ResearchOnline@JCU

JAMES COOK UNIVERSITY AUSTRALIA

This file is part of the following work:

Keys, Damien Leslie (2008) ***Mechanical localisation of copper deposits in the Mt Isa Inlier, North Queensland.*** **PhD Thesis, James Cook University.**

Access to this file is available from:

https://doi.org/10.25903/zqvr%2Dgq06

Copyright © 2008 Damien Leslie Keys

The author has certified to JCU that they have made a reasonable effort to gain permission and acknowledge the owners of any third party copyright material included in this document. If you believe that this is not the case, please email researchonline@jcu.edu.au

Mechanical localisation of copper deposits in the Mt Isa Inlier, North Queensland

Thesis submitted by
Damien Leslie Keys BSc (Hons) (University of Melbourne)
in February 2008

for the degree of Doctor of Philosophy
in the School of Earth and Environmental Sciences at
James Cook University of North Queensland

STATEMENT OF ACCESS

I, the undersigned, author of this work, understand that James Cook University will make this thesis available for use within the University Library and, via the Australian Digital Theses network, for use elsewhere.

I understand that, as an unpublished work, a thesis has significant protection under the Copyright Act and;

I wish this work to be embargoed until 1st March 2009.

Signature

Date

STATEMENT OF SOURCES

I declare that this thesis is my own work and has not been submitted in any form for another degree or diploma at any university or other institution of tertiary education. Information derived from the published or unpublished work of others has been acknowledged in the text and a list of references is given.

Signature

Date

STATEMENT OF CONTRIBUTIONS

General contributions towards this study have included:

- Australian Postgraduate Award (APA) scholarship
- pmd*CRC top-up scholarship
- pmd*CRC educational and training fund

AKNOWLEDGMENTS

I would like to thank my principal supervisor and mentor, Nick Oliver for his patience, guidance and sense of humour. There have definitely been some funny times, particularly in the field.

This project was initiated by Nick and Xstrata Exploration geologists Dugi Wilson and Paul Gow. Several Xstrata Copper geologists are thanked for facilitating underground visits, accommodation and discussion. They include Ian Holland, Trev Shaw, Nath Bullock, Frank Santaguida, Tim Raggett, and Dwayne Povey and Karl Malitz (Ernest Henry). A substantial amount of time was spent at the Aditya Birla Mt Gordon Mine and geologists Steve Oxenburgh, Martin Bennett, Craig Irvine and Simon Tear are all thanked for their support and comments. Copperco have also contributed largely to this project. Many thanks to Paul Hogan, Ken Maiden and Rosie Da Costa for their input. Thanks also to the Copperco fieldies who did a fantastic job of fishing a dinged up Hilux out of Borstad Creek. Finally thanks to Matrix Metals (Greenmount) for access to the prospect and data. Bob Dennis, Tony Alston and Bryan Frew are thanked for their thoughts and comments on the findings of this study.

I have also been fortunate enough to complete this PhD as part of the pmd*CRC I7 project, lead by Barry Murphy. Thanks to the pmd*CRC and in particular Barry, Bob Haydon, Russell Korsh and Andy Barnicoat for encouraging student participation and providing funding to attend research meetings. I thank the other CRC researchers and contributors for their input into the PhD at various project delivery meetings.

Many thanks to James Cleverly and John Walshe for challenging me to think in terms of isotopes, fluids sources and pathways and of course the “black juice”. Unfortunately the thesis doesn’t contain the quite the geochemical bent you may have hoped for but all is not lost! John Miller is also thanked for his contribution to the Mt Isa genetic story. His thorough mapping and analysis paved the way for the modelling conducted at Mt Isa in this study.

Thanks go to John McLellan, Tom Blenkinsop and Mike Rubenach for fielding modelling, structural and geochemical questions at a moments notice. I’m sure without your assistance this project would have taken considerably longer to complete and I am extremely grateful.

Office mates Gustav Nortje, Jim Austin and Kris Butera have ensured that there was never a dull moment. Thanks for being the sounding boards for some of the lesser ideas that have arisen, for your help in the field (at times) and for your friendship. To the EGRU PhD students (Dave, Louise, Julie, Arianne and Mark) of the last three years thanks also.

Last but most certainly not least, I'd like to thank my beautiful wife. Although not at all geologically inclined, she has never ceased to be totally supportive and caring, and was an amazing help with the drafting and checking references.

ABSTRACT

Copper mineralisation in the Mt Isa Inlier is typically associated with brittle deformation that has taken place during the ESE-WNW oriented D_4 event of the Isan Orogeny. Distinct element modelling of deposit-scale fault arrays has provided an extraordinary tool in the elucidation of far-field stresses and prime conditions for rock failure associated with mineralisation. Not only does the deposit-scale modelling results match well with regional-scale models, they provide a future way in which prospectivity analysis can be improved.

With only one known exception (Osborne) the bulk of the copper mineralisation in the Mt Isa Inlier is aged between 1530 Ma and 1505 Ma. The only age constraints on the D_4 deformation event are from the Snake Creek Anticline (foliation development associated with the intrusion of the Saxby Granite) and from the dating of the specific mineral deposits e.g. Ernest Henry. The Snake Creek age of D_4 is 1527±4 Ma and age dates from mineralised structures within the individual deposits vary from 1530 Ma to 1505 Ma.

The typically brittle D_4 deformation event occurs late in the Isan Orogeny and is only seen to have a ductile character in deformation around the intruding granites of the Williams and Naraku batholiths. In these locations D_4 can be seen expressed as a ductile foliation and in limited sites is associated with porphyroblast growth.

The D_4 deformation event, when associated with economic copper grades, is typically brittle and as such requires specific mechanical conditions. Most importantly, it appears that temperature was a primary control, such that if temperatures exceeded the onset of quartz creep (350 ºC), brittle failure did not occur and conditions for mineralisation were inappropriate. Ar-Ar dating of minerals appears to be a useful way of discriminating between rocks that are likely to fail via brittle modes versus brittle-ductile or ductile conditions. Consequently it is apparent that most of the copper deposits are found in areas where biotite Ar-Ar ages indicate the rocks had cooled sufficiently to behave brittley at around 1530 Ma. Conversely, rocks adjacent to granites or otherwise showing protracted cooling histories (e.g. Ar-Ar in hornblende younger than 1520 Ma) did not cool to brittle conditions quickly enough to allow the coincidence of brittle deformation and copper mineralisation.

The host rocks to mineralisation are typically at depths of 5 to 8 km at the time of mineralisation. In a hot orogen, this implies that these rocks are nearly at the brittle-ductile transition themselves. Earthquake nucleation is known to occur at depth near this transition. Sibson (1989) proposed that rupture nucleation and the direction of earthquake rupture propagation could be a useful tool in prediction of dilatant sites and hence prospective sites for Mt Isa style copper mineralisation. An example of how this technique could be used was conducted on the Mt Gordon Fault Zone.

The D_4 mineralisation event also coincides with cratonisation of the Mt Isa Inlier and a large change in the apparent polar wander path. This may have been triggered by collision of Baltica with the Laurentian supercontinent, causing a switch in convergence along the Laurentia-NAC boundary and providing the right conditions for low strain strike slip deformation and the ingress of copper-bearing fluids into the exhuming Isan orogenic belt.

1 INTRODUCTION.....1
PART 1 – THESIS OVERVIEW AND REGIONAL GEOLOGY 1
1.1 Project Overview 1
1.1.1 Thesis Aims 1
1.1.2 Research Methodology.....2
1.2 Overview of Mt Isa Geology 3
1.2.1 Sedimentology.....3
1.2.2 Magmatism.....5
1.2.3 Metamorphism and Metasomatism.....7
1.2.4 Structure.....12
PART 2 – ANALYTICAL METHODS 14
1.3 Structural Analytical Techniques.....14
1.3.1 Overview.....14
1.3.2 Brittle failure modes 14
1.3.3 Temperature conditions for brittle failure.....17
1.4 Palaeostress analysis and stress inversion.....18
1.4.1 Stereographic Methods - fault plane solution and P & T dihedra 19
1.4.2 The Multiple Inverse method 21
1.4.3 Grid search methods - SLICK.BAS.....23
1.4.4 Palaeostress analysis in relation to the Mt Isa Inlier study.....24
1.5 Numerical Modelling – UDEC (Universal Distinct Element Code) 24
1.5.1 Overview.....24
1.5.2 UDEC software.....25
1.5.3 Mechanical principles.....26
1.5.4 Constitutive models.....27
1.5.5 Stress Mapping in UDEC and implications for Mt Isa modelling.....27
1.5.6 Interpreting UDEC outputs – implications for likely failure mode.....29
1.5.7 Limitations of 2-dimensional simulation 29
2 MT GORDON COPPER MINES.....32
PART 1 – GEOLOGY AND GEOMECHANICAL SETTING 32
2.1 Introduction.....32
2.2 Discovery and Mine History.....33
2.3 Geological Setting.....34
2.3.1 Previous work on structural controls on mineralisation.....37
2.4 3D Modelling of the Mammoth Mine.....39
2.5 Structural Mapping of the Mammoth Mine.....42
2.5.1 Methodology 42
2.5.2 Mammoth Mine Faulting 44
2.5.3 Mammoth Fault and similarly oriented faulting.....44
2.5.4 130º Striking Fault Set.....46
2.5.5 Portal Fault Set.....47
2.5.6 North East Striking Fault Set.....48
2.5.7 Stress inversion of Mammoth Faults.....49
2.6 Mammoth Mine orebody breccias 53
2.7 Conclusions of underground mapping study 58
PART 2 – NUMERICAL MODELLING 59
2.8 Introduction.....59
2.9 Modelling Assumptions and Evidence 60
2.10 Numerical Modelling –Methodology and Conceptual Model.....62

2.11 Numerical Modelling Results 67
2.11.1 Connors NE-SW shortening model (Figure 2.23; pg 69) 67
2.11.2 Askew ENE-WSW shortening model (Figure 2.24; pg 70) 67
2.11.3 ERA Maptec E-W shortening model (Figure 2.25; pg 71) 67
2.11.4 Keys 124 SE-NW shortening model (Figure 2.26; pg 72) 68
2.11.5 The Keys 101 Model 73
2.11.6 Model utilizing Stress Inversion Parameters 78
2.12 Sensitivity Testing – Architecture vs. Rheological Contrast 81
2.13 Conclusions and Discussion 84
3 MT ISA COPPER MINES 87
3.1 Introduction 87
3.2 Geological Setting 88
3.2.1 The Mt Isa Valley 88
3.2.2 Host Sequence and Sedimentology 89
3.2.3 Alteration 91
3.2.4 Mineralisation 92
3.2.5 Structure 95
3.3 Previous Syn-Copper Kinematic Studies 97
3.3.1 Perkins (1984) 97
3.3.2 Bell, Perkins and Swager (1988) 98
3.3.3 Miller (2006) 99
3.4 Implications of Miller (2006) structural study 105
3.5 Proposed localisation mechanisms 106
3.6 Previous Numerical Modelling 108
3.6.1 Oliver et al (2001) 108
3.6.2 Gessner et al., (2004) and Gessner et al., (2006) 112
3.6.3 Mattai et al. (2004) 114
3.7 Numerical Modelling 117
3.7.1 Model Justification and Assumptions 117
3.7.2 Conceptual models 118
3.8 Numerical Modelling Results 122
3.8.1 Whole model metabasalt (northern section only) 122
3.8.2 Metabasalt basement and Urquhart Shale 122
3.8.3 Leapfrog modelled quartzite 124
3.8.4 Thin quartzite 125
3.8.5 Two quartzites (northern section only) 127
3.8.6 Variable basement with fine-grained pyrite 128
3.8.7 Variable basement and orebody faulting – southern section only 129
3.8.8 Variable basement and Pb-Zn orebodies – northern section only 130
3.9 Modelling and Mapping Synthesis 132
4. MT KELLY COPPER MINE 134
4.1 Introduction 134
4.2 Exploration History 136
4.3 Geological setting 136
4.4 Structural Field Studies at Mt Kelly 139
4.4.1 Diamond Drill Core Logging 139
4.4.2 Mt Kelly mapping 142
4.5 Numerical Modelling – Conceptual Model 143
4.6 Numerical Modelling Results 145
4.6.1 NE-SW shortening 145

4.6.2 ENE-WSW shortening 145
4.6.3 E-W shortening 146
4.6.4 ESE-WNW – Spinifex Fault Model vs Spinifex Fault Excluded Model 148
4.6.5 ESE-WNW shortening - Spinifex Fault Excluded Model at Mt Clarke and MK475 151
4.6.6 ESE-WNW shortening - Spinifex Fault Excluded Model at Mt Kelly Workings and Flying Horse 152
4.7 Summary of Numerical Modelling Results 153
5. INVESTIGATOR FAULT ZONE 155
5.1 Introduction 155
5.2 Geological setting 156
5.3 Exploration History 159
5.4 Numerical Modelling –Methodology and Conceptual Model 161
5.5 Numerical Modelling Results 162
5.6 Field Mapping – Model Validation and other areas of interest 167
5.6.1 Locality 1 – South Investigator Fault 169
5.6.2 Locality 2 – Prospect Fault 171
5.6.3 Locality 3 – South Investigator Fault Zone Bend 173
5.6.5 Locality 5 – North Investigator Fault near Mid Investigator Fault Junction 175
5.7 DISCUSSION 178
6. ERNEST HENRY COPPER-GOLD MINE 180
6.1 Introduction 180
6.2 Geological setting 181
6.3 Syn-Cu Structural Kinematics 189
6.3.1 Valenta (2000) Structural Hypothesis 189
6.3.2 Coward (2000) Structural Hypothesis 190
6.3.3 Laing (2003) Structural Hypothesis 192
6.4 Leapfrog modelling 193
6.4.1 Leapfrog 3D model assumptions and techniques 194
6.4.2 Leapfrog 3D model outputs 195
6.5 Numerical modelling – Conceptual Model 204
6.6 Numerical modelling results 206
6.7 Discussion 211
7. GREENMOUNT COPPER-GOLD DEPOSIT 215
7.1 Introduction 215
7.2 Exploration History 216
7.3 Geological Setting 216
7.3.1 Overview 216
7.3.2 Metasomatism - Sodic Alteration 218
7.3.3 Metasomatism - Potassic Alteration and Mineralisation 218
7.3.4 Metasomatism - Kaolinisation and Sericitization 220
7.3.5 Structure - Ductile Deformation 220
7.3.6 Structure - Brittle Deformation 220
7.3.7 Structure - Ductile or brittle deformation – Staveley Breccia Ridge? 221
7.4 Previous Syn-Copper Kinematic Studies 223
7.5 Deposit 3D Reinterpretation 227
7.5.1 Methods 227

7.5.2 Structural Mapping Results 228
7.5.3 Lithological / Alteration Relationships 231
7.6 Numerical Modelling - White Range Anticline 241
7.6.1 Conceptual Model 241
7.6.2 Numerical Modelling Results – White Range Anticline 242
7.6.3 Numerical Modelling Results – Greenmount 243
7.7 Discussion 245
8. DISCUSSION 247
8.1 Other studies showing evidence of an ESE – WNW D_4 shortening event 249
8.1.1 Regional stress mapping 249
8.1.2 Regional Fault Studies 252
8.1.3 Ductile deformation studies 254
8.1.4 Summary of ESE-WNW observations 258
8.2 Relationship of ESE-WNW D4 to prospectivity studies 259
8.3 Deformation and exhumation of the Inlier 263
8.4 Other mechanical factors potentially influencing localisation 270
8.5 Geodynamic setting of Mt Isa at 1530 Ma 276
8.5.1 Cratonisation of the Mt Isa Inlier 276
8.5.2 Polar wander and palaeomagnetic continental reconstruction 277
8.5.3 Mineralisation at 1530 Ma in Baltica 281
CONCLUSIONS 284
REFERENCES 286

TABLE OF FIGURES

1. INTRODUCTION

1.1 The copper deposits studied in the Mt Isa Inlier 2

1.2 Heat production of northern Sybella batholith at D_2 6

1.3 Metamorphic zones west of Mt Isa – Sybella Granite 9

1.4 Isograd map for part of the Mt Isa Inlier 11

1.5 **(a)** An 'Andersonian' extensional stress state 15

(b) Shear stresses and normal stresses acting on a plane 15

1.6 Modes of failure in relation to differential stress

(a) Extensional fracturing (hydraulic fracturing), 16

(b) Extensional shear (combination of hydraulic fracturing and shear), 16

(c) Shear fracturing 16

1.7 Schematic block diagram of variation with depth of the type of fault rock within a fault zone. 18

1.8 Stereonet showing P & T axes and P & T quadrants relative to the fault plane and movement plane. 20

1.9 Example of output plots of the Multiple Inverse Method. 22

1.10 Example of SLICK.BAS output. 23

1.11 Easily measurable features in UDEC 29

2. MT GORDON COPPER MINES

2.1 Mt Gordon Copper Mines location. 33

2.2 The Esperanza deposit occurs at the intersection of the Mammoth, Mammoth Extended and Esperanza Faults. 35

2.3 A plan view schematic diagram of the various Mammoth Mine orebodies 35

2.4 The Mt Gordon mine area stratigraphic column 36

2.5 **(a)** Leapfrog output of copper grade shells 40

(b) Section view of Mammoth Mine looking north. 40

(c) Plan view of Mammoth Mine. 40

2.6 Leapfrog output of breccia intensity and copper grade. 41

2.7 Leapfrog output of moderate chlorite alteration intensity related to the 1% Cu shells 41

2.8 Leapfrog output of moderate earthy hematite intensity related to the 1% Cu shells 41
2.9 Example of company geologist level plan mapping. 42
2.10 **(a)** Looking north onto the FW of a Mammoth Fault parallel 45
(b) Stereographic projection of fault and striation data for Mammoth Fault 45
(c) Fault plane solution plot for the data presented in (b) 45
2.11 **(a)** Stereographic projection of fault and striation data for the 130 striking set 46
(b) Fault plane solution plot for the data presented in (a) 46
2.12 **(a)** Stereographic projection of fault and striation data for the Portal Fault 47
(b) Fault plane solution plot for the data presented in (a) 47
2.13 The 2 Lens orebody on 4785rL showing the intensity of NE to NNE striking faulting 48
2.14 Palaeostress analysis using the Multiple Inverse Method 50
2.15 P solution grid for fault striation data proven valid in the Multiple Inverse Method 51
2.16 Slick (Ramsay and Lisle, 2000) output file. 52
2.17 Intensely brecciated unit cutting an ENE striking fault parallel to the Mammoth Fault. 55
2.18 4825rL level plan mapping showing interpreted faulting and relationship to the most intense brecciation 56
2.19 4785rL level plan mapping showing interpreted faulting and relationship to the most intense brecciation 57
2.20 Simplified mohr circle diagram showing uses of the data that can be easily acquired from UDEC model outputs 63
2.21 Geological map of the Mt Gordon Copper Mines Lease 64
2.22 Conceptual model geometry and scenarios. 65
2.23 The Connors Model Outputs 69
2.24 The Askew Model Outputs 70
2.25 The ERA Maptec Model Outputs 71
2.26 Keys 124 SE-NW Model Outputs 72
2.27 Keys 101 Model – Whole Model 74
2.28 Keys 101 Model - Mammoth Mine UDEC outputs 75
2.29 Keys 101 Model - Esperanza Mine UDEC outputs 76

2.30 Comparison between Keys 101 Model and Stress Inversion model at Mammoth 78
2.31 Comparison between Keys 101 Model and Stress Inversion model at Esperanza 80
2.32 Comparison between Keys 101 and All Quartzite model - Mammoth 82
2.33 Comparison between Mammoth Mine and All Quartzite – Esperanza 83
2.34 Mohr circle diagram showing the proposed failure modes within the Mammoth Mine. 84
2.35 Mohr circle diagram showing the proposed failure modes within the Esperanza Mine. 85

3. MT ISA COPPER MINES
3.1 Orebody long section looking west. 89
3.2 Idealised cross section looking north through the Upper Mt Isa Group stratigraphy 90
3.3 Orebody schematic showing the relative positions of the main Mt Isa copper orebodies. 93
3.4 Section through 3600mN (mine grid) 94
3.5 Section through 4400mN (mine grid) 94
3.6 Section through 6207mN (mine grid) 95
3.7 Isotropic Leapfrog models constraining the distribution of units defining the lower basement. 100
3.8 Syn-copper breccia veins that grade into a small package of breccia. 101
3.9 Stereonet plotting bedding/extension vein data from copper breccias 102
3.10 Jog-related chalcopyrite (slip along an S_3 cleavage plane). 103
3.11 Plan vein leapfrog model of lower basement contact (red) and 2% Cu (orange) distribution Enterprise Mine area. 104
3.12 Leapfrog model highlighting strike-trends of different Cu ore bodies 105
3.13 Hangingwall transport directions 105
3.14 Section through 4930mN (mine grid) showing the Basement Contact Fault and the fine-grained pyrite rib 107
3.15 Geology and numerical modelling of coupled deformation and copper mineralization at the Hilton mine. 110
3.16 Numerical modelling of the Hilton Mine. Contours of mean stress. 111

3.17 Architectures used in the Gessner (2004) modelling 112
3.18 Deformation scenarios tested by Gessner (2004) 113
3.19 Thermal modelling of Mattai et al. (2004) 115
3.20 Orientation of the sections that have subsequently been numerically modelled in UDEC 121
3.21 Greenstone only UDEC results 122
3.22 Greenstone basement under shales UDEC results northern section 123
3.23 Greenstone basement under shales UDEC results southern section 123
3.24 Split basement under shales UDEC results northern section 124
3.25 Split basement under shales UDEC results southern section 125
3.26 Thin quartzite in basement UDEC results northern section 126
3.27 Thin quartzite in basement UDEC results southern section 126
3.28 Two quartzites in basement UDEC results northern section 127
3.29 Fine-grained pyrite UDEC model results. Northern section 128
3.30 Fine-grained pyrite UDEC model results. Southern section 129
3.31 Mine faulting UDEC model results, southern section 130
3.32 Pre-existing Pb-Zn UDEC model results, northern section 131
3.33 An example of simple shear in two dimensions on a simple grid 133

4. MT KELLY COPPER MINE

4.1 Mt Kelly location map 135
4.2 Mt Kelly camp scale geological mapping showing known breccia locations and deposit locations. 135
4.3 Example of box folding in the Paradise Creek Fm 137
4.4 Surface outcrop of the limonitic shales in the approximate position of the Spinifex Fault 138
4.5 Breccia styles (from Laing, 2003). 139
4.6 Section through 7799285mN, showing the diamond drill hole MK475A. 140
4.7 Section through 7799275mN, showing the diamond drill hole MK513. 141
4.8 The simplified conceptual model used for UDEC modelling. 144
4.9 The Spinifex Fault Included Model and the Spinifex Fault Excluded Model UDEC model results. – all orientations of σ_1 147
4.10 The Spinifex Fault Included Model and the Spinifex Fault Excluded Model UDEC model results – Whole model ESE-WNW shortening 149

4.11 UDEC model outputs for the Spinifex Fault Excluded Model at Mt Clarke and MK475 151
4.12 UDEC model outputs for the Spinifex Fault Excluded Model at Mt Kelly and Flying Horse 152
4.13 Mohr Circle plots for MK475 deposit and the Mt Clarke deposit 153
4.14 Mohr Circle plots for Flying Horse deposit and the Mt Kelly deposit 154

5. INVESTIGATOR FAULT ZONE
5.1 The location of the Investigator Fault Zone relative to the Mt Gordon Copper Mines 156
5.2 Geological map of the Investigator Fault Zone 158
5.3 Geology with some constrained rock chip samples and drill holes. 160
5.4 Conceptual model geometry. The arrows reflect the σ_1 orientation that was tested. 161
5.5 Plot of minor principal stress for the Investigator Fault Zone. 163
5.6 Plot of mean stress for the Investigator Fault Zone. 164
5.7 Plot of fluid pressure required for failure for the Investigator Fault Zone. 165
5.8 Plot of differential stress for the Investigator Fault Zone. 166
5.9 The circles indicate the areas that modelling has predicted low minor principal stress, low mean stress, low fluid pressures for failure and low differential stress within the Investigator Fault System. 166
5.10 Sample localities (within black stars) mapped in detail within the Investigator Fault Zone. 168
5.11 Photographs from Locality 1 – South Investigator Fault 170
5.12 Geological map of the area around the Investigator Prospect and the position of Locality 2. 171
5.13 Locality 2 quartz breccia 172
5.14 Surface expression of the South Investigator Fault at Locality 3 173
5.15 Mid Investigator Fault breccia comprised of angular to sub-angular clasts of feldspathic quartzite in a quartz matrix. 174
5.16 Splay fault of the Mid Investigator Fault at Locality 4 175
5.17 Locality 5 breccia styles. 177

6. ERNEST HENRY COPPER-GOLD MINE

6.1 The location of the Ernest Henry mine. 180

6.2 The revised interpretation of the diorites from the sterilisation drilling and previous aeromagnetic interpretation. 182

6.3 Leapfrog 3D model outputs of the 1% copper grade shell (green) within the Ernest Henry Mine 185

6.4 Schematic diagram showing the orebody position relative to the interpreted shear zones 185

6.5 Schematic representation of a possible model for the formation of the duplex of shear zones interpreted from the aeromagnetic image 186

6.6 Ernest Henry pit map showing the locations of the major faults and shears in relation to the ore zone and alteration suite 187

6.7. Syn-mineralisation kinematic model proposed by Valenta. SE-NW shortening results in reverse movement on the northern side of the SZ bend near the deposit, 190

6.8. (from Coward, 2000) Representation of fault and vein trends in plane view showing the orientation of the principle maximum stress direction (σ_1) inferred from the extensional vein geometry. 191

6.9 Inferred mineral zonation pattern in a proposed single fault intersection breccia - replacement model 193

6.10 Ni-rich andesites and biotite schists dominate the hangingwall to orebody and the high Mn alteration seems to be associated with the biotite-calcite-actinolite schists 195

6.11 Cross-sectional view of the mineralisation associated with the Ernest Henry Mine, looking east. 196

6.12 Leapfrog 3D outputs of 1.5% copper, 25% iron, 0.75g/t gold and 50ppm uranium, looking north ` 197

6.13 Chalcopyrite abundance shells seen looking east 198

6.14 Pyrite abundance shells seen looking east 199

6.15 Magnetite abundance shells seen looking east 200

6.16 3D model outputs displaying the relationship between the low abundance shells of chalcopyrite (1%), pyrite (2.5%) and magnetite (10%). 201

6.17 3D model outputs displaying the relationship between the high abundance shells of chalcopyrite (1%), pyrite (2.5%) and magnetite (40%). 202

6.18 One proposed fault orientation based on the truncation of 20% magnetite shells and 10% pyrite shells 203
6.19 Conceptual model geometry containing the 1660 Ma diorites, the NE striking shear zones and the NW striking shear zones/faults. 205
6.20 Numerical modelling output of the 1660 Ma diorite and all shear zone model tested in a NNE-SSW compression event. 207
6.21 Numerical modelling output of the 1660 Ma diorite and all shear zone model ested in a ESE-WNW compression event. 208
6.22 The calculated areas of likely tensile failure and extensional shear and/or compressional shear failure for the ESE-WNW shortening model. 209
6.23 Plot of fluid pressure required for failure for the ESE-WNW shortening model. 210
6.24 The proposed fault may have been a possible pathway for the fluidised breccia that hosts the Ernest Henry Cu-Au Mine. 214

7. GREENMOUNT COPPER-GOLD DEPOSIT

7.1 Location of the Greenmount Cu-Au Deposit 215
7.2 Geology of the east limb of the White Range Anticline 217
7.3 Gross positive relationship seen between copper grades and gold grades. 219
7.4 The major faults of the White Range area 221
7.5 Simplified geological interpretation of cross section 9500mN. The Staveley breccia has been exhumed by a series of faults 222
7.6 Schematic cross section of the “Anticlinal Staveley Hill Model” through 9300mN 222
7.7 Schematic diagram of the fault swarm model proposed by King and Hy (1994) 223
7.8 Schematic diagram of the Kink model proposed by King and Hy (1994) 224
7.10 Schematic diagram showing the flat ramp model proposed by Krcmarov (1994). 225
7.11 Schematic diagram of the Laing (2004) genetic model 226
7.12 Field measurements and relationships 229
7.13 Field mapping of bedding, S2 cleavage and microcline–quartz vein orientations around the Staveley Breccia Hill. 230
7.14 Leapfrog 3D model outputs of the top of the Staveley Formation 232

7.15 2D sectional interpretation of 9900m and 9925mN 233
7.16 Albitic alteration (pale grey) is preferentially assuming two orientations. The orientation of albitic selvedge almost parallel to the core is in the S_2 cleavage orientation and the cross cutting orientation is the albitic selvedge associated with the bedding planes (S_0) 234
7.17 Mapping data showing two locations with microcline quartz veining that are seen in Leapfrog 3D model 235
7.18 150RL flitch plan of the 0.5% copper grade shell relative to the Staveley Formation and Greenmount Fault 236
7.19 Leapfrog 3D model outputs of the microcline-quartz breccia bodies over the top of the Staveley Formation 237
7.20 Leapfrog 3D model outputs of moderate to intense kaolin alteration, microcline-quartz breccia bodies and the top of the Staveley Formation 238
7.21 Leapfrog 3D model outputs of albitite moderate to intense kaolin alteration, microcline-quartz breccia bodies and the top of the Staveley Formation 240
7.22 White Range Anticline numerical modelling outputs 242
7.23 Greenmount numerical modelling outputs 244

8. DISCUSSION

8.1 Western Succession UDEC modelling showing predicted sites of dilation correlating well with known copper deposits 251
8.2 The mapped exposure of the Spillway Fault Area. 253
8.3 Schematic interpretation of the D_3 and D_4 structural events along the Cloncurry Fault Zone. 254
8.4 Two conflicting hypotheses on porphyroblast growth and development of inclusion trails. 255
8.5 Equal area rose diagrams for successive FIA sets and their proposed correlation across the Eastern Fold Belt. FIA 5 correlates to an ESE – WNW shortening event. 257
8.6 The various locations documented that show evidence of an ESE-WNW oriented shortening event associated with D4 (~1530 Ma). 258
8.7 The three highest ranking fault bend orientations of Mustard et al. (2005), related to the ESE-WNW D_4 shortening orientation. 262

8.8 The three highest ranking fault intersection orientations of Mustard et al. (2005), related to the ESE-WNW D_4 shortening orientation. 262
8.9 Suggested temperature-time diagram, for the Osborne/Cannington Mines and the Snake Creek Anticline/Eloise Mine 266
8.10 Strike-slip earthquake rupturing within the seismogenic regime in the vicinity of the transition from unstable frictional (FR) faulting to localised quasi-plastic (QP) shearing flow 271
8.11 Cartoon map illustrating the changing response of an isolated fault bend to rupture directivity on a right-lateral strike-slip fault. 272
8.12 Suggested paleo-fault rupture nucleation and directivity along the Mt Gordon Fault Zone 274
8.13 Faults of the Investigator Fault Zone with proposed rupture points (circles) located along the NNE-SSW striking faults of the Mt Gordon Fault Zone, near fault intersections. 275
8.14. The 1530 Ma age data also correlates with an inferred change in the polar wander path for the Australian continent. 278
8.15. AUSWUS reconstruction for two Proterozoic time slices. 279
8.16 The proposed Hudsonland (Columbia) supercontinent configurations showing Laurentia, Baltica, North Australia and Siberia. 281
8.17 Tectonic outline of the western part of East European Craton 282

LIST OF TABLES

2. MT GORDON COPPER MINES

2.1 Fault characteristics compiled from level plan mapping (mapped by company geologists). . 44

2.2 A summary of stress inversion outputs from each of the inversion methods used. 52

2.3 Clarke (2003) breccia classification system. 53

2.4 Mt Gordon models run, with the σ_1 orientation and a brief summary. 66

2.5 Sensitivity tests run, with the σ_1 orientation and a brief summary. 66

2.6 Model rock and contact input parameters used in all UDEC modelling. 66

3. MT ISA COPPER MINES

3.1 Basement geometry variations modelled. 119

3.2 Localisation mechanisms modelled. 120

3.3 Model rock and contact input parameters used in all UDEC modeling 120

4. MT KELLY COPPER MINE

4.1 Mt Kelly models with the σ_1 orientation and a brief summary. All models were run with and without the Spinifex Fault. 143

4.2 Mt Kelly conceptual model inputs. 144

4.3 Values obtained from UDEC model outputs when σ_1 is oriented NE-SW. Values of σ_3, σ_m and Pf_F are extremely high in all deposit locations. 145

4.4 Values obtained from UDEC model outputs when σ_1 is oriented ENE-WSW. Values of σ_3, σ_m and Pf_F are extremely high in all deposit locations. 146

4.5 Values obtained from UDEC model outputs when σ_1 is oriented E-W. 146

4.6 Values obtained from UDEC model outputs when σ_1 is oriented 112º-292º. 148

5. INVESTIGATOR FAULT ZONE

5.1 Rock chip sample assays for chips shown on geological map of Investigator (in Figure 5.3). 160

5.2 Conceptual model lithological and fault contact input parameters. All contacts in the model are treated as faulted contacts 162

6. ERNEST HENRY COPPER-GOLD MINE

6.1 (from Mark et al., 2006) The paragenetic sequence and spatial distribution of pre and syn-ore hydrothermal alteration in the Ernest Henry lease. 184

6.2 Characterisation of Ernest Henry faults 188

7. GREENMOUNT COPPER-GOLD DEPOSIT

7.1 Occurrences of copper species from core logging. Table adapted from Laing (2004). 219

7.2 Model lithological and fault contact input parameters. All contacts in the model are treated as faulted contact 241

8. DISCUSSION

8.1 (from Mustard et al., 2005) Rankings of the twelve critical ingredients for copper mineralisation in the Eastern Succession of the Mt Isa Inlier. 260

8.2 (from Ford and Blenkinsop, 2007) Results of correlation between clustering of copper occurrences and clustering of geological features using fractal analysis and contrast values obtained from weights of evidence analysis with corresponding confidence values. 261

8.3 (from Blenkinsop, 2005) Table summarises the roughness measurements and mineral endowments, arranged in order of decreasing roughness as measured by the fractal dimensions. 270

1 INTRODUCTION

PART 1 – THESIS OVERVIEW AND REGIONAL GEOLOGY

1.1 Project Overview

1.1.1 Thesis Aims

Several different styles of mineralisation are found in the Mt Isa Inlier including Pb-Zn-Ag (syn-sedimentary or epigenetic), unconformity-related and skarn-related uranium, vein and shear zone-hosted gold, carbonate-hosted copper and iron oxide copper-gold (IOCG), making it one of the richest base metal provinces in the world.

All deposits styles display some degree of structural control in the localisation of ores into their current locations. The structural controls on localisation of the copper deposits are of particular interest as the mineralisation in many of the copper deposits, both carbonate-hosted and IOCG has been dated at ~1530 Ma ($^{40}Ar/^{39}Ar$ - Perkins and Wyborn, 1998; Perkins *et al.*, 1999; U-Pb $_{(titanite)}$ - Mark *et al.*, 2006) (Figure 1.1).

There has been a large effort directed towards determining the structural controls of the Mt Isa Inlier copper deposits. However because these have typically been done by researchers or students on individual deposits, there have been no attempts to try to determine the overall controlling mechanical factors in the localization of deposits, or whether there are common architectural or kinematic ingredients that link them. The specific aims of the thesis are as follows:

(i) To determine whether or not the structural controls on copper localisation at individual deposits could be correlated to produce a broader structural framework for copper mineralisation either at a sub-regional, regional or at Inlier-wide scale.

(ii) To determine the significance of variations (if any) between the structural controls for the Mt Isa Eastern and Western successions, and

(iii) To determine how the structural controls fit into the overall geodynamic history of the Mt Isa Inlier.

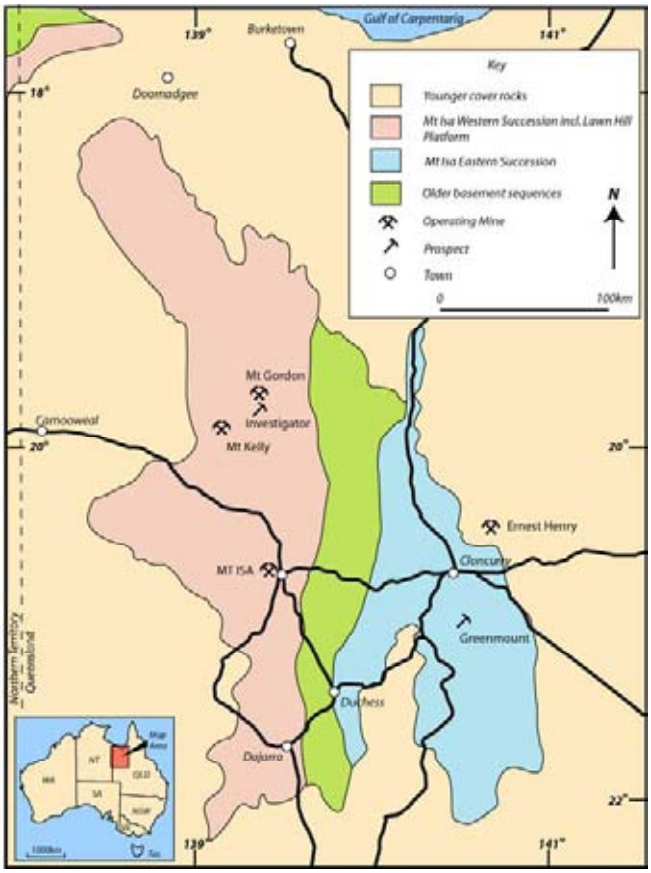

Figure 1.1 The copper deposits studied in the Mt Isa Inlier.

1.1.2 Research Methodology

The research methods employed in this study were:

(i) Structural and metasomatic mapping of local controls on mineralisation at a variety of scales. Surface mapping was conducted at the Mt Kelly Mine, the Investigator Fault Zone and at the Greenmount copper-gold deposit. Underground mapping was conducted in the Mt Gordon Mines (Mammoth Mine) and in the Mt Isa Mine.

(ii) Drill core logging of breccia characteristics and alteration assemblages related to copper mineralisation. Characterisation of breccias in drill core was conducted at the Mt Kelly Mine. Alteration assemblages and breccia characteristics were logged in drill core at the Greenmount copper-gold deposit.

(iii) Three-dimensional spatial modelling of alteration assemblages and copper grade distributions in relation to mine structural models. This was done for all deposits in an attempt to determine any spatial relationships between structures and fluid pathways.

(iv) Simulation of stress fields and fluid flow using paleostress indicators from geological data, and finite element modelling of fractured rock networks.

1.2 Overview of Mt Isa Geology

The Inlier can be divided into three separate north-south trending tectonostratigraphic domains; the Mt Isa Western Succession, the Kalkadoon-Leichhart Belt and the Mt Isa Eastern Succession.

1.2.1 Sedimentology

The Mt Isa Inlier records an extensive history of sedimentation between ~1880 Ma and 1575 Ma. The stratigraphic sequence is particularly well preserved in the Mt Isa Western Succession, where low metamorphic grades associated with the Isan Orogeny and extensive outcrop allow detailed description. The stratigraphic relationships are more difficult to determine in the Eastern Succession where the metamorphic grade is typically higher (greenschist to amphibolite facies) but variable.

Within the Mt Isa Inlier, three distinct superbasins have been determined. These superbasins are the Leichhardt Superbasin, the Calvert Superbasin and the Isa Superbasin. The Leichhardt Superbasin comprises a basal sequence of metabasaltic flows, volcanogenic sediments and minor quartzite up to 6 km thick, overlain by a thinner (2-3 km) succession of immature quartzofeldspathic sandstones with suboridinate amounts of poorly sorted siltstones and redbeds (Derrick, 1982; Jackson et al., 2000; Gibson, 2006). The Upper Leichhardt Superbasin (younger sediments) was deposited between 1780 and 1750 Ma into fluviatile and lacustrine depositional environments (Eriksson et al., 1993; Jackson et al., 2000). Deposition was focussed into NNW-trending basins (half-graben) that deepened toward the eastern margin of the Western Succession (Gibson, 2006). The Eastern Succession Leichhardt Superbasin time equivalent unit is the carbonate facies sediments of the Corella Formation. The Corella Formation comprises a large area of the current Eastern Succession surface and is seen to have a strong spatial association with copper deposits.

Deposition of sediment into the Calvert Superbasin coincided with the onset of rifting. Coarse sandstones and fanglomerates were deposited into fault-angle depressions and fluviatile environments. Calvert Superbasin sedimentation was interrupted by a phase of volcanism during the emplacement of the Fiery Creek Volcanics (1710 Ma; Gibson, 2006) and intrusion of the Weberra Granite (also 1710 Ma; Gibson, 2006). Siliciclastic sedimentation recommenced with the deposition of the Prize Supersequence, which was deposited into a deltaic to shallow marine environment. Thickening of these units towards E- or NE- trending

growth faults is inferred to represent a syn-rift origin for most of the Calvert Superbasin (Derrick, 1982; O'Dea *et al.*, 1997; Gibson, 2006). Magmatic rocks (1690 Ma peperites and 1678 Ma Carters Bore Rhyolite; U-Pb, Page and Sweet, 1998) are intercalated with the Calvert Superbasin siliciclastics and their dates represent the best age constraint on sedimentation.

Calvert Superbasin sedimentation was followed by a phase of magmatism in both the Mt Isa Eastern and Western Successions. Following the post-Calvert magmatism another phase of sedimentation produced the Isa Superbasin. The Isa Superbasin sequences are commonly seen to host copper and lead-zinc orebodies in both the Western and Eastern Successions. Deposition of the Isa Superbasin sequences occurred between 1670 Ma and 1645 Ma (U-Pb $_{(zircon)}$ - Neumann et al, 2006).

Sedimentation associated with the Isa Superbasin showed a gradual deepening of depositional environment to the east. In the Mt Isa Western Succession the lower McNamara Group, in the Leichhardt River Fault Trough, and the lower Mt Isa Group are typically siliciclastic. These units grade into carbonate-rich units in the upper McNamara and Mt Isa Groups.

The expression of the Isa Superbasin varies significantly in the Mt Isa Eastern Succession. West of the Cloncurry Fault the sediments show a change from siliciclastic sequences (Staveley Formation) to carbonaceous sequences such as the Marimo Slate. East of the Cloncurry Fault in the Mt Isa Eastern Succession, the Soldiers Cap Group contains turbiditic carbonaceous sediments, indicative of deep water depositional environments.

Units to the west of the Soldiers Cap Group are believe to have accumulated on a platform or ramp that accumulated in a deeper water basin and developed oceanward of the platform. Soldiers Cap Group time equivalent facies are lacking on the platform and deposition coincided with the platform-wide unconformity at the base of the Isa Superbasin or Gun Supersequence (Neumann et al, 2006).

Deposition of the Isa Superbasin sequences was complete by approximately 1645 Ma in most areas except the Lawn Hill Platform where sedimentation continued until ~1595 Ma, and the Tommy Creek Block in the Eastern Succession where the Quamby Conglomerate marks the last sedimentary sequence. Depositional age dates for the Quamby

Conglomerate have not been ascertained but are thought to be approximately 1610 Ma, coinciding with the onset of the Isan Orogeny.

1.2.2 Magmatism

The Kalkadoon-Leichhardt Belt (pre 1850 Ma) and Mt Isa Eastern Succession (younger than 1800 Ma) preserve the oldest igneous rocks in the Mt Isa Inlier. The dacitic-rhyolitic volcanism of the Argylla Formation occurred at about 1780 Ma (Blake, 1987). Overlying the Argylla Formation volcanic sequence is the Marraba Volcanics, correlatives of the Eastern Creek Volcanics in the Western Succession.

The Eastern Creek Volcanics are comprised of tholeiitic basalts, widely interpreted as continental flood basalts (Glikson et al., 1976). Basaltic magmatism associated with the Eastern Creek Volcanics was complete by 1770 Ma (Neumann et al., 2006). Leaching of the Eastern Creek Volcanics during metamorphism (associated with the Isan Orogeny) has long been considered a possible source of copper in the Western Succession copper deposits (Heinrich et al, 1995).

The Inlier-wide volcanism was followed by bimodal magmatism, in the Eastern Succession, between 1760 to 1720 Ma forming the Wonga Batholith. Intrusion of the tholeiitic basic rocks and granites of the Wonga Batholith is inferred to be related to a phase of extension, named D_w (Pearson et al., 1992). Similar aged meta-igneous rocks are seen in the Cloncurry area and include a 1754±25 Ma microgranite and 1740 to 1725 Ma porphyry bodies (Page, 1998). These bodies include the Gin Creek Granite (1741±7 Ma; Page and Sun, 1998) in the Selwyn area, the Jessie Granite (1746±8 Ma; Davis et al., 2001) and the Dipvale Granite (1746±7 Ma; Davis et al., 2001). The Ernest Henry Mine host sequence, the Mt Fort Constantine Volcanics (at the top of the Corella Fm), has been dated by Page and Sun (1998) at 1746±9 Ma and 1742±6 Ma. The Mt Fort Constantine Volcanics and metasedimentary sequence was subsequently intruded by two discrete diorite bodies at 1660 Ma (Pollard and McNaughton, 1997).

Butera et al. (2005) demonstrated that the dolerite dykes of the Llewellyn Creek Formation, near Snake Creek in the Eastern Succession, have an emplacement age of 1686 Ma. Butera et al. (2005) proposed that subsequent amphibolitisation of these volumetrically

significant doleritic dykes may account for some of the copper metal budget of the Eastern Succession.

In the Western Succession, volcanism associated with the Carters Bore Rhyolite (1678±2; Page, 1983) immediately preceeds the intrusion of the Sybella Granite. The Sybella Granite has been dated at 1673±3 Ma (Hoadley et al., 2001) and 1655±4 Ma (Connors and Page, 1995). The Sybella Granite is a composite of intrusive phases, often expressed as a coarse-grained granodiorite to alkali-feldspar granite. McLaren et al. (1999) described the Sybella Granite as being extremely rich in radiogenic elements (Figure 1.2) and being capable of generating steep upper crustal thermal gradients immediately prior to the Isan Orogeny. The gradients were appropriate to peak metamorphic conditions, such that the ensuing Isan Orogeny, was thought to require no significant additional heat input (McLaren et al., 1999), although this is disputed (Foster and Rubenach; 2006). Like the Wonga Batholith, the Sybella Granite was emplaced into a shallow level shear zone, most likely during extension (Hoadley et al., 2001).

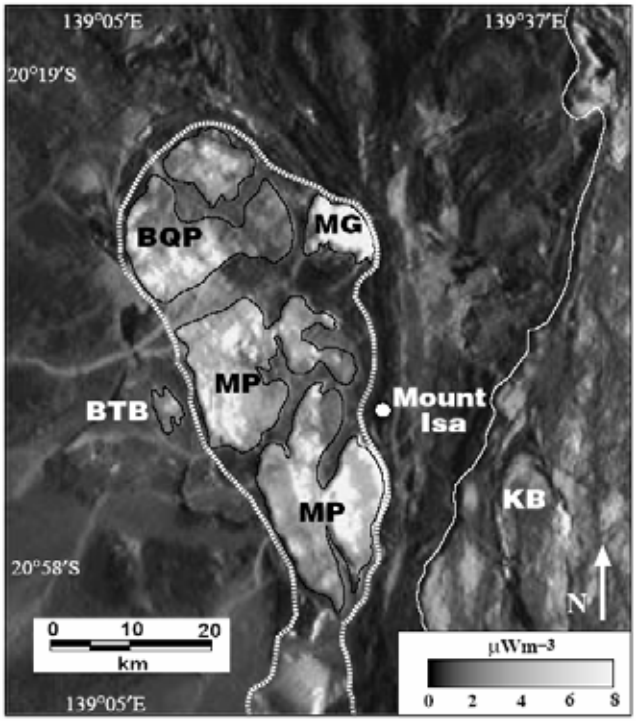

Figure 1.2 (from McLaren et al., 1999) Heat production of northern Sybella batholith (mWm–3) around time of peak metamorphism. Heat-production values are calculated from calibrated radiometric data. All values above 8 mWm–3 (to maximum of ~16 mWm–3) are shown in white. Approximate outcrop extents of Sybella batholith are shown and include MG—microgranite phase, BQP—beta-quartz phase, MP—main phase, BTB—Big Toby Granite. Kalkadoon batholith (KB) to east also shows elevated heat production.

The last magmatic event in the Mt Isa Inlier was the intrusion of the Williams-Naraku Batholith in the Eastern Succession. This felsic suite was intruded mainly over a 30 Ma period between 1530 Ma and 1500 Ma with minor earlier phases at c. 1550 Ma. The most volumetrically abundant of the intrusions (that comprise the Williams-Naraku Batholith) are typically K-rich granites, emplacement of which was coincident with major phases of Na-(Ca) alteration and Fe-oxide-Cu-(Au) mineralisation in the Cloncurry District (Perring et al., 2000; Mark et al., 2006; Oliver et al., 2004).

The recognition of distinct phases of geochemically similar, LILE (large-ion-lithophile-element) enriched, potassic intrusions across the Eastern Succession implies that these batholiths were derived from previously unmelted crustal material of tonalitic composition (Blenkinsop et al., 2005). The prolonged duration over which steep NS tectonic fabrics were produced throughout the Eastern Succession suggests that subhorizontal EW compression was dominant during that time, and that the higher apparent strain around the intrusions was associated with localised thermal weakening linked to heat advection from the crystallizing intrusions (Blenkinsop et al., 2005).

Areas proximal to the Williams-Naraku Batholiths locally achieved high temperature contact metamorphic conditions (Rubenach, 2005; Rubenach et al., 2007). The deformation style around these granites is typically documented as ductile deformation, including some foliation development at the Snake Creek Anticline (Rubenach et al., 2007).

1.2.3 Metamorphism and Metasomatism

The Mt Isa Block is characterised by high temperature, low pressure metamorphism, with peak metamorphic conditions in higher grade zones estimated at 400-500 MPa and 650º-700 ºC (Foster and Rubenach, 2006). Most of the region is characterised by greenschist to upper amphibolite facies rocks, with metamorphic grades typically increasing to the southwest of the Mt Isa Eastern Succession (Figure 1.3). In the areas of the highest metamorphic grade, upper amphibolite mineral assemblages of cordierite-andalusite-sillimanite are common (Figure 1.4).

Prograde metamorphism produced chlorite, biotite, garnet, cordierite or staurolite and/or andalusite, sillimanite, and sillimanite/K-feldspar zones within pelites and biotite,

hornblende and clinopyroxene within rock buffered calc-silicate rocks (Foster and Rubenach, 2001).

The P-T-t path for the Cloncurry/Osborne zone is quite complex but exhibits an overall clockwise pattern but which also incorporated isobaric heating or cooling episodes. The maximum pressure of 5-6 kbar occurred during D_1 to early D_2, and was followed by a pressure and temperature drop. Temperature then rose to a peak during D_{2b} at 4 kbar/590 °C for the sillimanite isograd and up to 710 °C in the sillimanite/K-feldspar zone at the Osborne Mine.

The majority of the metamorphism of the Mt Isa Western Succession is associated with radiogenic heating due to enrichment of heat-forming elements within the Sybella Granite (McLaren et al., 1999). Cordierite-anthophyllite replacement of mafic schist (metasomatised basalt) is common above the sillimanite isograd west of the Mt Isa Fault (Foster and Rubenach, 2006).

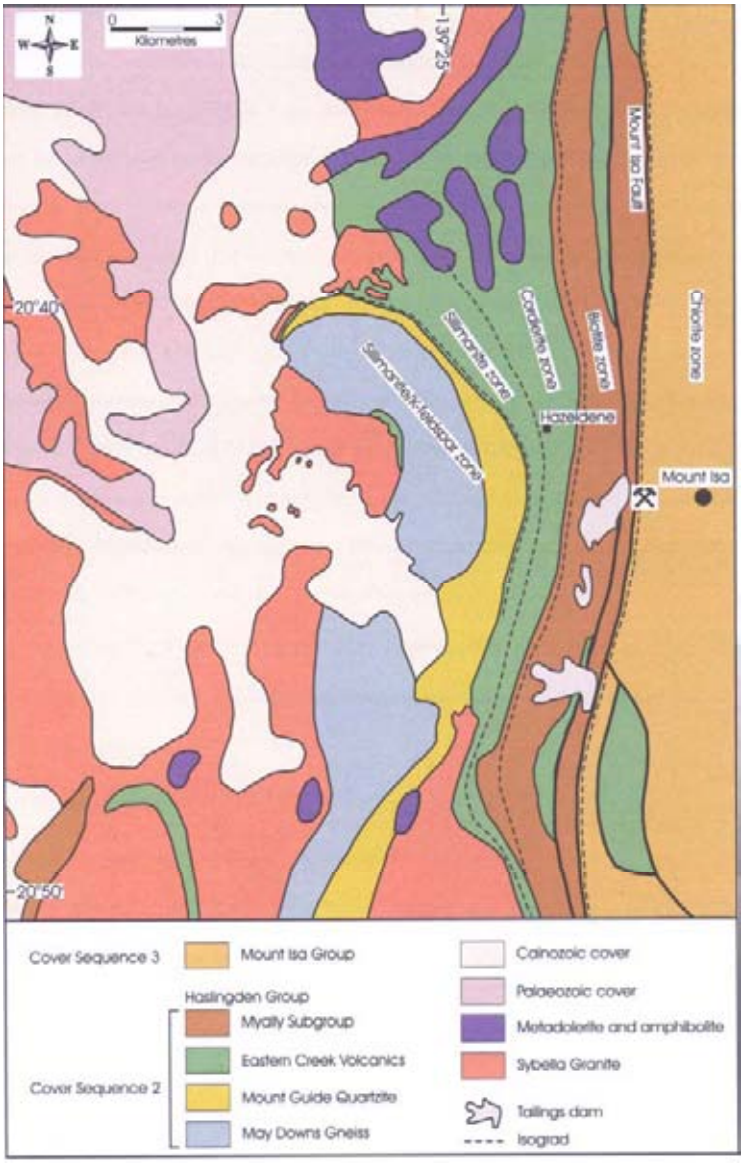

Figure 1.3 (from Foster, 2003) Part of the Western Fold Belt to the west of Mount Isa showing the distribution of the major rock units, and highlighting the metamorphic zones (in pelites) that go from chlorite zone near Mount Isa to sillimanite/K-feldspar zone in the west. Geology after Blake (1987). Isograd distribution after Rubenach (1992) and simplified to omit local complexity due to faulting. Notice that the Sybella Granite (1675-1655 Ma) postdates the Haslingden Group but predates and perhaps temporally overlaps with the Mount Isa Group (Urquhart Shale- ca.l655-1652 Ma). The undifferentiated metadolerite and amphibolite are undated and are likely to include more than one intrusive episode, some of which are likely to be coeval with the Eastern Creek Volcanics, and others with the Sybella Granite

Fault zones and/or major lithostratigraphic changes mark most of the boundaries between the high- and low- grade metamorphic belts. Juxtaposition of terranes of similar grade but different ages indicates that the stratigraphic sequences were disrupted by D_1 folding and/or thrusting prior to the metamorphic peak (Foster, 2003). Variable (and locally

extreme) metamorphic field gradients, and a broad correspondence between high-grade zones and anticlinal cores, indicate that the isograd surfaces were relatively shallow but that the overall distribution of isograds has been influenced by post-peak metamorphic folding and reverse faulting (Foster, 2003).

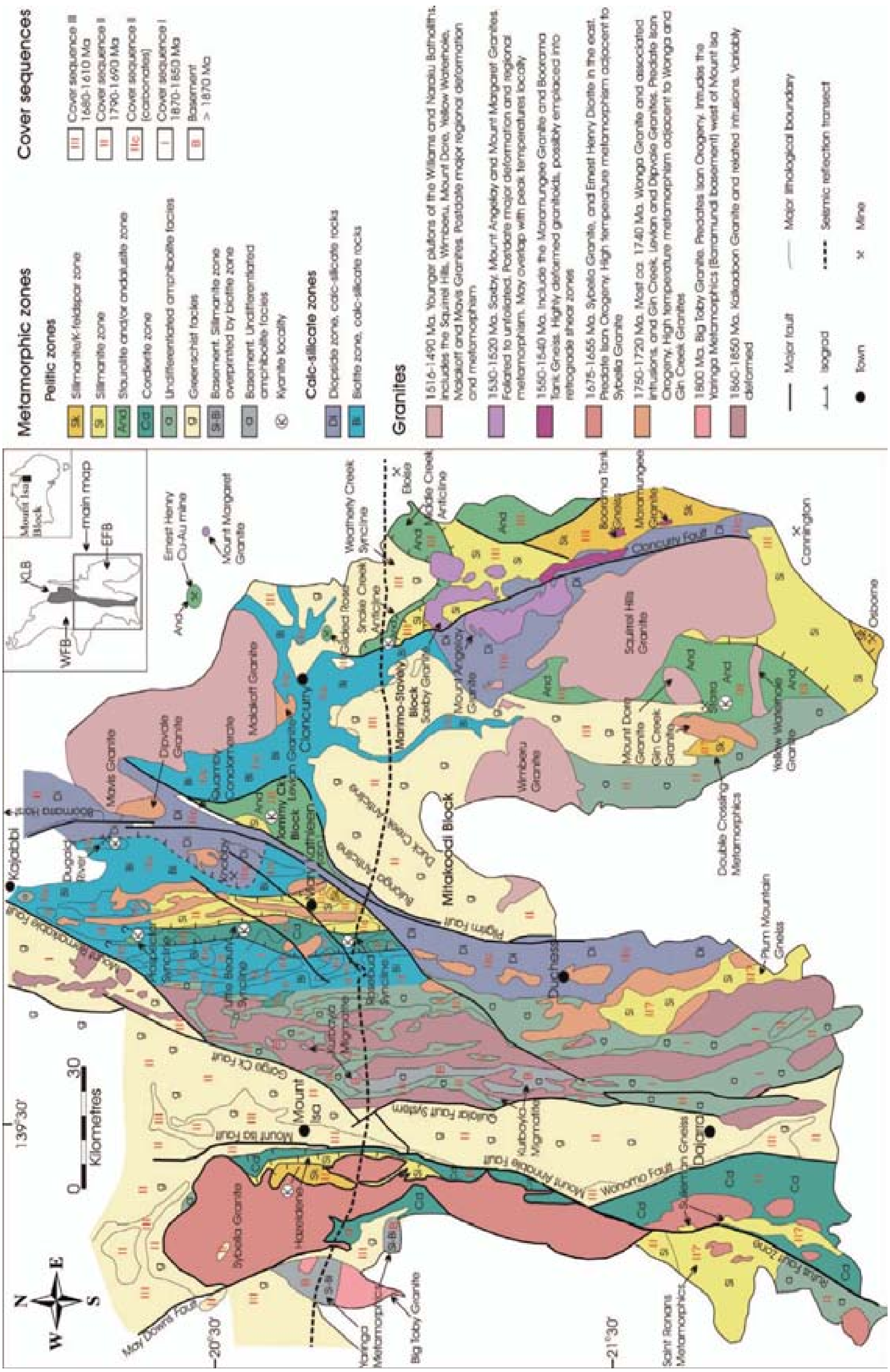

Figure 1.4 (from Foster and Rubenach, 2006) Isograd map for part of the Mt Isa Inlier, northeastern Australia (modified from Foster 2003) showing the broad distribution of metamorphic zones, large granite bodies and key localities.

1.2.4 Structure

Although the copper deposits of the Mt Isa Inlier vary considerably in host-rock lithology, all deposits have a close spatial association with faulting (Mustard et al., 2005; Ford and Blenkinsop, 2007). Furthermore, the vast majority of these copper deposits are hosted in hydrothermal breccias, fault breccias and display characteristics of brittle failure.

The prolonged structural history of the Mt Isa Inlier can be divided into two distinct timeframes. Structural histories that were contemporaneous with sedimentation and basin formation include:

D_w Wonga Event (~1750 Ma)

D_s Sybella Event (~1670 Ma)

Growth faults have also been proposed during sedimentation of the Mt Isa Group and McNamara Group at ~1650 Ma (Neudert, 1983; Askew, 1992; Connors, 1997). The Mammoth Extended Fault is proposed to be an example of growth faulting in the Mt Gordon Mine area, due to abrupt thickness changes of units across the fault from north to south (Askew, 1992; Connors, 1997)

The second and most easily recognisable structural features of the Mt Isa Inlier can all be attributed to a series of shortening events known as the Isan Orogeny. The Isan Orogeny commenced in ~1610 Ma

D_1 D_1 has been designated the first shortening event of the Isan Orogeny (Bell, 1991). It is related to N-S to NNW-SSE shortening. In the Western Succession of the Mt Isa Inlier D_1 folds are most intense north of Lawn Hill around the Murphy Tectonic Ridge (Queensland Department of Mines and Energy et al. 2000). Further south, D_1 is expressed as reactivated and inverted north-dipping normal faults (Gibson, 2006). East-west slaty cleavage in the Lake Moondarra area just north of Mount Isa has also been assigned to D_1 (Windsor 1986). North-south compression is mostly expressed as north-over-south thrusting but this may reflect deformation that has occurred prior to the onset of the Isan Orogeny (Gibson, 2006). This folding and thrusting in many instances involved the reactivation of pre-existing normal faults, not all of which necessarily dipped northward and were therefore favourably oriented for reverse movement (Gibson, 2006). Timing of this deformation is not well constrained

except by monazite dating of U-Pb dating of porphyroblast includion trails, prominent in the 1640-1610 Ma range (Rubenach, 1995).

D_2 A second contractional event which is associated with the peak of metamorphism (low-P/high-T metamorphism) in both the Mt Isa Eastern and Western Successions. D_2 produced north-south folding, a pervasive regional slaty cleavage, and east-over-west directed thrusting has been designated D_2 (Bell 1983; Winsor 1986; Blake 1987; Oliver et al. 1991). D_2 shortening locally caused west-directed thrust reactivation of older structures, particularly those defining the Leichhardt River Fault Trough. This event emplaced older Kalkadoon-Leichhardt basement rocks over the eastern margin of the Leichhardt River Fault Trough and produced upright synclines on both flanks of the Mount Gordon Arch (Gibson, 2006).

D_3 A third contractional event has an ENE-WSW to E-W orientation, producing structures not to dissimilar to those produced during D_2 (Page and Bell, 1986; Oliver et al., 1991). The activation of large-scale wrench faults, which cut the inlier, is considered to be due to D_3 deformation.

D_4 While D_3 was long considered the last event of the Isan Orogeny, evidence for a brittle deformation event is proposed in this study. The D_4 stress event involves ESE-WNW oriented shortening that is coincident with the formation of deposit-scale ore-hosting breccias and probably mineralisation itself. D_4 is seen to exhibit ductile characteristics in one location adjacent to the intruding Saxby Granite which is dated at 1527 Ma (Rubenach, 2005).

D_5 Significant dextral reactivation of NE striking faults is seen at a mine-scale and a regional-scale but the timing of this event is unclear. In the Mt Isa Copper Mine the NE-striking S48 Fault is seen to displace ore by approximately 200 m in an apparent dextral wrench. The NE-striking Fountain Range Fault in the Mt Isa Eastern Succession provides further evidence for one or more late-stage significant dextral wrench events.

PART 2 – ANALYTICAL METHODS

1.3 Structural Analytical Techniques

1.3.1 Overview

Tectonic forces are often described in terms of stresses acting at some distance from the locality where the structure (breccia, vein, shear zone etc.) has developed (e.g. Hafner 1951, Hubbert 1951, Ode 1957, Couples 1977, Muller & Pollard 1977; Pollard *et al.*, 1993). This distance is often large compared to the characteristic length of the structure and these 'regional' stresses are assumed to be homogeneous, so they are typically specified by a single stress tensor (Pollard *et al.*, 1993).

Several factors can influence the orientation of these stress tensors, based on the orientation of the stress field at the time of fault inception (Anderson, 1951). Complex fault geometries (Petit and Mattauer, 1995), areas of fluid overpressure (Bradshaw and Zoback, 1988) and intrusions (Parsons and Thompson, 1993) may affect the local stress geometry. Furthermore, stress heterogeneity may arise as a consequence of material inhomogeneities (Oliver et al., 1990; Sibson, 2001).

1.3.2 Brittle failure modes

Brittle failure can be most simply differentiated from ductile failure when described as a surface or zone across which the material loses cohesion (Twiss and Moores, 1992). Conversely ductile deformation occurs when the material becomes permanently deformed without losing cohesion (Twiss and Moores, 1992) on the scale of observation.

The major controls on the orientation of brittle structures at the time of their formation are effective stress, pore fluid pressure, and the stress geometry, which is defined by three orthogonal principal compressive stresses $\sigma_1 > \sigma_2 > \sigma_3$ (Figure 1.5). The orientation of σ_1, σ_2, and σ_3 may be affected by pre-existing anisotropy in the rock-mass (Anderson, 1951).

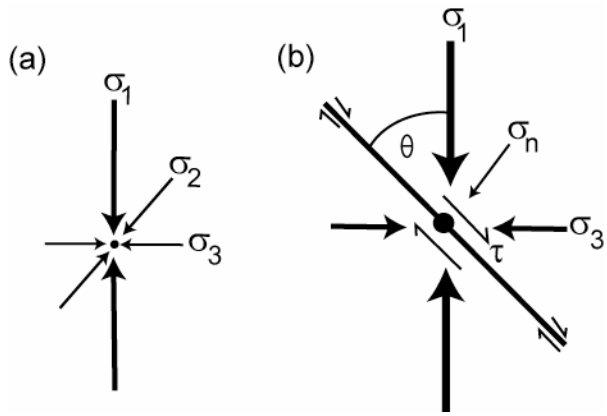

Figure 1.5 - (a) An 'Andersonian' extensional stress state where $\sigma_1 > \sigma_2 > \sigma_3$; and (b) shear stresses and normal stresses acting on a plane in a normal fault setting where θ is the angle between σ1 and the fault plane (Sibson, 2001).

Anderson (1951) realised that the earth's free surface can not sustain shear stress, therefore, the vertical stress must also be a principal stress, i.e. $\sigma_v = \sigma_1$, σ_2, or σ_3. Brittle faults typically form according to Coulomb failure criteria along planes containing the σ_2 axis at θ = 25° to 30° to σ_1 where θ (Figure 1.5b) is the angle between σ_1 and the failure plane. This angle depends on the coefficient of internal friction (Byerlee, 1978).

Coulomb failure envelopes may be constructed assuming any orientation of a plane of weakness. A stress regime in which the Mohr circle overlaps the failure envelope for planes of weakness, but does not touch the envelope for intact rock, will fail along that plane of weakness.

Three modes of brittle failure can occur in intact isotropic rock with predictable orientations of the principal stress axes (Holyland and Ojala, 1997; Sibson, 2001):

(i) pure extension fractures (Figure 1.6a),

(ii) shear fractures (faults) (Figure 1.6c), and

(iii) hybrid extensional-shear fractures (Figure 1.6b).

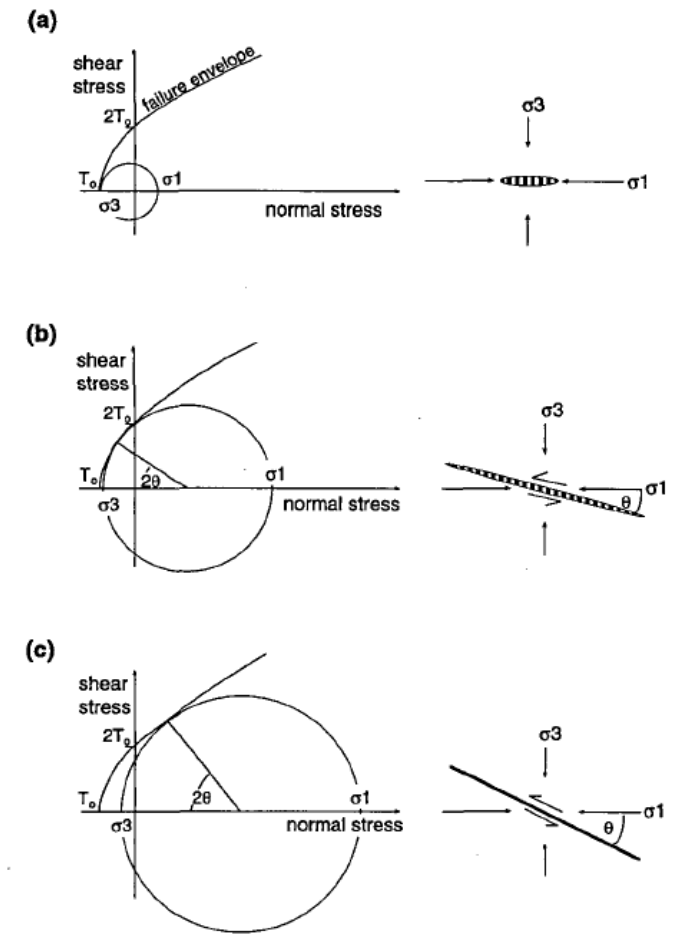

Figure 1.6 (from Holyland and Ojala, 1997) Modes of failure in relation to differential stress in homogeneous, isotropic rock. Mohr diagrams illustrate the general failure envelope for intact rock and the stress conditions for the three modes of failure. Modified from (Sibson 1989). (a) Extensional fracturing, (b) Extensional shear (combination of fracturing and shear), (c) Shear fracturing, σ_1, Maximum principal stress; σ_3, minimum principal stress; θ, angle of failure to σ_1; T_o , tensile strength of the rock.

The Griffith failure criterion (Griffith, 1924): $\tau^2 = 4\sigma_n^{'}T + 4T^2$ predicts shear strength, $\tau = 2T$ when $\sigma_n^{'} = 0$. The Coulomb failure criterion predicts failure with cohesive shear strength, C, and coefficient of internal friction, when: $\tau = C + \mu_i\sigma_n^{'} = C + \mu_i(\sigma_n - P_f)$ (Griffith, 1924). Brittle failure may arise by increasing differential stress and/ or by increasing fluid-pressure (Figure 1.6). The mode of failure depends on the balance between differential stress (σ_1 - σ_3) and tensile strength, T (Secor, 1965; Sibson, 1989). When (σ_1 - σ_3) > 4T, pure extension fractures form along planes perpendicular to the least compressive stress, σ_3, (Figure 1.6). When (σ_1 - σ_3) > 5.66T, shear fractures form along planes containing the σ_2 axis at angles to θi = 27° ± 5° to σ_1 in compliance with Coulomb criterion and the internal

coefficient of friction ($0.5 < \mu i < 1.0$). When $4T < (\sigma_1 - \sigma_3) > 5.66T$, extensional-shear fractures form along planes containing the σ_2 axis at angles ($\theta < \theta i$) to σ_1 (Figure 1.6) (Secor, 1965; Byerlee, 1978; Sibson, 1998).

1.3.3 Temperature conditions for brittle failure

A simple rheological model of shearing of the lithosphere that has gained wide acceptance is a three layer model with an upper brittle zone in which deformation takes place by frictional sliding on discrete fault surfaces, a lower plastic zone in which deformation takes place by bulk viscous flow and an intermediate transitional zone (brittle-ductile transition) which is assumed to be indicated by the lower limit of seismicity (Scholz, 1988; Sibson, 1989; Ranalli, 2000).

Conditions of brittle failure are dependent on the interactions between changes in the stress field and the rheological properties of the upper lithosphere. The rheology varies in time and space as a function of strain rate, composition, temperature, and pore-fluid pressure (Ranalli, 2000). The predicted depth of the brittle/ductile transition depends strongly on composition and geotherm, varying from <10 km for hot felsic crust to >30 km for cold mafic crust (Ranalli, 2000).

The brittle-ductile transition is broad transitional field of semi-brittle behaviour, which for quartzofeldspathic rocks lies between the onset of quartz plasticity at about 300 °C and feldspar plasticity at about 450 °C (Scholz, 1988). Quartz creep is hypothesised to mark the depth limit of earthquake nucleation, but large earthquakes can propagate to a greater depth (Sibson, 1989). The lower brittle-ductile transition is typically characterised by mylonites interlaced by pseudotachylytes and other signs of dynamic faulting (Scholz, 1988).

The upper brittle-ductile transition is also marked by a change in the generation mechanism of fault rocks, from abrasive wear above which produces cataclastites, to adhesive wear below, which is proposed as an important generation mechanism of mylonites in the upper part of the semi-brittle field (Figure 1.7) (Scholz, 1988).

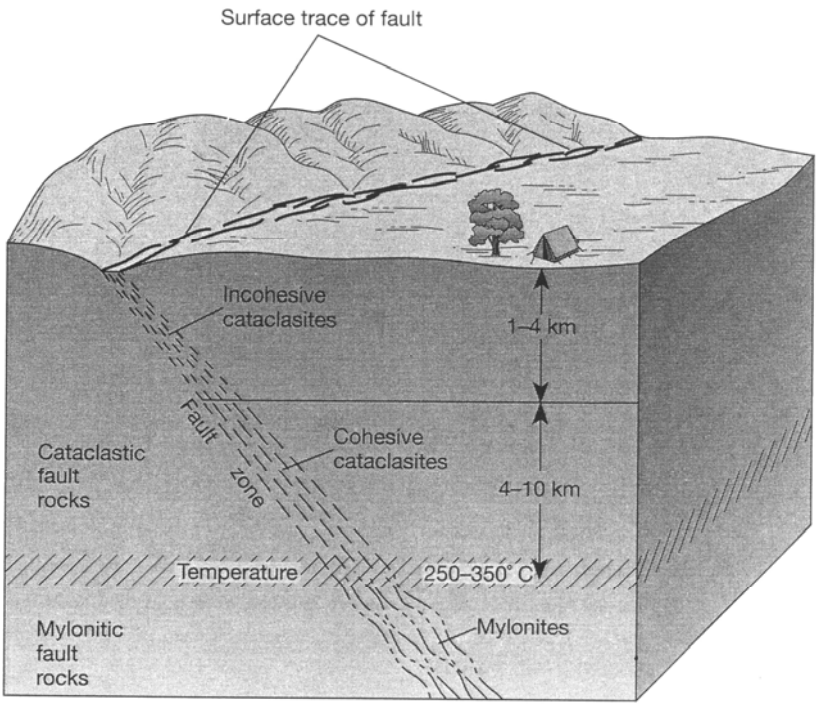

Figure 1.7 (from Twiss and Moores, 1992) Schematic block diagram of a portion of the earth's crust showing the surface trace of a fault zone (i.e., its exposure on the Earth's surface) and the variation with depth of the type of fault rock within the fault zone. Incohesive cataclasites (plus pseudotachylite if dry) characterise depths above 1-4 km. Below that, cohesive cataclasites (plus pseudotachylite if dry) are present at depths of up to 15 km. Mylonites are present at depths greater than 10-15 km and temperatures greater than 250-350 ºC.

1.4 Palaeostress analysis and stress inversion

Palaeostress analysis is a technique concerned with determining the nature of past states of stress in rocks (Lisle and Orife, 2002). Palaeostress analysis has some important practical applications. Miller and Wilson (2004) showed how the mineral exploration industry can benefit from palaeostress analysis, when they determined an orebody extension to the Stawell Gold Mine that had been offset during a late stage deformation event. Palaeostress analysis has the potential to be an extremely useful exploration tool when combined with numerical modelling, in which the appropriate stress field for the model has not always been quantitatively constrained (Blenkinsop and Lisle, 2006).

There are many different approaches to palaeostress analysis. The most common methodology is to estimate the macroscopic stress tensor from the geometrical features of faults present within a rock volume (Angelier *et al.*, 1982; Yamaji, 2000; Lisle and Orife, 2002;

Miller and Wilson, 2004). These methods are known often as fault-slip methods. These methods vary in terms of the data required and the assumptions they incorporate.

Fault slip methods treat faults and their slip vectors as palaeostress gauges recording the direction of maximum resolved shear stress on the planes of the faults. The directional characteristics of shear stress on planes of different attitude are sufficient to constrain certain features of the geological stress tensor; namely, the orientations of the principal stress axes and the stress ratio (phi value), a parameter describing the ratio of the principal stress differences.

The two basic assumptions behind these methods are that striae on a fault record the direction of shear stress at the time of movement and that the stress regime is consistent (Angelier, 1989; Fry, 1992). Any discrepancies are typically attributed to errors in measurement or to fluctuations from these assumptions. Such methods often indicate that one principal stress is approximately vertical (Fry, 1992). By incorporating the Andersonian assumption of a vertical principal stress (here σ_2), the determination can be greatly simplified. There then exist only three degrees of freedom amongst the stress tensor (fully specified absolute magnitudes), the orientation of a fault plane and the shear direction of that plane.

1.4.1 Stereographic Methods - fault plane solution and P & T dihedra

Compression and extension (P and T respectively) axes are a simple and direct representation of fault geometry and the sense of slip. Fault plane solutions are based on the determination of P and T axes, which is strictly a kinematic analysis method (Stein and Wysession, 2002). This is due to the contention of Marrett and Allmendinger (1990) that data obtained from the orientation of striae relative to the fault plane is a direct representation of strain. The maximum incremental shortening direction is equivalent to the maximum principal stress in a homogeneous, isotropic material.

The P and T dihedra method is based on the m – axis method developed by Arthaud (1969). For any fault zone, a movement plane containing the slip vector and pole to the fault plane is identified. The P & T axes are located in the movement plane at 45º to the fault pole. The principal stresses and the P & T axes don’t necessarily match up. In fact, the greatest

principal stress may occur anywhere within the P-quadrant, and the least principal stress may likewise occur anywhere within the T-quadrant.

An effective way of displaying the P & T axes is through the creation of “beach-ball” plots. By defining an auxiliary plane that is orthogonal to the fault plane (Figure 1.8) (Stein and Wysession, 2002), the reference sphere can be cut into four quadrants, (though sometimes only three quadrants are visible on the stereonet). By convention the quadrants in tension are shaded and the quadrants in pressure (compression) are white. σ_1 can occur anywhere within the P-quadrants (white) and σ_3 can occur anywhere in the T-quadrants (shaded).

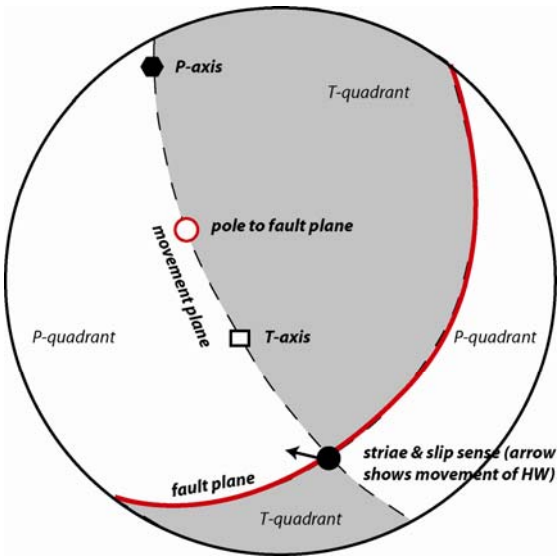

Figure 1.8 (adapted from Nortje, 2004) Lower hemisphere equal stereonet showing P & T axes and P & T quadrants relative to the fault plane and movement plane.

The major assumptions of the method are:

(i) bulk stress field is uniform (Gapais et al., 2000)

(ii) the major principal stress axis, σ_1, forms at 30° to the fault plane (Chapt. 1.3.2 *Brittle failure modes*) based on empirical data from Byerlee’s (1978) experiments on rock friction;

(iii) the major and least principal compressive stresses lie in the movement plane (m - plane) of the fault while the m - axis broadly corresponds to σ_2

(iv) fault measurements belong to a single tectonic event governed by a single stress tensor;

(v) faults may propagate through pre-existing discontinuities; and

(vi) stress fields may change through space and time during a single faulting event so one assumes motion along a fault is independent and occurs in the shear direction governed by a single mean stress deviator (Angelier, 1979, 1984, 1989).

It must be emphasised that striations yield information on the final faulting event and may not bear any relation to the main offset along faults.

1.4.2 The Multiple Inverse method

The Mulitple Inverse Method is an inversion technique designed to separate stresses from heterogeneous fault-slip data, which record polyphase stress history, without *a priori* information on the stresses or on the classification of faults according to the stresses (Yamaji, 2000). Heterogeneous data can also be obtained also from an area where stress state has a spatial variation. The validity of the method relies on the Wallace-Bott hypothesis, the basis of stress tensor inversion, which infers that it is highly probable that a state of stress activated faults with small misfit angles. The threshold set for the misfit angles is arbitrarily established at 20º.

The Mulitple Inverse Method delivers the principal stress tensors (σ_1, σ_2, and σ_3) as well as a stress shape ratio (Φ value). Significant solutions are identified as clusters in parameter space. Stresses are represented by clusters of dot-and-bar symbols in an ordinary lower-hemisphere, equal-area projection stereonet (Figure 1.9). The direction of the σ_3 axis is indicated by the position of a dot. The direction and length of the bar attached to the dot show the azimuth and plunge of the σ_1 axis of the stress state, respectively. Separate clusters of data, or data that doesn't cluster is considered to be heterogeneous and not related to the same deformation event (Yamaji, 2000).

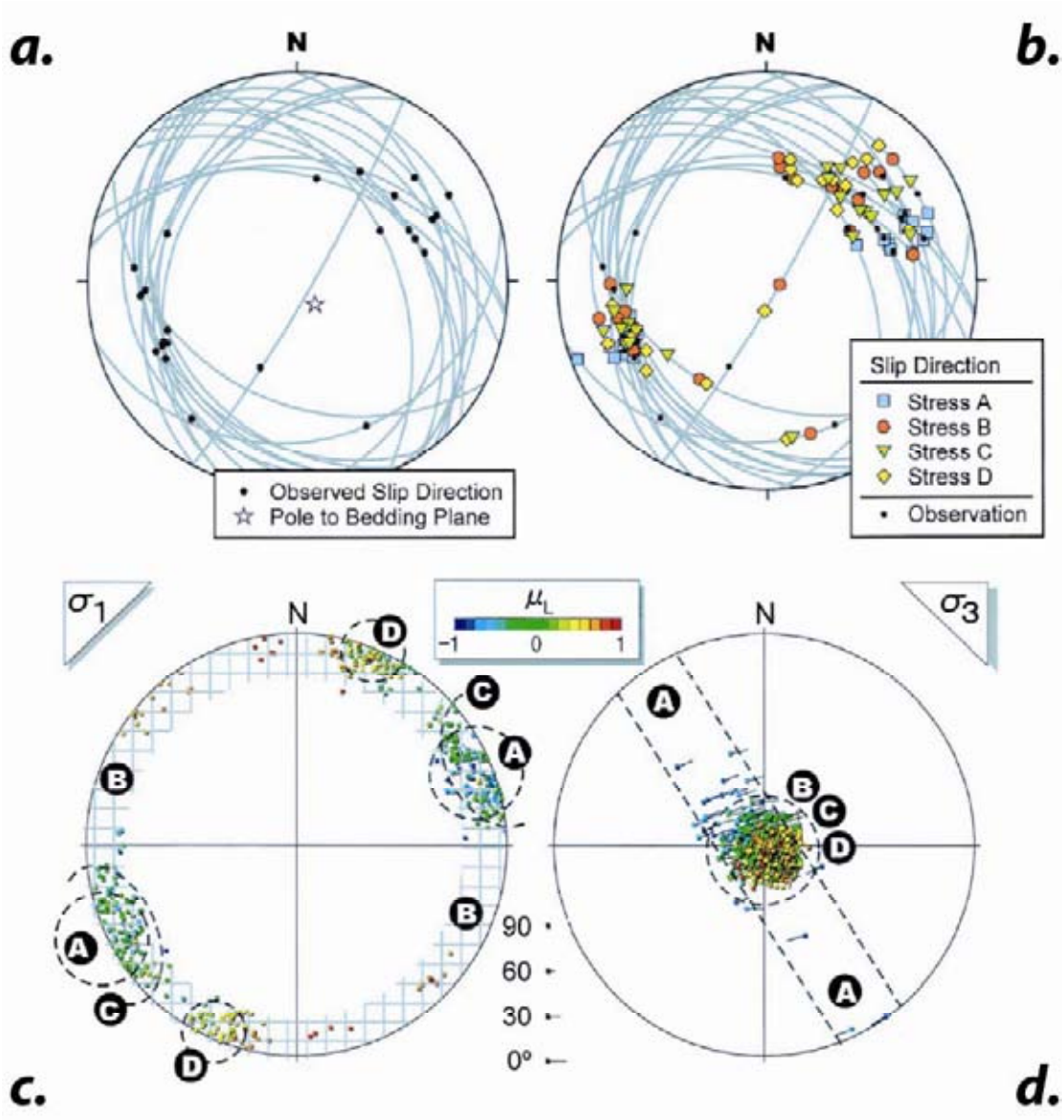

Figure 1.9 (adapted from Yamaji, 2000) Example of output plots of the Multiple Inverse Method. Dataset is from the Tano Formation, Miyazaki Group, Japan ***(a)*** *Reverse and oblique-reverse faults observed at an outcrop of the Tano Formation, Miyazaki Group. Lower hemisphere, equal angle projection. Solid circles indicate the slip direction of footwalls.* ***(b)*** *Theoretical slip directions by the stresses A-D that were identified by the multiple inverse method from the fault-slip data shown in (a)* ***(c)*** *Clusters representing the direction of σ_1 axes is shown. Dot-and-bar symbol length reflects the plunge of σ_3 and the direction represents the azimuth of σ_3. The stresses A, B, and C are equally plausible solutions. The cluster of reddish symbols in the cross-hatched area labeled as B indicates a vertical, axial, deviatoric tensional stress.* ***(d)*** *Clusters representing the direction of σ_3 axes is shown. Dot-and-bar symbol length reflects the plunge of σ_1 and the direction represents the azimuth of σ_1.*

1.4.3 Grid search methods - SLICK.BAS

The SLICK.BAS, software developed by Ramsay and Lisle (2000) finds the stress tensor by a grid-search, trial-and-error method. The search for the best-fit tensor involves changing each of the four variables (σ_1, σ_2, σ_3 and Φ) progressively until a complete range of tensors is considered. SLICK.BAS also evaluates the average angular deviation (<º) of the slip data with the theoretical predicted directions. The assumptions are: (i) that the slip direction on a fault is parallel to the resolved shear stress; (ii) that slip data utilised reflects deformation within a homogeneous stress field; and (iii) that there is independent slip (Ramsay and Lisle, 2000).

Each tensor is used to calculate the direction of shear stress on each of the fault planes and these calculated directions are compared with those of the measured slip lineations. The program assesses the quality-of-fit by recording the mean deviation between observed and calculated slip directions (from slickhlp.txt, Ramsay and Lisle, 2000). As this process does not require a fault movement sense, two answers are produced (Figure 1.10). The calculation of the stress shape ratio (Φ) differs between the SLICK.BAS software and the work of Angelier (1975; 1984; 1989), Oriffe et al. (2002) and others.

SLICK.BAS calculates Φ as

$$\Phi=(\sigma_1-\sigma_2)/(\sigma_1-\sigma_3)$$

whereas Angelier (1975, 1984, 1989) and others calculate Φ as

$$\Phi=(\sigma_2-\sigma_3)/(\sigma_1-\sigma_3)^*$$

*preferred calculation method

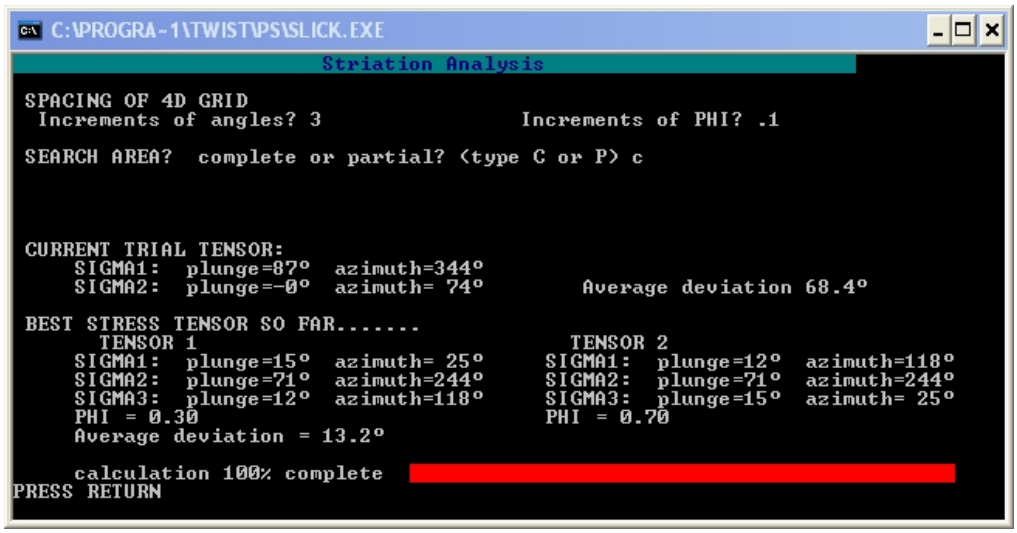

Figure 1.10 Example of SLICK.BAS output. Two sets of stress tensor are possible as no fault-slip sense is required for the analysis.

1.4.4 Palaeostress analysis in relation to the Mt Isa Inlier study

The palaeostress techniques outlined in Chapter 1.3.4, have been employed, where possible, in various deposit analyses incorporated in this study.

Striated fault surfaces mapped in underground exposures at the Mammoth Mine (part of the Mt Gordon Copper Mines – Chapter 2) were analysed using several palaeostress techniques. The multiple inverse method was employed to determine which fault striations were related to the same deformation event. The inversion result was then compared to further palaeostress analyses using SLICK.BAS (Ramsay and Lisle, 2000).

Miller (2006) determined the σ_1 palaeostress orientation at mineralisation by mapping extension veins in the Mt Isa Copper Mine (Chapter 3). The Miller (2006) palaeostress analysis results were compared to numerical modelling outputs at both Mt Isa and Mt Gordon.

1.5 Numerical Modelling – UDEC (Universal Distinct Element Code)

1.5.1 Overview

For the purpose of numerical modelling, the upper crust can be broadly described as a system continuous blocks that may be separated by weak faults which may be filled with fluids (Zhang and Sanderson, 2002). Such systems exhibit complex, discontinuous behaviour and generally are anisotropic and spatially heterogeneous. The rock-block systems may be subject to a complex loading history due to superposed tectonic events at various scales (Zhang and Sanderson, 2002).

The fractures associated with such rock-block systems were described by Pollard and Aydin (1988) as an influence on mineral deposition by guiding ore-forming fluids, and providing fracture permeability for water, magma, geothermal fluids, oil and gas. The principles of fracture permeability in mineralisation are fairly well understood (e.g. Phillips, 1972; Sibson, 1996). However very complex fault arrays are difficult to analyse from first principles or even palaeostress analysis.

Consequently, numerical modelling aims to numerically reconstruct a physical reality and to simulate the evolution of the physical system under a variety of initial conditions and external loads (Zhang and Sanderson, 2002). Modelling the likely behaviour of such rock-block systems is a useful tool in the understanding of the mechanical response to deformation

and its likely effect on fluid flow through fracture created permeability, particularly in complexly deformed mineralised terranes (Mair *et al.*, 2000).

Distinct element modelling has been used in a variety of modelling scenarios including stress mapping simulation in gold deposits (Ojala *et al.*, 1993; Holyland and Ojala, 1997; Mair *et al.*, 2000) copper deposits (McLellan, 2004, McLellan and Oliver, 2006), tin deposits (Jiang *et al.*, 1997) regional metamorphism and uranium deposits (Oliver *et al.*, 1990, 1999) and stress perturbation around major fault zones (Homberg *et al.*, 1997).

1.5.2 UDEC software

UDEC is a two dimensional numerical modelling program that is based on the distinct element method for discontinuum modelling (Cundall, 1980; Itasca, 2000). The code enables a numerical simulation of the response of discontinuous media (jointed and fractured rock mass) that is subject to either static or dynamic loading (McLellan and Oliver, 2007).

The modelling simulates an assemblage of discrete blocks, which interact through corner and edge contacts (e.g. Holyland, 1990a, b; Holyland and Ojala, 1997). Properties, such as density, bulk modulus, shear modulus, tensile strength and cohesion of the rock, are assigned to the individual blocks. The blocks can be coded to behave as either rigid or deformable material. These blocks can also be separated by discontinuities (faults, joints, lithological boundaries) which are prescribed their own contact properties (Holyland 1990; McLellan and Oliver, 2007). A stress field is applied in accordance with the inferred orientations and magnitudes of far-field stresses at the time of interest (Mair *et al.*, 2000).

UDEC calculates force and displacement according to Newton's laws of motion. As the force depends on displacement, the force/displacement calculation is done over one time instant (McLellan, 2004). This explicit time-stepping (dynamic) algorithm does not limit displacements or rotations for both the matrix and discontinuities (Holyland, 1990; Holyland and Ojala, 1997).

Another significant feature of UDEC is the coupling of the mechanical deformation and hydraulic behaviour (Zhang and Sanderson, 2002). Fluid pressure at block boundaries exerts a force which contributes to the deformation of the block (Zhang and Sanderson, 2002).

1.5.3 Mechanical principles

The simplest form of mechanics that concerns us are geology is the concepts of stress and strain. Although UDEC can calculate incremental strain, in this study it is primarily used for quantifying stress states and determining stress tensor orientations.

The stress component perpendicular to a surface is known as normal stress (σ_n) and a stress component that is parallel to a surface is known as shear stress (e.g. Hobbs et al., 1976). In 2-dimensional stress space the normal stresses are considered as σ_{xx} and σ_{yy}, and shear stresses as σ_{xy} and σ_{yx}. In order to prescribe a 2-dimensional state of stress in UDEC, three independent components σ_{xx}, σ_{xy} and σ_{yy} must be specified.

Within any column of rock the vertical stress acting upon it increases approximately linearly with depth. Assuming a constant density of the column of rock, and knowing the depth or height of the column of rock we can calculate the vertical stress acting upon the point of interest using:

$$\sigma_v = \rho g h$$

where σ_v is the vertical stress (MPa), ρ is the rock density (kg m^{-3}), g is acceleration due to gravity (ms^{-1}) and h is the depth or height of the column of rock overburden (m). For fault geometries modelled in plan view, σ_v is considered to be σ_2.

As there are normal forces acting on horizontal planes in the earth we also need to consider normal forces acting on the vertical planes. These horizontal normal stress components σ_{xx} and σ_{zz} are typically tectonic forces e.g. deviatoric stress, and this usually results from disequilibrium where:

$$\sigma_{xx} \neq \sigma_{zz} \neq \sigma_{yy}$$

When all three stresses are in equilibrium (approximately equal e.g. stable continental crust) the balance between this and the weight of the overburden is known as a lithostatic state of stress. When tectonic forces are present, the horizontal force F_c acting on a section of rock at depth is made up of both the lithostatic part and a tectonic part:

$$\sigma_{xx} = \rho_c g h + \Delta\sigma_{xx}$$

1.5.4 Constitutive models

Constitutive models are a mathematical description of how a rock will respond to an applied force. Widely used constitutive models include:

(i) the Cam-clay model - used to represent soft materials such as clay when the influence of volume change on bulk property and the resistance to shear need to be considered

(ii) the Drucker-Prager model – to model soft materials such as clay or soil with low friction angles, and

(iii) the Mohr-Coulomb model – which is the most conventional model used to represent shear failure in consolidated soils and rock.

The Mohr-Coulomb model with non-associated plasticity is regarded as a reasonable representation of the rheology of mid to upper crustal rocks (Vermeer & de Borst, 1984; Hobbs et al., 1990; Ord & Oliver, 1997). This is the constitutive model used in the elastic-plastic coupled deformation and fluid flow models in this study.

The Mohr-Coulomb model can be modified to incorporate strain hardening/softening behaviour by varying model properties such as cohesion, friction, dilation or tensile strength, as a function of the deviatoric plastic strain. These material properties are allowed to increase (hardening) or decrease (softening) following the onset of plastic yield, in contrast to the standard Mohr-Coulomb model in which the material properties are assumed to remain constant.

1.5.5 Stress Mapping in UDEC and implications for Mt Isa modelling

Stress mapping examines the variation in strain and stress through an inhomogeneous terrain on imposition of a regional stress field (Holyland and Ojala, 1997; Jiang et al., 1999). When stressed, an inhomogeneous model develops an inhomogeneous stress field whose components vary with rheological properties and geometry (Holyland and Ojala, 1997; Zhang and Sanderson, 2002). The modelling is considering only elastic and plastic stresses and strains, and, for instance, deformation dilatancy due to viscous strains is not considered (Holyland and Ojala, 1997; Zhang and Sanderson, 2002).

Depths to ore deposition levels are typically calculated from geobarometry in most Mt Isa Inlier deposits. Typically ore deposition was between 5 km and 7 km paleodepth and provides an estimate of mean stress for modelling purposes (Heinrich *et al.*, 1989; Clark, 2003; Mattai *et al.*, 2004).

Holyland and Ojala (1997) proposed that stress mapping could be used as a basis for prediction of hydrothermal fluid flow and mineralisation based on the following assumptions:

(i) Low minimum principal (σ_3) stress indicates proximity to failure and therefore possible deformation-enhanced permeability (this is more important in modelling of high crustal level deformation);

(ii) At depths of more than a few kilometres fluid pressure is buffered to be close to lithostatic pressure and the control on fluid pressure is mean stress;

(iii) Variations in mean stress result in variations in fluid pressure; and

(iv) Fluid flow is both upwards and towards zones of low mean stress.

The work of Holyland and Ojala (1997) suggests that structurally controlled mineralisation that is late in the tectonic history of a terrain coupled with evidence for fluid overpressuring, enables the prediction of zones of failure from areas of low mean or minor principal stress, provided that the orientation of the far-field stress can be determined or a reasonable orientation assumed.

Many of the deposits in the Mt Isa Inlier have formation ages of ~1530 Ma, nearing the end of the Isan Orogeny, and the majority of the deposits are hosted by large hydrothermal breccias providing evidence of fluid overpressuring. Given the proposed conditions of Holyland and Ojala (1997), this should enable a stress analysis relating to late tectonic faulting and ore genesis. As the locations of the deposits are known in relation to the fault geometries and lithological units, distinct element modelling can be used to test orientations of far-field stress. Far-field stress orientations that produce areas of low mean stress (o_m) or low minimum principal (o_3) stress in the locations of the copper deposits, can be considered viable options for the far-field stress orientation responsible for their formation.

1.5.6 Interpreting UDEC outputs – implications for likely failure mode

Failure may be initiated by:

- an increase in σ_1 or a decrease in σ_3, in either case increasing the differential stress (σ_1 - σ_3).
- increasing the fluid pressure and hence reducing the applied stresses and moving the Mohr circle to the left;
- decreasing σ_3 and hence decreasing mean and increasing differential stresses.

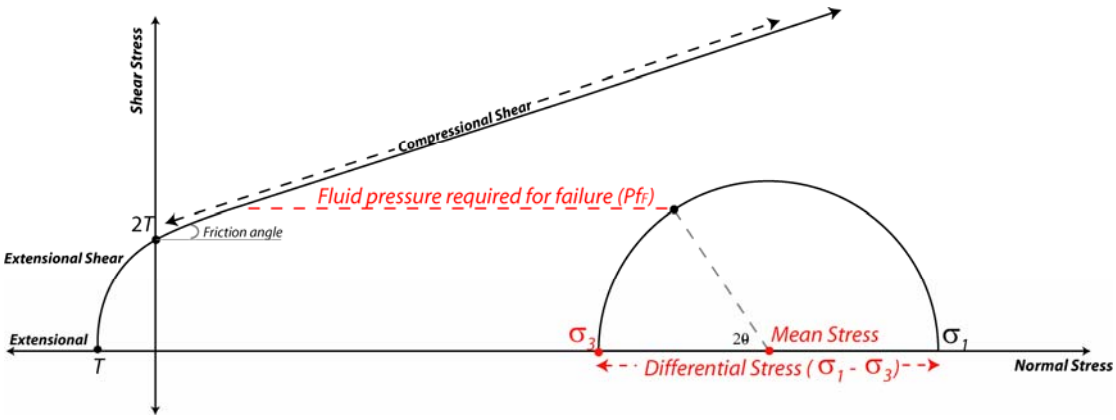

Figure 1.11 Easily measurable features in UDEC that can be used to determine the likely failure mode are seen in red. The failure modes (extension, extensional shear, and compressional shear) are discussed in Chapter 1.3.2. The shape of the failure envelope is determined by the tensile strength of the rock (T) and the friction angle. These are inputs into the UDEC block (rock mass) parameters. The limit of extensional (tensile) failure must be less than four times the tensile strength of the rock.

1.5.7 Limitations of 2-dimensional simulation

Several authors indicate that the most severe limitation of two-dimensional modelling is that the plane of a map does not accurately reflect the stress pattern in an area with a complex three-dimensional geometry (Holyland *et al.*, 1993; Holyland and Ojala, 1997; Zhang and Sanderson, 2002; McLellan 2004; McLellan and Oliver, 2007). This is not necessarily a critical restriction in the Mt Isa Inlier as many of the mapped ore hosting structures and other faults, are seen to dip very steeply.

Stress mapping has been questioned in terrains where faults and strata commonly dip at low angles. The accuracy of the three-dimensional geological interpretation becomes

especially important in deposit-scale modelling where the extent of interest of the vertical dimension is similar to horizontal dimensions (Holyland and Ojala, 1997).

Hu *et al.* (1996) completed a study on the effects of modelling deformation in two-dimensions versus modelling in three-dimensions. This study was completed on the active deformation of southern Taiwan and was supported by the present-day velocity field of southern Taiwan estimated based on geodetic data obtained through the Global Positioning System (GPS). Hu *et al.* (1996) posed the question "Is the 2-D approximation reasonable for solving 3-D geodynamic problems?".

The two-dimensional concerns with the Taiwan modelling were that:

(i) it implies drastic simplification (such as neglecting the vertical change of the rheological properties and the dips of major structures),

(ii) major discontinuities are not vertical - the main fault, the Longitudinal Valley Fault (LVF) dips at ~55° (Tsai et al., 1977), and

(iii) the main faults have a left-lateral thrust component (Hsu, 1976; Barrier and Angelier, 1986)

Despite the 50 ° dip attributed to the LVF in the 3-D model, in contrast with its implicit vertical attitude in the 2-D model, the results of determining the principal stress orientations and active plate velocity rates were nearly equivalent (Hu *et al.*, 1997). Hu *et al.* (1997) effectively obtained similar stress fields and similar deformation fields and concluded that the 2-D approximation was a reasonable simplification in this case.

The case study also incorporated testing finite element modelling in two-dimensions. The finite-element modelling at the scale of several hundred kilometres, was unable to account for the deviations analysed at the scale of several tens of kilometres (Hu *et al.*, 1997). This was largely due to the effects of mechanical decoupling across discontinuities that were unaccounted for, although they result in significant deviation of principal stress (Hu *et al.*, 1997). These effects were taken into account in the distinct-element modelling

This conclusion is important in practice, because the 2-D numerical models are much faster to construct and run, and enables one to use more sophisticated representation of regional patterns than the 3-D modelling for a similar memory size and run time (Hu *et al.*, 1997).

The implications of the Hu *et al.* (1997) study are potentially significant for the numerical modelling of copper deposits in the Mt Isa Inlier, where lithological associations and fault geometries are particularly complex. This issue will be discussed for individual deposits.

2 MT GORDON COPPER MINES

PART 1 – GEOLOGY AND GEOMECHANICAL SETTING

2.1 Introduction

The Proterozoic Mt Isa Block is endowed with a large number of small to medium sized copper deposits and two world class orebodies, Mt Isa and Ernest Henry. A high proportion of these deposits appear to have developed by the focussing of hydrothermal fluids through structural features such as faults, fault irregularities, shear zones or breccias (Perkins, 1984; Swager, 1985; van Dijk, 1986; Laing, 2003; McLellan and Oliver, 2007).

However the origin and controls on the largest deposits are not as clear as some of the smaller ones, due to their size and complexity, most noticeably Mt Isa copper, Ernest Henry and Osborne; the three largest mined copper deposits to date. In the Western Succession of the Mt Isa Block, the second largest known resource after Mt Isa is Mt Gordon (formerly known as Gunpowder), comprising the Mammoth and Esperanza mines. These deposits are relatively small and high grade, are hosted in an area of very good outcrop and are not associated with any other nearby deposit (unlike Mt Isa copper adjacent to the Pb-Zn orebodies). Thus they form a very suitable location for attempting to determine the specific mechanical controls on copper mineralisation.

The aim of this chapter is to use the map patterns, orientation and detail of faults and veins in Mammoth and Esperanza to try to constrain the orientation and the magnitude of the principal stresses acting on the host rocks at the time of primary copper mineralisation. The results form the basis for numerical models of deformation and fluid flow (Chapter 2.9) and a comparison with the Mt Isa Copper Mines (Chapter 3).

2.2 Discovery and Mine History

Mt Gordon is located approximately 120 km north of Mt Isa (Figure 2.1). The discovery of copper mineralisation at the Mammoth deposit was made in 1923 by two Afghan cameleers, the Shah brothers (Richardson and Moy, 1998). The Shah brothers operated a small open cut mine from 1927 to 1959. Various companies, including Surveys and Mining Ltd and Gunpowder Copper Ltd, worked the Mammoth Mine for approximately 110,000 tonnes of copper metal between 1959 and 1998 (Richardson and Moy,1998). Production increased in 1998 when Western Metals Ltd began production from the Esperanza open-cut. Upon acquiring the mine and surrounding leases, Western Metals renamed the operation (previously known as the Gunpowder Mine) to Mt Gordon. In 2004 the mine was acquired by Aditya Birla, the current mine operators. The Esperanza Mine mineral resource was exhausted and the mine closed in 2006. Underground resources, as at December 31, 2005 were in the order of 2.66 Mt @ 2.8% copper. The Mammoth Mine is expected to close in late 2008. Extraction of copper from both the hypogene and supergene ores is through leaching, followed by solvent extraction and electrowinning (Richardson and Moy, 1998).

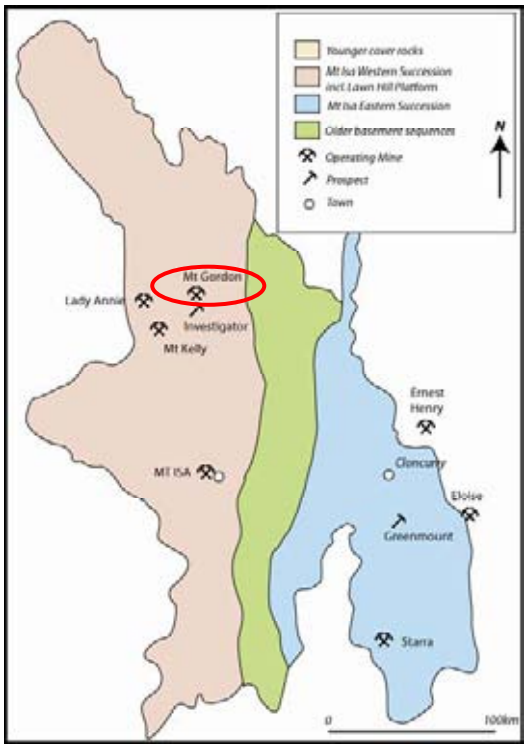

Figure 2.1 Mt Gordon Copper Mines location. Mt Gordon is located approximately 120 km north of Mt Isa in the Western Succession of the Mt Isa Inlier.

2.3 Geological Setting

The Esperanza Mine is located at the intersection of the north-south trending Esperanza Fault and the ENE trending Mammoth and Mammoth Extended Faults (Figure 2.2). It is hosted in the mid-Proterozoic Esperanza Formation, a series of well bedded to locally massive, black carbonaceous to locally grey or grey-green, weakly dolomitic siltstone and shale (Richardson and Moy, 1998). The Esperanza deposit has a significant supergene component in which copper species include digenite, djurleite, covellite and chalcocite (Richardson and Moy, 1998). The deeper hypogene component of the Esperanza ore system is dominated by chalcopyrite (Richardson and Moy, 1998).

The Mammoth Mine is located approximately 1.5 kilometres east of the Esperanza Mine (Figure 2.2). It is hosted by the Palaeoproterozoic Whitworth Quartzite, a buff to pale brown, thickly bedded, medium to coarse feldspathic quartzite (Hutton and Wilson, 1985). The Whitworth Quartzite dips to the west between 60º and 80º, striking roughly north-south in the mine area. The most significant mineralisation is located in the intersection of the north-south striking Portal Fault and the east-northeast trending Mammoth Fault. This mineralisation is hosted by several discrete orebodies (Figure 2.3) in dilational veins and breccias. The mineralisation is comprised of a range of copper species, dominantly chalcopyrite, bornite, chalcocite. The Whitworth Quartzite is unconformably overlain by the Surprise Creek Formation. The unconformity strikes north-south but dips at approximately 50º to the west, giving an angular discordance of 20º to 30º between units above and below (Clarke, 2003). The position of these two structurally controlled orebodies relative to the stratigraphy is shown in Figure 2.4.

A chlorite and hematite alteration suite is found proximal to both of the deposits. A large chloritic breccia crops out south of the Mammoth Mine, on Micks Fault to the west of the Portal Fault intersection. No copper mineralisation is associated with this breccia. At depth in the Mammoth Mine, the hematite alteration is associated with large faults (e.g. Mammoth and Mammoth Extended Faults) and has a clayey texture. The chlorite alteration at depth is usually confined to fault fills however in places in the footwall of D Lens, the chlorite alteration has been mapped as pervasive.

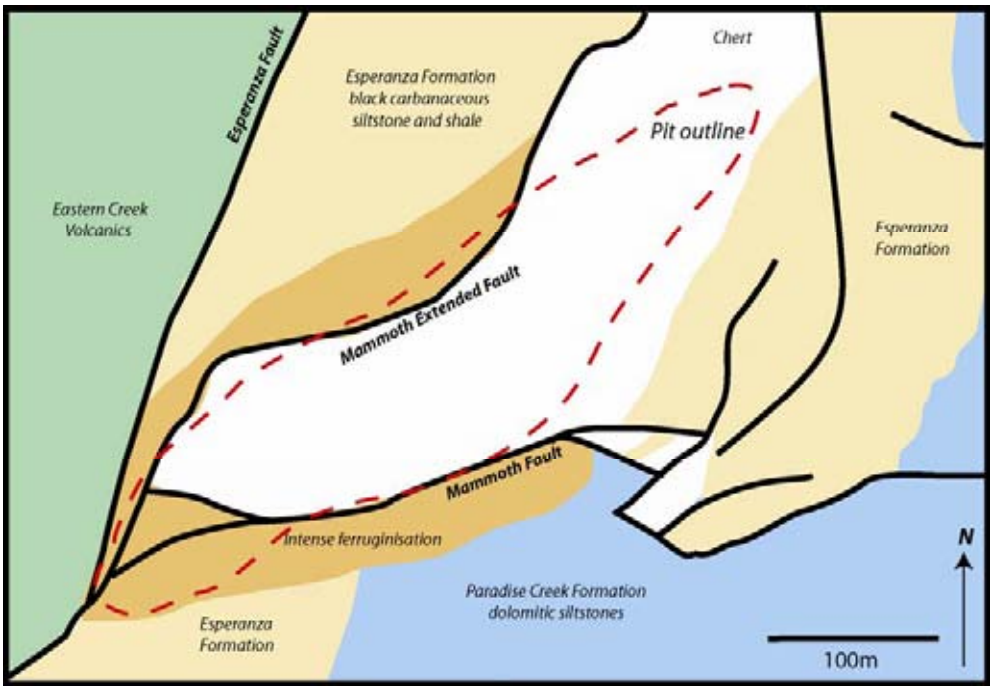

Figure 2.2 (adapted from Richardson and Moy, 1998). The Esperanza deposit occurs at the intersection of the Mammoth, Mammoth Extended and Esperanza Faults. The orebody sits below a laminated and brecciated chert supergene cap (white) and the deposit contains a large hematitic halo.

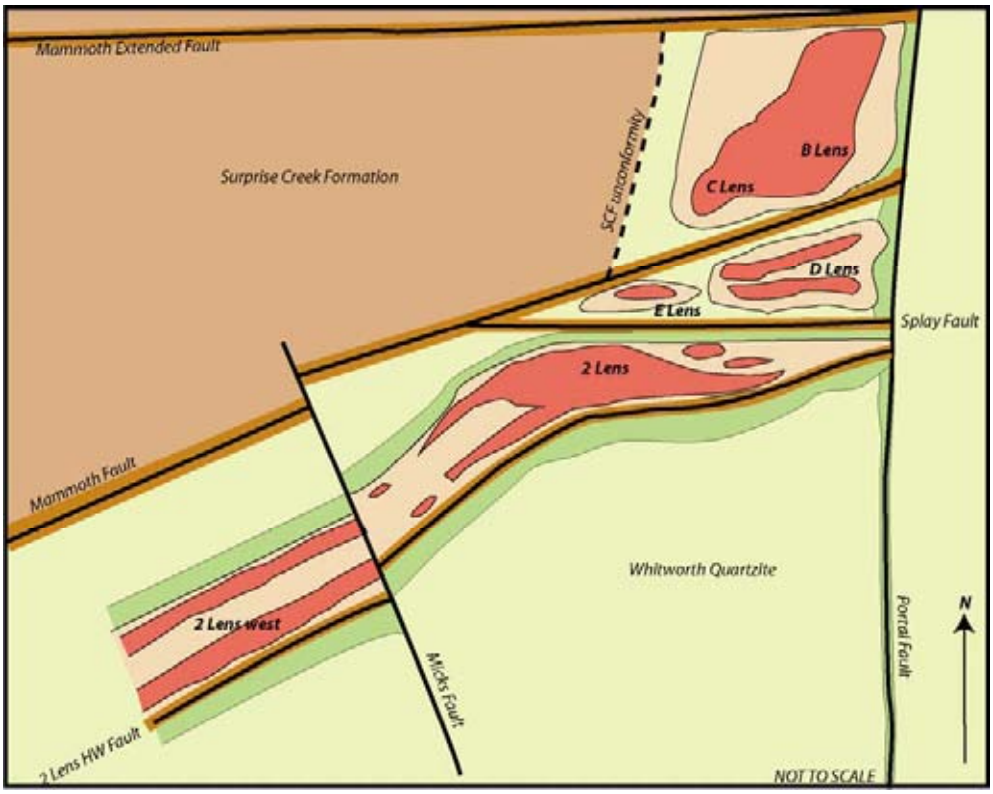

Figure 2.3 A plan view schematic diagram of the various Mammoth Mine orebodies (red) and their relative positions and orientations (adapted from Tear, 2005). The sub-grade breccias (pink) are encapsulated in a chlorite alteration halo (green) and the ENE striking faults commonly contain an earthy hematite alteration (brown). Both chlorite and earthy hematite are also present within ore zone faulting. To the east of the Portal Fault, the Whitworth Quartzite is relatively unbrecciated and unmineralised.

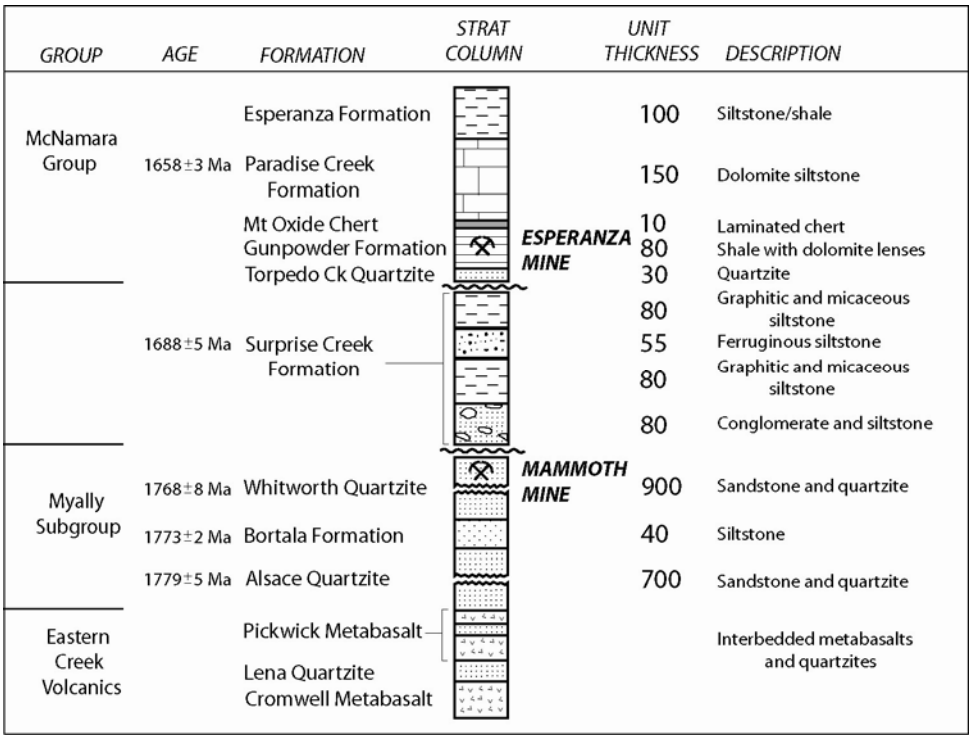

Figure 2.4 The Mt Gordon mine area stratigraphic column (adapted from Moore and Stoakes, 1975; Richardson and Moy, 1988). The column includes age dates (Foster, 2004; Neumann et al., 2006), lithological descriptions and unit thicknesses within the Esperanza and Mammoth Mine areas (Moore and Stoakes, 1975; Richardson and Moy, 1998).

2.3.1 Previous work on structural controls on mineralisation

The Mammoth deposit was first inspected by Commonwealth Government geologist C.S. Honman (1938) who described the Mammoth lode as “a replacement of a brecciated zone in quartzite and red sandstone … The ore occurs principally in the fractures of the breccia, and is associated with a fault or fissure of veined quartzite…”. Subsequent geological appraisals were conducted by government survey geologists (Shepherd, 1946; Brooks, 1957; Brooks, 1962).

A diagenetic model for the deposition of copper mineralisation at Mammoth was proposed by Mitchell and Moore (1975). They concluded that copper mineralisation in the No.1 Orebody was structurally controlled; associated with the intersection of strike-slip faulting with competent sandstone units.

Van Dijk (1986) made a significant contribution to the architectural story, suggesting that the Mammoth Fault was a steep subsidiary D_1 oblique ramp. Van Dijk (1986) interpreted the Portal Fault zone as a narrow NNW trending faulted F_3 fold, thus constraining the timing of the Portal Fault (and subsequently mineralisation) to syn-D_3. He inferred brecciation at Esperanza to be syn-D_3 also.

More recent studies have produced conflicting structural theories inferred for the orientation of the stress field at the time of mineralisation at Mt Gordon Copper Mines. Three main deposit structural studies are cited with regularity in in-house company reports:

1. Askew (1992) proposed ENE-WSW compression during D_3 timed mineralisation. This would have resulted in a dextral reverse sense of movement along the Mammoth and Mammoth Extended Faults;
2. ERA Maptec (Anonymous, 1994) proposed late N-S extension (D_3) along Mammoth and Mammoth Extended Faults, prior to late movements on the Portal Fault. σ_1 was thought to plunge steeply to the south (~60°). In the EW shortening event, a dextral sense of movement is invoked on the Mammoth Extended and Mammoth Faults; and
3. Connors (1997) proposed NE-SW transpression during D_4. Copper deposition was during D_4 sinistral reverse movement on the Mammoth and Mammoth Extended Faults.

The PhD completed by Clarke (2003) focused primarily on geochemical issues however he conducted a cursory review of the structural theories and favoured E-W shortening (sub-horizontal) during D_3 timed mineralisation.

2.4 3D Modelling of the Mammoth Mine

In order to gain an understanding of the distribution of mineralisation, brecciation, and alteration in respect to the mine scale faulting, the deposit was modelled using Leapfrog 3D, a software package by Zaparo Ltd. Leapfrog 3D is a 3D contouring and surface rendering package, that is well suited for visualizing deposits with a high density of drilling (Cowan *et al.*, 2002).

The 3D shells created in Leapfrog rapidly created mine scale models for copper abundance and location. As per the current site model, the highest grade copper was seen to occur in the Portal Fault hangingwall, in the Mammoth Fault-Portal Fault intersection. The footwall of the Portal Fault was seen to be unmineralised (Figure 2.5a, 2.5b, 2.5c), as was the Surprise Creek Formation west of the SCF unconformity.

3D modelling confirmed that the highest copper grades are coincident with the most intense brecciation (Figure 2.6). Chlorite alteration intensity, as logged by company geologists, was also able to be plotted. The plots show that weak chlorite alteration is coincident with copper mineralisation throughout the Mammoth Mine. When strong chlorite alteration was modelled it showed a distinct separation from the orebodies and was predominantly found to the south of the 2 Lens and D Lens orebodies (Figure 2.7).

Earthy hematite alteration was also modelled and its distribution was spatially similar to that of the chlorite. The hematite alteration intensity was seen to be particularly strong around faults, especially those in an ENE orientation such as the Mammoth Fault (Figure 2.8).

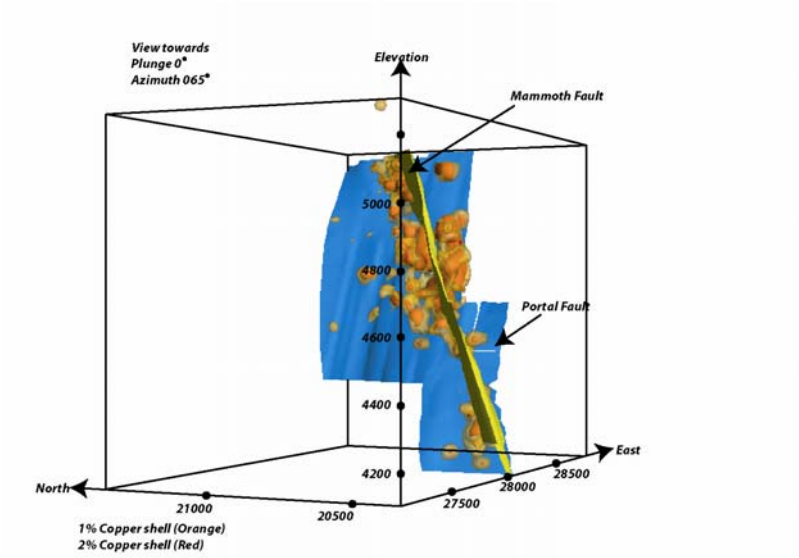

Figure 2.5a Oblique view looking along the Mammoth Fault. Leapfrog output of copper grade. The orange shell is 1% Cu, encapsulating a 2% Cu contour (red shell). The blue surface is the Portal Fault and the yellow surface is the Mammoth Fault.

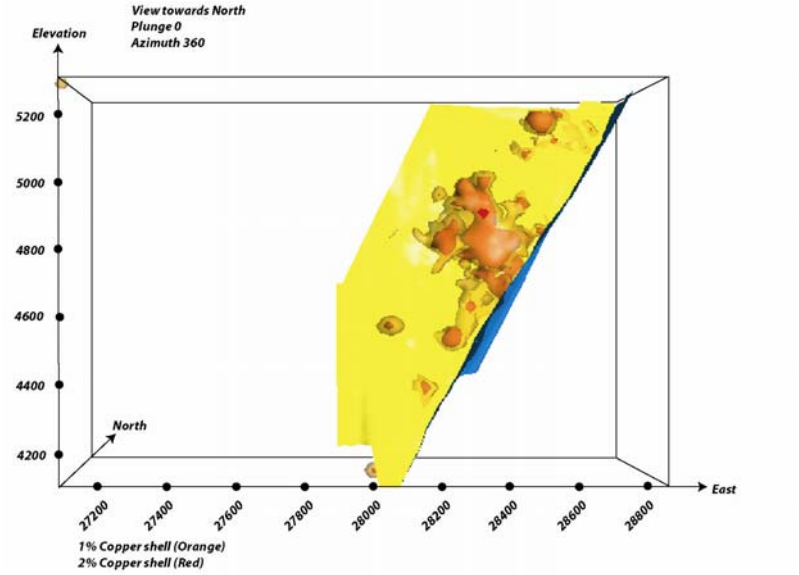

Figure 2.5b Section view of Mammoth Mine looking north. Shells and surfaces as per Figure 2.5a (above).

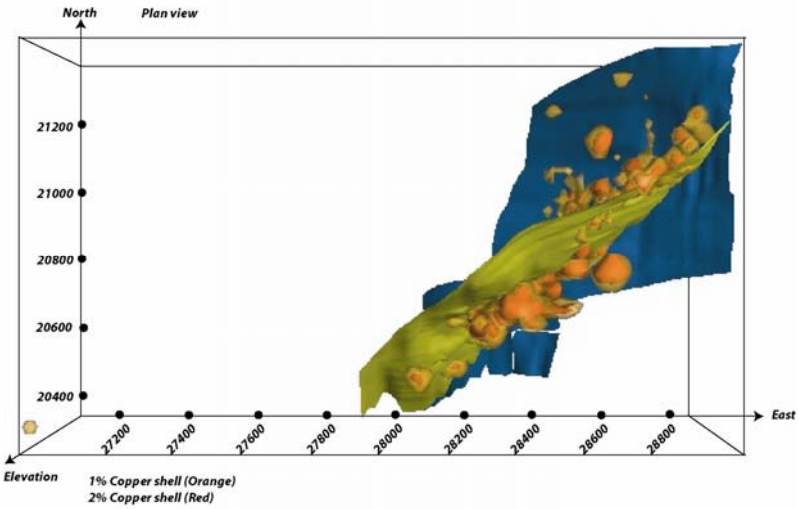

Figure 2.5c Plan view of Mammoth Mine. Shells and surfaces as per Figure 2.5a (above).

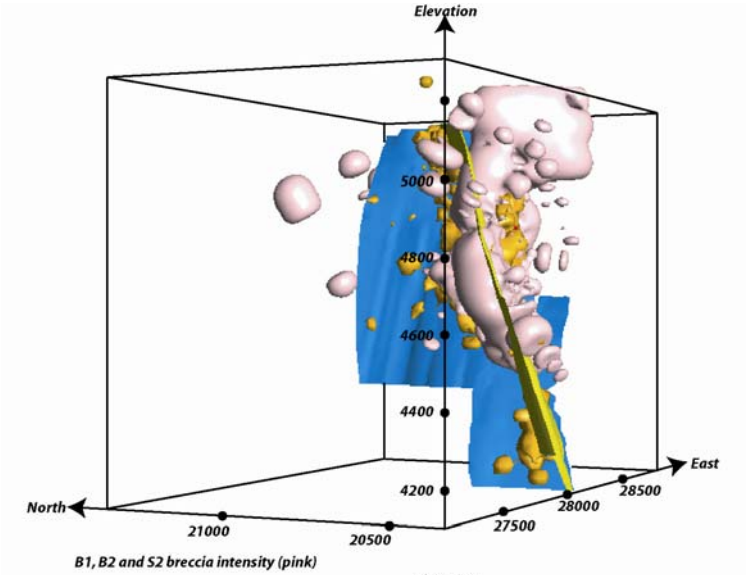

Figure 2.6 Leapfrog output of breccia intensity and copper grade. Pink shells represent the most intensely brecciated units and orange shell is 1% Cu. The blue surface is the Portal Fault and the yellow surface is the Mammoth Fault.

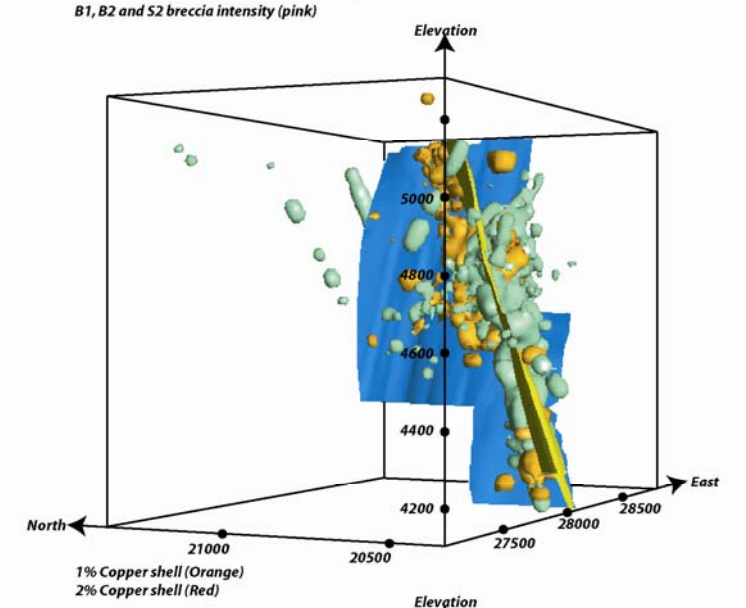

Figure 2.7 Leapfrog output of moderate chlorite alteration intensity (green) related to the 1% Cu shells (orange), Portal Fault (blue) and Mammoth Fault (yellow).

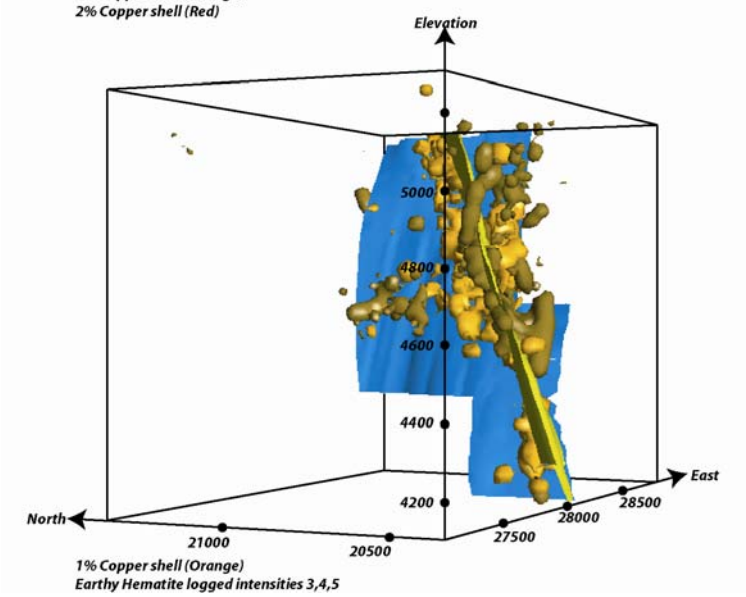

Figure 2.8 Leapfrog output of moderate earthy hematite intensity (brown) related to the 1% Cu shells (orange), Portal Fault (blue) and Mammoth Fault (yellow).

2.5 Structural Mapping of the Mammoth Mine

2.5.1 Methodology

As access was prohibited to the walls of the Esperanza open cut, the underground Mammoth Mine provided the best exposure to the mineralised breccias for structural mapping.

The Mammoth Mine is a large mine that is in the final stages of production. As the bulk of the orebody had already been mined, it was logistically difficult to access much of the mine. This in turn made identifying key areas to map a major problem. The Mammoth Mine has an extensive set of wire frames of major structures and breccia styles that have been mapped in drill core and via systematic underground drive mapping by company geologists (Figure 2.9).

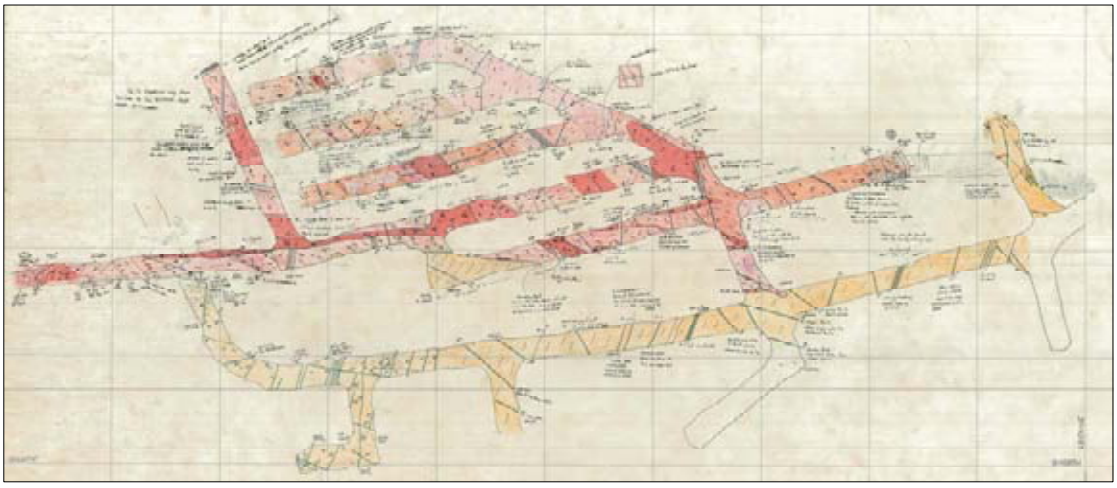

Figure 2.9 Example of company geologist level plan mapping. The 4825 rL level mapping completed by Aditya Birla geologists.

Orientations of faulting and intense brecciation were re-interpreted from the company level plan mapping in an attempt to constrain meso-scale controls on mineralisation.

The level mapping conducted in this study focused on recording fault orientations and striations, extension vein orientations and relative timing between faulting, veining and mineralization. The structural data collected was analysed and subsequently compared to structural data collected by Clarke (2003) and Richardson (2000). Fault-striation pair data was also obtained from the ERA Maptec (Anonymous, 1994) report, level plan mapping and the Clarke (2003) thesis.

Fault orientation and fault striation pairs were compiled for use in stress inversion. The Multiple Inverse Method (Yamaji, 2000) was used to determine which of the fault-striation pairs formed in the same deformational event. Conventional stress inversion, P and T dihedra method (Angelier, 1984), was then conducted on the consistent fault striation pairs. The P and T dihedra method is able to constrain the orientations of the principal stresses but is unable to deliver a ratio of these stresses. The fault-striation pair analysis was further validated using Slick (Ramsay and Lisle, 2000), a stress inversion program, that is also able to provide a best fit ratio of principal stress tensors.

2.5.2 Mammoth Mine Faulting

The ENE striking Mammoth and Mammoth Extended Faults, together with the NS striking Portal Fault are the dominant structural features within the Mammoth Mine. They are continuous through to surface, are found in close proximity to mineralisation, have fills of earthy hematite and consequently have produced a range of geotechnical issues in the underground mine.

There are however other orientations of faults, some of which have an association with mineralisation, that have often been neglected in previous studies. Prior to the collection of any data in this study, company geologist mapping was interrogated for fault orientation, characteristics and any relevant kinematic data, summarised below.

Table 2.1 Fault characteristics compiled from level plan mapping (mapped by company geologists). Movement sense of the faults is determined by company geologists during underground mapping.

Fault Strike	Fault Dip	Movement Sense	Fault Spacing	Associated Alteration	Example
070-080	Steeply south	Dextral-reverse	~ 50 m	Mineralisation, earthy hematite	Mammoth, Mam Extended, 2LHW Faut
120-130	Steeply south	Sinistral	~ 20 m	Mineralisation, earthy hematite, chlorite	Micks Fault
170-190	Steeply west or east	Reverse	~ 50 m	Mineralisation, earthy hematite	Portal Fault
220-230	Steeply west	?	~ 20 m	Hematite, chlorite	faults in 2 Lens HW.

2.5.3 Mammoth Fault and similarly oriented faulting

Several striations identified on the Mammoth and Mammoth Extended Fault surfaces (Figure 2.10a, 2.10b) pitch at low angles (~15° E) supporting dominantly strike-slip movement on these E-W to ENE-WSW oriented faults. Clarke (2003) identified these striations as being

consistent with north block east movement (dextral sense) and this is supported by steps on slickenlines observed during this study. Clarke (2003) also observed a second set of steeper, east plunging striations on these faults that were overprinted by the shallower (~15° E) set of striations. A sense of movement was unable to be obtained off the steeper, older striations.

The later stage, shallow, dextral movement on the Mammoth and Mammoth Extended Faults is inferred to be related to mineralisation. Fault plane solution plots (Figure 2.10c) for the Mammoth Fault are consistent with a dextral-reverse sense of movement on the Mammoth and Mammoth Extended Faults.

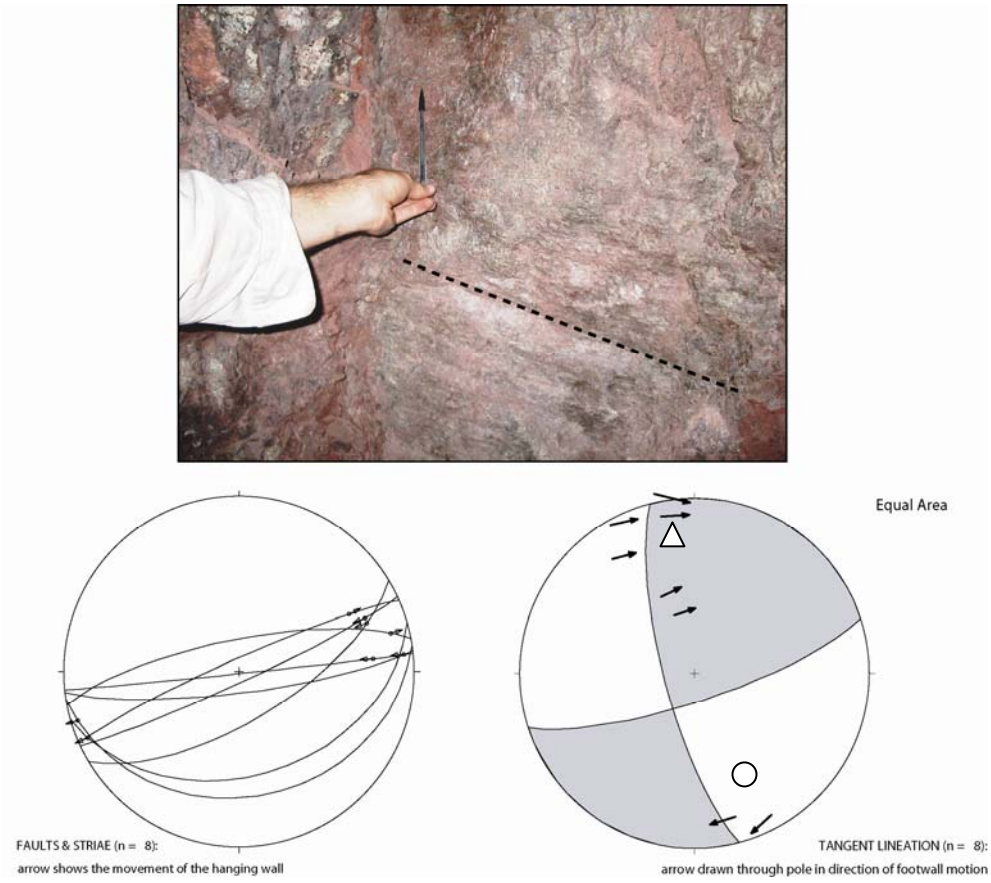

Figure 2.10 ***(a)*** *Looking north onto the FW of a Mammoth Fault parallel in the 4745 W1ext. The striations (parallel to the dashed line) step ~15° up to the west giving a dextral reverse sense of movement. The fault contains an earthy hematite fill and in this location is within the 2 Lens orebody.* ***(b)*** *Stereographic projection of fault and striation data for Mammoth Fault and associated smaller parallel faults (data collected by Keys, this study, and collated with data from Clarke, 2003). The great circles reflect the orientation of the fault plane and the arrows indicate the direction of hangingwall transport.* ***(c)*** *Fault plane solution plot for the data presented in (b). The darker shaded areas reflect areas in tension with the white representing areas in pressure. Hence the triangle reflects an approximate position of* σ_3 *based on this data and the circle being the approximate position of* σ_1*. The dark arrows indicate the footwall transport direction. Equal area stereonet projection used, north is up on all stereonets.*

2.5.4 130º Striking Fault Set

Micks Fault is the largest example of the 130 striking fault set in the Mammoth Mine and displaces the 2 Lens orebody to the south. Micks Fault strikes northwest, between 120°-130° (Figure 2.11a) and dips subvertically. Smaller faults of this orientation are frequently seen in the underground mapping data from all Mammoth orebodies. These faults typically dip steeply to the northeast and are intimately associated with mineralisation in the Mammoth Mine. Ore bearing breccias commonly form parallel and in close proximity to the 130° faults. Their influence on mineralisation has not been previously documented.

The 130° striking fault set is also associated with fault fills of chlorite and lesser hematite, particularly in the hangingwall and footwall of the deposit.

The 130° oriented faults are consistently mapped by company geologists as having an apparent sinistral sense of displacement. Within the mine these faults have preserved shallow slickenlines.

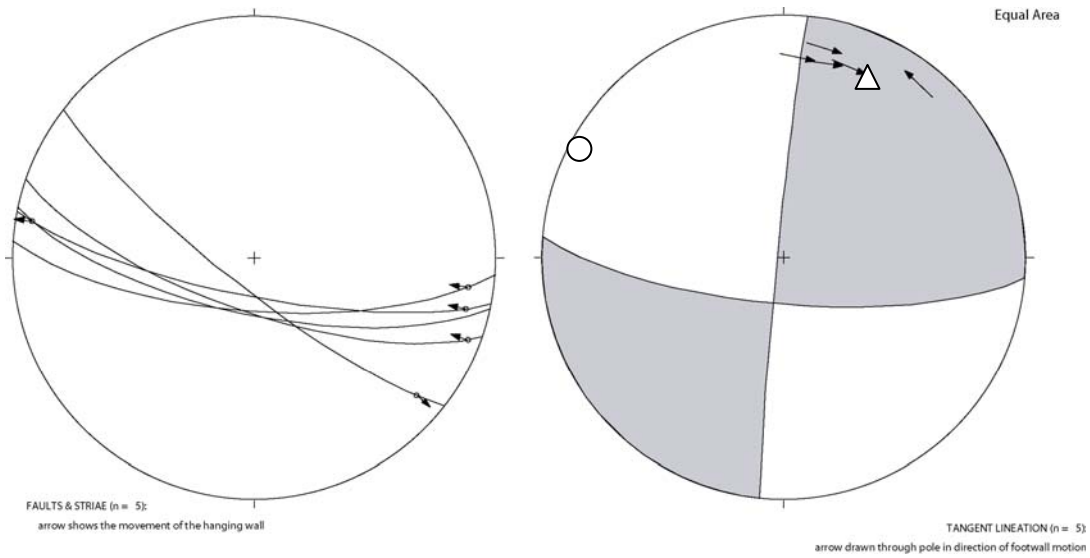

Figure 2.11 ***(a)*** *Stereographic projection of fault and striation data for the 130 striking fault set (data collected by Keys, this study, and collated with data from Clarke, 2003). The great circles reflect the orientation of the fault plane and the arrows indicate the direction of hangingwall transport.* ***(b)*** *Fault plane solution plot for the data presented in (a). The darker shaded areas reflect areas in tension with the white representing areas in pressure. Hence the triangle reflects an approximate position of σ_3 based on this data and the circle being the approximate position of σ_1. The dark arrows indicate the footwall transport direction. Equal area stereonet projection used, north is up on all stereonets.*

2.5.5 Portal Fault Set

Because the bulk of the Mammoth Mine mineralisation is localised in the Portal Fault-Mammoth Fault intersection, the Portal Fault has long been considered an important ore localising feature (Askew, 1992; Connors, 1994; Anonymous *ERA-Maptec*, 1994). The Portal Fault itself varies in strike between about 160° to 180° and dips west at approximately 70° (Figure 2.12). It crops out at surface, where it has little surface expression. Both steep and shallow striations are commonly found on the Portal Fault. The ERA Maptec (Anonymous, 1994) mapping campaign focussed almost exclusively on the steep southerly plunging set of striations. They invoked a reverse sense of movement on the Portal Fault due to S and C fabric relationships. A shallower set of striations was recorded by Clarke (2003), level plan mapping (company geologists) and in this study. Clarke (2003) also preferred a reverse sense of movement (west block up) on the Portal Fault.

The Portal Fault contains an earthy hematite fill and has an obvious proximal relationship to mineralisation.

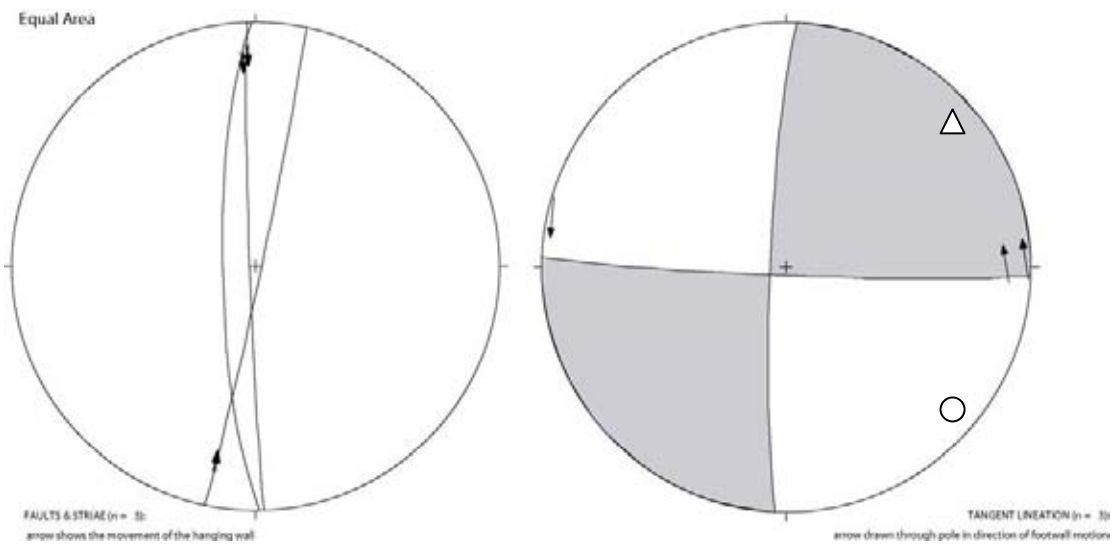

Figure 2.12 ***(a)*** *Stereographic projection of fault and striation data for the Portal Fault set (data collected by Keys, this study, and collated with data from Clarke, 2003). The great circles reflect the orientation of the fault plane and the arrows indicate the direction of hangingwall transport.* ***(b)*** *Fault plane solution plot for the data presented in (a). The darker shaded areas reflect areas in tension with the white representing areas in pressure. Hence the triangle reflects an approximate position of σ_3 based on this data and the circle being the approximate position of σ_1. The dark arrows indicate the footwall transport direction. Equal area stereonet projection used, north is up on all stereonets.*

2.5.6 North East Striking Fault Set

The north east striking fault set is the least common orientation of faulting in the Mammoth Mine. These faults commonly dip steeply to the east or west. This set of faults is best developed in the hanging wall (south) of 2 Lens, D Lens and E Lens (Figure 2.13). In this hangingwall position the north east faulting can occur as regularly as 1 fault per 5 metres. This amount of faulting is never seen within the breccia hosted orebodies. This could be attributed to

1. the NE faulting being earlier than brecciation and obliterated through the breccia process
2. the NE faulting occurring after mineralisation and terminating on the rheologically softer copper sulphide body

The north east faulting also contains a set of striations, commonly plunging between 15º and 40º to the SE.

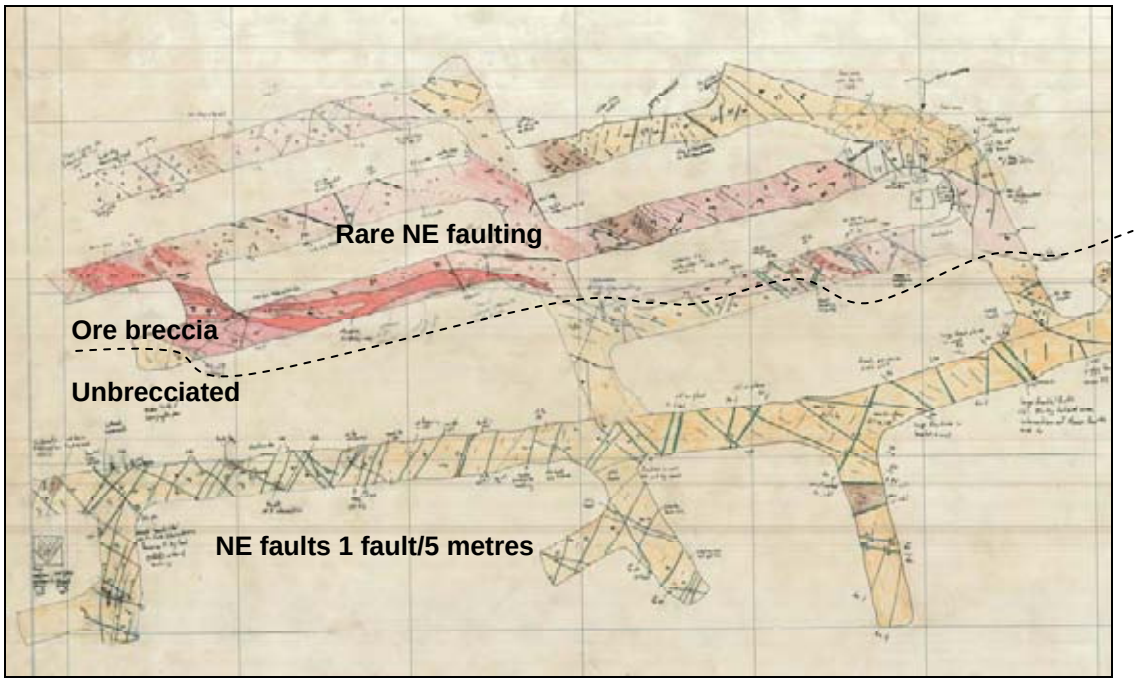

Figure 2.13 The 2 Lens orebody on 4785 rL showing the intensity of NE to NNE striking faulting in the hangingwall quartzites (yellow). This intense NE striking faulting is not observed in the ore zone (reds and pinks). The green colour of the fault traces indicates the presence of chlorite on or in those fractures.

2.5.7 Stress inversion of Mammoth Faults

The measurement locations of the Clarke (2003) fault-striation data pairs are unknown. Although spatially the data is poorly constrained, it is still quite useful in determining potential shortening orientations.

In order to determine whether the striated faults were active under the same stress field, the Multiple Inverse Method (Yamaji, 2000) of stress inversion was adopted. The Multiple Inverse Method is used to separate stresses from heterogeneous fault-slip data without *a priori* information on the stresses or on the classification of faults according to the stresses (Yamaji, 2000). The method produces values of σ_1, σ_2 and σ_3 as well as a ratio of the principal stress tensors (phi value) and relates the misfit angles of the data through a table or stereographic plot. If the misfit angle of the fault-striation data is greater than 20º the fault movement is deemed to be unrelated to the stress orientation (Yamaji, 2000).

Multiple Inverse Method (MIM) stress inversion was conducted for all fault striation pairs recorded. Of these pairs, the data from the Mammoth parallel faulting (shallow striations), Portal Fault parallel faulting and 130º oriented faulting were related to each other. The NE striking faults however are considered unrelated. The orientation of σ_1 was 8º towards 116º (Figure 2.14a, 2.14b) with σ_3 being oriented 14º to 024º (Figure 2.14c). There was not enough data to constrain any orientations of σ_1, σ_2 or σ_3 for the NE striking fault set. Although it is a valuable tool for discriminating separate stresses from heterogeneous data, the MIM relies on a degree of user input and is therefore be open to some conjecture over the validity of inversion results. Alternate stress inversion techniques were employed to clarify any ambiguity over the orientations of the principal stresses and their ratios.

The P and T dihedra for the faults deemed to be related by the MIM were plotted to confirm an approximate orientation for σ_1 (Angelier, 1979; Angelier, 1984). Orife and Lisle (2006) stated that stress estimates based on less than eight faults should be treated with grave suspicion. The total data utilised for these stress analyses numbered 16. The preferred orientation of σ_1 from the P and T dihedra plots was horizontal toward 127º (Figure 2.15). Hence σ_3 is oriented horizontal toward 037º. This technique does not however provide a ratio of the principal stress tensors (phi value).

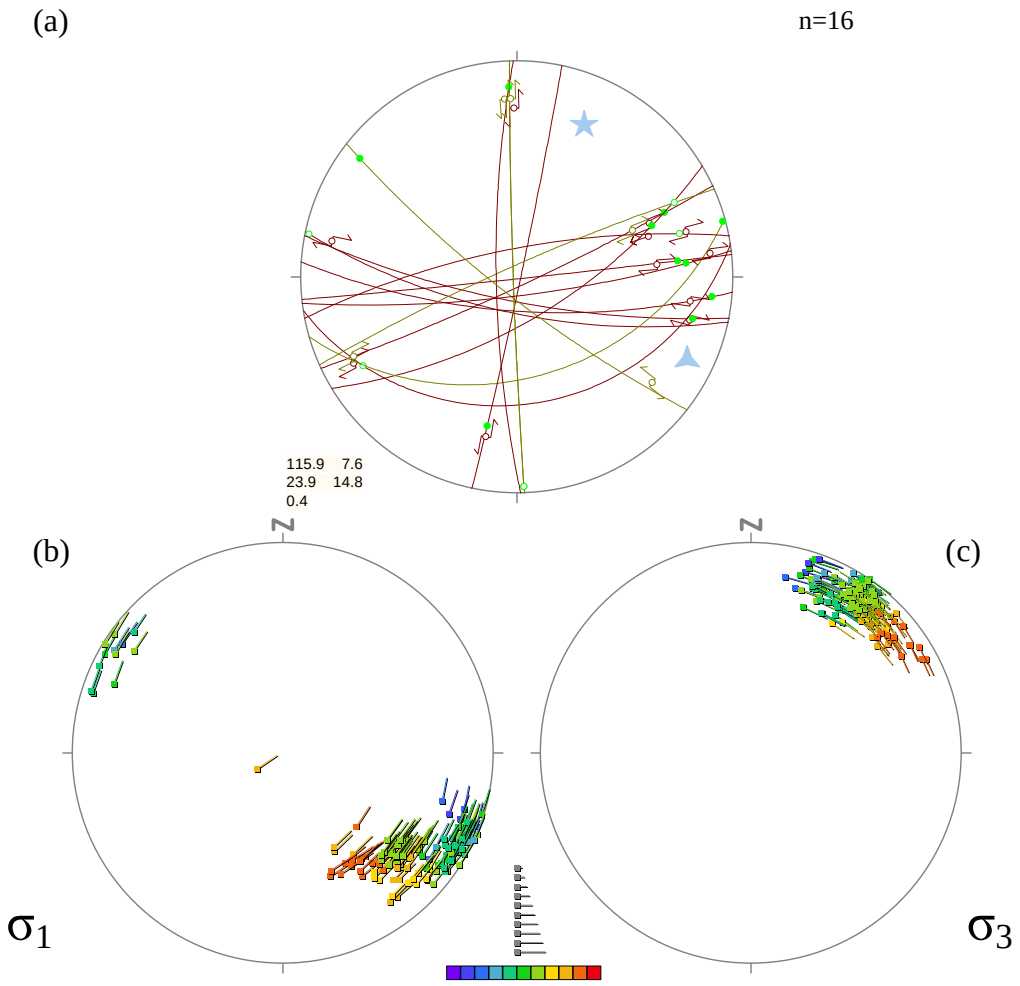

Figure 2.14 Palaeostress analysis using the Multiple Inverse Method ***(a)*** *Stereonet of all fault and striation pairs. The blue triangle represents a best fit σ_1 with the blue star representing σ_3 (Yamaji et al, 2000).* ***(b)*** *Output showing the preferred σ_1 orientations from Multiple Inverse Method Software (Yamaji et al, 2000). The "tadpoles" show stress inversion solutions for different possible phi values. The position of the head of a tadpole symbol indicates a σ_1 orientation. The clusters indicate that all fault and striation pairs inputted can be attributed to the same stress event and that the σ_1 orientation of that stress event was shallow and ESE-WNW.* ***(c)*** *Output showing the preferred σ_3 orientations from Multiple Inverse Method Software (Yamaji et al, 2000). In this instance "tadpole" head reflects a σ_3 orientation and the tails reflect the azimuth and plunge of the σ_1 orientation.*

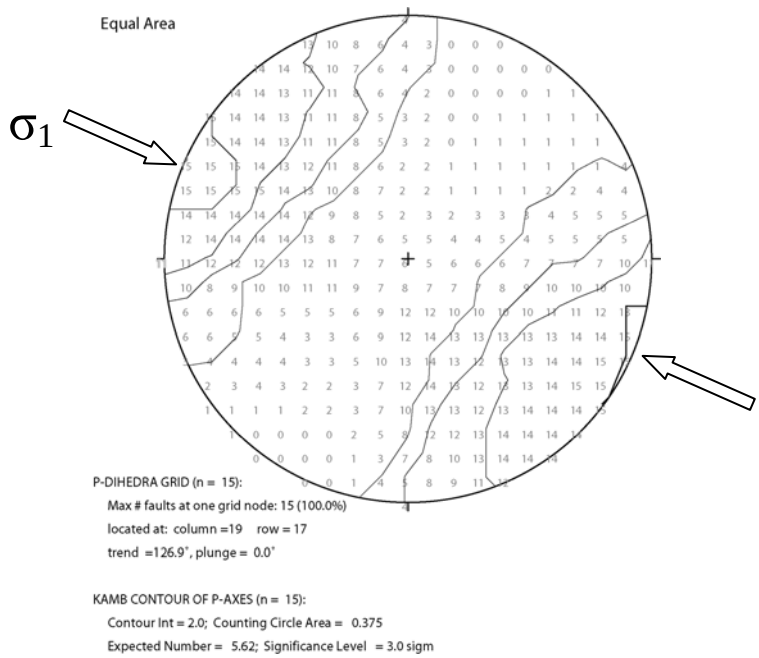

Figure 2.15 P solution grid for fault striation data proven valid in the Multiple Inverse Method inversion (see Figure 2.14a). Kamb contours for the P dihedra grid showing an approximated best fit σ_1 orientation of horizontal toward 127º.

Slick, software developed by Ramsay and Lisle (2000) finds the stress tensor by a trial-and-error method. The search for the best-fit tensor involves changing progressively each of the four variables (σ_1, σ_2, σ_3 and Φ) until a complete range of tensors is considered. Each tensor is used to calculate the direction of shear stress on each of the fault planes and these calculated directions are compared with those of the measured slip lineations. The program assesses the quality-of-fit by recording the mean deviation between observed and calculated slip directions (from slickhlp.txt, Ramsay and Lisle, 2000). As this process does not require a fault slip movement sense, two answers are produced (Figure 2.16).

Based on the similarity to the results of the other stress inversion techniques (Multiple Inverse Method and P and T dihedra) the preferred σ_1 orientation from Slick was 12º to 118º, σ_2 was 71º to 244º and σ_3 was 15º to 025º. A phi value of 0.3 was produced.

The Multiple Inverse Method relies somewhat on the user's interpretation of the best fit to the data and the P and T dihedra don't produce a phi value. The Slick value is derived by computing best fit stress tensors to the mapped data. Thus the Slick outputs are deemed to be the most reliable of the stress inversions conducted. In any case the three methods produce similar results (Table 2.2).

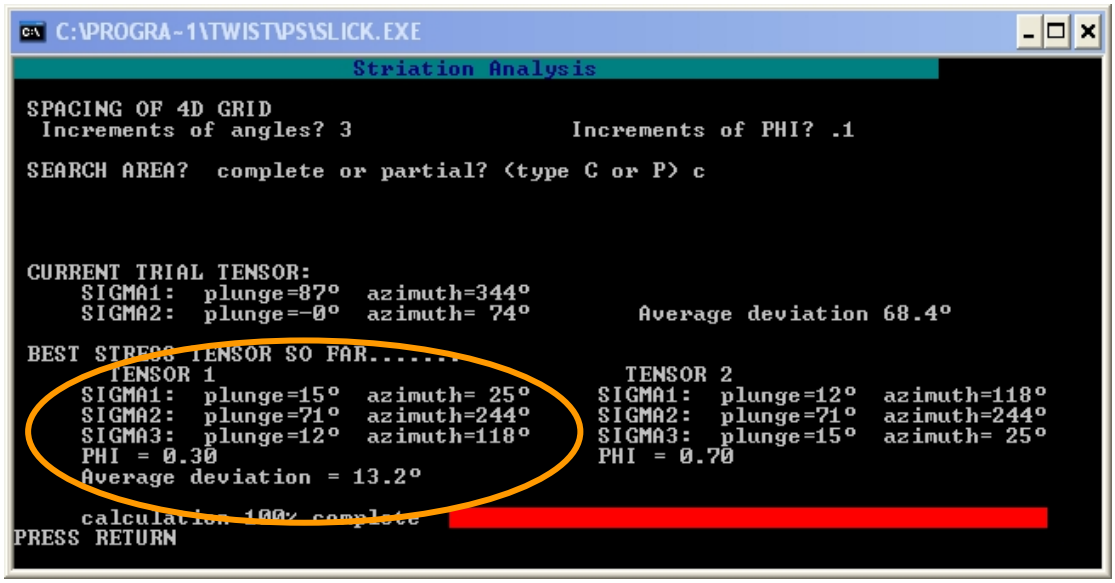

Figure 2.16 Slick (Ramsay and Lisle, 2000) output file. Two best fit stress tensor orientations are produced because no fault slip movement sense is used as input. Recalling that phi as calculated by Slick (Ramsay and Lisle, 2000) differs from the phi calculated by Angelier (1989) (see Chapter 1.4.3) then the orientation of Tensor 1 would give σ_1 of 118º (here shown as σ_3). Tensor 1 (circled) is seen to best fit the recorded data, and is a good match with the other methods.

Table 2.2 A summary of stress inversion outputs from each of the inversion methods used.

Stress Inversion Technique	Papers	σ_1 plunge	σ_1 azimuth	σ_2 plunge	σ_2 azimuth	σ_3 plunge	σ_3 azimuth	Phi
Multiple Inverse Method	*Yamaji, 2000*	*8*	*116*			*24*	*014*	*0.4*
P and T Dihedra	*Anglier, 1984*	*0*	*126*	*90*	*-*	*0*	*036*	*-*
Slick	*Ramsay and Lisle, 2000*	*12*	*118*	*71*	*244*	*15*	*025*	*0.3*

2.6 Mammoth Mine orebody breccias

The brecciation within the Mammoth Mine initiated with a period of open space filling, as indicated by the occurrence of coarse grained and crystalline pyrite followed by Cu and Cu-Fe sulfides (± chlorite) (Clarke, 2003). Replacive hydrothermal alteration and open space filling by sulfides seen in all Mammoth Mine breccias and stockworks, indicate that the alteration and mineralisation were linked to the breccia and stockwork processes. (Richardson and Moy, 1998; Clarke, 2003).

Clarke (2003) devised a new method for categorising the Mammoth Mine breccias (Table 2.3). Logging and mapping of mine breccias by company geologists has since been tailored to fit the Clarke breccia codes.

Table 2.3 Clarke (2003) breccia classification system.

Unit	Characteristics	
Unfractured Host Rock	**S0** ▪ No significant veins, fracture patterns, or brecciation developed	
Fractured Host Rock	**S1** ▪ **<** 100 veins over 1 metre ▪ Individual veins are typically <4 mm thick ▪ Veins consistently cross cut at a high angle to each other ▪ No significant wall rock bleaching at the hand specimen scale	**S2** ▪ **>** 100 veins over 1 metre ▪ Localised in situ brecciation ▪ Replacement of host rock components by sulfides along vein edges ▪ Veins consistently cross cut at a high angle to each other ▪ Significant wall rock alteration is often visible at the hand specimen scale
Brecciated Host Rock	**B1** ▪ Clast supported breccia ▪ Subangular to rounded clasts ▪ Clasts **rarely** contain disseminated sulfides	**B2** ▪ Matrix supported breccia ▪ Rounded clasts dominate ▪ **Common** replacement of breccia clasts by sulfides

The bulk of the company level plan mapping that has incorporated the breccia criteria of Clarke (2003) is from 2, D and E Lens. The focus of the breccia analysis will therefore be on these three orebodies. Level plan mapping showed two distinct orientations of intense brecciation (B2 – Clarke breccia code) in the vicinity of 2 and D Lens. These orientations have significance when trying to determine which faulting is critical for ore stage breccia development.

Level plan mapping shows two preferred orientations of intense brecciation. The first orientation is an E-W to ENE-WSW trending intense breccia set, parallel to the overall 2 Lens orebody orientation (Figure2.17; Figure 2.18; Figure 2.19).

These breccias are often closely associated with smaller faults that are parallel to the Mammoth Fault. The second orientation of intense breccia is oriented NW-SE (striking ~130°) and is well developed around faults of the same orientation (Figure2.17; Figure 2.18; Chapter 2.5.4.130° Striking Fault Set). This suggests that the intense mineralised breccias formed in response to movement on these 130º faults or that the mineralised breccias have been re-oriented post mineralisation into the 130º orientation.

The 130º breccias are also seen to locally cross cut the ENE striking fault set with little displacement (Figure 2.17) implying that during breccia formation the gross net movement on the ENE striking fault set was minimal.

However, when the faults cross-cut each other the fault-slip timing relationship is less clear. Locally the 130 faults experience small dextral offsets when crossing the ENE striking fault set. Likewise, there appears to be small sinistral offsets of the ENE striking fault set across the 130 fault set.

The fault striation data collected from these faults show that they were active under the same far-field stress regime (Chapter 2.5.7) which implies that the faults experienced small, variable displacements locally.

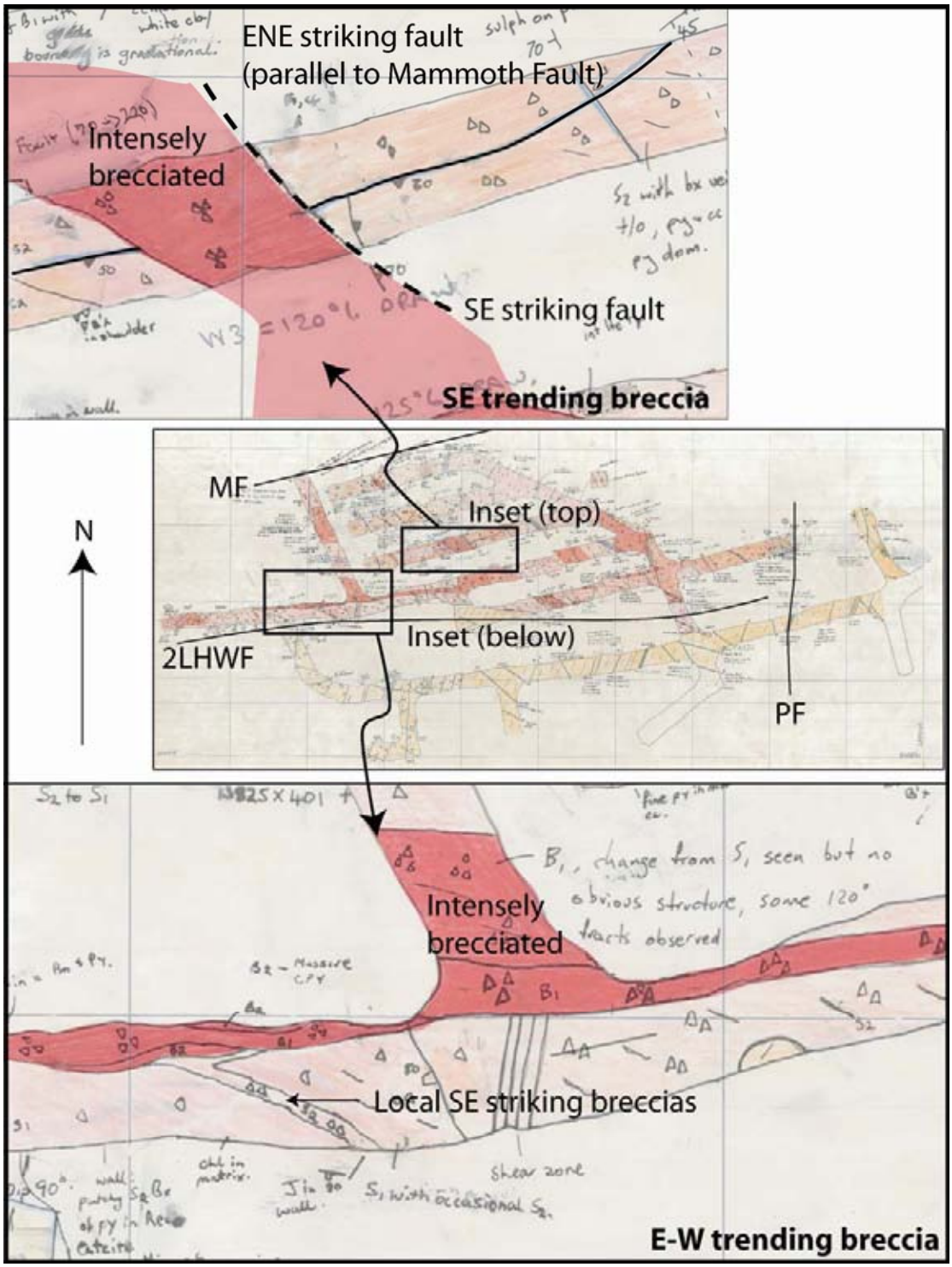

Figure 2.17 Intensely brecciated unit (red) cutting an ENE striking fault parallel to the Mammoth Fault. The intense breccia is found in the footwall of a steeply NE dipping 130º striking fault .Mapping is of 4825rL W3 120 DPT, in the middle of 2 Lens, from Aditya Birla company geologist mapping.

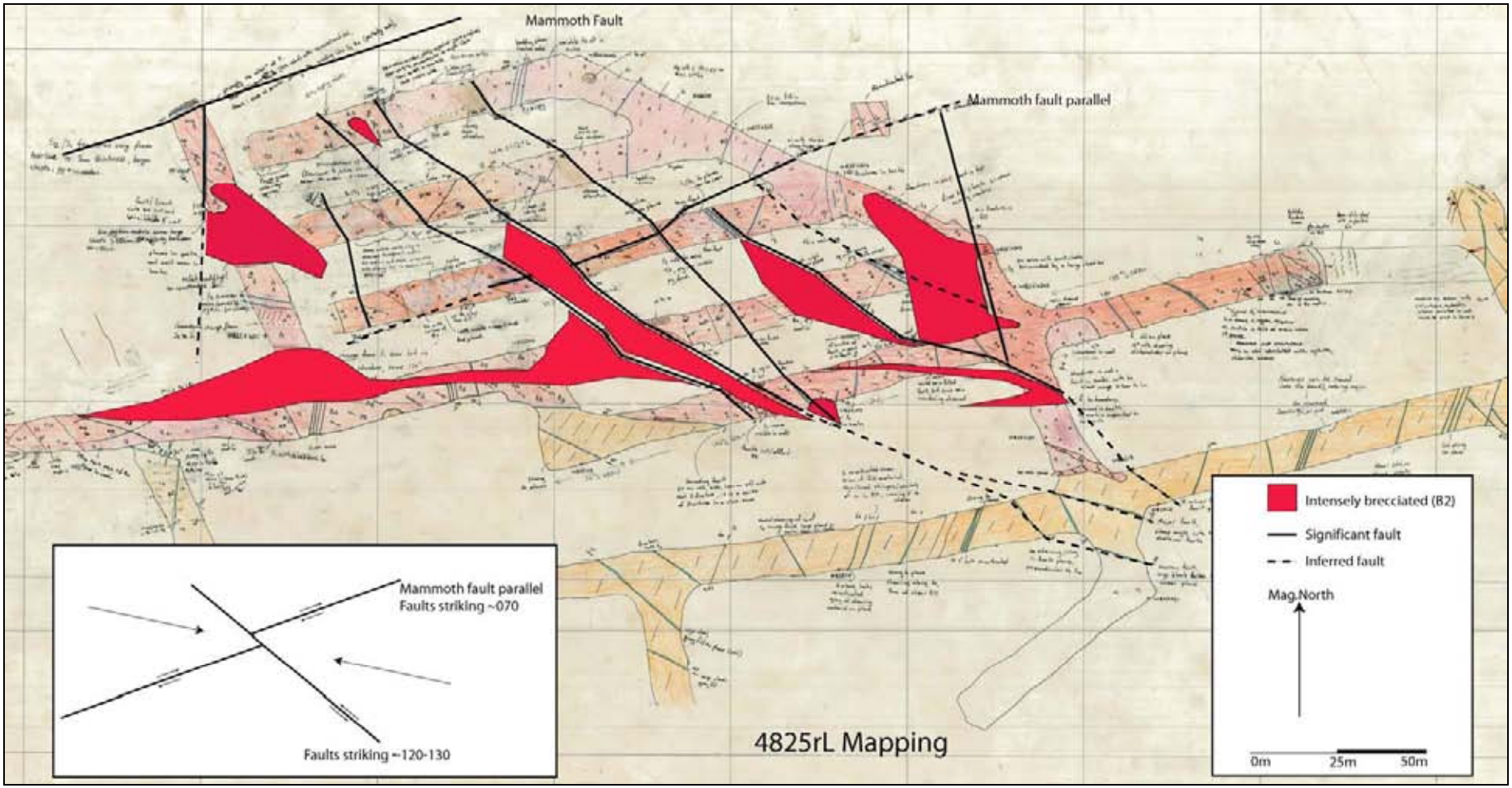

Figure 2.18 4825 rL level plan mapping showing interpreted faulting and relationship to the most intense brecciation (B2 breccias of Clarke, 2003). Two preferred orientations of breccia can be seen. One breccia set is oriented along 130° and appears related to similarly oriented faults. The other east - west trending breccia has a closer affinity with the small ENE striking fault, parallel to the Mammoth fault. The yellow shading represents unbrecciated, unmineralised Whitworth Quartzites. The pink shading relates to variably brecciated, copper bearing Whitworth Quartzite.

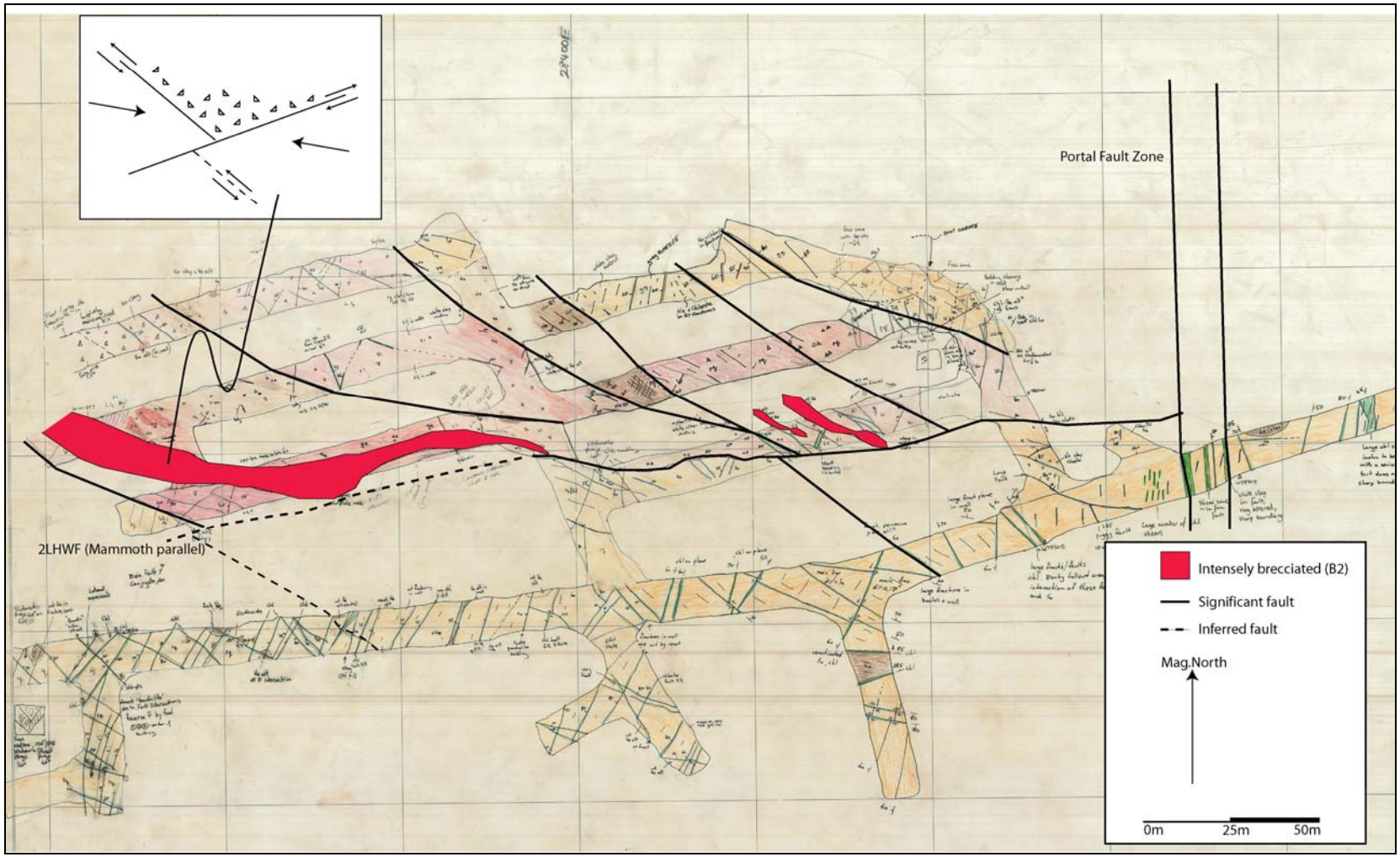

Figure 2.19 4785 rL level plan mapping showing interpreted faulting and relationship to the most intense brecciation (B2 breccias of Clarke, 2003). Two preferred orientations of breccia can be seen. One breccia set is oriented toward 130° and appears related to similarly oriented faults. The other, an east west trending breccia, has a closer affinity with the 2LHWF; a smaller fault parallel to the Mammoth Fault. The intersection of the 2LHWF and the 130° fault (see inset) reflects the thickest part of the intense breccia.

2.7 Conclusions of underground mapping study

Late deformational, dextral strike-slip movement on the Mammoth and Mammoth Extended Faults, as indicated by low angle striations (Figure 2.10) appears to be related to the copper mineralising event at Mammoth.

Reinterpretation of level plan mapping shows two orientations of intense mineralised brecciation. The most intense breccias are typically either oriented E-W or NW-SE. The E-W trending breccias are always located in close proximity to the 070º oriented faults (Mammoth Fault parallels). The NW-SE breccias are bound by faulting of similar orientation (130º Fault set) and it would appear these faults were active at the time of mineralisation.

Using several methods, it is apparent that the bulk of the mineralisation was emplaced during horizontal shortening with σ_1 oriented shallow towards 116º. This is different from the proposed orientations of σ_1 from previous authors.

Stress inversion completed on faulting active during mineralisation in the Mammoth Mine, shows a sub-horizontal orientation for both σ_1 and σ_3. This contrasts with the model of ERA Maptec who proposed a moderately north plunging σ_3 orientation. The stress inversion and fault plane solution also ruled out the proposed σ_1 orientations of Askew (1992) and Connors (1997). The Connors (1997) proposed NE – SW shortening orientation does not account for the“unfavourably oriented 130º breccias.

PART 2 – NUMERICAL MODELLING

2.8 Introduction

The results and conclusions from the mapping component of this study (Chapter 2 – Part 1) contradicted the conclusions of previous authors. The numerical modeling approach was designed to independently test the differing structural theories.

The ability to rapidly simulate the effects of deformation through numerical modelling helps to resolve conflicting structural theories, as at the Mt Gordon Copper Mines. Such modelling can have predictive capability when input data are appropriate.

Distinct element modelling of deforming rocks has been used to determine the magnitudes and orientations of stresses in many mineralised terranes (Oliver et al, 1990, 2001; Jiang et al, 1991; Holyland and Ojala, 1997; Mair et al, 2000; McLellan and Oliver, 2007). This so-called “stress mapping” attempts to produce numerical, spatial solutions of the stress field to meshes of rock and boundary properties (Chapter 1). UDEC, Universal Distinct Element Code (Itasca, 2000), is best applied to upper crustal epigenetic hydrothermal mineral deposits, where fluid flow is focussed in faults, rather than through the bulk rock mass (Mair *et al*, 2000). Much of this type of stress mapping is carried out in two dimensions in plan view using geological maps partly due to the computational difficulty of running and visualising 3D problems. It is suitable for terranes with steeply dipping lithostratigraphy and faults, and an inferred strike-slip movement on those contacts. The effectiveness of this numerical modelling is maximised if mineralisation was late in the evolutionary history of the host terrane, and hence the structural geometry of the terrane and contained deposits similar to that observed today (Mair *et al*, 2000). In this situation, a knowledge of the total strain history is not required; rather, if it is assumed that mineralising fluids were late, then the present geometry becomes a reasonable approximation of the geometry at the time of mineralisation (such that there is little geometrical change over the duration of the mineralising event). This assumption can be tested by comparing the results to independent determinations of the mineralising stress field, such as that presented in the previous sections. Mt Gordon with its steeply dipping faults, predominant strike-slip movement and late-stage deformation related to epigenetic mineralisation, is an ideal candidate for UDEC modelling. Mt Isa and Ernest Henry have a

greater degree of complexity and more protracted ductile histories so the model results need to be treated more cautiously (Chapter 3; Chapter 6).

2.9 Modelling Assumptions and Evidence

Underground mapping (Richardson , 2000; Clark, 2003; and this study) and 3D orebody modelling (Chapter 2.4) in Leapfrog 3D provided much of the background data for the inputs made to the numerical modelling, along with surface mapping by Crossing (2004)

Mineralisation is hosted in large breccia zones at both Mammoth and Esperanza. Breccias vary in style from the S1 local breccia class comprising weakly fractured host rock (Clark, 2004) to the B2 local breccia class comprising rounded breccia clasts in a dominantly sulphide matrix (Clark, 2004). Breccias can also vary in composition from chlorite and hematite dominated breccias to infills dominated by chalcopyrite, bornite or chalcocite. The chlorite-hematite breccias have a spatial association with mineralisation (Chapter 2.4) and will therefore be used to validate areas of the numerical model outputs, e.g. the chlorite-hematite breccia mapped at the intersection of the Portal Fault with Micks Fault (Crossing, 2004).

There is a spatial and temporal relationship between faulting and mineralisation at both the Mammoth and Esperanza Mines. Previous studies (van Dijk, 1986, Askew, 1992; Anonymous (ERA Maptec), 1994; Connors, 1997; Richardson and Moy, 1998; Clark, 2003) have all constrained mineralisation to be syn- or post- regional D3 (Bell *et al.*, 1988). These studies have also documented the rock mass failure associated with mineralisation to be directly attributed to fault slip during during deformation. The evidence for the rock mass failure relationship to mineralisation is the presence of the mineralised breccias (Richardson and Moy, 1998; Clark, 2003) and mineralised extension veins (Richardson, 2000) at both the Mammoth and Esperanza deposits. This rock mass failure occurs concurrently in the Gunpowder Creek Formation (Esperanza Mine) and the Whitworth Quartzite (Mammoth Mine).

There is also evidence for multiple modes of failure within each deposit. The dominance of large jigsaw breccias near the Portal Fault-Mammoth Fault intersection within the Mammoth Mine is indicative of tensile failure. For these breccia styles to occur areas of low minor principal stress and low differential stress are required. The peripheries of the

orebody are commonly logged as fractured host rock, locally as breccia class S1 (Clark, 2003). These areas are dominated by vein arrays of multiple orientations. The vein arrays are indicative of areas of low σ_3, high differential stress ($\Delta\sigma$) and fluid pressures exceeding the tensile strength of the host rock (Sibson, 1986).

2.10 Numerical Modelling –Methodology and Conceptual Model

The 2.3 km x 2.3 km model geometry was created from detailed field mapping conducted by Crossing (2004) (Figure 2.21). It was assumed that all the faults in the models were already present their current configuration, as there is little evidence for any major fault displacement post-mineralisation.

The orientation of the maximum principal stress was varied from SW-NE to SE-NW (Figure 2.22 pg 67; Table 2.4 pg 66) to test the range of hypotheses proposed by previous authors and by the geology-based conclusions of this study (Chapter 2.3.1). The stress conditions for the model are set at ratios of σ_1/σ_2=1.2 and σ_3/σ_2=0.8, resulting in a phi (Φ) value of 0.5. These ratios are similar to those used by Mair *et al.* (2000), Zhang and Sanderson (2002) and McLellan and Oliver (2007), for typical upper crustal stresses acting on faulted rocks, showing Mohr-Coulomb behaviour. The imposed stresses (σ_1=210 MPa, σ_2=175 MPa, σ_3= 140 MPa) represent 7 km of overburden and are within reasonable ranges of CO_2 fluid inclusion entrapment pressures based on isotope fluid inclusion work at Mammoth Mine completed by Clarke (2003). The stresses were later adjusted to a phi value of 0.3 to be consistent with the stress inversion calculations completed on the faulting (Chapter 2.5.7).

Sensitivity tests are tests in which the effect of systematically changing particular model input parameters is studied. A series of sensitivity tests was initiated to better constrain the importance of contrasting rheology in the localization of dilation, the effect of changing the principal stress ratios (phi values) and the effect of the Portal Fault on brecciation (all sensitivity tests in Table 2.5 pg 66).

In order to ascertain whether the fault architecture was the primary control on the specific sites of dilation, a series of single lithology models were initiated. Rock properties, fault properties, fluid pressures (Table 2.6) and the orientation of σ_1 (101º - 281º) were identical to the Keys Model 101, as was the conceptual model geometry. The difference between the sensitivity test and the Keys Model 1 was that the rock type of the whole model was changed to Whitworth Quartzite (Mammoth Mine host rock). If the fault architecture was the dominant control on localizing dilation, then the known mine areas would be expected to be dilatant regardless of rock type. Alternatively the contrasting rheology (varying rock types),

as per the Keys Model 101, may be required to provide the necessary rheological contrast to assist fault movement and subsequent dilation in areas of known mineralisation.

Many aspects of the models were investigated (e.g. displacement vectors, shear displacement, shear stress, dilation and principal strain); however, this study will focus on the criteria required for rock failure, given the occurrence of ore in veins and breccias. Some conditions required for determining failure mode criteria, that can be quantified using UDEC, are the minimum principal stress (σ_3), the effective mean stress (σ_m), the differential stress ($\Delta\sigma$) values and the fluid pressure required for failure (Pf_F). The aforementioned parameters are also important in determining failure mode through mohr circle diagrams (Figure 2.20) and so provide a useful comparison point with this traditional method (Chapter 1).

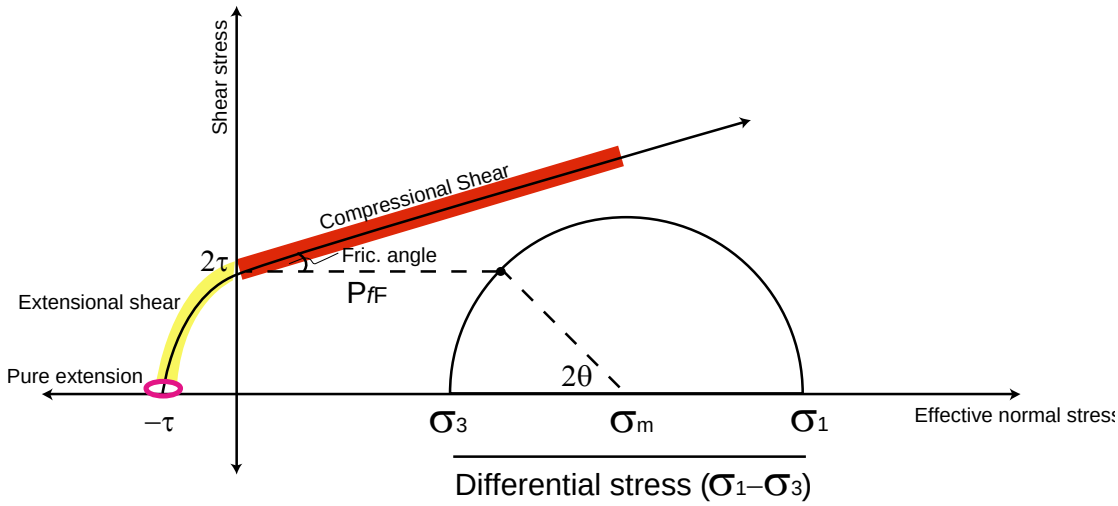

Figure 2.20 Simplified mohr circle diagram showing uses of the data that can be easily acquired from UDEC model outputs. Using σ_3, σ_m and the differential stress, the mohr circle itself can be created. By determining 2θ, in this case, 2 x (angle from EW plane) we can determine the failure point. From here a horizontal line is drawn to intersect the failure envelope. This line represents the fluid pressure required for failure (Pf_F;) another measurable UDEC output. Where this line intersects the failure envelope will determine the likely failure mechanism.

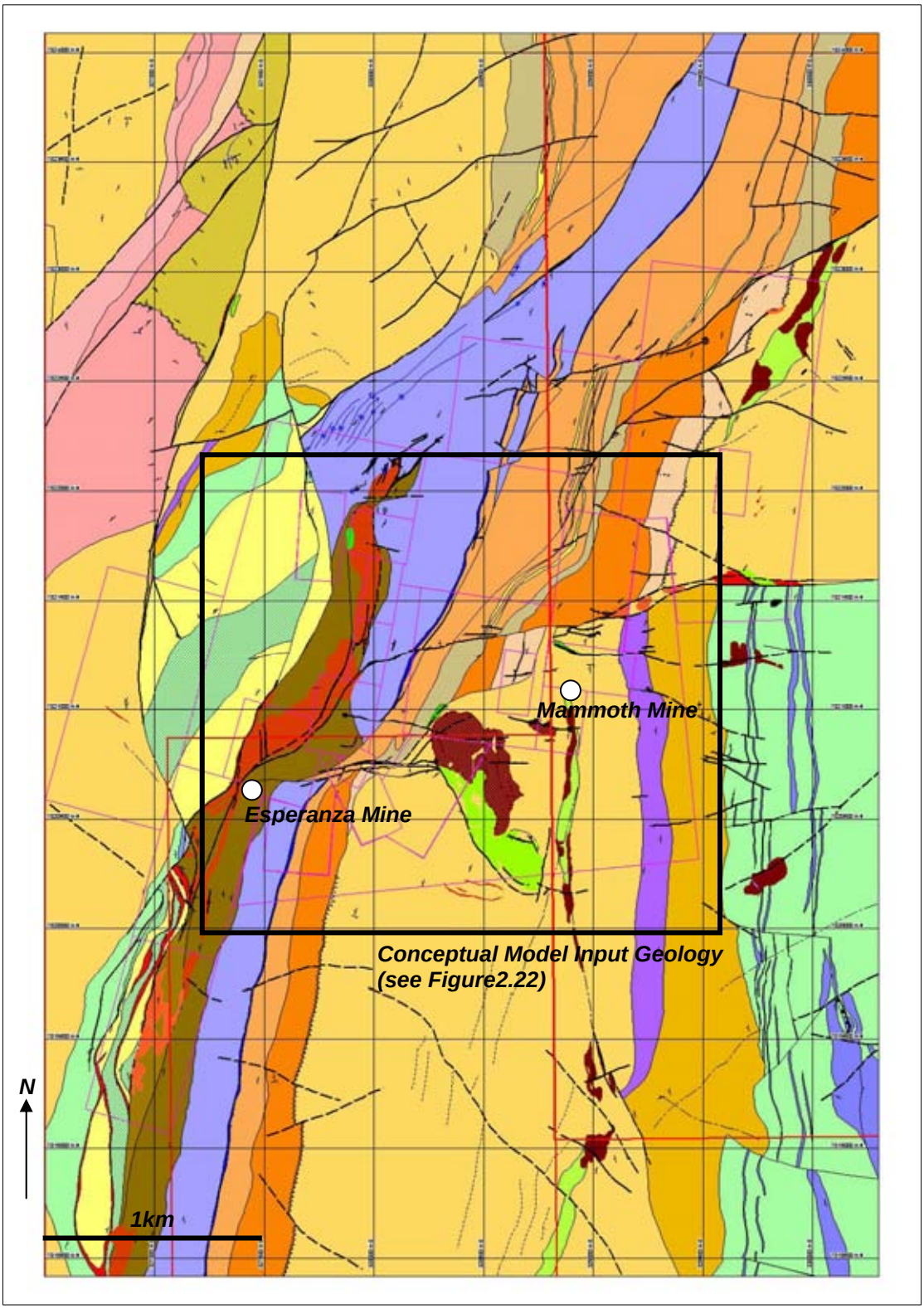

Figure 2.21 Geological map of the Mt Gordon Copper Mines Lease as mapped by Crossing (2004). Inset, approximately 2.3 km x 2.3 km, shows geology used for input into the numerical modelling.

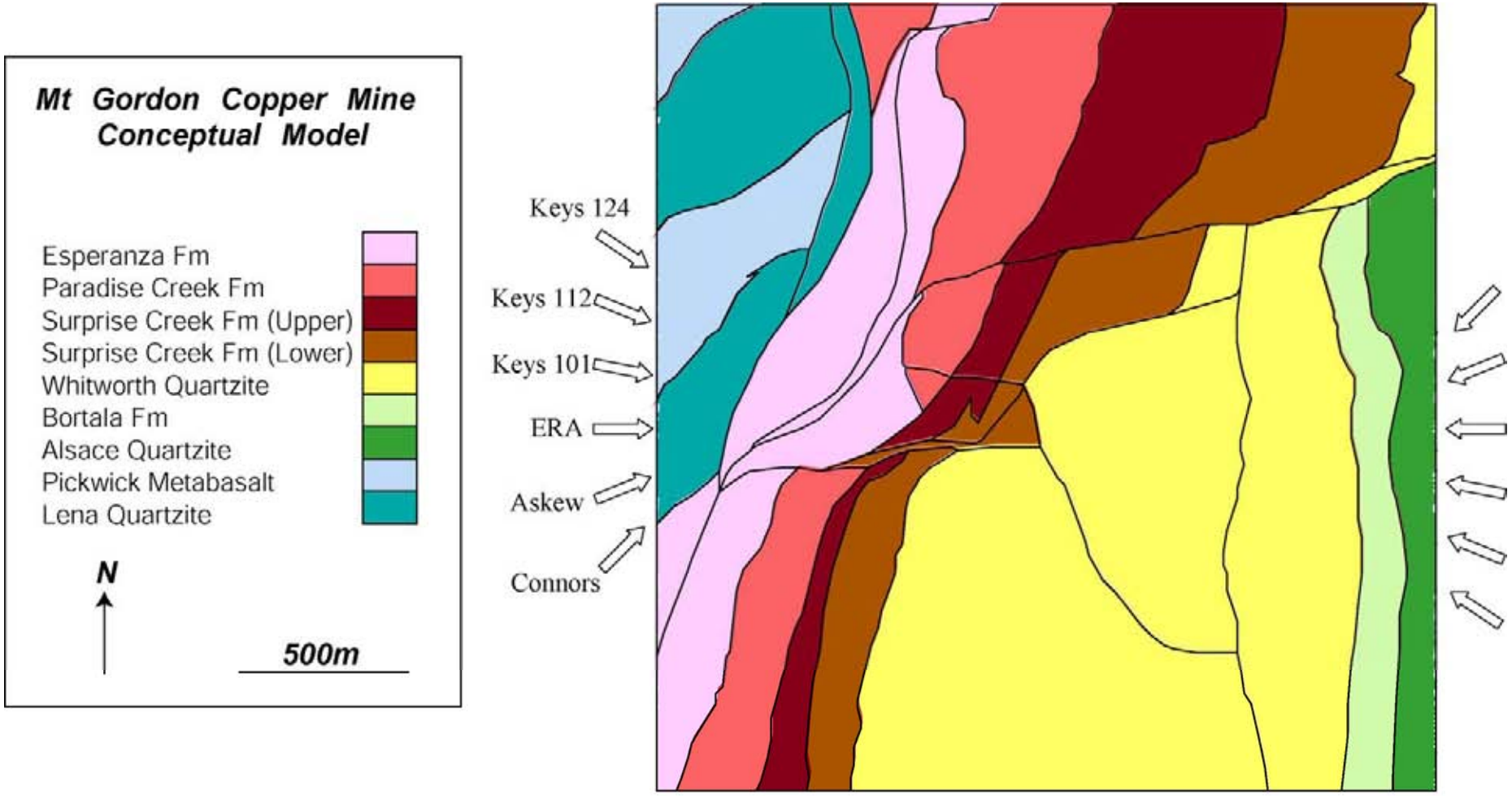

Figure 2.22 Conceptual model geometry and scenarios. The arrows reflect the σ_1 orientations proposed by the various authors (see Chapter 2.3.1).

Table 2.4 Mt Gordon models run, with the σ_1 orientation and a brief summary. Locations of the detailed results of each model are also tabulated.

Model	σ_1 Orientation	Summary of Outcome	Detailed Results
Connors	*045*	*Poor visual fit with known brecciation.*	*2.12.1*
Askew	*067*	*Poor visual fit with known brecciation.*	*2.12.2*
ERA Maptec	*090*	*Identifies known breccias, but dilates areas known to not be brecciated*	*2.12.3*
Keys 101	*101*	*Good visual fit with known brecciation*	*2.12.5*
Keys 112	*112*	*Identifies known breccias, but dilates areas known to not be brecciated*	-
Keys 124	*124*	*Poor visual fit with known brecciation*	*2.12.4*
Stress Inversion	*112 Phi=0.3*	*Excellent visual fit with known breccias*	*2.12.6*

Table 2.5 Sensitivity tests run, with the σ_1 orientation and a brief summary. Locations of the detailed results of each model are also tabulated.

Model	σ_1 Orientation	Summary of Outcome	Detailed Results
All Whitworth	*101*	*Good visual fit with known breccias*	*2.13*
Lower diff. stress	*101 Phi=0.5*	*Less definition between dilatant & non dilatant zones*	*Appendix …*
Lower diff. stress	*112 Phi=0.3*	*Less definition between dilatant & non dilatant zones*	*Appendix …*

Table 2.6 Model rock and contact input parameters used in all UDEC modelling

Property	Quartzite	Shale	Siltstone	Metabasalt	Lithological contact	Fault
Density (kg/m3)	*2600*	*2650*	*2400*	*2650*		
Bulk modulus (Pa)	*40e9*	*40e9*	*16e9*	*49e9*		
Shear modulus (Pa)	*25e9*	*7e9*	*11e9*	*27e9*		
Cohesion (Pa)	*24e7*	*5e7*	*10e7*	*20e7*	*3e3*	*5e2*
Tensile strength (Pa)	*12e7*	*3e7*	*5e7*	*10e7*	*3e6*	*2e6*
Friction angle (°)	*31*	*37*	*32*	*31*	*35*	*30*
Dilation angle (°)	*2*	*5*	*2*	*2*	*5*	*5*
Normal stiffness (Pa/m)					*2e9*	*5e9*
Shear stiffness (Pa/m)					*5e5*	*8e4*
Permeability factor (Pa/s)					*238*	*300*
Aperture at zero normal stress (m)					*0.03*	*0.05*
Residual hydraulic aperture (m)					*0.01*	*0.03*

2.11 Numerical Modelling Results

2.11.1 Connors NE-SW shortening model (Figure 2.23; pg 69)

When modelled the proposed σ_1 orientation of NE-SW produces results with high minor principal stress and high mean stress in the known mine locations. The Mammoth Mine location requires high fluid pressure for failure, however the Esperanza Mine requires low fluid pressures for failure. These results would suggest that a σ_1 orientation of NE-SW would not produce the necessary dilation for copper bearing breccias at mineralisation time at Mt Gordon.

2.11.2 Askew ENE-WSW shortening model (Figure 2.24; pg 70)

The proposed model of Askew resulted in high values of minor principal stress in both mine locations. High mean stress values and high fluid pressure for failure are seen in the Mammoth Mine location. High mean stress values are also seen in the Esperanza Mine location although low fluid pressure for failure is observed there. Areas of low values of σ_3, σ_m and Pf_F were cross referenced with detailed mapping conducted by Crossing (2004) and seen to occur in areas that had little to no brecciation evident. The σ_1 orientation of NE-SW during mineralisation was considered unlikely on the basis of this UDEC modelling. On the basis of the fault mapping (Chapter 2.5), stress inversion (Chapter 2.5.7) and UDEC modelling a σ_1 event oriented ENE-WSW at mineralisation is unlikely.

2.11.3 ERA Maptec E-W shortening model (Figure 2.25; pg 71)

Although a small zone of low σ_3, σ_m and Pf_F are seen in the Mammoth Mine location, the zone of low σ_3 extends across the Portal Fault. The Leapfrog 3D modelling (Chapter 2.4) completed shows that both copper grade and intense brecciation does not occur on the eastern side of the Portal Fault. The Esperanza Mine location shows low values of σ_m and Pf_F but has high values of σ_3 and is therefore unlikely to dilate in an E-W oriented σ_1 event at mineralisation.

2.11.4 Keys 124 SE-NW shortening model (Figure 2.26; pg 72)

The Keys 124 model shows moderate values of σ_3, σ_m and Pf_F in the Esperanza and Mammoth Mine locations. Although these are not the worst models, they do not define the brecciated areas clearly and are therefore not preferred.

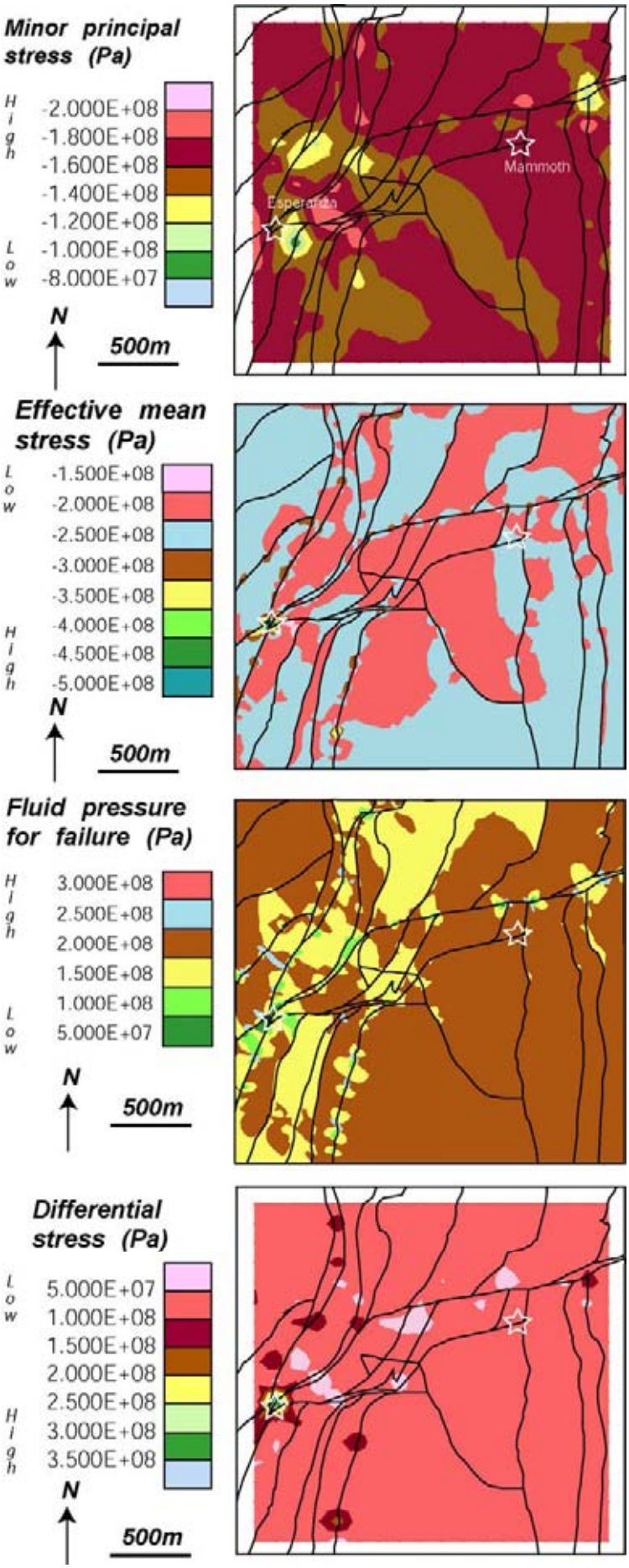

Figure 2.23 The Connors Model Outputs

a. *High values of σ_3 are seen in both the Mammoth and Esperanza Mine locations (~160 MPa Mammoth and 140 MPa at Esperanza).*

b. *Values of effective mean stress are higher in the Mammoth Mine location (250 MPa), than surrounding areas (200 MPa). Mean stress values are even higher in the Esperanza Mine location (~ 450 MPa).*

c. *High Pf_F values are seen in the Mammoth Mine location (200 MPa). Furthermore, there is no discrepancy between the Pf_F values seen on either side of the Portal Fault.*

d. *Differential stress values within the Mammoth Mine are not too dissimilar to input differential stress values (70 MPa). Far higher differential stress values are seen in the Esperanza Mine location (~350 MPa).*

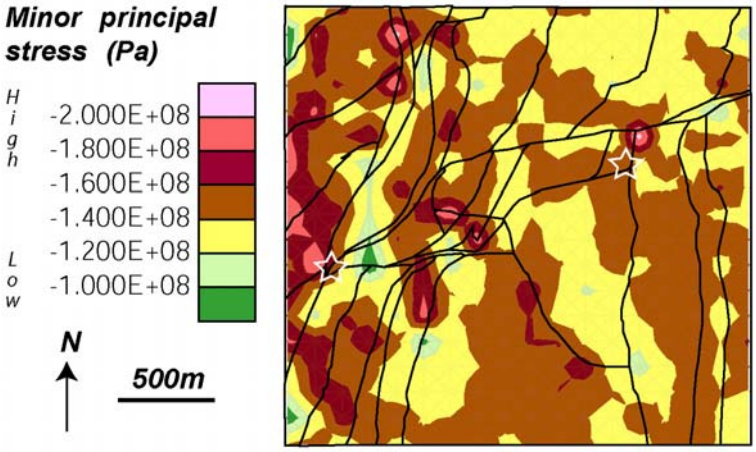

Figure 2.24 The Askew Model Outputs

a. *High values of σ_3 are seen in the known mine locations (~140 MPa at both).*

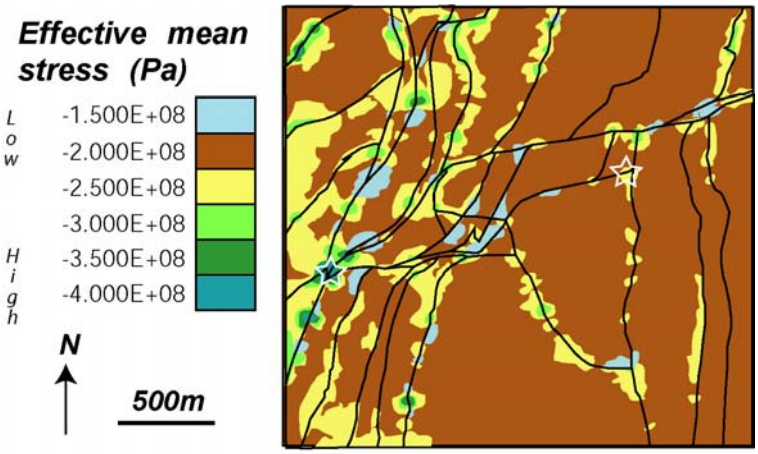

b. *High values of mean stress are seen in the mine locations (400 MPa Esperanza and 250 MPa Mammoth).*

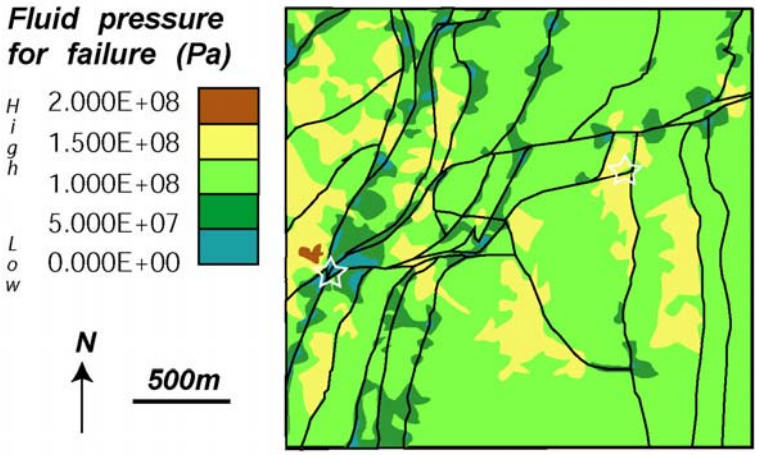

c. *High fluid pressures are required for failure in the Mammoth Mine area (~150 MPa). Low P_{fF} values are seen at Esperanza ~10 MPa.*

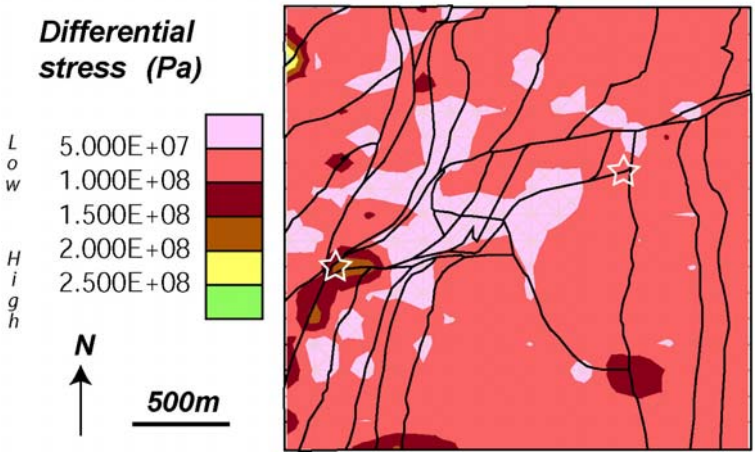

d. *Differential stress values are low at Mammoth (~50 MPa) and extremely high at Esperanza (~200 MPa).*

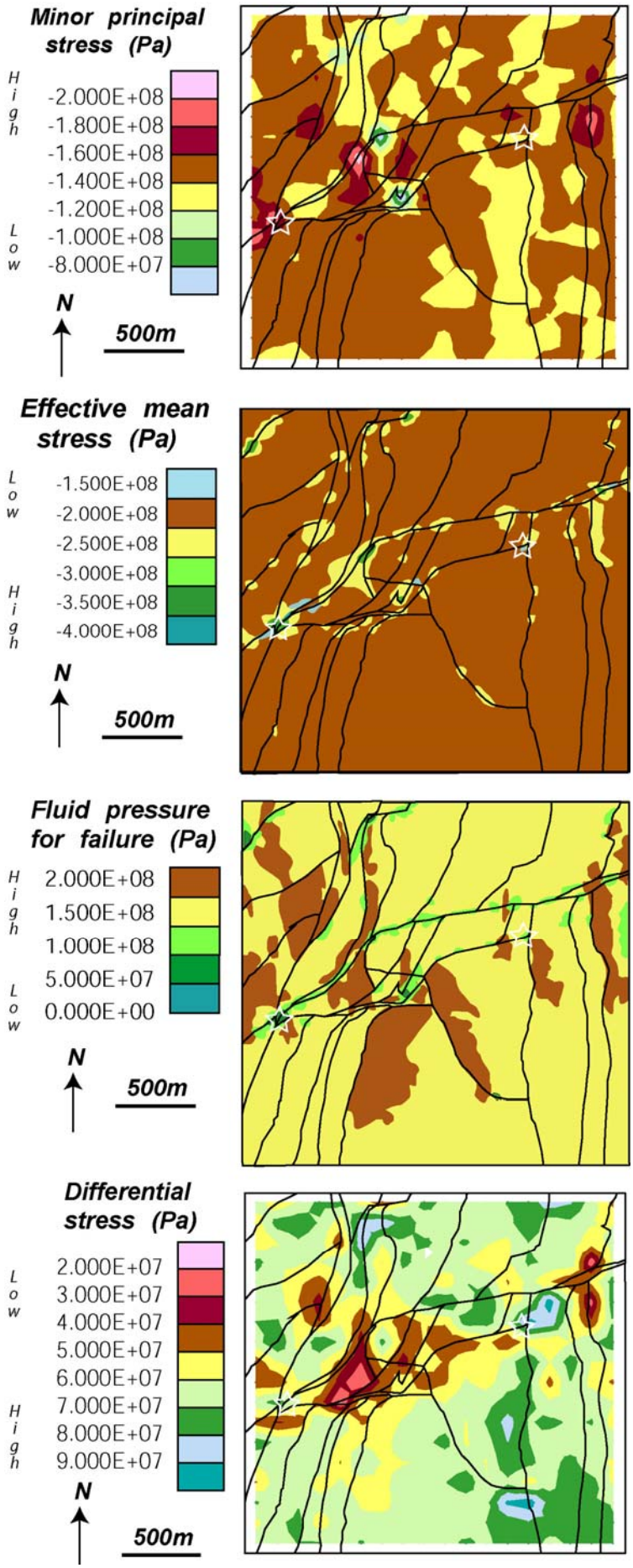

Figure 2.25 The ERA Maptec Model Outputs

a. *High values of σ_3 are seen in the known mine locations (~ 120 – 140 MPa at both).*

b. *Moderate mean stress values are seen at both the Mammoth Mine and Esperana Mine locations (~120 MPa).*

c. *Moderate fluid pressures are required for failure in both mine locations (~100 MPa Mammoth and ~75 MPa Esperanza).*

d. *Differential stress values are high at the Mammoth Mine (~80 MPa), and also high at the Esperanza Mine location (~70 MPa).*

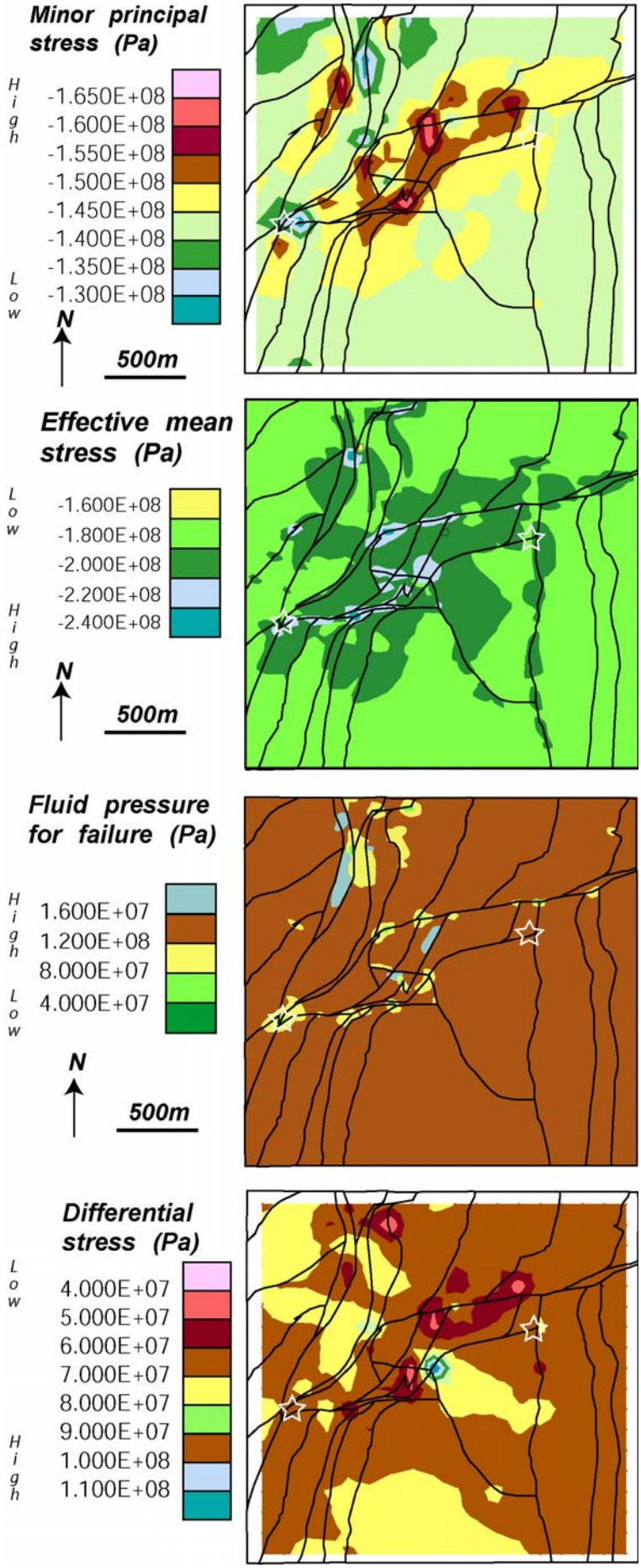

Figure 2.26 Keys 124 SE-NW Model Outputs

a. *Moderate values of σ_3 are seen in both of the known mine locations (~135 MPa at Esperanza and ~ 145 MPa at Mammoth).*

b. *Moderate mean stress values are seen at both mine locations (~200 MPa).*

c. *Moderate fluid pressures are required for failure in both mine locations (~120 MPa Mammoth and ~40 MPa Esperanza).*

d. *Differential stress values are extremely high in both mine locations (~90 MPa in both mines).*

2.11.5 The Keys 101 Model

Areas of low σ_3, σ_{eff} and P_{fF} produced in the Keys 101 Model showed a good correlation with the known mine locations (Figure 2.27). By focusing in on the deposit scale, a more detailed distribution of σ_3, σ_m, $\Delta\sigma$ and P_{fF} could be determined.

Within the Mammoth Mine, the plot of minor principal stress (Figure 2.28a) showed values of 100 MPa along the western margin of the Portal Fault, from the Mammoth Extended Fault to south of Mammoth Fault, consistent with the bulk of the Mammoth Mine mineralised zone. The eastern side of the Portal Fault is seen to have high minor principal stress values (140 MPa to 200 MPa), which is consistent with the mapped unmineralised, unbrecciated Whitworth Formation in this part of the Mammoth Mine. Likewise the unmineralised, unbrecciated Surprise Creek Formation proximal to B Lens is also seen to have high σ_3 values (140 MPa to 200 MPa).

The mean stress acting over the Mammoth Mine region was seen to be lowest in the vinicinty of the Mammoth Fault – Portal Fault intersection (Figure 2.28b). The combination of low σ_m (~120-150 MPa) and low σ_3, represent ideal conditions for dilation and fluid focusing.

Fluid pressures required for failure (P_fF) with the ore zones require ~50 MPa of fluid pressure for failure compared to values of 100 MPa to 150 MPa to the east of the Portal Fault (Figure 2.28c).

A range of differential stress values ($\Delta\sigma$) are seen in the vicinity of the Mammoth Mine (Figure 2.28d). In the B Lens area, $\Delta\sigma$ values are typically higher than in the 2 and D Lens area. In the vicinity of D Lens, $\Delta\sigma$ values are commonly around 80 MPa whereas $\Delta\sigma$ values around the B Lens area are in the range of 120-140 MPa. This variation has potential implications for the failure mode of the different orebodies. Overall it would appear that the mine is localised across a steep gradient in σ_3 and $\Delta\sigma$.

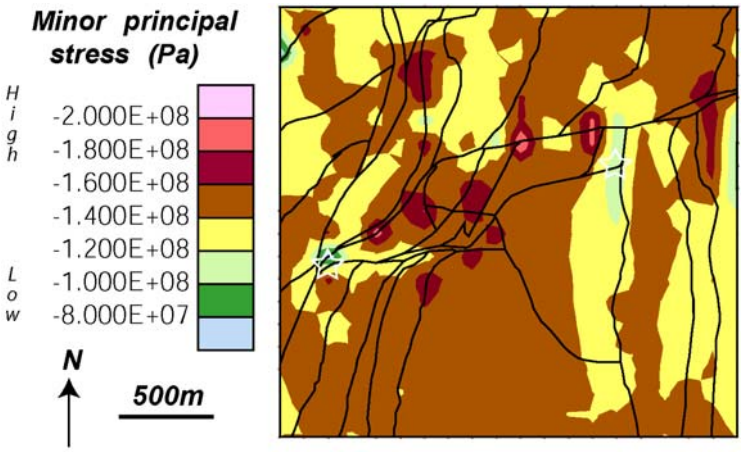

Keys 101 Model – Whole Model

Figure 2.27 ***(a)*** *A corridor of low σ_3 values runs along the western margin of the Portal Fault (Mammoth Mine location white star - east). Low values of σ_3 are seen in the Esperanza Mine location (white star – west).*

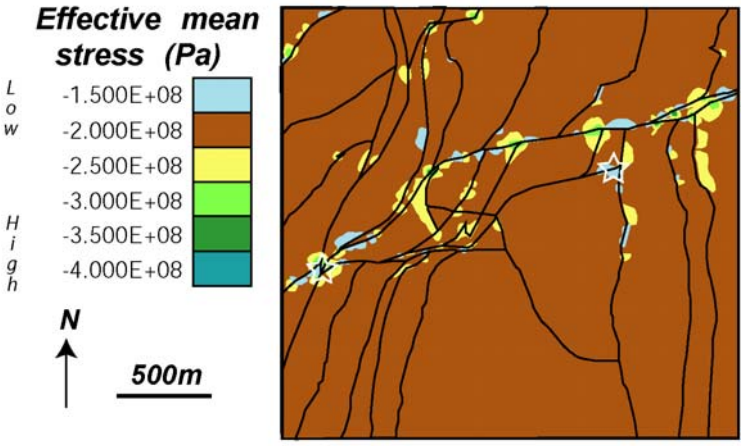

b. *Values of effective mean stress are relatively low in the Mammoth Mine location compared to the surrounding rocks. The Esperanza Mine contains low values of mean stress. Esperanza Mine in particular has very low mean stress values against very high mean stress values (steep mean stress gradient).*

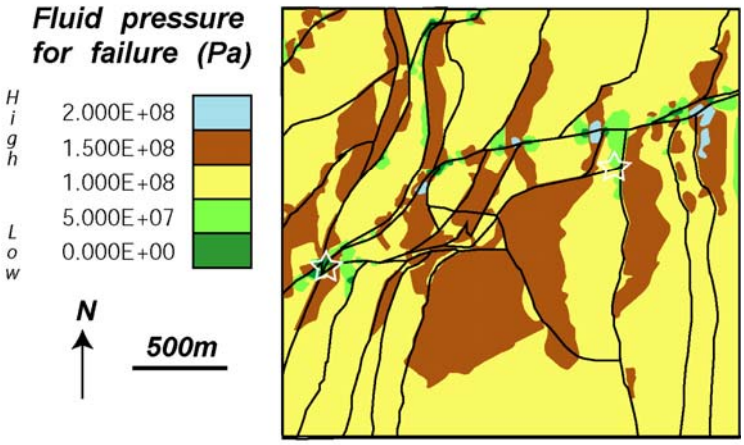

c. *Low Pf_F values are seen in the Mammoth Mine location (~50 MPa). The Esperanza Mine also contains low values of Pf_F (~15 MPa).*

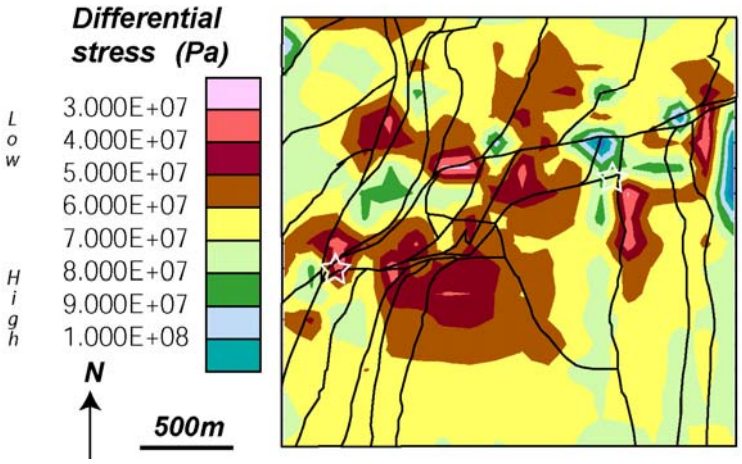

d. *Differential stress values appear to be quite low in the Esperanza Mine location relative to the values seen in the Mammoth Mine location.*

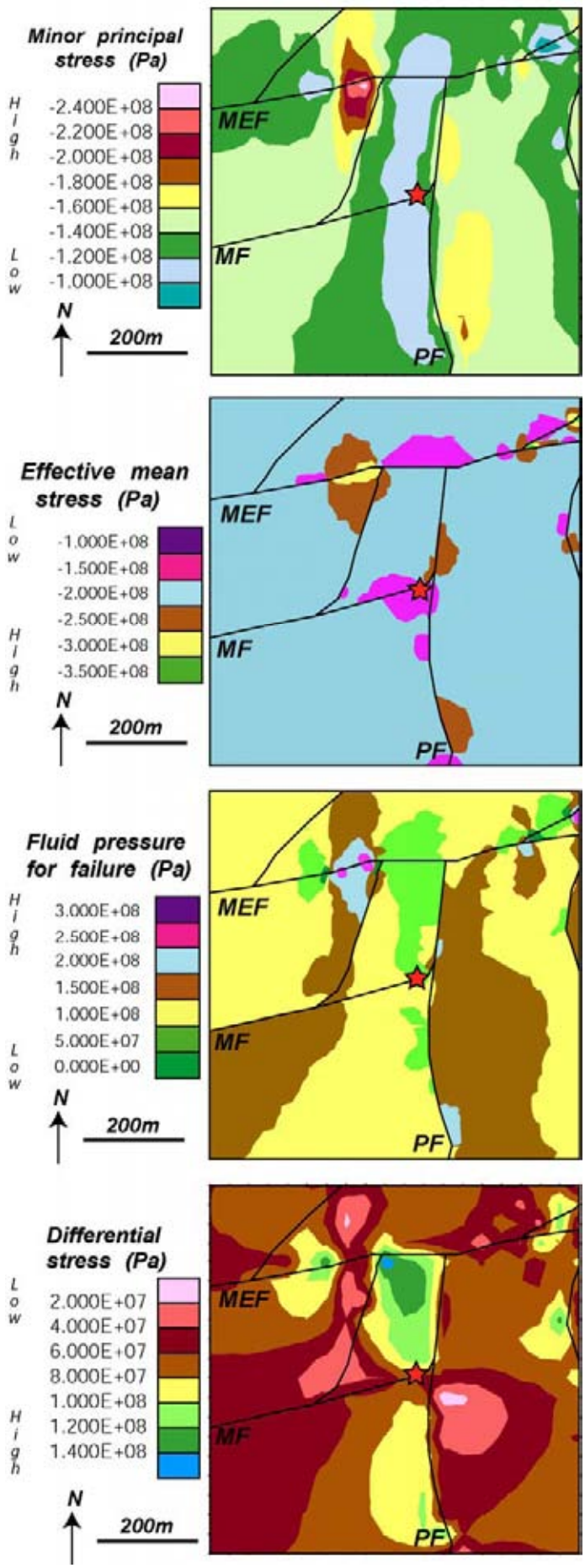

Mammoth Mine UDEC outputs (Keys 101 Model)

Figure 2.28 ***(a)*** *A corridor of low σ_3 values runs along the western margin of the Portal Fault (Mammoth Mine location red star).*

b. *Values of effective mean stress are significantly lower in the Mammoth Mine location than surrounding areas.*

c. *Low PfF values are seen in the Mammoth Mine location. Higher values of PfF are seen on the east of the Portal Fault*

d. *Differential stress values vary substantially between different areas around the Mammoth Mine. The mine lies on a steep gradient between values of high $\Delta\sigma$ and low $\Delta\sigma$.*

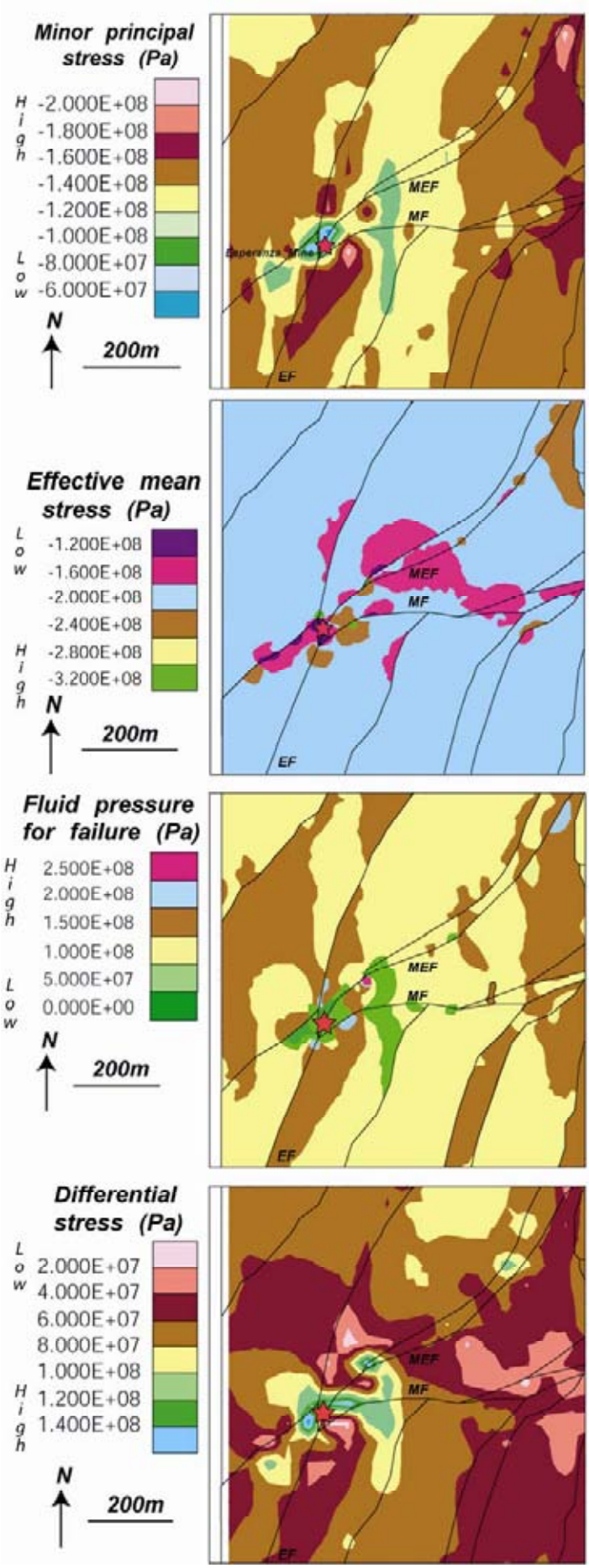

Esperanza Mine UDEC outputs (Keys 101 Model)

Figure 2.29 ***(a)*** *Low σ_3 values are concentrated at the intersection of the Mammoth Extended Fault (MEF), the Mammoth Fault (MF) and the Esperanza Fault (EF).*

b. *Values of effective mean stress are significantly lower in the Esperanza Mine location than surrounding areas.*

c. *Low Pf_F values are seen in the Esperanza Mine location. Higher values of Pf_F are seen on the immediately outside the intersection of the MEF, MF and EF.*

d. *Differential stress values are quite high near the Esperanza Mine location, but again the deposit is localised on a steep $\Delta\sigma$ gradient.*

The plot of minor principal stress (Figure 2.29a) showed values of 60-120 MPa in the intersection of the Esperanza Fault, the Mammoth Extended Fault and the Mammoth Fault. This zone represents the bulk of the mineralised Esperanza ore system. Distal to the fault intersection, high σ_3 values (160 MPa to 240 MPa) are observed.

The mean stress acting over the Esperanza Mine region was seen to be lowest in the vicinity of the intersection of the three faults (Figure 2.29b). The combination of low σ_m (120 MPa to 160 MPa) and low σ_3, make for ideal conditions for dilation and fluid focusing.

Fluid pressures for failure are extremely low, less than 10 MPa, at the Esperanza Mine location (Figure 2.29c). Fluid pressures for failure increase rapidly away from the mine location.

The differential stress is seen to be quite variable in the Esperanza Mine location (Figure 2.29d) as differential stress values reach ~150 MPa, but drop steeply to ~40 MPa. The Esperanza mineralisation straddles this steep gradient.

2.11.6 Model utilizing Stress Inversion Parameters

The stress inversion of the fault and striation pairs using Slick (Ramsay and Lisle, 2000; Chapter 2.5.7) provided statistical best fit orientations for σ_1, σ_2 and σ_3 as well as a best fit phi value. Although the σ_1 orientation (116º) was relatively close to the orientation tested by Keys Model 112, the Φ value differed. The Φ value in the stress inversion was 0.3 as opposed to the 0.5 value tested in the initial model runs.

To test the Φ=0.3 scenario, the values of σ_1, σ_2 and σ_3 had to be changed accordingly. As σ_2 related to the depth of deposition, this value was unchanged (175 MPa). As $\Phi=(\sigma_2-\sigma_3)/(\sigma_1-\sigma_3)$ (Angelier, 1984), the σ_1 value was increased to 210 MPa requiring the σ_3 value to be increased to 160 MPa. The model was run in the Keys Model 2 orientation (112º-292º). All lithologies and fault parameters were unchanged from the initial modelling.

The outputs from the model were slightly better than the best fit outputs of the Keys Model 101. Values of σ_3 (Figure 2.30a) are between 80-100 MPa, approximately 20 MPa lower than values of σ_3 seen in the Keys Model 101. Mean stresses (Figure 2.30b) in the Mammoth Fault-Portal Fault intersection are also slightly lower (120 MPa) than the σ_{eff} values of Keys Model 101 (150 MPa). Pf_F values (Figure 2.30c) of approximately 50 MPa are seen in the Mammoth-Portal intersection and are similar to the Keys Model 101 Pf_F values.

The stress inversion model differs only slightly from the Keys Model 101 in the differential stress values (Figure 2.30d).

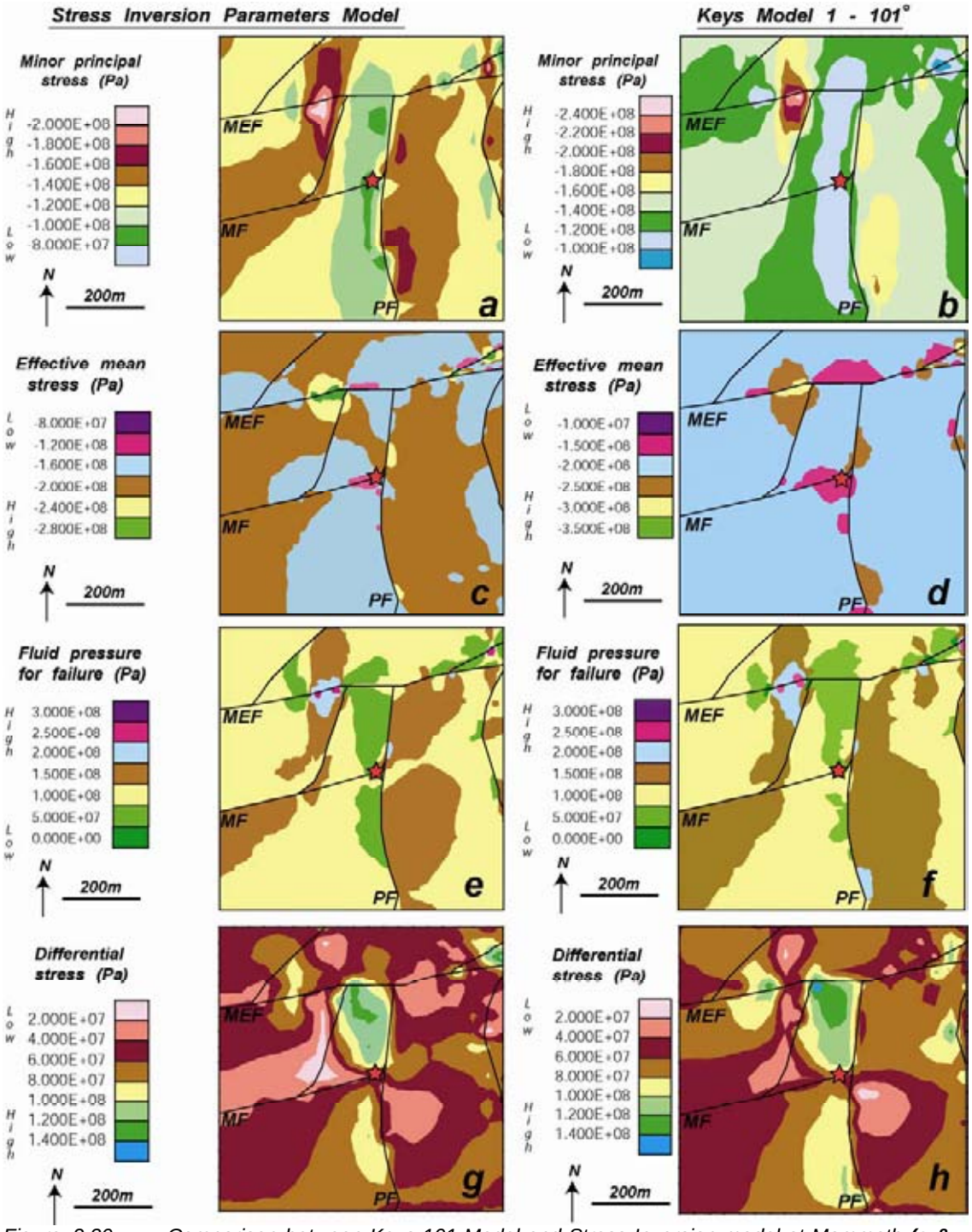

Figure 2.30 Comparison between Keys 101 Model and Stress Inversion model at Mammoth ***(a & b)*** *A corridor of low σ_3 values runs along the western margin of the Portal Fault (Mammoth Mine location red star). Lower values of σ_3 are seen in the Stress Inversion Model (a) and the low σ_3 corridor is better defined (a).*

(c & d) *Values of effective mean stress are significantly lower in (c) despite the area influenced being significantly smaller.*

(e & f) *Low Pf_F values are seen in the Mammoth Mine location in both models. Higher values of Pf_F are seen on the east of the Portal Fault*

(g & h) *Differential stress distributions appear similar between the models. The Stress Inversion model (g) is again has lower values of $\Delta\sigma$, than the Keys Model 101 (h).*

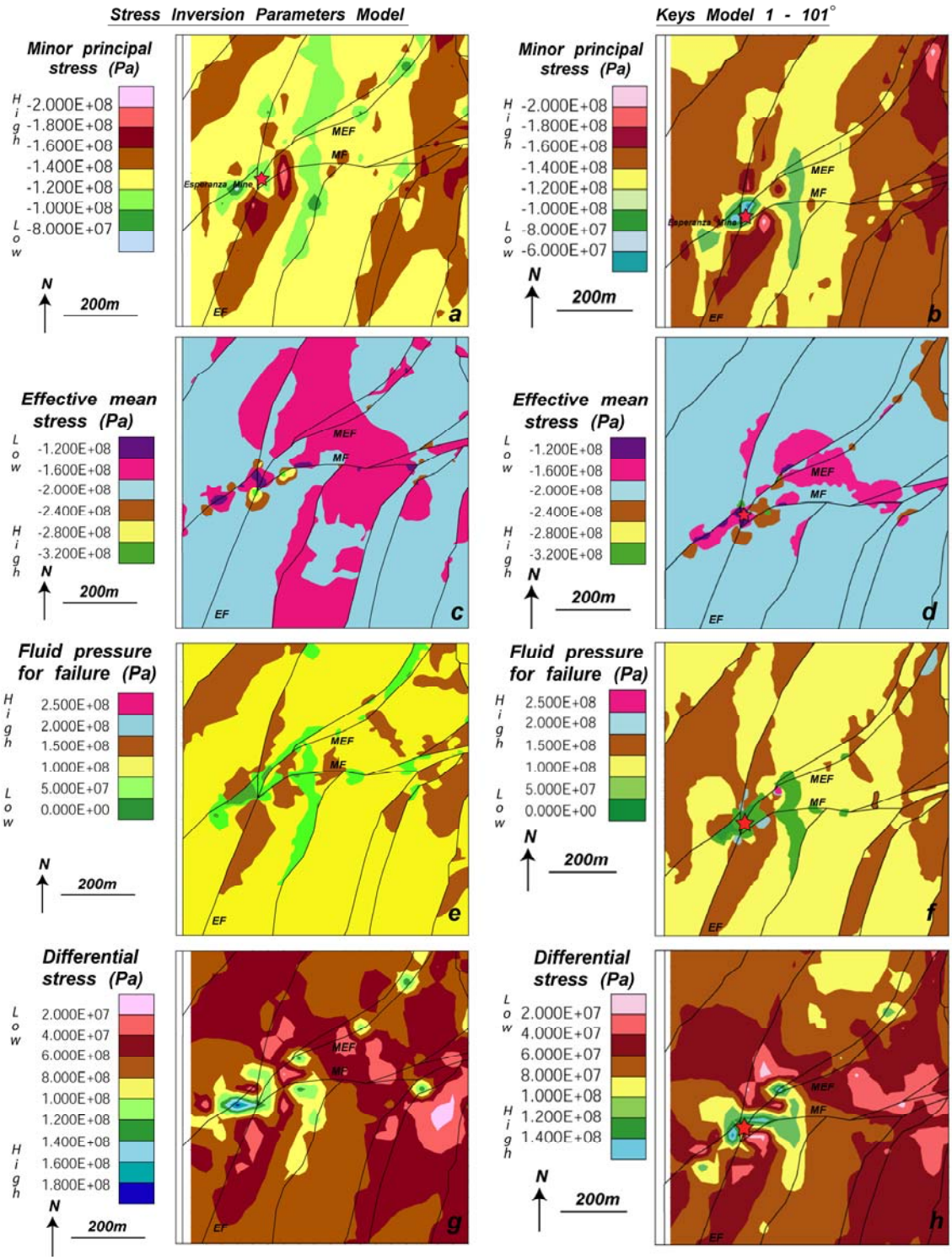

Figure 2.31 Comparison between Keys 101 Model and Stress Inversion model at Esperanza ***(a & b)*** *A concentration of low σ_3 values is found at the intersection of the Mammoth Extended Fault (MEF), the Mammoth Fault (MF) and the Esperanza Fault (EF).*

(c & d) *Values of effective mean stress are significantly lower in the Esperanza Mine location than surrounding areas and differ little between the two models.*

(e & f) *Little difference is seen between the two models (e & f). Low Pf_F values are seen in the Esperanza Mine location. Higher values of Pf_F are seen on the immediately outside the intersection of the MEF, MF and EF.* ***(g & h)*** *Differential stress values show a strong gradient with similar values in the Esperanza Mine location in both model runs (g and h).*

2.12 Sensitivity Testing – Architecture vs. Rheological Contrast

When the entire model was changed to Whitworth Quartzite, the Mammoth deposit exhibited similar values of σ_3, σ_m, $\Delta\sigma$ and Pf_F to the initial Keys 101 Model (Figure 2.32a-d). The intersection of the Mammoth Fault and Portal Fault was seen to be the site of the lowest σ_3, σ_m, and Pf_F in both the All Whitworth Model and Keys Model 1. Similarly the eastern side of the Portal Fault, which is known to be devoid of significant breccias and mineralisation, was seen to have relatively high values of σ_3, σ_m, and Pf_F in both models.

Around the Esperanza Mine, values of σ_3, σ_m, $\Delta\sigma$ and Pf_F were significantly higher than the Keys Model 1 (Figure 2.33a-d). Although values between the models differed, the areas exhibiting relatively low σ_3, σ_m and Pf_F were comparable to the areas of low σ_3, σ_m and Pf_F within the multi-lithological Keys 101 Model (Figure 2.32a-d). The focus of the low σ_3, σ_m and Pf_F was in the Mammoth Extended Fault – Mammoth Fault – Esperanza Fault intersection, in both models.

From these model results we can assume that the fault architecture is the dominant control on the sites of breccia localization. The variable lithology seems to have a significant but subordinate effect on the amount of dilation seen in each of the mine locations.

This has implications for the exploration of the Mt Gordon lease and regionally, as it suggests that good structural targets may be found, irrespective of the host lithology. Sulphur isotope data however, suggests that rock type did influence the specific mechanisms of sulphide precipitation (Clark, 2003).

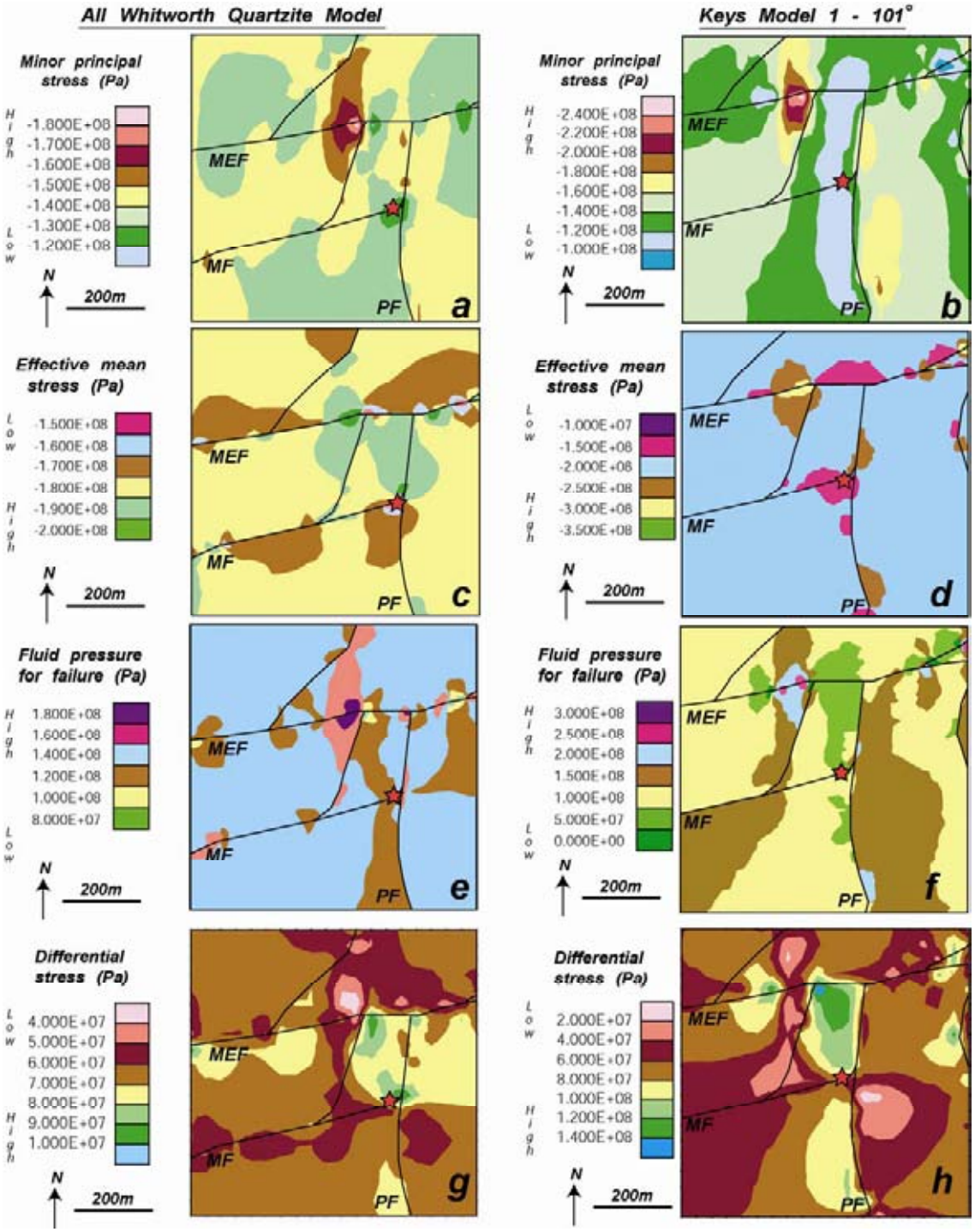

Figure 2.32 Comparison between Keys 101 and All Quartzite model ***(a & b)*** *Although values of σ_3 are higher in the Whitworth Model (a), the model shows higher values of σ_3 to the east of the Portal Fault (PF). The NS trending zone of low σ_3 is still evident in the Mammoth Mine location in (a).* ***(c & d)*** *Relatively low values of σ_m are seen in the Whitworth Model (c). Again these values are slightly higher than those in the Keys 101 model (d).* ***(e & f)*** *Due to the higher σ_3 values in (a), the Pf_F values in the Mammoth Mine location in (e) are significantly higher than those in (f). Despite this they are relatively lower than the Pf_F values seen to the east of the Portal Fault, maintaining the validity of the All Whitworth model.* ***(g & h)*** *Despite the zone of moderate $\Delta\sigma$ values extending through the PF in (g), the plots show similar patterns of areas of high $\Delta\sigma$ and low $\Delta\sigma$.*

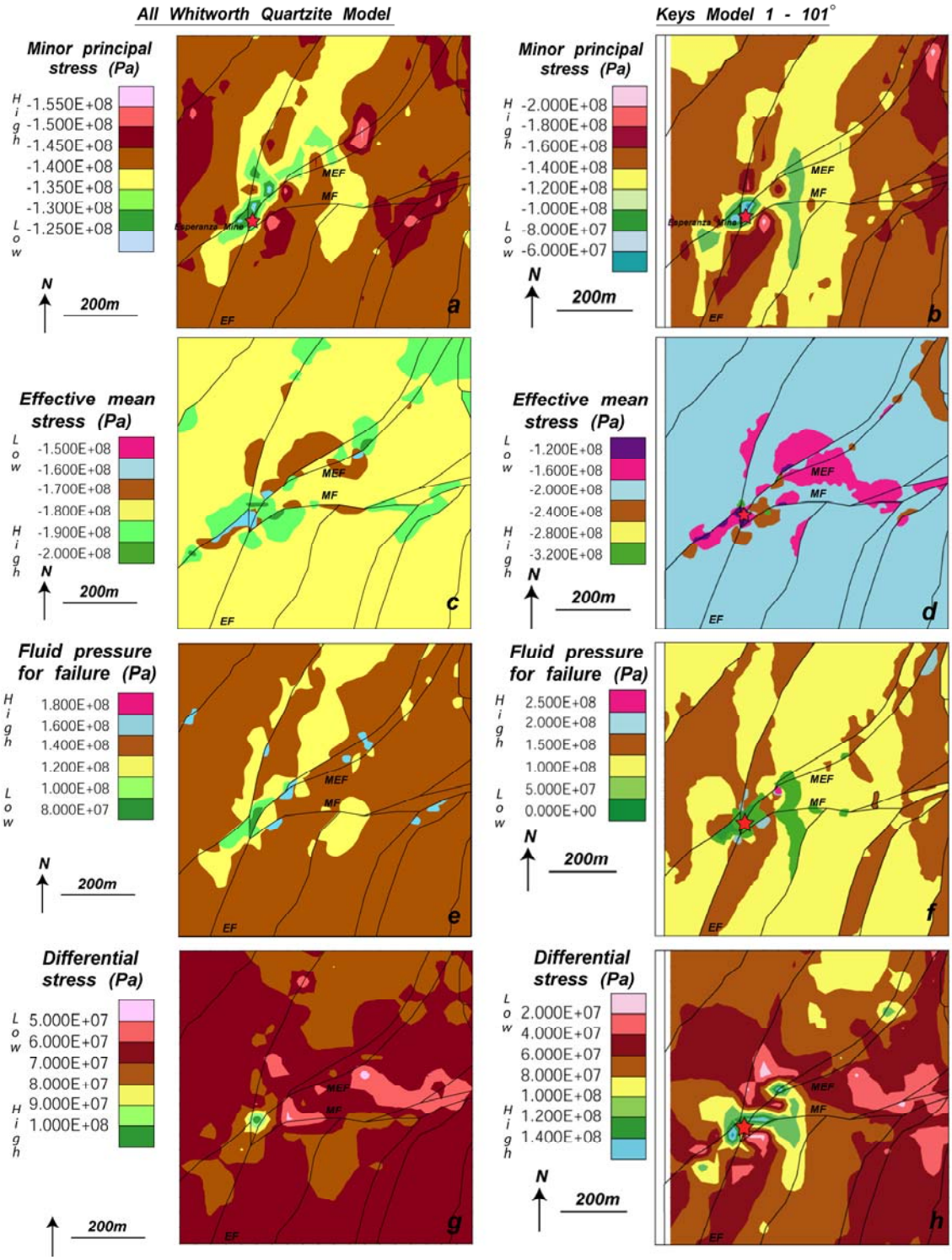

Figure 2.33 Comparison between Mammoth Mine and All Quartzite ***(a & b)*** *Although values of σ_3 are higher in the Whitworth Model (a), the zone of low σ_3 is still evident in the intersection of the MEF, MF and PF in (a) as it is in (b)..*

(c & d) *Relatively low values of σ_m are seen in the Esperanza location in (c). Again these values are higher than those in the Keys 101 model (d). but show the same patterns of σ_m as (d)*

(e & f) *Fluid pressures for failure are significantly higher in the All Whitworth model (e). Despite this a similar zonation of Pf_F trends is seen in both models.*

(g & h) *Relatively high $\Delta\sigma$ values are seen in the Esperanza location in both models.*

2.13 Conclusions and Discussion

The stress inversion derived models (~112º-292º shortening, Φ=0.3) produced the best visual fit for predicting known mine locations and breccia bodies. Low values of σ_3, σ_m and P_fF are typically indicative of dilation and focused fluid flow and known breccias and deposits are seen to correlate well with low values of σ_3, σ_m and P_fF in this model.

In the approximate location of D Lens, low Δσ values were observed, suggesting that failure in this area was likely to be the result of extensional shear failure (Figure 2.34).The values of Δσ were somewhat higher in the Mammoth Fault – Portal Fault intersection although when plotted, the inferred failure mode is still extensional shear.

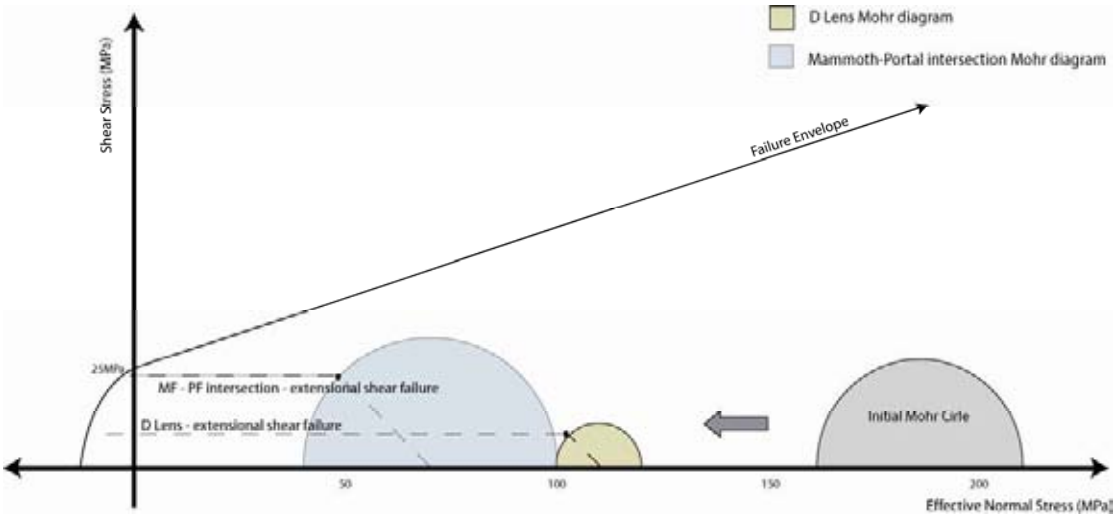

Figure 2.34 Mohr circle diagram showing the proposed failure modes within the Mammoth Mine. Data from the Stress Inversion Model suggests that failure in the Mammoth Fault – Portal Fault intersection is a result of extensional shear failure. This is consistent with the observed jigsaw brecciated orebodies in the mapped areas of D Lens and 2 Lens.

Within the Esperanza Mine area, a zone of high Δσ exists between the NE-SW striking Mammoth Extended Fault and the N-S striking Esperanza Fault. The inferred failure mode in this location is expected to be compressional shear failure (Figure 2.35. This differs significantly from the failure mode anticipated between the Mammoth Fault and Mammoth Extended Fault. Low Δσ values are observed in this area, which when plotted would indicate an extensional shear failure mode. This area is also coincident with the highest copper concentrations in the Esperanza Mine.

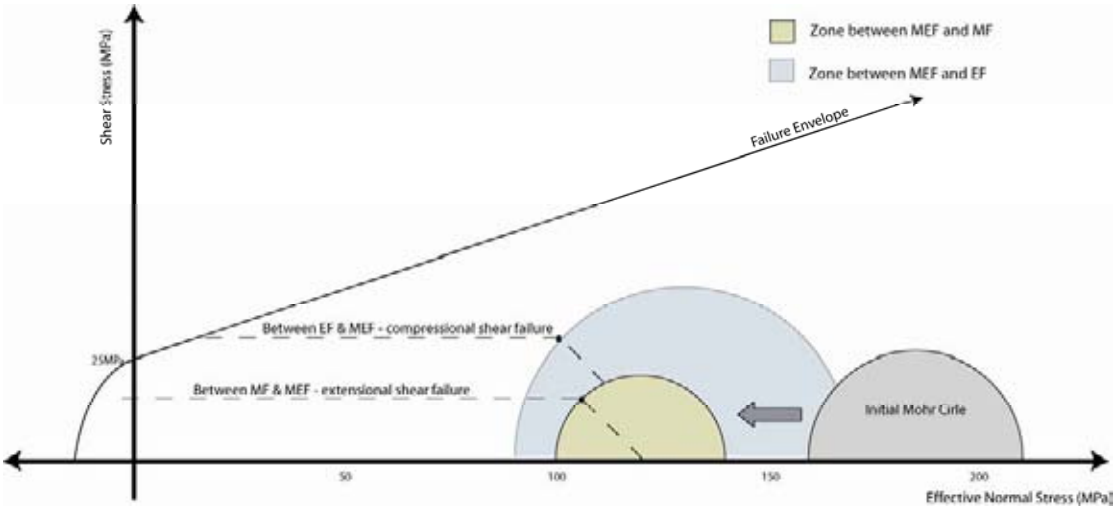

Figure 2.35 Mohr circle diagram showing the proposed failure modes within the Esperanza Mine. Data from the Stress Inversion Model suggests that failure in between the Mammoth Fault – Mammoth Extended Fault intersection is a result of extensional shear failure. Conversely any failure between the Esperanza Fault and the Mammoth Extended Fault is inferred to be the result of compressional shear failure.

For both deposits, it would thus appear that mineralisation is located on steep gradients of minor principal stress and mean stress. There are also steep gradients of differential stress from the orebodies to the surrounding, unmineralised host rock.

UDEC modelling shows that the proposed mineralisation models of Askew (1992) (ENE-WSW shortening) and Connors (1994) (NE-SW shortening) result in anti-dilatant settings at mine locations. They also give sinistral movement on the Mammoth Extended Fault. This is inconsistent with obvious dilation at the mine sites and dextral movement indicators on the Mammoth and Mammoth Extended Faults (Chapter 2.5).

The ERA Maptec (Anonymous, 1994) proposed model (E:W shortening), and Keys Model 2 (ESE-WNW shortening) were interpreted to give dilation in mine locations but also give significant dilation in known unbrecciated areas.

The Keys Model 1 (101°-281° shortening) showed a good correlation of low minor principal stress, low mean stress and low fluid pressures for failure with the known deposits. However the best fit model was the model that employed the stress inversion derived (Chapter 2.5.7) principal stress tensors and ratios. There was an excellent fit between zones

of low σ_3, σ_m and P_{fF} with the known deposits and breccias. Inferred failure modes were consistent with observed breccia characteristics (Chapter 2.7).

It appears the brecciation observed in the Esperanza/Mammoth system is dominantly a result of the existing fault architecture. Changes in lithology may influence the amount of dilation, but ultimately the sites for brecciation are determined by the interplay of the fault architecture. This has implications for the exploration for the Mt Gordon lease and for the exploration of other similarly oriented fault arrays along the Mount Gordon Fault Zone, such as the Investigator Fault System.

3 MT ISA COPPER MINES

3.1 Introduction

The Mt Isa Copper Mine is the largest copper mine in the Mt Isa Inlier and Australia's second largest copper producer.

Discovery of the Mt Isa lead-zinc system was made in 1923 with mining commencing in 1925. Copper was intercepted in drilling in the early 1930's (the 650 Orebody). No further copper exploration was done until the early years of World War Two. It was the war time demand for copper that provided the real impetus for the development of the near surface copper resource (Blainey, 1965). A long history of mining at Mt Isa has also included a long history of research, conducted by many different authors and groups.

Several advances have been made on the geological understanding of the system as mining and technology have progressed. Ore genesis models for copper have evolved with an epigenetic origin for mineralisation being related to a fault and fold controlled, brecciation event (Wilson, 1973; Perkins, 1984; Bell *et al.*, 1988; Davis, 2004; Miller, 2006).

The most recent addition to this research was a structural study commissioned by Xstrata as part of the pmd*CRC I7 project. The study was conducted by John Miller (University of Western Australia) and ran concurrently with this PhD. Some of the key geological observations of the Miller (2006) study have been numerically modelled in this study, in an attempt to further understand the geological processes involved with ore breccia formation.

Although many deposit scale structural studies have been undertaken in the past, little work has been done on collating these thoughts and putting them into a regional framework. This study will attempt to put recent structural advances and modelling analyses into such a context.

3.2 Geological Setting

3.2.1 The Mt Isa Valley

The Mt Isa Valley is the name given to the 30 km long x 5 km wide zone of Mt Isa Group metasedimentary rocks that outcrop east of the Sybella Granite. The Mt Isa Valley is bound to the south by the Crystallena Fault, a NNW striking fault that juxtaposes Eastern Creek Volcanics (emplacement age 1770 Ma – U-Pb $_{zircon}$ SHRIMP; Neumann *et al.*, 2006) against a N-S striking suite of Mt Isa Group sediments (depositional ages of 1670 to 1645 Ma; U-Pb $_{detrital\ zircon}$ SHRIMP; Neumann *et al*., 2006). The western margin of the Mt Isa Valley is bound by the steeply west dipping Mt Isa Fault. To the west of the Mt Isa Fault is the Sybella Granite, which has crystallization ages of 1673 ± 3 Ma (U-Pb $_{zircon}$ SHRIMP; Hoadley *et al*., 2001) and 1655 ± 4 Ma (U-Pb $_{zircon}$ SHRIMP; Connors and Page, 1995). The Mt Isa Valley continues north beyond the Hilton and George Fisher lead-zinc-silver mines, and east to the outcropping Eastern Creek Volcanics.

Lead-zinc-silver (Pb-Zn-Ag) mineralisation is found in the Urquhart Shales of the Mt Isa Valley at the Mt Isa Mine and approximately 22 km north at the George Fisher and Hilton Mines. The genetic history of the lead-zinc-silver ores is controversial, with research being split between syngenetic and diagenetic origins (Perkins, 1984; Valenta, 1994, Chapman, 2001) and an epigenetic origin (Bell *et al.*, 1988; Painter *et al.*, 1999; Davis, 2004).

Copper mineralisation is limited to the southern end of the Mt Isa Valley, approximately 3 km north of the Crystallena Fault. The Mt Isa Copper Mines are comprised of several orebodies over a 4 km strike length. The largest of these orebodies is the 1100 orebody, which is approximately 3 km in length, 450 m wide and currently at ~ 1 km depth (Figure 3.1).

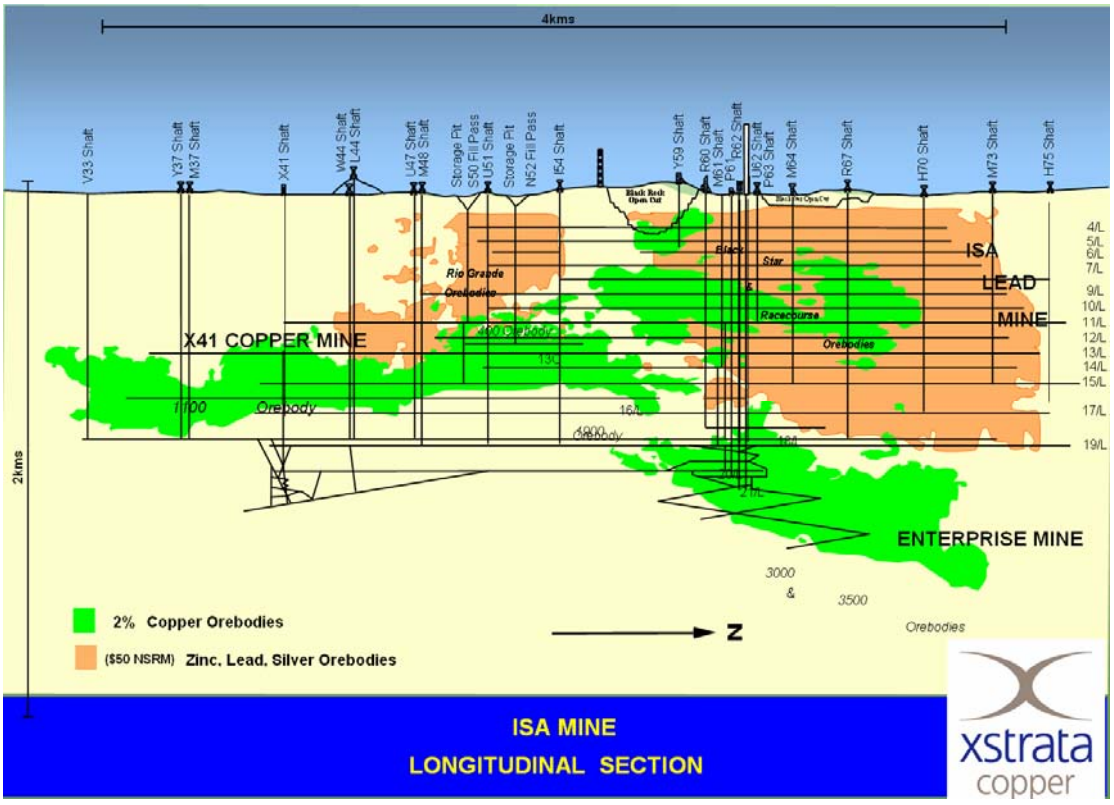

Figure 3.1 (figure from Miller, 2006) Orebody long section looking west. The brown shading is the extent of the lead-zinc lodes and the green shading reflects the relative positions of the various copper orebodies. The total strike length of the copper deposit is ~4 km.

3.2.2 Host Sequence and Sedimentology

The Mount Isa Copper Mines are hosted within the Urquhart Shales of the Mt Isa Group. The ore hosting shales dip 60º to 80º to the west. The Mount Isa Group is subdivided into upper and lower Mount Isa Groups on the basis of local unconformities occurring at the contact of the Breakaway Shale with the Native Bee Siltstone (Figure 3.2) (Neudert, 1983). This boundary also marks a lithological change from predominantly siliceous (Lower Mt Isa Group) to the predominantly dolomitic rocktypes of the Upper Mt Isa Group (Neudert, 1983). The Lower Mt Isa Group is comprised of the Warrina Park Quartzite, Moondarra Siltstone and Breakaway Shale.

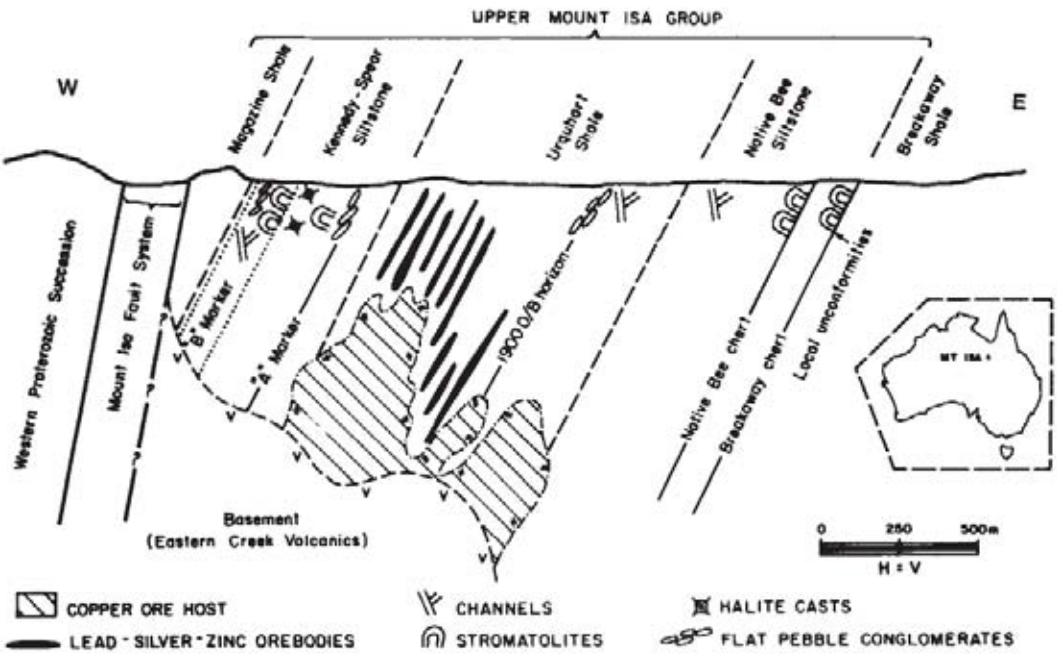

Figure 3.2 (from Neudert, 1983) Idealised cross section looking north through the Upper Mt Isa Group stratigraphy highlighting several sedimentological features.

In detail, the Urquhart Shale contains a cyclic succession of carbonate rich and carbonate poor facies. Four facies types are distinguished (Neudert, 1983):

(i) Dark grey, carbonate-poor and carbonaceous rhythmite (centimetre thick couplets of parallel-laminated siltstone and non-laminated mudstone).

(ii) A carbonate-rich variant of (i) which contains a significant proportion (~50%) of carbonate cemented siltstone and/or mudstone layers.

(iii) A dark grey rhythmite facies similar to (i) but containing numerous carbonate crusts and nodules (mainly calcite).

(iv) A carbonate-rich siltstone facies, which often contains current-laminated deposits, erosional contacts and flutes.

Pyritic siltstones occur throughout the Urquhart Shales as bedding parallel layers that consistently show a uniformity of thickness over a long strike length. The distribution of fine-grained pyrite is facies controlled. Pyrite is most abundant in the rhythmite facies with crusts and nodules (iii) and is least abundant in the carbonate-rich siltstone facies (iv) (Neudert, 1983). The fine-grained pyrite has a close spatial association with both the copper and lead-

zinc ores. The fine-grained pyrite is commonly found on the peripheries of the copper orebodies.

Painter *et al.* (1999) hypothesised that the fine-grained pyrite formed by thermochemical sulphate reduction during diagenesis. Consistency between fine-grained pyrite, Pb-Zn and Cu ore sulphur isotope values (Robertson, 1982) led Painter *et al.* (1999) to the hypothesis that the Pb-Zn and Cu systems reflect a chemically and thermally zoned, evolving system, or discrete Cu and Pb-Zn mineralising events linked by a common sulphur source.

The Mt Isa Group sediments within the Mt Isa Valley and locally within the mine, unconformably and disconformably overlie the Eastern Creek Volcanics. Within the mine, the Paroo Fault juxtaposes the Eastern Creek Volcanics against the younger Urquhart Shale.

3.2.3 Alteration

Several authors have documented the presence of a zonal distribution of siliceous and dolomitic metasomatic rocks, particularly within the 1100 Orebody (Figure 3.1, Figure 3.3) (Perkins, 1984; Swager, 1985; Bell *et al.*, 1988; Waring, 1990). An inner siliceous zone occurs immediately adjacent to the Paroo Fault. An outer zone of dolomitic alteration surrounds the siliceous core. The margin of the two zones is irregular and contacts between the dolomitic and siliceous rocktypes may be “knife-edged” or gradational. Features such as stylolitic seams, carbonaceous fault planes or stratiform pyrite define abrupt contacts between the dolomitic and siliceous rocktypes (Law, 2001). Gradational contacts result from partial dolomitisation, such as incipient development of recrystallised shale or through partial silicification (Law, 2001). Silicification does occur away from the inner core, typically in up-dip extensions of the orebody associated with orebody faulting. Silicification and copper mineralisation are closely associated. Copper grades decrease outwards and upwards with the change from the core of silica-rich/dolomite-poor ‘rock types’ to the outer dolomite-rich/silica-poor ‘rock types’ (Law, 2001).

Perkins (1984), Swager (1985) and Waring (1990) describe the formation of the silica-dolomite as a system involving three stages of silicification and dolomitisation, which

took place during the regional D_3 deformation. The formation of the silica dolomite is described below:

Stage 1 - Early syn-D_3 recrystallisation and silicification.

Stage 2 - Extensive dissolution of dolomite by the silicifying fluids changed the fluid composition until it became over-saturated with carbonate components and started to redeposit and promote growth of dolomite (irregularly brecciated dolomitic shale).

Stage 3 - Chalcopyrite and quartz precipitated, replacing dolomite. Dissolution of dolomite and precipitation of chalcopyrite are presumed to have occurred simultaneously. In the Enterprise orebodies (Figure 3.1, Figure 3.3) the association of economic concentrations of chalcopyrite with silicification is ubiquitous.

Talc occurs widely through the copper lodes at Mt Isa. Talc alteration is most intense in both the footwall and hanging wall of the northern 3500 orebody (Figure 3.1, Figure 3.3), the Footwall Lens of the 1100 orebody and in the 1900 orebody (Figure 3.1, Figure 3.3) at Mt Isa. The talc occurs in Mg-rich assemblages that may include quartz, dolomite, chlorite, pyrite, pyrrhotite and chalcopyrite (Foster *et al.*, 2006). Foster *et al.* (2006) concluded that talc did not form by isochemical metamorphic reactions and that talc, phlogopite and chlorite were formed during metasomatism. The metasomatic events that formed the talc are believed to have removed K^+ and Ca^{2+}. The recrystallisation of the coarse talc to fine foliation parallel talc implies that the talc formation could be pre- to syn- regional D_3. Foster *et al*. (2006) suggest that the changing mineralogy across the entire metasomatic system was controlled by the relative activities of Si, Mg, Ca, K (possibly Al), and x_{CO2} and S and O fugacity.

3.2.4 Mineralisation

Although several sulphide species exist in the Mt Isa Copper Mines (fine-grained and coarse grained pyrite, pyrrhotite, galena and sphalerite) the principal copper sulphide is chalcopyrite.

The main copper mineralisation occurs directly above the basement contact fault (1100 and 3000 orebodies) with smaller orebodies present at higher levels detached from the contact (650/500 orebodies and upper 3500 Orebody) (Figure 3.3). The detached orebodies

show that copper bearing fluids have most likely been transported upwards, most likely along fault or fracture networks (Law, 2001).

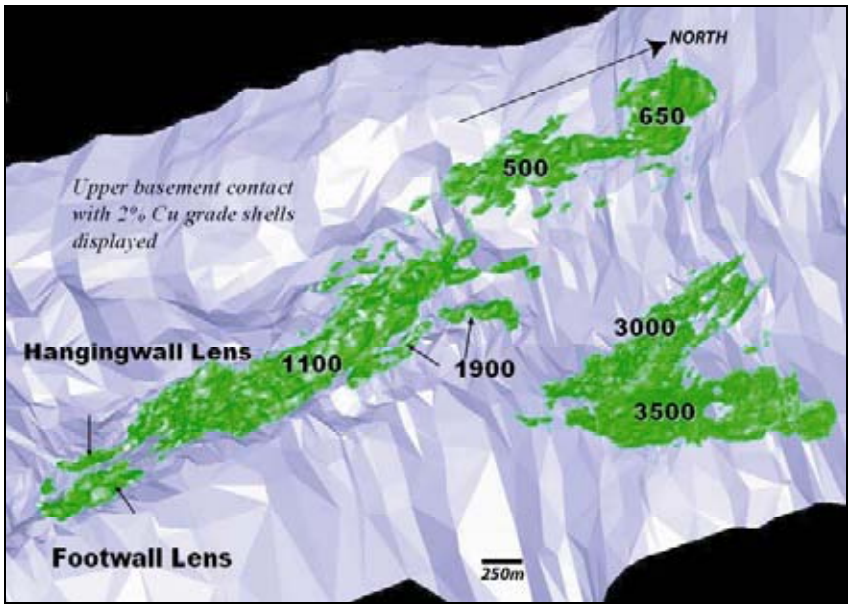

Figure 3.3 (from Keys, 2002) Orebody schematic showing the relative positions of the main Mt Isa copper orebodies. The blue wireframe is the Basement Contact Fault (Paroo Fault) and the green shells are the 2% copper grade shells. The 1100 orebody is the largest of the orebodies and occupies a basement ramp position. The 1100, 1900, HW Lens and FW Lens comprise the X41 Mine. The 3000 and 3500 orebodies form the Enterprise Mine. The 500 and 650 orebodies are known to Mt Isa geologists as the perched orebodies as they do not contact the basement contact.

Basement contacting orebodies such as the 1100 orebody, 3000 orebody and 1900 orebody are seen to be contain highly siliceous cores with dolomitic haloes (Figures 3.4, 3.5, 3.6). The 200 orebody, 500 orebody and 650 orebody have a weak siliceous alteration associated but are primarily dolomitically altered.

The lead-zinc orebodies however are seen to die out on the contact with dolomitic alteration (Figure 3.6). At a meso-scale, dolomitic veins are seen to cross-cut lead-zinc lodes (Valenta, 1994).

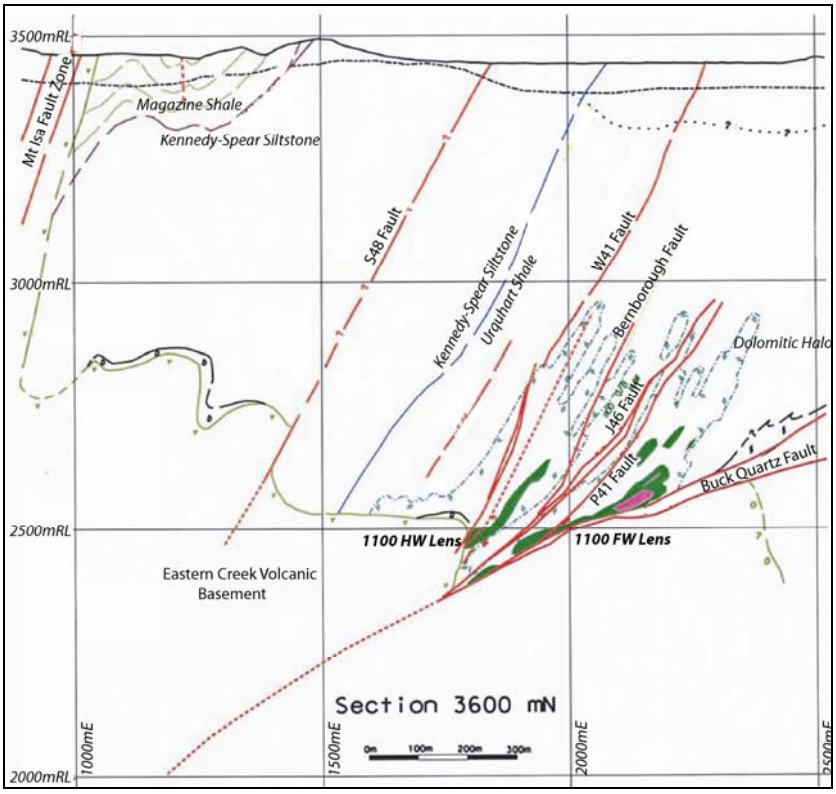

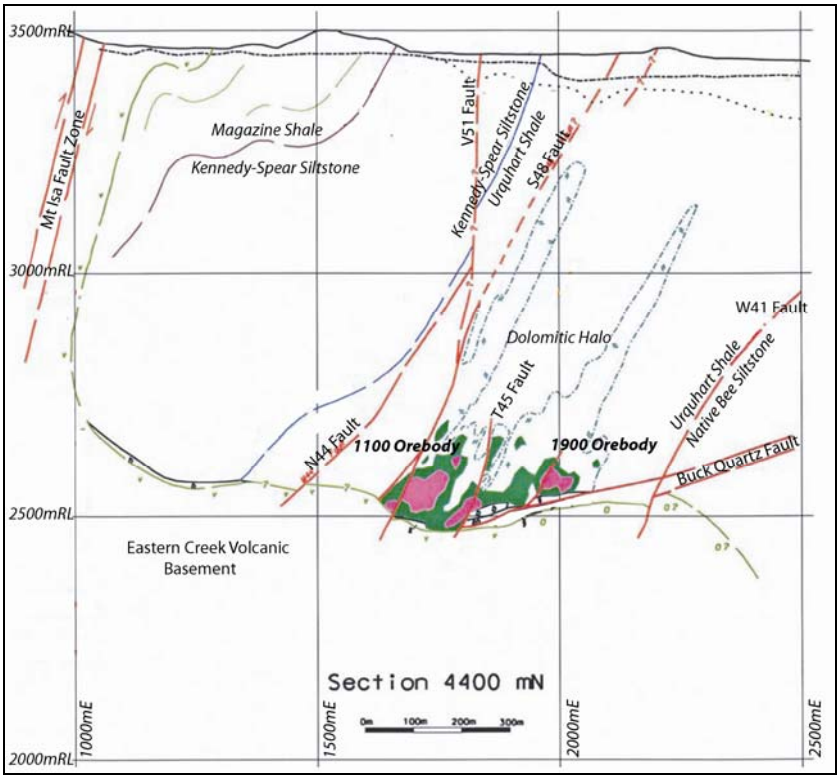

Figure 3.4 (above) (adapted from Law, 2001) Section through 3600 mN (mine grid). This section is at the south end of the Mt Isa copper mine, where the mineralisation is located in the 1100 HW Lens and the 1100 FW Lens. The green solid is 2-4% Cu and pink solid is indicative of >4% Cu. The dolomitic halo around the orebodies is shown by a dashed blue line. Major faults are marked in red.

Figure 3.5 (below) (adapted from Law, 2001) Section through 4400 mN (mine grid). This section is at the cuts both the 1100 orebody and the 1900 orebody.

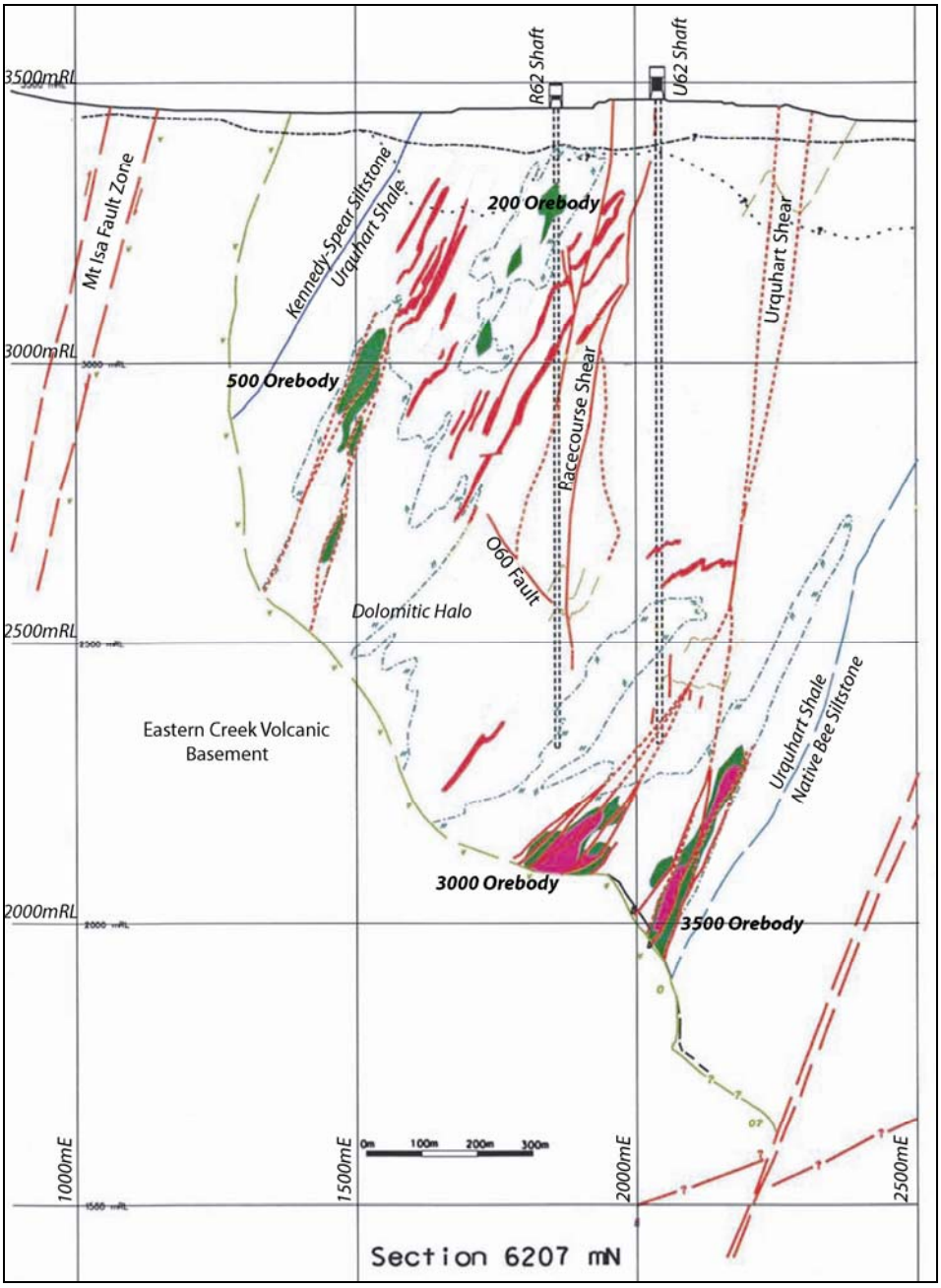

Figure 3.6 (adapted from Law, 2001) Section through 6207 mN (mine grid). This section cuts the 200, 500, 3000 and the 3500 orebodies. Lead-zinc lodes are seen as thick red lines on the section. The dolomitic halo around the orebodies is seen as a dashed blue line. Major faults are marked in red. The green solids are 2-4% Cu grade shells and pink solids are >4% Cu.

3.2.5 Structure

The basement contact fault is a complex structure, which forms the base beneath the copper orebodies. It juxtaposes upper Mount Isa Group against the older Eastern Creek Volcanics. It is analogous to the Paroo Fault, which is mapped at the surface west of the mine sequence (Law, 2001). The Paroo fault crops out east of the Mount Isa Fault and dips steeply

west approximately parallel to bedding. At depth it curves sharply to form an almost flat-dipping structure beneath the Mount Isa copper mines (Law, 2001).

The basement contact fault is a major zone of shearing of variable width and complex history, incorporating both Mount Isa Group rocks and Eastern Creek Volcanics. At depth, it has flat lying sections that cross-cut the Urquhart Shales at a high angle, which change to steep sections trending towards parallelism with bedding near the 1100HW orebody (Law, 2001). The flatter lying sections of the basement contact fault generally have a thick intensely sheared, carbonaceous mylonite zone between the Urquhart Shales and the Eastern Creek Volcanics. This geometry is postulated to have developed via folding, the flat sections being fold hinge zones. There is a broad parallelism between the hinge lines in the basement contact fault and the axial plane to folding in the mine.

Bell *et al.* (1988) described the fault as having formed as a lateral thrust ramp during D_1 and to have essentially reached its present day configuration after D_2. There are small inflections within the basement contact that are parallel to the axial plane of D_3 folding within the mine sequence. These are inferred to be the expression of the F_3 folding event on the basement surface (Keys, 2002; Miller 2006).

On a large scale the basement contact fault forms an almost flat to very shallowly dipping structure beneath the 1100 and 1900 orebodies. The relationship to folding is not particularly clear beneath the main body of the 1100 Orebody (section 4400mN). However moving northwards to where the 1100 Orebody narrows and the adjacent 1900 Orebody has developed, the basement contact fault has a geometry similar to that described beneath the Deep Copper orebodies (Figure 3.5). The 1100 Orebody seems to sit in a synformal hinge whereas the 1900 orebody is positioned more towards an anticlinal inflection point where the fault is interpreted to dip steeply away to the east (Figure 3.5).

Faulting is prevalent throughout the copper orebodies. Major mapped faults are inferred to have been long lived, active during D_3, D_4 and also after copper deposition. Faults active during mineralisation typically have fills of quartz, dolomite, graphite and chalcopyrite. Faults showing evidence for movement immediately after copper deposition have fills that

include quartz, chalcopyrite (minor) and trace galena. Clark (1992), Keys (2002) and Krois (2002) have noted fills of sepiolite, gypsum and calcite in the youngest post-copper faults.

Few faults displace the copper orebodies. The NE striking S48 Fault displaces the 1100 and 1900 copper orebodies by approximately 200 m in an apparent dextral sense.

3.3 Previous Syn-Copper Kinematic Studies

Perkins (1984) and Bell *et al.* (1988) offer hypotheses on the mine-scale to sub-regional structural history, the implications of the structural history for the genesis of the copper and lead-zinc, and the relationships between grade and alteration. These papers will be briefly reviewed in this chapter to provide a framework for further work.

More recently, Miller (2006) completed a structural analysis of the Enterprise Mine copper orebodies, the 3000 orebody and 3500 orebody. This was primarily focussed on determining modes and mechanisms of failure for the genesis of the ore breccias and the relationships between copper and basement rocks.

3.3.1 Perkins (1984)

Perkins (1984) argued against co-genetic Pb-Zn-Ag and Cu, suggesting that genesis of the copper ores reflected a complex hydrothermal alteration system postdating deposition of the Mount Isa Group and the lead-zinc-silver orebodies. A regional folding event (D_2) formed the fold limb, which constitutes the ore setting. The fold limb is inferred to rest against the post-lithification pre-D_2 fault contact and the chlorite schists beneath it (Perkins, 1984).

Perkins (1984) showed that the silica-dolomite alteration resulted from differential progressive metasomatic alteration (phyllosilicate development, dolomitization, and silicification) of the entire range of microfacies constituting the lead-zinc sequence. This was the first work to formally document the relationship of all stages of alteration, from incipient bedding and vein-controlled alteration to to a deformational history of folding, cleavage development, faulting and brecciation (Perkins, 1984).

The study showed that dolomitizition of the Urquhart Shale host developed dolomite replacement veins and pseudobreccias of varying intensity. The veins and breccias developed along bedding and fractures until total dolomitization of the former shales occurred

in much of the mine sequence. All forms and stages of dolomitic pseudobreccias are preserved by pseudomorphic quartz replacement in silicification zones which form the core of the orebody systems (Perkins, 1984).

The observations made on the silica-dolomite led Perkins (1984) to infer a separation in timing and mode of formation of the lead-zinc and copper orebodies. Perkins hypothesised that the lead-zinc mineralization appeared to accumulate either syngenetically or at a very early stage in diagenesis, but the copper had a formed during the Isan Orogeny and had a dominantly structural control. From dates of sedimentation and deformation elsewhere in the Mt Isa Inlier, Perkins (1984) suggested that copper mineralisation is estimated to have been introduced at least 150 m.y. later than the lead-zinc mineralisation.

3.3.2 Bell, Perkins and Swager (1988)

Using the timing relationships determined by Perkins (1984), *Bell et al.* (1988) determined the structural controls and constraints on the silica-dolomite alteration and the subsequent copper mineralisation.

The study determined that three major deformation events were responsible for the structural relationships seen in the mine. The first of these deformation events involved the formation of the Basement Contact Fault during D_1 thrusting. The fault was rotated and overturned by the combined effects of D_1 and D_2 into a shallowly dipping attitude on the western limb of a regional-scale upright D_2 antiform in the mine location (Bell *et al*., 1988). Bell *et al.* (1988) then determined that a relatively flat basement fault provided a plane of considerable anisotropy and competency contrast between the dolomitic shales and siltstones (above) and the greenschists (below).

Bell *et al.* (1988) also observed a consistent steep W-dipping foliation which transected the basement contact (mapped as S_3) in both the volcanic rocks and the overlying shale. The F_3 folding generated opposite senses of shear across the fault, resulting in differential movement across the fault and particularly near fold hinges. The reactivation of bedding during the folding and unfolding of the shale unit during D3, in conjunction with the competency contrast created by the shales over greenschists, lead to localised fracture and opening of the contact. Bell *et al.* (1988) inferred that a rapid drop in fluid pressure was

associated with the opening of the contact, causing the explosive brecciation, particularly of the dolomitically altered shales, that hosts the copper orebodies.

3.3.3 Miller (2006)

The most recent of the structural analyses has been conducted by Miller (2006). Miller focussed on mapping extension veins (both syn- and post-Cu), cleavage and bedding orientations in the Enterprise Mine (3000 and 3500 orebodies). The structural mapping was integrated with 3D models of the ECV basement to determine key structural controls on copper mineralisation. Leapfrog 3D modelling of the basement primary rock types showed the majority of quartzite occurs in flatter dipping lower basement zones. Miller (2006) suggested that this may reflect early dip refraction of the lower basement fault (Paroo Fault) through rheologically different units during D_1 or D_2 thrusting – this geometry is substantially modified by folding during the D_3 deformation event. Alternatively the quartzites in the basement may represent an intense to total silicification of the pre-existing metabasalt. Significantly, the flatter dipping zones of lower basement have previously been linked to focussing of Cu-bearing fluids (Perkins, 1984; Swager, 1985; Bell *et al.*, 1988). Miller (2006) also noted the presence of a NNW-trending lower basement lineament beneath the 3000 ore body that correlated with the trend of the copper breccias. He realised that the lineament was not related to any late faulting that affects the shales (as all late faulting is N- to NE-trending through the area) and as such inferred that the basement trend correlates with an F_3 axial trace. The steeply W-dipping basement overhangs are associated with strongly developed zones of S_3 cleavage.

A relationship between basement lithology and the copper grade distribution was also observed by Miller (2006). Miller (2006) noticed that where basement quartzites were absent, “dead zones” or zones of low copper grade were seen in the orebodies. Two such zones were noticed in the 3000 and 3500 orebodies (Figure 3.7). Miller (2006) hypothesised that the quartzite units may be linked to silicification of the overlying shale producing a unit rheologically favourable for breccia development or that the quartzite may have been a fluid conduit for Cu-bearing fluids sourced from deeper units.

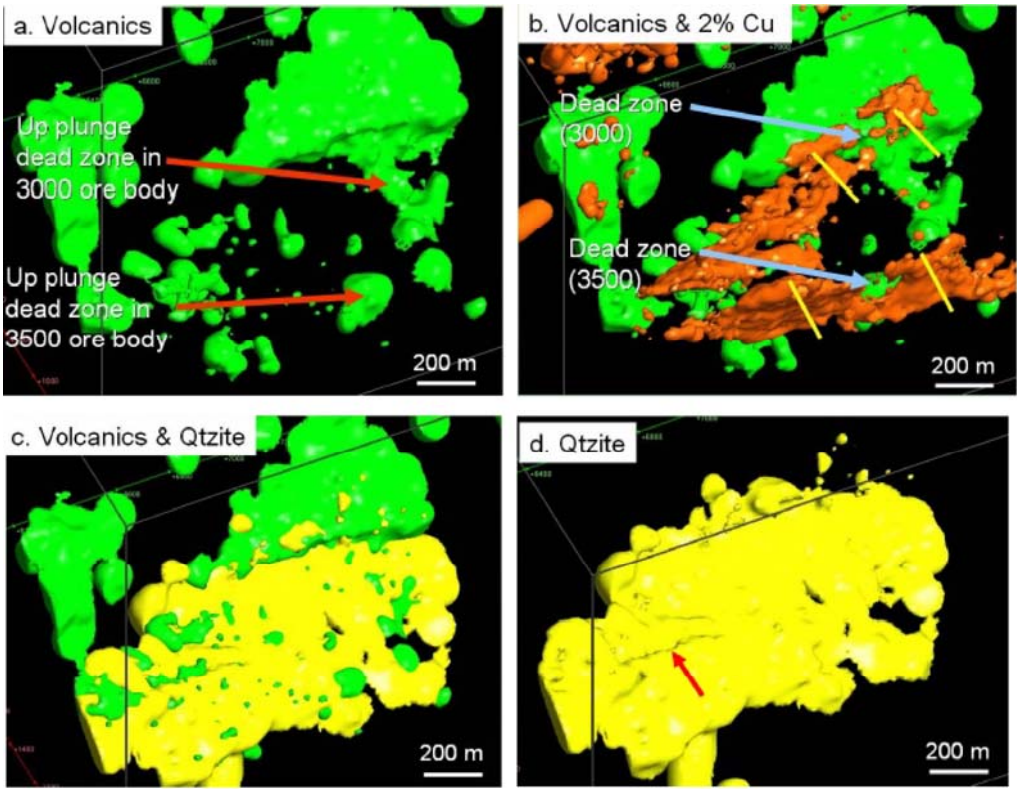

Figure 3.7 (from Miller, 2006) Isotropic Leapfrog models constraining the distribution of units defining the lower basement. Viewed looking NW – note that the volcanic rocks and quartzites are inter-layered in many areas. (a) Leapfrog model of volcanic rocks – coherent zones of volcanic rocks correspond to dead zones of low Cu grades in the over-lying shale units. (b) Volcanic rocks and 2.5% Cu (Leapfrog model). Yellow lines highlight F_3 fold plunge direction, which is a control on ore shoot plunge (e.g., Perkins, 1984). (c) Volcanic rocks and quartzites – note the quartzites sit in the flatter dipping area of the lower basement. (d) Leapfrog model of quartzites. Red arrow highlights basement trend defined by a depression within the quartzites (this is filled by volcanics –see (c)). This basement trend is parallel to a copper lode within the 3000 ore body and is not obvious in the lower basement contact wire frame that includes both units.

Miller (2006) determined bedding parallel slip along planes dipping ~60º to the west to be the key structural control on the development of copper breccias (Figure 3.8). Miller (2006) also recognised the ore brecciation tended to overprint the S_3 cleavage and hence brecciation post-dated the D_3 event. The extension orientation determined by Miller (2006) related to a hangingwall transport direction of southeast (sinistral-reverse movement on north-south bedding; Figure 3.9). This inference was consistent with copper mineralisation seen in localised jogs that would be dilatant in a sinistral-reverse environment. To create this observed slip vector, the stress field associated with the copper breccias would have had a σ_1 orientation in the northwest-southeast quadrant on a stereonet.

Importantly, the observed slip direction associated with the formation of the copper ore-breccias was independent of fold plunge, ore body trend (i.e. N-S or NNW-SSE) and the location of the breccias bodies with respect to basement.

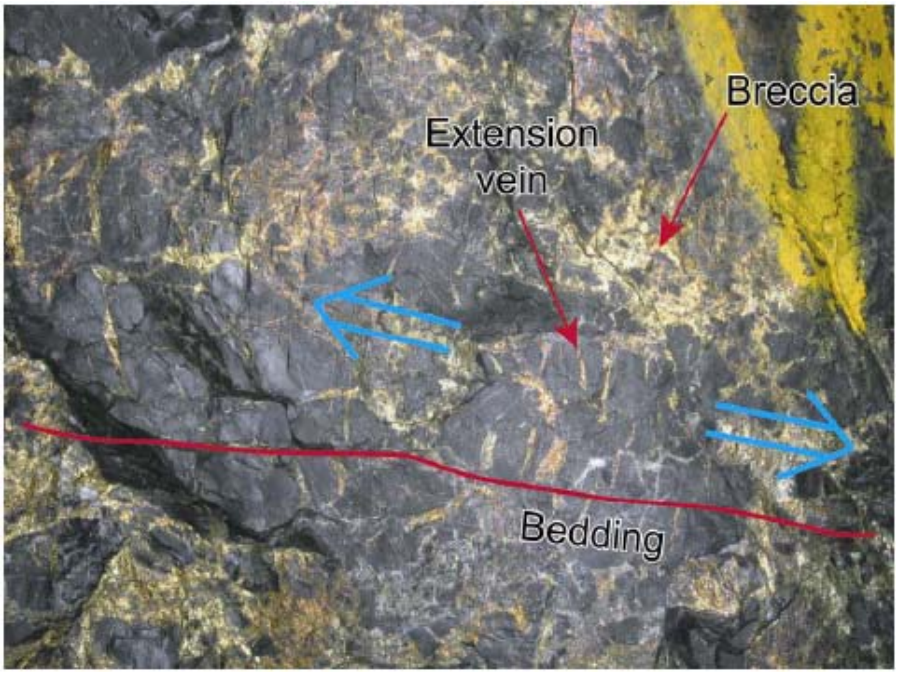

Figure 3.8 (from Miller, 2006) Syn-copper breccia veins that grade into a small package of breccia. M65 SEDR, 26b, 3000 ore body.

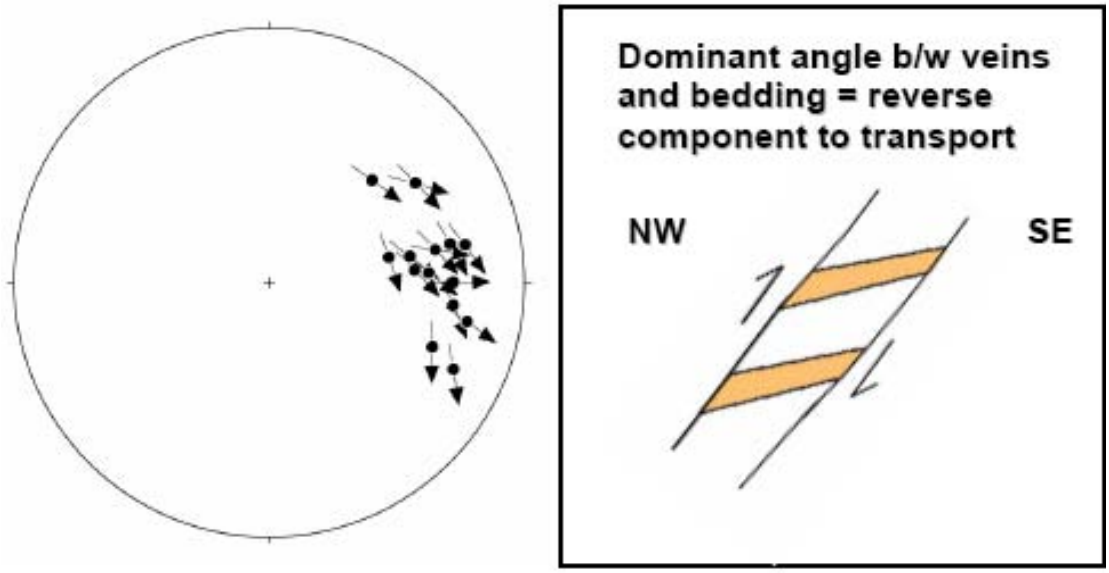

Figure 3.9 (from Miller, 2006) Stereonet plotting bedding/extension vein data from copper breccia bodies as projected hangingwall palaeotransport direction. Hangingwall paleotransport directions (see Miller and Wilson 2004) were calculated for all of the data by taking the average intersection direction between the extension veins and bedding for each data locality and assuming the deformation had a component of reverse movement. These arrows represent the transport direction of the rocks in the hangingwall of the fault calculated at the faults pole. The figure on the right highlights dominant bedding extension vein geometry (see Figure 3.8).

The presence of prior S_3 cleavage acted to increase permeability with the L^0_3 lineation (F_3 fold plunge) being a key control on ore shoot plunge (Miller, 2006) (Figure 3.10). Copper ore shoot plunges are typically parallel to the L^0_3 orientations (Miller, 2006). However, L^0_3 is not a consistent orientation over the extent of the copper mineralisation and as such ore shoot plunges are variable. Through systematic mapping of the copper ore bodies, Miller (2006) was able to determine the consistent extension direction along bedding planes (the slip vector orientation) and along the S_3 cleavage.

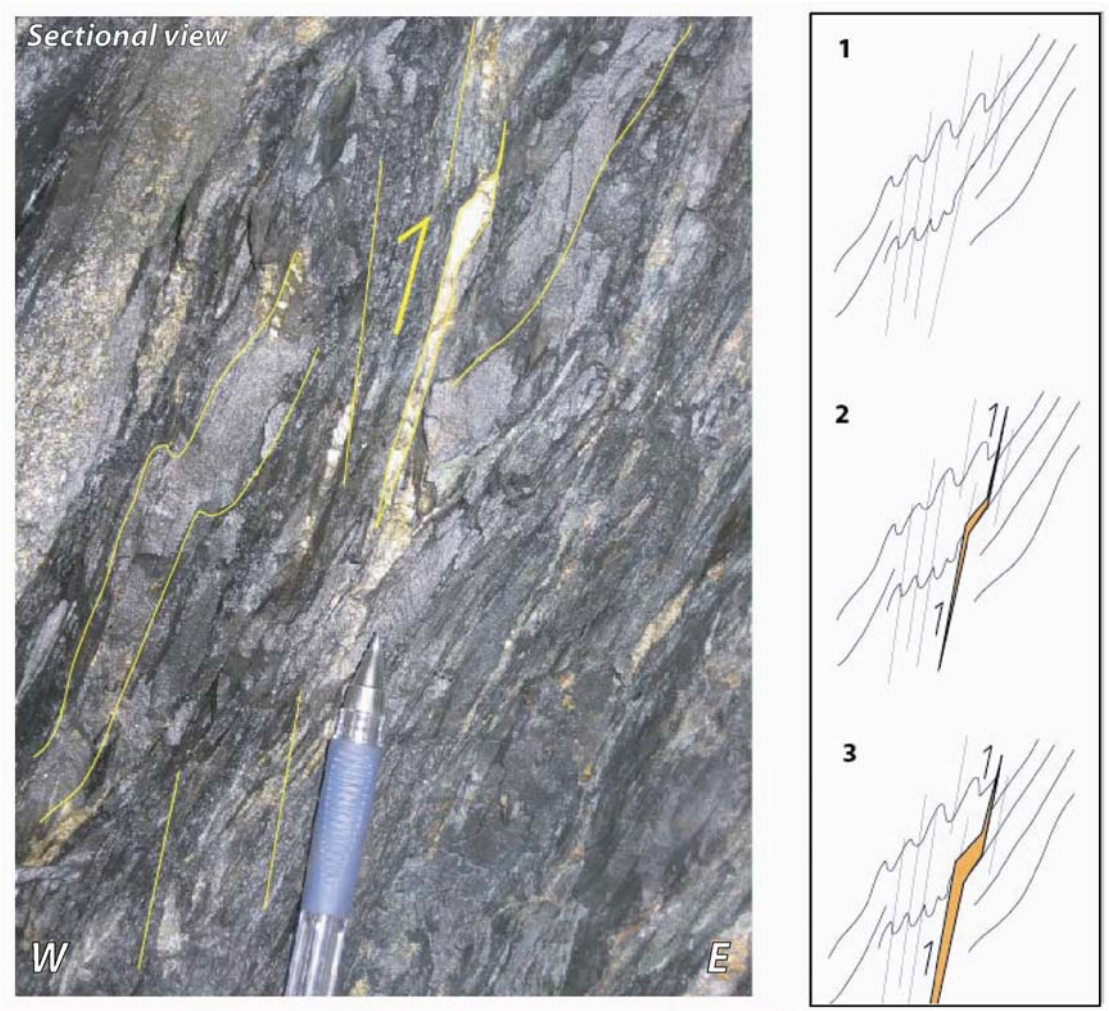

Figure 3.10 (from Miller, 2006) Jog-related chalcopyrite (slip along an S_3 cleavage plane). V624 6240 XC 27C, 3500S ore body.

Copper brecciation is inferred to be a single discrete event as there is no mesoscopic evidence for multiple phases of brecciation (Miller, 2006). The brecciation event was probably low strain with a limited net amount of slip along bedding surfaces (Miller, 2006).

This orientation of σ_1 was also related back to the distribution of high grade copper. Three dimensional modelling of the copper distribution at 2.5% showed geometries consistent with a sinistral component of movement at mineralisation (Figure 3.11).

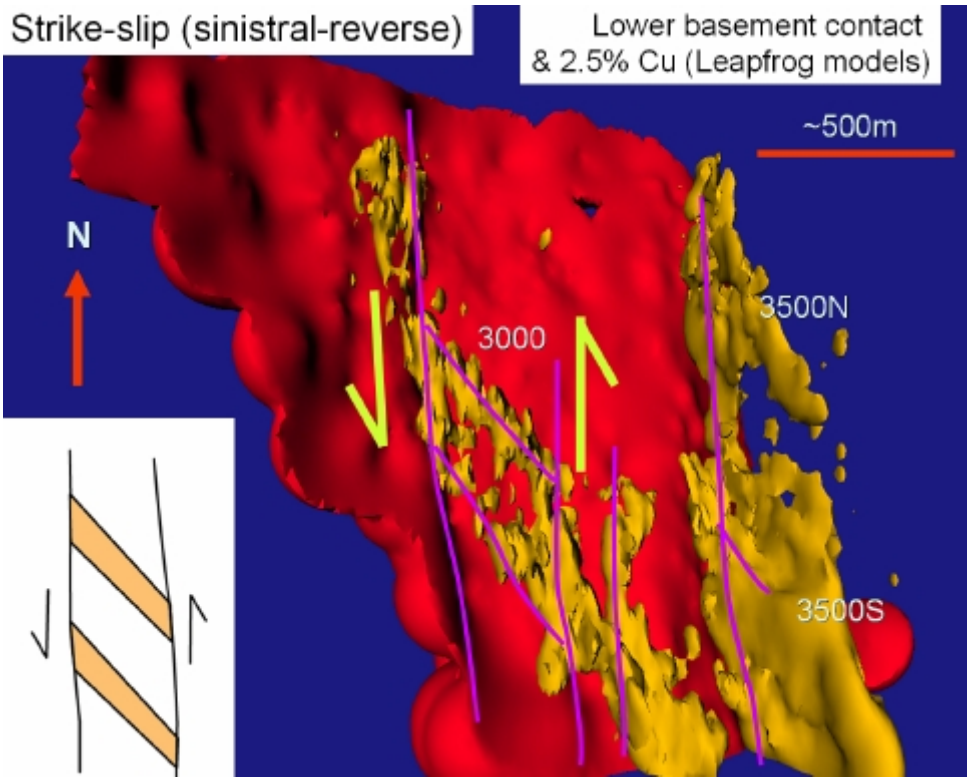

Figure 3.11. (from Miller, 2006) Plan vein leapfrog model of lower basement contact (red) and 2% Cu (orange) distribution Enterprise Mine area. Kinematic interpretation utilises slip data in Figure 3.10. Bedding strikes N-S and on average dips at 60° to the W.

Miller (2006) hypothesised that the mechanism for localisation of the bulk of the 3000 orebody and the 1900 orebody was linked to the dilation of NNW-trending basement lineaments that are inferred to be F_3 axial traces. Other ore bodies are linked to dilation of strong NNW-trending cleavages within the shale – these can occur off the basement (perched ore bodies). Miller (2006) observed that copper was more strongly linked to the S_3 cleavage in the dolomite hosted ore bodies (Figure 3.12).

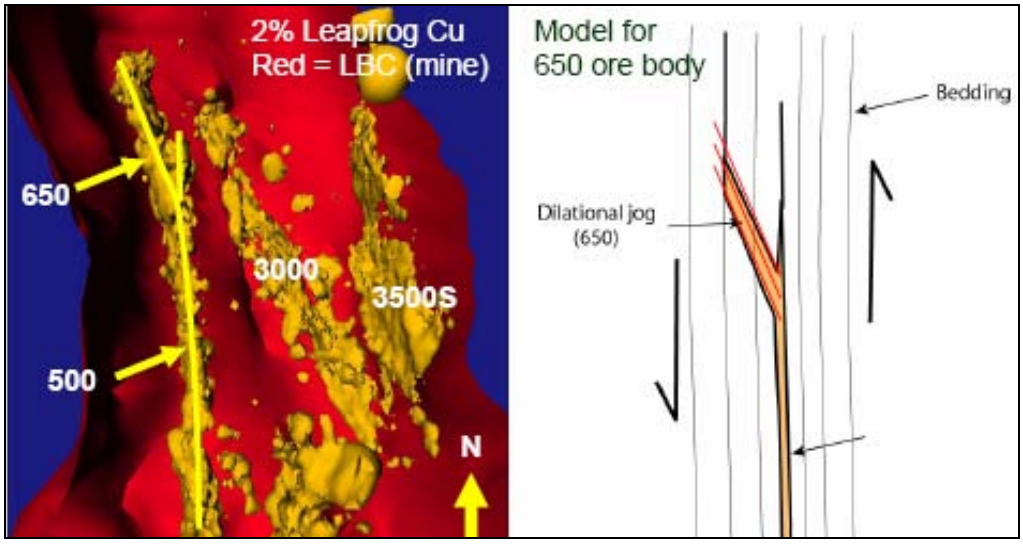

Figure 3.12 (from Miller, 2006) Leapfrog model highlighting strike-trends of different Cu ore bodies (orange) (c) Model for 650 ore body forming as a dilatant jog via failure of a pre-existing S3 cleavage (cleavage depicted as red lines).

Miller (2006) also deduced the kinematics of post-copper faulting. These are faults that offset the orebodies but still maintain minor chalcopyrite in the fault infill. He noted two sets of post-copper structures. The first set are W- and NW-dipping reverse and dextral reverse faults (these have quartz, pyrite and chalcopyrite fills) with consistent top-to-the-E hangingwall transport (Figure 3.13). These have been previously assigned a D_4 age, and have a talc association (asymmetric talc pressures shadows on pyrite). The second set of post-copper breccia structures are NE- and ENE-dipping dextral-reverse faults that offset some of the copper ore bodies.

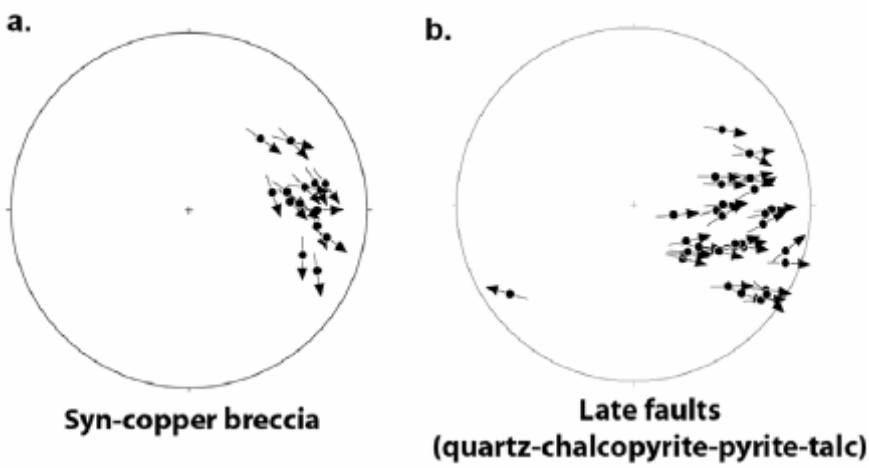

Figure 3.13 (from Miller, 2006) Hangingwall transport directions (see Miller and Wilson, 2004) plotted at the pole to the slip surface (commonly bedding). (a) Cu breccia (hangingwall top-to-SE). (b) Later W and NW-dipping faults (hangingwall top-to-E). Note different transport directions.

3.4 Implications of Miller (2006) structural study

The orientation of σ_1 that was responsible for the ore stage breccias at Mt Gordon was ESE-WNW (Chapter 2). The proposed SE-NW orientation of σ_1 responsible for the ore stage brecciation at Mt Isa by Miller (2006) is similar to that proposed for the ore breccia stage at Mt Gordon (Chapter 2). Mineralisation is inferred to occur late in the deformational history at both Mt Isa and Mt Gordon.

The results from these individual studies therefore suggest that far field maximum principal stress orientation of ESE-WNW to SE-NW, was responsible for formation of the breccias hosting copper mineralisation at the Mt Gordon and Mt Isa mines. It thus appears that there may have been a consistent far field stress regime responsible for copper mineralisation in the Western Succession of the Mount Isa Inlier during a late stage (D_4) in the Isan Orogeny (c. ~1530 - 1510 Ma).

3.5 Proposed localisation mechanisms

Perkins (1984), Bell *et al.* (1988), Davis (2004) and Miller (2006) document the importance of fold geometry and S_3 cleavage as important means of localising fracture, brecciation and the influx of copper-bearing fluids. Perkins (1984) proposed that the silica-dolomite lobe containing the 650 orebody (perched orebody) developed in a D_3 fold zone. The localisation of mineralisation and alteration within this fold zone provides an explanation for the attitude of the silica-dolomite body which is steeper than the transgressive to bedding (Bell *et al.*, 1988).

Bell *et al.* (1988) observed that the D_3 folds occur on a range of scales. They proposed that the bulk of the 1100 orebody lies adjacent to a large D_3 fold in the greenschist contact. The reactivation of bedding during the folding and unfolding of the shale unit during D_3, is one component of the failure mode proposed by Bell *et al.* (1988).

Several studies have been commissioned on-site into the effects of faulting on ore localisation within the mine (Foy, 1964; Bridges, 1970, 1971; Stoker, 1976; Mills, 1978; Raymond, 1990; Secis, 1992; Sims, 1992; Clark, 1994; Keys, 2002; Krois, 2002). These studies focussed primarily on characterising fault fills and relationships to ore, fault displacements of ore and alterations and determining fault timing. Many of these reports show that there is a close spatial association between intense faulting and high grade ore (Bridges, 1970; Sims, 1992; Keys, 2002), particularly in the perched orebodies (500 and 650 orebodies).

Robertson (1982) documented the importance of the pre-existing sulphides in the formation of the copper ores at Mt Isa. Robertson (1975; 1982) made the observation that the 1100 orebody with a massive core of chalcopyrite, was developed at the same stratigraphic horizon as rich pyrite mineralisation (>20% fine-grained pyrite) outside the ore zone, with a reduction of pyrite in this core. The highest grade copper zones are consistently stratigraphically equivalent to the external zones of abundant fine-grained pyrite (Figure 3.14).

The similarity in sulphur isotope composition between the chalcopyrite, the fine-grained pyrite and the lead-zinc ores was noticed by Robertson (1982). Robertson (1982) hypothesises that the pre-existing sulphur-rich horizons were the source of sulphur for the invading cupriferous solutions, resulting in the deposition of copper and silica. The dissolution

of the fine-grained pyrite would have released the sulphur, which was then used in the chalcopyrite formation.

The validity of the pre-existing sulphides as a sulphur source is disputed by Waring *et al.* (1998) who hypothesised that pyrite was added to the system during mineralisation rather than consumed. Despite the geochemical contribution (or lack there of) of the fine-grained pyrite, the undeniable spatial link between the early sulphides and the copper ores remains. I propose that the pre-existing sulphides may reflect zones of significant rheological contrast, and hence a structural localisation agent rather than be purely of chemical significance, as pyrite-rich layers may be considerably more competent than adjacent carbonaceous and/or carbonate-rich shale.

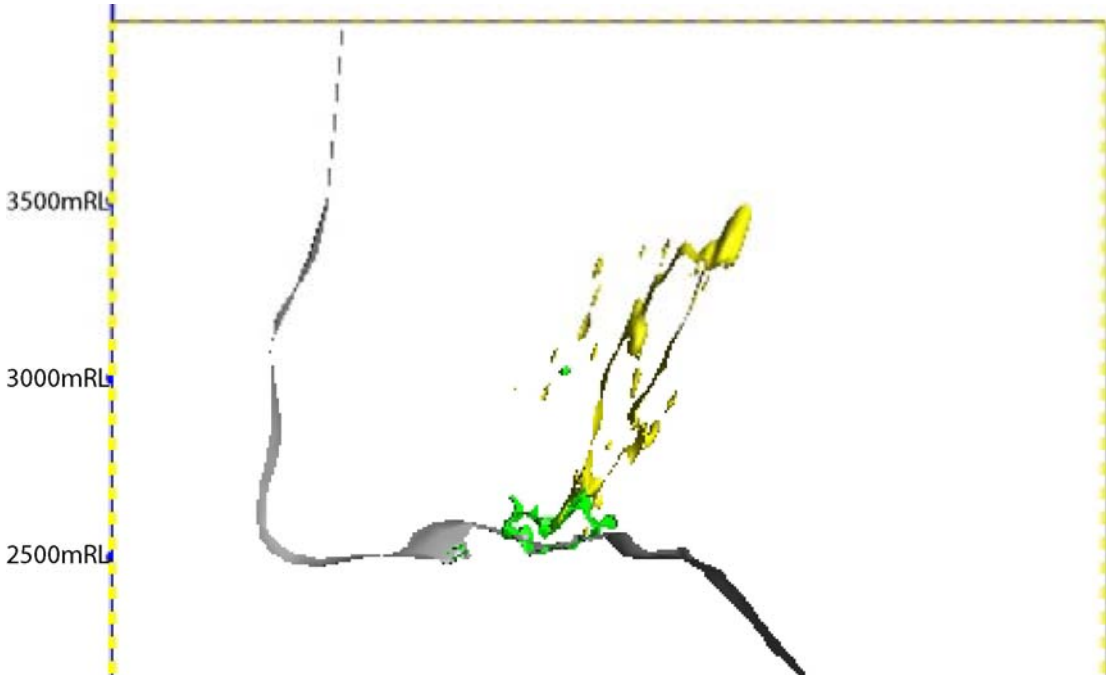

Figure 3.14 Section through 4930mN (mine grid) showing the Basement Contact Fault (grey), the fine-grained pyrite rib (yellow) and the 2% copper grade shell (green). The fine-grained pyrite horizon extends down-dip into the northern 1100 orebody.

3.6 Previous Numerical Modelling

With the improvement in computer technology many of the structural, geodynamic, and chemical hypotheses proposed for the genesis of the Mt Isa copper mines have been able to be simulated. Three examples of recent modelling of different structural hypotheses for the Mt Isa copper system are discussed below in detail.

3.6.1 Oliver et al (2001)

This modelling focussed on the syn-tectonic copper mineralisation at the Hilton Pb-Zn-(Cu) mine ~22 km north of the Mt Isa mine. Oliver *et al.* (2001) presented and discussed results from the structural mapping of Valenta (1989) and Valenta *et al.* (1994). Valenta's (1994) inferred structural history comprised early thrusting (D_1), regional north-trending folding (D_2) and late faulting and development of fold zones in various orientations (D_3-D_5). Rocks in the Hilton area lie on the west limb of a large scale D_2 anticline, contain a weak but penetrative S_2 cleavage, and have undergone intense faulting and block rotation associated with the D_2 to D_5 deformation episodes (Valenta, 1994).

Valenta (1994) demonstrated that the stratiform lead-zinc mineralisation and the associated stratiform pyritic shales were syn-sedimentary and predated any copper mineralisation by ~140 m. y. The Hilton Mine stratigraphy and lead-zinc mineralisation is cross-cut by dolerite dykes that predate the minor copper mineralisation (Valenta, 1994). The copper-rich zone of the Hilton Mine is associated with an area of high strain within the three hanging-wall lead-zinc orebodies where they are cut by a vertical extensional fault adjacent to a pre-copper dyke (Figure 3.15). The lead-zinc orebodies are bound by the Paroo Fault (west) and the Barkly Shear Zone (east) and it was inferred that there was a component of reverse movement on these faults during copper mineralisation (Valenta, 1994; Oliver *et al*., 2001).

The numerical modelling was conducted in UDEC, and was run for an E-W oriented cross-section (two dimensions). The modelling tested the effect of the rheological contrast of the Pb-Zn sulphides, intercalated shales and the discordant dolerite during E-W oriented shortening, the inferred orientation of σ_1 during copper mineralisation (Valenta, 1994).

The model runs showed significant perturbations in the stress orientations around the dolerite dyke during the E-W shortening, particularly early in the model runs (Figure 3.15c;

Figure 3.16 top). These perturbations were also accompanied by zones of low to moderate differential stress and high mean stress adjacent to the dyke (Oliver *et al.*, 2001). Late in the model runs, mean stress values around the dyke were seen to decrease, whereas differential stress values were seen to remain low (Figure 3.15d; Figure 3.16 bottom) (Oliver *et al.*, 2001). These model results were directly related to the rheological contrast between dyke rocks, and the shales and Pb-Zn orebodies (Oliver *et al.*, 2001) and lead to an increase in the fracture permeability of the dolerite dyke and the Pb-Zn layers (Oliver *et al.*, 2001). The inferred increase in fracture permeability is consistent with the mapped and logged intensity of alteration within and around the dyke.

Copper mineralisation is also associated with the intersection of the dyke and the Paroo Fault Zone, and is expressed as a zone of intense veining. The UDEC modelling produced a zone of high mean stress but very low differential stress (Oliver *et al.*, 2001) in this intersection. Oliver *et al.* (2001) hypothesised that if fluid pressures were high enough, it would be possible to form veins perpendicular to the maximum principal stress in this intersection.

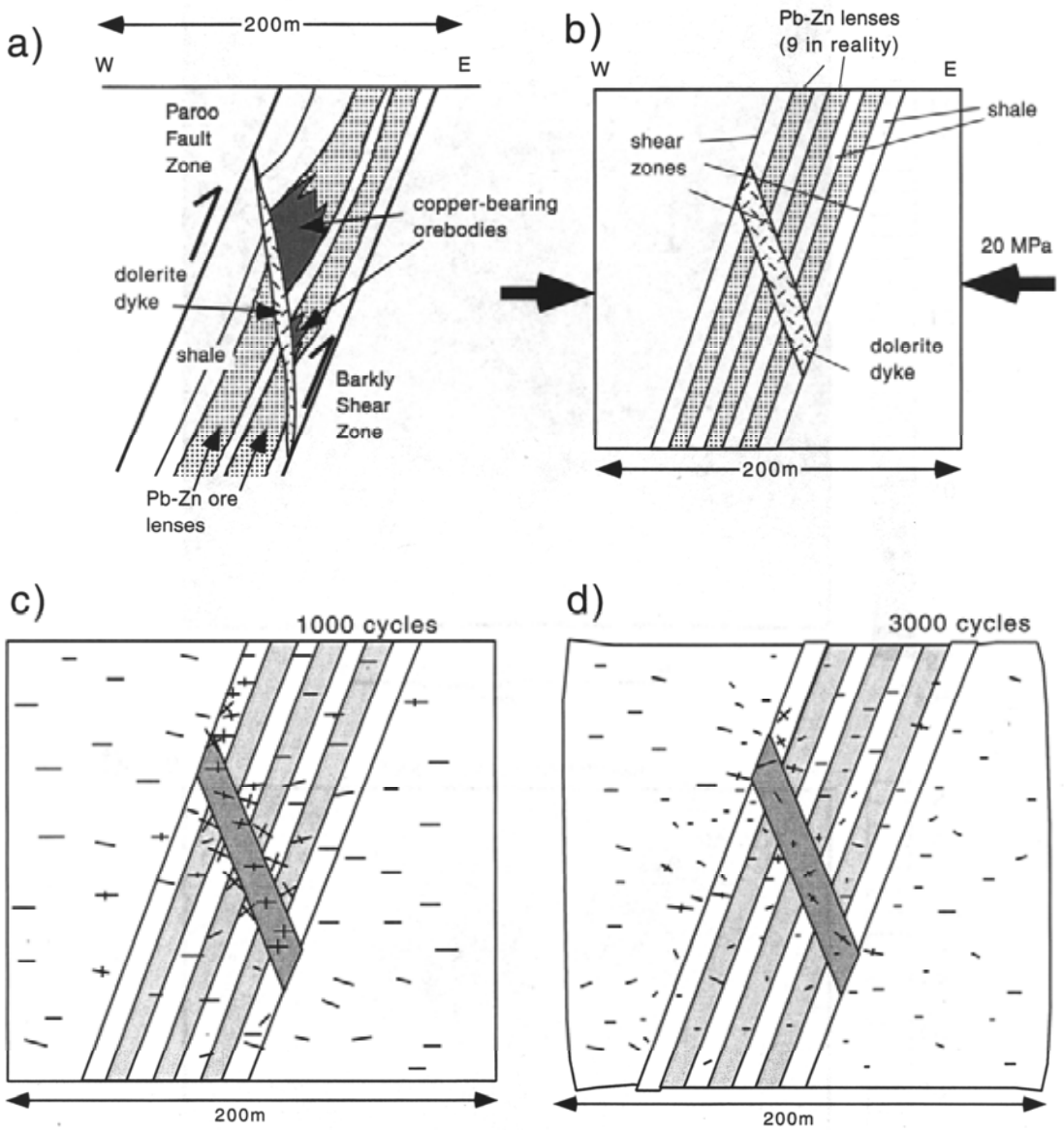

Figure 3.15 (from Oliver et al., 2001, adapted from Valenta, 1989) Geology and numerical modelling of coupled deformation and copper mineralization at the Hilton mine. ***(a)*** *Cross section of geology, showing interaction of Paroo and Barkly fault zones with a package of layered rocks (lead-zinc ore and shale), and an east dipping dyke that predates copper mineralization.* ***(b)*** *Input geometry for UDEC models, with E-W shortening and initial hydrostatic fluid pressure gradient, and an imposed E-W far-field differential stress of 20 MPa; rock and contact properties are listed in Table 3.* ***(c)*** *Two dimensional stress field after 1000 cycles. If the minimum stress is not shown then its magnitude is less than the line width; note variation in stress orientation and magnitudes around the dyke.* ***(d)*** *Stress field after 3000 cycles: note the overall lowering of stresses compared to 1000 cycles as strain is accumulated; also note zones of very low differential stress developed near where the dyke tips intersect the Paroo fault, which is a zone of intense alteration in the mine.*

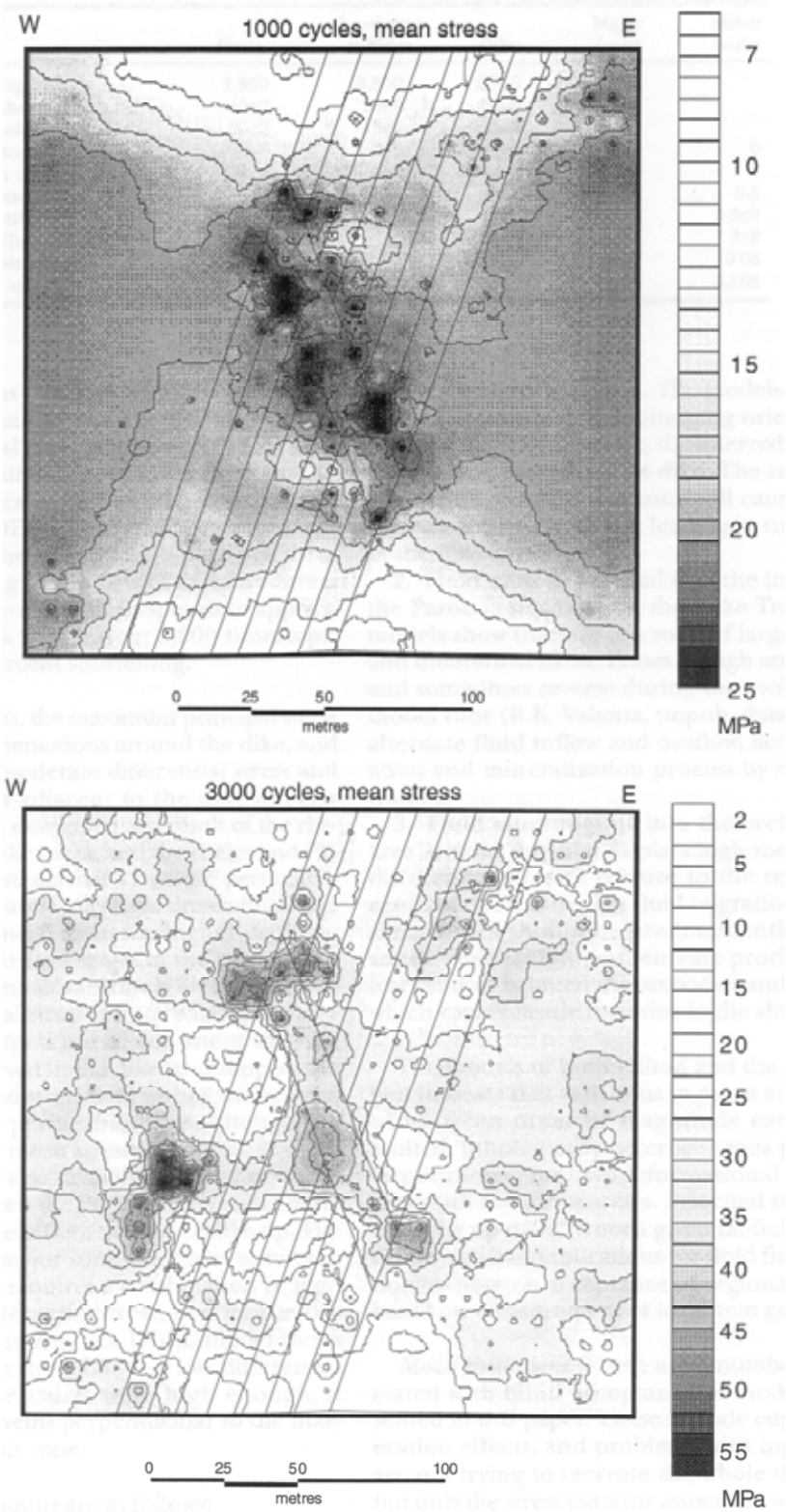

Figure 3.16 (from Oliver et al., 2001) ***Above*** *- Contours of mean stress at 1000 cycles equivalent to 3.15c.* ***Below*** *Contours of mean stress at 3000 cycles, equivalent to Figure 3.15d. Note correspondence of ore zones with zones of low Mean stress at 1000 cycles. At 3000 cycles, high mean stresses correspond with low effective stress and low differential stress around the dyke tips and where the dykes intersect the lead-zinc orebodies. Intense alteration of dykes and fault zones is found in these locations in the mine.*

3.6.2 Gessner et al., (2004) and Gessner et al., (2006)

This modelling investigated which deformation geometry localised strain in the Urquhart shale, and how strain geometry and structural architecture impacted on the fluid flow pattern. The modelling was conducted in FLAC^{3D} (ITASCA, 1997-2003) on a series of conceptual geometries. The base geometry contained of all the mapped stratigraphic units (Figure 3.17A). Variations of this model included the addition of the W41 and S48 faults (Model B; Figure 3.17B), a fault in the ECVs and the Lena quartzite (Model C, Figure 3.17C) and a combination of all models A, B and C (Model D, Figure 3.17D).

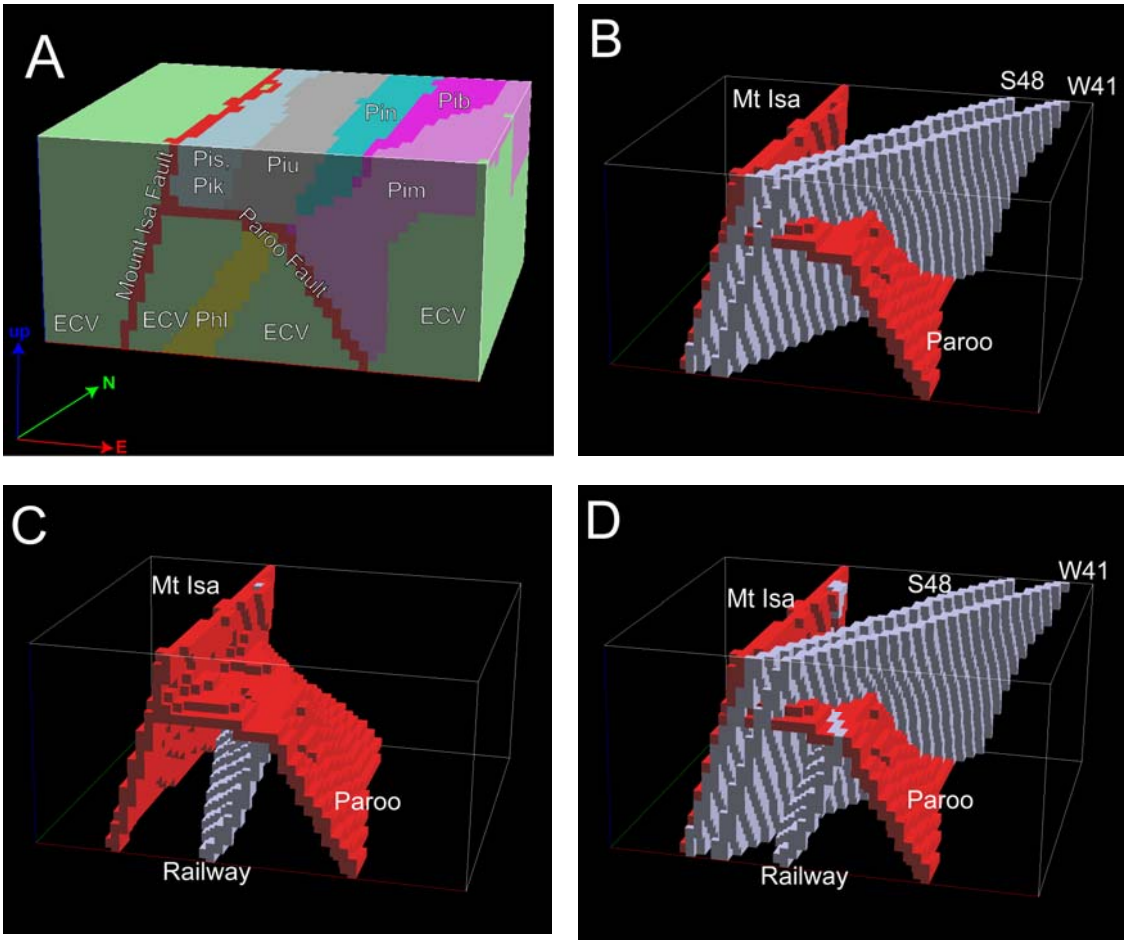

Figure 3.17 (from Gessner, 2004) Architectures used in the module. Image A shows all stratigraphic units of the model with the Mt Isa fault and the Paroo fault (Model 1). Images B-D show how additional faults were combined in the other models. View is towards NW

To account for the different tectonic events from syn- to post-D_2 to syn- to post-D_4, E–W contraction, top-to E simple shear strain and oblique dextral strike slip geometries were simulated (Figure 3.18). Gessner (2004) inferred that contraction was likely to have occurred

during the silica-event (Stage 1 – late D_2 to early D_3), because the ore breccia shows characteristics of hydraulic over-pressuring, which is less likely to occur in extension and strike-slip tectonic settings. The D_4 oblique strike-slip model was shortened from the ENE-WSW, consistent with the conventional syn-copper kinematic hypothesis at the time, of Bell *et al.* (1988).

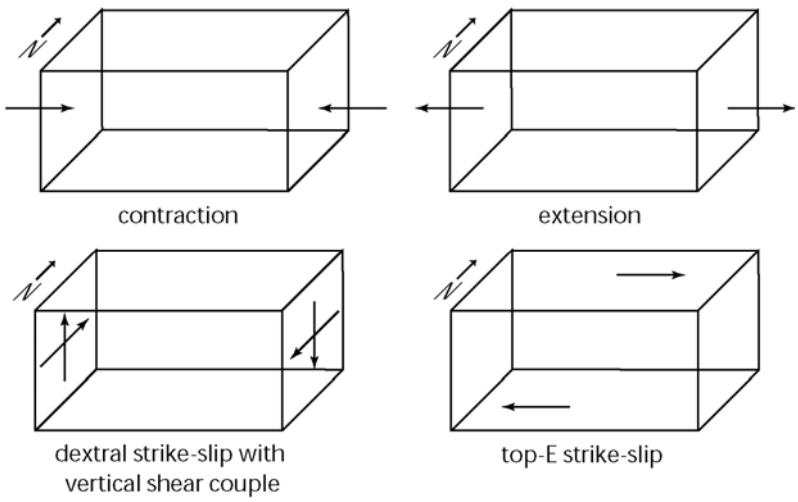

Figure 3.18 Deformation scenarios tested by Gessner (2004)

From the E-W contraction model results, Gessner (2004) inferred that the main structures which localised strain are the lower, E-dipping part of the Paroo fault, and the Urquhart shale itself, in the lower portion of which a shear strain maximum formed. A W-dipping, reverse-sense shear zone ('back-shear') branched off the zone of maximum shear strain. This structural arrangement resulted in a bulge in the Urquhart shale, which popped out between the two shear zones (Gessner, 2004). The occurrence of a strain maximum in the Urquhart shale represented a good fit with field observations (Gessner, 2004). Gessner (2004) also infer from the modelling that fracturing is limited to the Urquhart shale, mainly because of its favourably dipping anisotropy, but also because of its position in a shear strain maximum

The strain maximum and the back-shear patterns are also observed when the rockmass properties of the Urquhart Shale are changed to the rockmass properties of the Breakaway shale, or the Native Bee siltstone. In a case where all Isa Group rocks are assigned identical anisotropic properties, the strain maximum developed in the same location, however the back-shear did not develop at all. This means that the strain maximum in the Urquhart shale is mainly due to its position in the architecture, and only to a lesser extent

influenced by the material property distribution. Fracturing is limited to the Urquhart shale, mainly because of its favourably dipping anisotropy, but also because of its position in a shear strain maximum.

Gessner (2004) modelled oblique strike-slip deformation, which produced a range of steep NNE-SSW trending dextral shear zones and reactivation of the Mount Isa Fault. The relevant model run was seen to show strain patterns with little relevance to actual field observations and was a poor fit with known copper breccia locations. Model fracturing during oblique strike-slip deformation initiated in the Urquhart shale, the Lena Quartzite, and parts of the ECVs close to the Mount Isa fault, because these rocks were anisotropic, brittle, and/or located close to shear strain maxima, respectively (Gessner, 2004).

When the extension model was run (Gessner, 2004), model normal sense shear zones formed along the lower part of the Paroo fault, across the Isa Group stratigraphy in the eastern part of the model, and a normal sense (west side down) shear zone also reactivating the Mount Isa fault. This scenario also represented a poor match with field observations.

Overall, the simulated fracture patterns suggested that a component of top-to east simple shear was required to form the hydraulic breccia, which hosts the Cu-mineralisation, most likely in conjunction with contraction (Gessner, 2004).

3.6.3 Mattai et al. (2004)

The modelling of Mattai *et al.* (2004) was not specifically designed to test the structural controls on the copper orebodies. Rather, the modelling was conducted to test the potential for forced fluid convection as a method of driving hydrothermal fluids to the ore deposition site. Although not specifically mechanically oriented, the modelling does make some interesting, and hotly debated, assumptions on the magnitude and permeability of faulting in and around the mine sequence.

Geochemical and mass-balance constraints in conjunction with stable isotope data indicate that the Mount Isa copper deposit formed by mixing of a reduced sulphur-rich fluid from overlying Mount Isa Group metasedimentary rocks with a copper rich oxidised fluid entering a brecciated contact zone from underlying metabasalts (Mattai *et al.*, 2004).

The modelling hypothesised that differential uplift along the north-trending Mount Isa fault zone (Figure 3.19) was a plausible energy source for late-metamorphic fluid transport. Some 13 km were eroded from high-grade metamorphic rocks west of Mount Isa (Rubenach, 1992). The lower-grade region east of the Mount Isa fault zone, from which ~5 km were eroded, shows field evidence for widespread downward flow (oxidation, carbonation, desilicification) through highly fractured metabasalts. A marine evaporitic cover is indicated by high Br/Cl ratios in the infiltrating brines, but no stratigraphic record of the paleosurface is preserved.

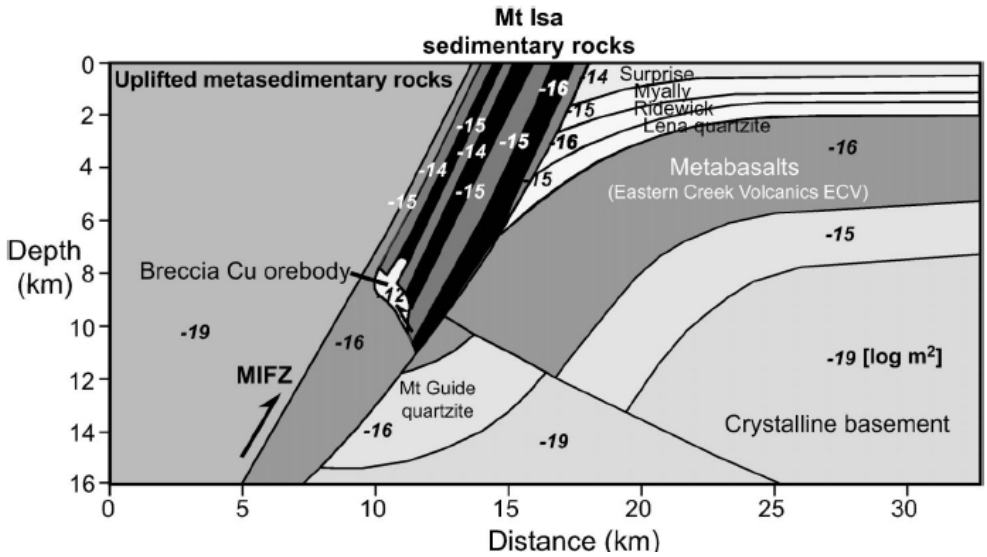

Figure 3.19 (from Mattai et al., 2004.) Interpreted cross section of late-metamorphic hydrothermal ore system, showing geometry of two geochemically distinct rock reservoirs: thick pile of metabasalts and wedge of metasedimentary rocks with pre-existing stratiform pyrite and lead-zinc sulfide layers. West of Mount Isa fault zone (MIFZ), hot high-grade metamorphic rocks are thrust upward. This displacement is predicted to induce copper mineralization by forced fluid convection in tectonic breccia situated above earlier Paroo fault. Constant permeabilities (shown as log10 m2 values) capture layered structure of intensely fractured rock pile.

Numerical simulations were run to test whether the deposit may have formed by forced fluid convection driven by progressive displacement on the Mount Isa fault zone, with the driving thermal gradient produced by an ~200 ºC offset in metamorphic grade. Results indicate that uplift of ≥1 mm/yr induces regional fluid flow organizing into a stable, permeability-controlled circulation system. Far-field advection through the oxidised metabasalts is superimposed on smaller-scale convection in the metasedimentary rocks beneath the fault. As convection on the large scale gains momentum, the breccia

progressively cools, consistent with mineralogic and fluid-inclusion evolution. For realistic uplift rates, the measured silica enrichment in the orebody (~190 Mt SiO_2) is achieved in ~1 m.y. Reduced and oxidised fluids mix at the proportions required for high-grade copper-iron sulfide precipitation, aided by rapid oscillations in the influx ratio of the two fluids into the most permeable and vigorously convecting orebody region.

Wilde and Gessner (2005) questioned the validity of the modelling on several levels, in particular the conclusion of Matthäi *et al.* (2004) that uplift is the driving mechanism on hydrothermal convection. Wilde and Gessner (2005) also argued that significant components of the Mattai *et al.* (2004) model were at odds with the current understanding of Mount Isa geology, particularly the architecture represented in the model, the magnitude and distribution of permeability, and the interaction of heat transport mechanisms (Wilde and Gessner, 2005).

Wilde and Gessner (2005) also claimed that there is ample evidence in the Mount Isa area for substantial fluid flow along faults, in particular along the Mount Isa and Paroo faults, which dilated in several tectonic events. While Matthäi *et al.* (2004) considered the permeability change due to deformation within the wall rock and the mineralised breccia, the faults were not considered as potential pathways. Matthäi *et al.* (2004) considered the Mt Isa Fault as the least permeable feature noting that the core of transcrustal faults in compressive settings as often being the least permeable (Evans *et al.*, 1997).

Oliver et al. (2006) also demonstrated that rapid deformation events such as those expected during faulting and brecciation have a strong tendency to disrupt convection cells. Mechanically-driven stress and fluid pressure changes must be considered in any thermal modelling which involves active faults.

3.7 Numerical Modelling

3.7.1 Model Justification and Assumptions

Gessner (2004) and Miller (2006) observed a relationship between Eastern Creek Volcanic basement lithology and copper distribution in the overlying Urquhart Shale. Where basement contained only metabasalts the copper grades above were seen to be low. Copper mineralisation was seen to be most pronounced when the basement beneath was comprised of silicified metabasalts and quartzites. There may be several interpretations of these observations;

- the quartzite units may be linked to silicification of the overlying shale by dissolution below the basement contact and re-precipitation above, producing a unit rheologically favourable for subsequent breccia development
- the quartzite may have been a preferred fluid conduit for copper-bearing fluids sourced from deeper units, such that mineralisation was then localised immediately above or
- the quartzites may have acted as a rigid body in basement, altering the mechanical behaviour of the basement contact fault, allowing fluid focussing at and above the contact.

Specific lines of numerical modelling have been employed to analyse the relationship between ore brecciation and basement lithology further.

The work of Oliver *et al.* (2001) provided protential insights into the localisation mechanisms at 100 metre scales. Deformation was seen to be localised in shales around the margins of a rigid body (a dolerite dyke), whilst only weak deformation was focussed into the pre-existing lead-zinc orebodies. The Gessner (2004) and Gessner et al. (2006) modelling results also showed that contrasting rheology is significant for the localisation of the copper orebodies. This study will also focus on the mechanisms of localisation for copper ore brecciation. The close spatial association between high grade mineralisation and fine-grained pyrite (Chapter 3.5) is one particular feature of the localisation mechanisms that will be analysed, that was not considered by earlier workers.

3.7.2 Conceptual models

The use of two-dimensional numerical modelling software UDEC requires that modelling must be carried out in cross-section or in plan. The use of UDEC in cross-sectional analysis on Mt Isa orebodies has been previously conducted successfully by Oliver *et al.* (2001) (Chapter 3.6.1). The 3D geometry shown in Figure 3.17 and the cross-sections shown in Figures 3.4 and 3.6 demonstrate the degree to which 2D cross-sections can be used.

As Miller (2006) had inferred an ESE-WNW to SE-NW shortening orientation for the formation of the copper breccias at Mt Isa, two sections through the orebodies oriented ESE-WNW, were sliced for numerical modelling (Figure 3.20; page 122). The two sections were chosen as they represented a flat basement ramp (northern section; e.g. Figure 3.6), and a ramp with a basement overhang (southern section; e.g. Figure 3.4). These geometries account for all of the styles of copper mineralisation that are proximal to the basement contact.

The three dimensional lithological shells, fault wireframes and silica-dolomite alteration shells created in Leapfrog 3D were all sliced along these two cross-sections. The resultant sections were then traced and converted into UDEC geometries. Due to limitations in the UDEC software, all fractures and contacts must join an edge or another contact. This affected several shells and wireframes including the fault wireframes. Fault wirefames are typically only constructed to the limits of development or drilling or until they terminate up-dip. In this instance the fault wireframes are extended to the model boundary. Other shells that were extended to model boundaries included the basement quartzites (lower boundary), fine-grained pyrite (upper boundary) and the Pb-Zn orebodies (upper boundary).

Two distinct lines of UDEC modelling were conducted:

(i) the effects of basement geometry and basement lithology on the localisation of copper (Table 3.1), and

(ii) other mechanisms assisting the localisation of copper ores (Table 3.2)

Regarding basement geometry, the models commence with the single basement lithology to determine the effect of the Basement Contact Fault only on the distribution of the Mt Isa copper orebodies. The Basement Contact Fault was the only structural feature inputted into the conceptual model geometries for this line of modelling.

Following the single lithology tests, a basement quartzite unit was added to the modelling runs. The basement quartzite was initially tested in its actual Leapfrog 3D modelled position. The effects of a thinner basement quartzite, multiple quartzite units and the quartzite above and below the basement ramp were also tested (Table 3.1). These permutations of the known geometries were run due to uncertainty of basement composition north and south of the current mine extents.

Table 3.1 Table summarising the basement geometry variations modelled.

MODEL NAME	MODEL OUTCOME	MODEL DESCRIPTION
SINGLE LITHOLOGY MODELS		
Whole model metabasalt	Poor visual fit with known position of copper orebodies	3.8.1
Metabasalt basement + Urquhart	Poor visual fit with known position of copper orebodies	3.8.2
VARIABLE BASEMENT MODELS		
Leapfrog modelled quartzite	Very good visual fit with orebody locations	3.8.3
Thin quartzite	Poor visual fit with known position of copper orebodies	3.8.4.
Two quartzites	Poor visual fit with known position of copper orebodies	3.8.5

The specific conceptual model geometries can be found with the results of each line of basement modelling.

The second line of modelling was directed at mechanisms assisting the localisation of the copper ores. All localisation modelling was superimposed on the best fit basement model that incorporated the actual Leapfrog 3D quartzite unit (Chapter 3.8.3).

Robertson (1982) considered the fine-grained pyrite rib to have a chemical control on the distribution of copper ore, but did not consider the possible mechanical localisation effect. The fine-grained pyrite was modelled as a rheologically competent unit that was stronger than the surrounding shales.

Orebody faulting was another localisation mechanism that previous authors have considered as important on ore distribution (Bridges, 1970; Sims, 1992; Keys, 2002). Mine fault wireframes were particularly detailed in the southern section. Thus all mine fault wireframes that intersected the southern cross-section plane, were incorporated into the UDEC model.

Many authors believe the Pb-Zn orebodies that sit above the 3000 and 3500 Orebodies, and much of the 1100 Orebody, were formed syn-genetically (Perkins, 1984; Valenta, 1994). The Pb-Zn grade shells were particularly well developed over the northern section. As such, the effect of a pre-existing Pb-Zn system has also been modelled on the northern section.

Table 3.2 Table summarising the localisation mechanisms modelled.

MODEL NAME	MODEL OUTCOME	MODEL DESCRIPTION
LOCALISATION MODELS		
Variable basement (3.8.3) + fine grained pyrite	Poor visual fit with known position of copper orebodies	3.8.6 Page 130.
Variable basement (3.8.3) + Orebody faulting	Poor visual fit with known position of copper orebodies	3.8.7 Page 130
Variable basement (3.8.3) + Pb/Zn	*Good visual fit with Cu ores*	3.8.8 Page 131

Table 3.3 Model rock and contact input parameters used in all UDEC modelling

Property	Metabasalt	Quartzite	Shale	Pb/Zn	Pyrite	Lith contact	Fault
Density (kg/m3)	*2650*	*2600*	*2650*	*2400*	*2650*		
Bulk modulus (Pa)	*49e9*	*40e9*	*40e9*	*16e9*	*49e9*		
Shear modulus (Pa)	*27e9*	*25e9*	*7e9*	*11e9*	*27e9*		
Cohesion (Pa)	*20e7*	*24e7*	*5e7*	*10e7*	*20e7*	*3e3*	*5e2*
Tensile strength (Pa)	*10e7*	*12e7*	*3e7*	*5e7*	*10e7*	*3e6*	*2e6*
Friction angle (°)	*31*	*31*	*37*	*32*	*31*	*35*	*30*
Dilation angle (°)	*2*	*2*	*5*	*2*	*2*	*5*	*5*
Normal stiffness (Pa/m)						*2e9*	*5e9*
Shear stiffness (Pa/m)						*5e5*	*8e4*
Permeability factor (Pa/s)						*238*	*300*
Aperture at zero normal stress (m)						*0.03*	*0.05*
Residual hydraulic aperture (m)						*0.01*	*0.03*

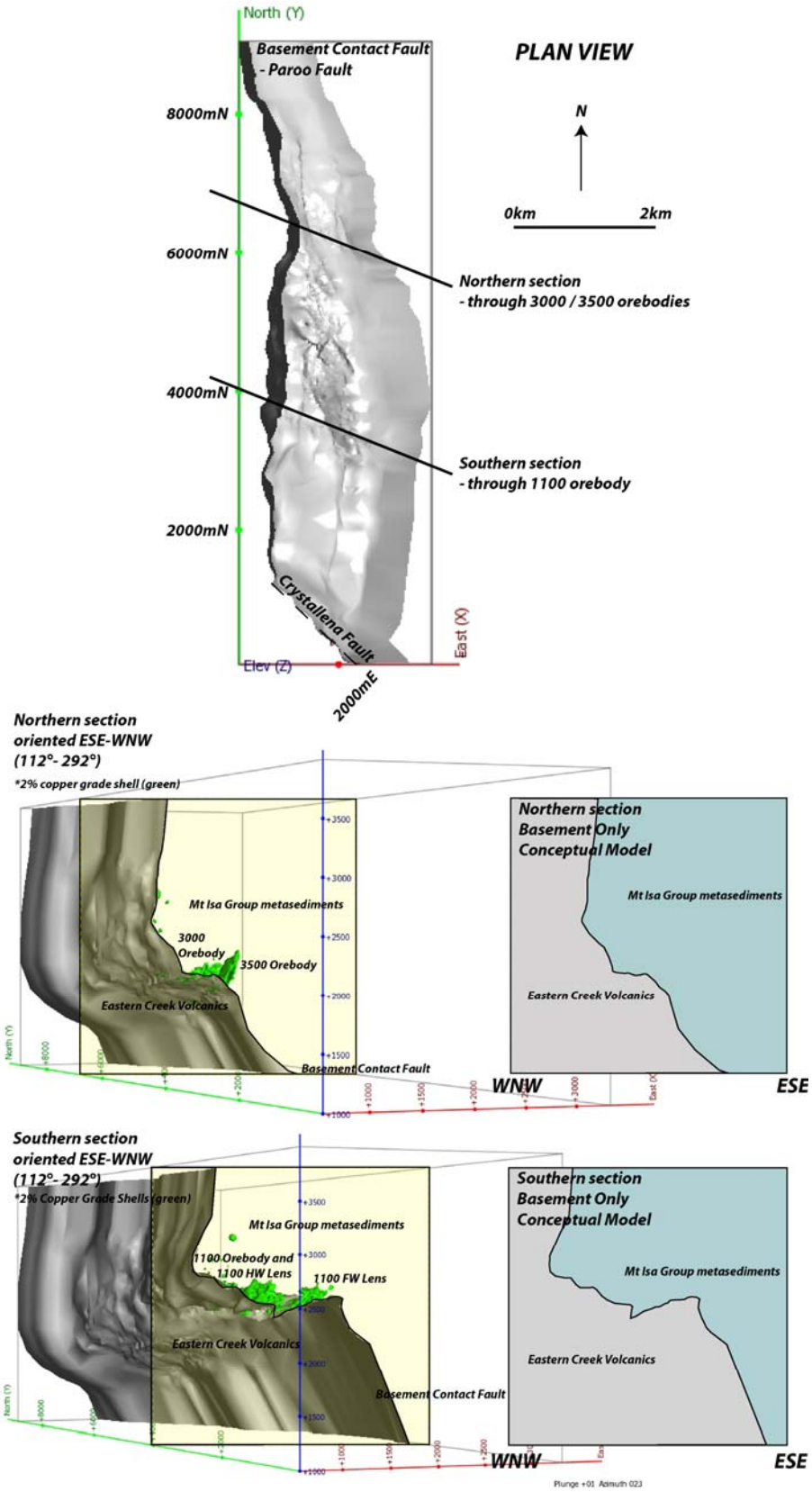

Figure 3.20 Plan view of the upper basement contact (provided by Xstrata Copper), with the black lines showing the orientation of the sections that have subsequently been numerically modelled in UDEC. The sections are oriented ESE-WNW to match the inferred σ_1 orientation responsible for the formation of mineralised breccias (Miller, 2006). The green shells represent the 2% copper grade shells.

3.8 Numerical Modelling Results

3.8.1 Whole model metabasalt (northern section only)

This conceptual model geometry (Figure 3.21) was designed to determine whether the Basement Contact Fault would preferentially dilate in the orebody locations, irrespective of rocktype, during ESE-WNW shortening. Results show small differences in the values of σ_3 and Pf_F between the rock above and below the fault. In both the northern and southern models, slightly lower values of fluid required for failure and lower values of minor principal stress were seen on the bottom side of the fault. This would normally be more indicative of failure below the fault, and is inconsistent with the known copper locations.

From this model we can infer that contrasting lithologies are required for failure within the Urquhart Shales, and the Basement Contact Fault geometry was not the sole cause of copper localisation.

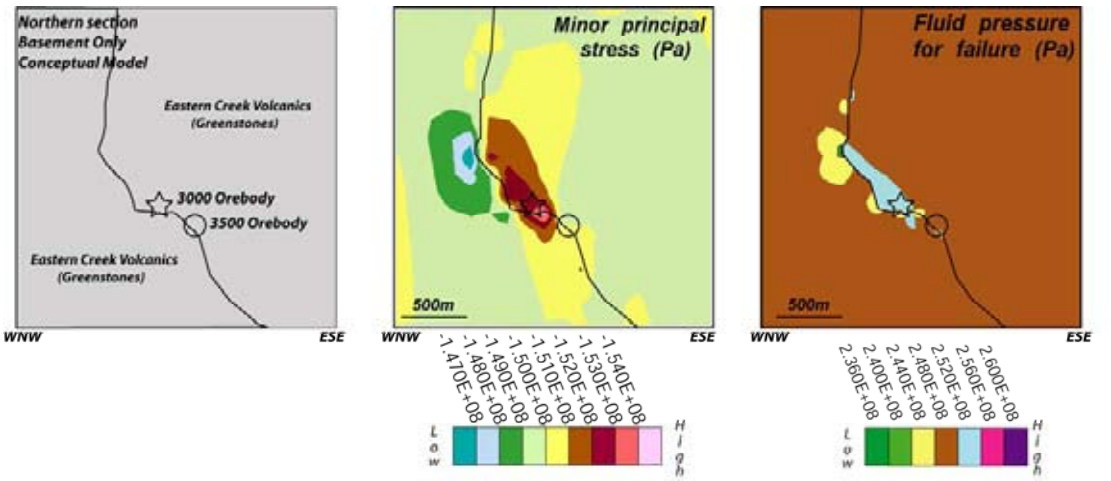

Figure 3.21 Greenstone only results (left) Conceptual model geometry for the northern section. (centre) Plot of minor principal stress showing relatively high σ_3 values in the known deposit locations. However the variation in minor principal stress values is only 10 MPa across the entire model. (right) Plot of fluid pressure for failure showing slightly lower fluid pressures required for failure beneath the basement fault.

3.8.2 Metabasalt basement and Urquhart Shale

The entire basement was modelled as metabasalt with a sequence of metasediment modelled above the ramp (Figure 3.22 and 3.23). The Mt Isa Group sediments above the fault (Magazine Shale, Kennedy-Spear Siltstone, Urquhart Shale, Native Bee Siltstone) were modelled as one unit. Despite this simplification, the plots of minor principal stress were again

slightly higher in the known mine locations (Figure 3.22 and 3.23). However due to the higher tensile strength and cohesion of the metabasalts, the basement of both models was seen to require much higher fluid pressures for failure (Figure 3.22 and 3.23). These models provided a modest fit with the known copper locations and show that at the very least, the basement contact fault and contrasting lithologies on either side are required for failure.

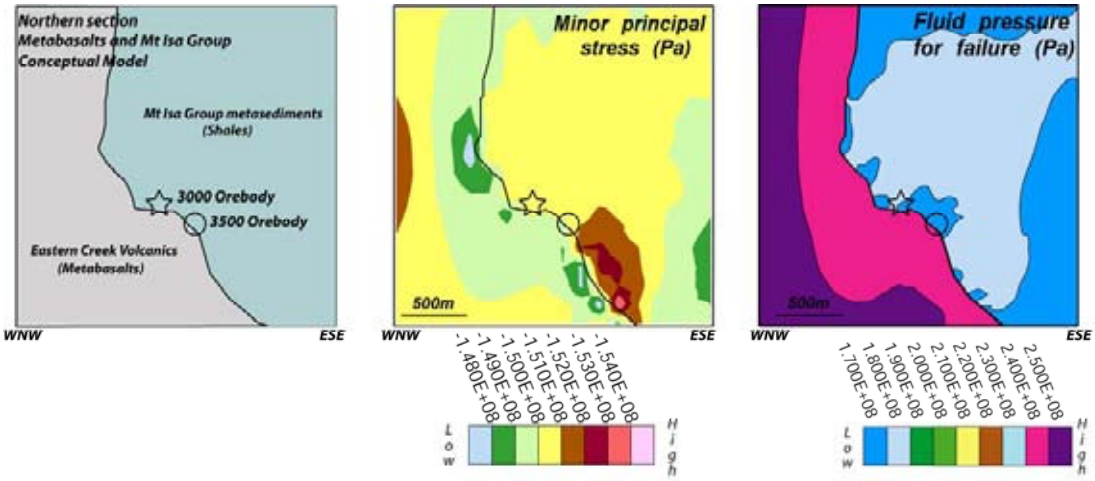

Figure 3.22 Greenstone basement under shales UDEC results (left) Conceptual model geometry for the northern section. (centre) Plot of minor principal stress showing relatively high σ_3 values in the known deposit locations. However the variation in minor principal stress values is only 7 MPa across the entire model. (right) Plot of fluid pressure for failure showing significantly lower fluid pressures required for failure in the known mine locations. The 3000 Orebody requires 170 MPa of fluid pressure for failure relative to the basement which requires 240 MPa.

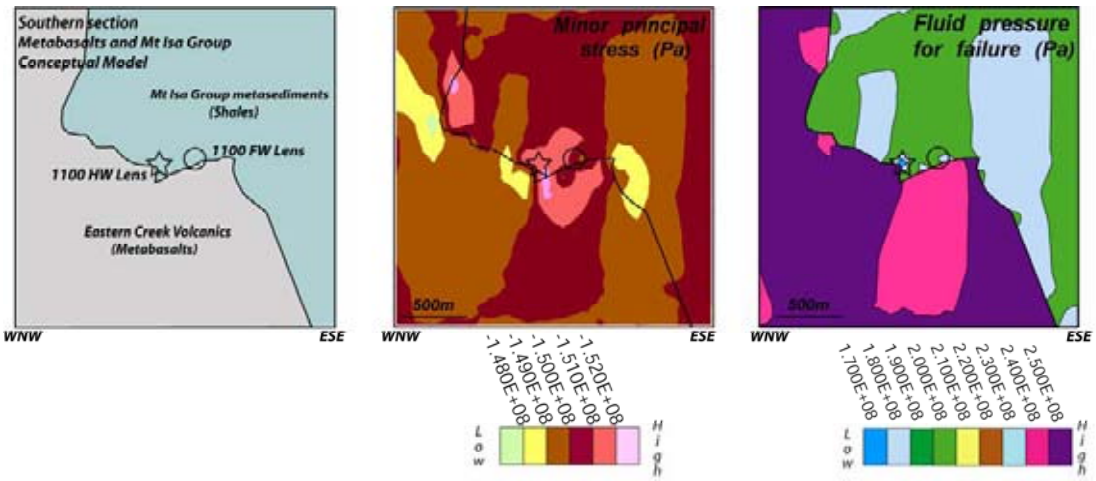

Figure 3.23 (left) Conceptual model geometry for the southern section. (centre) Plot of minor principal stress showing relatively high σ_3 values in the known deposit locations. However the variation in minor principal stress values is only 4 MPa across the entire model. (right) Plot of fluid pressure for failure showing significantly lower fluid pressures required for failure in the known mine locations. The 1100 HW Lens location requires 170 MPa of fluid pressure for failure relative to the basement which requires 250 MPa.

3.8.3 Leapfrog modelled quartzite

The conceptual model geometries were derived from the 3D modelling of basement lithologies conducted by Miller (2006). The presence of quartzite broadly correlates with the flattening of the basement ramp, and refraction of the basement fault through the quartzite is one explanation for the ramp formation (Bell et al., 1988; Miller, 2006).

The northern section model showed a good correlation between the location of the 3000 Orebody and the lowest σ_3 and Pf_F values (Figure 3.24). The values of σ_3 are ~50 MPa lower than any of the previous models (Chapters 3.7.1 and 3.7.2). The 3500 Orebody was located on a gradient between high and low values of both σ_3 and Pf_F. Large gradients of σ_3 and Pf_F are seen to correlate well with known deposits in the Mt Gordon modelling (Chapter 2.9).

The southern section models show similar trends (Figure 3.25). The 1100 HW Lens sits on a gradient of high and low σ_3 values and requires low fluid pressures for failure. The 1100 FW Lens sits in an area of low σ_3 values but requires slightly higher fluid pressures for failure. This model has produced results that are a good fit with the known deposit sites in both the north and south sections. From these results we can infer that basement heterogeneity is required for the formation of basement associated copper orebodies at Mt Isa.

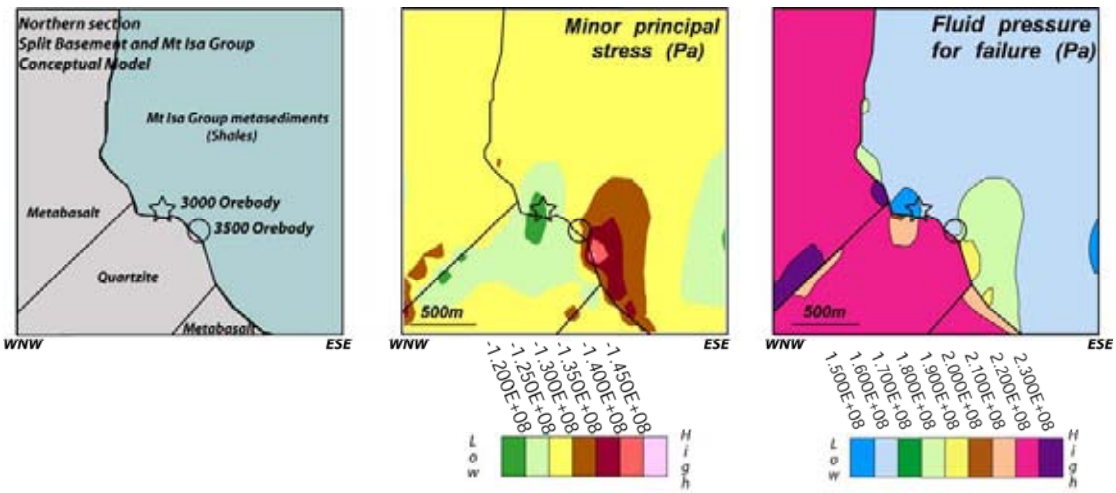

Figure 3.24 Split basement under shales UDEC results (left) Conceptual model geometry for the northern section. (centre) Plot of minor principal stress showing relatively low σ_3 values in the known deposit locations. The σ_3 values are significantly lower than in the previous models. There is a gradient between low and high σ_3 values in the 3500 Orebody location. (right) Plot of fluid pressure for failure showing significantly lower fluid pressures required for failure in the known mine locations. The 3000 Orebody location requires 150 MPa of fluid pressure for failure and again the 3500 Orebody sits on a

gradient between high and low Pf_F values. Values of σ_3 and Pf_F are not as low in the 3500 orebody location as the 3000 Orebody location suggesting further localisation mechanisms are required for its formation.

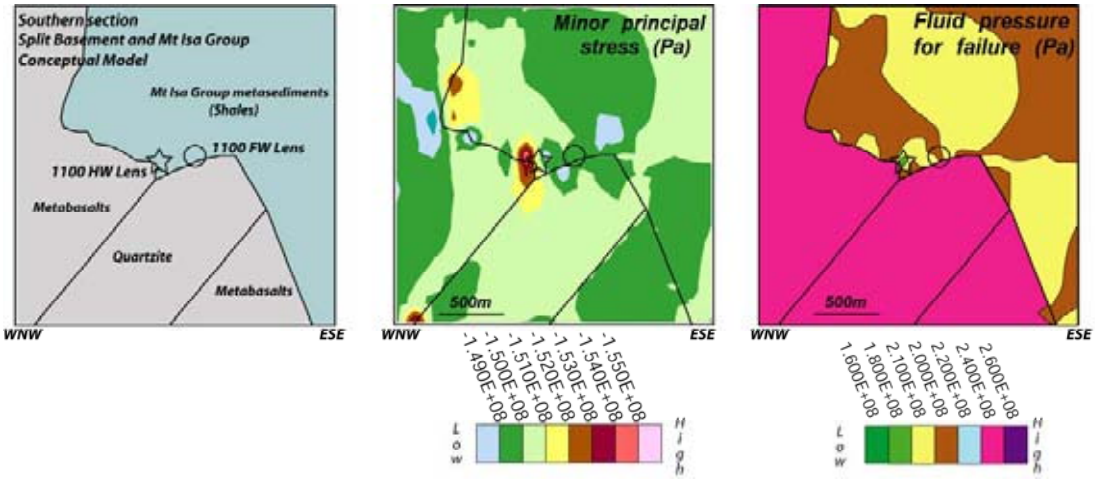

Figure 3.25 Split basement under shales UDEC results (left) Conceptual model geometry for the southern section. (centre) Plot of minor principal stress showing relatively low σ_3 values in the 1100 FW Lens location. The 1100 HW Lens straddles a gradient between high and low σ_3 values. (right) Plot of fluid pressure for failure showing significantly lower fluid pressures required for failure in the 1100 HW Lens location. The 1100 FW lens is seen to require moderate fluid pressures for failure, indicating that there may be further localisation controls required.

3.8.4 Thin quartzite

The nature and distribution of the quartzite unit is not well understood. Perkins (1984) and Miller (2006) suggested that the basement quartzite may in fact be silicified greenstones and not a stratigraphic quartzite unit. Due to a lack of drilling data, the thickness, or presence, of the basement quartzite is unknown, particularly at the south of the 1100 orebody near the Crystallena Fault. This model was designed to test the mechanical effect of thinning the basement quartzite unit. When the thickness of the quartzite is reduced, stress is redistributed around the quartzite body and into the shales. The result is that a zone of low σ_3 and low fluid pressure for failure extends out from the quartzite into the shale unit (Figure 3.26 and 3.27). The lowest values of σ_3 are ~30 MPa higher than for the thicker quartzite model (Chapter 3.7.3). Again the 3500 orebody and the 1100 HW Lens are located on relatively weak gradients of both σ_3 and Pf_F. These gradients are seen to represent a change of ~5 MPa for the σ_3 and ~10-20 MPa for the Pf_F.

Although these models still produce a fairly good visual comparison between areas of low σ_3 and Pf_F, comparison with the previous model leads to the inference that a thicker

quartzite unit beneath the basement contact is desirable when exploring basement contact related copper.

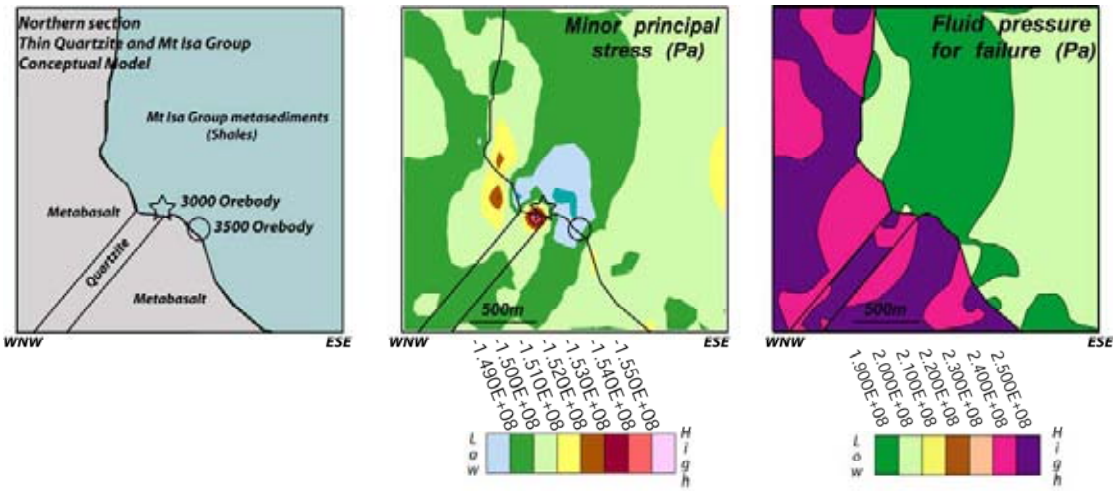

Figure 3.26 Thin quartzite in basement (left) Conceptual model geometry for the northern section. (centre) Plot of minor principal stress showing relatively low σ_3 values in the known deposit locations. There is a gradient between low and high σ_3 values in the 3000 Orebody location that appears to be associated with stress redistribution around the top of the quartzite. (right) Plot of fluid pressure for failure showing low fluid pressures required for failure in the known mine locations relative to the surrounding rock mass.

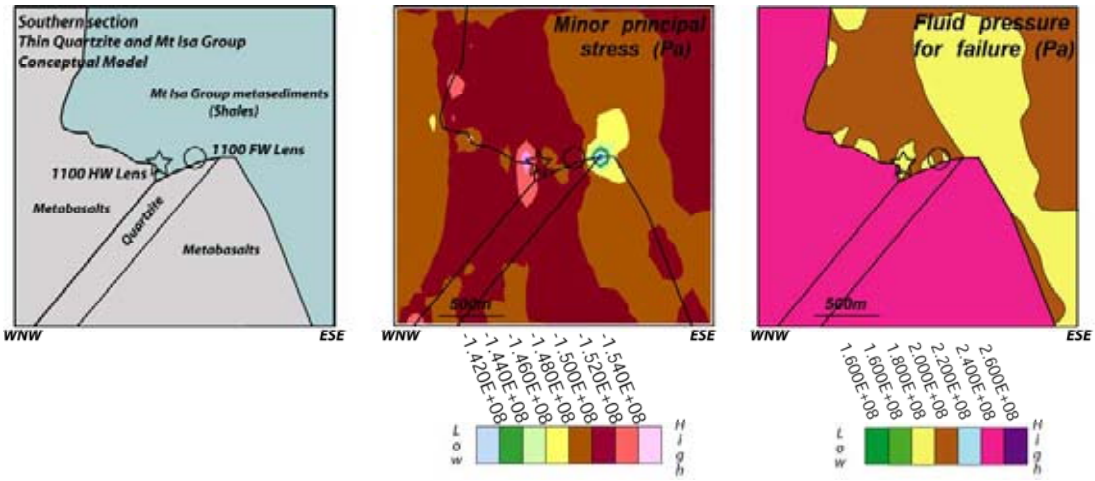

Figure 3.27 (left) Conceptual model geometry for the southern section. (centre) Plot of minor principal stress showing relatively low σ_3 values in the known deposit locations. This model is not a particularly good fit with the known orebody locations. (right) Plot of fluid pressure for failure showing moderate fluid pressures required for failure in the known mine locations relative to the surrounding rock mass. It would appear that a thinner basement quartzite is not desirable for mineralisation on a very flat basement ramp.

3.8.5 Two quartzites (northern section only)

If the basement quartzite unit is an alteration product associated with the pre-mineralisation silicification of the greenstones and shales, then it is possible that there are several small bodies of quartzite as opposed to one larger quartzite body, as previously modelled. This may reflect more than one fluid conduit at the time of the silicification. Miller (2006) documented the irregularity of the quartzite unit under the 3000 and 3500 orebody. This line of modelling seeks to determine the effect of two or more discrete quartzite units, particularly in the northern section of the mine.

The modelling shows a particularly good fit with relatively low σ_3 and Pf_F seen in the 3500 Orebody location, although the size of the anomaly is quite small. The 3000 orebody deposit location shows relatively high values of σ_3 (~152 MPa) and moderate values of Pf_F (~200 MPa) (Figure 3.28). Despite the good visual fit with the 3500 orebody, the values of σ_3 and Pf_F are still very high relatively high leading to the inference that two smaller quartzite units in basement are less likely to form large breccias in the overlying metasediments.

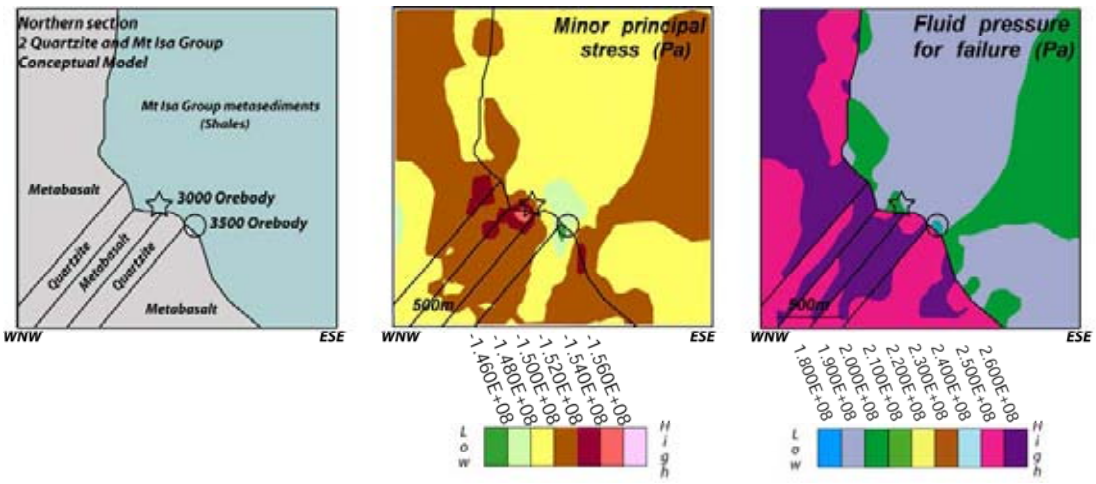

Figure 3.28 Two quartzites in basement UDEC results (left) Conceptual model geometry for the northern section. (centre) Plot of minor principal stress showing relatively low σ_3 values in the 3500 orebody location. There is a gradient between low and high σ_3 values in the 3000 Orebody location that appears to be associated with stress redistribution around the top of the quartzite. (right) Plot of fluid pressure for failure showing low fluid pressures required for failure in the 3500 orebody location.

3.8.6 Variable basement with fine-grained pyrite

The geochemical importance of the fine-grained pyrite on copper localisation (Robertson, 1982) has been since disputed by Waring *et al.* (1998). Despite this, there is still a close spatial relationship between the distribution of fine-grained pyrite and high grade copper in both the 3000 and 3500 orebodies and the 1100 orebodies. This line of modelling set out to determine the mechanical localising capacity of a rigid pyrite body between shales.

In the northern section there are two distinct fine-grained pyrite ribs. One is located in the hangingwall of the 3000 orebody and the other in the footwall of the 3500 orebody (Figure 3.29). UDEC models show a very good visual fit with known copper distributions. Values of σ_3 and Pf_F were the lowest of any of the models run to this point. The σ_3 were ~100 MPa in both the 3000 and the 3500 orebody locations. Pf_F values in both northern orebody locations were ~100 MPa, approximately 50 MPa better than any of the UDEC models to this point.The southern model produced a poor set of results, whereby high values of σ_3 and Pf_F were seen in the 1100HW location (Figure 3.30).

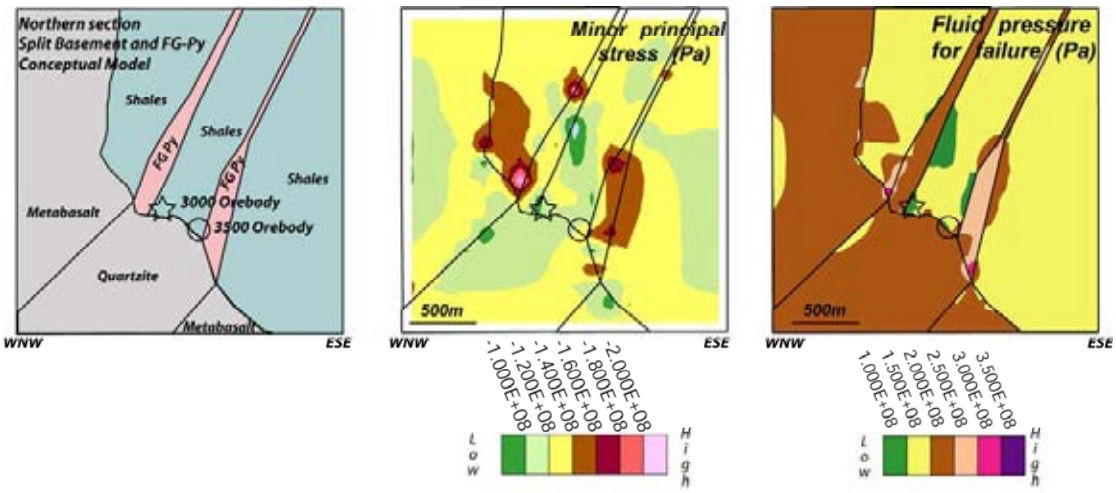

Figure 3.29 (left) Conceptual model geometry for the northern section incorporating fine grained pyrite.. (centre) Plot of minor principal stress showing ow σ_3 values in the 3500 orebody location. There is a gradient between low and high σ_3 values in both deposit locations that appears to be associated with stress redistribution around the top of the quartzite. (right) Plot of fluid pressure for failure showing low fluid pressures required for failure in both orebody locations.

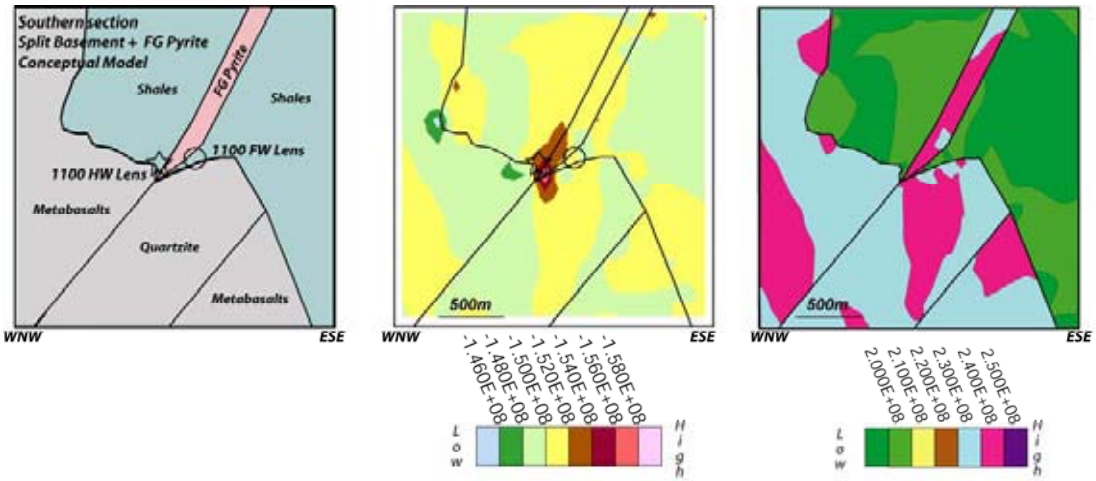

Figure 3.30 (left) Conceptual model geometry for the southern section with a fine-grained pyrite rib running into the overhang area. (centre) Plot of minor principal stress showing relatively low σ_3 values in the 1100FW location but a relatively high value in the 1100HW location.. This model is not a particularly good fit with the known orebody locations. (right) Plot of fluid pressure for failure showing moderate fluid pressures required for failure in the known mine locations relative to the surrounding rock mass. It would appear that the presence of fine-grained pyrite in an overhang–type of basement geometry is not conducive to brecciation. The results from Figure 3.29 however show that fine-grained pyrite can be a reasonable localising agent in the right geometrical situations.

3.8.7 Variable basement and orebody faulting – southern section only

Orebody faulting was seen to be a far more efficient localisation mechanism for predicted brecciation. Both the 1100FW and 1100HW deposits were defined in both the plots of minor principal stress and fluid pressure for failure (Figure 3.31). Although the models produced lower values of σ_3 and Pf_F in the known deposit locations, values of both were still relatively high compared to previous models (σ_3=145 MPa and Pf_F = 170 MPa). From these results we can infer that orebody faulting is preferable but not essential for breccia development in the Mt Isa Copper Mines.

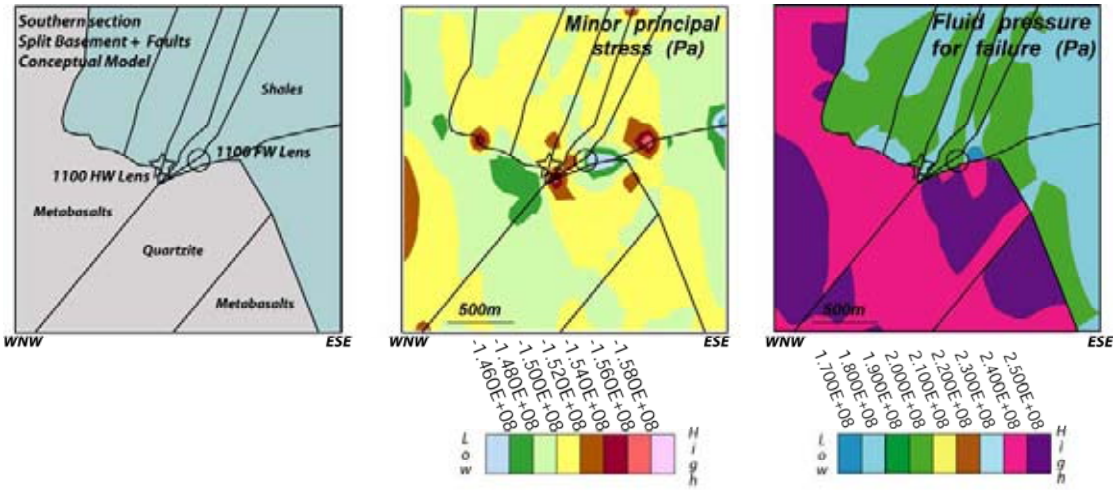

Figure 3.31 (left) Conceptual model geometry for the southern section with mine faulting incorporated. (centre) Plot of minor principal stress showing relatively low σ_3 values in the 1100FW location but a relatively high value in the 1100HW location.. This model is not a particularly good fit with the known orebody locations. (right) Plot of fluid pressure for failure showing moderate fluid pressures required for failure in the known mine locations relative to the surrounding rock mass. It would appear that the presence of fine-grained pyrite in an overhang –type of basement geometry is not conducive to brecciation. The results from Figure 3.30 however show that fine-grained pyrite can be a reasonable localising agent in the right geometrical situations.

3.8.8 Variable basement and Pb-Zn orebodies – northern section only

The model incorporating the Pb-Zn orebodies was seen to show low values of σ_3 and Pf_F in the 3000 and 3500 orebody locations (Figure 3.32). Values of σ_3 reached ~90 MPa and values of Pf_F were approximately 120 MPa. This is a significant lowering of both values and would imply that the presence of the Pb-Zn may improve the rheological contrast required to brecciate and dilate the rock mass.

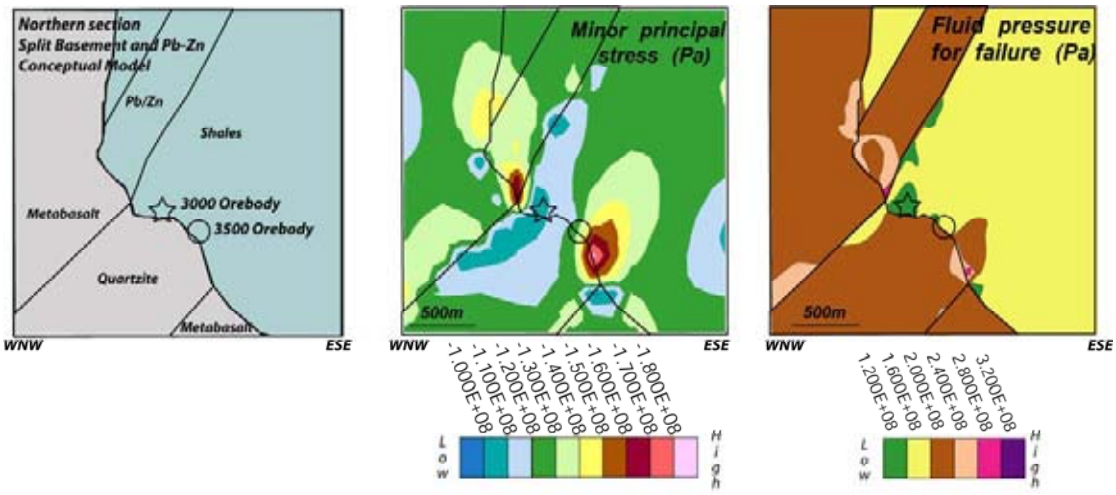

Figure 3.32 (left) Conceptual model geometry for the northern section incorporating a thick unit of dominantly Pb-Zn in the HW of the 3000 orebody. (centre) Plot of minor principal stress showing low σ_3 values in the 3000 orebody location. There is a gradient between the location of the 3500 orebody and the 3000 orebody.. (right) Plot of fluid pressure for failure showing low fluid pressures required for failure in both orebody locations.

3.9 Modelling and Mapping Synthesis

The modelling of simplified basement geometries in this study produced some interesting results. A metabasalt only basement was seen to show values of minor principal stress and fluid pressure for failure that were relatively low in the mine location. The model was improved significantly when the quartzite was widened, to represent the actual quartzite thickness in basement.

The distribution, thickness and position of the basement quartzite is poorly constrained to the north and south of the current resource. Several variations of the basement quartzite were modelled to test the effects of subtle changes to quartzite geometry, but no model results replicated the successful models of the known quartzite thickness.

Localisation mechanisms were also tested within the Urquhart Shales with quite mixed results. The presence of fine-grained pyrite was seen to be advantageous in the northern section, but didn't improve the localisation of dilatancy in the southern section. Orebody faulting appeared to have a little success and most certainly wasn't detrimental to the brecciation of the Urquhart Shale. The Pb-Zn seemed to localise deformation along the basement contact, coincident with the known deposits.

On the basis of some simple 2D UDEC modelling, it would appear that basement heterogeneity and possibly some pre-existing soft sulphides are preferable for localising brittle deformation above the basement contact.

Consideration of the modelling results of Gessner (2004), in conjunction with the structural observations of Perkins (1984), Bell et al. (1988) and Miller (2006), suggests that some of the initial conceptual models established by Gessner (2004) may have utilised kinematic information related to pre-ore alteration.

The oblique strike-slip model (Gessner, 2004) was designed to model a syn-copper deformation event. However, when related to the observations of D_3 mine-scale folding by Bell et al (1988), Davis (2004) and Miller (2006), the oblique strike-slip (dextral reverse on N-S striking bedding) models may more accurately reflect the D_3 event, immediately prior to ore genesis. Some of the oblique strike-slip model observations that are consistent with mapped D_3 features include the formation of steep NNE-SSW trending dextral shear zones.

The alternative simple-shear model of Gessner (2004) provides a better fit with known mineralisation, as the model effectively creates a zone of low strain in the approximate orebody location (Figure 3.33). Top to the east simple-shear, would also induce reverse movement on faulting and bedding, which has been documented by Miller (2006). The lack of a sinistral component of displacement to the N-S oriented bedding and faulting may explain why the model provides only a reasonable fit with the orebody locations.

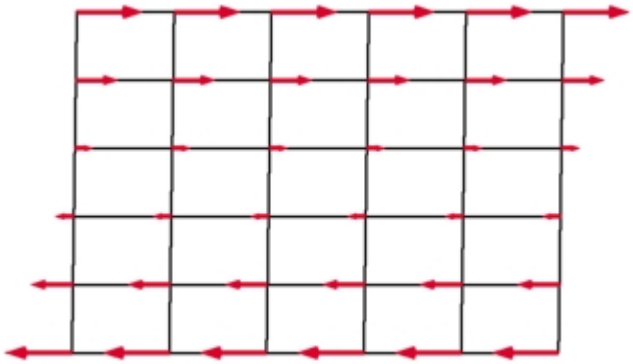

Figure 3.33 (from Gessner, 2004) An example of simple shear in two dimensions on a simple grid. The arrows represent the magnitude of the strain. This implies that the centre of the model is in a zone of relatively low strain to the outer margins of the model.

The contraction model of Gessner (2004), effectively tested horizontal E-W shortening, may better reflect either a transient stage between the proposed ENE-WSW D_3 event and the proposed ESE-WNW copper breccia forming D_4 event, or the E-W directed post copper deformation event associated with E-W shortening. Components of the model may well be applied to both scenarios.

When the Gessner (2004) results are considered in this context they correlate nicely with a range of timeframes in the deformation history of the Mt Isa Mine.

Kendrick *et al* (2006) documented fluid mixing of metamorphically derived fluids (from the Barramundi basement) and bittern brines for the formation of the Mt Isa copper orebodies. This implies the introduction of the metamorphic fluids from depth. The strike-slip nature of the D_4 copper event may allow the tapping of deep fluids and the brittle nature of the D_4 deformation may provide the locus for fluid mixing.

4. MT KELLY COPPER MINE

4.1 Introduction

The Mount Kelly Copper Mine, located 110 km north northwest of Mount Isa has a long history of exploration and only limited exploitation (Figure 4.1). Mount Kelly is a series of small deposits 20 km south west of Lady Annie. The Mt Kelly copper deposits include Mt Kelly, Mt Clarke, Flying Horse and MK475 (Figure 4.2).

The Mt Kelly Copper Mine is thought to be of similar age to the Mt Gordon and Mt Isa Copper mines (Stephens, 2001; Maiden *et al.*, 2000; Da Costa, 2005) and as such an understanding of the structural controls on copper mineralisation may be of significance in this Inlier-wide study.

Limited outcrop exists over the mineralised breccias, hence there is little knowledge of the structural controls on copper. This gap in understanding and the successful application of the numerical modelling at the Mt Gordon Mine, provide the framework for study at Mt Kelly. A more comprehensive knowledge of deposit scale structural controls on mineralisation will be sought, primarily through the use of numerical modelling. Thus, the use of the numerical modelling is more of a predictive exercise than for the Mt Gordon study.

Primary copper mineralisation consists dominantly of chalcopyrite and pyrite, concentrated in the matrix of breccia zones and in quartz-carbonate stockwork veins. Gold is locally present, both as discrete grains and locked in chalcopyrite and pyrite (Maiden *et al*, 2000). The main copper oxide mineral is malachite, with minor azurite, chrysocolla, cuprite and tenorite. Both the sulphide ores and the copper oxide mineralisation appear to be shear and fault controlled.

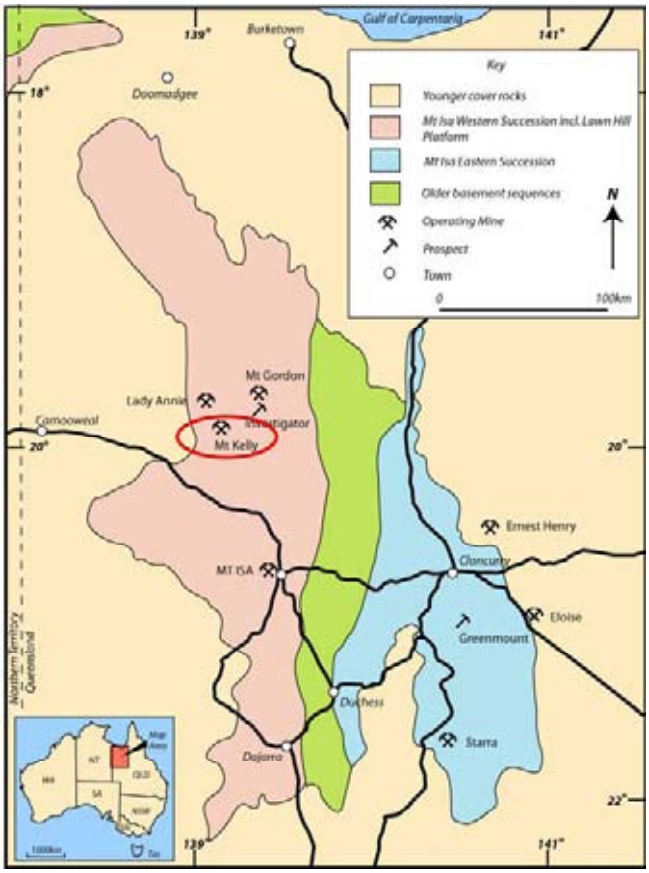

Figure 4.1 Location of the Mt Kelly Mine.

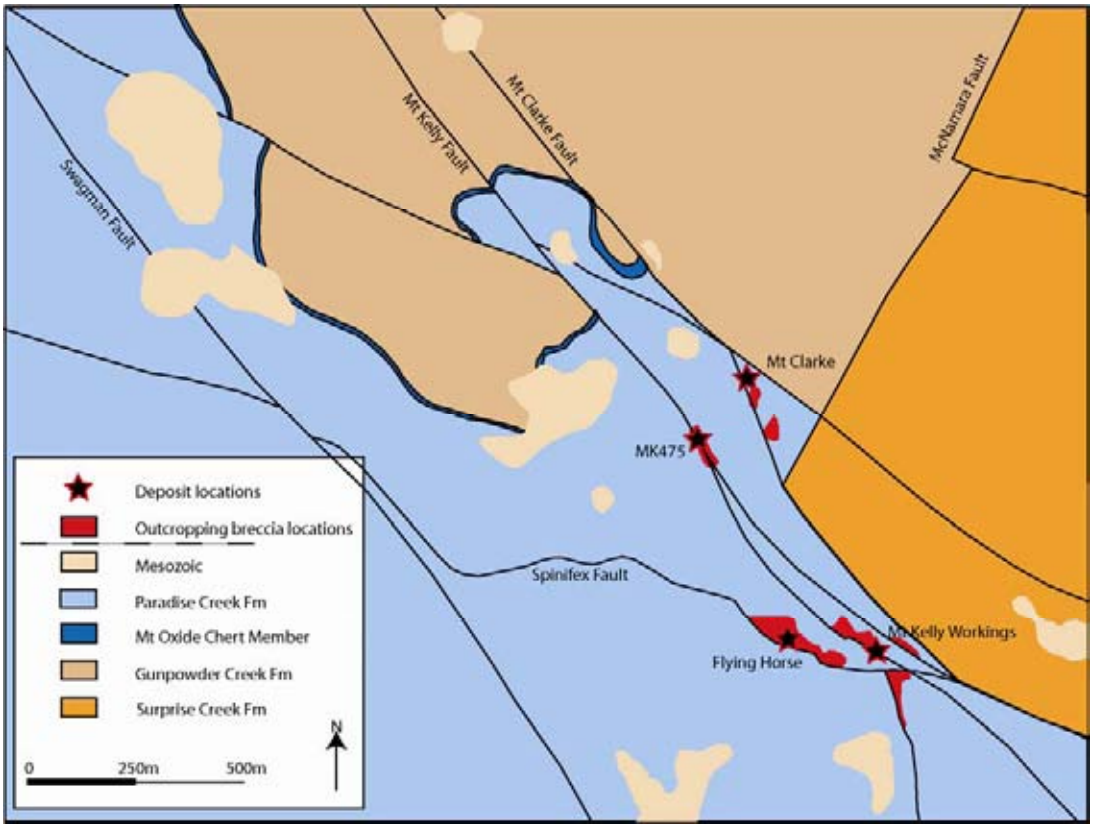

Figure 4.2 Mt Kelly camp scale geological mapping (adapted from Stegman, 1994). The map shows known breccia locations and deposit locations.

4.2 Exploration History

Since the 1960's, the Mount Kelly area has been the subject of several exploration campaigns, mainly directed towards the potential for primary copper and gold mineralisation. Secondary copper mineralisation has been prospected and worked in the area since the 1950's. The largest of the historic workings is the Mount Kelly mine, which produced 2,360 t of copper oxide ore averaging 7% Cu to 1958. A further 115 t at 3.9% Cu was mined between 1958 and 1968. The lease was explored by CRA and later Reefway through the 1980's until 2003. The area was extensively mapped and this mapping forms the basis for much of the work conducted in this study.

Most recently, Mt Kelly has been the subject of an extensive reverse circulation drilling program conducted by Copperco Ltd. that commenced in October 2004. Copperco have successfully delineated a significant oxide resource and have subsequently begun mining. Further exploration of sulphide extensions to the ore zones has yielded significant copper and gold intersections, particularly around the MK475 and Mt Kelly Workings areas.

4.3 Geological setting

The Mt Kelly Copper Mine is hosted by early to mid Proterozoic siltstones and dolomitic siltstones of the Paradise Creek Formation. The dominant structural feature of the Mt Kelly area is the broadly north-south striking McNamara Fault, traceable for approximately 150 km in limited outcrop and geophysics.

Within the mine area, the regional scale McNamara Fault juxtaposes Paradise Creek Formation and Gunpowder Creek Formation sediments (west of the McNamara Fault) against the older Surprise Creek Formation (east of the McNamara Fault). Small outcrops of Eastern Creek Volcanic basalt have also been found on the eastern side of the McNamara Fault, although they have not been recognised at 1:100,000 scales within several kilometres of the mine area. The presence of the basalt indicates a structural high, which is important as the basalt is a possible source of copper and such a small structurally controlled culmination or basement high may have provided a focal point for up-welling hydrothermal fluids (Crossing, 2007).

The rock sequence is strongly deformed by multiple stages of folding and faulting (Da Costa, 2005). A complex fold history is recorded in the Paradise Creek Formation west and south of the known deposits. South of Flying Horse, east-west oriented F_1 folds have been refolded by F_2 (north-south shortening) and F_3 (NNW-SSE shortening) (Da Costa, 2005). F_2 folds are often seen to be refolded during D_3 and fold geometries such as kink folding and box folding are common (Figure 4.3). To further complicate matters, several generations of faulting have disrupted the stratigraphic sequence. The McNamara Fault and regional stratigraphy is displaced by several northwest trending faults, including the Mt Kelly, Mt Clarke and Swagman Faults. Movement has occurred on the northwest striking faults post regional D_2, as F_2 fold traces are significantly displaced.

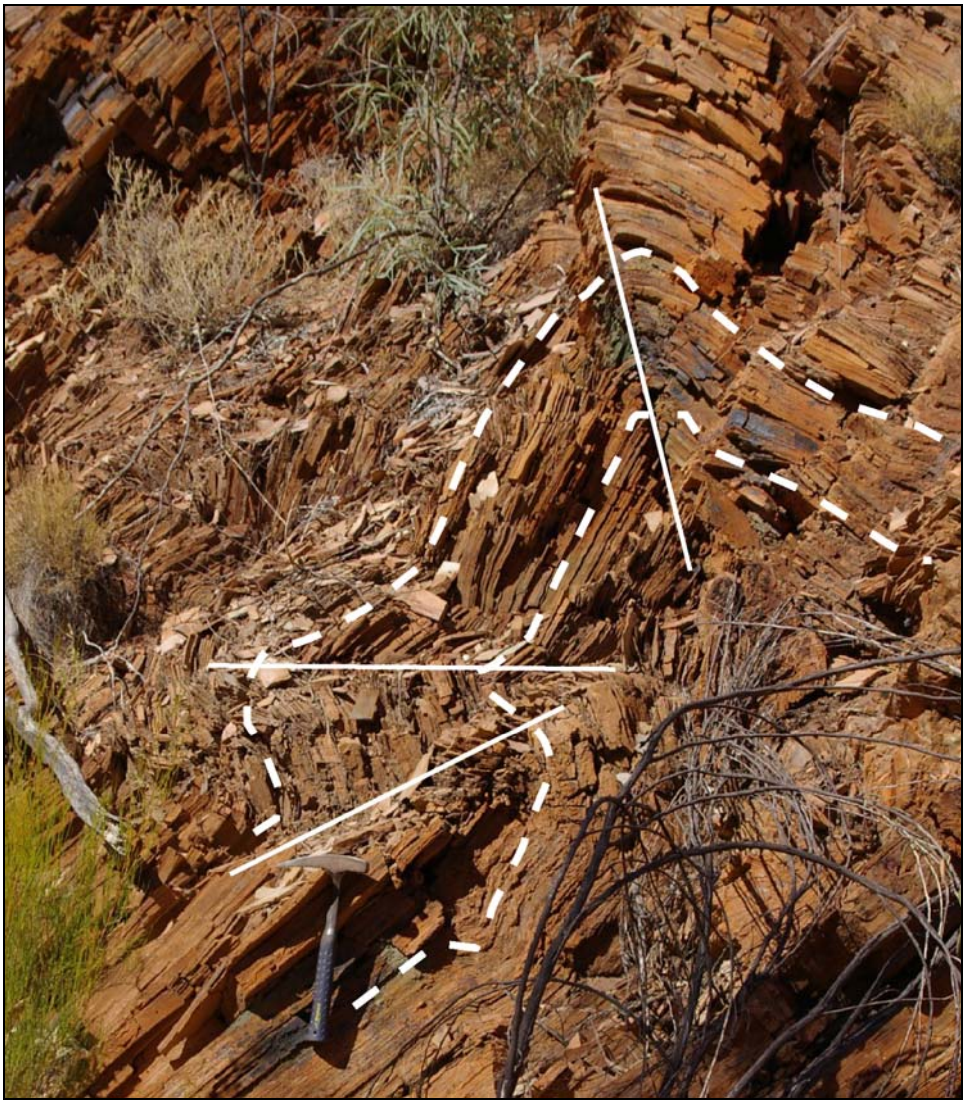

Figure 4.3 Example of box folding in the Paradise Creek Fm south west of the Mt Kelly Deposit, near the Swagman Fault. Dashed white lines reflect bedding trends around the fold and solid lines indicate kinks and/or small detachments necessary to accommodate strain within the box fold.

Primary copper mineralisation is intimately associated with these northwest trending faults, with the biggest deposits located on the Mt Kelly Fault and Mt Clarke Fault. Company mapping (Stegman, 1994) shows another orientation of fault. The Spinifex Fault is interpreted as an east-west striking fault, located south of the Flying Horse deposit. Weakly brecciated and weathered limonitic shales are seen in the approximate vicinity of this postulated fault and typically trend toward 100º with a steep dip to the north. The lack of any measurable surface outcrops, have led other geologists to question the existence of the Spinifex Fault. Aerial photographic interpretation by Da Costa (2005) noted WNW trending structures to the west of the Flying Horse region, although no faults were clear within the Flying Horse/Mt Kelly area itself. East-west oriented creeks were seen in an area south of Flying Horse, leading the hypothesis that the WNW faults to the west had changed orientation, accommodating strain with jogs and splays (Da Costa, 2005). This zone of WNW-ESE and E-W oriented faulting was interpreted to reflect the trace of the Spinifex Fault. Da Costa (2005) did not record any specific measurements off the supposed Spinifex Fault, but did note ironstones outcropping along the approximate location of the proposed fault trend (Figure 4.4).

Figure 4.4 Surface outcrop of the limonitic shales in the approximate position of the Spinifex Fault. The outcrop is weakly brecciated. Looking south, at 305024E 7798981N (location in AGD 84). Photo from Da Costa (2005).

4.4 Structural Field Studies at Mt Kelly

4.4.1 Diamond Drill Core Logging

The intersection of the Mt Kelly Fault and the supposed Spinifex Fault is often used to explain a high-grade gold intersection found in the MK475 locality. Four diamond holes were examined for breccia style (Figure 4.5), breccia relationships to mineralisation, alteration intensity and alteration relationships to mineralisation.

The logged drill hole that contained the most mineralisation was the MK475A drill hole. The intensity of brecciation was directly proportional to the distance from the Mt Kelly Fault, i.e. the closer the sampled interval to the Mt Kelly Fault, the more intense the brecciation. The style of brecciation also changed depending on the proximity to the Mt Kelly Fault (Figure 4.6). Breccias containing breccia clasts themselves were found in the inferred Mt Kelly Fault position downhole. This would imply two episodes of brecciation within the Mt Kelly Fault, with the latter event most likely related to copper mineralisation. If the copper is associated with the second breccia phase, then this is consistent with the model assumption that the Mt Kelly Fault was present and active before mineralisation.

The MK513 hole, located approximately 15 m south of the MK475A hole, was also logged. Like MK475A, this drill hole showed an increase in breccia intensity nearer to the Mt Kelly Fault. It also showed a change in breccia style from crackle and mosaic breccias, to rubble and rebrecciated breccias, as the Mt Kelly Fault was neared (Figure 4.7).

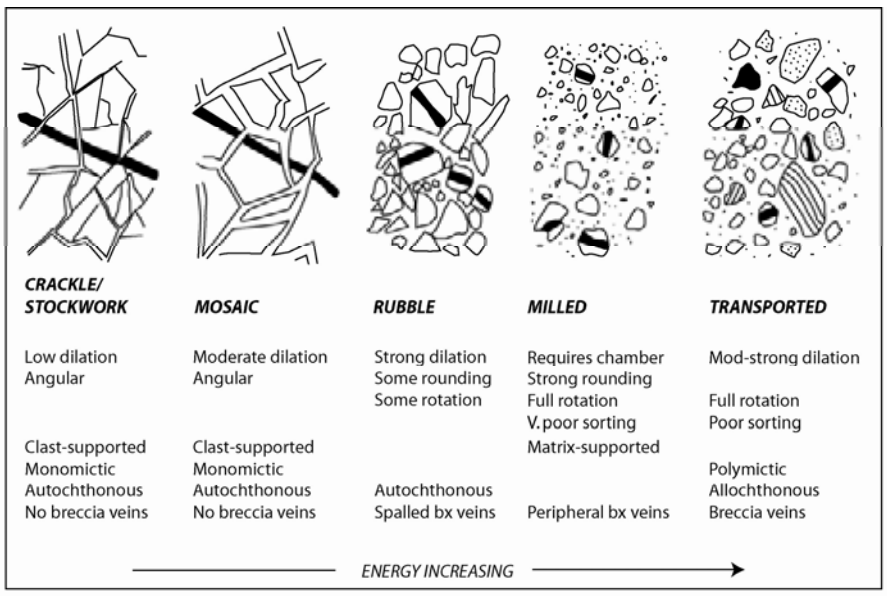

Figure 4.5 Breccia styles (from Laing, 2003).

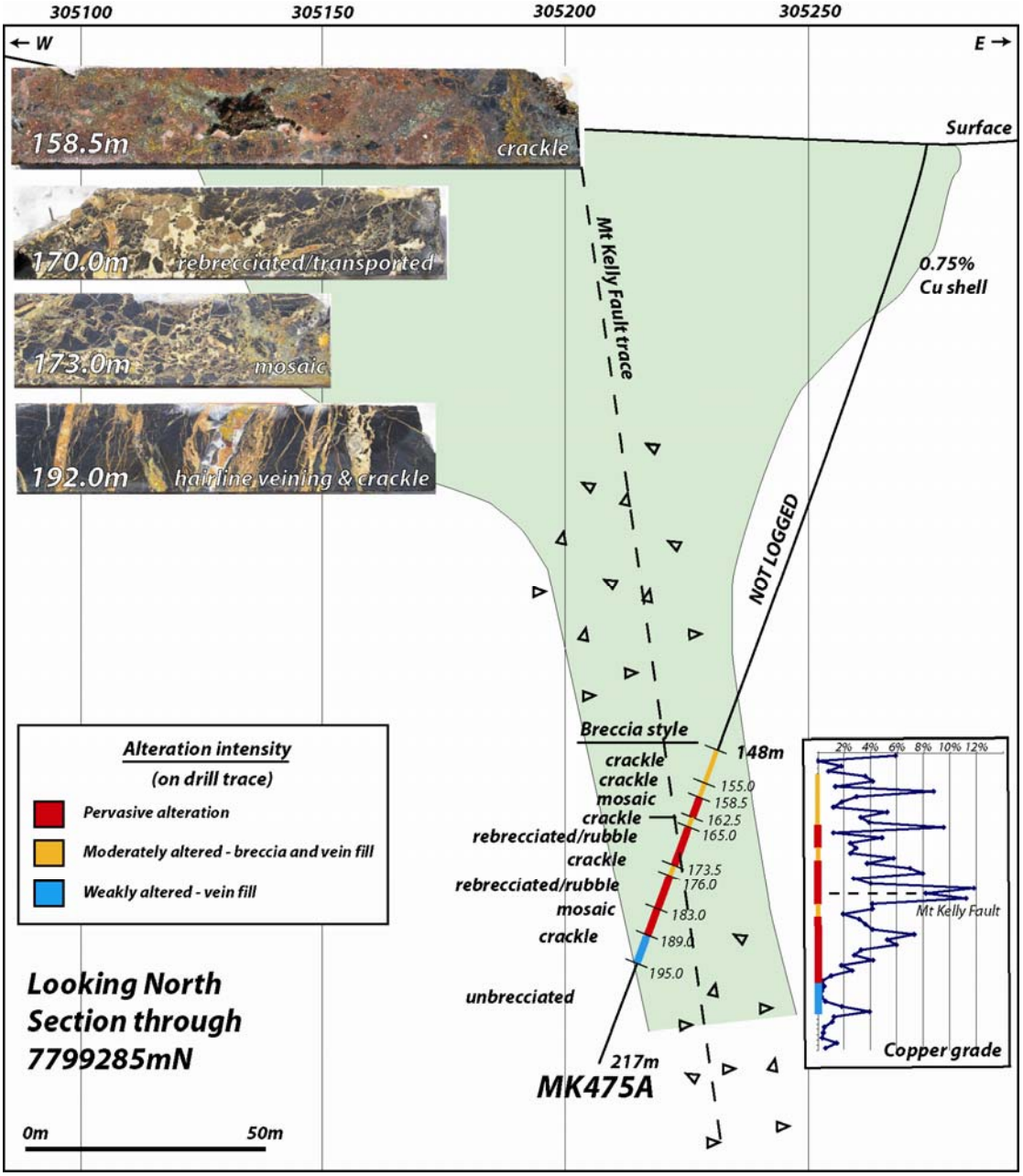

Figure 4.6 Section through 7799285mN (AGD 84 Datum), showing the diamond drill hole MK475A. Breccia styles and intensities are seen to directly correlate with proximity to the Mt Kelly Fault. The copper grades through the ore zone are seen to correlate well with alteration intensity. Photographs representing each of the logged breccia styles are shown.

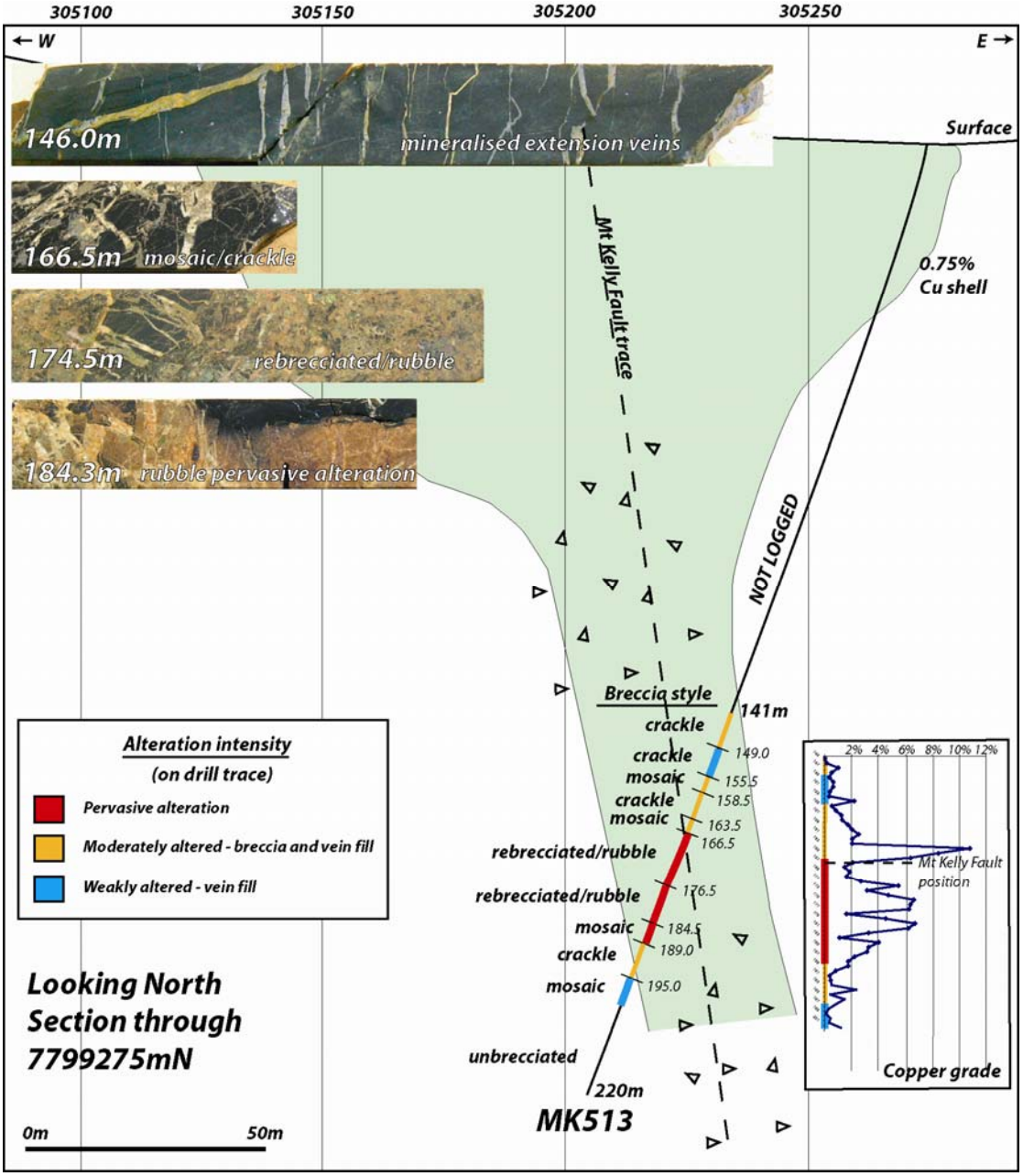

Figure 4.7 Section through 7799275mN (AGD 84 Datum), showing the diamond drill hole MK513. Breccia styles and intensities are seen to directly correlate with proximity to the Mt Kelly Fault. The copper grades through the ore zone are seen to correlate well with alteration intensity. Photographs representing each of the logged breccia styles are shown.

4.4.2 Mt Kelly mapping

Field mapping of the Mt Kelly deposit area and Flying Horse South was conducted, as part of this study, to attempt to locate the position, thickness, dip and dip direction and fill of the Spinifex Fault, but failed to confidently identify the fault. Small outcrops of locally sheared and weakly brecciated, limonitically altered shale were observed but these dipped steeply similar to the nearby black shales, whereas Stephens (2001) and Maiden *et al.* (2000) proposed a 25º northerly dip to the Spinifex Fault.

Several sub-vertical, short-lengthed, dominantly east-west striking fault strands were mapped south of the Spinifex Fault map position. These faults were commonly between 10 and 15 cm thick and were spaced approximately 15 metres apart.

4.5 Numerical Modelling – Conceptual Model

The model geometry was created from detailed field mapping conducted by Stegman (1994). It consists of an area of 1.2 km x 2 km (Figure 4.8). The orientation of the maximum principal stress was varied from SW-NE to SE-NW to test the range of hypotheses proposed for the Mount Gordon Copper Mines (Chapter 2.11), located approximately 50 km south east of Mt Kelly (Figure 4.1). The stress conditions for the model are set at ratios of σ_1/σ_2=1.2 and σ_3/σ_2=0.8, resulting in a phi (Φ) value of 0.5, as per the initial Mt Gordon modelling. The same values of imposed stresses (σ_1=210 MPa, σ_2=175 MPa, σ_3= 140 MPa) used in the Mt Gordon and Mt Isa modelling, were used in the Mt Kelly modelling. The vertical stress (σ_2=175 MPa) is applied to the models to represent 7 km of overburden, similar to copper deposition depths for the Mt Gordon and Mt Isa Copper deposits (Clarke, 2003; Heinrich *et al*, 1989). It was assumed that all the faults in the models were already present their current configuration, as there is little evidence for any major fault displacement post-mineralisation.

Field mapping completed in this study failed to locate a shallow dipping Spinifex Fault. Conjecture over the existence and character of this fault has dominated the literature on the Mt Kelly deposit (Stephens, 2001; Maiden *et al.*, 2000; Da Costa, 2005). The model was therefore run with and without the Spinifex Fault.

The model runs, both with and without the Spinifex Fault, have a best fit of predicted dilational sites to known breccias when σ_1 is oriented 112º-292º, the same as the Mt Gordon Copper Mine numerical modelling.

Table 4.1 Mt Kelly models with the σ_1 orientation and a brief summary. All models were run with and without the Spinifex Fault. Locations of the detailed results of each model are also tabulated.

σ_1 Orientation	Summary of Outcome	Detailed Results
NE-SW	*Poor visual fit with known brecciation.*	*Chap 4.6.1*
ENE-WSW	*Poor visual fit with known brecciation.*	*Chap 4.6.2*
E-W	*Reasonable visual fit with known brecciation*	*Chap 4.6.3*
101º-291º	*Identifies known breccias, but dilates areas known to not be brecciated*	
ESE-WNW	*Best visual fit with known brecciation*	*Chap 4.6.4*
124	*Poor visual fit with known brecciation*	

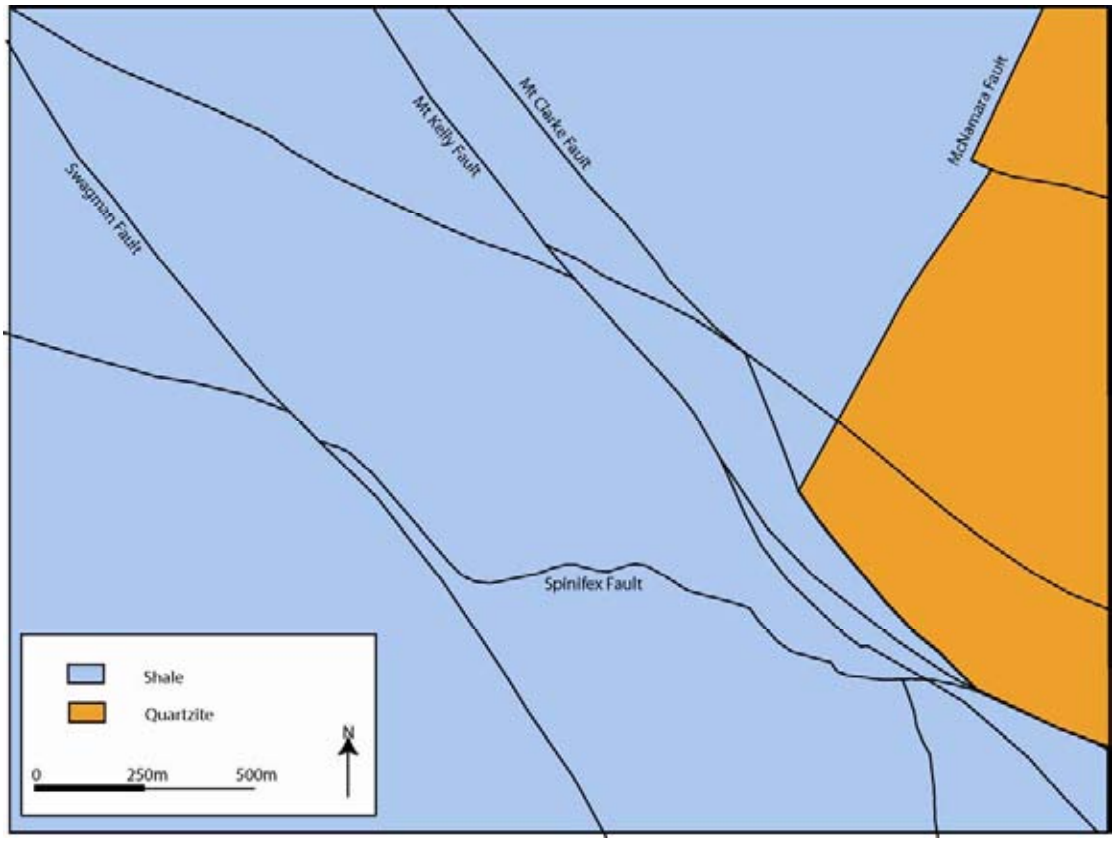

Figure 4.8 The simplified conceptual model used for UDEC modelling. The blue is Paradise Creek Fm shale and Esperanza Fm shale and the orange is Surprise Creek Fm quartzites. The model was also run without the Spinifex Fault.

Table 4.2 Mt Kelly conceptual model inputs.

Property	Quartzite	Shale	Lithological contact	Fault
Density (kg/m3)	2600	2650		
Bulk modulus (Pa)	40e9	40e9		
Shear modulus (Pa)	25e9	7e9		
Cohesion (Pa)	24e7	5e7	3e3	5e2
Tensile strength (Pa)	12e7	3e7	3e6	2e6
Friction angle (°)	31	37	35	30
Dilation angle (°)	2	5	5	5
Normal stiffness (Pa/m)			2e9	5e9
Shear stiffness (Pa/m)			5e5	8e4
Permeability factor (Pa/s)			238	300
Aperture at zero normal stress (m)			0.03	0.05
Residual hydraulic aperture (m)			0.01	0.03

4.6 Numerical Modelling Results

4.6.1 NE-SW shortening

In both the Spinifex Fault Included and the Spinifex Fault Excluded models, the proposed σ_1 orientation of NE-SW produces results with high minor principal stress in the known deposit locations (Figure 4.9 a and b). Values of mean stress and fluid pressure for failure are also high in the deposit locations (Table 4.3). These results would suggest that a σ_1 orientation of NE-SW would not produce the necessary dilation for copper bearing breccias at mineralisation time at Mt Kelly.

Table 4.3 Values obtained from UDEC model outputs when σ_1 is oriented NE-SW. Values of σ_3, σ_m and Pf_F are extremely high in all deposit locations. Values vary little in specific deposits between the two models.

Model	Deposit Name	σ_3 (MPa)	Mean stress (MPa)	Fluid pressure for failure (MPa)
Spinifex Fault Included	Mt Clarke	170	190	160
	MK 475	150	180	160
	Mt Kelly	140	165	125
	Flying Horse	145	175	140
Spinifex Fault Excluded	Mt Clarke	170	190	160
	MK 475	150	185	155
	Mt Kelly	140	170	140
	Flying Horse	155	180	150

4.6.2 ENE-WSW shortening

The ENE-WSW shortening model also shows high values of σ_3 in the known deposit locations, in both the Spinifex Fault Included and Spinifex Fault Excluded models (Figure 4.9 b and c). Both models exhibit high values of mean stress and fluid pressure for failure in all deposits (Table 4.4). These results would suggest that a σ_1 orientation of ENE-WSW would also not be favourable for the formation of copper bearing breccias at mineralisation at Mt Kelly.

Table 4.4 Values obtained from UDEC model outputs when σ_1 is oriented ENE-WSW. Values of σ_3, σ_m and Pf_F are extremely high in all deposit locations. Values vary little in specific deposits between the two models.

Model	Deposit Name	σ_3 (MPa)	Mean stress (MPa)	Fluid pressure for failure (MPa)
Spinifex Fault Included	Mt Clarke	165	185	150
	MK 475	155	180	155
	Mt Kelly	155	180	140
	Flying Horse	155	185	150
Spinifex Fault Excluded	Mt Clarke	165	195	160
	MK 475	155	180	160
	Mt Kelly	150	180	140
	Flying Horse	150	175	145

4.6.3 E-W shortening

The Spinifex Fault Included and Spinifex Fault Excluded models showed a substantial variation when σ_1 was oriented E-W. The Spinifex Fault Included model showed higher values of σ_3 (Figure 4.9), σ_m and Pf_F, particularly at the Mt Kelly deposit, than the Spinifex Fault Excluded model. Mean stress values were also seen to be significantly higher at the Mt Kelly deposit as well (Table 4.5).

Although the values of minor principal stress, mean stress and fluid pressure for failure are generally lower than the NE-SW models and the ENE-WSW models, the E-W shortening model still only provides a mediocre fit with the known deposits. Therefore a σ_1 orientation of E-W is not favoured for the formation of the copper bearing breccias at Mt Kelly.

Table 4.5 Values obtained from UDEC model outputs when σ_1 is oriented E-W.

Model	Deposit Name	σ_3 (MPa)	Mean stress (MPa)	Fluid pressure for failure (MPa)
Spinifex Fault Included	Mt Clarke	150	165	145
	MK 475	155	180	150
	Mt Kelly	150	180	145
	Flying Horse	150	180	150
Spinifex Fault Excluded	Mt Clarke	135	155	140
	MK 475	145	170	140
	Mt Kelly	170	230	160
	Flying Horse	145	170	150

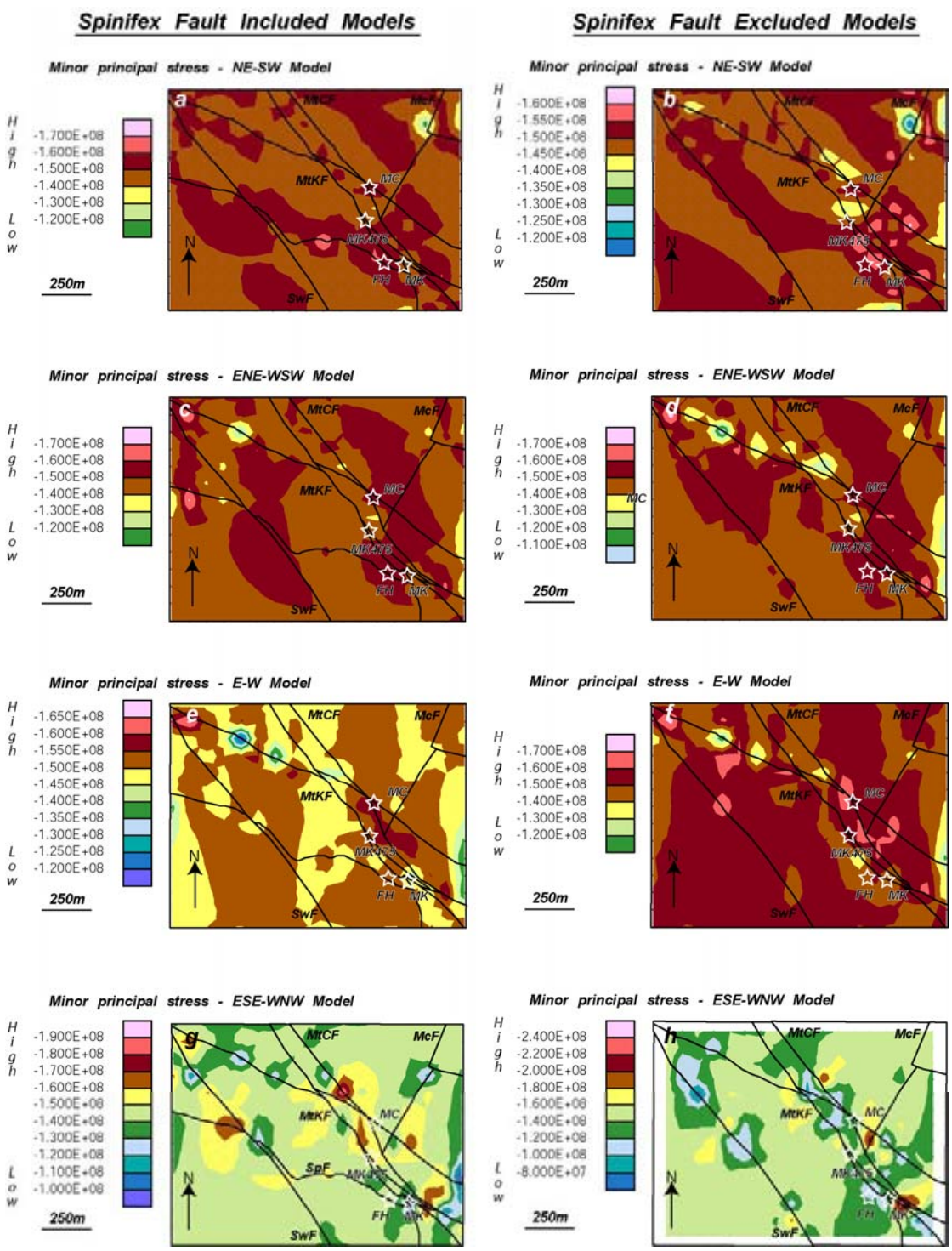

Figure 4.9 The Spinifex Fault Included Model (left) and the Spinifex Fault Excluded Model (right).
*(**a** and **b**) Plot of minor principal stress for the NE-SW shortening model. Values of σ_3 are seen to be high in the known deposit locations.*
*(**c** and **d**) Plot of minor principal stress for the ENE-WSW shortening model. Values of σ_3 are seen to be high in the known deposit locations.*
*(**e** and **f**) Plot of minor principal stress for the E-W shortening model. Values of σ_3 are seen to be high in the known deposit locations.*
*(**g** and **h**) Plot of minor principal stress for the ESE-WNW shortening model. Low values of σ_3 are seen to correlate well with the known deposit locations. This is the preferred model.*
Note: SpF=Spinifex Fault, SwF=Swagman Fault, MtCF=Mt Clarke Fault, MtKF=Mt Kelly Fault, McF=McNamara Fault. White stars show position of known deposits; MC=Mt Clarke deposit, MK=Mt Kelly deposit, FH=Flying Horse and MK475.

4.6.4 ESE-WNW – Spinifex Fault Model vs Spinifex Fault Excluded Model

Subtle differences were seen between the Spinifex Fault Included and Spinifex Fault Excluded Models (Table 4.6, Figure 4.10). The Spinifex Fault is thought to be critical in localising the brecciation of the Flying Horse deposit as copper is not found on the south side of the fault (Stephens, 2001; Maiden *et al*, 2000). In the Spinifex Fault Included Model, a zone of low σ_3 extends through the Flying Horse area. The plot of mean stress however shows the lowest values on the south side (unmineralised side) of the Spinifex Fault. The Spinifex Fault Excluded Model however shows low values of σ_3 extending west from the Mt Kelly Fault into the Flying Horse deposit. Significantly a large zone of low mean stress is seen to extend into the Flying Horse area and fluid pressures for failure are moderate.

Although this study cannot conclusively deny or confirm the existence of the Spinifex Fault, it shows that it is not a necessity for the brecciation all of the Mt Kelly Copper Mine deposits.

Table 4.6 Values obtained from UDEC model outputs when σ_1 is oriented 112º-292º. Although quite similar, the Spinifex Fault Excluded Model is preferred for its lower fluid pressure for failure values. The MK 475 and Mt Kelly deposits show the lowest σ_3 values and coincidently are the two highest grade deposits in the Mt Kelly mineralised system.

Model	Deposit Name	σ_3 (MPa)	Mean stress (MPa)	Fluid pressure for failure (MPa)	Differential stress (MPa)	Inferred failure mode
Spinifex Fault Included	Mt Clarke	105	120	100	15	Tensile
	MK 475	130	170	120	40	Tensile
	Mt Kelly	100	140	100	40	Tensile
	Flying Horse	140	160	140	20	Tensile
Spinifex Fault Excluded	Mt Clarke	120	140	100	40	Tensile
	MK 475	100	110	105	20	Tensile
	Mt Kelly	90	110	80	40	Tensile
	Flying Horse	120	130	130	20	Tensile

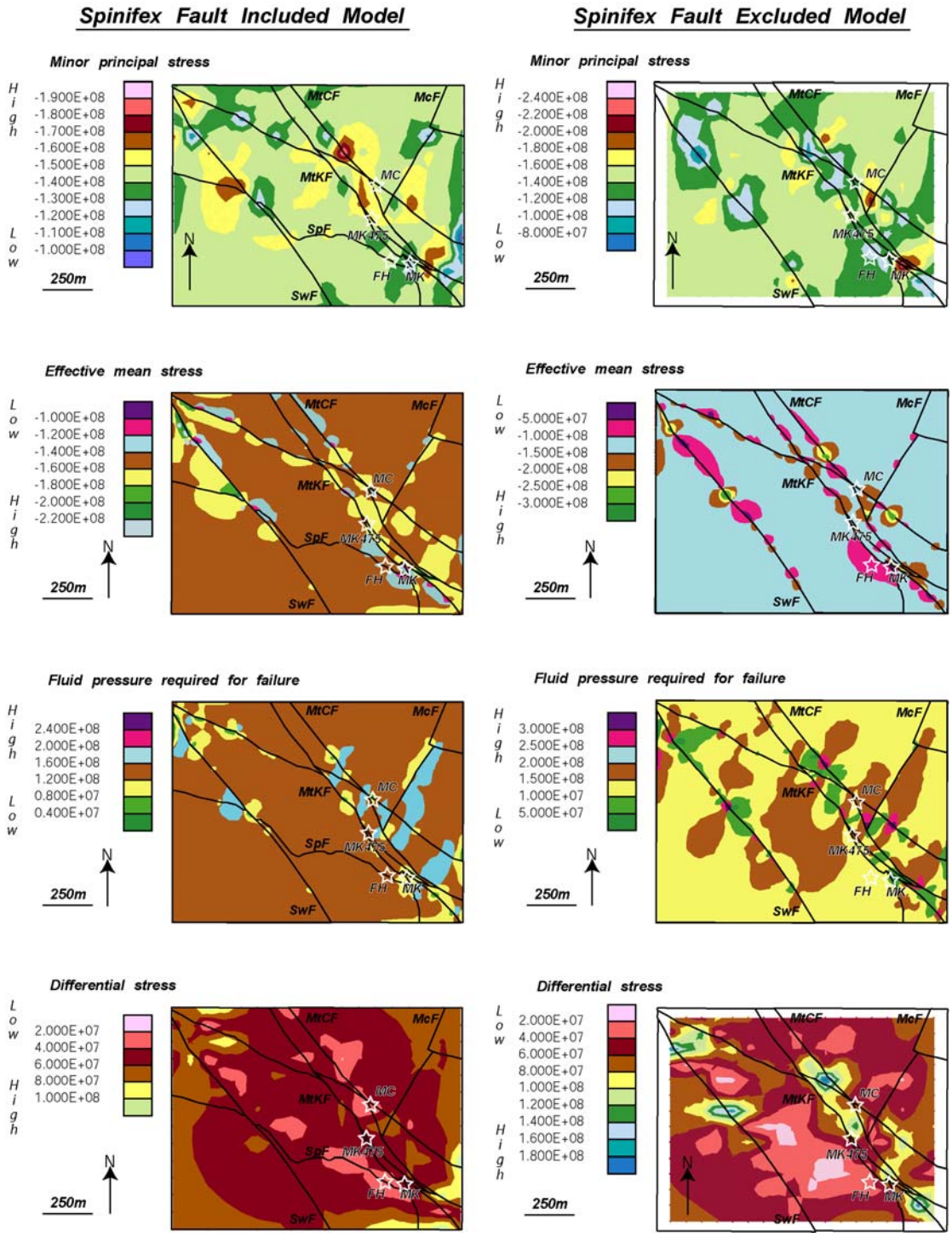

Figure 4.10 Comparative diagrams with the Spinifex Fault Included Model (left) and the Spinifex Fault Excluded Model (right). SpF=Spinifex Fault, SwF=Swagman Fault, MtCF=Mt Clarke Fault, MtKF=Mt Kelly Fault, McF=McNamara Fault. White stars show position of known deposits; MC=Mt Clarke deposit, MK=Mt Kelly deposit, FH=Flying Horse and MK475.

(a) *Showing contours of minor principal stress. The Spinifex Included Model shows quite localised areas of low σ_3 around the known deposit locations. The Spinifex Fault Excluded Model shows a far broader area of low σ_3 along the Mt Clarke Fault. The current knowledge of the extent of sulphide resource in this area is limited however the oxide resource extends for 450 m in strike length, potentially making the Spinifex Fault Excluded valid. Values of 3 are slightly lower in the Spinifex Fault Excluded in the known deposit locations.*

(b) *Showing contours of mean stress. The Spinifex Fault Included Model shows discrete zones of low mean stress around the known deposit locations. The Flying Horse deposit however only has moderate values of mean stress with the lowest values being on the southern side of the Spinifex Fault, an area known to be unmineralised. The Spinifex Fault Excluded model shows a large zone of low mean stress extending from the Mt Kelly Workings west to the Flying Horse deposit.*

(c) *Showing contours of fluid pressure required for failure. Both models show a NNW orientation to zones of high and low fluid pressures for failure. This is due to stress partitioning around the rigid Surprise Creek Quartzite body in the east of the model. Both models show low P_{fF} values in the known deposit locations and high P_{fF} values along the SCQ/Paradise Creek Formation contact.*

(d) *Showing contours of differential stress. Both models show low differential stresses between the Mt Kelly and Swagman Faults. In the Spinifex Fault Included Model the lowest differential stress is confined to the Spinifex Fault. In both models high differential stresses were seen along the Mt Kelly and Mt Clarke Fault corridor.*

4.6.5 ESE-WNW shortening - Spinifex Fault Excluded Model at Mt Clarke and MK475

The Surprise Creek Fm quartzites appear to act as a stress buffer with the highest stresses being redistributed along the western margin of the quartzite. This is evident in the plot of minor principal stress where the highest values of σ_3 are seen in the shales beside the McNamara Fault.

Low σ_3 values (80 MPa to 130 MPa) are seen in the deposit locations (Figure 4.11a), in the intersections of the anastomosing NW striking faults. These sites also require moderate fluid pressures for failure (Figure 4.11b) and have relatively low mean stress (Figure 4.11c). The relatively low differential stresses seen in both locations have implications for the failure mode of each deposit (Figures 4.11d).

A NNE trending zone of low σ_3, P_{fF}, σ_m and differential stress is seen to the NW of the existing deposit locations and is particularly well developed along the Mt Clarke Fault. This area may warrant further exploration.

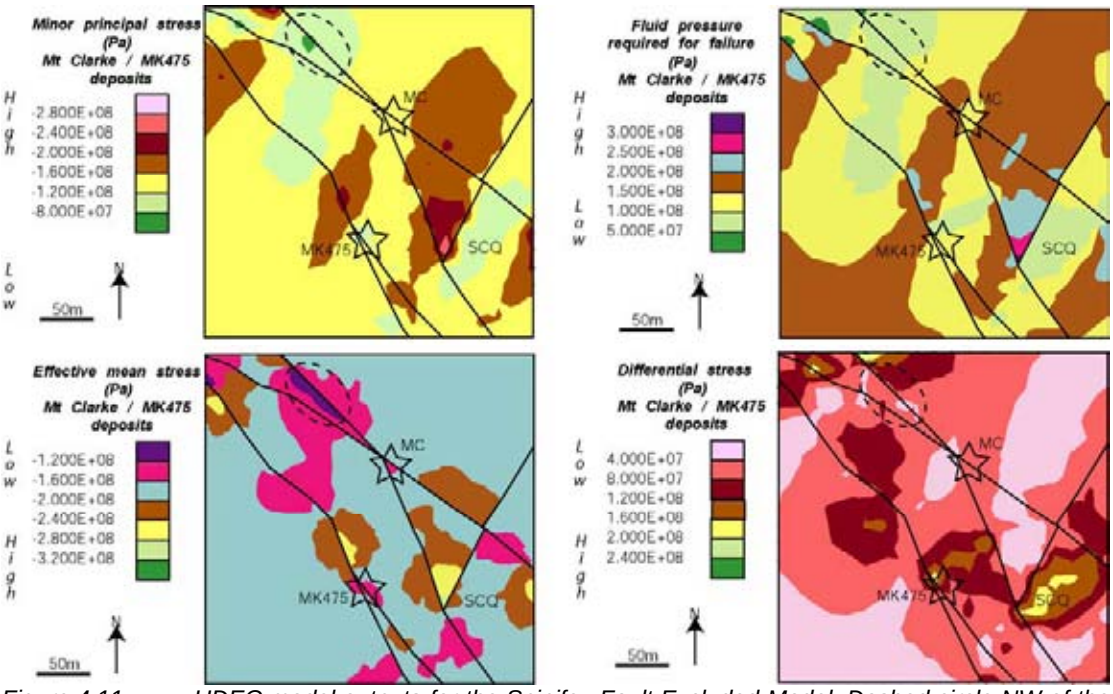

Figure 4.11 UDEC model outputs for the Spinifex Fault Excluded Model. Dashed circle NW of the Mt Clarke deposit represents an area of low σ_3, P_{fF}, σ_m and $\Delta\sigma$, that may warrant further exploration.
(a) *Showing contours of minor principal stress. NNW striking corridors of high σ_3 parallel the Surprise Creek Quartzite (SCQ) contact. Low σ_3 is seen in the deposit locations and along the Mt Clarke Fault*
(b) *Low values of mean stress are noted in the deposit locations and along the Mt Clarke Fault.*
(c) *Showing contours of fluid pressure required for failure. As per σ_3 values high P_{fF} parallels the SCQ contact.*
(d) *Moderate to high differential stresses are seen in the deposit locations.*

4.6.6 ESE-WNW shortening - Spinifex Fault Excluded Model at Mt Kelly Workings and Flying Horse

The Mt Kelly and Mt Clarke Faults are the focus for the bulk of the stress in the south of the model. It is just to the north of the Mt Kelly deposit that the Surprise Creek quartzites are juxtaposed against the Paradise Creek Formation shales. A stress shadow extends south west of the Surprise Creek quartzites, through the deposit sites of Mt Kelly and Flying Horse. Low values of minor principal stress are observed at both Mt Kelly and Flying Horse, from 90 MPa to 120 MPa (Figure 4.12a). A large zone of relatively low mean stress extends from the Mt Kelly Workings through the Flying Horse area (Figure 4.12b). Differential stresses in the Flying Horse and Mt Kelly Workings deposits are seen to be very low (<50 MPa) (Figure 4.12d).

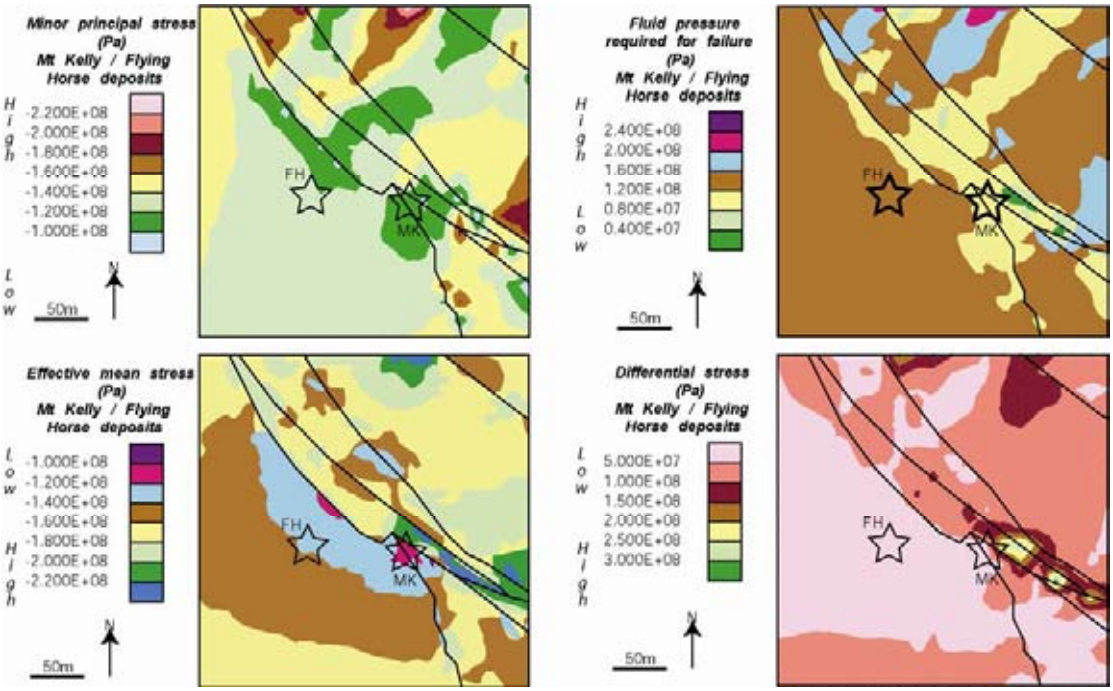

Figure 4.12 UDEC model outputs for the Spinifex Fault Excluded Model.

(a) *Showing contours of minor principal stress. A large zone of low σ_3 is found in the Mt Kelly Workings site and extends west from the Mt Kelly Fault through the Flying Horse area.*

(b) *The mean stress plot closely resembles the σ_3 plot with low values seen in the deposit areas.*

(c) *The lowest fluid pressure for failure is seen in the Mt Kelly Workings deposit. The Flying Horse area shows moderate P_{fF}.*

(d) *Moderate differential stress values are seen in the Mt Kelly Workings deposit. The Flying Horse deposit exhibits low differential stresses.*

MtCF=Mt Clarke Fault, MtKF=Mt Kelly Fault, McNF=McNamara Fault, MK=Mt Kelly Workings deposit and FH=Flying Horse.

4.7 Summary of Numerical Modelling Results

For both of the model runs (with and without the Spinifex Fault), the σ_1 orientation providing the best correlation with known deposits was 112°-292°. When σ_1 was oriented ESE-WNW, values of minor principal stress, fluid pressure required for failure and mean stress were seen to be relatively low in the specific deposit locations.

The Mt Kelly models run without the Spinifex Fault showed significantly lower values of fluid pressures required for failure than the model run with the Spinifex Fault included (Table 4.6; Figure 4.10). The UDEC outputs of minor principal stress, fluid pressure required for failure, mean stress and differential stress were plotted to Mohr circles to determine the likely failure mode at each deposit (Figure 4.13 MK475 and Mt Clarke; Figure 4.14 Mt Kelly Workings and Flying Horse). It is seen that the likely failure mode for each deposit is likely to be extensional shear.

The modelling does not definitively prove that the Spinifex Fault was or wasn't active at copper mineralisation time. It does however show that the Spinifex Fault is not necessary for dilation in the known breccia and deposit locations. The models also outline several prospective areas of low minor principal stress and low mean stress that warrant further exploration.

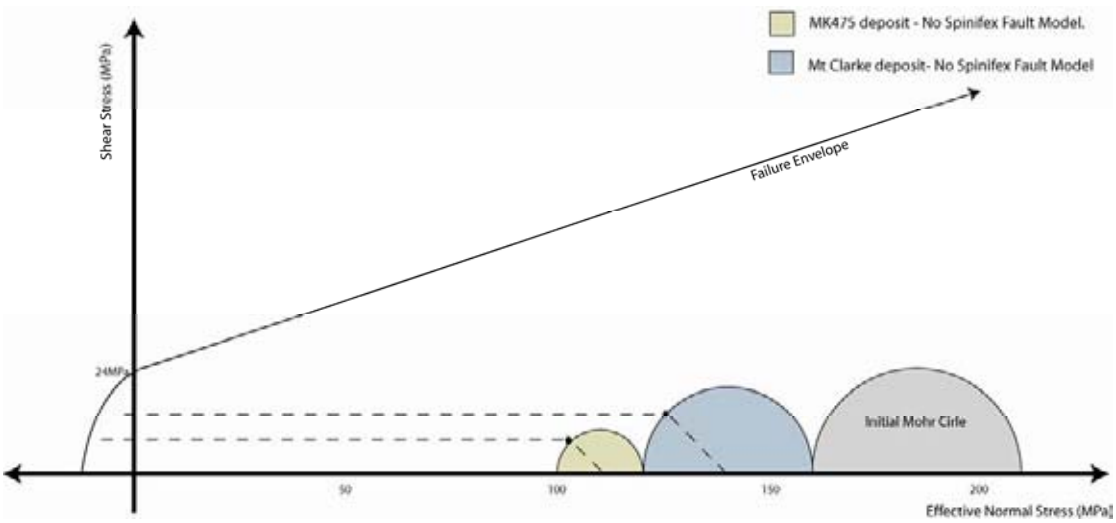

Figure 4.13 Mohr Circle plots for MK475 deposit and the Mt Clarke deposit (from Spinifex Fault Excluded Model). Dashed horizontal lines represent the fluid pressure required for failure. Both deposits are expected to fail in extensional shear.

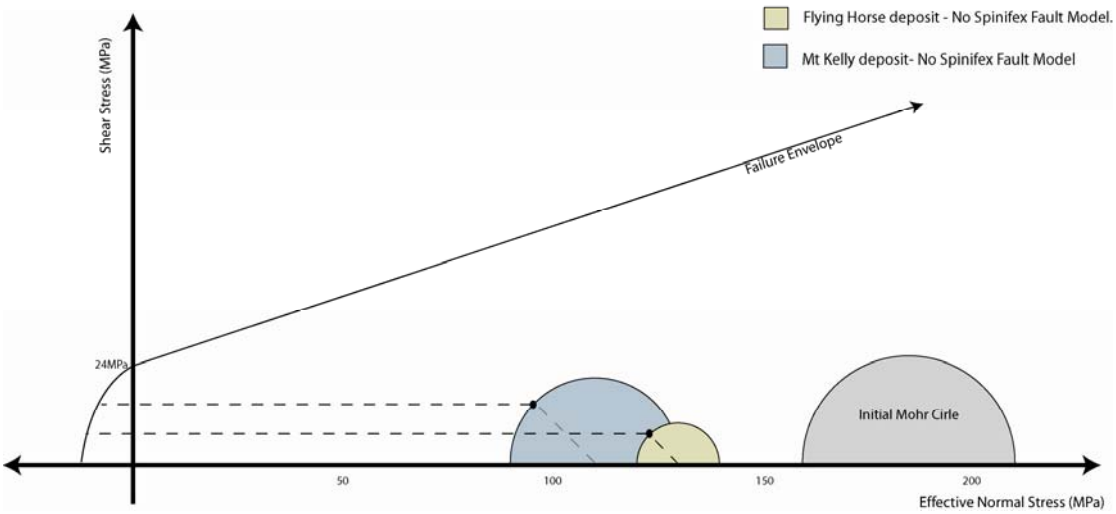

Figure 4.14 Mohr Circle plots for Flying Horse deposit and the Mt Kelly deposit (from Spinifex Fault Excluded Model). Dashed horizontal lines represent the fluid pressure required for failure. Extensional failure will be the likely failure mechanism for both deposits.

As with the Mt Gordon modelling, the Mt Kelly modelling suggests there is a relationship between the deposit locations and steep gradients in σ_3, σ_m and Pf_F values. The steep gradients are likely to reflect distinct, discrete, relatively intense breccia bodies, capable of hosting economic copper grades and tonnages. If the σ_3, σ_m and Pf_F value gradients are weaker, it would be more likely that the dilation would be less intense and dispersed over a larger area. This would probably not be as conducive to producing a deposit of economic grade or tonnage.

5. INVESTIGATOR FAULT ZONE

The field data pertaining to Chapter 5: Investigator Fault Zone was collected in collaboration with Gustav Nortje (PhD candidate, James Cook University). The photographs displayed throughout this chapter were taken by G. Nortje and are being used with his permission.

5.1 Introduction

The Investigator Fault Zone is an exploration tenement located approximately 100 km north of Mount Isa, approximately 4 km west of the Mt Isa-Gunpowder road. To date no economic mineralisation has been identified in the Investigator Fault Zone. The prospect is of particular interest to this study as it shares many characteristics with the Mt Gordon Copper Mines, only 12 km to its north. These similarities include similarly oriented major faults and the same stratigraphic repetition (Figure 5.1). The Investigator area has only been lightly explored, as previous companies specifically targeted “Mt Isa-style” stratabound mineralisation in the south of the tenement area. Unlike the Mt Gordon and Mt Kelly Copper Mines, the Investigator area has no known copper bearing breccias and therefore no obvious validation points for the numerical modelling outputs. Here, the Investigator Fault Zone was forward modelled in UDEC, followed by a field mapping campaign in order to validate the model. In this sense both the predictive capacity of UDEC and the suitability of UDEC as a 2-dimensional modelling tool are being tested.

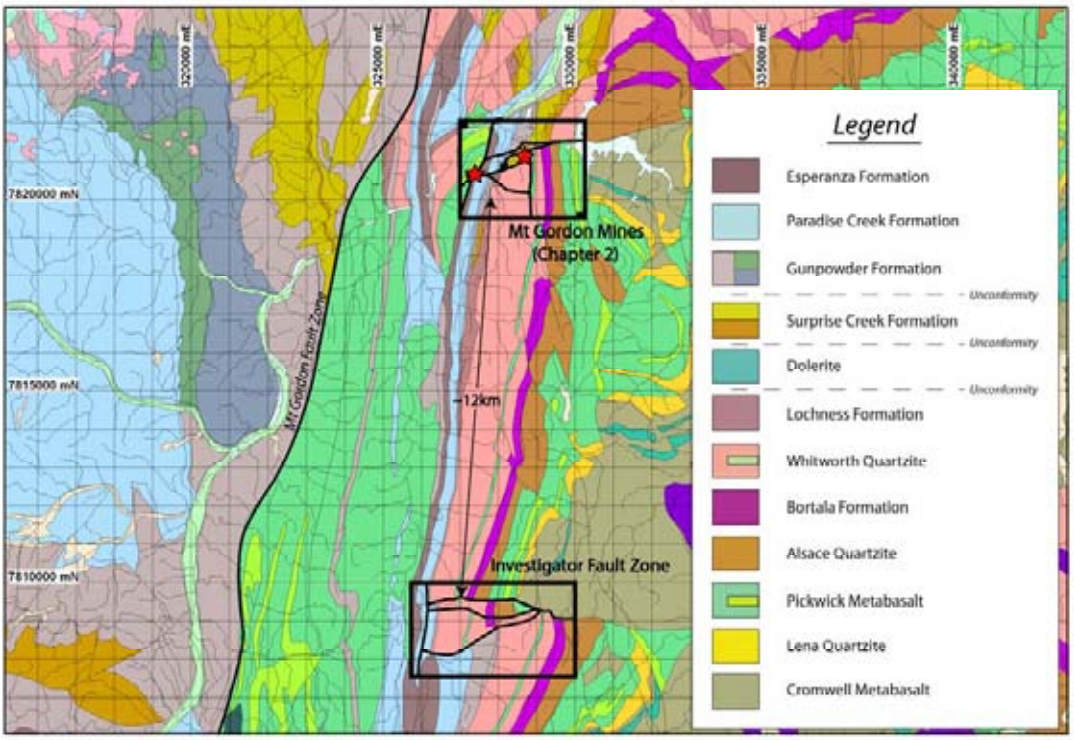

Figure 5.1 (adapted from Hutton et al., 1985) The location of the Investigator Fault Zone relative to the Mt Gordon Copper Mines (Chapter 2). Note the proximity of the two deposits, the similarities in the relative structural settings and lithological setting.

5.2 Geological setting

The Investigator area covers a complex north-trending package of Haslingden Group and McNamara Group strata within the Mount Gordon Fault Zone, strongly faulted by the north- to NNE-trending Mount Gordon Fault, Esperanza Fault and related splays.

The Investigator Fault Zone is comprised of three main east-west striking faults; the South Investigator Fault, Mid Investigator Fault and North Investigator Fault. These faults merge into one in the east of the field area (Figure 5.2).

The Investigator faults terminate to the west on the N-S to NNE-SSW striking Stockyard Creek Fault and the Esperanza Fault. The Esperanza Fault and related splays cut a north-trending syncline of lower McNamara Group strata, cored by the Esperanza Formation. These faults form part of the greater Mt Gordon Fault Zone and continue through to Mt Gordon to the north (Figure 5.1). Another NNE-SSW splay of these fault zones, the Prospect Fault, terminates on the South Investigator Fault.

Stratigraphically it is similar to the Mt Gordon Mines area, in that the Bigie Formation, Fiery Creek Volcanics and Quilalar Formation are not exposed in the area. Unlike Mt Gordon,

the Surprise Creek Formation is not present in the Investigator area, so the Torpedo Creek Quartzite (basal McNamara Group) rests with a slight angular unconformity on the Whitworth Quartzite (upper Myally Subgroup) (Figure 5.2). In the northeast of the Investigator area, the east-trending Investigator Fault juxtaposes the lower McNamara Group and Myally Subgroup (to the south) against the ECV and Myally Subgroup (to the north). The 100,000 scale Mammoth Mines Sheet (Hutton *et al*., 1985) shows that the Investigator Fault terminates just east of the Esperanza Fault. However, unpublished detailed mapping by Anaconda (1981) shows that the Investigator Fault swings sharply southward to become a north-trending fault lying parallel to, and a few hundred metres east of, the Esperanza Fault. This will be of significance when the constructing the numerical model geometries.

Aeromagnetic images show a sliver of ECV extending northwards immediately west of the Esperanza Fault. The images also show other bodies of ECV at shallow depth beneath Myally Subgroup within the Eastern Creek EPMA (Maiden, 1999).

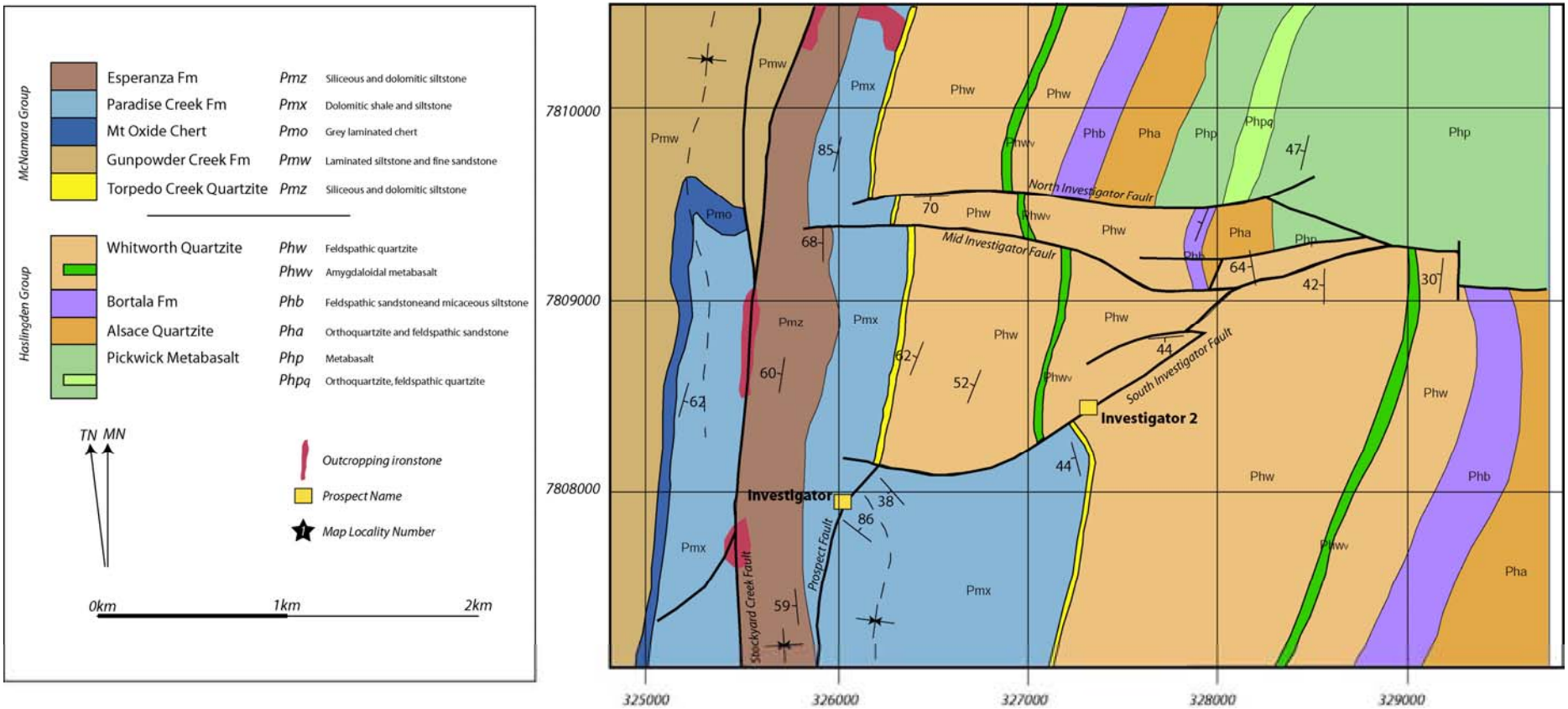

Figure 5.2 Geological map of the Investigator Fault Zone (adapted from Hutton et al., 1985 and Connors, 1997).

5.3 Exploration History

Exploration at Investigator has previously targeted Mt Isa-style, black shale-hosted, silica-dolomite alteration type copper deposits. For this reason the bulk of the historical drilling has been within the Paradise Creek Fm near the Stockyard Creek Fault (Figure 5.3).

During 1969-74, Carpentaria Exploration Company drilled five diamond holes (total 1105 m) to test the Prospect Fault, south of the South Investigator Fault. Holes intersected minor copper close to the fault plane - up to 0.3% Cu in Hole #1 and 0.64% Cu in Hole #3. Rock descriptions in the drill logs identify silica-dolomite alteration associated with the mineralisation. This alteration and mineralisation was not followed up with further drilling. 452 rock chip samples were reported on, however the report is in poor condition and results were unable to be plotted.

During 1980-82, Anaconda carried out detailed mapping between the Investigator and Bluff prospect (5 km to the south of the Investigator Prospect). The Bluff prospect contains a small resource of 75,000 t at 0.9% Cu, hosted by sheared and brecciated Whitworth Quartzite of the Myally Subgroup, in fault contact with the Paradise Creek Formation. With this in mind, Anaconda drill tested the Whitworth – Paradise Creek contact in the south of the Investigator Area. Four diamond holes (total 2661 m) and 14 percussion drilling (total 1 974 m) intersected up to 0.15% Cu and up to 0.18% Co near the Investigator Prospect. Minor chalcopyrite was present in quartz-carbonate veinlets and disseminated in siltstone. A small rockchip sampling campaign was conducted and the assay results for 10 well constrained and described samples can be seen in Table 5.1. These exploration programmes were conducted prior to the research which led to the realisation that the Mount Isa copper system is epigenetic, related to late folding and fault movement (Perkins, 1984; Swager,1985; Bell *et al.*, 1988). Although no high grade copper was intersected in either of these exploration programs, drilling showed indications of what is now recognised as Mount Isa-type copper mineralisation and alteration - including silica-dolomite alteration and laminated fine grained pyrite, one of the characteristic features of marginal parts of the Mount Isa ore system. The Investigator Fault Zone's similarity to the Mammoth and Mammoth Extended Fault Zone (Mt Gordon Copper Mines) 12 km to the north should not be overlooked. The Mammoth Mine is hosted by Whitworth Quartzites and appears to be a dominantly

structurally controlled deposit. No exploration at Investigator has yet targeted Mammoth-style copper mineralisation.

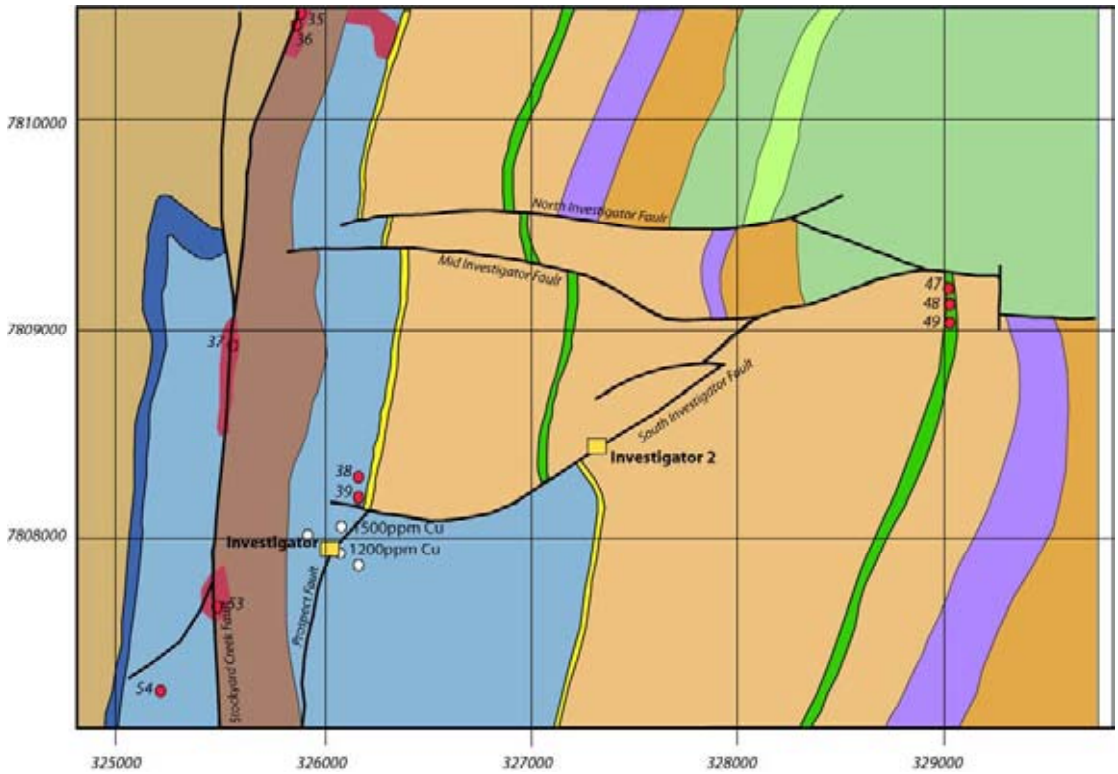

Figure 5.3 Geology with some constrained rock chip samples and drill holes. Rock chip samples (red dots) are numbered and corresponding assays seen in Table 5.1. Drill holes (white dots) with significant intersections are labelled next to some drill collars. Outcropping ironstones are shaded pale red.

Table 5.1 Rock chip sample assays for samples on geological map of Investigator (Figure 5.3).

Rock Chip	Description	Cu (ppm)	Co (ppm)	Pb (ppm)	Zn (ppm)	Ag (ppm)	Fe (%)	Mn (ppm)	As (ppm)
35	Stratigraphic ironstone (fault?)	190	1	66	47	7	20.8	160	522
36	Ferruginous chert	570	38	140	38	17	37.6	1510	333
37	Ferruginous chert	58	1	9	27	1	3.9	290	72
38	Stratigraphic ironstone	99	220	160	150	22	42.7	3260	11
39	Stratigraphic ironstone	450	83	190	82	24	47.1	1230	137
47	Ferruginous weathered syenite	170	77	44	80	9	6.3	330	14
48	Hematitic syenite	69	40	59	48	10	16.1	970	7
49	Micro syenite	42	56	26	23	1	5.6	75	7
53	Fault ironstone	73	5	74	48	10	24.0	270	92
54	Hematitic siltstone	39	1	26	35	1	4.4	2490	31

5.4 Numerical Modelling –Methodology and Conceptual Model

The 4.7 km x 3.1 km model geometry (Figure 5.4) was created from field mapping and air photo interpretation conducted by Connors (1994). Due to limitations of the UDEC program, no fractures can be inserted that are not directly or indirectly connected to the model edges, hence all fractures are joined (McLellan and Oliver, 2007). For this reason the various east-west trending Investigator Fault strands were connected to the north-south striking Stockyard Creek Fault. The orientation of the maximum principal stress tested was horizontally directed along 112.5º-292.5º as per the best fit models for Mt Gordon (Chapter 2) and Mt Kelly (Chapter 4). The stress conditions for the model are set at a phi (Φ) value of 0.3 (as per Chapter 2.12.6. Stress Inversion Models). The imposed stresses (σ_1=190 MPa, σ_2=175 MPa, σ_3= 140 MPa) also remained unchanged from the Mt Gordon stress inversion numerical model. Approximately 7 km of overburden is represented by an initial σ_2 value of 175 MPa. Rock and fault properties remain unchanged from the Mt Gordon modelling (Table 5.2). It was assumed that all the faults in the models were already present in their current geometric configuration.

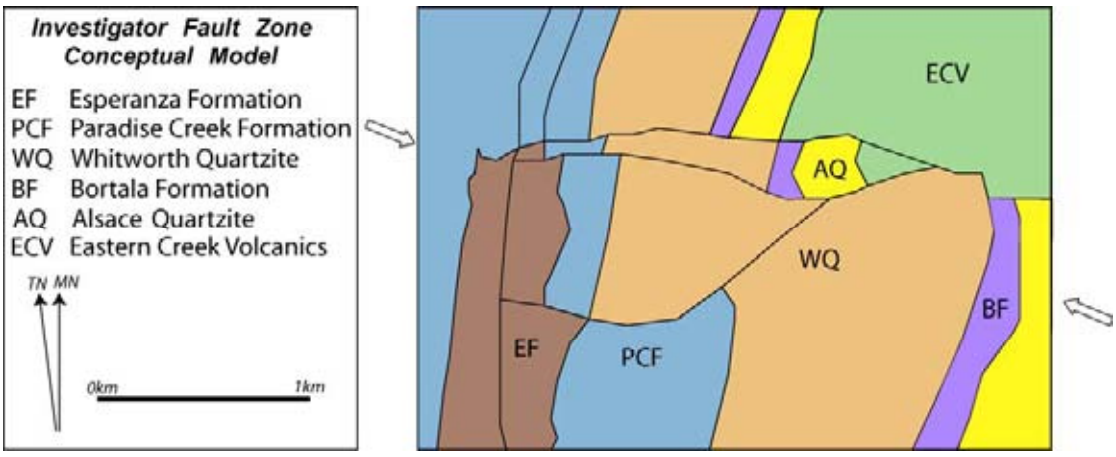

Figure 5.4 Conceptual model geometry. The arrows reflect the σ_1 orientation that was tested.

Table 5.2 Conceptual model lithological and fault contact input parameters. All contacts in the model are treated as faulted contacts.

Property	Quartzite	Shale	Siltstone	Metabasalt	Lithological contact	Fault
Density (kg/m3)	2600	2650	2400	2650		
Bulk modulus (Pa)	40e9	40e9	16e9	49e9		
Shear modulus (Pa)	25e9	7e9	11e9	27e9		
Cohesion (Pa)	20e7	5e7	10e7	20e7	3e3	5e2
Tensile strength (Pa)	10e7	3e7	5e7	10e7	3e6	2e6
Friction angle (°)	31	37	32	31	35	30
Dilation angle (°)	2	5	2	2	5	5
Normal stiffness (Pa/m)					2e9	5e9
Shear stiffness (Pa/m)					5e5	8e4
Permeability factor (Pa/s)					238	300
Aperture at zero normal stress (m)					0.03	0.05
Residual hydraulic aperture (m)					0.01	0.03

5.5 Numerical Modelling Results

The numerical modelling sought areas of (i) low minor principal stress (σ_3), (ii) low mean stress (σ_m), (iii) low fluid pressure for failure (Pf_F), and (iv) low differential stress ($\Delta\sigma$), as potential structural targets favourable for mineralisation. The modelling predicted four zones of low minor principal stress (σ_3) (Figure 5.5). The largest area of low σ_3 was found near the junction of the North and Mid Investigator Faults at approximately 330000mE. A broad zone of low σ_3 extends south west from this fault intersection to the south of the South Investigator Fault Zone.

Another significant area of low σ_3 was located at the intersection of the Stockyard Creek Fault and the South Investigator Fault. The σ_3 value in this fault intersection was approximately 125 MPa. Two zones of low σ_3 were located in Whitworth Quartzites between the North Investigator and Mid Investigator Faults. Values of minor principal stress within these areas of low σ_3 were approximately 120 MPa. This area is of particular interest as the

gross scale fault geometry and lithological host rock are similar to the Mammoth copper deposit 12 km to the north.

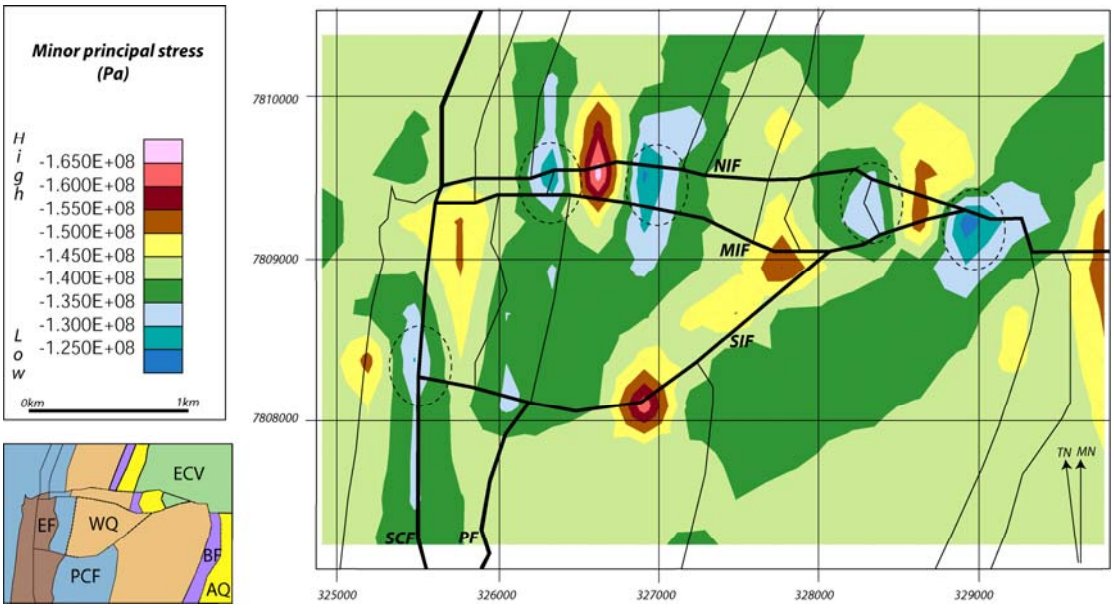

Figure 5.5 Plot of minor principal stress for the Investigator Fault Zone. The conceptual model input (bottom left corner) is present for reference. Areas of low minor principal stress values (dashed circles) can be seen between the North and Mid Investigator faults, at the junction of the North and Mid Investigator faults and at the intersection of the Stockyard Creek Fault and South Investigator faults.

The lowest values of mean stress were seen in the junction of the North Investigator Fault and the Mid Investigator Fault (Figure 5.6) coincident with the same zone of low σ_3 (Figure 5.5). North of the intersection of the Prospect Fault and the South Investigator Fault was also a broad area of low mean stress. This is also coincident with an area of low minor principal stress (Figure 5.5).

Localised areas of low mean stress are also seen along the North Investigator Fault. The low mean stress is confined to the southern side of the North Investigator Fault within the Whitworth Quartzite, the Bortala Formation and the Alsace Quartzite. The ECV's (Pickwick Metabasalt) north of the North Investigator Fault are seen to contain relatively high mean stress values. A thin sliver of low mean stress is seen to trend up the western margin of the Stockyard Creek Fault, north of the South Investigator Fault.

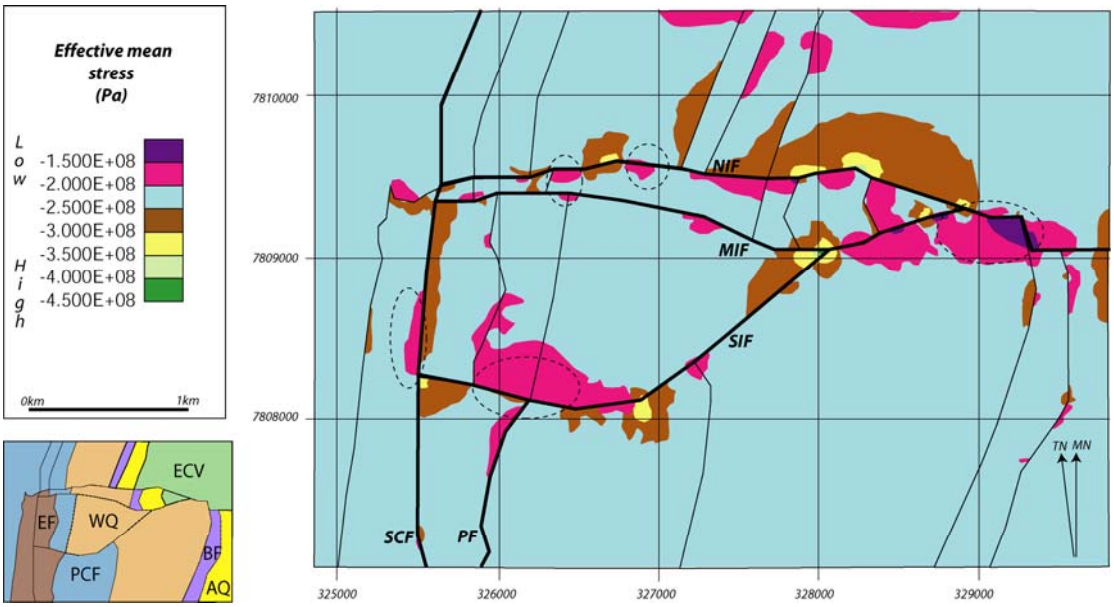

Figure 5.6 Plot of mean stress for the Investigator Fault Zone. Areas of low mean stress values (dashed circles) can be seen between the North and Mid Investigator faults, at the junction of the North and Mid Investigator faults and at the intersection of the Stockyard Creek Fault and South Investigator faults.

Areas of low fluid pressure for failure (Figure 5.7) are generally consistent with the areas of low minor principal stress and low mean stress, however the areas of low Pf_F are more tightly defined.

The junction of the North Investigator Fault and Mid Investigator Fault is an area where low fluid pressure is required for failure (~40 MPa). This modelled area thus shows very low fluid pressure for failure, low mean stress and low minor principal stress making it an area that should theoretically be very favourable for rock failure and fluid flow.

The North Investigator Fault also has two small zones of low fluid pressure for failure (~40 MPa) that sit around a zone of high fluid pressure for failure. As seen with the Mt Gordon Mines numerical modelling (Chapter 2), some deposits seem to be associated with steep gradients in fluid pressure for failure, minor principal stress and mean stress. These two discrete zones of low Pf_F, also correlate with discrete zones of low σ_3 and σ_m either side of an area of high σ_3 and σ_m.

Other areas that developed low σ_3 and σ_m and also show low Pf_F are the intersection of the Prospect Fault and the South Investigator Fault (Pf_F ~ 90 MPa) and the north-western intersection of the South Investigator Fault and the Stockyard Creek Fault (Pf_F ~ 90 MPa).

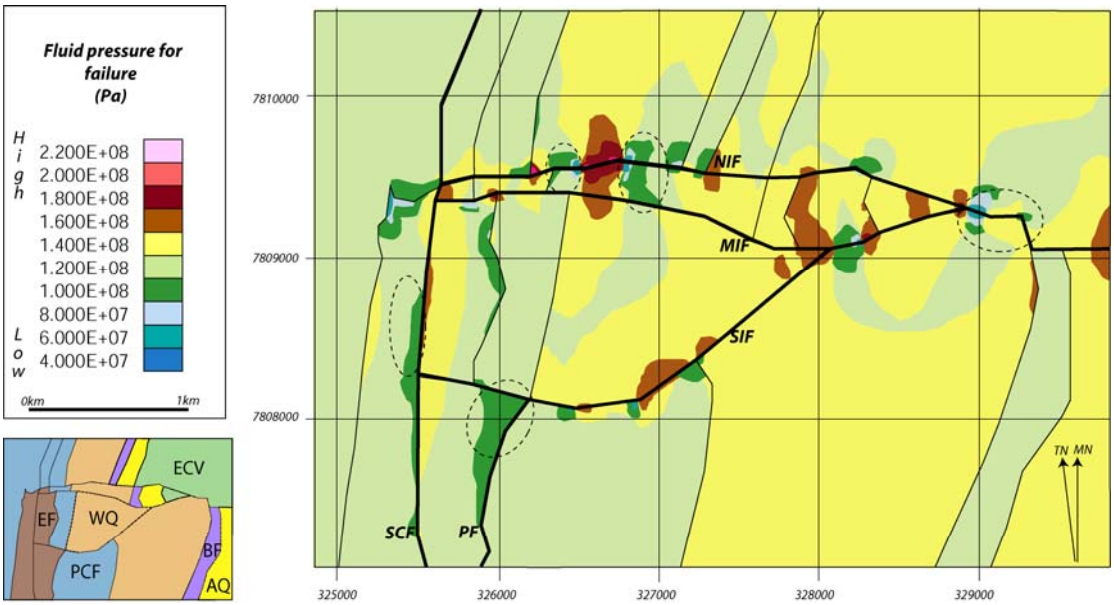

Figure 5.7 Plot of fluid pressure required for failure for the Investigator Fault Zone.

Areas of low differential stress in the Investigator Fault Zone, that are coincident with areas of low σ_3, σ_m and Pf_F, may be indicative of areas more likely to fail in tension or extensional shear. Conversely areas of high differential stress that are coincident with areas of low σ_3, σ_m and Pf_F, are more likely to fail in contractional shear.

Areas of low differential stress coincident with areas of low σ_3, σ_m and Pf_F are developed in several places between the North Investigator Fault and Mid Investigator Fault (Figure 5.8). Coincident areas of low σ_3, σ_m, Pf_F and differential stress are shown in Figure 5.9.

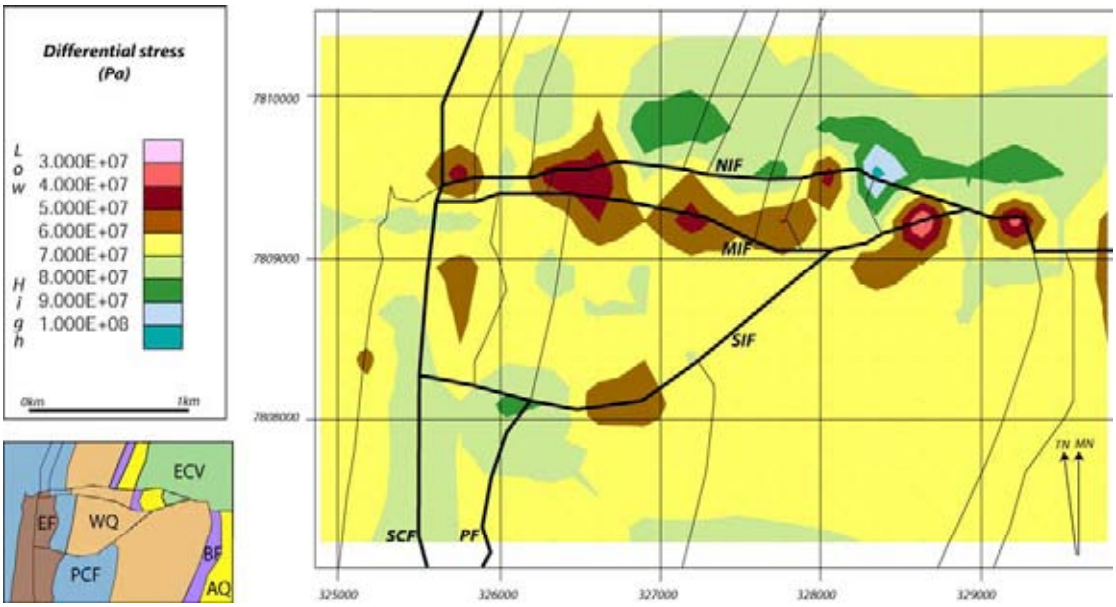

Figure 5.8 Plot of differential stress for the Investigator Fault Zone. Areas of low Δσ (dashed circles) have developed in several places between the North Investigator Fault and Mid Investigator Fault, as well as at the junction of these two faults.

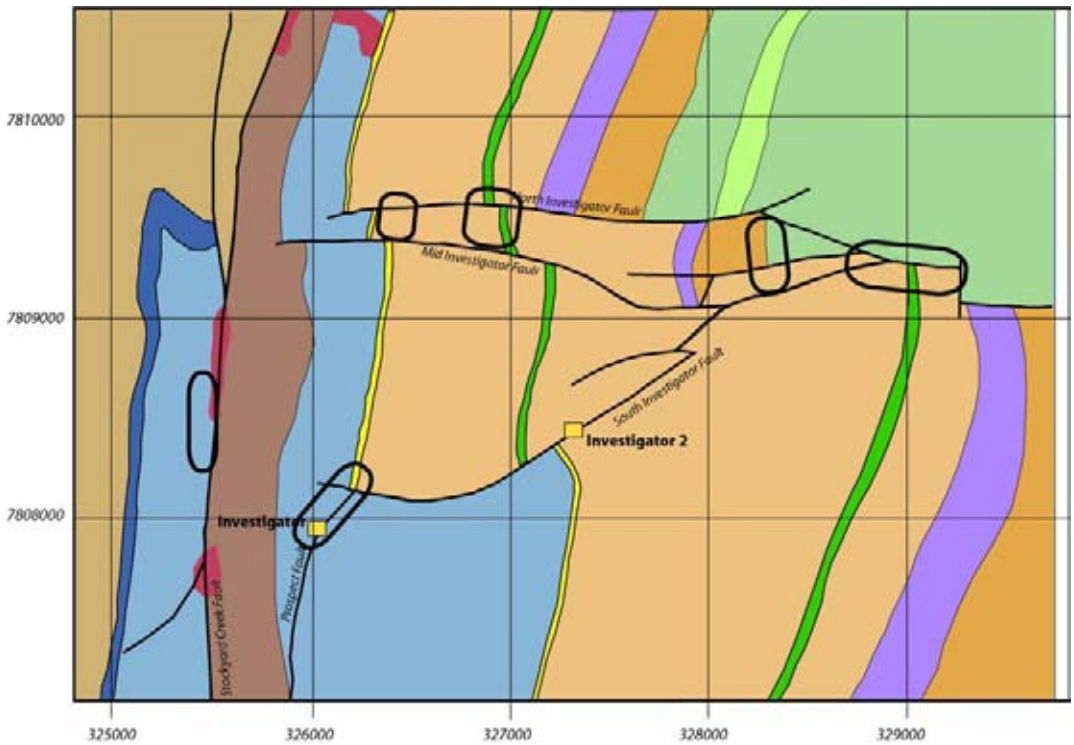

Figure 5.9 The circles indicate the areas that modelling has predicted low minor principal stress, low mean stress, low fluid pressures for failure and low differential stress within the Investigator Fault System. The core of these areas are predicted to develop failure in tension (and possible hydraulic brecciation) and the edges of these areas are expected to fail in extensional shear. Modelled boundaries between areas of predicted tensile and shear failure are known to contain mineralisation at Mt Gordon (Chapter 2).

5.6 Field Mapping – Model Validation and other areas of interest

Field mapping was conducted in an effort to validate the outputs of the numerical models completed for the Investigator Fault Zone. Several traverses were walked in order to ascertain the expression of the fault (i.e. discrete fault or series of sheeted veins etc.), the locations of significant breccias and the type of fault fills.

Several localities of interest are discussed in further detail in this section (Figure 5.10)

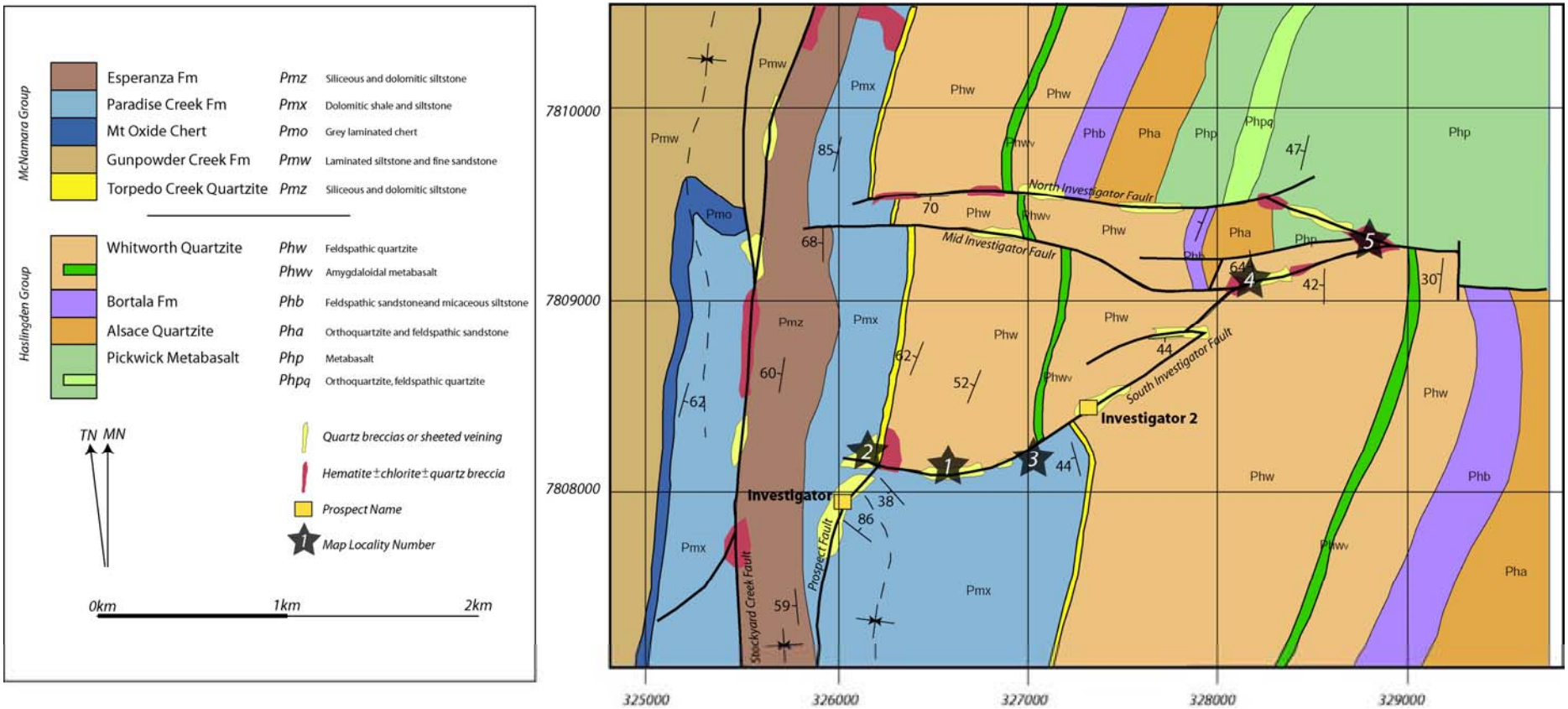

Figure 5.10 Sample localities (within black stars) mapped in detail within the Investigator Fault Zone. The map also contains outcropping fault fills mapped in this study, and areas of ironstone along faults recognised earlier.

5.6.1 Locality 1 – South Investigator Fault

At this locality the South Investigator Fault juxtaposes Whitworth Quartzite against younger Paradise Creek Formation shales. UDEC modelling shows this area to have low σ_3, σ_m and P_{fF}, reflecting a likely site of dilation.

The South Investigator Fault was seen to strike east west in Locality 1 but was poorly exposed. A splay approximately 15 metres north of the South Investigator Fault contained slickenlines. It was found to strike toward 061º with a steep dip to the south. The South Investigator Fault splay was seen to be approximately 3 metres wide in this location. The fault breccia contained angular to sub-rounded, silicified quartzite clasts 2 to 20 cm in size (Figure 5.11a).

Two sets of slickenlines are present on the fault margin; one set of steeply plunging slickenlines and another shallow set (Figure 5.11b) that overprint the steep ones. This is consistent with slickenlines seen in the Mammoth Mine where a steep early set of slickenlines are seen to be overprinted by a shallow slickenline set on similarly oriented fault surfaces. The shallow slickenline set at Mammoth was associated with the stress field acting during ore breccia development. When plotted on a stereonet, the fault plane solution suggests this slickenside set is consistent with ENE-WSW to SE-NW shortening (Figure 5.11c).

At Locality 1, the South Investigator Fault shows evidence of at least two phases of displacement, with the youngest fault displacement potentially being related to the ESE-WNW oriented deformation event associated with copper breccia formation at Mt Gordon.

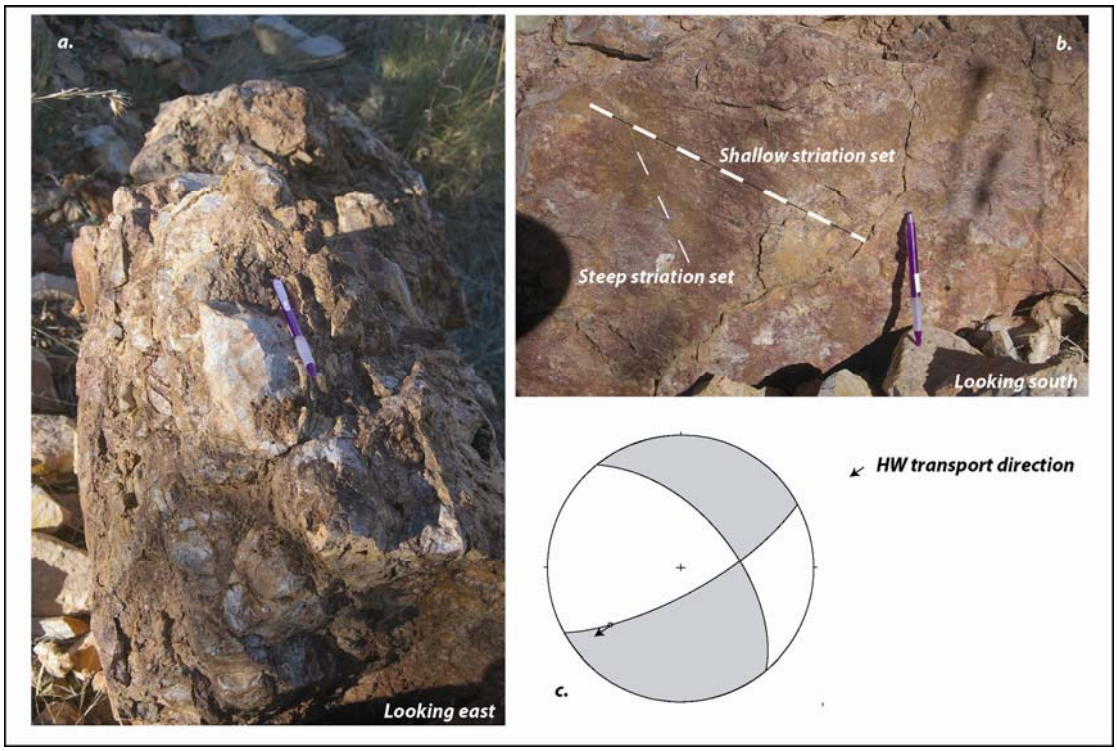

Figure 5.11 Locality 1 – South Investigator Fault ***(a)*** *Looking east down a splay off the South Investigator Fault. The fault breccia contains clasts that vary in size from 2 to 20 cm.* ***(b)*** *A fault surface containing two sets of slickenlines. A shallow set of slickenlines are seen to overprint a steeper set. This was observed on the Mammoth Fault (Chapter 2.5.3 this study; Clark, 2004) within the Mt Gordon Mines. The Mammoth Fault was oriented similarly to the South Investigator Fault in Locality 1.* ***(c)*** *Stereonet showing the fault plane solution for the fault striking 061, and the shallow slickenside set. As the white areas reflects an area in pressure, σ_1 must be oriented between ~060º and ~150. The small arrow reflects the direction of hangingwall transport.*

5.6.2 Locality 2 – Prospect Fault

Locality 2 is located at the inferred intersection of the Prospect Fault – South Investigator Fault (Figure 5.12). The South Investigator Fault has juxtaposed Whitworth Quartzites against Paradise Creek Formation shales. The Paradise Creek Formation is heavily folded in this area and the Prospect Fault runs parallel to the axial plane of a north-south anticline (likely D_2 fold). The intense folding and faulting within the shale unit makes this area quite undulating, and the Prospect Fault trace tracks along one of the ridge lines.

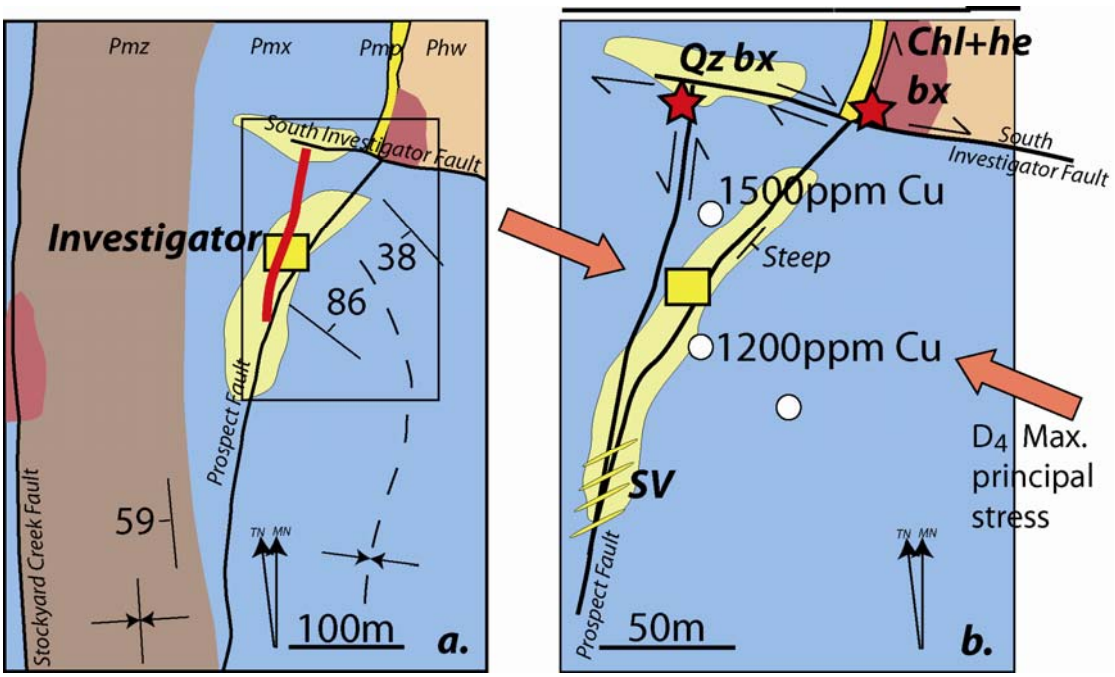

Figure 5.12 ***(a)*** *Close up of the area around the Investigator Prospect and the position of Locality 2. The red line indicates an extension to the Prospect Fault as mapped in this study. Colours reflect lithology and alteration as per Figure 5.10.* ***(b)*** *An inset to the area denoted by a square in Figure 5.12a. The figure shows positions of drill hole collars (white circles), with significant assay results alongside the relevant collar. The model also shows the ESE-WNW orientation modelled and the likely location of significant brecciation associated with this event (red stars). The red star in the east matches with a mapped hematite-chlorite-breccia body. Expression of the Prospect Fault to the south is as a sheeted vein set (SV) with weak brecciation locally. Colours reflect lithology and alteration as per Figure 5.10.*

The Prospect Fault's expression grades from a series of sheeted veins approximately 250 metres south of the intersection to a 10 m wide quartz flooded jigsaw-fit breccia. The 10 m wide fault breccia still shows evidence of failure along bedding planes as shown in Figure 5.13. This change in fault expression can possibly be related to a change in minor principal stress value as determined by the UDEC modelling. Lowest values of σ_3 are seen in the intersection itself, with the location of the

sheeted veins corresponding to an increase in σ_3 value of approximately 25 MPa. UDEC modelling of the fault intersection shows relatively low σ_3, σ_m and Pf_F values reflecting a site likely to dilate.

Figure 5.13 Locality 2 quartz breccia. The breccia has preferentially terminated against a bedding plane associated with the surrounding Paradise Creek Formation shales and siltstones.

Chlorite-hematite-quartz breccias are seen in the north-eastern quadrant of the Prospect Fault and South Investigator Fault intersection. This is coincident with an area that conventional structural analysis would predict to be dilatant during an ESE-WNW shortening event (Figure 5.12b). The numerical modelling outputs (Chapter 5.5) also suggest this area to be favourable for brecciation during an ESE-WNW shortening event. Little outcrop existed over the south-western quadrant of the Prospect Fault and South Investigator Fault intersection although modelling results also show this area to be a favourably oriented structural target.

The quartz breccias are seen to occur in areas that would not be expected to be conducive to dilation during an ESE-WNW shortening event. Quartz veins as part of a sheeted vein set to the south of the Investigator prospect (Figure 5.12b) are also unlikely to be related to an ESE-WNW shortening event on the basis of their orientations. It is likely that the quartz dominated breccias and veins represent a different structural event, possibly during the initial faulting event, prior to the ESE event.

5.6.3 Locality 3 – South Investigator Fault Zone Bend

Locality 3 is located on the northwestern side of a mapped bend in the South Investigator Fault. As for Localities 1 and 2, the South Investigator Fault juxtaposes Whitworth Quartzites against Paradise Creek Formation shales at Locality 3.

The South Investigator Fault Zone had a significant change in fault expression at Locality 3. Just west of the Investigator 2 prospect, the South Investigator Fault was seen to contain an intense shear fabric (Figure 5.14) and little brecciation whereas the same fault was seen to have angular clasts in breccia up to 20 cm near the Prospect Fault (Figure 5.11). At map scale, the only obvious difference between the brecciated and non brecciated South Investigator Fault areas was the orientation of the fault zone in each location. The fault strike in Locality 3 is toward 072º, a change of approximately 25º from the almost east-west striking fault plane at Locality 1. The truncation of small F_3 folds by the shear fabric suggests that the shear fabric was developed post D_3. Numerical modelling indicates that Locality 3 would have contained the highest values of σ_3 in the entire Investigator Fault Zone during an ESE-WNW shortening event. High values of mean stress and fluid pressure for failure would imply that this area was unlikely to dilate during ESE-WNW shortening.

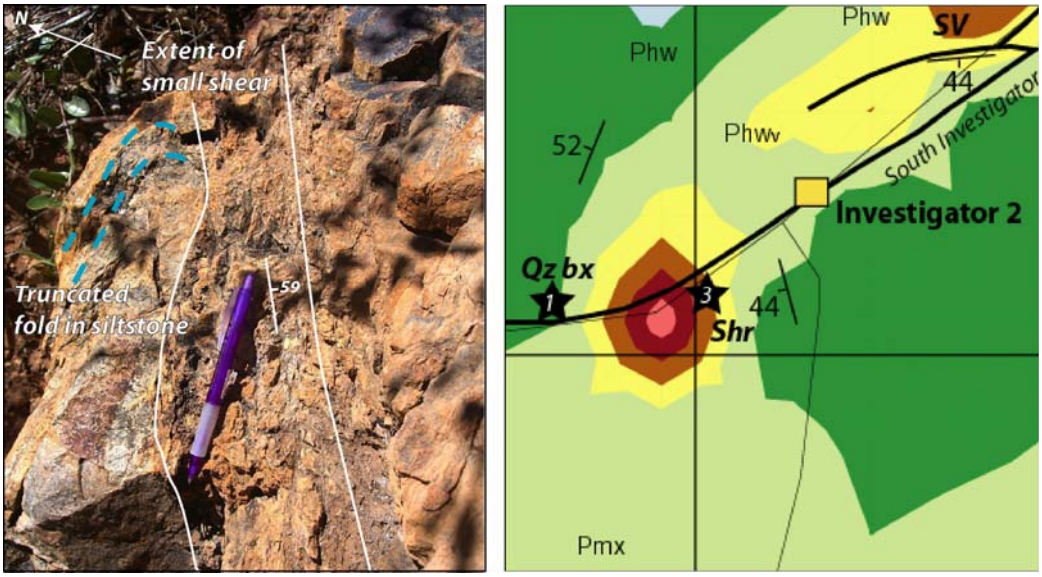

Figure 5.14 ***(a)*** *Surface expression of the South Investigator Fault at Locality 3 showing strong shear fabric and only minor cataclastic brecciation. The main fault/shear plane here was found in the bottom of the creek and outcropped poorly. The shear truncates a small fold.* ***(b)*** *Plot of contours of minor principal stress for Localities 1 and 3. Significantly higher values of σ_3 are seen at Locality 3 than at Locality 1. The change in orientation is the only obvious physical difference between the two localities, but the expression of the South Investigator Fault at Locality 1 is a hydraulic breccia and at Locality 3, a shear zone.*

5.6.4 Locality 4 – Mid Investigator Fault

Locality 4 is located on the Mid Investigator Fault, approximately 75 m east of the intersection with the South Investigator Fault. Several differing breccia bodies were present within and around the Mid Investigator Fault at Locality 4. A large quartz dominated breccia was seen in the Mid Investigator Fault location. The fault breccia was comprised of angular to sub-angular clasts of feldspathic quartzite that ranged in size from <1cm to 25 cm diameter (Figure 5.15), set in a matrix comprising hydrothermal quartz infill.

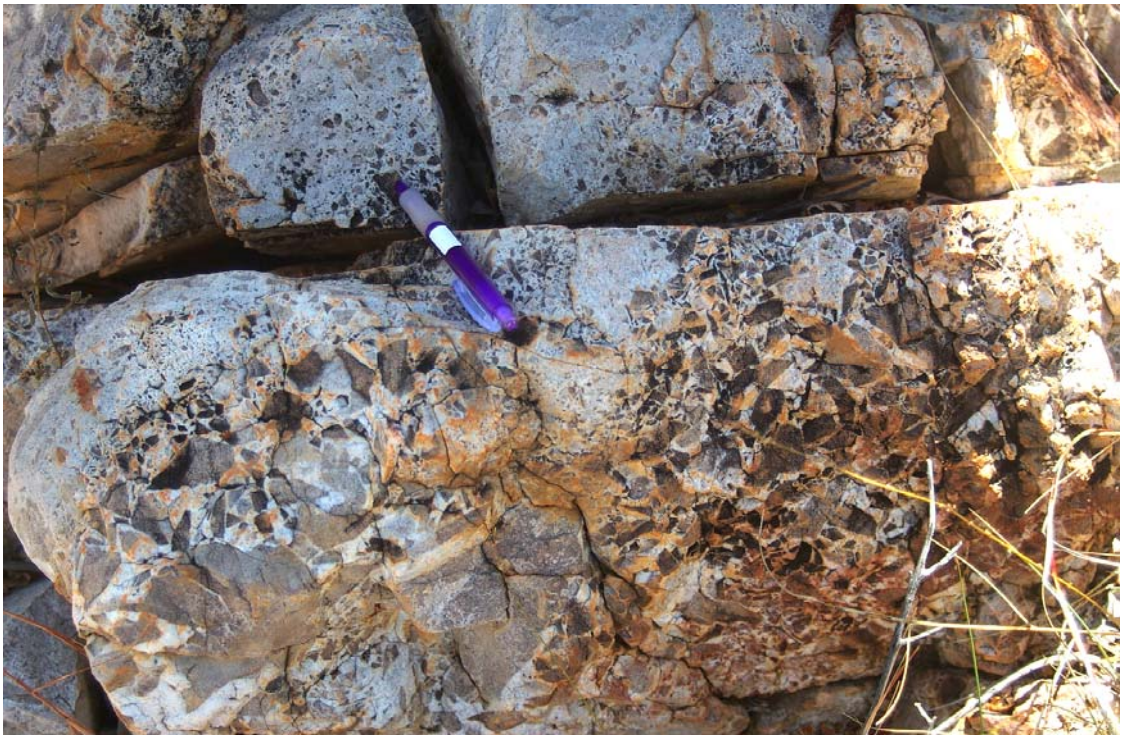

Figure 5.15 Mid Investigator Fault breccia comprised of angular to sub-angular clasts of feldspathic quartzite in a quartz matrix.

A small splay fault (~8 cm width) from the Mid Investigator Fault was seen to have an associated extension vein array at Locality 4. The splay fault and vein array were of interest because the dominant vein fill was hematite, chlorite and quartz, differing from the quartz dominated Mid Investigator Fault proper. The extension veins were seen to have a preferred orientation of sub-vertical, striking toward approximately 115º. Shortening from the ESE-WNW would have produced a dextral sense of shear on the fault and tensile failure of the quartzites proximal to the fault (Figure 5.16).

The hematite-chlorite veining is younger than the bulk of the quartz breccias. As with Locality 2, it seems likely that the quartz dominated breccias have formed in a separate stress event to the hematite-chlorite veining and breccias.

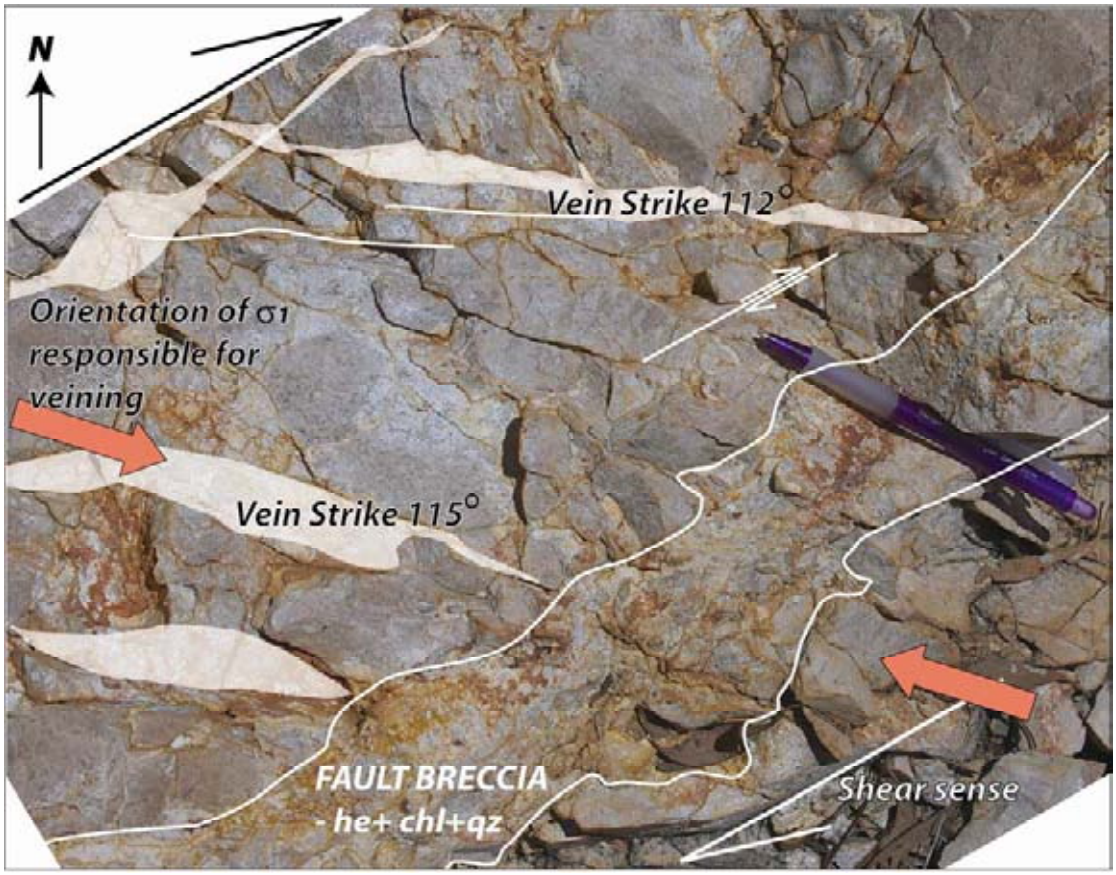

Figure 5.16 Splay fault of the Mid Investigator Fault at Locality 4. The fault (within the white lines) has a fill of hematite-chlorite and quartz. Extension veins (shaded white) with a similar fill are seen to strike ESE-WNW. A σ_1 orientation parallel to these veins would have produced a dextral shear sense on the fault (and other faults of similar orientation) if it is assumed the veins were a tensile en echelon vein array.

5.6.5 Locality 5 – North Investigator Fault near Mid Investigator Fault Junction

Locality 5 is situated on the North Investigator Fault approximately 100 metres north-west of the junction with the Mid Investigator Fault. The North Investigator Fault strikes towards 110º at Locality 5, juxtaposing a sliver of Whitworth Quartzites south of the North Investigator Fault against Eastern Creek Volcanics to the north of the fault.

The breccia body is approximately 50 metres wide and contains differing breccia fills over its width. The peripheries of the fault are dominated by quartz breccias (Figure 5.17a), similar to Locality 4 (Figure 5.14), with angular to sub-angular clasts of Whitworth Quartzite varying in size from 2 to 30 cm. Some quartz breccias show evidence of re-brecciation, with local clasts of quartzite and quartz engulfed by further quartz fill.

The quartz breccias are occasionally cross cut by breccias containing a hematite-chlorite dominated fill with minor quartz (Figure 5.17b). These breccia orientations were not mapped as in situ examples of this breccia style were not located, but individual boulders contained several parallel breccia sheets.

The final breccia style is a hematite-chlorite-quartz breccia (Figure 5.17c and d) that is seen to cut through quartz dominated breccias and also to abut on weakly brecciated to unbrecciated Whitworth Quartzites. Clasts are typically small 1 cm to 6 cm and are typically sub-angular to rounded, suggesting an explosive-type or abrasive brecciation event.

The presence of quartz breccias overprinted by later hematite-chlorite confirms the observations made at Locality 2 and Locality 4, that the bulk of the quartz breccias and veining seen around the Investigator Fault Zone, are unrelated to the hematite-chlorite stress event. This observation is important when differentiating between breccias more likely to be related to mineralisation (hematite-chlorite breccias) from those likely to have pre-dated the ESE-WNW shortening event (quartz dominated breccias).

Figure 5.17 Locality 5 breccia styles. ***(a)*** *Quartz dominated breccia with 2 cm to 20 cm angular to sub-angular clasts of variably fedspathic quartzite.* ***(b)*** *Quartz dominated breccia showing signs of re-brecciation and infill of hematite and chlorite locally.* ***(c)*** *Angular clasts (1 cm to 5 cm) of feldspathic quartzite within a hematite-chlorite matrix.* ***(d)*** *A hematite-chlorite dominated breccia with small (~1 cm) sub-rounded breccia clasts. The breccia is bound on one side (right of photo) by a feldspathic quartzite.*

5.7 DISCUSSION

The previously limited exploration of the Investigator Fault Zone means the area remains a prospective area for both Mt Isa-style and Mammoth-style mineralisation. The previous sampling and drilling campaigns were primarily targeting Mt Isa-style copper deposits, and as such the bulk of the collected data was from the McNamara Group shales. Little data was acquired from the Haslingden Group quartzites in the north and east of the Investigator Fault Zone; areas that from camp-scale mapping, would appear prospective for Mt Gordon Mammoth-style mineralisation.

The successful numerical modelling of the Mt Gordon Copper Mines (Chapter 2) and the Mt Kelly Copper Mine (Chapter 4) provided evidence of a σ_1 orientation of ESE-WNW to form the ore-bearing breccias. The structural mapping of Miller (2006) showed the Mt Isa Copper Mine ore breccias formed under a similar tectonic regime. The Investigator Fault Zone was therefore modelled with a σ_1 orientation of ESE-WNW.

The numerical modelling of the Investigator Fault Zone has predicted several areas of coinciding low minor principal stress, low mean stress, low fluid pressures for failure and low differential stress. Steep gradients of high to low values of σ_3, σ_m, Pf_F and particularly $\Delta\sigma$ have proven particularly indicative of areas likely to dilate from the modelling conducted at Mt Gordon and Mt Kelly. The core of these areas is predicted to develop failure in tension (and possible hydraulic brecciation) and the edges of these areas are expected to fail in extensional shear. Modelled boundaries between areas of predicted tensile and shear failure are known to contain mineralisation at Mt Gordon (Chapter 2).

With no known economic copper deposits found to date at Investigator, the numerical modelling outputs required field validation. Breccia styles and breccia fills were mapped and related back to the model outputs.

Mapping consistently located hematite-chlorite-quartz breccia bodies in areas predicted to be dilatant from the numerical modelling. In some cases multiple breccia events preserved a transition from early quartz rich breccias to these later stage hematite-chlorite-quartz breccias (Locality 5). Significantly no hematite-chlorite-quartz brecciation was seen to preserve cross-cutting veins or itself be re-brecciated, suggesting that this breccia event occurred late in the deformational history. At Locality 4, hematite-chlorite-quartz extension veins were inferred to have formed in response to ESE-WNW shortening.

It is therefore proposed that evidence for a D_4 ESE-WNW shortening event is preserved within the Investigator Fault Zone in the form of hematite-chlorite-quartz brecciation and veining.

As a consequence of this work, Copperco Ltd. have decided to re-explore the Investigator Fault Zone. An extensive soil and rock chip sampling campaign has been conducted and an airborne geophysical survey flown over the area. Plans for drilling are dependent on the results of the geophysics. Unlike previous exploration campaigns, the Copperco Ltd. exploration team is not discounting Mammoth-style mineralisation models.

6. ERNEST HENRY COPPER-GOLD MINE

6.1 Introduction

The Ernest Henry Mine is located approximately 35 km northeast of Cloncurry (Figure 6.1). It is the largest copper deposit in the Eastern Succession and Australia's third largest copper producer with a total reserve and resource prior to the commencement of mining in 1998 of 166 Mt @ 1.1% Cu, 0.54 g/t Au (Ryan, 1998). As of June 2006 the remaining resource (proved and probable) totalled 106 Mt @ 1.10% Cu, 0.56 g/t Au (Xstrata Annual Report, 2006).

Copper mineralisation has been dated by U-Pb (titanate) at 1529 +11/-8 Ma (Mark *et al.*, 2006), giving it a similar age to the copper deposits at Mt Isa, Mt Gordon and Mt Kelly Mines in the Mt Isa Western Succession. Although similarly aged to the Western Succession deposits, the Ernest Henry deposit differs significantly in host rock, alteration style and apparent structural controls. Like many of the Western Succession deposits, several authors (Valenta, 2000; Coward, 2000; Laing, 2003) have postulated different structural theories for the formation of the Ernest Henry deposit. This study hopes to resolve the nature of the structural setting during ore genesis and if possible place this into a regional structural framework.

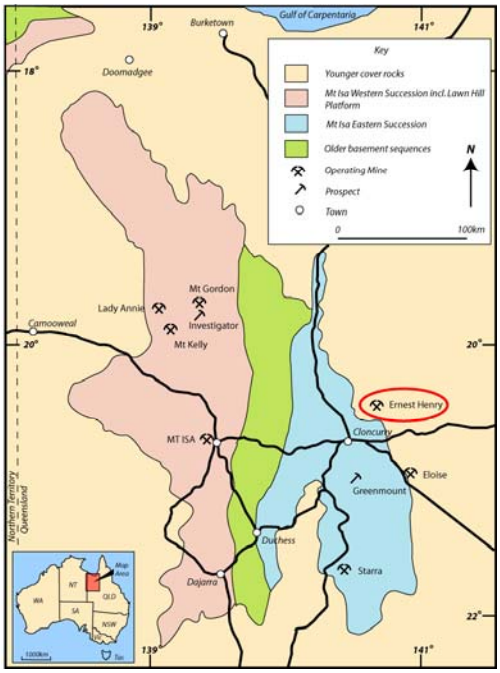

Figure 6.1 The Mt Isa Inlier with the Ernest Henry Mine circled. The deposit is concealed beneath a Phanerozoic sedimentary cover sequence, but is considered part of the Mt Isa Eastern Succession.

6.2 Geological setting

The Ernest Henry ore deposit lies to the east of the Cloncurry Fault, within the Cloncurry-Selwyn zone of the Mt Isa Eastern Succession. The orebody lies beneath ~75 m of Phanerozoic cover and was discovered when WMC Ltd. targeted a coincident aeromagnetic (Figure 6.2a) and TEM anomaly (Craske, 1995; Webb and Rowston, 1995). The anomalism was created by the magnetite-rich nature of the deposit alteration and the presence of native copper in the supergene portion of the ore zone (Craske, 1995; Webb and Rowston, 1995).

The Ernest Henry deposit fits the generic orebody classification of iron oxide copper-gold type (IOCG) (Hitzman *et al*, 1992; Williams, 2000; Mark *et al*, 2000, 2006; Williams and Pollard, 2001; Williams *et al*, 2005). Mineralisation in all IOCG deposits is dominated by magnetite or hematite. IOCG's are typically polymetallic often containing elements such as Cu, Au, Ag, U, Mo and REE (Hitzman, 1992). IOCG host sequences are generally intensely altered. Aside from intense Fe-metasomatism throughout IOCG deposits, Hitzman (1992) defined general trends in alteration from sodic alteration at deep levels, to potassic alteration at intermediate to shallow levels and sericitic alteration and silicification at very shallow levels.

Williams and Pollard (2001) hypothesise that the Ernest Henry IOCG mineralisation was probably dominated by processes such as CO_2-phase separation, fluid cooling, wall-rock reactions that buffered pH, or fluid mixing constrained by the structural environment at the time of mineralisation. Williams and Pollard (2001) describe the deposit as poorly zoned, with respect to Cu-Fe species, with the relative homogeneity of sulphur and ore minerals potentially reflecting large fluid masses.

The Ernest Henry deposit is hosted in an interlayed intermediate metavolcanic and metasedimentary (calc-silicate, psammite, pelite and carbonaceous meta-siltstone) sequence (Twyerould, 1997; Mark *et al.*, 1998). A metavolcanic sequence at Mt Fort Constantine (~5 km south west of Ernest Henry) is thought to be stratigraphically equivalent to the Ernest Henry ore host sequence. The Mt Fort Constantine metavolcanics have been dated by Page and Sun (1998) with crystallisation ages of 1746±9 Ma and 1742±6 Ma. The Ernest Henry metavolcanic and metasedimentary sequence has been intruded by diorite (Figure 6.2b). The diorites have a crystallisation age of ca. 1660 Ma (Pollard and McNaughton, 1997). The diorites, metavolcanics and metasediments were all metamorphosed to lower amphibolite facies (Twyerould, 1997; Mark *et al.*,

1999) during regional peak metamorphism at regional D_2 (ca. 1585 – 1595 Ma; Page and Sun, 1998; Gauthier *et al.*, 2001; Giles and Nutman, 2002; Rubenach *et al.*, 2007).

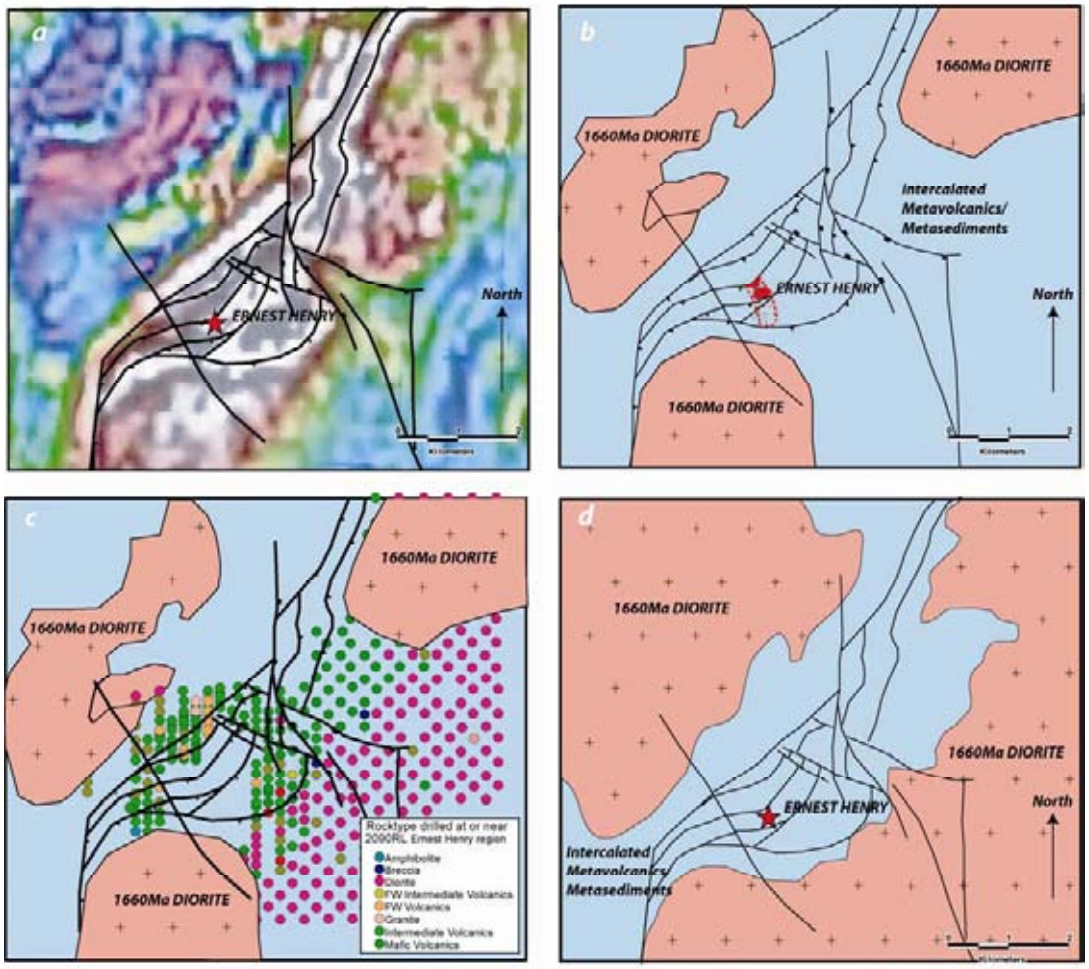

Figure 6.2 ***(a)*** *Aeromagnetic image with interpreted faulting marked in black. The fault traces were primarily constructed from rapid changes in magnetic response. Interpretation of shear zone provided by S. Coates and R. Valenta (ex company geologists).* ***(b)*** *Interpretation of the position of the diorite bodies relative to the Ernest Henry deposit. The diorite interpretation utilised the aeromagnetic image S. Coates and R. Valenta (ex company geologists).* ***(c)*** *Diorite and fault interpretation (Valenta and Coates), with sterilisation drilling results overlaid. The sterilisation drilling shows dominantly diorite intercepts between the north-eastern and southern diorite bodies.* ***(d)*** *The revised interpretation of the diorites from the sterilisation drilling and previous aeromagnetic interpretation.*

The host metavolcanic and metasedimentary sequence has also been subjected to extensive metasomatic alteration over a protracted time frame. The generations of alteration can be broadly grouped into four main categories (*from* Mark *et al.*, 2000, 2006):

Stage 1 - Regional Na-Ca alteration – mainly as albitic plagioclase with magnetite-, clinopyroxene- and amphibole rich veining. These assemblages are thought to have formed ca.

400-500 ºC (Mark *et al*, 2000) and are identical to regional Na-Ca alteration suites described by Oliver (1995), de Jong and Williams (1995), Mark and Foster (2000), Oliver *et al.* (2004).

Stage 2 - Early mineralisation-related alteration – mainly as multiple phases of K-feldspar-, biotite-, amphibole-, magnetite-, garnet-, carbonate- and minor sulphide bearing veins and fault related breccia. Homogenisation temperatures suggest formation temperatures of 400-550 °C (Blake *et al.* 1997; Mark *et al.*, 2000; Mark *et al.*, 2006).

Stage 3 - Cu-Au mineralisation – hydrothermal breccia with a matrix of magnetite, calcite, pyrite, biotite, chalcopyrite, K-feldspar, titanite and quartz. Accessory minerals include garnet, barite, molybdenite, fluorite, amphibole, apatite, monazite, arsenopyrite, galena, cobaltite, sphalerite, scheelite, uraninite and tourmaline (Mark *et al.*, 2000). The waning stages of mineralisation are characterised by a network of veins that cut earlier infill-supported ore breccias. These veins contain the same mineralogy as the breccias implying a close relationship to the earlier mineralisation.

Stage 4 - Post mineralisation alteration – Characterised by late carbonate veining and replacement. The carbonate (mainly calcite and dolomite) is accompanied by quartz, biotite, actinolite, pyrite, magnetite and minor garnet and chalcopyrite (Mark *et al.*, 2000). Some researchers have proposed that at least part of the carbonate is primary, in the form of intensely brecciated and altered marble, colloquially known as 'marble matrix breccia' (Marshall *et al.*, 2006).

U-Pb_{rutile} age determination on Cu-Au mineralisation returned an age of 1538±37 Ma (Gunton, 1999). More recent U–$Pb_{titanite}$ age determination (Mark *et al.*, 2006) indicates early Stage 2 Na–Ca alteration occurred at 1529 +11/-8 Ma. Stage 3 biotite-magnetite alteration returned a U-$Pb_{titanite}$ date of 1514±24 Ma (Mark *et al.*, 2006). The three U-Pb dates are consistent within error. These dates also overlap with the emplacement age of some phases of the Williams and Naraku Batholiths (Pollard and McNaughton, 1997; Page and Sun, 1998; Davis *et al.*, 2001) including the nearest exposed granite, the Mount Margaret Granite (ca 1530 Ma; Page and Sun, 1998), ~15 km NE of Ernest Henry. Granite-related fluids have been inferred to be important for Na-Ca alteration (Oliver *et al.*, 2004) and IOCG mineralisation (Perring et al, 2000; Pollard, 2001; Williams *et al.*, 2005). Ar^{40}/Ar^{39} dates of

alteration biotite, associated with mineralisation, from the Ernest Henry Cu-Au yields ages of 1515±15 Ma (Perkins and Wyborn, 1998).

Table 6.1 (from Mark et al., 2006) The paragenetic sequence and spatial distribution of pre and syn-ore hydrothermal alteration in the Ernest Henry lease. The width of the individual lines reflects the relative abundance of each mineral during a particular stage. Black fill denotes relatively Na-rich pre-ore mineral assemblages and grey fill highlights K-rich mineral assemblages deposited prior to ore-related K-feldspar alteration (Mark et al., 2006).

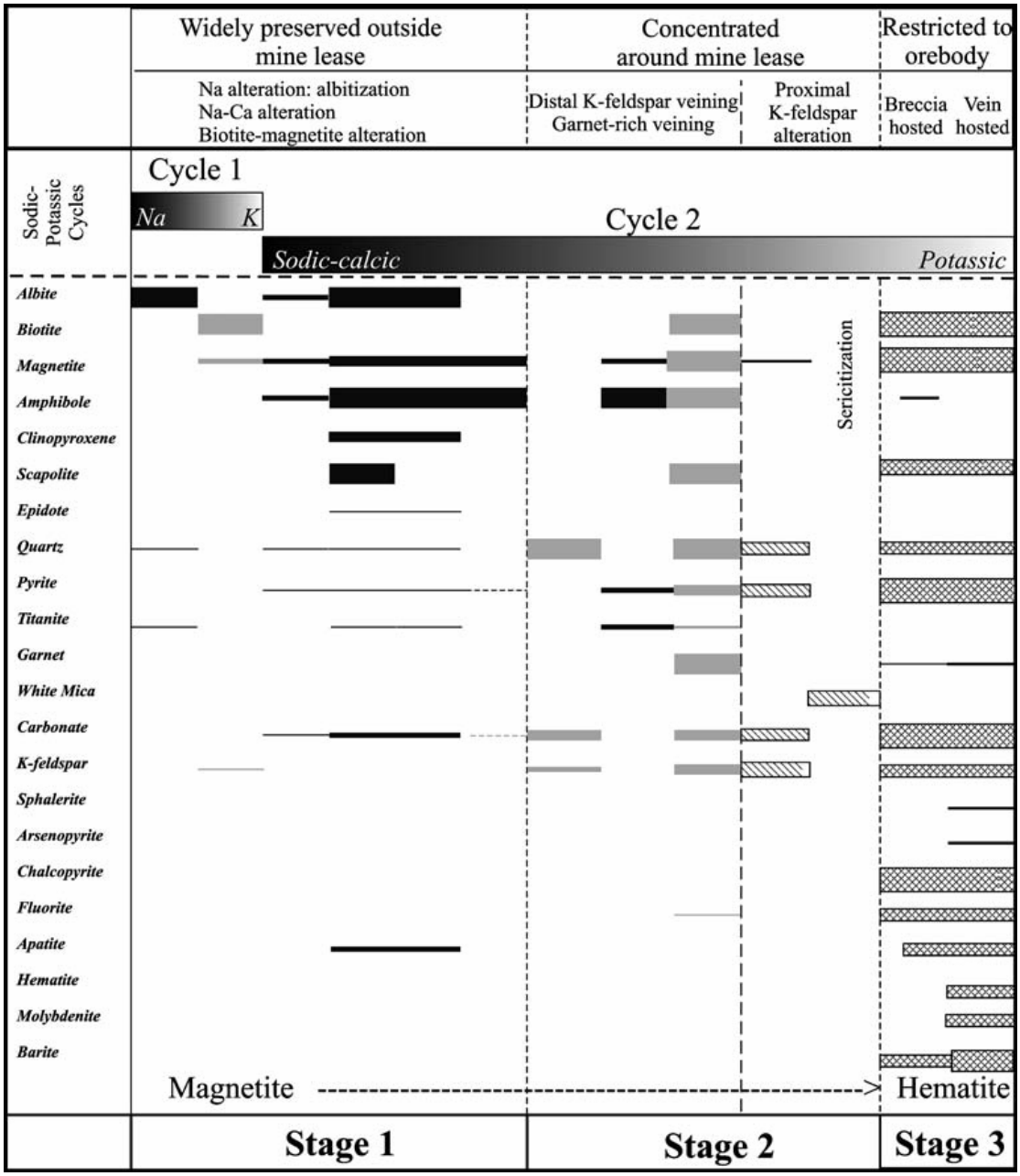

The bulk of the Ernest Henry ore zone occurs in the matrix of a pipe-like breccia body that plunges ~45º SSE. The pipe has a subtle change of orientation at depth to a S plunge (Figure 6.3).

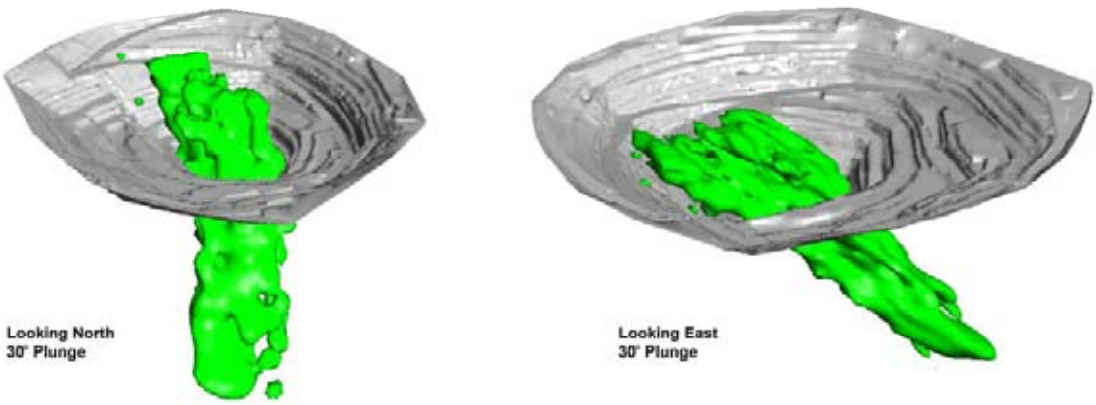

Figure 6.3 Leapfrog 3D model outputs of the 1% copper grade shell (green) within the Ernest Henry Mine (pit as at November 30, 2005). The subtle change in plunge direction of the orebody, from SSE plunging (shallow) to S plunging (at depth) is most obvious in the view looking north.

The pipe is bound on the top and bottom by the Footwall (FWSZ) and Hangingwall Shear Zone (HWSZ), which appear to run parallel to the breccia pipe along the extent of drilling. The FWSZ and HWSZ are distinguished as heterogeneous zones of higher strain and foliation development within a variably, but weakly foliated sequence of metavolcanics (Coward, 2000). Both shear zones change orientation around the ore breccia from a ENE strike west of the ore zone, to a NNE orientation east of the ore zone (Figure 6.4).

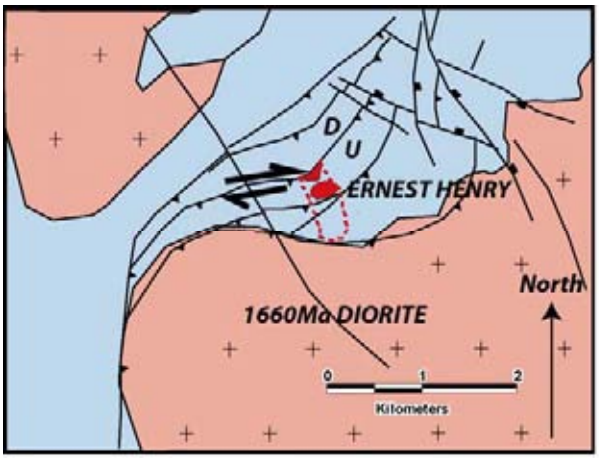

Figure 6.4 (adapted from Valenta, 2000) Schematic diagram showing the orebody position relative to the interpreted shear zones. The Ernest Henry Mine is located at an inflection point on one of the inferred shears, where the shear zone orientation changes from an E-W orientation to a broadly NE-SW orientation .The pink bodies represent the 1660 Ma diorites and the pale blue is an intercalated volcanic and metasedimentary sequence (as per Figure 6.2b).

Coward (2000) proposed a genetic model for the formation of the FWSZ and HWSZ at the time of regional D_2 (Figure 6.5). The model revolved around the refraction of a shear zone around two competent diorite bodies during E-W to ENE-WSW shortening. The pervasive fabric within the metavolcanics which parallels the shear zone is widely recognised as an S_2 fabric further validating the syn-D_2 timing of the Coward (2000) shear zone genetic model.

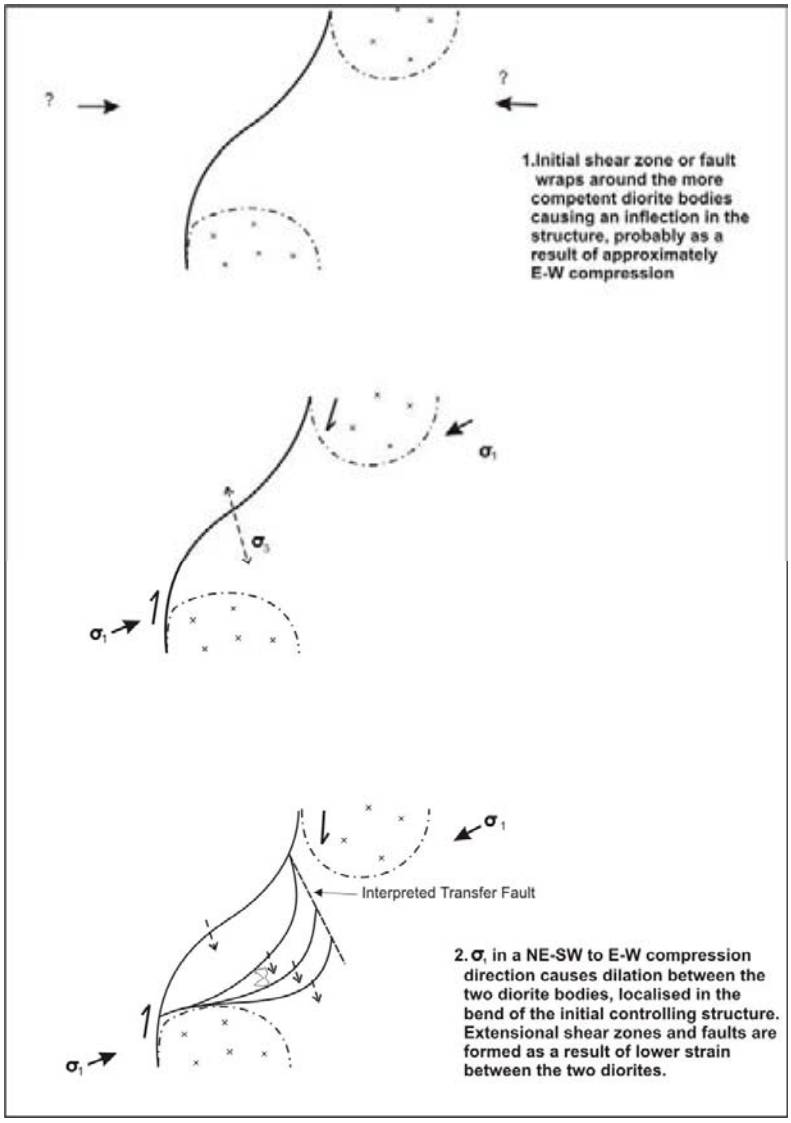

Figure 6.5 (from Coward, 2000) Schematic representation of a possible model for the formation of the duplex of shear zones interpreted from the aeromagnetic image. Note, it is likely that the two discrete diorites shown here are continuous along the eastern side (see Figure 6.2d).

Two main brittle faults run parallel to the FWSZ and HWSZ; they are Fault 2 and Fault 4 (Figure 6.6). Fault 2 divides the high grade mineralisation (i.e. >1.5% Cu) within the mineralised breccia pipe, into an upper lens and a lower lens. Fault 2 dips between 35º and 50º to the south and is often expressed as a ~30 m wide zone of numerous shear planes, with smaller zones of cataclasite

and fault gouge (Coward, 2000). Fault 2 shows signs of reactivation, containing sheared carbonate cementing and overprinting slickenside sets (Coward, 2000; Laing, 2003). Fault 4 is of similar orientation, contains similar fault fills and expressions, but is located on the orebody side of the Hangingwall Shear Zone.

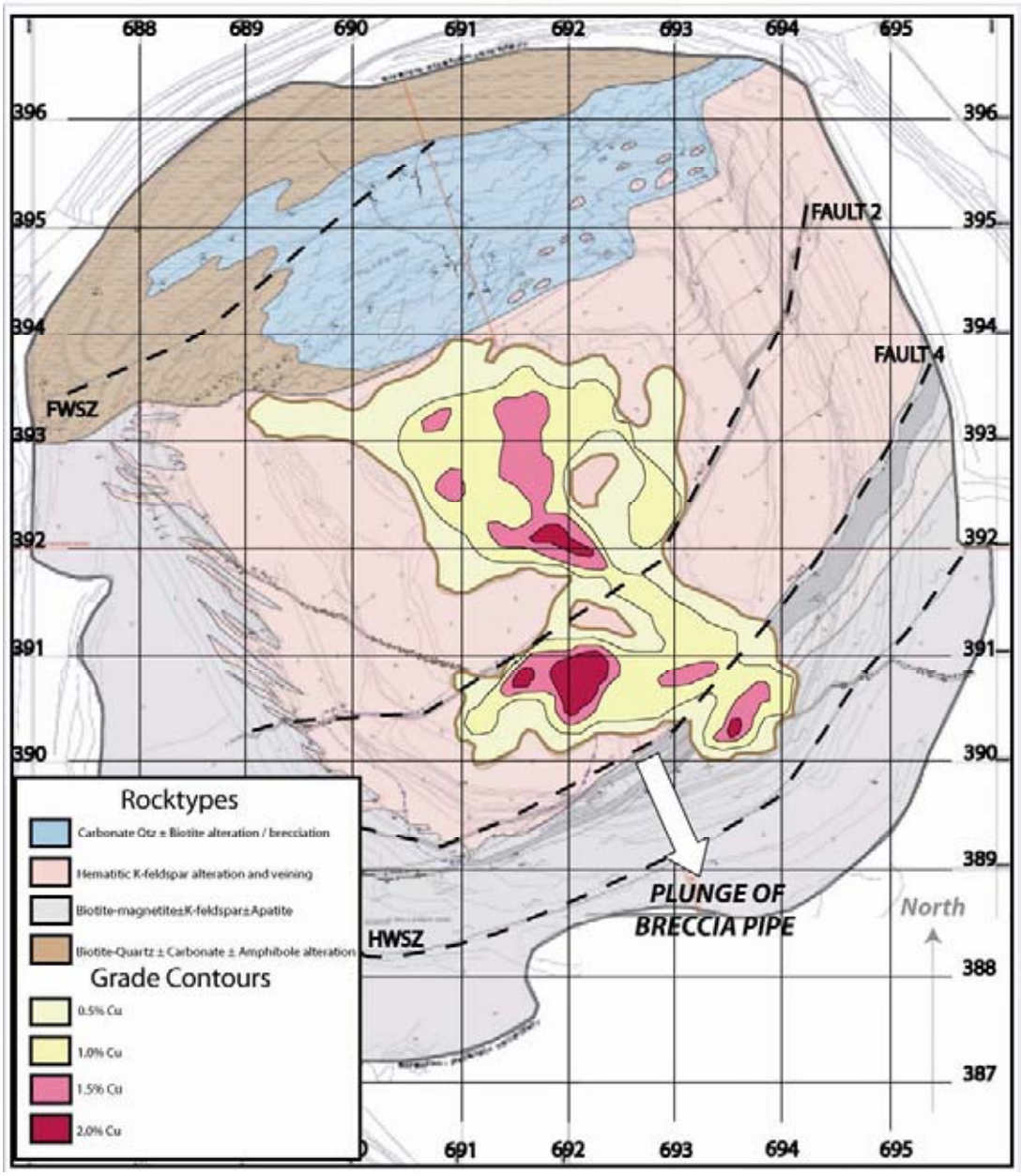

Figure 6.6 (adapted from Coward, 2000) Ernest Henry pit map showing the locations of the major faults and shears in relation to the ore zone and alteration suite.

Table 6.2 (modified from Laing, 2003) Characterisation of Ernest Henry brittle and ductile faults.

FAULT SETS - ORIENTATION					
EVENT	FAULT	DIP IN PIT*	LINEATION	DISPLACEMENT VECTOR	DISPLACEMENT SENSE & MAGNITUDE
3	F1 & F1FZ	40 to 055	None seen	Not known	Strike-slip=small, dextral? (offsets F2, 2014 bench E wall); mainly dipslip? reverse (TFA)
2b	F4	45 to 130	Khaki chlorite fibres	Inferred 45 to 130	Dipslip; sense uncertain; truncate orebody
2a ORE EVENT	F2/HWSZ reactivated	50 to 135	Biotite-chlor lineation	50 to 135	Reverse in ore event (TVA); normal later (s-c planes; Coward?); control ore shape
1 EARLY DUCTILE	FWSZ	45 to 155	Biotite-chlor lineation	45 to 155	Dipslip - sense unknown (biotite/chlorite lineation)
1 EARLY DUCTILE	HWSZ	50 to 140	Biotite-chlor lineation	50 to 140	Dipslip - sense unknown (biotite/chlorite lineation)

* Structures change orientation downdip in the orebody, generally steepening

The ore breccia is dominated by milled, rounded and locally chemically corroded clasts of altered metavolcanic rocks, cemented by a matrix dominated by the ore minerals. It has the characteristics of a fluidised breccia in which clasts were physically transported (Oliver *et al.*, 2006; Oliver *et al.*, 2007).

Conflicting theories on the nature and genesis of the Ernest Henry ore breccia exist. Laing (2003) proposed the ore breccia is a purely tectonic breccia dominated by replacement, localised at the intersection of faults striking 050º and 110º. Oliver *et al* (2006) however propose that the dominant mechanism for brecciation was not primarily tectonic, but was caused by overpressured magmatic-hydrothermal fluids being driven off the crystallising magmatic bodies of the Williams and Naraku Batholiths.

Discordant breccia dykes and pipes are seen in several localities in the Cloncurry district (Oliver *et al.*, 2006). These breccias have a similar mineralogy to the Stage 1 alteration of the Ernest Henry deposit, and commonly contain an assemblage of albite + magnetite + quartz + titanite + apatite + calcite + actinolite (Oliver *et al.*, 2006). The breccia pipes are seen to extend upwards and outwards from the contact aureoles of the 1530 Ma Williams Batholith. They are inferred to be explosive rather than implosive breccias, such that pressure within the pipe was sufficient to restrict inward spalling of fragments from pipe walls (Oliver *et al.*, 2006). The textural and mineralogical relationship of the regional breccias to the Stage 1 alteration of the Ernest Henry deposit, suggests the breccias may have been sources of fluids or mechanical energy for ore genesis. Alternatively these breccias may provide permeable pathways for later ore fluids (Oliver *et al.*, 2006).

6.3 Syn-Cu Structural Kinematics

The Ernest Henry Mine has been the focus of three main structural studies (Valenta, 2000; Coward, 2000; Laing, 2003). All three studies had conflicting views on the syn-mineralisation kinematics. Each author however reached a general consensus on the timing of mineralisation as being syn- to late-regional D_3. Each structural hypothesis and its supporting evidence is summarised.

6.3.1 Valenta (2000) Structural Hypothesis

Valenta (2000) utilised the aeromagnetic data to compile a sub-regional interpretation of the major magnetite-bearing faults. From observations of foliations, lineations and veins in drill core, coupled with the regional fault interpretation, Valenta suggested that the syn-mineralisation structures were the SE-dipping shear zones with a SE-plunging downdip lineation and associated subhorizontal “birdswing” veins.

East – west shortening associated with the D_2 regional peak metamorphic event caused the shear zones to bend around the pre-existing diorite bodies.

During the mineralising event, the bend hosting the orebody marks an easterly transition from oblique dextral to pure reverse shear, and the mineralization formed associated with sub-horizontal dilational structures in the zone of pure reverse displacement (Figure. 6.7). The orebody is therefore hosted in a compressional bend in plan view.

Valenta (2000) doesn’t discount the chance that there may have been a contribution of vertical dilation association with a flattening of dip in the shear zone as well. Valenta reports some of the orebody block models show a slight steepening in plunge as depth increases, but that this increase in dip does not appear to terminate the down-dip extent of the orebody.

It is also noteworthy that both pre-mineralization (Isan orogeny) structures and post-mineralization structures are consistent with EW shortening, while syn-mineralization structures are associated with apparent NW-SE shortening. Valenta (2000) speculates that there is a rotation in the stress field synchronous with the main intrusive event and mineralisation.

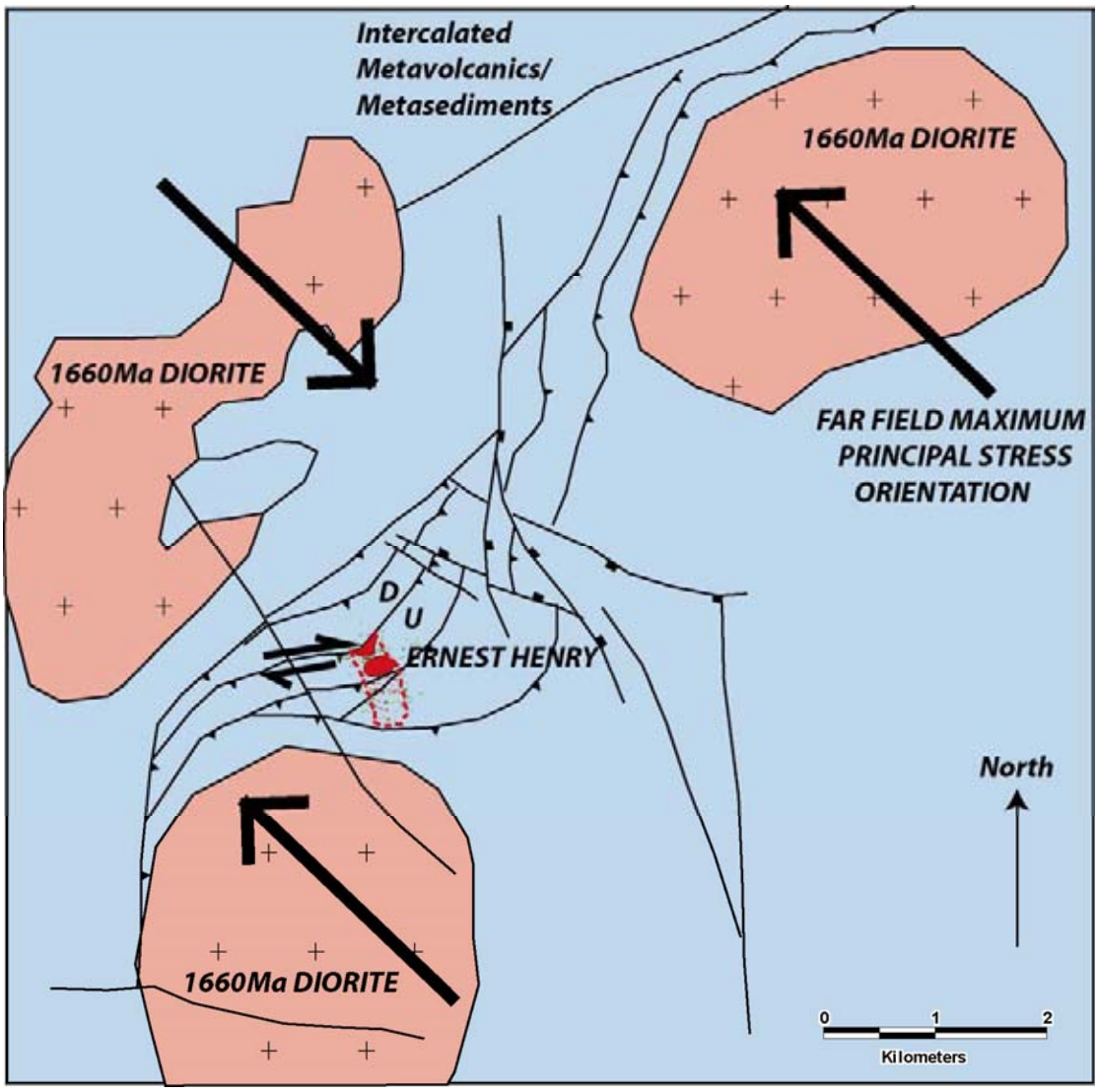

Figure 6.7. (adapted from Valenta, 2000) Syn-mineralisation kinematic model proposed by Valenta. SE-NW shortening results in reverse movement on the northern side of the SZ bend near the deposit, whereas west of the deposit the SZ goes into oblique dextral slip. This results in a dilatant zone at the inflection point of the SZ. Note however the diorite distribution is probably oversimplified, with the drilling results suggesting a semi-continuous body along the eastern flank (Figure 6.2d).

6.3.2 Coward (2000) Structural Hypothesis

Coward (2000) demonstrated that the local S_2 fabric was overprinted and destroyed in part by hematitic K-feldspar alteration related to the main mineralising event. This suggested that the timing of the shear zones was before mineralisation. Coward also mapped an early stretching lineation on the shear zones. The stretching lineation was consistent with a south-plunging antiform in the S_2 fabric, implying the shear zone flexure (in the Ernest Henry deposit location) formed syn-shear zone development (syn-D_2).

A D_3 ductile precursor to mineralisation is seen in the form of a NNW striking, steeply west dipping S_3 cleavage. The S_3 cleavage was recognised in the HWSZ as fine seams of medium-grained biotite and magnetite. Although not observed in field mapping in the FWSZ, the S_3 cleavage was seen in thin section in the form of fine-grained biotite seams.

Coward (2000) identified a series of faults near the FWSZ that were cemented by K-feldspar, carbonate and specular hematite. Veins of similar mineralogy were associated with this faulting. The Footwall Faults varied in strike from 330º to 040º but those faults with associated veining commonly strike NNW (330º-350º). Shallow slickenlines on these faults suggest that the last phase of movement on these faults was oblique strike-slip (Coward, 2000). Steeply dipping extension veins emanating from the Footwall Faults are also indicative of dominantly strike-slip movement. The Stage 3 assemblage veins have a strike and dip of 012/58º NW. From the fault and vein data Coward inferred a σ_1 orientation of NNE-SSW during mineralisation. (Figure 6.8).

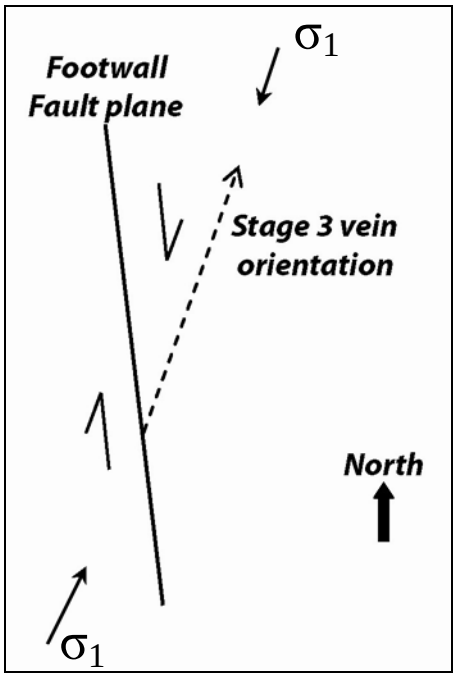

Figure 6.8. (from Coward, 2000) Representation of fault and vein trends in plane view showing the orientation of the principle maximum stress direction (σ_1) inferred from the extensional vein geometry.

6.3.3 Laing (2003) Structural Hypothesis

Laing (2003) bases his hypotheses primarily on ore distributions on bench grade control data. He argues that at orebody scale chalcopyrite, gold, pyrite and magnetite show strong spatial controls, bound both internally and externally by sides trending 050º and 110º (Figure 6.5). The 050º sides parallel the F2 fault/shear set, but the 110º oriented side does not parallel any known orientation of faulting. "*The strength of this orebody pattern suggests a dual fault control, and the overall architecture is strongly reminiscent of an intersection pipe*" (Laing, 2003). In addition to the 050º and 110º structures delineated from bench plan interpretation, Laing argues for a "Central Structure" oriented 350º which passes through the centre of the orebody and is the fundamental feeder structure. This feeder structure is based on the sub-regional aeromagnetics interpretation, in which N-S pattern breaks are magnetite-depositing metasomatic feeders (Laing, 2003). In order to create these N-S to NNW-SSE metasomatic feeders, either tension fractures or transfer faults, Laing (2003) proposes a σ_1 orientation during mineralisation of approximately N-S.

Laing (2003) argues that the breccia pipe was formed in a single event which occupied the dilatant core of an interpreted fault intersection zone. The breccia is single stage, was not reworked, and remained a coherent breccia pipe with spatially consistent mineral zoning (Figure 6.9) and a simple orebody shape which persists downplunge. The metasomatic (mineral) zoning is consistent around the pipe and comprises a simple increasing sulphide, increasing Cu:Fe, more reducing gradient inward to the dilatant core. Replacement was inferred to be the principal depositional mechanism, but was largely confined to the stockwork around the fault intersection.

6.4 Leapfrog modelling

The inferences made from a stacked set of 2D images by Laing (2003), highlighted the need to determine the spatial relationships of mineralisation and alteration mineralogy in three dimensions.

Other than testing the Laing (2003) mineral zonation hypothesis, the orebody 3D modelling set out to determine the relationships between modelled breccia, fault and mineral distributions with the intention of determining potential fluid pathways within the Ernest Henry system. It was thought that the relationships of mineral assemblages and 3D modelled structure may provide insights into which faults were active at the different stages of mineral deposition, with a view to furthering a structural model in areas drilled away from the main breccia pipe.

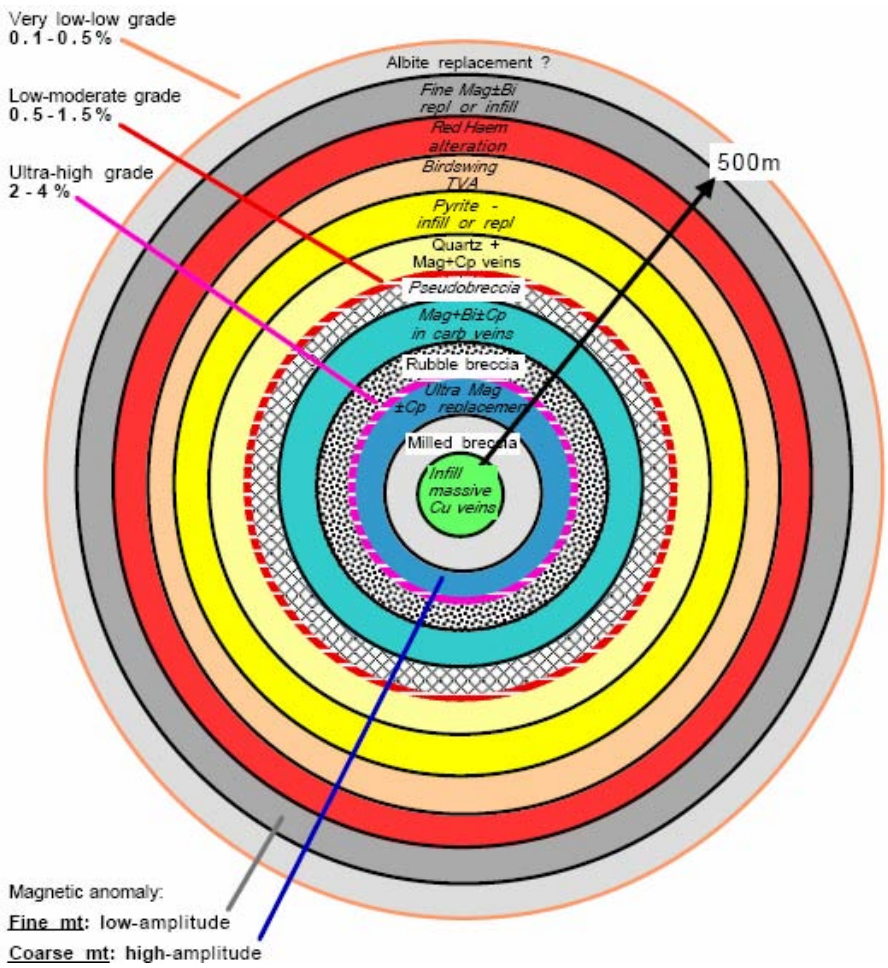

Figure 6.9 (from Laing, 2003) Inferred mineral zonation pattern in a proposed single fault intersection breccia - replacement model. The centre of the breccia pipe should therefore contain the highest copper values (2-4%), a magnetite – pyrite rim (0.5-1.5%) to the high grade mineralisation.

6.4.1 Leapfrog 3D model assumptions and techniques

Two assay databases were made available for analysis within the Ernest Henry mine; the resource drilling database and the bench grade control database. The resource drilling database was preferred as it contained assay data beyond 1 km depth (bench grade control data only to ~200 m depth). The resource drilling database was coded and modelled using Leapfrog 3D for a range of elements including Cu, Au, Ag, Mo, U, Fe, S, As, Co, Mn and Ni. Two distinct sets of three dimensional orebody models were created:

- Modelling of element abundances, to determine relationships between individual elements.
- Modelling of mineral abundances, calculated from the resource drilling assay results stoichiometrically, using assumptions based on the dominant mineralogy of the deposit.

Mineral assemblage maps were created for Ernest Henry prior to this study (Gow, 2004), however a large drilling campaign has since been conducted, adding to the geochemical database.

All assayed copper was treated as chalcopyrite ($CuFeS_2$) and hence the equivalent amount of iron and twice the sulphur was consumed in creating the mineral chalcopyrite.

The other dominant sulphide in the deposit is pyrite. Therefore when all the assayed copper was accounted for (chalcopyrite), the remaining sulphur was consumed in creating pyrite (FeS_2). This required using the remainder of the sulphur in assay, and consuming half the sulphur value of iron. The local development of minor barite is ignored.

Iron is required to create both magnetite (Fe_3O_4) and hematite (Fe_2O_3). As magnetite is the dominant iron oxide and both minerals have similar weight percentages of iron, the remaining iron (after chalcopyrite and pyrite were calculated) was used to create magnetite only. Iron in minor biotite, garnet and amphibole was also ignored.

Another limitation associated with the mineralogical assumptions is the presence of a large amount of barite ($BaSO_4$) within the orebody, which would account for some of the sulphur. Barium has not been routinely assayed for and therefore cannot be factored into the stoichiometric calculations. Although these assumptions on the element partitioning into different minerals are not exact, the resultant shells provide a reasonable approximation of mineral distribution for broad scale analysis.

6.4.2 Leapfrog 3D model outputs

Three dimensional modelling of the raw assay data showed certain elements that preferentially co-exist with copper at Ernest Henry, and certain elements that are not found with copper. The minerals which do not co-exist closely with copper at Ernest Henry are manganese, nickel and arsenic. The elevated nickel and manganese assays outside the ore zone can be attributed to lithological and alteration changes outside the breccia pipe. The elevated manganese in the footwall of the breccia pipe (Figure 6.10) appears to be associated with biotite-calcite-actinolite rocks. The elevated nickel in the hangingwall of the Ernest Henry deposit (Figure 6.10) is associated with andesites and biotite-rich schists.

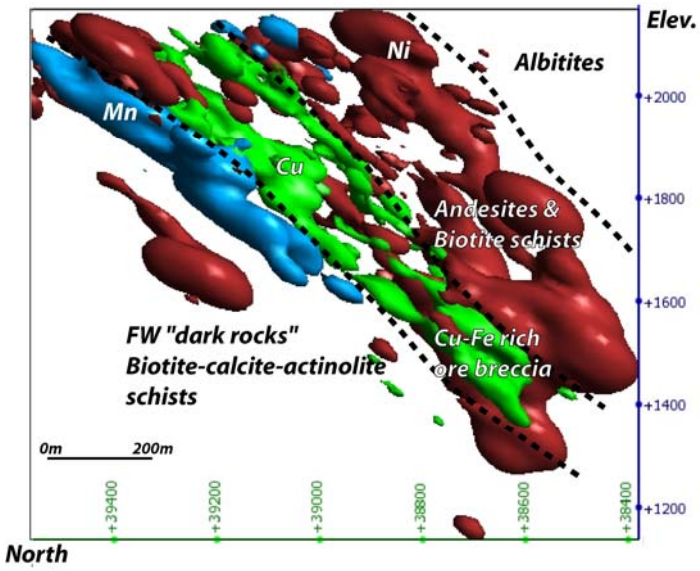

Figure 6.10 Two of the elements seen to be unrelated to the copper (Cu) spatially are nickel (Ni) and manganese (Mn). Ni-rich andesites and biotite schists dominate the hangingwall to the orebody and the high Mn alteration seems to be associated with the biotite-calcite-actinolite schists. Elevated Ni is seen in the footwall of the deposit and maybe related to the intercalated nature of the metavolcanic/metasediment host suite.

Elements such as iron, uranium, gold, cobalt, molybdenum and silver are seen to be spatially related to the copper mineralisation (Figure 6.11).

The change in orientation of the pipe from a SSE plunging body to a S plunging body at depth, has been recognised primarily from the resource copper grade shells. This change has been documented by previous workers (Laing, 2003; Gow, 2004; Cleverley, 2006), however the no change in orientation has been documented for any of the other elements or minerals. When the 3D shells were created, it was noted that all elements that were seen to co-exist with the copper, exhibited the same change in down-plunge orientation (Figure 6.12). As well as the change in orientation, all

elements (including copper) showed a distinct narrowing at the inflection point (Figure 6.12). This was particularly obvious in the higher grade shells of the respective elements.

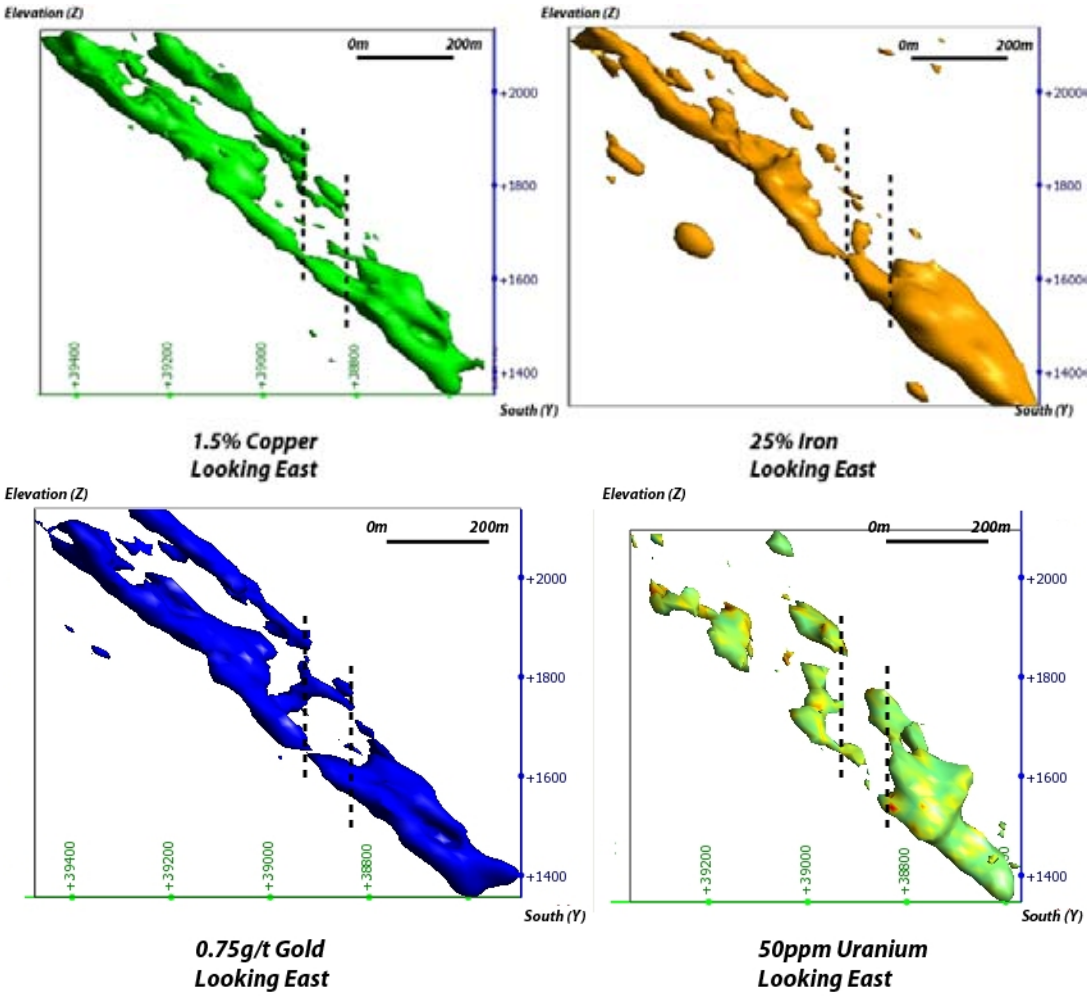

Figure 6.11 Cross-sectional view of the mineralisation associated with the Ernest Henry Mine, looking east. Shells include 1.5% copper, 25% iron, 0.75 g/t gold and 50 ppm uranium. All elements displayed appear to co-exist at these grades. . Each shell displays a zone of depletion at approximately 1550RL and between 38920mE and 38820mE. This zone of depletion may possibly represent a structural break.

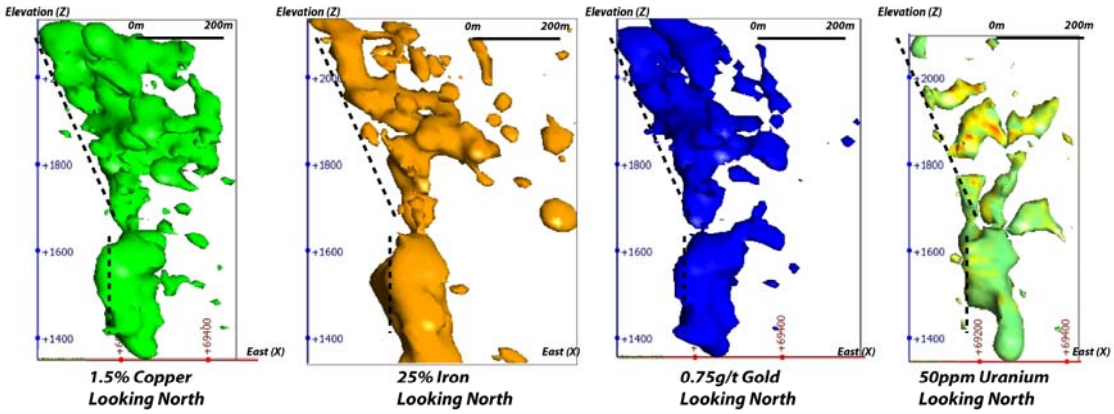

Figure 6.12 Leapfrog 3D outputs of 1.5% copper, 25% iron, 0.75 g/t gold and 50 ppm uranium, looking north. All elements appear to co-exist at these grades, despite all assay shells showing two distinct plunge orientations (dashed black lines). At the change in pipe orientation, all grade shells are seen to pinch out, before thickening out again below the inflection point.

There was little evidence of the flattening of plunge in the shear zone as documented by Valenta (2000). A very slight steepening in plunge was noticed as depth increases, but that increase in plunge was only in the order of 1º to 5º. This slight steepening was not obvious in the high grade copper shells (Figure 6.12), but was more obvious in the low grade shells (Figure 6.13).

The mineral assemblage shells displayed similar spatial characteristics to the element shells. Chalcopyrite shells (Figure 6.13), pyrite shells (Figure 6.14) and Fe-oxide shells (modelled as magnetite) (Figure 6.15) were seen to have a close spatial association at lower grades (Figure 6.16). The zone of depletion associated with the inflection point (Figures 6.11 and 6.12) is obvious in the high grade chalcopyrite (Figure 6.13d, Figure 6.17a & e) and Fe-oxide shells (Figure 6.14d, Figure 6.17c & e). The high grade pyrite shells (Figure 6.15c & d, Figure 6.17a & e) are seen to thicken across this zone. The high grade pyrite shell is also seen to be dominant in the upper of the two orebody lenses, whereas the chalcopyrite and Fe-oxides dominate the lower lens.

High grade shells of chalcopyrite, pyrite and the Fe-oxides are seen to occur as continuous to semi-continuous bodies along the western margin of the orebody. Small occurrences of high grade chalcopyrite, pyrite and Fe-oxide occur through the eastern side of the mine, but are limited to discrete and isolated pods of up to 40 m strike length.

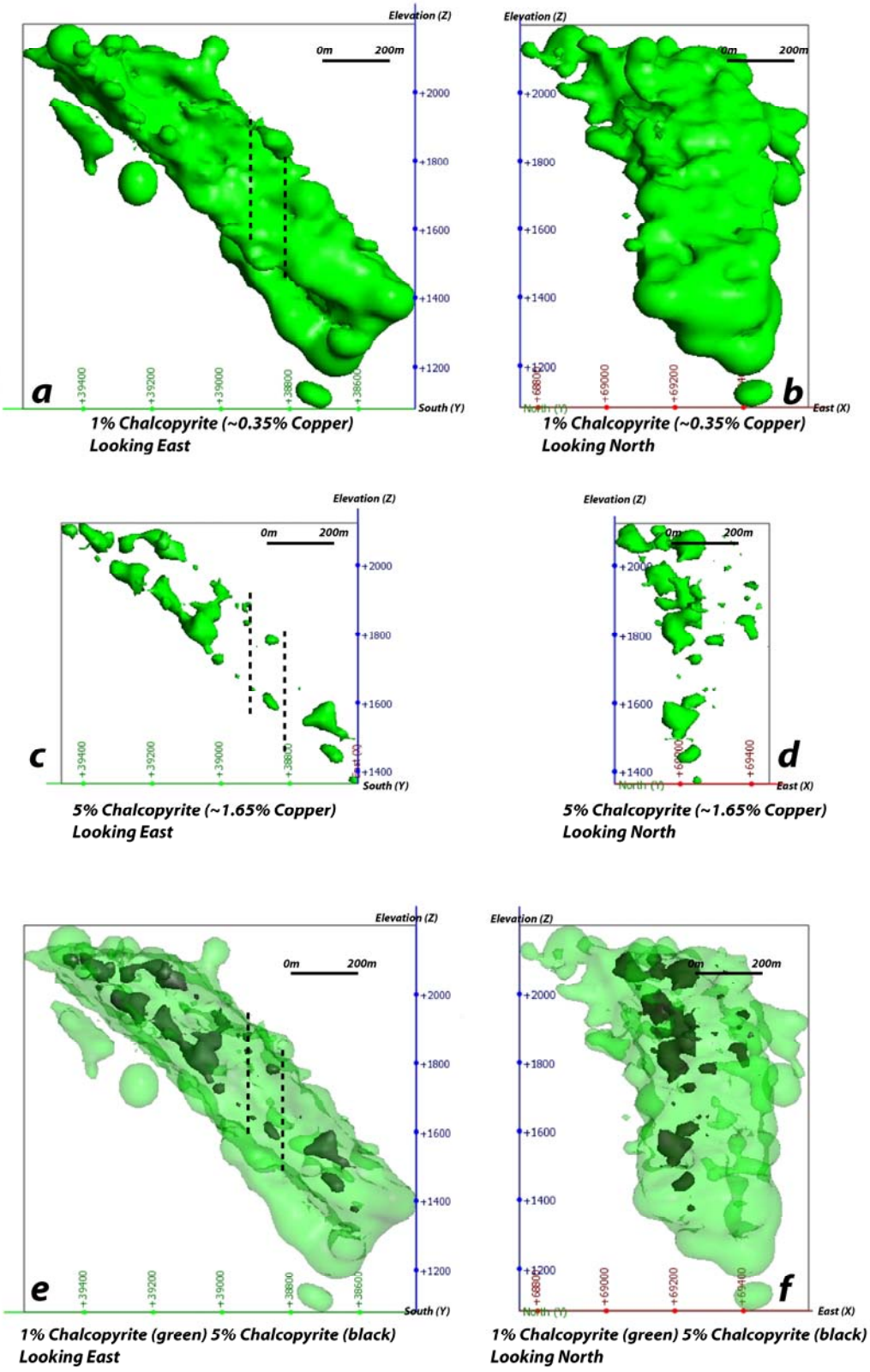

Figure 6.13 Chalcopyrite abundance shells seen looking east (left - a,c,e) and north (right – b,d,f). Two distinct lenses of high grade mineralisation can be seen in (c). The depletion zone (as observed in Figure 6.12), is again witnessed in (c) and (d). The depletion zone is associated with the inflection point and is evident in the 5% chalcopyrite shells (c & d). High grade mineralisation generally occurs near to the footwall of the deposit (e) and on the western margin of the breccia pipe (f).

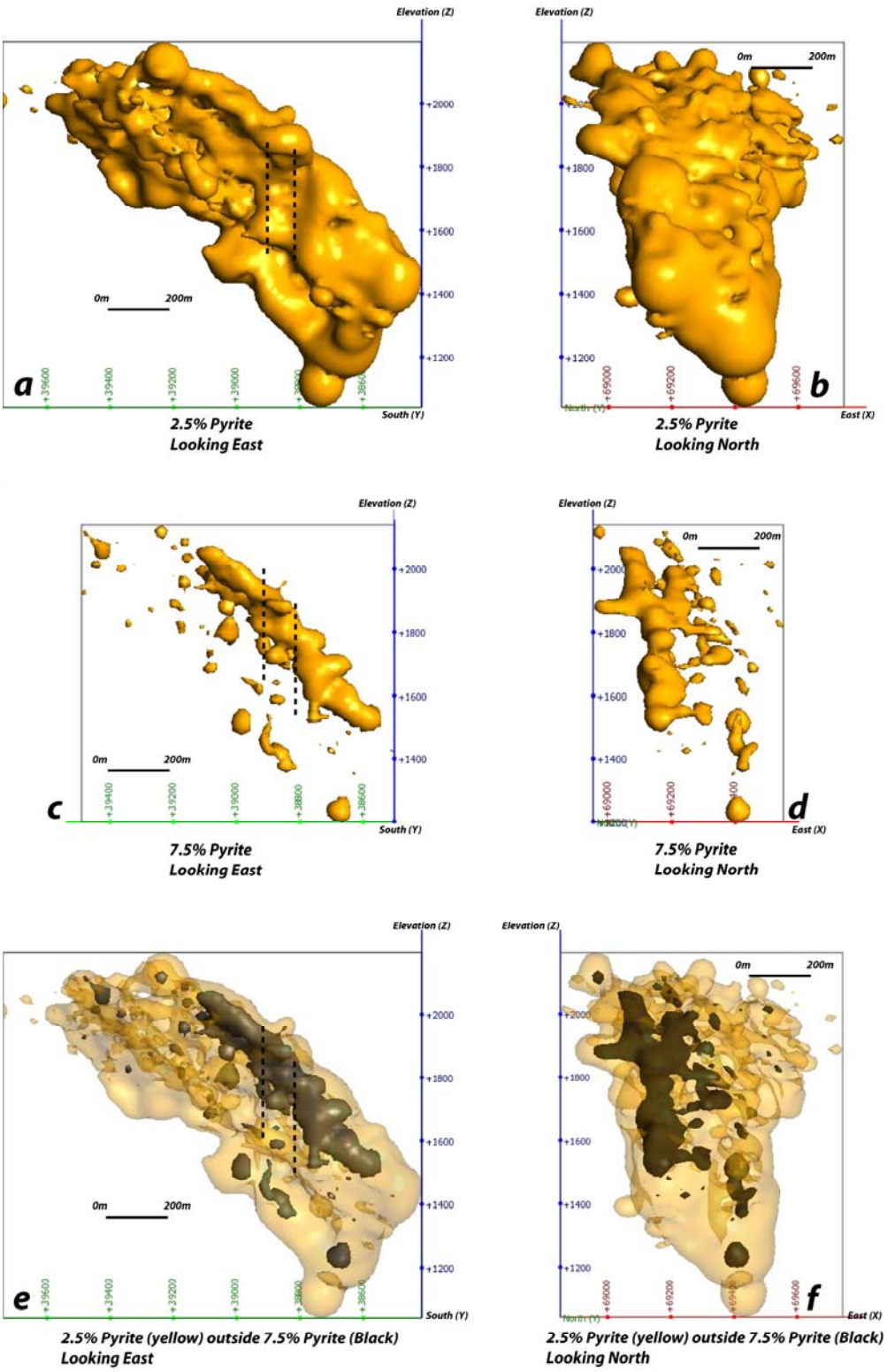

Figure 6.14 Pyrite abundance shells seen looking east (left - a,c,e) and north (right – b,d,f). Two distinct lenses of high grade pyrite can be seen in (c). The depleted zone (as observed in Figure 6.12 and Figure 6.13), is not evident in the high grade pyrite shells (c) and (d). Pyrite shells are actually seen to thicken across this zone (c) and (d). Unlike the chalcopyrite shells (Figure 6.13) high grade pyrite generally occurs toward the hangingwall of the ore breccia (e). The high grade pyrite is also found on the western margin of the breccia pipe (f).

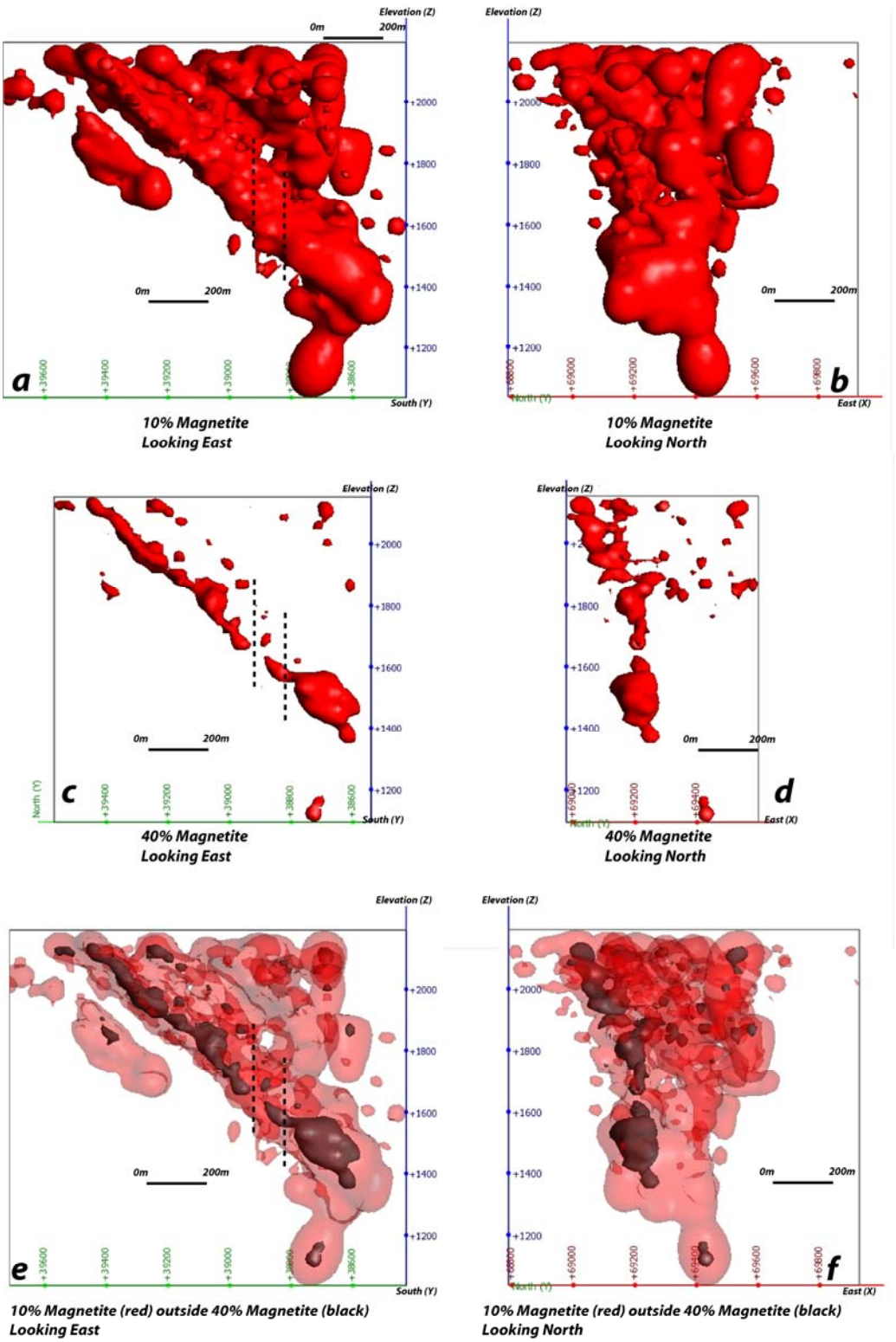

Figure 6.15 Magnetite abundance shells seen looking east (left - a,c,e) and north (right – b,d,f). A distinct lower lens of high grade mineralisation is in contrast to a poorly developed upper lens of high grade (c). The depletion zone associated with the inflection point (as observed in Figure 6.12), is again witnessed in (c) and (d). High grade mineralisation generally occurs near to the footwall of the deposit (e) and on the western margin of the breccia pipe (f).

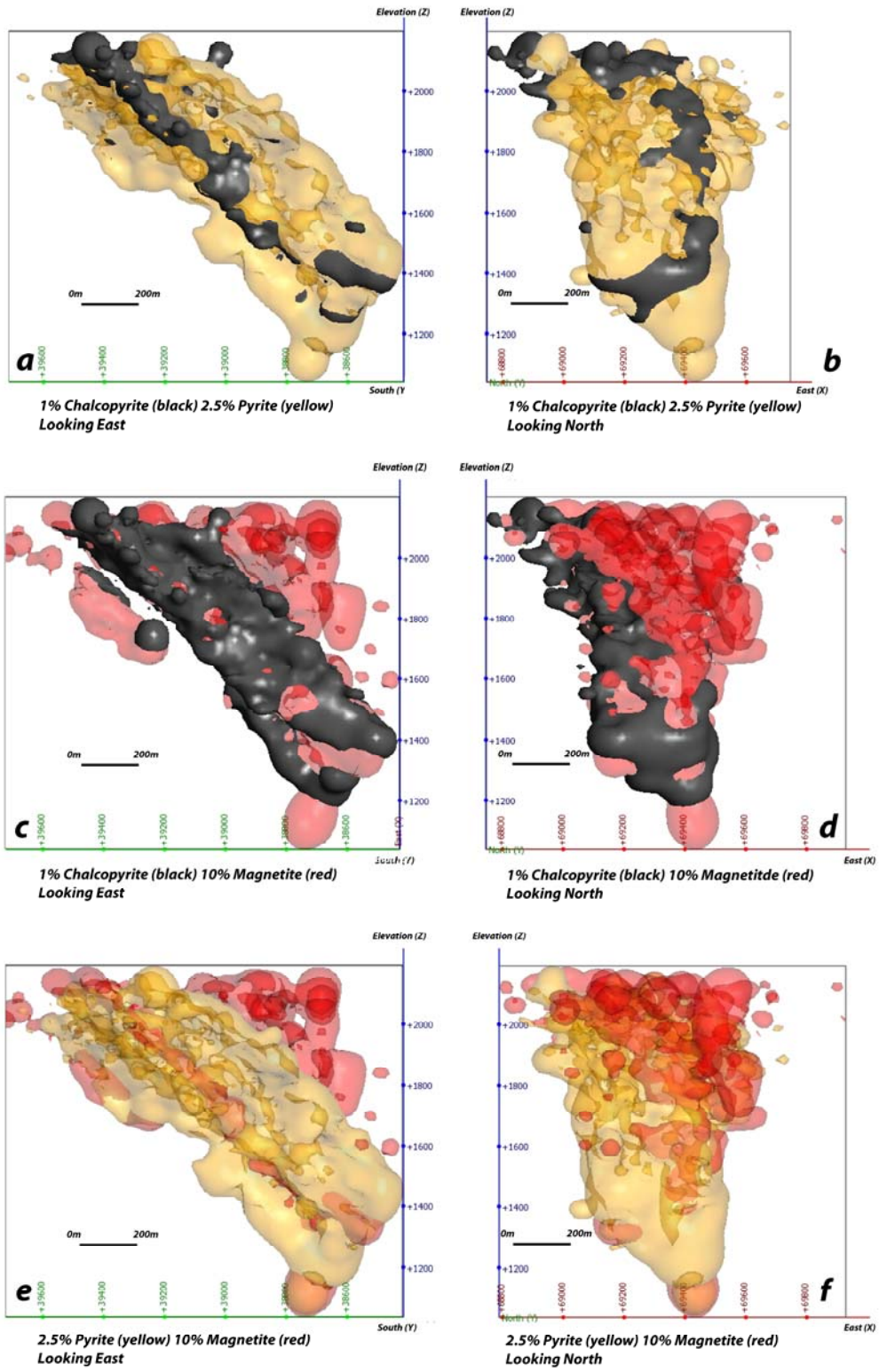

Figure 6.16 3D model outputs displaying the relationship between the low abundance shells of chalcopyrite (1%), pyrite (2.5%) and magnetite (10%). At low grades the shells are spatially relatively similar. The chalcopyrite contains a slightly larger pyrite halo (a & b), which in turn is surrounded by a magnetite (e & f). 10% magnetite also extends off into the upper hangingwall (f).

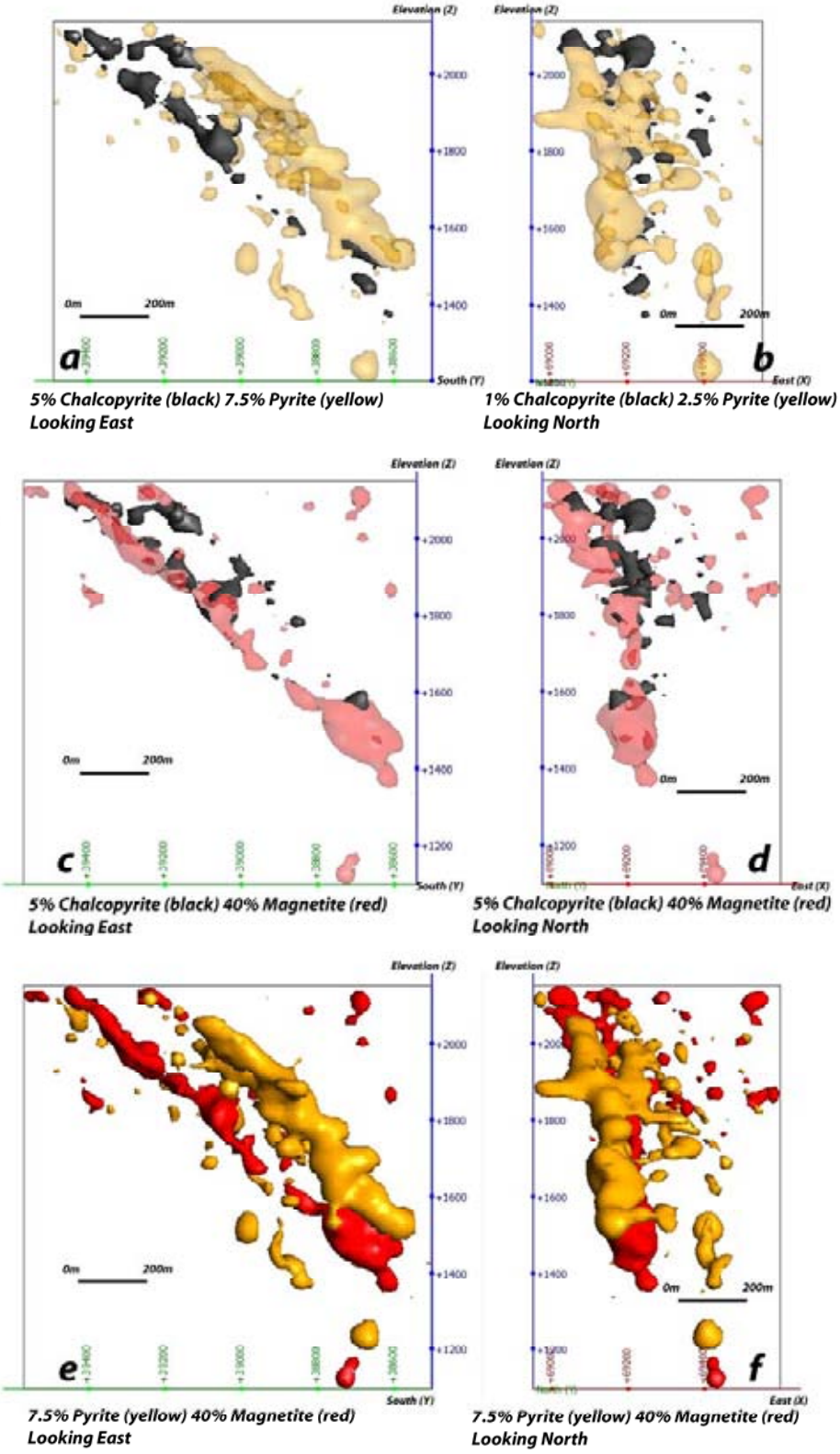

Figure 6.17 3D model outputs displaying the relationship between the high abundance shells of chalcopyrite (1%), pyrite (2.5%) and magnetite (40%). At high grades the chalcopyrite and magnetite shells dominate the lower lens of the orebody (a, c & e), whereas the high grade pyrite is seen to occur more prevalently in the upper lens (a & e). All high grade shells are located in the west of the breccia pipe (b, d & f).

Above the lower lens depletion zone associated with the orebody inflection point, some Fe-oxide grade shells, high pyrite shells and copper shells appear to be truncated or to terminate. Two possible explanations for the terminations or truncations of mineralisation shells, (i) the shells are offset by a fault or (ii) there has been an introduction of orebody fluids to a new area through an unrecognised feeder fault. Any proposed fault would be well below the current pit floor and would have only been observed in diamond drill core. An example of a potential through going fault is seen in Figure 6.18.

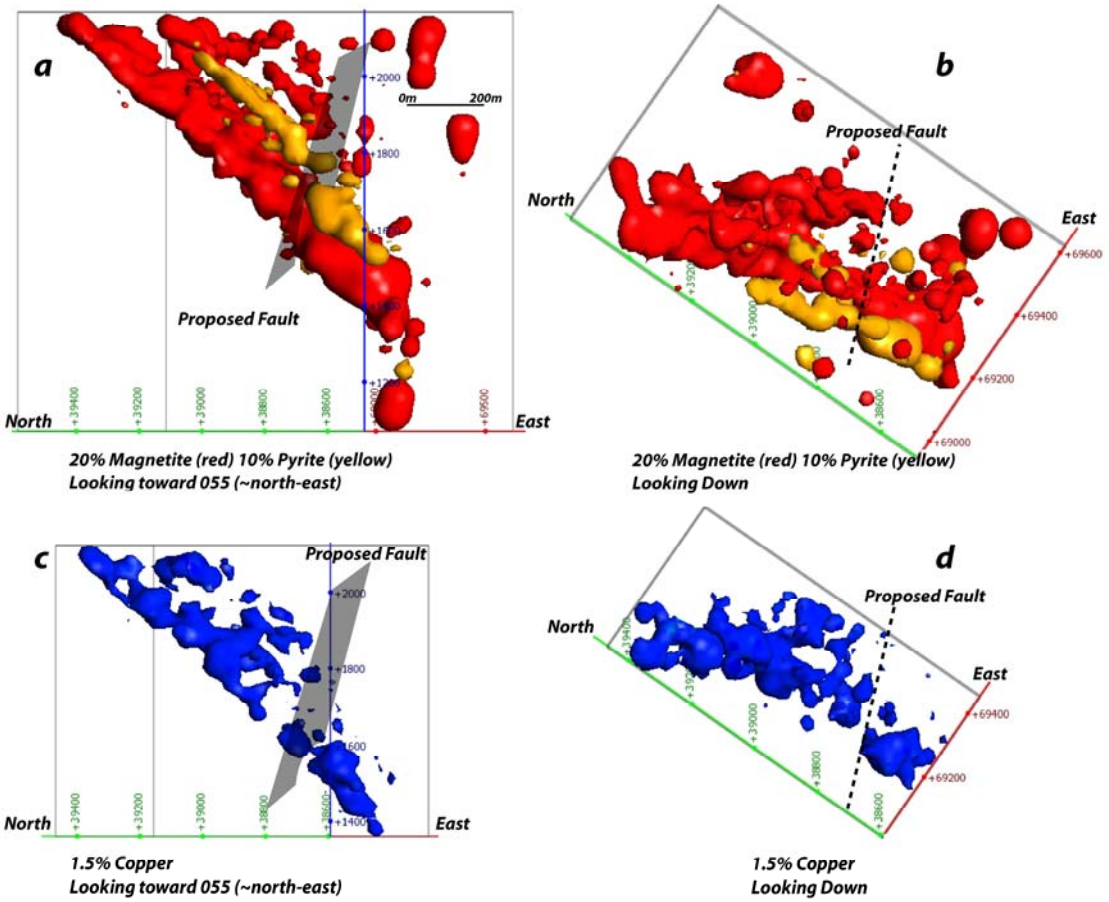

Figure 6.18 One proposed fault orientation based on the truncation of 20% magnetite shells and 10% pyrite shells in (a) and (b) and in the ore depletion zone in 1.5% copper grade shells in (c) and (d).

From the 3D element and mineral shells created, it is apparent there is an asymmetric lateral zonation to the orebody. Marshall *et al.* (2005) determined that the copper percentages at Ernest Henry showed a strong positive correlation with breccia intensity.

The western margin of the orebody is seen to contain the highest copper, iron, gold, uranium and molybdenum assay values, as well as having abundant pyrite and Fe-oxides. At higher grades, these abundances rapidly decrease to the east, however the minerals are still present in significant

quantities at lower grades. This may indicate a fluid path vector from west to east, or be indicative of less intensive breccia development to the east.

6.5 Numerical modelling – Conceptual Model

The UDEC modelling set out to determine the effects of stress partitioning around the 1660 Ma diorites during the late stages of the Isan orogeny. The modelling was not intended to provide a definitive σ_1 orientation at mineralisation, as all previous authors agree that a significant amount of dip slip movement has occurred on the FWSZ and HWSZ during D_2 and D_3. Of all of the deposits modelled to date in this study, Ernest Henry has the most apparent 3-dimensional shape variability. The 2D modelling is thus only considering the extent to which a horizontal shortening component influenced the structural evolution.

The 8.8 km x 7 km model geometry was created from the aeromagnetic and sterilization drilling interpretation of the 1660 Ma diorite bodies and shear zones. The effects of the orientation of the maximum principal stress were tested at 22.5º intervals. The values of imposed stresses was set at σ_1=200 MPa, σ_2=175 MPa, σ_3= 150 MPa. The vertical stress (σ_2=175 MPa) is applied to the models to represent 7 km of overburden during the D_3 regional metamorphism and the deformation event associated with mineralisation. A depth of 6 km was modelled to comply with geobarometry conducted by Oliver *et al* (2006), which concluded that mineralisation occurred at pressures less than 3kbars.

The conceptual model geometry comprised the 1660 Ma diorites, the NE striking shear zones and the NW striking shear zones/faults (Figure 6.19). This numerical model was designed to test a syn-mineralisation D_4 scenario. The model set out to determine a far field orientation of maximum principal stress (σ_1) that would provide a NNE-SSW trending to N-S trending local σ_1 orientation around the FWSZ, to be consistent with the mapped mineralised extension veins (Coward, 2000; Laing, 2003)

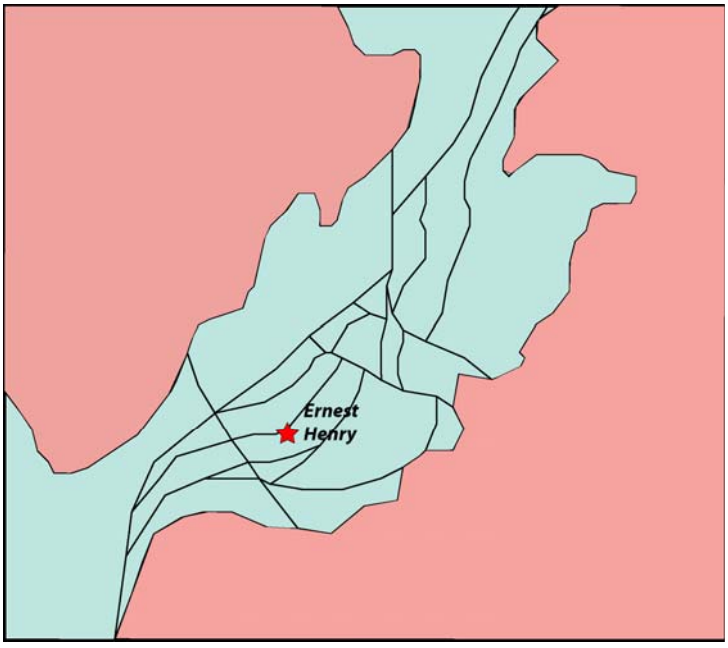

Figure 6.19 Conceptual model geometry containing the 1660 Ma diorites, the NE striking shear zones and the NW striking shear zones/faults.

6.6 Numerical modelling results

Both Coward (2000) and Laing (2003) suggest σ_1 orientations based on the orientation of mineralised extension veins relative to brittle faulting. Coward (2000) suggested the mineralisation σ_1 orientation of NNE-SSW based on observations of similarly oriented mineralised veins near the FWSZ. Laing (2003) proposed a σ_1 orientation of N-S to locally NNW-SSE based on extension vein measurements near the F2 and F4 faults in the centre and hangingwall of the deposit.

The UDEC modelling revealed that these local σ_1 orientations could be achieved during far field σ_1 stress orientations of ESE-WNW or NNE-SSW compression. Models involving a far field σ_1 orientation of N-S or SE-NW (Figure 6.20) also produced local σ_1 orientations in the mine area of N-S to locally NNW-SSE.

The plots of differential stress for both the ESE-WNW and NNE-SSW directed models (Figure 6.21) show a strong correlation between low differential stress and the location of Ernest Henry copper mineralisation. The differential stress values can be further analysed for a likely failure mode.

Brittle failure may arise by increasing differential stress and/ or by increasing fluid-pressure (Chapter 1 – Structural Techniques incl. paleostress analysis). The mode of failure depends on the balance between differential stress (σ_1 - σ_3) and tensile strength, T (Secor, 1965; Sibson, 1998). When (σ_1 - σ_3) > 4T, pure extension fractures form along planes perpendicular to the least compressive stress, σ_3.

By calculating four times the tensile strength of the rockmass modelled (~48 MPa), we can determine the area likely to fail in extension from the differential stress model outputs. The result is that during an ESE-WNW far-field σ_1 event, the area of tensile failure coincides with the economic grades of copper within the orebody (Figure 6.22). The orebody is surrounded by an area that is more likely to fail in compressional shear (Figure 6.22).

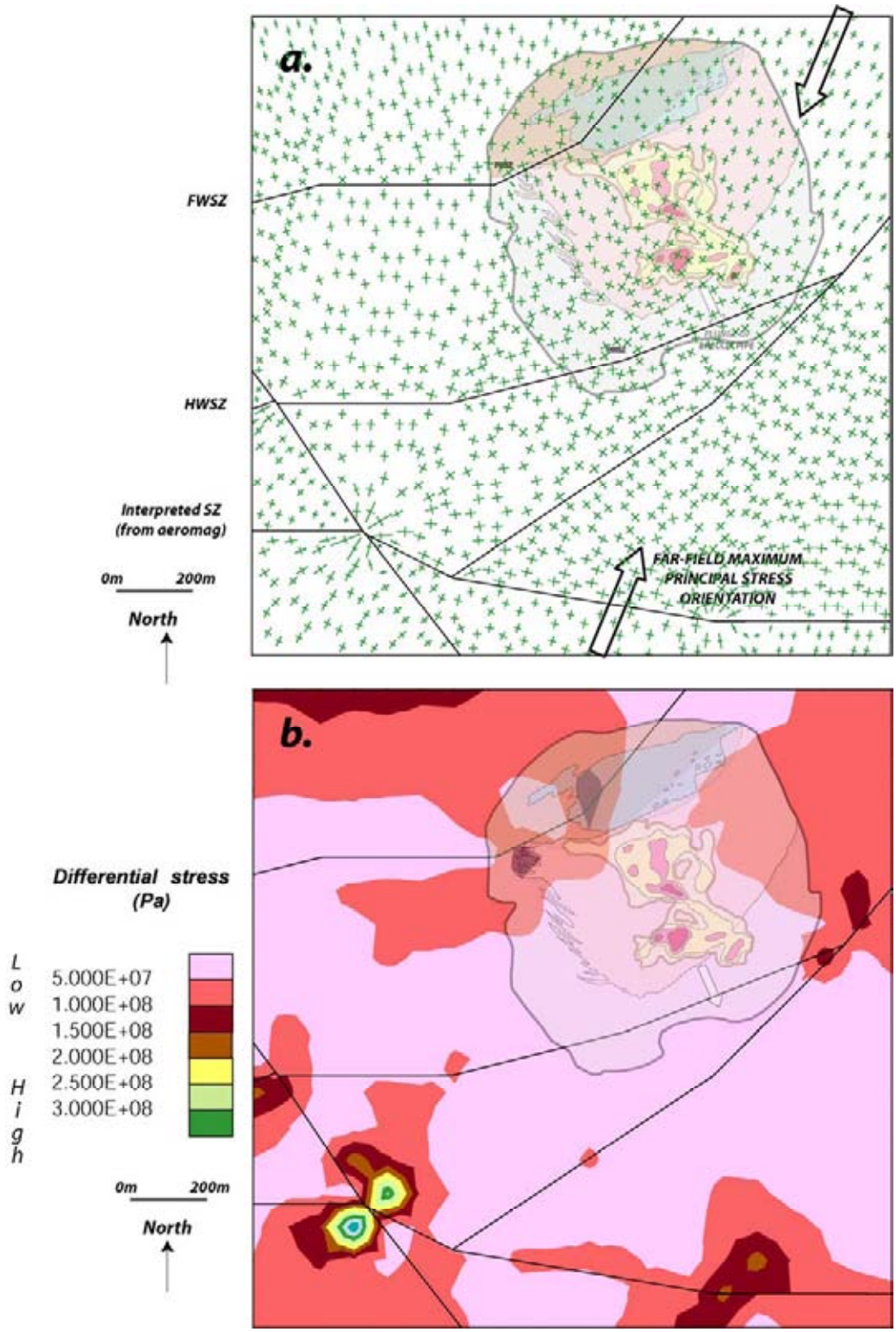

Figure 6.20 Numerical modelling output of the 1660 Ma diorite and all shear zone model tested in a NNE-SSW compression event. The Ernest Henry pit (as per Figure 6.6) is marked on the figures for reference. ***(a)*** *Plot of the principal stress tensors during a NNE-SSW compression event. The green crosses reflect the orientation of the principal stress tensors, with the cross length being proportional to the magnitude of the stress. The orientation of the maximum principal stress within the deposit varies between NNW and NNE trending.* ***(b)*** *The differential stress model output shows mineralisation forming in an area of low differential stress.*

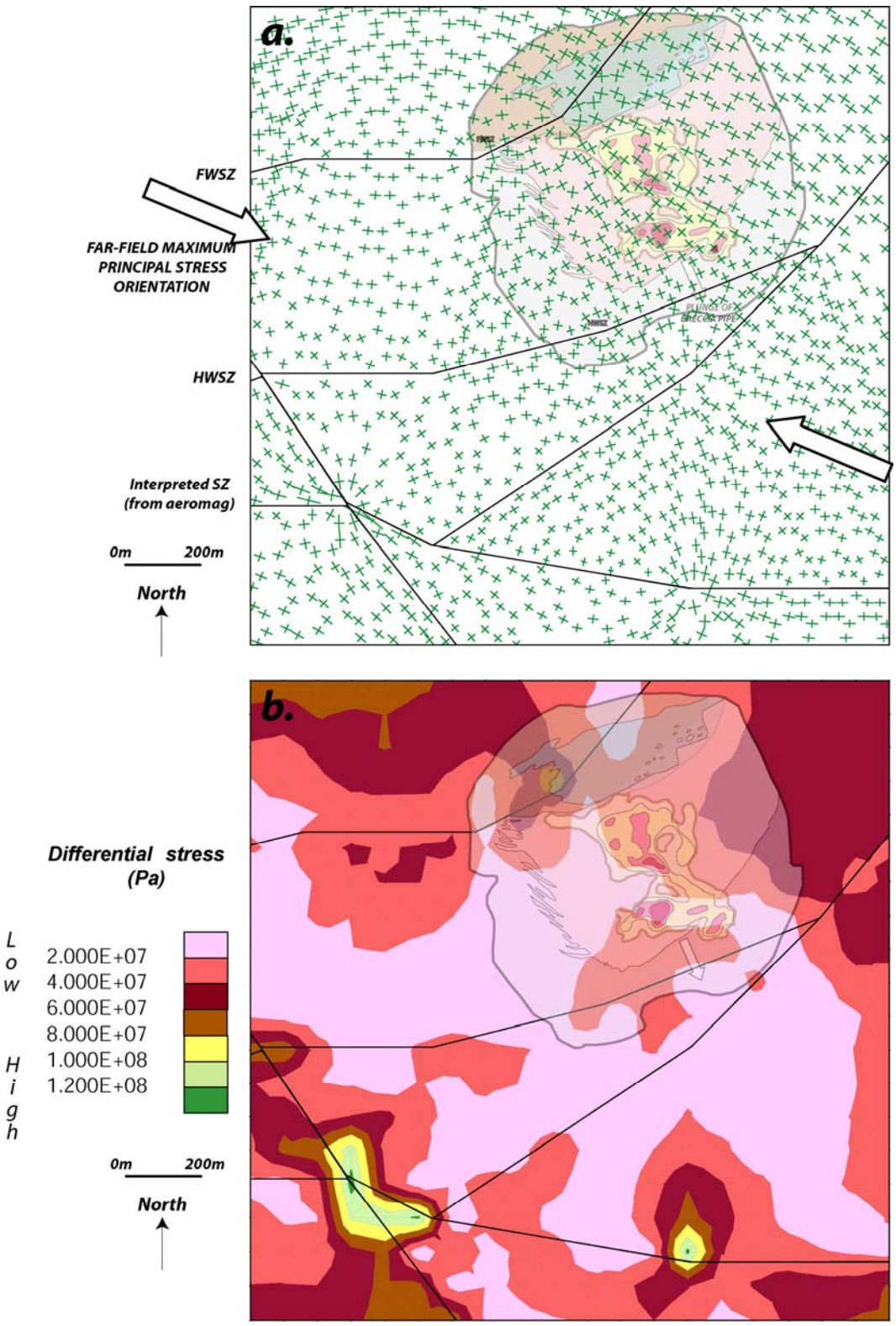

Figure 6.21 Numerical modelling output of the 1660 Ma diorite and all shear zone model tested in a ESE-WNW compression event. The Ernest Henry pit (as per Figure 6.6) is marked on the figures for reference. ***(a)*** *Plot of the principal stress tensors during a ESE-WNW compression event. The green crosses reflect the orientation of the principal stress tensors, with the cross length being proportional to the magnitude of the stress. The orientation of the maximum principal stress within the deposit varies between NNW and NNE trending.* ***(b)*** *The differential stress model output shows mineralisation (particularly the high grade mineralisation) forming in an area of low differential stress.*

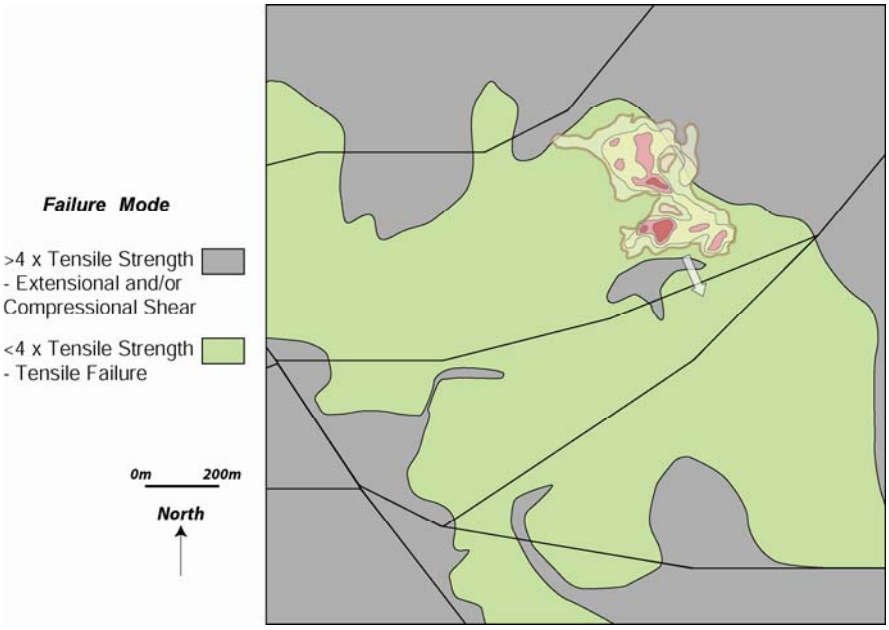

Figure 6.22 The calculated areas of likely tensile failure and extensional shear and/or compressional shear failure for the ESE-WNW shortening model. The Ernest Henry copper grade shells (as per Figure 6.6) are seen to occur in an area of tensile failure, on the margins of a large zone of extensional and/or compressional shear.

Laing (2003) hypothesised that the highly magnetic N-S striking shear zones, were indicative of tension fractures accommodating mineralisation stage magnetite metasomatism. The presence of widespread fine-grained magnetite-biotite alteration, that overprints much of the original metavolcanic sequence near the deposit, has been documented by several authors (Twyerould, 1997; Ryan, 1998; Mark and Crookes, 1999; Mark *et al.*, 2000, 2006; Williams and Pollard, 2001). This fine-grained magnetite event predates coarser type of magnetite that occurs with sulphides in the ore (Ryan, 1998; Williams and Pollard, 2001). With at least two separate and quite distinct magnetite events being identified, it may be that the magnetite occupying the N-S shear zones represents multiple metasomatic events. This line of justification for a regional N-S oriented σ_1 event, required for tensional failure of the N-S shear zones, may be overly simplistic.

If the magnetite in the N-S shear zones was precipitated in the same shortening event as the copper and gold mineralisation, then the numerical models may potentially provide some insight into the localisation process. Plots of fluid pressure required for failure is one of several parameters that have proved an important guide to finding sites of likely dilation in the modelling conducted on the Mt Gordon, Mt Isa and Mt Kelly mines. Areas of low fluid pressure for failure are typically indicative of rocks likely to fail in extensional shear or as a result of tensile failure and are therefore potentially favourable sites for the precipitation of minerals.

Areas of low fluid pressure for failure, in this instance used as a proxy for areas more likely to dilate than areas of high fluid pressure for failure, showed a strong correlation with the areas of high aeromagnetic response in the models with far field σ_1 orientations of ESE-WNW (Figure 6.23) and SE-NW. The N-S and NNE-SSW σ_1 oriented models showed a poor correlation between the areas of low fluid pressure and the areas of high magnetic response.

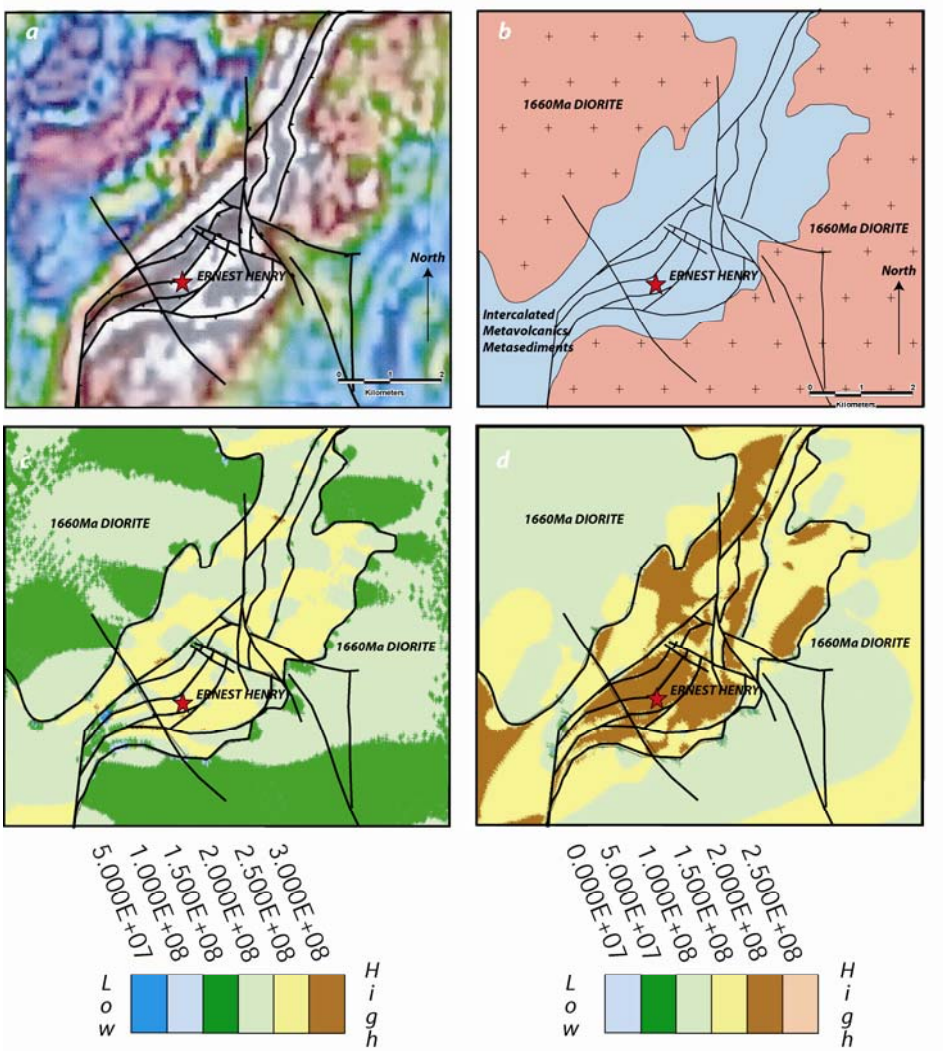

Figure 6.23 ***(a)*** *Magnetic image with interpreted faulting marked in black. The fault traces were primarily constructed from rapid changes in magnetic response. Interpretation of shear zone provided by S. Coates and R. Valenta (ex company geologists).* ***(b)*** *Input conceptual geometry for UDEC modelling.* ***(c)*** *Plot of fluid pressure required for failure for the N-S shortening model. There is a reasonable visual correlation between areas of low fluid pressure for failure and high magnetic response in (a), along the E-W striking portions of the shear zones. The correlation is quite poor along the N-S striking shear strands. Laing (2003) hypothesised that the highly magnetic N-S striking SZ (a), were indicative of tension fractures accommodating mineralisation stage magnetite metasomatism.*

(d) *Plot of fluid pressure required for failure for the ESE-WNW shortening model. There is a good visual correlation between areas of low fluid pressure for failure (yellow and green) and the areas of high magnetic response in (a). The areas of high magnetic response are indicative of areas of magnetite metasomatism (Laing, 2003), the Stage 2 or 3 fluids of the mineralising event.*

6.7 Discussion

The previous structural interpretations of Coward (2000) and Laing (2003) inferred far field stress orientations of NNE-SSW and N-S respectively, based on the orientations of the extension veins around the periphery of the Ernest Henry breccia pipe. Neither Coward (2000) nor Laing (2003) determined the effect of stress partitioning around the 1660 Ma diorite bodies. However from the mine-scale observations of the inferred orientation of the maximum principal stress, Laing (2003) hypothesised that a N-S shortening event was responsible for brecciation and subsequent magnetite mineralisation within the mine and in several sub-regional N-S striking shear zones. From the deposit scale 3D modelling there was little evidence for a major N-S oriented metasomatic channel in deposit as proposed by Laing (2003).

Coward (2000) proposed a σ_1 orientation of NNE-SSW during mineralisation on the basis of mineralised fault and mineralised vein measurements on the Footwall faults. The 1660 Ma diorites acted as rigid bodies, often redistributing far field σ_1 into unusual orientations at a local scale. Numerical models showed NNE-SSW shortening could be achieved locally in and near the Ernest Henry FWSZ during either an NNE-SSW far field σ_1 orientation or a ESE-WNW far field σ_1 orientation.

When the far field σ_1 was oriented NNE-SSW, differential stress values were seen to be low in the Ernest Henry location (20 to 50 MPa). Mineralisation was not present where differential stresses exceeded 50 MPa.

Similarly when the far field σ_1 was oriented ESE-WNW, differential stresses seen in the Ernest Henry location were extremely low (5 to 20 MPa). The highest grade sections of the Ernest Henry deposit were coincident with the areas of lowest differential stress. Conversely, in areas where the differential stresses reached ~40 MPa, the mineralisation was seen to be sub-economic or non-existant. Vein hosted and disseminated chalcopyrite is typical of mineralisation styles in the peripheries of the orebody (Laing, 2003).

During an ESE-WNW oriented σ_1 event, the N-S striking sections of the regional shear zones are seen to require low fluid pressures for failure. This is consistent with the highly magnetic response in the aeromagnetic image, presumably developed by the precipitation of magnetite (Stage 2 or 3 alteration). On a regional scale, the N-S oriented modelling results showed a poor correlation of fluid pressure for failure with the aeromagnetic response image. In the mine scale N-S oriented σ_1

numerical modelling results, local orientations of σ_1 were seen to consistently be oriented NNW-SSE, which was not consistent with the vein orientations of Coward (2000).

The ESE-WNW orientation of σ_1 is therefore the preferred model for the likely orientation of far field σ_1 during mineralisation. This is not dissimilar to the deposit genetic model stress orientation proposed by Valenta (2000), although the modes of failure differ. Valenta (2000) had interpreted two distinct diorite bodies in the south-east of the Ernest Henry Mine, with a SE oriented σ_1 event causing reverse movement on one segment of the bend in the FWSZ, and a dextral reactivation of the other segment. Reinterpretation of the diorite body and numerical modelling, show that during ESE-WNW shortening, extremely low strain and low differential stresses are created in the mine location. Stress partitioning around the 1660 Ma diorites leads to a local σ_1 orientation of NNE-SSW, as mapped by Coward (2000) and Laing (2003). The pipe preferentially occupies an area with extremely low differential stress, with mineralisation decreasing as the differential stress increased. In these areas of higher differential stress (still relatively low) crackle breccias and extension veins formed, similar to the extension veins mapped by Coward (2000) and Laing (2003).

U-$Pb_{rutile/titanite}$ age determination on Cu-Au mineralisation returned an ages of ~1530±20 Ma (Gunton, 1999; Mark *et al.*, 2006). These dates also overlap with the emplacement age of the Williams and Naraku Batholiths, and the nearby Mt Margaret Granite (Pollard and McNaughton, 1997; Page and Sun, 1998; Davis *et al.*, 2001). The ~1530 Ma age for mineralisation is also consistent with a 1527 Ma date on an ESE-WNW shortening event seen and dated at Snake Creek (Rubenach *et al*, 2007), 60 km south of Ernest Henry. The age date on an ESE-WNW σ_1 event (Rubenach *et al.*, 2007) is consistent with orebody age dating and a numerically modelled far field σ_1 orientation of ESE-WNW at mineralisation. The proposed σ_1 event at mineralisation also matches the proposed σ_1 orientations for the ore breccia forming event at Mt Gordon (Chapter 2), Mt Isa (Chapter 3) and Mt Kelly (Chapter 4).

The overpressured breccia pipe model proposed by Oliver *et al.* (2006), whereby brecciation is initiated by the abrupt release of overpressured magmatic-hydrothermal fluid several kilometres upward and outward from the contact aureole of the ~1530 Ma Williams Batholith is preferred. Despite the breccia pipe being extremely overpressured (pressure variations to 150 MPa) (Oliver *et al.*, 2006), it still seeks a path through an area of low differential stress.

Regional mapping of fluidised breccias of similar composition and style to the Ernest Henry ore breccia (Marshall, 2003; Oliver *et al.*, 2006), shows fluidised breccia pathways preferentially followed faults, lithological contacts and other planes of weakness. The proposed fault at depth (Figure 6.18), which is inferred from the mineral abundance and the element abundance grade shells, may provide one such pathway for the mineralising fluidised breccia.

Fluidised breccias that may have exploited the Proposed Fault would have been intercepted by the SE dipping shear zones that bound the Ernest Henry breccia, or Fault 2 and Fault 4 which run through the Ernest Henry breccia. Some of the fluidised breccia may have progressed up the shear zone to the upper shear zone, which could explain the presence of a lower and upper lens (Figure 6.24).

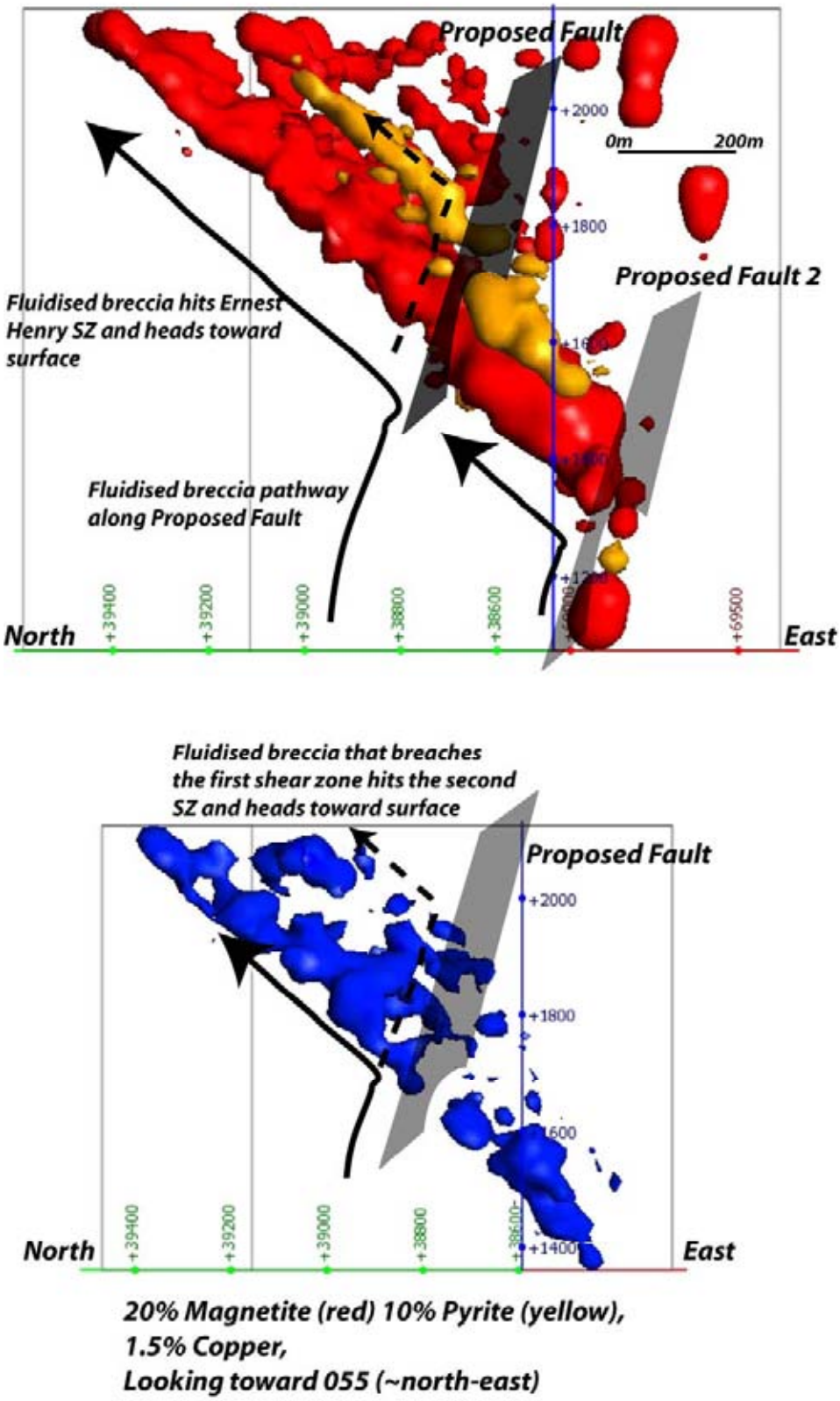

Figure 6.24 The proposed fault may have been a possible pathway for the fluidised breccia that hosts the Ernest Henry Cu-Au Mine. Fluid that breached the first shear zone (SZ) may have exploited the second SZ.

7. GREENMOUNT COPPER-GOLD DEPOSIT

7.1 Introduction

The Greenmount Cu-Au-Co deposit is located approximately 40 km south of Cloncurry, in the Marimo Basin (Figure 7.1). Greenmount is hosted by the Marimo Slate, a regressive unit which shows poor outcrop in the study area. The Greenmount deposit and its satellite prospects have been extensively drilled with a resource of 14.8 Mt @ 1.1% Cu. An understanding of the mineralised system has been attained primarily from RC and diamond drilling with a few surface observations both by previous authors (King and Hy, 1994; Krcmarov, 1995; Laing, 2004) and in this study. Because the drilling has taken place sporadically over approximately 20 years and the logging of these drill holes has lacked consistency. This lack of logging consistency has made 3D interpretation of the deposit extremely difficult.

Previous authors (King and Hy, 1994; Krcmarov, 1995; Laing, 2004) have interpreted the orebody differently, although all agree that the deposit has formed syn to post regional D_3, in the late stages of the 1600-1500 Ma Isan Orogeny. This study aims to determine the controls on ore localisation by combining detailed relogging of drill holes (both RC and diamond), 3D modelling of the relogged data and surface mapping of key structural elements (where exposed).

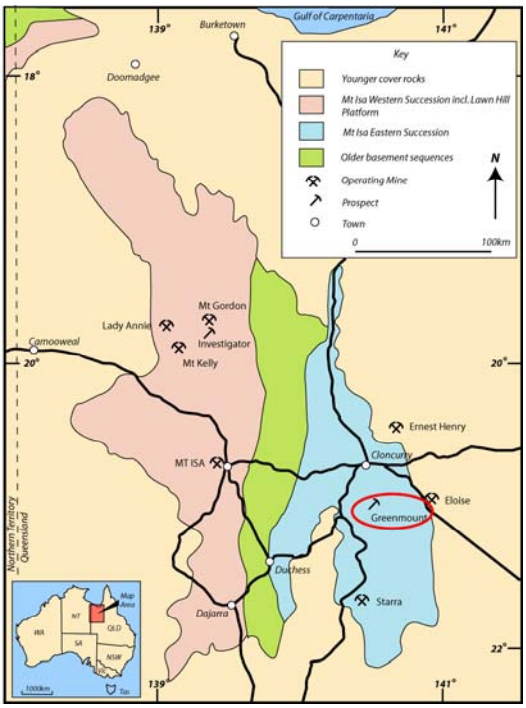

Figure 7.1 Location of the Greenmount Cu-Au Deposit.

7.2 Exploration History

The White Range exploration tenements have been the focus of several companies seeking copper mineralisation. In the late 1980's, Valdora Minerals and Homestake Australia formed a joint venture with a primary focus on finding gold and PGE mineralisation. During this study, BLEG (bulk leach extractable gold) anomalies were identified. The anomalies stretched from Greenmount to Vulcan, some 1.5 kilometres. Follow up RAB and RC percussion drilling identified the Greenmount orebody in 1991. However to date it has proven uneconomical to mine.

7.3 Geological Setting

7.3.1 Overview

The Greenmount Cu-Au-Co deposit is situated in greenschist facies black shales of the Marimo Slate belt (Figure 7.2, Rubenach et al, 2007). The Marimo Slate conformably overlies the Staveley Formation, a variably ferruginous, calcareous and siliceous arenite (Derrick, 1980).

Greenmount is the largest of several copper deposits located in Marimo Slate around the White Range Anticline. Other copper deposits include Mt McCabe, Vulcan, Pete's, Mt Leone, Blue Flag, Desolation and Painted Peaks (Figure 7.3). Of these deposits, the Mt McCabe and Vulcan deposits have been mined with limited tonnage.

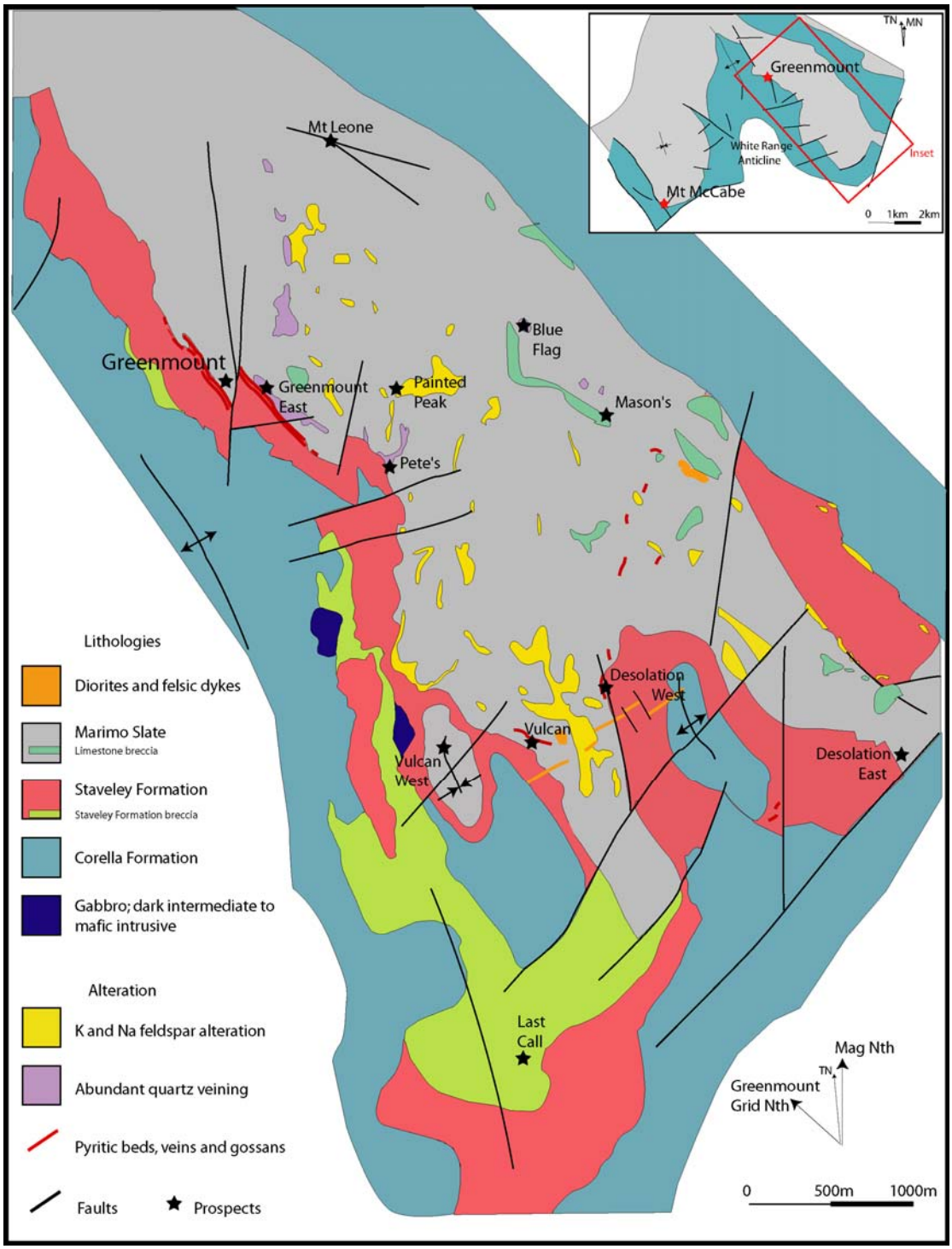

Figure 7.3 Geology of the east limb of the White Range Anticline (see inset). The Greenmount deposit occurs on the boundary of the Marimo Slate and Staveley Formation.

7.3.2 Metasomatism - Sodic Alteration

The Marimo Slate is pervasively albitised (locally sericitised) in the immediate vicinity of the ore zone. The albitised black shales (± coarse pyrite), are poorly exposed over an area of up to about 120 m wide and 1150 m long (Stewart, 1991).

The fine-grained pervasive albitisation accompanied elimination of organic matter, giving a distinct bleached appearance (Krcmarov and Stewart, 1998). XRD analysis was conducted by Mason (1994) on five samples from both mineralised and barren drill intersections at the Pete's and Painted Peaks Prospects west of Greenmount. The samples were dominated by albite with varying amounts of microcline and quartz and lesser phlogopite, quartz, pyrite, chlorite, dolomite and smectite.

The Staveley Formation is also locally albitised, but the extent of albitisation is far weaker than in the overlying Marimo Slate. Mason (1994) also noted the presence of tourmaline, apatite and rutile in the Staveley Formation. The tourmaline crystals were aligned parallel to the S_2 cleavage suggesting their growth pre or syn D_2. The less common rutile aggregates are assigned to the same metamorphic event (Krcmarov, 1995).

7.3.3 Metasomatism - Potassic Alteration and Mineralisation

Veins of microcline and quartz occur within the Marimo Slates and are typically spatially coincident with mineralisation. Disseminated chalcopyrite, often since altered to malachite, chrysocolla and chalcocite, is found within these microcline and quartz veins. The microcline-quartz veins are rarely seen in non-albitised shale.

The mineralisation at Greenmount is characterised by elevated Au, Cu, Co, As, Mo and W. Data from Krcmarov (1995) shows gross positive correlations between Au and Cu (Figure 7.4), As and Co and a weak positive correlation between Cu and K. Krcmarov (1995) states that minute inclusions of microcline in chalcopyrite may have affected the Cu-K analyses and he inferred that microcline and chalcopyrite were co-precipitating. This association of Cu-Au±Co-As with potassic alteration, overprinting earlier sodic alteration, is reminiscent of many of the iron oxide-Cu-Au deposits of the district (e.g. Williams et al., 2005). Iron oxides are absent (uncommon at Greenmount but magnetite-hematite alteration is found at depth (Stewart, 1991).

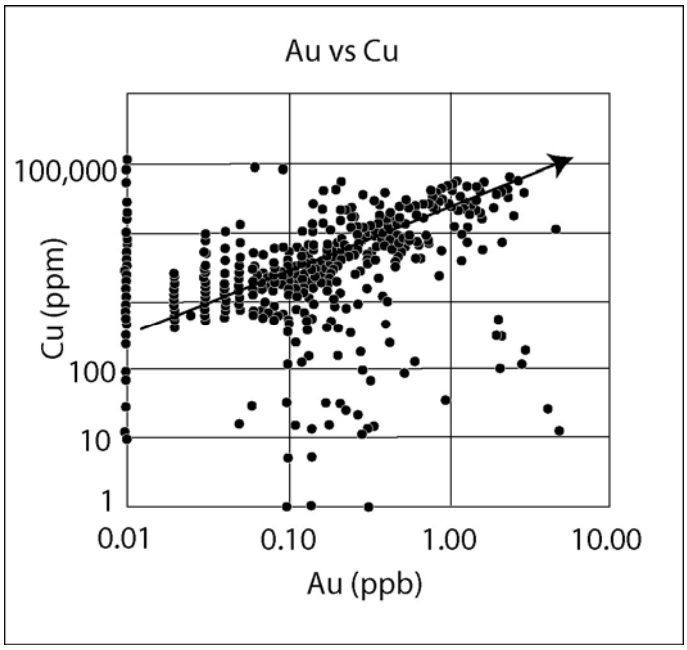

Figure 7.4 Gross positive relationship seen between copper grades and gold grades. Figure from Krcmarov (1995).

Supergene processes have obscured many of the in situ characteristics of the ore zone. Copper species assumed to originally be dominated by chalcopyrite, now consist dominantly of malachite, azurite, chrysocolla and chalcocite (Table 7.1). From the limited amount of holes drilled into the primary ore zone, mineralisation is disseminated within microcline and quartz veins or disseminated in the adjacent microcline, quartz or albite vein selvedges. Some primary mineralisation is also found in quartz only veins.

Table 7.1 Occurrences of copper species from core logging. Table adapted from Laing (2004).

Copper Species	***Description***	***% of Mineral***			***% of resource***
		Cpy	*Cc*	*Az+Mal*	
Chalcotrichite	Infill in late secondary joints				<1%
Azurite, malachite	Infill in dissolution cavities & secondary joints.			80	30%
	Replacement of sulphide/wallrock.			20	
Chalcocite	Replaced chalcopyrite in microcline veins /selvedge.		70		70%
	Infill in secondary joints		30		
Chalcopyrite	Infill in microcline-quartz vns, ?also pyritic vns	?>95			Primary zone 100%
	Replaced wallrock in microcline vn selvedge	?<5			

7.3.4 Metasomatism - Kaolinisation and Sericitization

X-ray diffraction analysis (Mason, 1994) on samples from the Petes and Painted Peaks showed weathering of albite and microcline to kaolinite and alunite.

Similar mineralogies are observed within the Greenmount ore system, suggesting to Krcmarov (1995) and Krcmarov and Stewart (1998) that the kaolinisation and sericitization of the Greenmount deposit also reflects weathering of albite and microcline.

7.3.5 Structure - Ductile Deformation

The White Range Anticline is the largest regional fold in the Marimo Basin. It is an 8 km wavelength, NNW plunging fold (plunges approximately 20°) and is inferred to have formed during the D_2 event of the Isan orogeny (Stewart, 1991; King and Hy, 1994; Krcmarov, 1995; King and Hy, 1997; Laing, 2004). The White Range Anticline has developed an upright, NNW trending S_2 cleavage, best developed in the Marimo Slates. S_2 is also weakly defined by mineral alignment of tournamaline crystals and rutile aggregates in the Staveley Formation near the Greenmount deposit (Stewart, 1991; Krcmarov, 1995). On close inspection the S_2 cleavage is often crenulated. This crenulation is associated with the ENE-WSW shortening D_3 event (Laing, 2004).

The large-scale geometry of F_2 folds, though now partly obscured by F_3 effects, is believed to be influential in the ductile architecture of the prospect (Laing, 2004). Regionally F_3 folds have a strong and characteristic brittle-ductile component: disharmonic, polyclinal, and kink folds are common and axial planes vary in orientation.

7.3.6 Structure - Brittle Deformation

The mapping campaigns of King and Hy (1994, 1997) identified four dominant orientations of faults around the Greenmount deposit.

The earliest is a moderately (45° to 65°) east dipping NW trending set of faults, inferred to be sinistral and reverse at the time of mineralisation (King and Hy, 1997). This class of faulting includes the Caravan Fault Zone and Mt Leone Fault Zones (Figure 7.5). A set of NNW trending faults was considered important during mineralisation (King and Hy, 1997). King and Hy (1997) inferred these faults had a sinistral sense of movement due to the geometry of minor folds and were one of the main

controls on mineralisation. The NW and NNW faults are broadly parallel with the bedding and S_2 cleavage orientations respectively. An ESE trending set of sinistral faults is thought to have developed after mineralisation. Post mineralisation, dextral reactivation of the NNW faults is also inferred from the apparent displacement of the Marimo-Staveley contact (King and Hy, 1997).

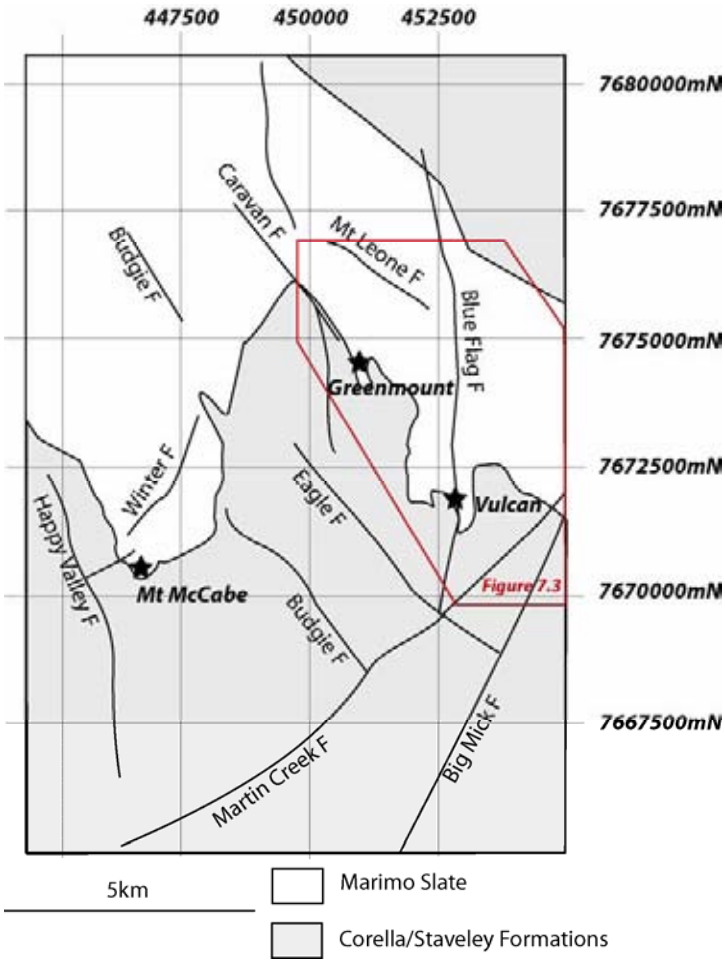

Figure 7.5 The major faults of the White Range area (adapted from King and Hy, 1994). Significant copper deposits are marked. The location of the detailed map (Figure 7.3) is illustrated.

7.3.7 Structure - Ductile or brittle deformation – Staveley Breccia Ridge?

South of the Greenmount Fault lies the enigmatic Staveley Breccia Ridge, a prominent hill of "potassified and hematite dusted arenaceous and pelitic clasts, cemented by calcite, which forms a distinctly orange coloured ridge, paralleling the main ore zone for at least 600 m" (Krcmarov, 1995). Several authors have disputed the origins of the ridge, with some authors preferring a fault/shear model with the Staveley breccia exhumed in a braided fault system (King and Hy, 1994; Krcmarov, 1995) (Figure 7.6). Others prefer the hypothesis that the ridge is an anticlinal fold closure, with mineralisation folded around the hinge (Stewart, 1991; Laing, 2004) (Figure 7.7).

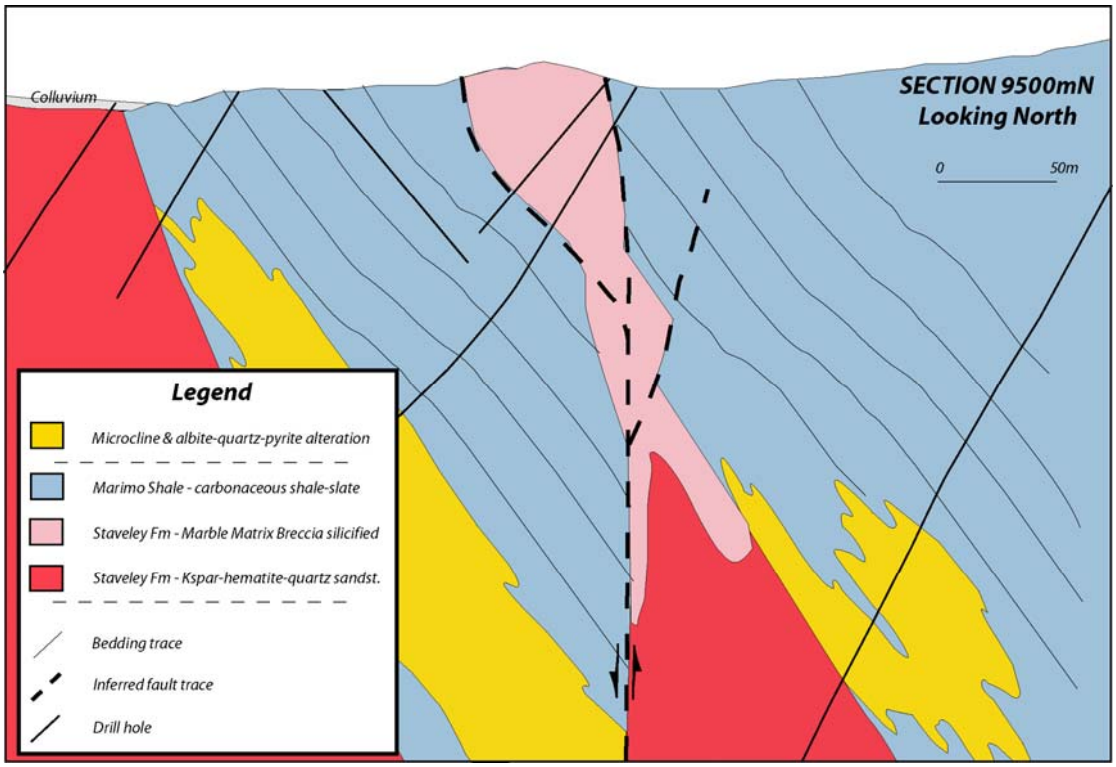

Figure 7.6 (adapted from Krcmarov, 1995) Simplified geological interpretation of cross section 9500 mN. The Staveley breccia has been exhumed by a series of faults (King and Hy, 1994; Krcmarov, 1995).

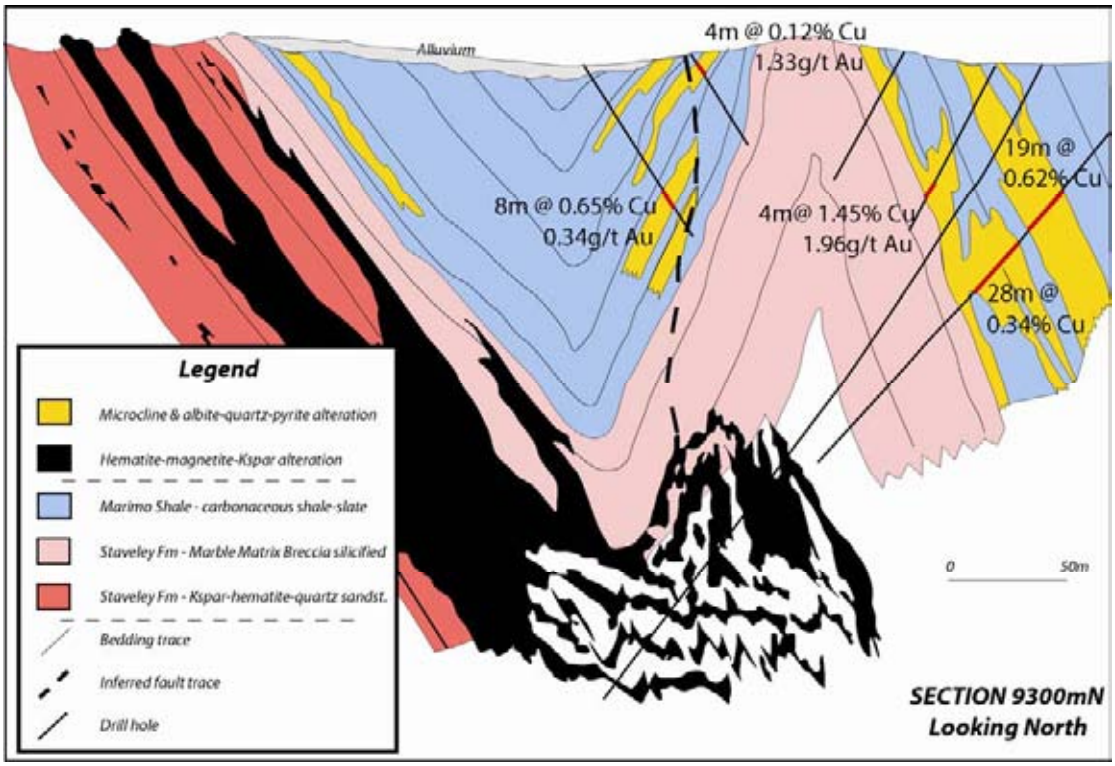

Figure 7.7 (adapted from Stewart, 1991) Schematic cross section of the "Anticlinal Staveley Hill Model" through 9300mN (grid north), ~300 m south of the Greenmount Fault (Stewart, 1991; Laing, 2004). Note this section is 200 m south of the section in Figure 7.6.

7.4 Previous Syn-Copper Kinematic Studies

The Greenmount deposit and smaller satellite deposits (Vulcan, Mt McCabe and Copper Canyon) have been extensively mapped by several companies and authors. Much previous work (Stewart, 1991; Krcmarov, 1995) focussed primarily on the geochemistry of the Greenmount system.

Three structural studies have been undertaken at Greenmount – by King and Hy (1994, 1997), Krcmarov (1995) and by Laing (2004). A field mapping campaign of the eastern limb of the White Range Anticline was conducted by King and Hy in 1994. The King and Hy (1994) study concluded that mineralisation was controlled by a swarm of structures at a high angle to bedding and the bulk of the ore zone (Figure 7.8). The case for the fault swarm argument revolved around the fact that few structures were found to parallel the ore zone, and that many mineralised veins and structures were found to parallel the N-S striking Greenmount Fault. As these N-S faults pass through the Marimo-Staveley contact, they widened to create local dilation zones. The other alternative put forward by King and Hy (1994) was that refraction of the fault swarm through the Marimo-Staveley contact would result in N-S oriented dilatant zones (Figure 7.9 – Kink model).

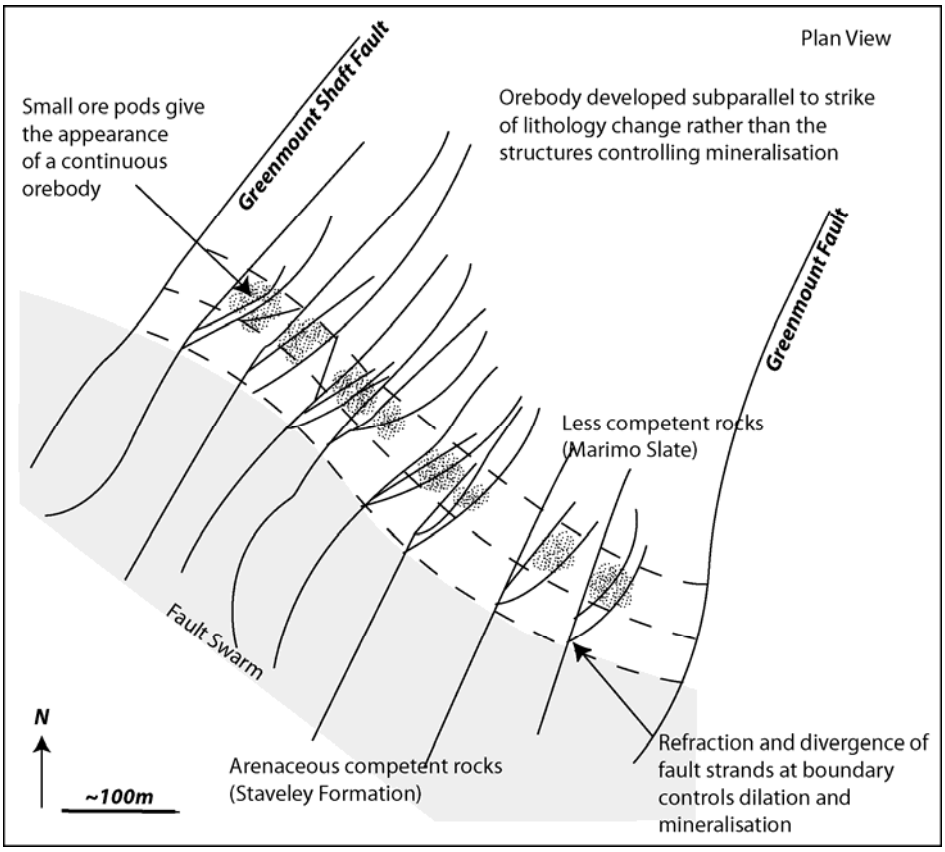

Figure 7.8 Schematic diagram of the fault swarm model proposed by King and Hy (1994) (adapted from Krcmarov and Stewart, 1998).

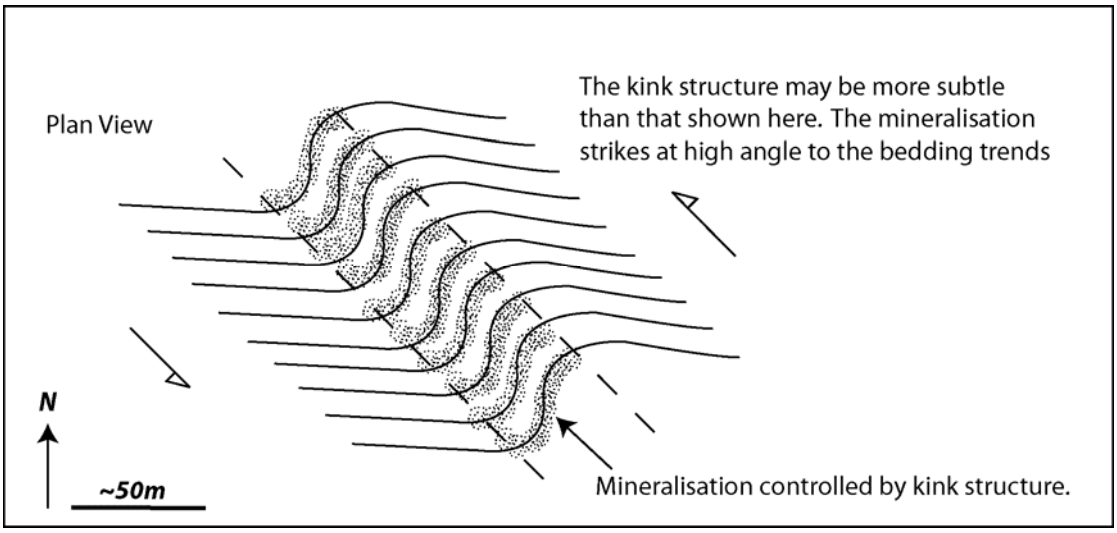

Figure 7.9 Schematic diagram of the Kink model proposed by King and Hy (1994) (adapted from Krcmarov and Stewart, 1998).

Krcmarov (1995) contended that there was little evidence from the limited outcrop for either of the King and Hy (1994) scenarios. Instead Krcmarov proposed that reverse faulting of flat ramp on the Marimo-Staveley contact was responsible for the ore breccias (Figure 7.10). Krcmarov (1995) concluded that the most altered and mineralised part of the system occurred where the Marimo-Staveley contact was shallowest.

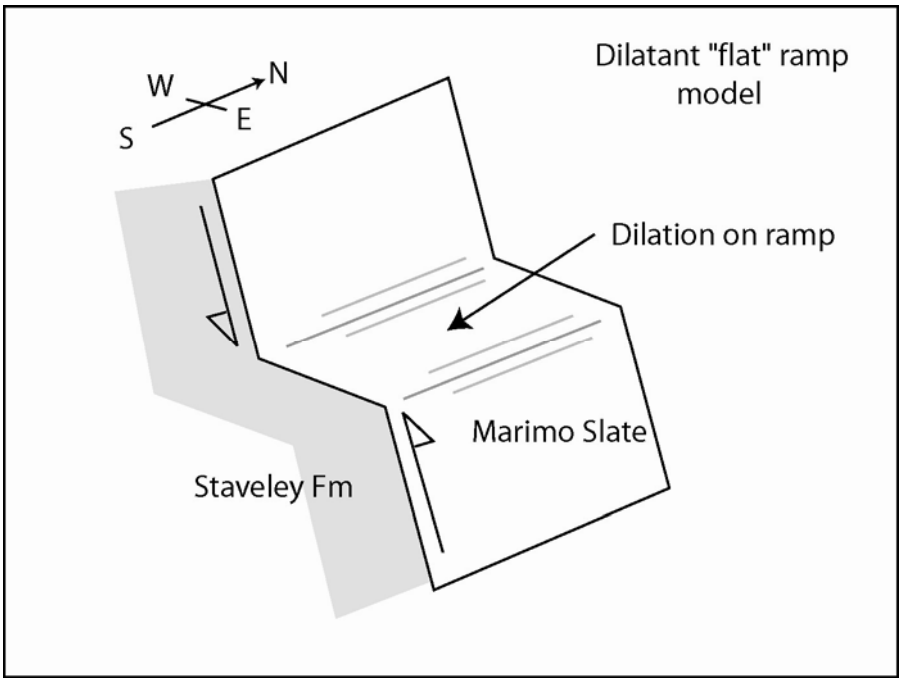

Figure 7.10 Schematic diagram showing the flat ramp model proposed by Krcmarov (1994).

The structural report of Laing (2004) focussed on drill core observations. Measurements were taken on the un-oriented drill core using the regionally consistent S_2 cleavage as a reference structure. Laing inferred the bulk of the mineralised microcline-quartz veins were NNE striking and tensional. From vein orientations, Laing assumed a dextral sense of slip on a bedding parallel shear zone, the "Greenmount Shear Zone", located beyond the mineralised zone (Figure 7.11). From the tensile veins and the dextral sense of shear on the Greenmount Shear Zone, Laing inferred a mineralising σ_1 orientation of NNE-SSW.

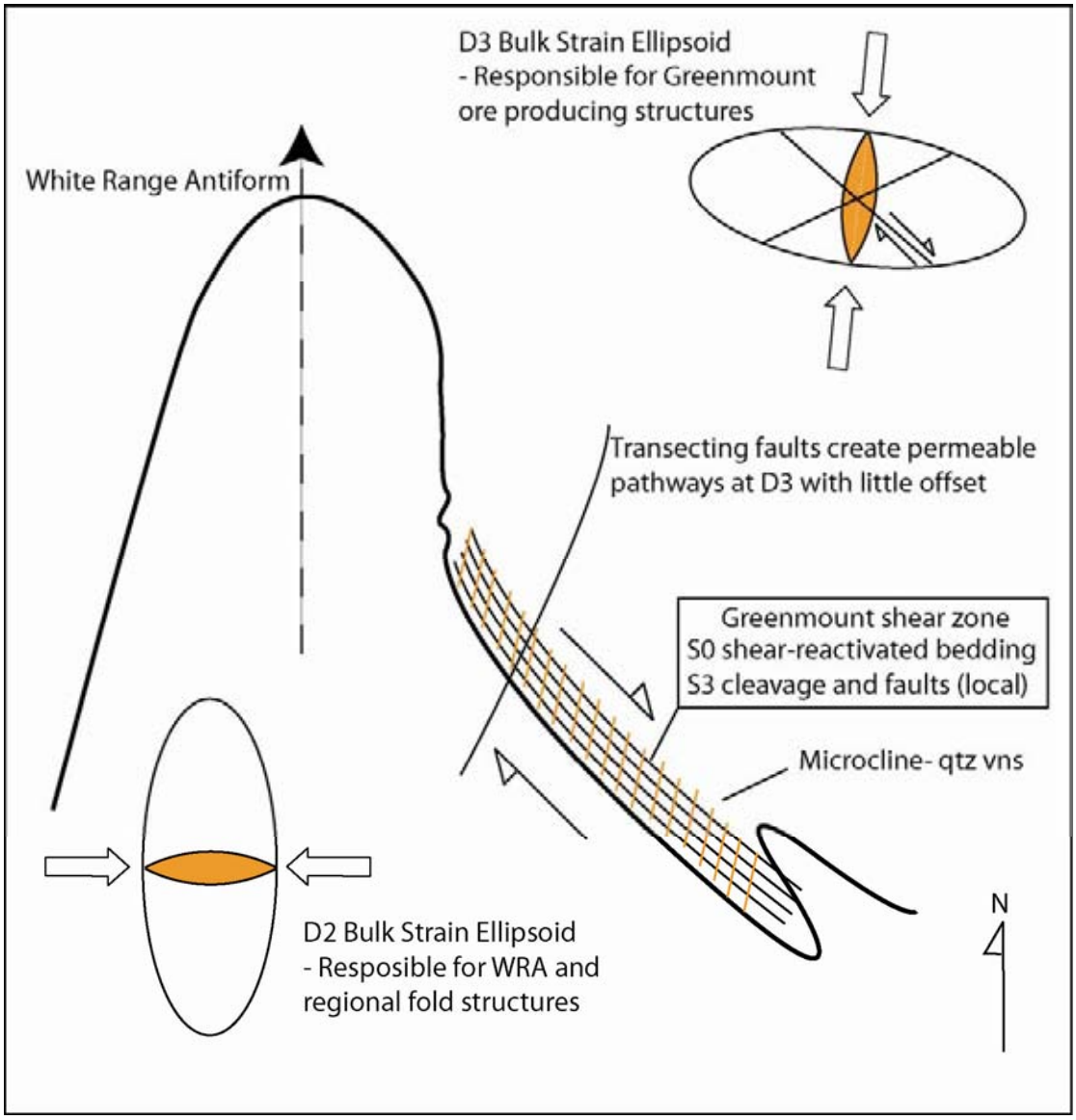

Figure 7.11 Schematic diagram of the Laing (2004) genetic model revolves around far field σ_1 orientation NNE – SSW shortening at mineralisation time to create the bedding parallel, dextral Greenmount Shear Zone and to produce NNE striking tension veins. Note: diagram not to scale.

The structural studies completed have focussed either on mapping the limited amount of outcrop (King and Hy, 1994), comparing copper grade distributions and models from other Mt Isa Inlier deposits to Greenmount (Krcmarov, 1995), or logging drill-core (Laing, 2004), in order to come to their conclusions. The variety of structural models produced from these isolated studies suggests that several datasets must be interrogated in order to truly define structural controls on mineralisation at Greenmount.

7.5 Deposit 3D Reinterpretation

7.5.1 Methods

As previously discussed, the mineralisation at Greenmount has a clear association with microcline-quartz veins (Stewart, 1991; Krcmarov, 1995). Laing (2005) determined the orientations of the mineralised veins from unoriented drill core, using the S_2 cleavage as a reference structure (method in Scott and Berry, 2004). A select area of the Greenmount deposit was structurally mapped, with particular focus on the orientation and nature of the microcline-quartz veins, in order to attempt to validate the Laing (2005) and earlier logging.

Data collection, in the form of core and chip logging of drilled holes, has occurred over a 20 year time frame at Greenmount. Changes in logging codes, logging requirements and many different core/chip logging geologists have led to inconsistencies in drilled geology database. These inconsistencies made interrogation of the geological database very difficult.

All existing RC (115 holes) and diamond drill holes (30 holes) through the Greenmount deposit, north of 9300mN (mine grid) were relogged for primary rocktype, alteration style and intensity and fault position and thickness (where possible).

Three dimensional modelling of the Greenmount deposit has in the past been limited to a Staveley – Marimo contact wireframe and orebody kriging of the copper resource.

Here, the relogged drill data was converted into database format and inputted into Leapfrog 3D. 3D shells were created for the primary lithologies; the Staveley Formation and the Marimo Slates. The different styles of alteration were also modelled in 3D; microcline-quartz alteration, albitisation and kaolinisation. The lithological and alteration 3D shells were related to the copper and gold assay data in an attempt to determine any spatial relationships.

7.5.2 Structural Mapping Results

Structural mapping of the immediate Greenmount ore zone is limited by poor outcrop due to a cover of ~10 m thick colluvium over much of the deposit. The only significant outcrop in the Greenmount deposit is around the Staveley Breccia Hill. Small exposures are otherwise sparsely distributed in narrow gullies.

King and Hy (1997) conducted mapping and aerial photographic interpretation of the Greenmount deposit. They produced a 1:2500 scale map of the major faults, rocktypes and interpreted bedding traces. This scale of mapping was not sufficient to deduce the distribution of the microcline-quartz-copper veining. Mapping transects were conducted over the Staveley Breccia Hill, south of the Greenmount Fault, during this study. The primary focus of the mapping was to determine the dominant orientations of the microcline-quartz veins and the relationships of these veins to bedding, S_2 cleavage and any faulting.

King and Hy (1997) and Laing (2004) document significant variations in bedding orientations and dips, due to parasitic folding during D_2 and local refolding of F_2 folds during D_3. However, mapped bedding orientations in the areas of outcrop during this study were seen to be moderately to steeply, north-east dipping (Figure 7.12b), more consistent with the Krcmarov (1995) work (Figure 7.6).The north east dipping bedding plane measurements are consistent with expected bedding orientations on the eastern limb of a gently north plunging anticline (i.e. the White Range Anticline, Figure 7.12a). The author does not completely dismiss the possible presence of local mesoscopic F_3 folds, but was unable to locate or measure any in the field.

The dominant fabric in the field area mapped was the S_2 foliation. The S_2 foliation was subvertical, NNW trending (Figure 7.12c) and was often weakly crenulated by F_3 microfolds (i.e. <2 mm). The orientation of the S_2 foliation is consistent with the NNW trending axial trace of the White Range Anticline.

Orientations of microcline-quartz veins were somewhat variable but most were northwest-southeast striking to north-south striking and moderately to steeply dipping (Figure 7.12d). Approximately one third of the measured veins were aligned parallel to the bedding and another third of the veins aligned with the S_2 cleavage. The remainder of the measured veins were found to lie between bedding and cleavage orientations but intersect along the bedding-S_2 cleavage intersection.

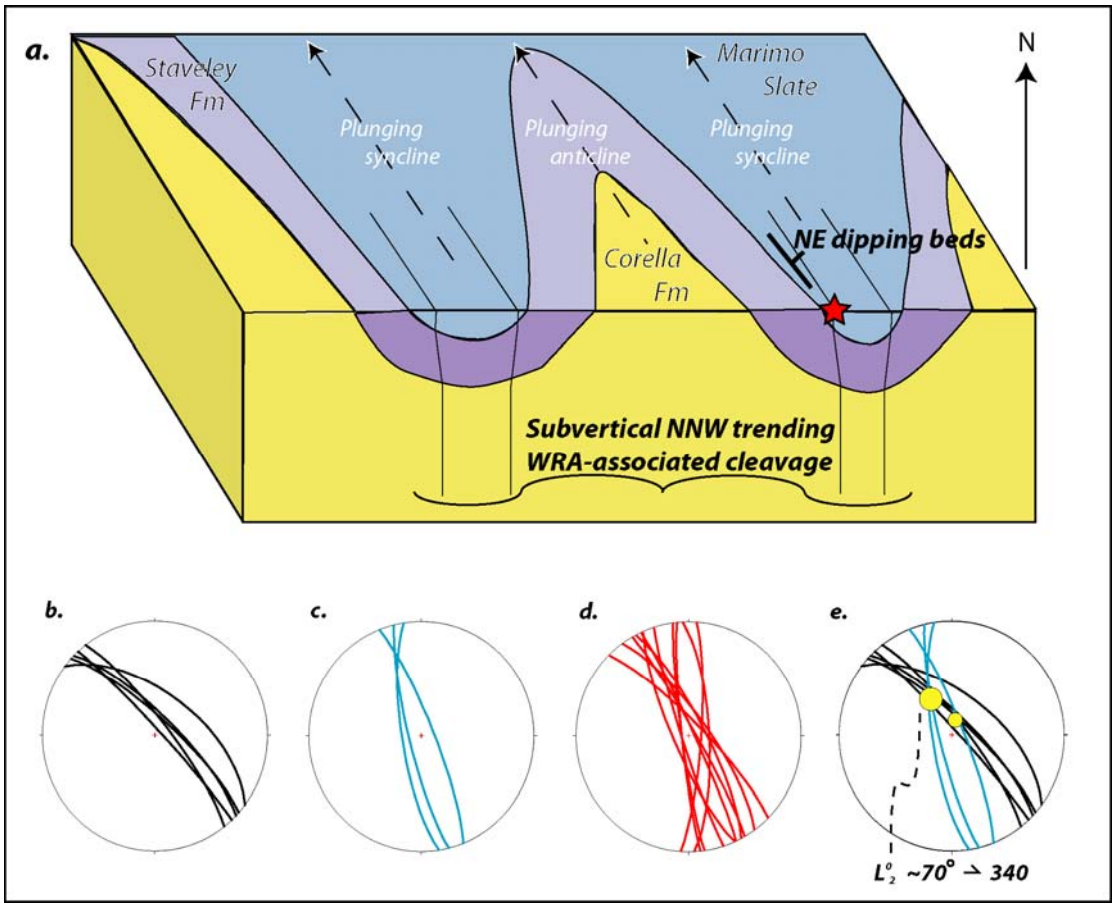

Figure 7.12 ***(a)*** *Simplified view of the White Range Anticline (WRA) showing the relative position of Greenmount (red star).*

(b) *measured bedding orientations from Marimo Slate outcrops around the Staveley Breccia Hill, steeply dipping to the north-east. This is consistent with the Greenmount deposit being on the eastern limb of a NNW trending anticline.*

(c) *S_2 cleavages are seen to be sub-vertical, NNW trending. The S_2 cleavage measurements strike parallel to the axial trace of the White Range Anticline.*

(d) *microcline - quartz ± copper veins are seen to vary in strike from northwest-southeast to north-south. They vary in dip from moderate to steeply dipping.*

(e) *bedding and S_2 cleavage orientations have been overlayed to determine an average L^0_2 orientation. Two clusters of intersections are seen. The largest cluster orientation for L^0_2 is ~70º→340º. The smaller cluster trends L^0_2 ~80º→005º*

The distribution of vein orientations around the Staveley Breccia Hill provided some insight into the significance of the microcline-quartz vein orientations (Figure 7.13). The northernmost extent of the Staveley Breccia Hill had the largest amount of veins and most diversified vein orientations in the one locality. Veins were seen to be parallel to bedding, parallel to the S_2 cleavage and the microcline-quartz veins also assumed an orientation parallel to the trend of the bedding-cleavage intersection.

The western side of the Staveley Breccia Hill showed two of the three microcline-quartz vein orientations seen to the north. Veins parallel to the S_2 cleavage and to the bedding-S_2 cleavage intersection was mapped in this locality. The bedding parallel vein set was not seen in this location.

The bedding parallel vein set was the only microcline-quartz vein set mapped on the eastern side of the Staveley Breccia Hill. Coincidently, the eastern side of the Staveley Breccia Hill does not contain significant amounts mineralisation. An albitite is present nearby and contains trace amounts of chalcopyrite and a silver-purple mineral, possibly cobaltite.

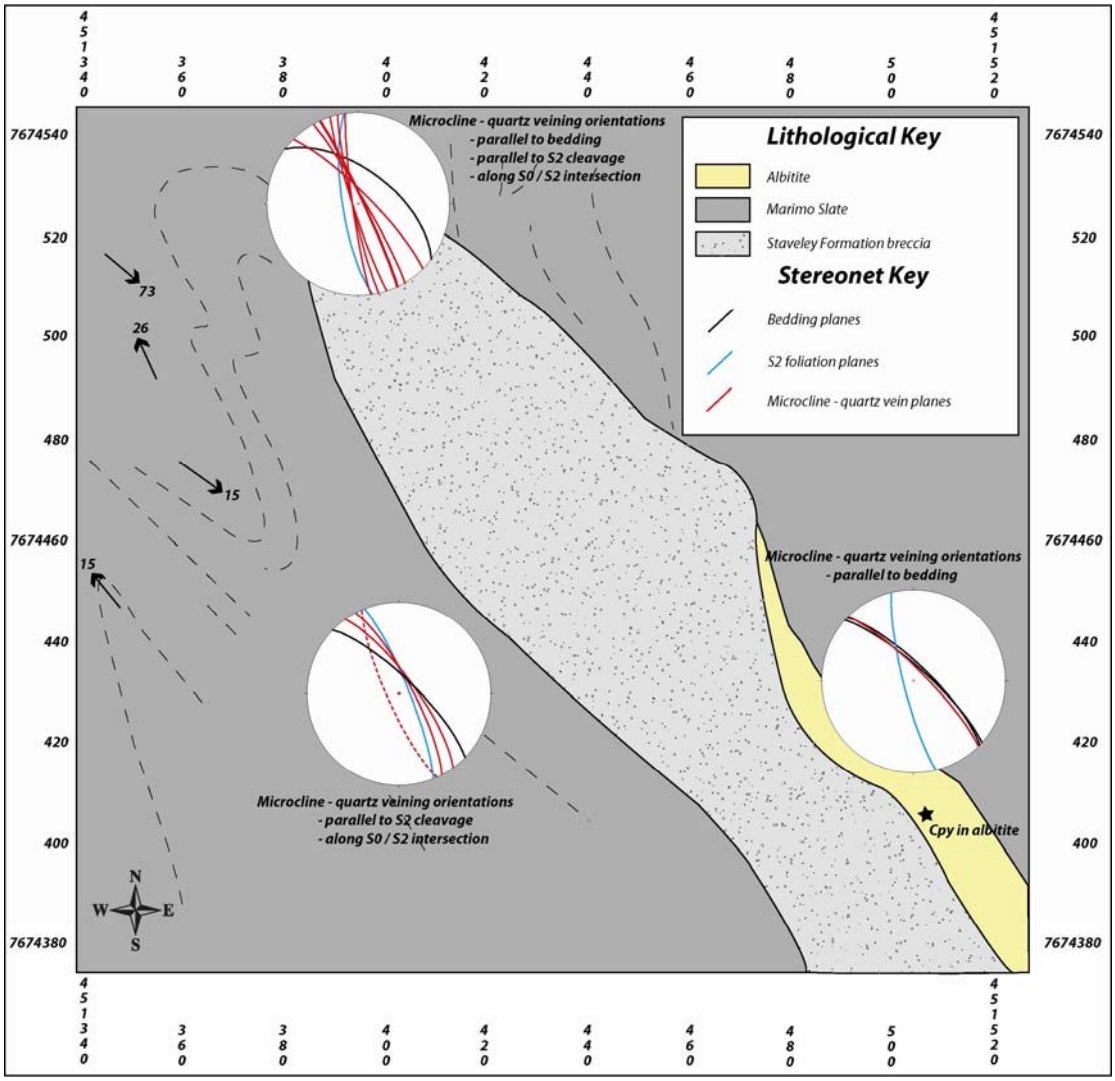

Figure 7.13 Field mapping of bedding, S_2 cleavage and microcline–quartz vein orientations around the Staveley Breccia Hill.

7.5.3 Lithological / Alteration Relationships

The previous three dimensional modelling of the Greenmount deposit focussed on copper and gold grade shells, assisted by geostatistics (King and Hy, 1994). Here, 3D lithological and alteration models are generated to better define high grade ore shoots and the geometric, structural and lithological controls on mineralisation.

The position of lithological contacts, styles of alteration, alteration intensities and relationships between the alteration phases and wallrock were relogged from the diamond drill holes existing in 2005. These drill holes constituted ~20% of the total drilling at Greenmount. Lithotypes and alteration assemblages were logged in RC chip trays for use in 3D model construction.

Prior to construction of the 3D models, the relogging data was interpreted in 2D on drill sections (e.g. Figure 7.15) and related to both the copper and gold assayed drilling intercepts. From a series of 25 m to 50 m spaced sections there appeared to be a positive relationship between elevated copper grades and the eastern boundary of the microcline-quartz breccias, and between elevated copper grades and the eastern margin of the kaolin altered shales with the unaltered black shales. Grades in these locations were significantly higher than in the bulk of the pervasively kaolin altered rock.

The first 3D surface created was the Staveley-Marimo contact surface, including the Staveley Breccia Hill. North of the Greenmount Fault Zone (Figure 7.14), the contact dips steeply to the east, aside from a small step (~15 m wide). The Greenmount Fault Zone offsets the Marimo-Staveley contact significantly with a south block west (apparent dextral) displacement.

Segments of narrow N-S trending Staveley breccia emanate from the Staveley-Marimo contact within the Greenmount Fault Zone (Figure 7.14 bottom). These N-S striking, narrow breccias are parallel to the Staveley Breccia Hill, located on the south side of the Greenmount Fault Zone. These short breccia strands may be a) faulted offsets of the Staveley Breccia Hill, b) small exhumed braids of Staveley Formation along faulting parallel to the main Staveley Breccia Ridge or c) parasitic fold closures.

The Staveley Breccia Hill is an extremely narrow breccia body (~30 m wide) at depth. With the White Range Anticline being a large upright open fold, it would be unlikely for the parasitic folding on the eastern limb to form such tight isoclinal folding.

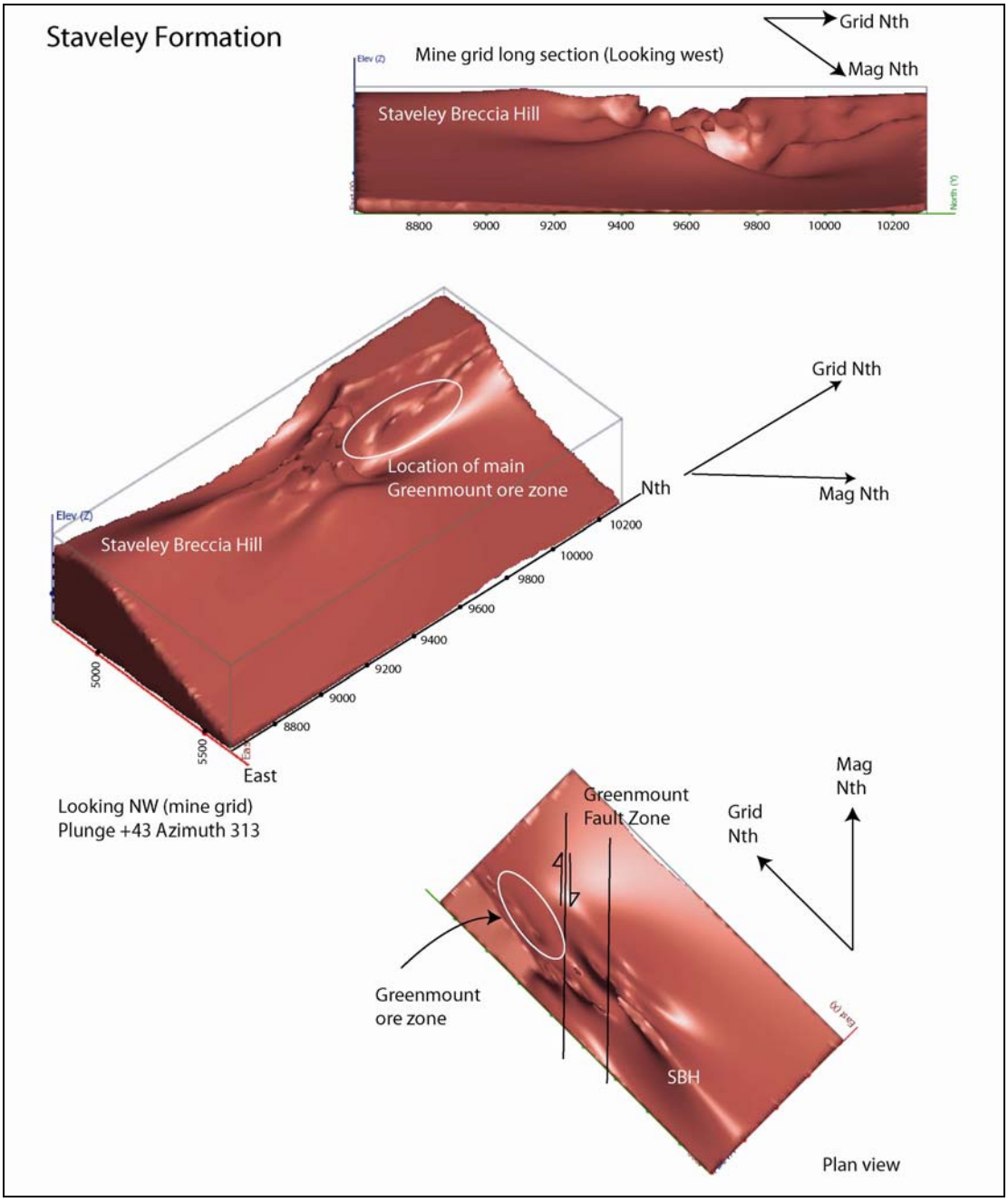

Figure 7.14 Leapfrog 3D model outputs of the top of the Staveley Formation. In long section (top) the Staveley Breccia Hill is apparent, as is the small ridge in the north of the deposit. When viewed from the south east (middle) the disruption of the Staveley – Marimo contact around the Greenmount Fault Zone can be seen. The narrow nature of the Staveley Breccia Hill is apparent in plan view (bottom). The surface projection of the Greenmount Fault and an associated fault (from King and Hy, 1994 map) are shown.

From the cross-section interpretation, it also appeared that the microcline-quartz breccia bodies are plunging steeply to the north (Figures 7.15a & b). Close visual inspection of the drill core showed two preferred orientations of albitisation and microcline-quartz veins. The preferred orientations were along bedding planes and the S_2 cleavage planes (Figure 7.16). Along the

intersection of these planes (S_0/S_2 intersection), the thickness of the albitic selvedge increased significantly.

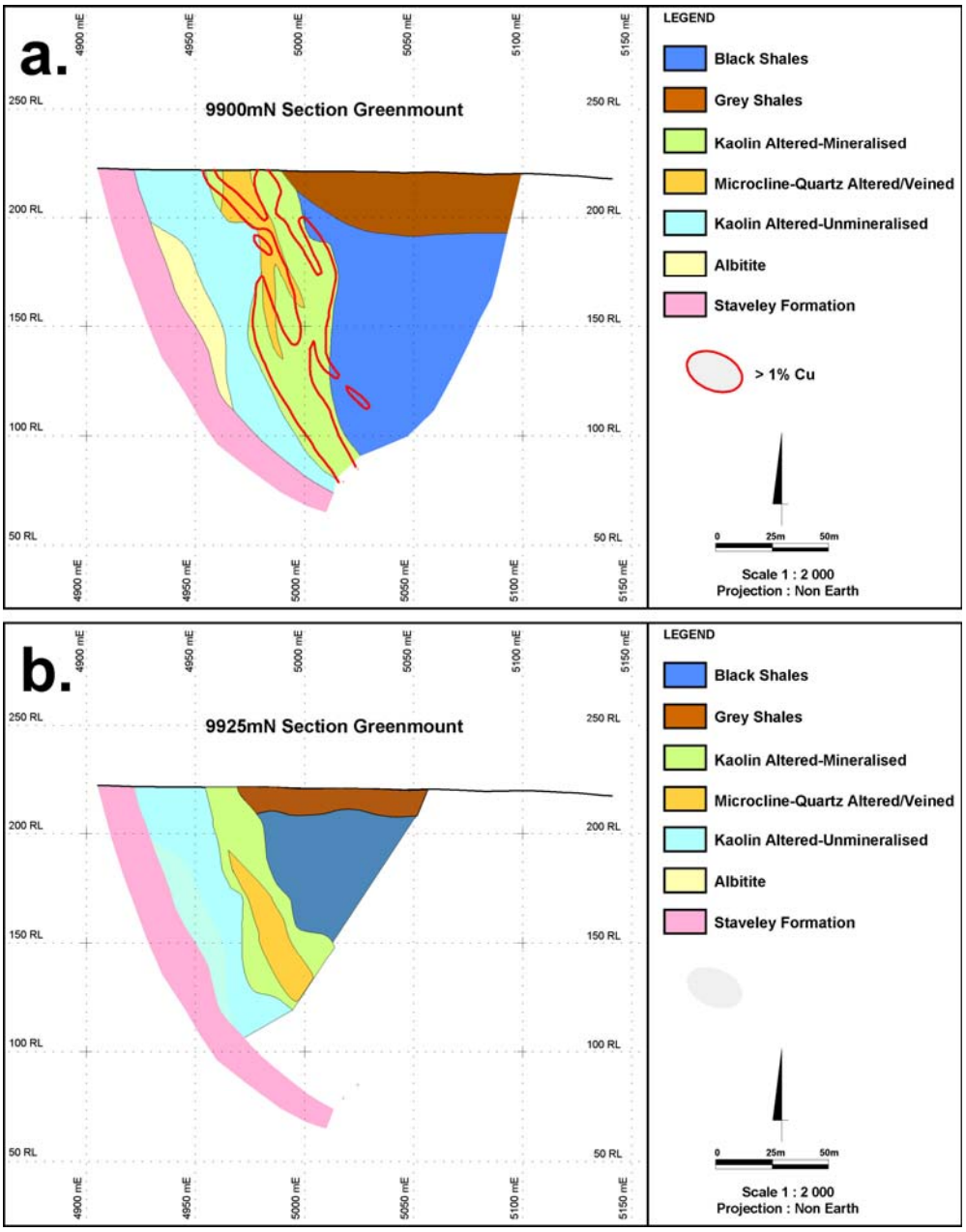

Figure 7.15 a) 2D sectional interpretation of 9900mN (mine grid) from relogged drill holes.
b) 2D sectional interpretation of 9925mN (mine grid) from relogged drill holes. Note the position of the microcline-quartz altered/veined unit relative to its position in (a). Over a strike distance of 25 m, the unit has gone from surface (220RL, 9900mN) to below surface (190RL, 9925mN). This gives a minimum plunge of 60 N for the microcline-quartz unit.

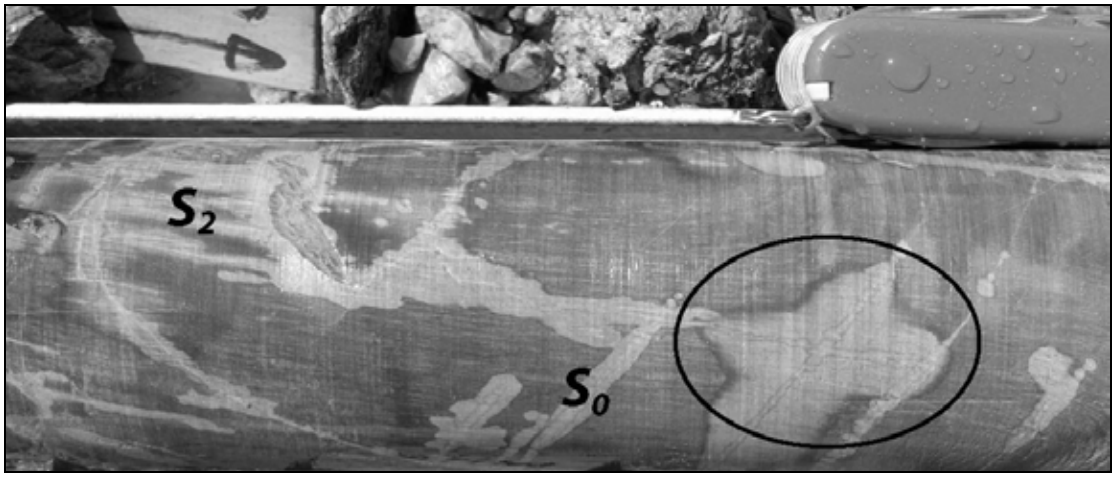

Figure 7.16 Photograph of HQ sized core from drillhole GDHM21 96.2 m depth. Albitic selvedge (pale grey) is preferentially assuming two orientations. The orientation of albitic selvedge almost parallel to the core is in the S_2 cleavage orientation and the cross cutting orientation is the albitic selvedge associated with the bedding planes (S_0). Note the selvedge thickness change at the intersection of the bedding and cleavage (black circle).

In order to accurately model the microcline–quartz breccia bodies in three dimensions, the preferred orientations seen in the core and mapping had to be considered. These preferred orientations can be modelled in 3D by applying an anisotropic fit to the data. Geostatistical anisotropy is where the continuity of data exhibits a longer range (i.e., better correlation) in one direction than another (Isaacs and Srivastava, 1989).

From the cross-section interpretation and field mapping of three preferred orientations of microcline-quartz veining, the bedding-cleavage intersection orientation was seen to be the orientation most likely to have the greatest lateral and vertical continuity. Diamond core logging suggested that ore shoots parallel to the S_0/S_2 intersection lineation would be at least three times as long as they are wide. A strong anisotropy (5:1.5:1; plunge:plunge azimuth:pitch) was determined on the basis of these diamond core results with the mean plunge and plunge direction of 75º toward 335º assigned to the intersection lineation. This L^0_2 orientation is similar to the L^0_2 orientation proposed from mapping around the Staveley Breccia Hill (Figure 7.12e) where L^0_2 is ~70º→340º.

The result of applying this anisotropy to the relogged drill-hole dataset, was to produce microcline-quartz shoots in approximately 7 locations. The only place these shoots could be validated was around the mapped area of the Staveley Breccia Hill (Figure 7.17).

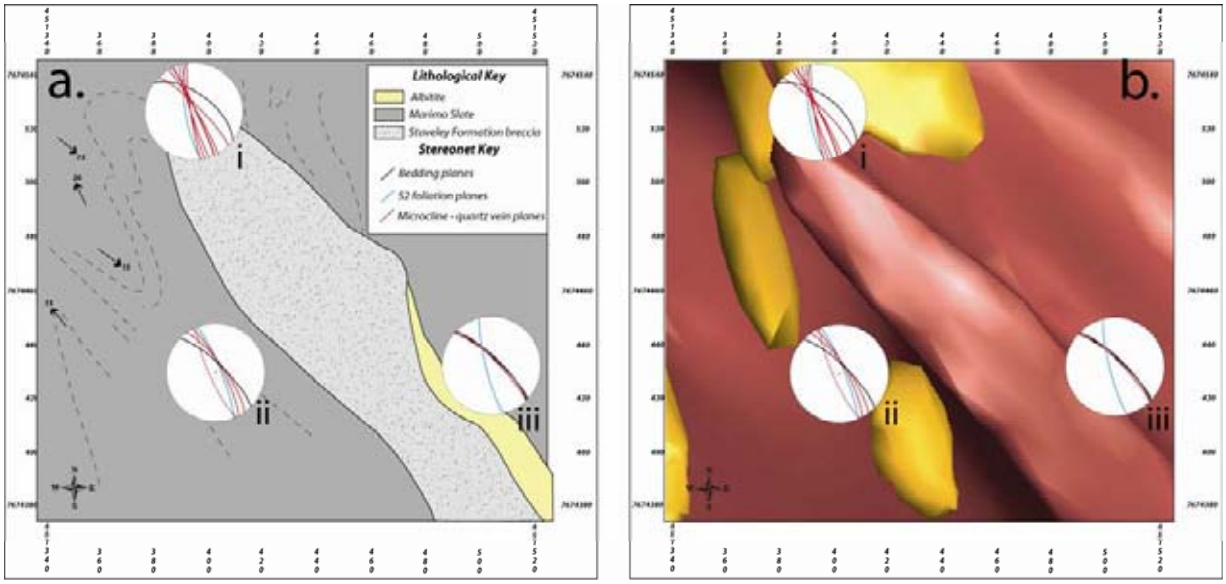

Figure 7.17 ***(a)*** *Mapping data showing two locations with microcline quartz veining in a bedding-cleavage intersection orientation (locations i and ii). Location iii contains bedding parallel microcline quartz veining only.* ***(b)*** *The 3D model outputs with the Staveley Formation in red and the steeply plunging microcline-quartz shoots in orange. The mapping localities where the microcline-quartz veining was seen in a bedding-cleavage intersection orientation (a. i and ii) match the 3D modelled relogged drilling data (b. i and ii). No microcline-quartz veining was modelled in a bedding-cleavage intersection orientation in location iii.*

The microcline-quartz shoots are also seen to terminate on the very small (~15 m wide) ramp on the Staveley-Marimo contact to the north and commonly extend to the shallower Staveley-Marimo contact in the south (Figure 7.19). These shoots may either indicate potential fluid pathways into the ore zone for the mineralising fluids, an inaccurate assessment of the anisotropic data, or some combination of these factors.

Flitch plan mapping by Alston (2004) showed two distinct orientations to the 0.5% copper grade shell (Figure 7.18). The copper grade shell assumes both the S_2 cleavage orientation (NNW striking) and the bedding orientation (NW striking). The albite/kaolin alteration, microcline-quartz veining and the copper distribution all co-exist suggesting timing of the three styles was similar if not coeval.

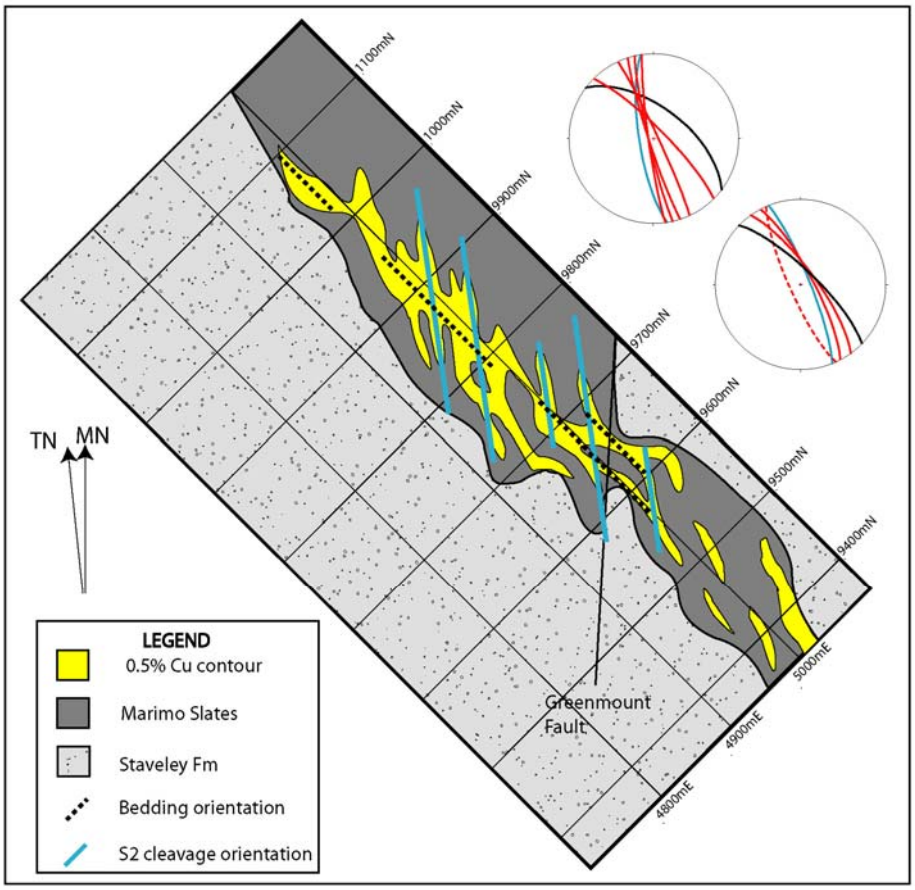

Figure 7.18 (adapted from Alston, 2004) 150RL flitch plan of the 0.5% copper grade shell (yellow) relative to the Staveley Formation and Greenmount Fault. The copper grade shell aligns with both the S_2 cleavage orientation and the bedding orientation. Thickenings of the grade shell are seen at 9850mN and 9900mN where the S_2 cleavage and bedding intersect. Stereonets of the mapping results are plotted with the blue plane showing the S_2 cleavage and the black plane showing the bedding orientation.

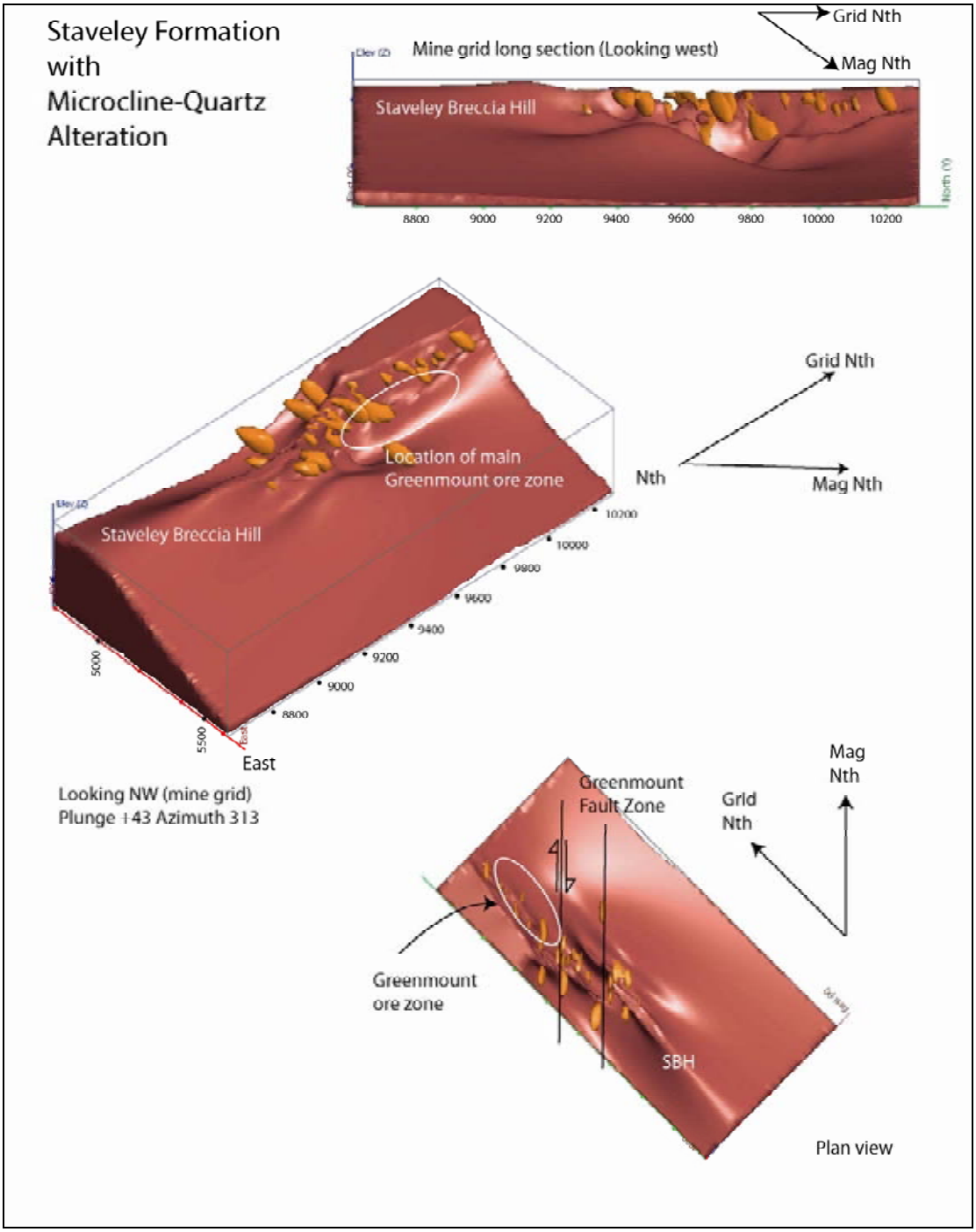

Figure 7.19 Leapfrog 3D model outputs of the microcline-quartz breccia bodies (orange) over the top of the Staveley Formation (red). In long section (top) the vertical extent of the breccia bodies is evident, with the breccias to the north extending to shallower depths than those in the south. When viewed from the south east (middle) the NNW plunge to the microcline-quartz breccias can be seen. In plan (bottom), the concentration of microcline-quartz brecciation around the Greenmount Fault Zone relative to the weak veining to the north is noticed. This is most likely due to the extensive kaolinitic alteration and overprinting of the northern mineralised veins. The surface projection of the Greenmount Fault and an associated fault (from King and Hy, 1994 map) are shown.

When the variably mineralised kaolin altered shales were added to the 3D model (Figure 7.20), further insights were made to the Greenmount ore system. The most striking feature was the prevalence of kaolin in areas around the microcline-quartz breccias. Other noticeable features of the kaolin model were the relatively shallow depth extent of the kaolin to the north and the small amount of kaolin alteration on the western side of the Staveley Breccia Hill. Kaolin alteration to the north of the model does not extend too far beyond the small step in the Staveley-Marimo contact.

Finally the albitites were added to the 3D model (Figure 7.21). The albitites were common through the Greenmount Fault corridor, particularly when in close proximity to the Staveley-Marimo contact. The albitite mapped on the eastern flank of the Staveley Breccia Hill was also recognised in drill core and RC chips. The albitites have a poor spatial relationship to copper mineralisation relative to the microcline-quartz shoots.

One explanation for this observation is that there are two distinct albitisation events. One of these albitisation events is associated with copper mineralisation and the other is either paragenetically earlier or later than the copper mineralisation.

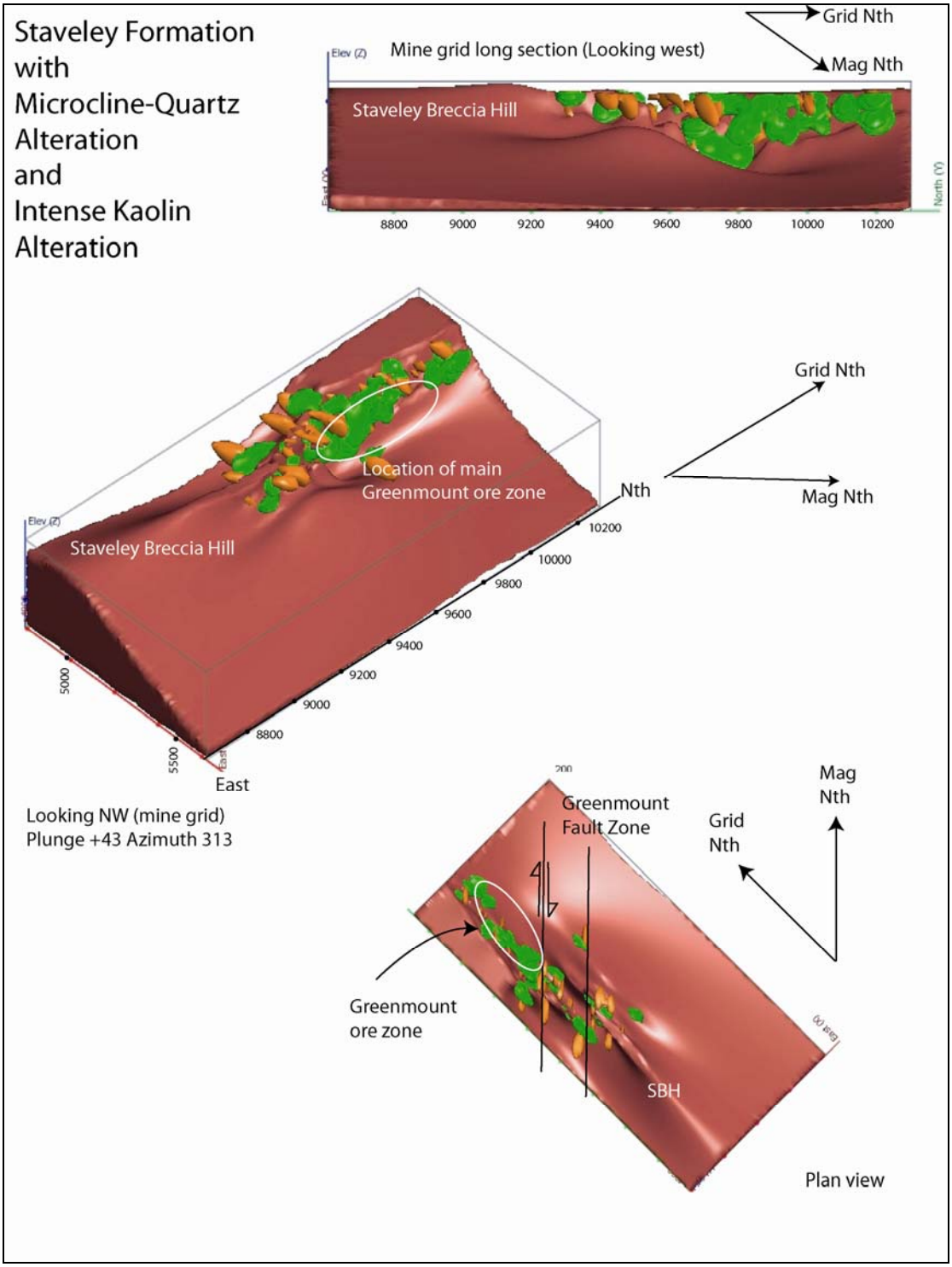

Figure 7.20 Leapfrog 3D model outputs of moderate to intense kaolin alteration (green), microcline-quartz breccia bodies (orange) and the top of the Staveley Formation (red). In long section (top) the vertical extent of the breccia bodies is evident, with the kaolin altered material to the north being far shallower than those in the south. The kaolin alteration to the north is not evident below the 15 m wide step in the Staveley-Marimo contact. When viewed from the south east (middle) the lack of kaolin alteration to the south of the model can be seen. The most intense and abundant kaolin alteration is present to the north of the projected Greenmount Fault Zone (middle, bottom).

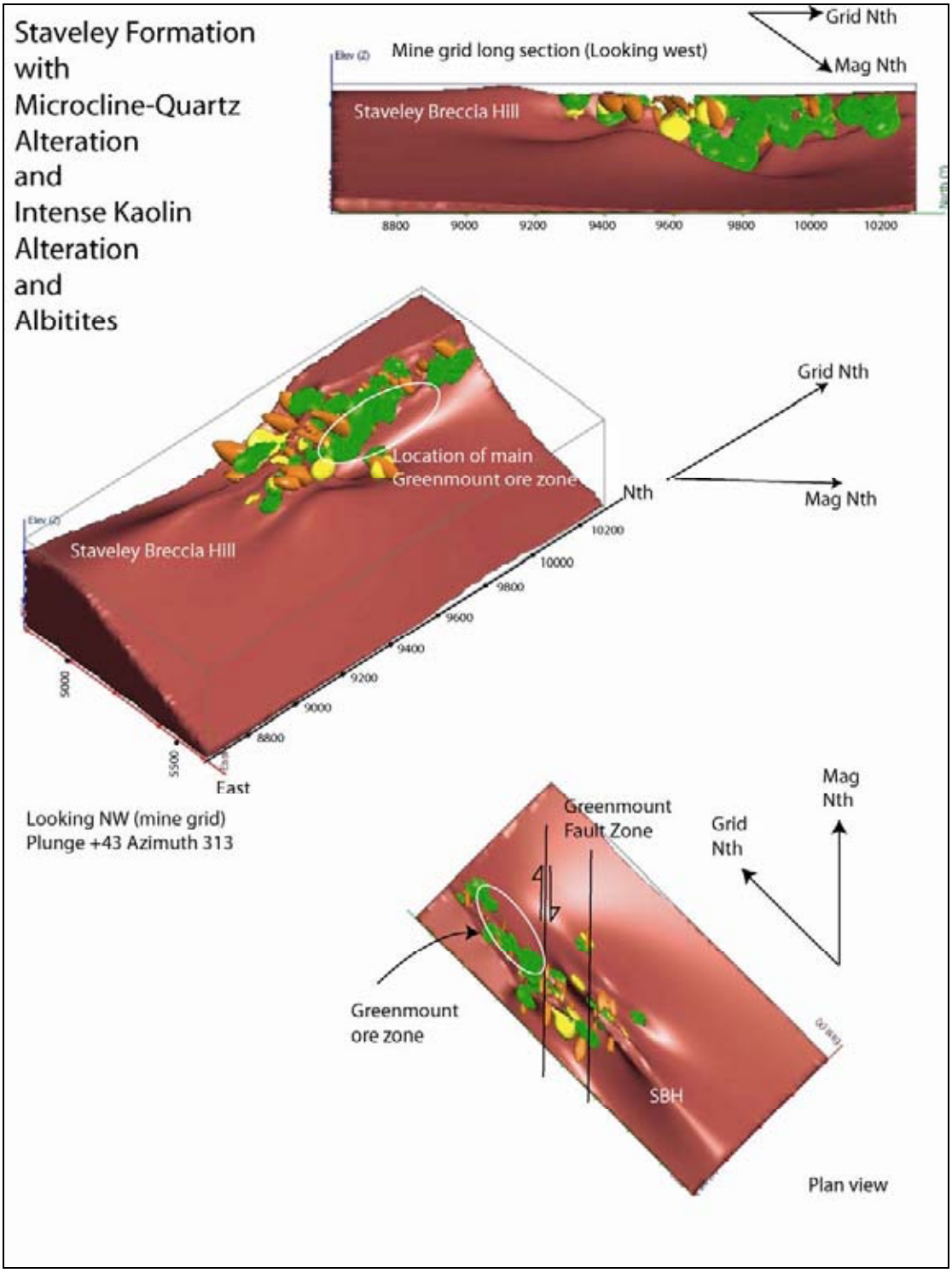

Figure 7.21 Leapfrog 3D model outputs of albitite (yellow), moderate to intense kaolin alteration (green), microcline-quartz breccia bodies (orange) and the top of the Staveley Formation (red). In long section (top) the albitite body on the eastern side of the Staveley Breccia Hill is evident. Albitites are most commonly present through the projected Greenmount Fault Zone (middle, bottom), particularly along the Staveley-Marimo contact. Little albitite is present to the north of the Greenmount Fault Zone.

7.6 Numerical Modelling - White Range Anticline

7.6.1 Conceptual Model

The 11.8 km x 8.5 km model geometry was created from mapping conducted by Rosenatreich *et al.* (1989). Due to limitations of the UDEC program, no fractures can be inserted that are not directly or indirectly connected to the model edges, hence all fractures are joined (McLellan and Oliver, 2007). For this reason the variably north-south trending Blue Flag Fault was connected to the Staveley Formation boundary in the north-east of the Greenmount area. A range of orientations of the maximum principal stress were numerically modelled to test the hypothesis of Laing (2004) amongst others. The stress conditions for the model are set at ratios of σ_1/σ_2=1.2 and σ_3/σ_2=0.8, resulting in a phi (Φ) value of 0.5.

The imposed stresses (σ_1=193 MPa, σ_2=175 MPa, σ_3= 157 MPa) represented approximately 7 km of overburden by an initial σ_2 value of 175 MPa. Rock and fault properties remain unchanged from the Mt Isa Western Succession modelling (Table 5.2). It was assumed that all the faults in the models were already present in their current configuration, based on observations that pre-ore albitite appears to passively overprint ductile deformation features (Figure 7.16).

Table 7.2 Model lithological and fault contact input parameters. All contacts in the model are treated as faulted contacts.

Property	*Quartzite*	*Shale*	*Siltstone*	*Metabasalt*	*Lithological contact*	*Fault*
Density (kg/m3)	*2600*	*2650*	*2400*	*2650*		
Bulk modulus (Pa)	*40e9*	*40e9*	*16e9*	*49e9*		
Shear modulus (Pa)	*25e9*	*7e9*	*11e9*	*27e9*		
Cohesion (Pa)	*20e9*	*5e9*	*10e9*	*20e9*	*3e3*	*5e2*
Tensile strength (Pa)	*10e9*	*3e9*	*5e9*	*10e9*	*3e6*	*2e6*
Friction angle (°)	*31*	*37*	*32*	*31*	*35*	*30*
Dilation angle (°)	*2*	*5*	*2*	*2*	*5*	*5*
Normal stiffness (Pa/m)					*2e9*	*5e9*
Shear stiffness (Pa/m)					*5e5*	*8e4*
Permeability factor (Pa/s)					*238*	*300*
Aperture at zero normal stress (m)					*0.03*	*0.05*
Residual hydraulic aperture (m)					*0.01*	*0.03*

7.6.2 Numerical Modelling Results – White Range Anticline

The best fit UDEC models were obtained when σ_1 was oriented ESE-WNW (112.5º-292.5º). Model success was based on low values of σ_3, σ_m and Pf_F occurring in at Greenmount, Vulcan and Mt McCabe locations.

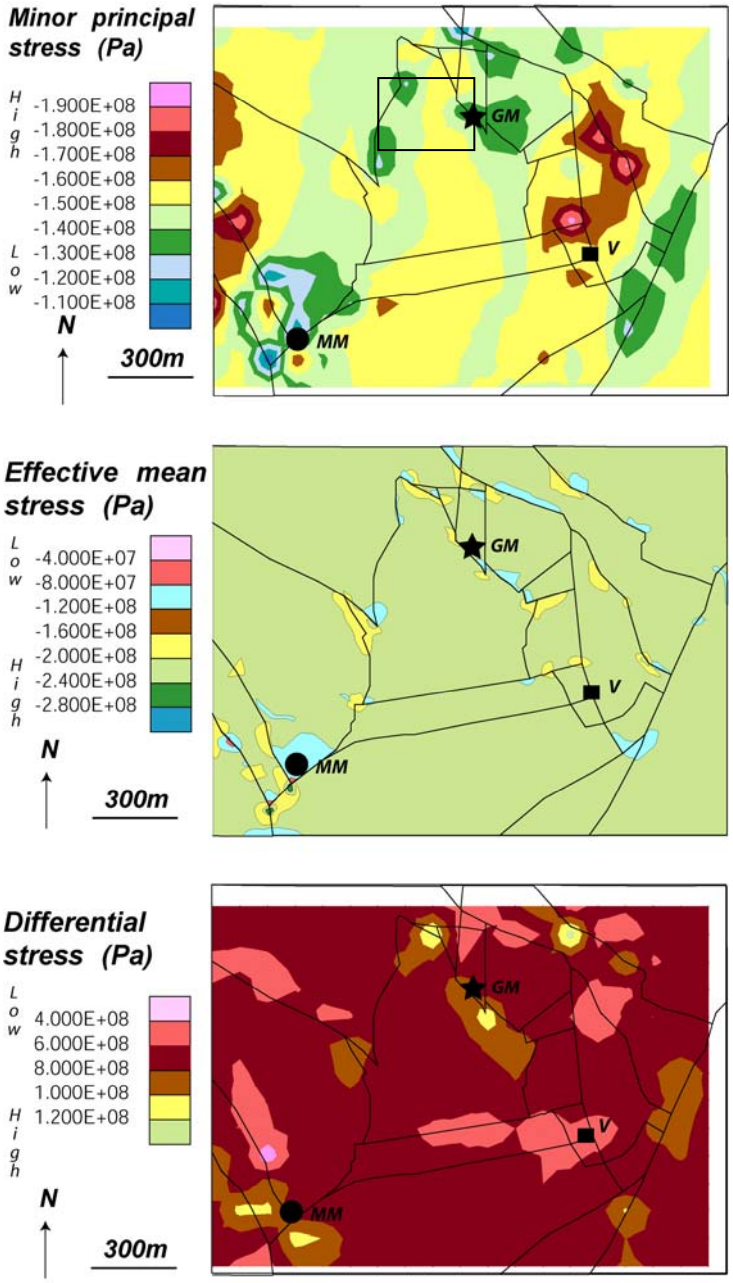

Figure 7.22 *White Range Anticline numerical modelling outputs. The conceptual model geometry was constructed from figure 7.5. The diagrams show the results from a whole White Range Anticline model run in an ESE-WNW orientation. MM=Mt McCabe, GM=Greenmount and V=Vulcan* ***(a)*** *Plot of minor principal stress. Low values of σ_3 are seen on the Marimo Slate side of the Marimo Staveley contact. Box over Greenmount will be further analysed in section 7.6.3 and Figure 7.23.* ***(b)*** *Plot of mean stress. Again low values of σ_m are seen on the Marimo Slate side of the Marimo Staveley contact.* ***(c)*** *Low differential stress values are seen on the north of the Marimo-Staveley contact.*

7.6.3 Numerical Modelling Results – Greenmount

This section will focus on the results within the immediate Greenmount area (see inset on Figure 7.22 top)

The plot of minor principal stress shows the lowest values within the Marimo Slates proximal to the Staveley Formation contact (Figure 7.23a). Minor principal stress values as low as 100 MPa were seen in the Marimo Shales relative to values of approximately 150-160 MPa in the Staveley Formation. The Staveley Breccia Hill however exhibited extremely low values of σ_3 also. This suggests that the hill would have preferentially brecciated during ESE-WNW shortening.

Plots of mean stress also showed significantly lower values within the Marimo Slates relative to the Staveley Formation (Figure 7.23b). The values of σ_m were approximately 140 to 160 MPa within the Marimo Slates as opposed to values of 200 to 220 MPa in the Staveley Formation. The lowest σ_m values were seen in the northern most section of the Staveley Breccia Hill where values of 100 to 120 MPa were reached.

Differential stress values (Figure 7.23c) in the Greenmount deposit area were extremely low (20-40 MPa) indicating a likelihood for the Marimo Slate to fail in extensional shear. Again the Staveley Breccia Hill showed low values of differential stress consistent with failure in tension, and or brecciation.

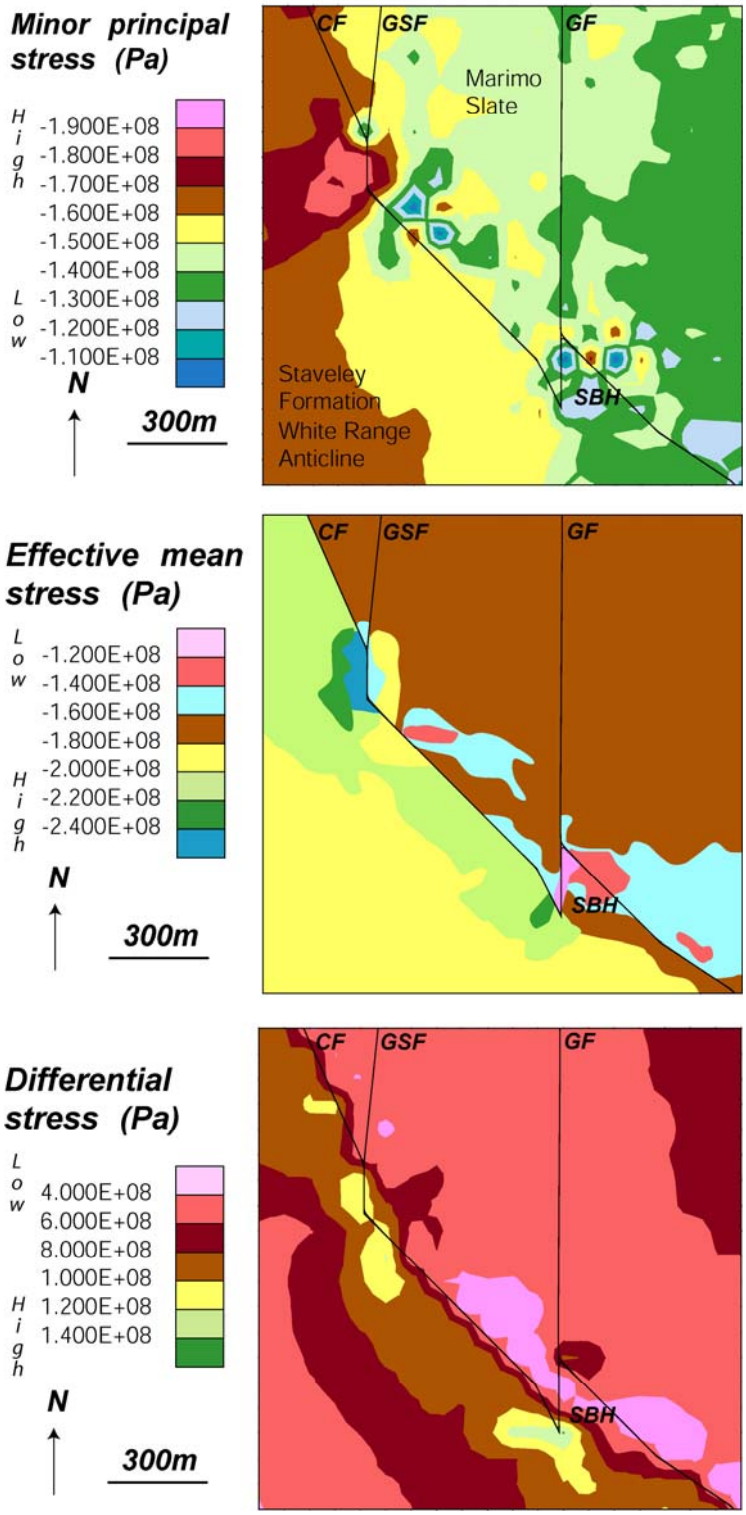

Figure 7.23 Numerical modelling outputs. The diagrams represent a zoom into the Greenmount ore zone, from a whole White Range Anticline model. SBH=Staveley Breccia Hill, GF=Greenmount Fault, GSF= Greenmount Shaft Fault and CF=Caravan Fault. ***(a)*** *Plot of minor principal stress. Low values of σ_3 are seen on the Marimo Slate side of the Marimo Staveley contact.* ***(b)*** *Plot of mean stress. Again low values of σ_m are seen on the Marimo Slate side of the Marimo Staveley contact.* ***(c)*** *Low differential stress values are seen on the north of the Marimo-Staveley contact.*

7.7 Discussion

The White Range Anticline formed at regional D_2 and developed a strong NNW trending S_2 fabric in the Marimo Slate. Regional D_2 occurred between 1595-1575 Ma (Rubenach *et al*., 2007) associated with the regional peak metamorphic event. This event also aligned tourmaline and rutile aggregates particularly in the Staveley Formation.

The ENE-WSW regional D_3 shortening event (Rubenach *et al.,* 2007) locally produced small NNW-trending folds, with steep axial surfaces. It produced a crenulation cleavage that is often recognisable in hand specimen. Brittle reactivation along S_2 has formed steeply dipping, large, N-S striking faults (Greenmount Fault and Greenmount Shaft Fault). These faults have displaced the Staveley-Marimo contact and the Staveley Breccia Ridge breccia with an apparent sinistral sense of movement.

The albite alteration in the Marimo Slate, in close proximity to the Staveley Formation contact, is concentrated around bedding and the dominant slaty S_2 cleavage, hence it can be inferred that albitisation was at least post-D_2.

The presence of a small suite of microdiorites along the eastern limb of the White Range Anticline, may be related to localised albitisation of the Marimo Slates. This suite of microdiorites is potentially related to either the nearby Mt Angelay Granite or Saxby Granite. The Saxby Granite has been dated at 1527 Ma (Rubenach et al, 2007). This would be broadly consistent with the timing of a regional sodic-calcic alteration event (Oliver et al, 2004).

In most instances the albite has been weathered to kaolin and/or alunite (Mason, 1994). The remaining albite is sparsely distributed on the Staveley-Marimo contact at ~9600 mN and on the eastern side of the Staveley Breccia Hill. Although sparsely distributed the albitisation of the precursor shales is extremely intense, to the point of complete replacement.

Mineralised microcline-quartz veins overprint albitite. Stewart (1991) and Krcmarov (1995) documented the relationship between the microcline-quartz veining and the copper mineralisation. The microcline-quartz veining also takes up the bedding and S_2 cleavages. Flitch plan interpretation of 0.5% copper grade distribution completed by Alston (2004) (Figure 7.18) also shows the bedding parallel and S_2 cleavage parallel orientations to the ore lodes. The complex nature of this copper distribution was unable to be replicated in 3D with the software available.

Numerical modelling has shown that an ESE-WNW σ_1 event was most likely responsible for the dilation at the Greenmount, Mt McCabe and Vulcan prospects.

Steep ore shoots, thickest along the S_0/S_2 intersection suggests that fluid migration and mineralization accompanied reactivation of earlier fabrics. The steep orientation of the L^0_2 intersection may have facilitated sub-vertical fluid movements tapping far field reservoirs.

Modelling at the broader scale than the WRA models shown here may provide an explanation of why brecciation occurred in the location of the orebodies. At the scale of this modelling, the most important control appears to be the contact between the Stavely and Marimo Formations.

8. DISCUSSION

This study indicates that fluid flow leading to copper mineralisation in many Mt Isa Inlier deposits was controlled by a far-field σ_1 orientation of ESE-WNW that occurred late in the Isan Orogeny. The ESE-WNW shortening event (D_4), has been recognised as a subtle deformational event that is expressed in the deposits by brittle fault reactivation-related brecciation and creation of mineralised extensional veins.

All Mt Isa copper deposits, both IOCG and carbonate hosted, display some degree of structural control in the localisation of ores into their current locations. Copper mineralisation is typically hosted by breccias, faults, shear zones and veins.

The structural controls on localisation of the copper deposits are of particular interest as the mineralisation in many of the copper deposits, both carbonate-hosted and IOCG, has been age dated at ~1530 Ma. The obvious exception to the ~1530 Ma mineralisation age is the Osborne Mine in the south of the Eastern Succession, which has two dates associated with mineralisation. Shear and D_2 foliation hosted ores at Osborne have been dated (U-Pb zircon) at 1595 Ma (Rubenach *et al.*, 2001), with a significant component of breccia hosted ores dated with an apparent maximum age of 1540 Ma (Perkins and Wyborn, 1998).

The 1595 Ma copper lies in D_2 flexures of a silicified halo that contains an S_1 fabric (Oliver et al., 2007). The 1595 Ma copper emplaced at Osborne represents the oldest dated copper mineralisation in the Mt Isa Inlier. There is speculation that 1595 Ma copper may also exist at the Selwyn - Starra orebodies and Eloise Mine (Davidson and Large, 1989; Oliver *et al.*, 2007). Overprinting structures at all of these deposits have the characteristics observed elsewhere in this study for later copper mineralisation.

Uranium enrichment at the Mary Kathleen orebody commenced as early as 1740 Ma, but final ore formation occurred between 1550 and 1500 Ma in fractures associated with the Mary Kathleen Shear Zone (Page, 1983; Oliver et al., 1999). Similarly the long-standing controversy over timing of Pb-Zn introduction in the district, centres on stratiform Pb-Zn (presumed syn-genetic by most researchers) and a very strong overprint or renewed mineralisation late in the Isan Orogeny (e.g. Mt Isa, Davis, 2005; Cannington, Chapman et al., 1998).

However, despite some deposits having formed pre-1530 Ma, the majority of copper deposits formed at 1530 Ma and most other deposits appear to have been strongly reworked or remineralised

at 1530 Ma (e.g. Oliver et al, 2007) under a stress regime consistent with that proposed in this study at D_4.

The proposal of this thesis, that much of the copper mineralisation in the Mt Isa Inlier was largely associated with ESE-WNW shortening at D_4 (~1530 Ma), raises several questions:

- With the exception of Osborne (dates on mineralisation ~1595 Ma and ~1530 Ma), why is all other copper mineralisation in the Mt Isa Inlier associated with a 1530 Ma time specifically?
- What changes are there in the structural localisation mechanisms at 1530 Ma, relative to earlier deformation events?
- How can an understanding of the mechanical processes assist in the exploration for further copper deposits?
- What are the potential fluid sources that would accommodate 1530 Ma mineralisation over an Inlier-wide scale?

These questions will be approached in this chapter by:

- Recognising the extent of the ESE-WNW shortening D_4 event across the Mt Isa Inlier. This section will compare and contrast the observations of previous workers against the conclusions of this study in an attempt to determine whether the D_4 event is truly a regional event.
- Reconciling the deformation and exhumation history of the Mt Isa Inlier in order to determine the specific conditions of each deformational stage of the Isan Orogeny. From this analysis, the specific nature of the 1530 Ma deformation will be compared to earlier phases of deformation, in order to determine the characteristics that made it suitable for ore formation.
- Explaining the relationship of mineralisation to faulting in the Mt Isa Inlier and determining possible mechanical processes that lead to the localisation of copper hosting-brecciation.
- Determining a geodynamic framework that can adequately explain the Inlier-wide mineralisation event.

8.1 Other studies showing evidence of an ESE – WNW D_4 shortening event

8.1.1 Regional stress mapping

Holyland (1990) and McLellan and Oliver (2007) conducted regional scale UDEC modelling of the Mt Isa district. Holyland (1990) used a fault database to identify the location of the Mt Isa copper deposits.

McLellan and Oliver (2007) conducted regional scale UDEC modelling of the Mt Isa Eastern Succession. Two primary conceptual models were based on distinct temporal periods. The first was based on a 1540-1530 Ma time frame, being post metamorphic peak and containing the older plutons of the Eastern Succession but being pre-emplacement of the Williams and Naraku Batholiths. The second model tested a 1530-1480 Ma time frame, where additional younger fault architectures and the Williams and Naraku Batholiths were added to the first model. Several permutations of both models were analysed including the orientation of σ_1 and the influence of changing fluid pressures.

McLellan and Oliver (2007) found that modelled areas of low minor principal stress and low mean stress spatially correlated best with the known deposits when σ_1 was oriented ESE-WNW (112.5º-292.5º), particularly in the post Williams–Naraku model. However these areas of low σ_3 and low σ_m, did not clearly correspond to specific fault orientations or configurations. Rather, the models produce complex zoning of stress anomalies in response to the partitioning of stress across complex fault blocks, and the interaction between more competent granitoid bodies, less competent meta-sedimentary rocks, and the fault and rock boundary complexities (McLellan and Oliver, 2007).

McLellan (2007) conducted a similar regional scale UDEC analysis of the Mt Isa Western Succession. For ease of interpretation the Western Succession modelling outputs were observed in two separate map areas. The map areas that will be further discussed are the Northern Leichhardt River Fault Trough (NLRFT) and the southern region, incorporating the Mt Isa Valley (Chapter 3.2.1) and the Sybella Granite. The Western Succession numerical modelling also tested a range of σ_1 orientations.

The overall values of dilation are similar in the E-W and SE-NW models; however the ESE-WNW shortening model has a notable increase in values of dilation in comparison to the other two models. The main interesting feature of this model is the broad dilation zone over the Mount Isa and Hilton location (Figure 8.1), which is not so evident in either the E-W or the SE-NW models. Similar patterns were observed in the distribution of low Pf_F and low σ_3 values where values are up to 20 to

40 MPa less in certain localities including Mt Isa, Hilton and other areas immediately east of the Sybella Granite.

In the northern region of the Leichhardt River Fault Trough, the distribution of σ_3 in the E-W shortening model, displays lowest values associated with fault intersections, bends and on the edges of competent intrusive bodies (McLellan, 2007). A somewhat similar distribution of σ_3 is seen when the stress field is rotated by 22.5° (ESE-WNW) with the ESE-WNW shortening model displaying lowest values around intrusive bodies and fault intersections, with a notable absence of lower values in the centre of the region. This observation is significant as the centre of the NLRFT is relatively devoid of mineralisation. Rotation of the stress field to and ESE-WNW direction has also resulted in lower overall values of σ_3 by around 40 MPa in some cases.

As with the McLellan and Oliver (2007) Eastern Succession modelling, the Western Succession modelling was also seen to show the best correlation between the modelled areas of low σ_3, low Pf_F, high volumetric increase or dilation (ψ) and the known areas of copper mineralisation when σ_1 was oriented ESE-WNW. This corresponds well with recent work carried out in the Eastern Succession of the Mount Isa Inlier, and suggests an inlier-wide stress regime may have been responsible for much of the Cu and Cu-Au mineralisation in the region (McLellan, 2007).

Again these modelled areas of interest do not clearly correspond to specific fault orientations or configurations, but again response to the partitioning of stress across complex fault blocks. In this sense, it is not possible to be entirely predictive only at prospect-scale because most of the known mineralisation discussed here lies within, (or is presumed to lie within), such favourable corridors.

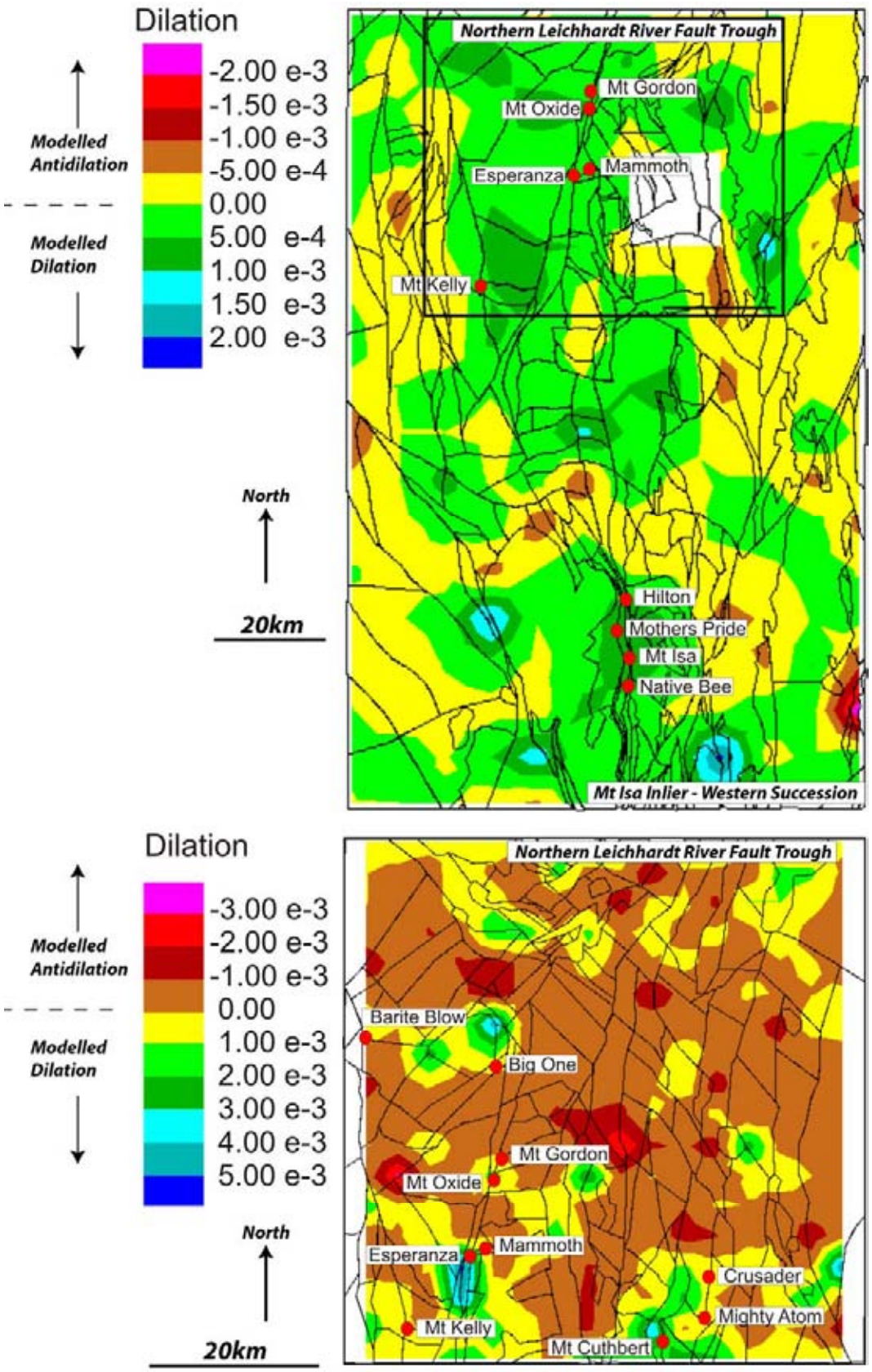

Figure 8.1 (from McLellan, 2007) Western Succession UDEC modelling showing predicted sites of dilation correlating well with known copper deposits (red dots). When viewed in detail, the Northern Leichhardt River Fault Trough (below) is seen to be a very good fit between predicted and actual sites of copper mineralisation.

8.1.2 Regional Fault Studies

Stark (2003) completed an Honours thesis on strike-slip faulting in the Mt Isa Inlier. The work was particularly focussed around three main regional faults, which vary widely in morphology and geological setting. The thesis aimed to analyse the fault slip data in order to evaluate the mechanics involved with their movement. The faults studied were;

- The Spillway Fault
- The Diagonal Fault
- The Thrust Fault
- The Overlander Fault
- The Fountain Range Fault

The absolute timing of these fault slip movements was not established in this study and limits the confidence to which these observations can be directly attributed to D_4. However the observations made by Stark (2003), that the slickenlines measured on the faults recorded a late-stage, strike-slip stress event, are consistent with D4 observations from elsewhere in the Inlier for the D_4 event.

The Spillway Fault is located near Lake Moondarra, some 20 km north east of the Mt Isa Mine. The Spillway Fault is well exposed over its 4 km strike length. The Spillway Fault is a NW-SE trending fault, inferred to be late deformational and one of a set of NW-SE trending faults that dominate the Leichhardt River Fault Trough. Stark (2003) inferred that the Spillway Fault had a series of conjugate faults locally (a NW-SE trending fault set and the ENE-WSW Spillway Fault) and that similar orientations to both fault sets were repeated often at a regional scale (Stark, 2003).

The kinematics of the faults as determined by Stark (2003) are evident of E-W to ESE-WNW shortening in all but one of the fault sets. The Overlander, Spillway and Thrust faults all showed evidence of E-W to ESE-WNW shortening, whereas the Diagonal Fault (which may be a different fault generation) did not.

The Overlander Fault is also an ENE striking fault that was incorporated into the Stark (2003) thesis. It is located approximately 10 km north of the Fountain Range Fault, which in turn is located approximately 100 km east of Mt Isa. Comparisons between the similarly oriented Diagonal Fault and Overlander Fault were conducted to determine whether these faults were potentially active in the same deformation event. Although similarly oriented, the two faults were mapped by Stark (2003) as having opposite senses of movement.

The results of this study are significant as the orientations of most faults mapped by Stark (2003) share similar characteristics to faults seen at Mt Gordon. Displacement vectors are also seen to be consistent with those mapped at the Mammoth Mine (Chapter 2.5) and Investigator Prospect (Chapter 5.6). Furthermore, the field relationships of brecciation and mineralisation mapped by Stark (2003) are similar to those associated with high grade mineralisation underground in the Mammoth Mine (Chapter 2.6). The mapping of Stark (2003) shows a skarn body near the intersection of a ENE-WSW trending fault and a NW-SE trending fault (Figure 8.2). This skarn is described in the accompanying text as fault and breccia infill of sulphide-rich quartz and bladed barite crystals (to 70%), with minor malachite and azurite (~2%). These are potentially significant quantities of mineralisation to be seen in outcrop, and such mineralisation correlates with the ENE-WSW and NW-SE fault orientation intersections at the Mammoth Mine, which were often seen to contain the strongest brecciation and the highest copper grades (Chapter 2.6).

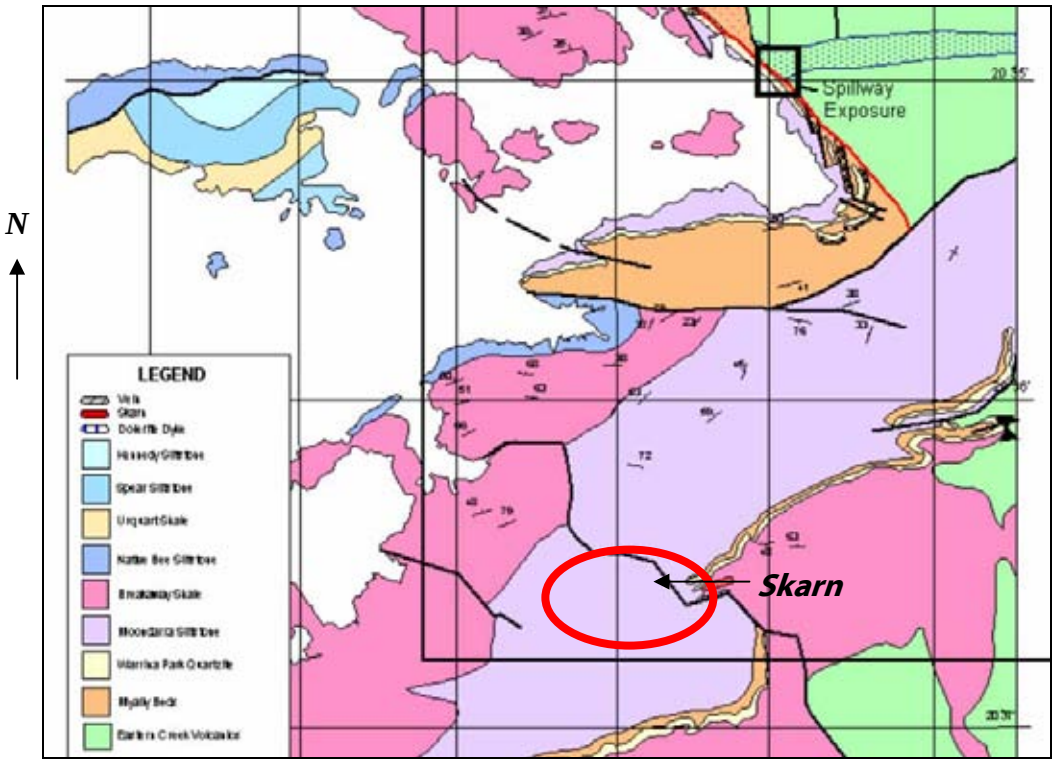

Figure 8.2 (from Stark, 2003) The mapped exposure of the Spillway Fault Area. The red circle highlights the location of a skarn body. This mineralised body sits in the intersection of an ENE-WSW striking fault and a NW-SE striking fault. These orientations of faulting are similar to those that are associated with the highest copper grades and most intense brecciation at the Mammoth Mine.

Austin and Blenkinsop (2008) confirm the extensive brecciation and albitisation at ~1530 Ma from regional field mapping of the Cloncurry Fault, in the Eastern Succession. Although not

specifically related to copper mineralisation, they document the transition from an ENE-WSW shortening producing NNW or SSE plunging folds at D_3, to a brittle strike-slip event coincident with massive Na-Ca brecciation at D_4 (figure 8.3). The inferred sense of movement on the NNW striking Cloncurry Fault is sinistral at D_4, from which Austin and Blenkinsop (*in press*) have inferred that the σ_1 orientation was approximately SE-NW. Intrusive magmatism and IOCG, Cu and Au mineralisation are spatially and temporally related to the D_3-D_5 history of the Cloncurry Fault Zone (Austin and Blenkinsop, *in press*).

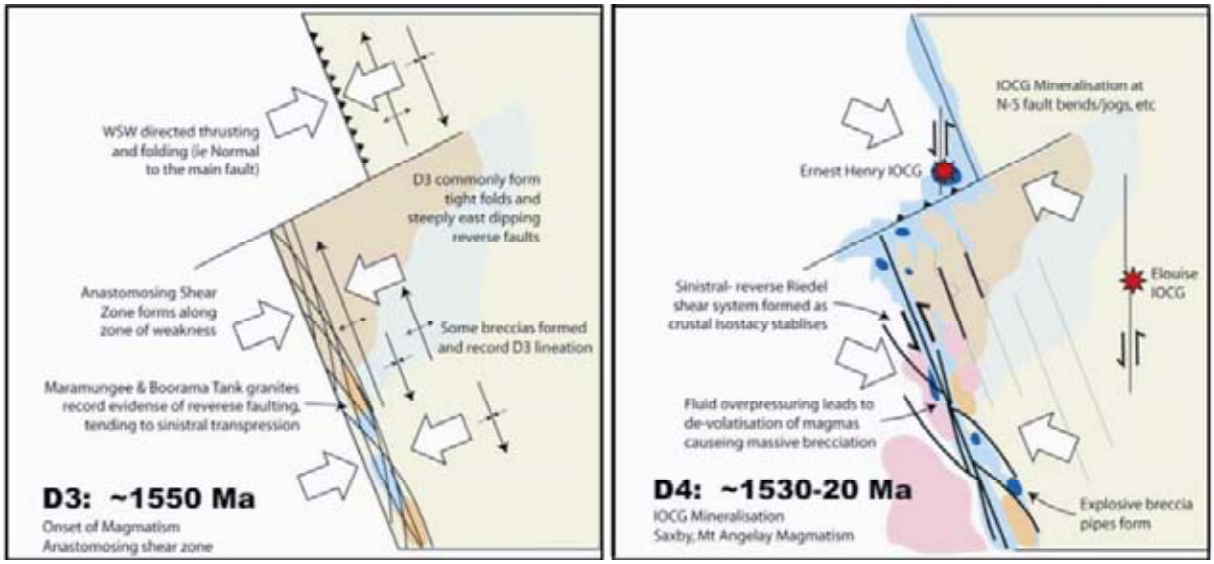

Figure 8.3 (from Austin and Blenkinsop, in press) Schematic interpretation of the D_3 and D_4 structural events along the Cloncurry Fault Zone.

8.1.3 Ductile deformation studies

The controversial FIA (foliation intersection axis) theory (Bell, 1995) proposes that porphyroblast inclusion trails can be used to define discrete periods and orientations of shortening events during regional metamorphism. The principle is that axes of curvature of discrete inclusion trail segments (FIAs) lie orthogonal to shortening vectors of individual deformation phases. Even if Bell's (1995) FIA theory is dismissed, the alternative theory maintains that the FIAs represent axes around which porphyroblasts rotated and could therefore approximate a line orthogonal to a shear vector (Figure 8.4).

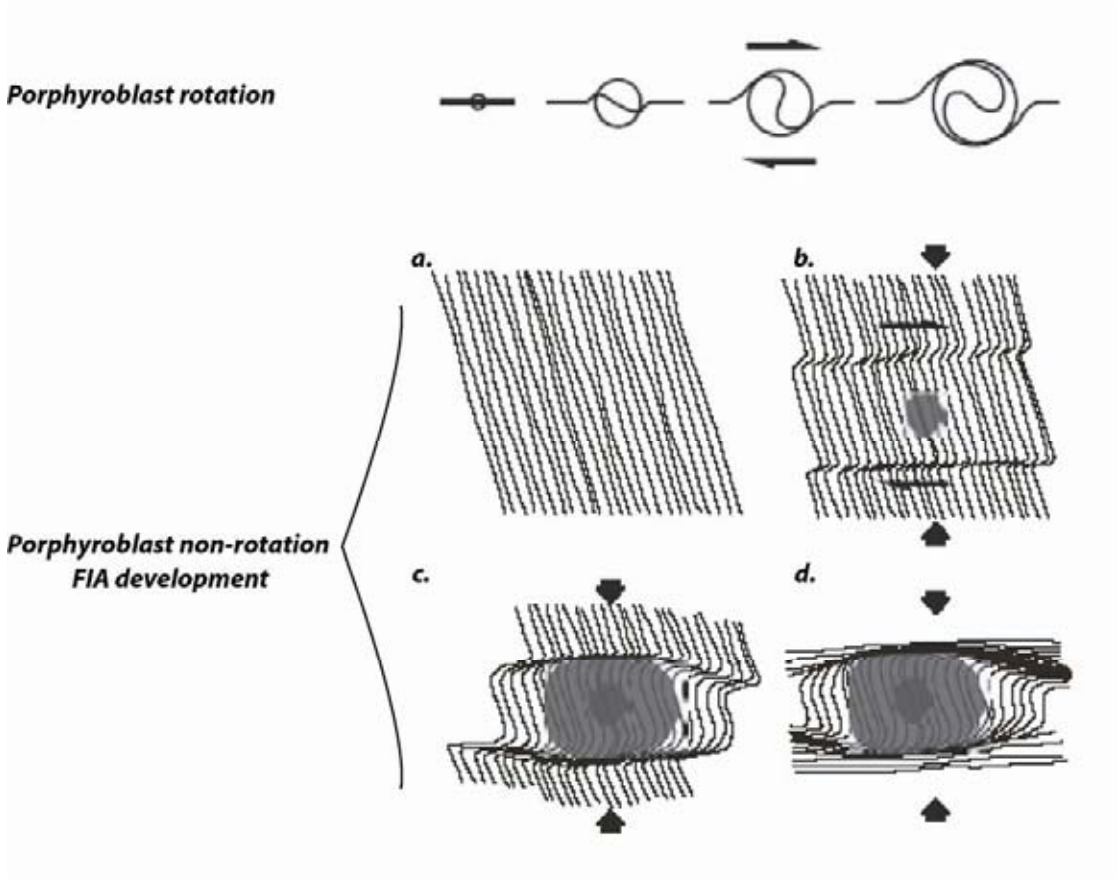

Figure 8.4 (adapted from Huddlestone-Holmes, 2005) Figure showing the two conflicting hypotheses on porphyroblast growth and development of inclusion trails. The porphyroblast rotation hypothesis (top) associates growth of the porphyroblast while being rotated by shear on the foliation. The stages of porphyroblast non-rotation hypothesis (FIA development) showing the progressive development of curved trails during deformation partitioning. (figures bottom) ***(b)*** *A porphyroblast grows in the crenulation hinge.* ***(c)*** *Porphyroblast eventually overgrows the curvature of the sub-vertical foliation into the flat foliation* ***(d)*** *The deformation intensifies against the edge of the porphyroblast which has stopped growing.*

None of the deposits studied here occurs in rocks that record porphyroblast growth during D_4, due to the low metamorphic grade. However, in several locations of high metamorphic grade, Sayab (2007) has recorded FIAs in porphyroblasts near granites of the Williams Batholith. Many phases of this batholith intruded at 1530-1520 Ma (Page and Sun, 1998). The last of the FIA sets recorded (FIA 5; Sayab, 2007), at the Snake Creek Anticline near the Saxby Granite, was inferred to have formed during a phase of ESE-WNW shortening (Figure 8.5).

Rubenach *et al.* (2007) also document an ESE-WNW shortening event in the Snake Creek Anticline area, expressed as NNE crenulations in several localities near the intruding Saxby Granite (1527 Ma). It is suggested that the granite intruded during D_4 and that deformation had ceased prior to

final solidification (Rubenach *et al.*, 2007). Microstructural analysis confirms that porphyroblast growth continued at least as far as the D_4 event, in the Snake Creek Anticline area (Rubenach *et al*., 2007).

This 1527 Ma Saxby Granite age also represents the D_4 (M_6 – low pressure metamorphism) event, and is consistent with the timing of extensive brecciation and late albitisation of calc-silicate rocks of the Corella Formation in the Selwyn Zone (Rubenach *et al.*, 2007). Thus these higher grade rocks appear to record evidence of an ESE-WNW shortening event synchronous with granite emplacement, and also synchronous with deposition of IOCG deposits at lower metamorphic grades elsewhere.

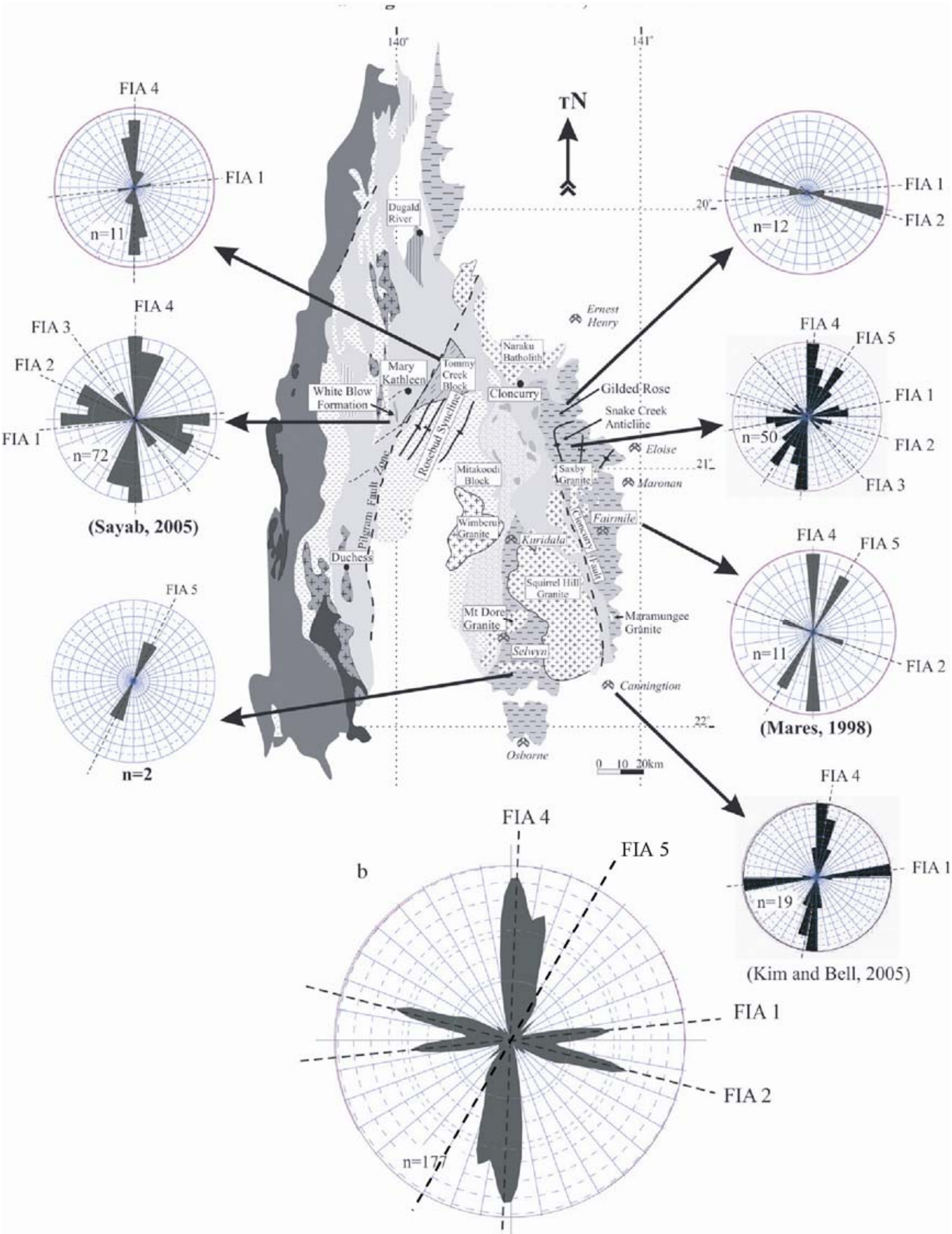

Figure 8.5 (adapted from Sayab, 2007) (a) Equal area rose diagrams for successive FIA sets and their proposed correlation across the Eastern Fold Belt of the Mount Isa Inlier. FIA sets are named in order of oldest to youngest, hence FIA set 5 is the last preserved deformational/metamorphic event. As FIA's are developed orthogonal to the direction of shortening, FIA 5 correlates to an ESE – WNW shortening event. It is inferred that Snake Creek Anticline, Fairmile and Selwyn preserve evidence of ESE-WNW shortening late in the deformational history. (b) Total FIA measurements from the Mount Isa Inlier at 1° interval using Spheristat software.

8.1.4 Summary of ESE-WNW observations

This study has shown five deposits for which the active σ_1 orientation at mineralisation was ESE-WNW. Constraints on the timing of this deformation event are from the Snake Creek Anticline D_4 age of 1527 Ma (Rubenach *et al.*, 2007) and the limited deposit depositional age dates of copper mineralisation between ~1510-1530 Ma (Perkins and Wyborn, 1998; Oliver et al., 2004; Mark et al, 2006).

Several authors have mapped or modelled the late Isan Orogeny (D_4), ESE-WNW event. With the exception of McLellan and Oliver (2007) and McLellan (2007), this D_4 event has only been determined locally, or on the one fault strand. As more of these studies have been collated, it seems possible, if not probable, that the ESE-WNW shortening event was an Inlier-wide occurrence (Figure 8.6).

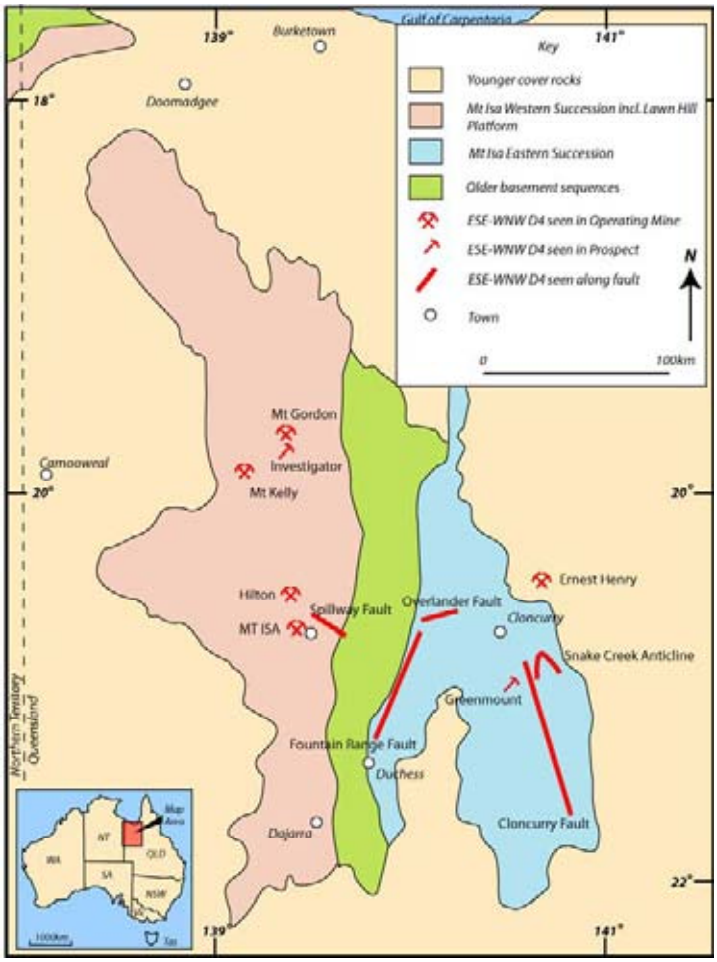

Figure 8.6 The various locations documented (in this study and discussed previously) that show evidence of an ESE-WNW oriented shortening event associated with D_4 (~1530 Ma). This map shows that much of the Mt Isa Inlier shows evidence of the ESE-WNW shortening event. In all localities except near to the intruding Saxby Granite, the expression of the D_4 event is by brittle deformational features (e.g. breccias, veins, faults) and related mineralisation and alteration.

8.2 Relationship of ESE-WNW D4 to prospectivity studies

Mustard *et al.* (2005) and Ford and Blenkinsop (2007) both conducted weights-of-evidence based prospectivity analysis of the Mt Isa Inlier and the Ford and Blenkinsop (2007) study also applied the fractal methods to the weights of evidence modelling results within the Mt Isa Inlier. There is future potential for fusion of the geomechanical modelling with the prospectivity analysis, using for example the methods of Ojala *et al.* (2007) for the Lapland Greenstone Belt.

The Mustard *et al.* (2005) weights of evidence analysis incorporated a training data set consisting of 567 copper occurrences including Ernest Henry, Eloise, Osborne, Mt Elliot, and the Selwyn line. The prospectivity analysis set out to investigate the spatial relationships to copper of a considerable range of potential geological controls on copper mineralisation. The prospectivity analysis was aimed at evaluating the relative importance of a range of spatial variables including: host rock type, proximity to felsic granites or mafic intrusives, stream geochemistry (Cu and Au), faults, and geophysics (including magnetics, gravity and wavelet-processed potential field data or “worms”). A data driven approach was taken in view of the considerable uncertainty in genetic models for IOCG deposits. Spatial correlations were calculated across the Eastern Succession of Mt Isa Inlier at a unit area of 0.25 km^2, assuming the known deposits have a 0.25 km^2 area of influence. The spatial correlations were determined by a contrast value and a confidence value, with higher contrast values (C) being more indicative of a good spatial association (Mustard et al., 2005). As a rule of thumb Contrast values above 0.5 are considered reasonable and Confidence values above 1.5 considered better than random.

Table 8.1 (from Mustard et al., 2005) Rankings of the twelve critical ingredients for copper mineralisation in the Eastern Succession of the Mt Isa Inlier. Ranking 1 represents the best spatial correlation with the copper deposit training set.

Ranking	***Evidential Layer***	***Contrast***	***Confidence***
1	*Copper in rockchips (>249 ppm Cu)*	*2.50*	*36.31*
2	*Gold in rockchips (>0.11ppm Au)*	*2.38*	*26.45*
3	*Corella-Soldiers Cap Contact (750 m buffer)*	*1.87*	*13.98*
4	*Aeromagnetics (magnetic highs)*	*1.82*	*14.36*
5	*N-S and ENE faults (650 m buffer)*	*1.45*	*17.20*
6	*Mafic Intrusives (750 m buffer)*	*1.25*	*7.47*
7	*Lithologies (dominantly Cover Sequence 3)*	*1.21*	*5.09*
8	*Gravity (Gradients)*	*1.03*	*15.91*
9	*Bends on N-S and ENE faults*	*1.03*	*2.33*
10	*Metamorphic Grade (Amphibolite Facies)*	*0.98*	*7.85*
11	*Radiometrics (U/Th)*	*0.83*	*4.46*
12	*Williams and Naruku batholiths (4 km buffer)*	*0.64*	*3.36*

The parameters analysed were ranked from one to twelve in terms of their spatial association with the copper deposits. Not surprisingly anomalous copper and gold in rockchip samples provided the best spatial correlation with known deposits. This form of dataset is only useful in areas of outcropping rock.

Aside from rockchip results, the proximity to the Corella Formation-Soldiers Cap Formation contact was the next highest parameter of known Cu-Au occurrences with a C value of 1.8 and ranked third on the list. Aeromagnetic highs are also strong predictor of known Cu-Au occurrences with a C value of 1.82 (Mustard *et al*., 2005).

The combined N-S and NE orientated faults is the next best parameter for Cu-Au occurrences with a C value of 1.45. Proximity to mafic intrusions, lithology, gravity and fault bends associated with N-S and NE orientated faults and metamorphic grade are all moderately strong predictors of know Cu-Au occurrences, with contrast (C) values greater than 1, except metamorphic grade.

Proximity to the Williams-Naraku batholith (4 km buffer) had the lowest contrast (C) value of 0.63 and is a weak predictor of know Cu-Au occurrences. This conflicted with previous research which suggested that the Williams-Naraku Batholiths were a significant source of copper in the Mt Isa Eastern Succession (Baker and Laing, 1998; Oliver et al., 2004; Williams et al., 2005).

Ford and Blenkinsop (2007) followed up on the Mustard *et al.* (2005) work and showed that there was a strong correlation between known copper deposits and fault bends and fault intersections in both the Mt Isa Western and Eastern Successions (Table 8.2). In conjunction with fractal analysis of the weights of evidence results, Ford and Blenkinsop (2007) showed that a positive correlation

between the logarithms of contrast values obtained from the weights of evidence analysis and the clustering correlations obtained from the fractal analysis. The positive relationship between the fractal analysis and weights of evidence can be interpreted to indicate that the features that controlled the clustering of the copper occurrences in the Mt. Isa Inlier also controlled the localisation of the copper occurrences (Ford and Blenkinsop, 2007). Though the results indicate that the spatial relationship between the faults and the copper occurrences is stronger in the Western Succession than the Eastern Succession, their control on the copper occurrences in the Eastern Succession is also significant (Ford and Blenkinsop, 2007).

*Table 8.2 (from Ford and Blenkinsop, 2007) Results of correlation between clustering of copper occurrences and clustering of geological features using fractal analysis and contrast values obtained from weights of evidence analysis with corresponding confidence values. Note: *indicates significance at the 95% confidence level.*

Location	***Cu occurrences correlated with***	***Correlation***	***Contrast***	***Confidence***
East. Succ.	*Fault bends*	*0.696**	*0.798*	*2.249*
	Fault intersections	*0.658**	*0.617*	*3.332*
	Mafic intrusions	*0.885**	*0.536*	*3.723*
	Mafic intrusions+extrusions	*0.600*	*0.567*	*4.261*
West. Succ.	*Fault bends*	*0.823**	*1.469*	*2.921*
	Fault intersections	*0.862**	*2.330*	*4.006*
	Mafic intrusions	*0.670*	*0.623*	*1.208*
	Mafic intrusions+extrusions	*0.620**	*0.460*	*1.883*
	Mafic extrusions	*0.604**	*0.643*	*1.989*

Mustard *et al.* (2005) ranked not only the various orientations of faulting to copper occurrences, but also the orientations of fault bends and fault intersections to copper occurrences. The three highest ranking orientations of fault bend were related to a far-field σ_1 orientation of ESE-WNW to determine whether the spatial association could be explained by D_4 tectonics (Figure 8.7, 8.8). The three highest ranking fault bend orientations were all consistent with formation of dilatant fault bends during an ESE-WNW shortening event.

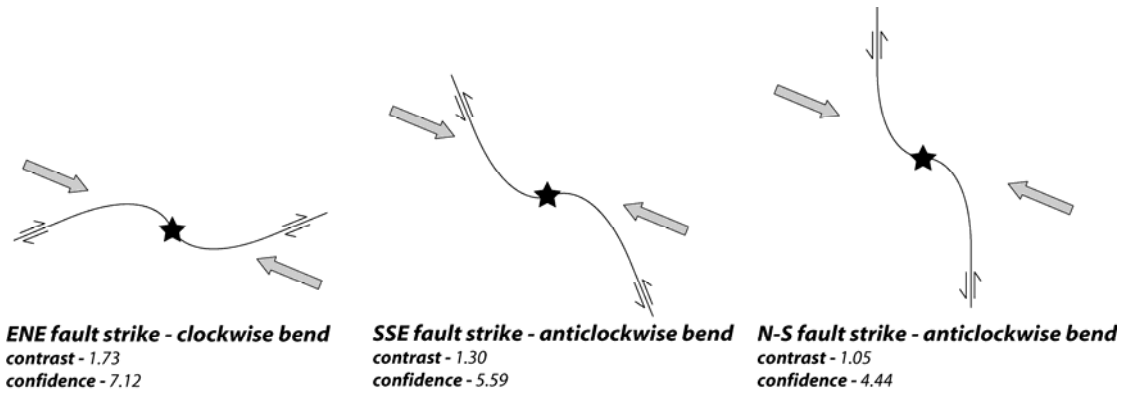

Figure 8.7 The three highest ranking fault bend orientations of Mustard et al. (2005), related to the ESE-WNW D_4 shortening orientation. All three orientations of fault bends would be predicted to be dilatant during ESE-WNW shortening.

Fault intersection weights of evidence analysis also predicted dilatant sites in intersection locations that match deposit scale scenarios. For example faults striking ENE-WSW and N-S, intersect at the Mammoth Mine (Chapter 2) in the location where the bulk of mineralisation is found. The N-S striking fault in this instance is the Portal Fault and the ENE striking fault is the Mammoth Fault.

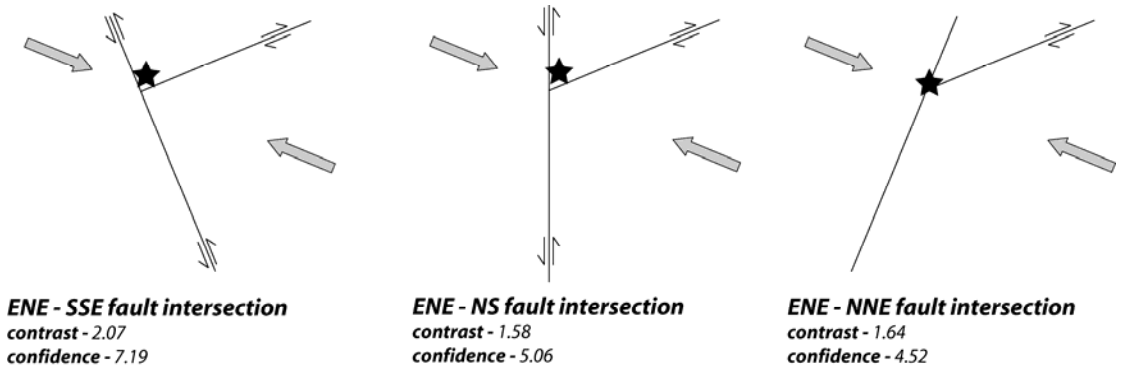

Figure 8.8 The three highest ranking fault intersection orientations of Mustard et al. (2005), related to the ESE-WNW D_4 shortening orientation.

Although some fault orientations, fault bend orientations and fault intersection orientations are seen to have better spatial relationships to mineralisation than others, not all favourably oriented structures are mineralised. It is worth re-iterating the observations of McLellan and Oliver (2007) and McLellan and Oliver (2007) that the interplay of faults and rock-blocks, often produce a complex zoning of stress anomalism in response to the partitioning of stress across complex fault blocks. This in turn may not create conditions whereby structures that are favourably oriented for brittle deformation do not respond predictably.

8.3 Deformation and exhumation of the Inlier

The Isan Orogeny (1610-1500 Ma) was the last major tectonic event and resulted in cratonisation by around 1500 Ma. Within that history, the D_4 deformation event appears to be the 'last gasp', synchronous with late-tectonic A-type granite emplacement and copper mineralisation.

Cratonisation can occur by removal of heat producing elements (K, U, Th) from the lower crust by granite genesis (e.g. McLaren et al., 1999). Alternatively, or in addition, exhumation of previously deeply buried crustal material can terminally affect continental plate boundaries, for example with trench retreat leaving continental interiors progressively removed from a heat source, thus cratonising it.

These two theories essentially appeal to a) internal processes of heat transfer versus b) external plate boundary considerations.

This brief review of the Isan Orogeny focuses on those parts of the tectonic evolution that could have given rise to the situation in which the last brittle deformation event was implicated in one of the world's most significant copper mineralising events. In the context of the Proterozoic evolution of north Australia, Mt Isa is particularly important as the Isan Orogeny may reflect the E-W collision of Laurentia and north Australisa (Giles and Betts, 2002). Whether elements of this collision relate specifically to the key ingredients for copper are explored here.

D_2

D_2 is recognised across the Mt Isa Inlier as a broadly ductile event. This E-W shortening event formed N-S folds with mainly steep axial planes and created an intense N-S oriented foliation across much of the inlier. D_2 represents the peak of metamorphism and is thought to have occurred at depths of 10-15 km, 500-700 ºC and 4 to 5 kbars (Rubenach and Foster, 2007; Rubenach et al., 2007; Sayab, 2007).

D_3

There is a noticeable change in the character of D_3 from D_2. D_3 is associated with significant faulting (e.g. Portal Fault at Mammoth, mine-scale faulting at Isa), local refolding of D_2 geometries (commonly into box folds and kink folds) and the formation of fracture cleavages and crenulation cleavages locally. The inferred orientation of σ_1 during D_3 varies locally between ENE-WSW (Snake Creek, Rubenach et al., 2007; and Mt Isa, Miller, 2006) and E-W (Page and Bell, 1986; Oliver et al.,

1991). The depth, temperature and pressure conditions on D3 are inferred to be ~10 km, 500 ºC and 4 kbars, but constraints are few (Rubenach et al., 2007).

D_4

Rubenach (2005), Sayab (2007) and Rubenach *et al.* (2008) document the specific nature of the D_4 event around the Snake Creek Anticline. When close to the intruding Saxby Granite (1527 ± 4 Ma) the expression of D_4 is NE- trending folds with steep axial surfaces, and crenulations and/or reactivation of the S_2 cleavage. These ductile D_4 structures are commonplace around the Saxby Granite but are not observed a few kilometres away from the Saxby Granite. Of the limited amount of documentation on the D_4 event, the only place that ductile deformation is associated with D_4 is around the Saxby Granite, apart from inclusion trails in porphryblasts in other rocks also proximal to the Williams Batholith intrusions (Sayab, 2007). Oliver et al. (2006) and Rubenach *et al.* (2008) mapped D_4 breccias cross cutting S_3 foliation that was associated with sodic-calcic alteration, some distance from the Saxby Granite. Elsewhere in the Inlier, D_4 is expressed as low strain deformation on brittle, often strike slip faults, as previously discussed. Orebodies formed during D_4 are hosted in large breccia zones, also formed in a brittle environment. This event is, in the literature, often lumped in with D_3, as previous authors have not recognised the significance of the ESE-WNW shortening, or overprinting of D_3 by D_4 was not observed, due to their discrete spatial localisation. The depth, temperature and pressure conditions on D_4 are inferred to be ~5 to 7 km, 300 ºC and 2.5 to 3 kbars, but constraints are limited to the Snake Creek Anticline area (Rubenach et al., 2007).

From this summation of the deformation events of the Isan Orogeny, it is not apparent that there has been a significant exhumation of the Mt Isa Inlier between D_2 and D_3. Between D_3 and D_4 however, it appears that there has been a pressure drop of approximately 1 to 1.5 kbars. This would imply an exhumation of ~3 - 3.5 km between D_3 and D_4.

Another noticeable feature of the deformation history of the Isa Inlier is the significant temperature change between the peak of metamorphism (D_2) and the mineralisation event (D_4). The rate of cooling is such that amphibolite grade rocks (~500 ºC) exhumed at D_3 may be at temperatures of 250–300 ºC by D_4.

Mustard *et al.* (2005) showed there was a poor spatial correlation with mineral deposits and the Williams and Naraku Batholiths in the Mt Isa Eastern Succession. In fact, of 12 critical parameters

for the formation of Mt Isa copper deposits tested using Contrast (a measure of association of training sites with the predictor features or patterns), the worst predictor for copper deposits was proximity to the Williams and Naraku Batholiths. This is a significant observation given that the Williams and Naraku Batholiths outcrop over 2400 km^2 and that many studies have suggested a magmatic component to the fluid source for some deposits (Baker and Laing, 1998; Oliver et al., 2004; Williams et al., 2005).

Areas proximal to the Williams-Naraku Batholiths are seen to locally achieve extremely high temperatures (Figure 8.9). The deformation style around these granites is typically documented as ductile deformation, including the foliation development at the Snake Creek Anticline (Rubenach et al., 2007). Across the Mt Isa Inlier, there appears to be a direct correlation between the deposition temperature and the deformation style, particularly around the Williams-Naraku Batholiths.

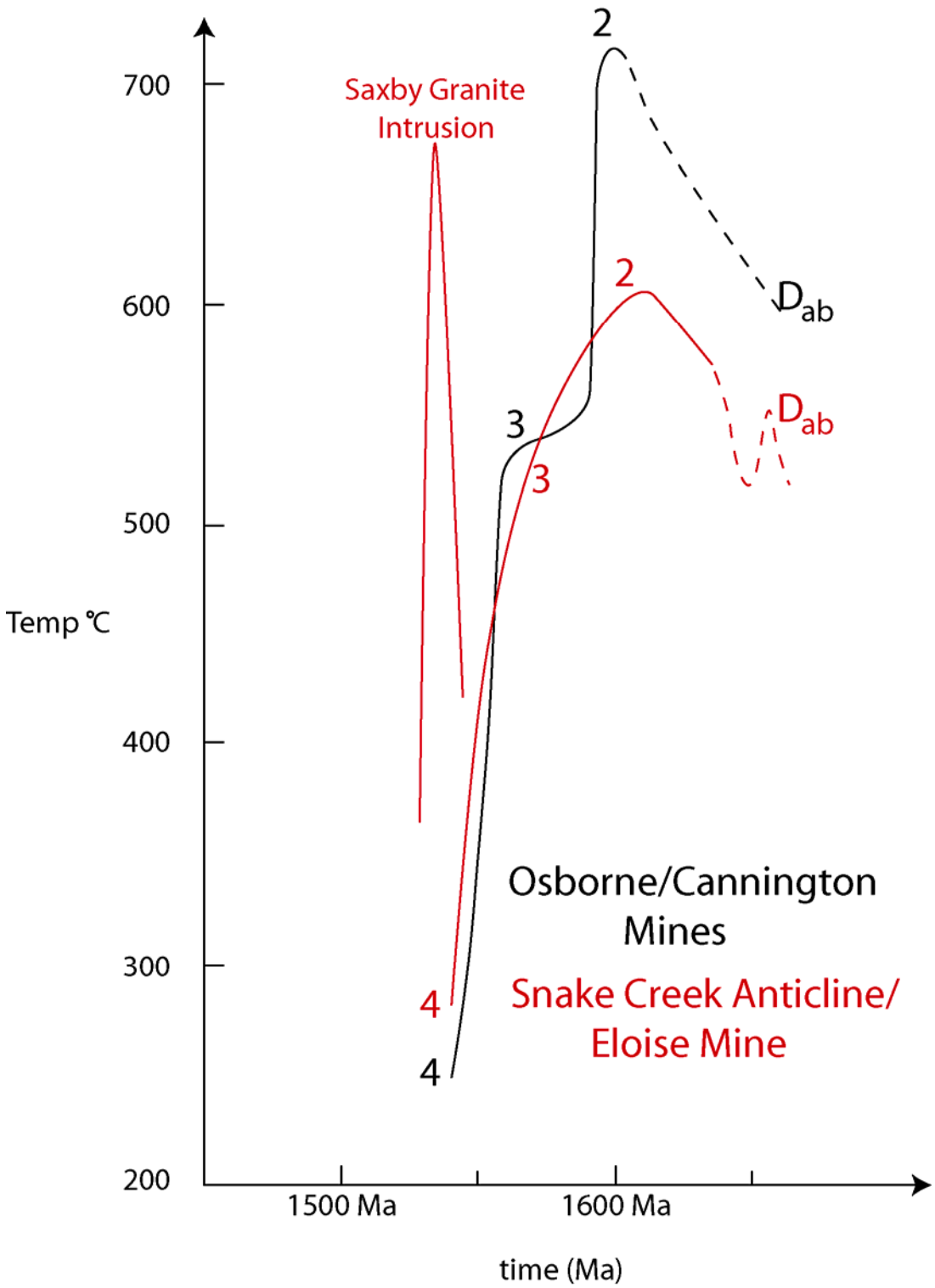

Figure 8.9 (from Rubenach, 2005) Suggested temperature-time diagram, for the Osborne/Cannington Mines (black) and the Snake Creek Anticline/Eloise Mine (red). D_{ab} –the intense albitisation event (~1640 Ma) of the Soldiers Cap Group. D_2 - metamorphic peak, followed by rapid cooling so that the 1595 Ma titanate ages were preserved at Osborne. D_3 – 1555 Ma closure for hornblende at Eloise. D_4 – 1530 Ma closure for biotite at Eloise (Baker et al., 2001). At the same time as biotite closure at Eloise, the Saxby Granite and gabbro intruded the southern part of the Snake Creek Anticline. Further west there was massive brecciation and albitisation around the Cloncurry Fault (Rubenach, 2005; 2007).

The temperature of the exhumed blocks may play an important role in the failure mode, and possibly mineralisation. Many authors have described the temperature conditions required for brittle failure, ductile failure and the brittle-ductile transition (Sibson, 1982; Scholz, 1988; Ranalli, 2000). Authors typically agree that the window for brittle failure is below ~350 ºC, which typically equates to depths of 8 to 10 km in an area with a high geothermal gradient (e.g. 30 to 40 ºC/km). This places some constraints on the ambient temperatures of the rock in the known deposit locations, although pore pressure and strain rate variations also influence failure mode for any given depth.

There are a few techniques that can be employed to determine the temperature of the host rock at mineralisation. One is Ar^{40}/Ar^{39} dating of mineralisation-related minerals such as hornblende, actinolite, muscovite (and other white micas) and biotite. U/Pb dating of monazite, hydrothermal zircon and apatite can also assist. There are uncertainties, but U/Pb closure temperatures for monazite and zircon are above 700 °C, U/Pb for titanite ~500-600 °C, Ar^{40}/Ar^{39} for hornblende ~450-525 °C, Ar^{40}/Ar^{39} for muscovite ~325- 375 °C, and Ar^{40}/Ar^{39} for biotite ~250-350 °C (Spear, 1993). For example an Ar^{40}/Ar^{39} date on hornblende will record the time that the hornblende stopped absorbing potassium, and hence the age that the rock temperature fell below 450-525 ºC. As brittle deformation is difficult to achieve above ~350 ºC, this rock would most likely experience ductile rather than brittle deformation at the Ar^{40}/Ar^{39} (hornblende) closure point. Similarly the closure temperature for biotite is ~250-350 ºC, meaning Ar^{40}/Ar^{39} (biotite) dates could reflect conditions under which rocks were more likely to undergo brittle deformation. At the lower temperature end, biotite Ar^{40}/Ar^{39} dates may represent a 250 ºC closure temperature, so the biotite age may even represent a time later (cooler) than that required for the onset of brittle failure.

From the Ar^{40}/Ar^{39} dating conducted by Perkins & Wyborn (1998), Baker *et al.* (2001), and Spikings *et al.*, (2001), hornblende closure at dates younger than 1530 Ma are often seen to occur in close proximity to the felsic granites of the Williams and Naraku batholiths. The data not surprisingly suggests that cooling may have been strongly influenced by proximity to plutonic intrusions. However, no exposed granites of Williams-Naraku Batholith age occur in the Mary Kathleen Belt where alteration-related hornblende and titanite ages of over 1524 Ma are recorded (Oliver et al., 2004; Rubenach, 2005). Also, there is scatter in the Ar^{40}/Ar^{39} data for amphibole and biotite for some localities, e.g. the Osborne Mine, suggesting processes such as ductile deformation, local high-

temperature fluid infiltration and veining may be important in addition to simple cooling through closure temperatures (Rubenach, 2005).

Rubenach (2005) has determined time-temperature curves for the Osborne Mine and the Eloise Mine (Figure 8.9). These mines are located in some of the highest metamorphic grade rocks in the Mt Isa Inlier. The rate of cooling following the metamorphic peak at D_2 is of particular interest as it may potentially represent a cooling rate for other exhumed blocks between D_2 and D_3, and D_3 and D_4.

From the time-temperature plots it is apparent that the highest metamorphic grade rocks in the Osborne Mine and Cannington Mine are cooling from over 700 °C at ~1600 Ma (D_2), to about 550 °C by 1550 Ma (D_3), to ~300 °C by 1530 Ma (Rubenach, 2005). This is an extremely rapid cooling rate which would typically correspond to the rate of exhumation at the onset of cratonisation in Phanerozoic belts. As the rate of exhumation may be relatively constant, the reason for the rapid cooling of rate between D_3 and D_4 is likely to be due to the onset of cratonisation accompanying final emplacement and cooling of the Williams Batholith.

Mustard et al. (2005) determined that there was a reasonable spatial association between amphibolite facies rocks and copper deposits, particularly in the Mt Isa Eastern Succession. The rapid cooling rate ensures that rocks that had reached amphibolite grade during D_2 or D_3 would still have had time to cool to within the brittle deformation limits of ~300-350 ºC (Scholz, 1988; Ranalli, 2000) by D_4.

The use of Ar^{40}/Ar^{39} closure dates may be useful in determining the likely nature of the mineralisation being explored for. Rocks showing Ar^{40}/Ar^{39} (hornblende) closure dates of 1530 Ma or younger were probably intrusion proximal or didn't cool quickly enough to deform brittley during D_4.

There is potential to take this technique even further and routinely Ar^{40}/Ar^{39} date rocks on either side of large fault zones to determine corridors or blocks that have potentially experienced brittle failure, for the 1530 Ma time period. Overlapping the cool rock corridors with the prospectivity study of Mustard et al. (2005) or the mechanical numerical modelling outputs of McLellan and Oliver (2007), may be useful exploration techniques.

An example of the application of this technique is proposed for the Mt Isa Copper Mine. An Ar^{40}/Ar^{39} cooling age for hornblende of 1460 Ma has been recorded west of the Mt Isa Fault, and Ar^{40}/Ar^{39} cooling age for biotite of 1523 Ma recorded in the mine sequence on the eastern side of the Mt Isa Fault (Perkins et al., 1999). This implies that there has been significant uplift of the high grade

rocks on the western side of the Mt Isa Fault no earlier than 1460 Ma or that the high radiogenic heat-producing granites (McLaren et al., 1999) to the west of Mt Isa (Sybella Granite) sustained temperatures of >550 ºC for ~200 million years. In either scenario the fact remains, that the western side of the Mt Isa Fault was far hotter than the ~350 ºC required for brecciation and brittle failure at 1530 Ma. The eastern side of the Mt Isa Fault however, is at temperatures well within the brittle failure window at 1530 Ma.

Conditions for the onset of brittle deformation are largely controlled by temperature, with temperatures greater than ~300 ºC indicative of the onset of quartz plasticity and a transition to ductile deformation (Scholz, 1988). There is a strong relationship between copper mineralisation and low temperature, brittley deformed rocks within the Mt Isa Inlier.

Conversely rocks preserving evidence of high temperatures during D_4 (1530 Ma) typically show evidence for ductile deformation (e.g. foliation development at the Snake Creek Anticline) and are rarely associated with economic copper mineralisation.

8.4 Other mechanical factors potentially influencing localisation

Mustard (2005) and Ford and Blenkinsop (2007) showed there is a close spatial association between long faults and copper occurrences in both the Mt Isa Western and Eastern Successions. Blenkinsop (2005) then observed that the longer faults are also seen to be rougher faults. Fault roughness is a function of the planarity or linearity of the fault and as such is affected by bends, intersections and offsets. Bends on fault surfaces affect fluid flow and can localise mineral deposits. The relation between roughness and length suggested that as faults grow, they become rougher. Blenkinsop (2005) hypothesised that it is the roughness, but not length of the fault that controls mineralisation. Fault roughness was calculated by the coastline method, which is a sensitive measure of fractal roughness (e.g. Aviles *et al.*, 1987). The exponent of a power law relationship between the length of a fault (P) and the ruler length (L) is used to derive D, a measure of the fault roughness:

$$P \sim L^{1-D}$$

D is the coastline dimension of the fault. A straight line has D = 1, and D increases with fault roughness (Aviles *et al.* 1987). Blenkinsop (2005) selected thirteen major well-exposed faults or fault segments from throughout the Mount Isa Inlier that dip vertically at surface, in order to exclude topographic effects, and to obtain reliable estimates of fault roughness. Copper mineralisation endowment (tonnes metal) was seen to be at least an order of magnitude greater along the rough faults relative to the intermediate and smooth faults.

Table 8.3 (from Blenkinsop, 2005) Table summarises the roughness measurements and mineral endowments, arranged in order of decreasing roughness as measured by the fractal dimensions. Rough faults are seen to contain copper endowments at least an order of magnitude greater than intermediate and smooth faults.

Fault	Fractal Dimension	Error	Cu* (t/km^2)	Pb* (t/km^2)	Zn* (t/km^2)	Ag* (kg/km^2)	Co* (t/km^2)
Rough faults							
Mt Gordon	1.008	0.0004	8.99E+02	0.00E+00	0.00E+00	6.91E-01	0.00E+00
Mt Isa	1.007	0.0013	1.13E+04	1.61E+04	1.52E+04	3.26E+04	1.09E+01
Intermediate faults							
Cloncurry South	1.005	0.0011	0.00E+00	0.00E+00	0.00E+00	0.00E+00	0.00E+00
Fountain Range	1.005	0.0005	8.44E+01	0.00E+00	0.00E+00	6.20E+00	0.00E+00
Mt Remarkable	1.004	0.0005	7.88E+00	0.00E+00	0.00E+00	6.39E-01	0.00E+00
Termite North&Central	1.004	0.0005	0.00E+00	0.00E+00	1.45E+04	5.68E+03	0.00E+00
Termite South	1.004	0.0011	0.00E+00	0.00E+00	0.00E+00	0.00E+00	0.00E+00
Pilgrim North	1.003	0.0001	3.33E-02	0.00E+00	0.00E+00	0.00E+00	0.00E+00
Smooth faults							
Pilgrim Central	1.002	0.0008	9.10E-03	0.00E+00	0.00E+00	0.00E+00	0.00E+00
Creek	1.001	0.0002	0.00E+00	0.00E+00	0.00E+00	0.00E+00	0.00E+00
Cloncurry North&Central	1.001	0.0007	6.90E-02	0.00E+00	0.00E+00	0.00E+00	0.00E+00
Pilgrim CentralSouth	1.001	0.0020	8.30E-03	0.00E+00	0.00E+00	0.00E+00	0.00E+00
Pilgrim South	1.001	0.0002	0.00E+00	0.00E+00	0.00E+00	0.00E+00	0.00E+00

* Resources and reserves associated with the faults

Sibson (1989) hypothesised that much of the displacement occurring in the upper half of the actively deforming continental crust was related to earthquake faulting (Figure 8.10). Sibson (1989) focussed on the effects of incremental slip within faults as opposed to the total displacement across faults and the finite deformation state associated with them. Earthquake and seismological theory suggests that there is continual stress cycling accompanying episodic incremental reactivation of active crustal faults (Sibson, 1989).

Sibson (1989) proposed that the base of the seismogenic zone represents a transition from unstable frictional (FR) faulting to quasi-plastic (QP) shearing flow localised in mylonite belts (Figure 8.10), and is inferred to be the region of peak shear resistance where larger earthquake ruptures tend to nucleate. This is potentially particularly relevant to this study as the base of the seismogenic zone is inferred to be restricted to temperatures of 300-350 ºC, the temperature conditions inferred for the D_4 event in the Mt Isa Inlier.

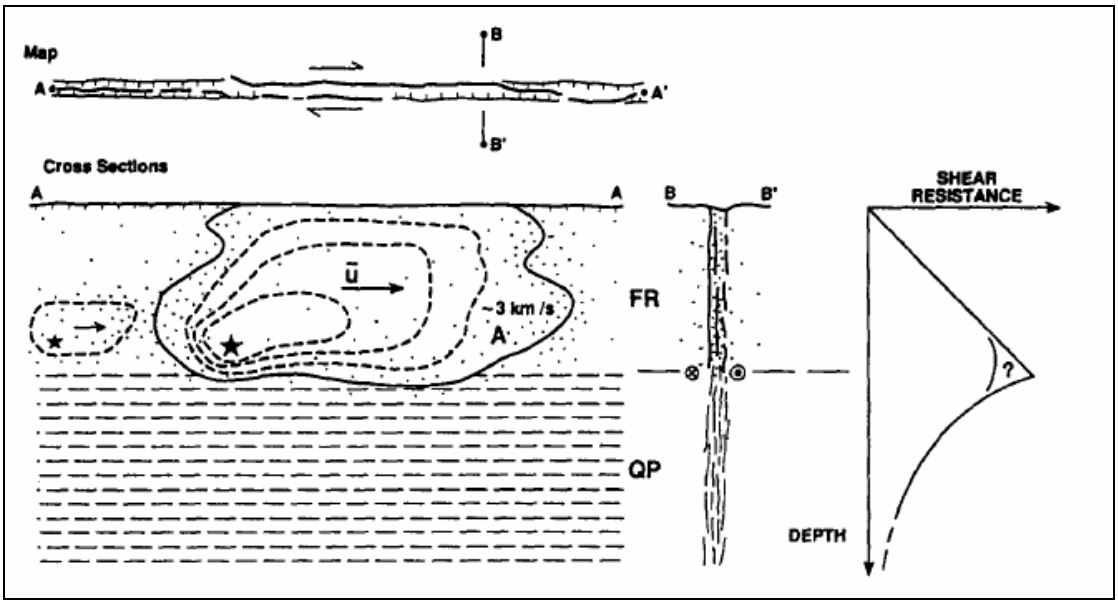

Figure 8.10 (from Sibson, 1989) Strike-slip earthquake rupturing within the seismogenic regime defined by background microseismicity and aftershock activity, shown in relation to a composite profile of fault shear resistance versus depth which peaks in the vicinity of the transition from unstable frictional (FR) faulting to localised quasi-plastic (QP) shearing flow (after Sibson 1986b). Longitudinal fault section shows large ruptures expanding over the fault surface at ~3 km s^{-1} from nucleation sites (stars) in the vicinity of the FR/QP transition. Mean slip, ũ is averaged over a final rupture area, A, which occupies all or part of the seismogenic zone,

Sibson (1989) suggested that future structural studies should be directed to the understanding of the dynamic character of fault reactivation during incremental slip. This would involve (Sibson, 1989);

- associating rheological and geometrical controls on the initiation, perturbation and termination of ruptures;
- rupture propagation direction effects;
- the recognition of structures resulting from repeated stress cycling within seismogenic crust, and
- identification of structural features diagnostic of shear stress levels during faulting.

Antidilational fault bends and jogs perturb ruptures and form obstacles to both incremental and long-term slip transfer along a fault (Sibson, 1989).

Dilational fault jogs however, are seen to be preferred sites of rupture termination (Sibson, 1986, Knuepfer et al., 1987). The rupture termination is generally followed by delayed slip transfer across the jog accompanied by localised aftershock activity, thus impeding rapid transfer but allowing slow slip transfer across the dilatant zone (Sibson, 1989).

The direction of rupture propagation is hypothesised to exert a significant control on the formation of cavity space at fault irregularities and hence have important implications for the development of fault-hosted mineralisation (Figure 8.11) (Sibson, 1989).

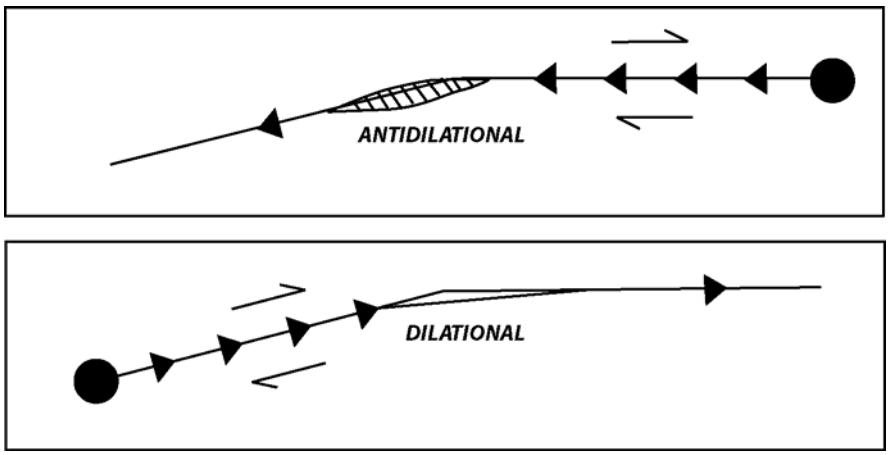

Figure 8.11 (from Sibson, 1989) Cartoon map illustrating the changing response of an isolated fault bend to rupture directivity on a right-lateral strike-slip fault. Solid circles represent earthquake epicentres.

Due to the complex deformation history of the Mt Isa Inlier and contention over the recognition of rupture points and indicators to the direction of rupture propagation, no definitive field evidence has been collected. However with significant amounts of exploration having been conducted in the Mt Isa Inlier, and with copper occurrences being well mapped, there is scope to use the locations of orebodies and deposits to speculate on potential directivity of rupture propagation. These directivity effects associated with rupture propagation may be relevant to determinations of potentially dilatant, and therefore potentially prospective areas for structurally controlled deposits.

The Mt Gordon Fault Zone, particularly between the Bluff prospect and the Mt Gordon deposit, is a good place to study the effects of earthquake faulting on copper mineralisation as it is a well explored section of a major fault zone, is one of the longest and roughest faults in the Mt Isa Inlier (Blenkinsop, 2005) and has been the focus of much work in this study. Although the cross and splay fault geometries are very similar, exploration of these systems isn't routine from one fault zone to another, due to subtle variations in fault geometry detail (pers. comm. S. Oxenburgh, 2008).

In order to propose the paleo-response of fault bends to rupture propagation directivity, large assumptions must be made. The biggest unknown is the actual epicentre of the earthquakes. From studies of the San Andreas Fault, the majority of earthquake epicentres concentrate around areas of structural complexity (Jennings, 1975; Scholz, 1977; Sibson, 1989). Sibson (1984, 1989) goes even further to say that because larger ruptures generally initiate towards the base of the seismogenic zone, it seems probable that rheological and geometrical irregularities play an important role in the nucleation process of these faults. Along the Mt Gordon Fault Zone the rheological contrast between the units is relatively minor, implying that geometrical irregularities may be more important in rupture nucleation. The main zones of structural complexity are associated with the ENE-WSW cross-faults, such as the Mammoth Extended Fault and the Investigator Fault. Numerical modelling conducted by McLellan (2007) also shows that these intersection areas are likely to yield early in the D_4 deformation event, as failure occurs first here during progressive deformation.

The ENE-WSW cross fault intersections with the NNE-SSW striking Mt Gordon Fault Zone corridor are therefore assumed to represent the most likely sites of intense earthquake epicentre activity (Figure 8.12). This assumption has particular significance when comparing the NNE-SSW faults associated with mineralisation (Esperanza Fault, Stockyard Creek Fault, Bluff Fault) to those NNE-SSW striking faults with little to no copper association (Mt Gordon Fault proper).

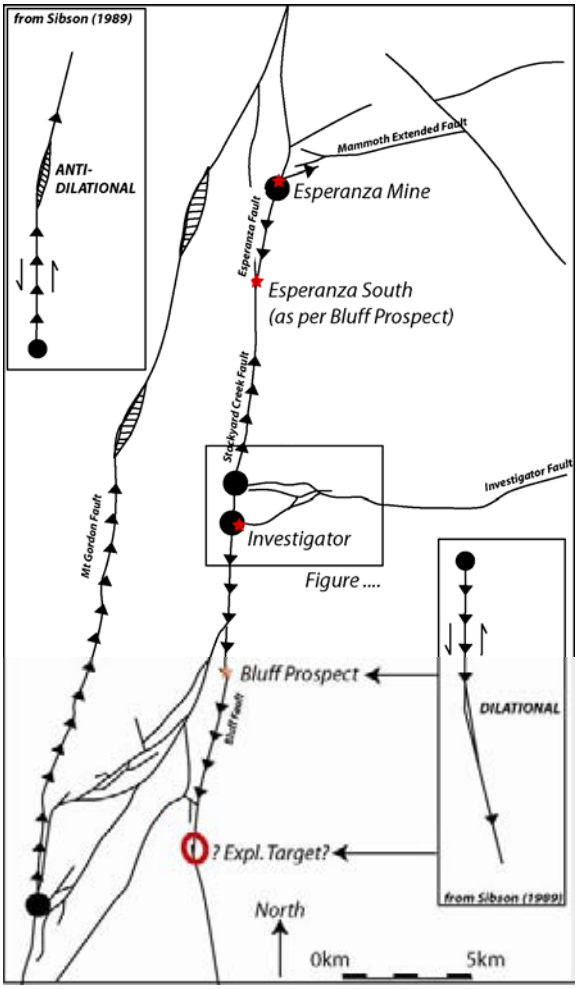

Figure 8.12 (adapted from Connors, 1994 and Sibson, 1989) Suggested paleo-fault rupture nucleation (black dots) and directivity (arrows) along the Mt Gordon Fault Zone between the Bluff Prospect and the Esperanza Mine. If the assumption of geological complexity being important on the sites of fault nucleation is correct, the north directed rupture propagation into right stepping antidilatant bends may explain why the Mt Gordon Fault itself is relatively unmineralised.

A brief review of rupture propagation and propagation direction at the Investigator Fault Zone may confirm the hypothesis that the rupture propagates along and away from the NNE-SSW to N-S striking faults of the Mt Gordon Fault Zone. Figure 8.13 shows the fault geometry of the Investigator Fault Zone and the breccia bodies present, along with proposed dilatant and antidilatant sites based on two notional rupture nucleation points. The rupture nucleation points were placed at the intersection of the ENE-WSW striking faults with the NNE-SSW striking faults (Stockyard Creek Fault and Prospect Fault).

The effect of these rupture nucleation points on propagation direction was that field mapped antidilational zones (e.g. South Investigator Fault; Chapter 5.6.1) correlated well with predicted

antidilational zones (Figure8.13). The predicted dilational sites from the inferred propagation direction also matched large field mapped hematite-chlorite breccias during dextral movement on the Investigator Faults. Some quartz breccias were seen to occur in areas that were predicted to be antidilational, reaffirming the hypothesis that at least some of the quartz breccias reflected an early deformation than the D_4 event.

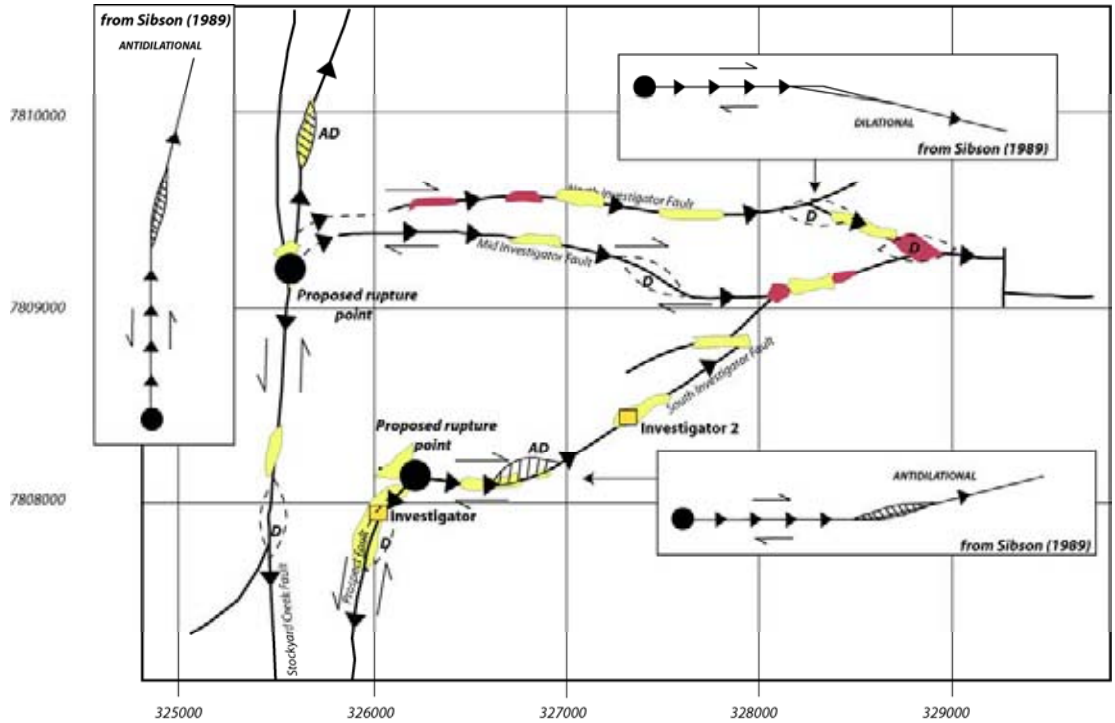

Figure 8.13 (insets adapted from Sibson, 1989) Faults of the Investigator Fault Zone with proposed rupture points (circles) located along the NNE-SSW striking faults of the Mt Gordon Fault Zone, near fault intersections. The quartz dominated breccias (yellow) were seen to predate the hematite-chlorite breccias (red) associated with D_4 (see Chapter 5.6). The proposed rupture nucleation points match dilatant sites with some of these hematite chlorite breccias and also match antidilatant sites with the section of the South Investigator Fault that was seen to contain shear fabrics rather than breccias (Chapter 5.6.1).

8.5 Geodynamic setting of Mt Isa at 1530 Ma

8.5.1 Cratonisation of the Mt Isa Inlier

The significant drop in the temperature of the D_4 event across the Mt Isa Inlier (D_2 600 °C to D_4 300 ºC), coupled with a change in pressure, implies that D_4 marks the final stages before cratonisation of the Mt Isa Inlier.

Mineralisation and widespread intrusion associated with the final stages of cratonisation is not an uncommon phenomenon. Examples of mineralisation and intrusion immediately preceding cratonisation include Archaen gold (Yilgarn; Lin et al., 2005; West Africa; Bowell et al., 1990) and copper-nickel-PGE systems such as the Superior Province (Thurston, 2002), and in Proterozoic copper-zinc-gold-lead systems (Arabian Shield; Moore, 1976).

Cratonisation is defined by the cessation of an increase in crustal thickness and a peak in lithospheric strength. Cratonisation can be caused by vertical accretion through asthenosphere-driven processes (e.g. plumes) that cool the interior of the Earth leading to lithospheric growth by mafic underplating and partial melting in an intra-continental setting (Etheridge et al. 1987). It can also be caused by lateral accretion through plate margin processes, allowing heat loss at the surface, with growth of the lithosphere through subduction/accretion and collision (Gibson et al., 2005). Combinations of both of these processes are the likely drivers for the geological evolution of the Proterozoic North Australia Craton (NAC; Giles et al. 2002; McLaren et al. 2005).

McLaren et al (2005) related an elevated thermal regime in the North Australian Craton to the heterogeneous distribution of heat-producing elements, chiefly from high heat producing granites, such as the Sybella Granite, in the upper 5-10 km of the crust. The final emplacement of the Williams Batholith would have left the lower crust incapable of further melting and resulted in transfer of heat-producing elements to the mid/upper crust, thus assisting, or causing, cratonisation.

In addition to these granites, thermal input related to the generation of abundant mafic rocks is also considered to contribute to the elevated thermal regime prior to cratonisation (Butera et al., 2005). Modelling of the evolution of the abundant high-Fe mafic rocks that characterise the Mount Isa Inlier suggests considerable fractionation in magma chambers below the current levels of emplacement (Oliver et al., 2007). This may explain the apparent lack of local large igneous intrusives corresponding to most of the metamorphic events, although some igneous rocks have the right timing for nearby metamorphism (Rubenach, 2005). For example, the dolerite dyke swarms at Snake Creek

could not by themselves explain the peak of metamorphism as they are volumetrically insignificant. However, they do indicate mafic intrusion was possible around the time of the peak metamorphic event, and as they are fractionated they could be linked to large bodies deeper in the crust (Rubenach, 2005).

It is suggested that gabbros ponded in the lower crust during the metamorphic episodes (i.e., 1630-1660 Ma, and 1527-1610 Ma) causing considerable partial melting. During the later part of the Isan Orogeny when the ductile strain was less intense, larger bodies (i.e. plutons) of granite and gabbro were able to intrude (e.g., Maramungee Granite, and the Williams and Naraku Batholiths) (Butera et al., 2005; Rubenach, 2005). The fractionation of these mafic bodies has been billed as a potential metal source for copper in both the Western and Eastern Successions (Western Succession – Heinrich et al, 1995; Eastern Succession – Butera et al., 2005).

Removal of younger mafic rocks and the Williams and Naraku batholiths from the lower crust, coupled with ~3 km of exhumation between the D_3 and D_4 deformational events (van Dijk, 1986; Rubenach, 2005), are thought to be the key drivers for cratonisation during the mid-Proterozoic, in the Mt Isa Inlier (McLaren et al., 2005).

The other alternative method for cratonisation may have been through lateral accretion and plate margin processes. At 1530 Ma Mt Isa, and the rest of the North Australian Craton, was colliding with Laurentia and Antarctica. These issues will be raised in the next section.

8.5.2 Polar wander and palaeomagnetic continental reconstruction

Tanaka and Irdnum (1994) constructed an apparent polar wander path for the North Australian Craton during the Proterozoic (Figure 8.14). At 1530 Ma the largest inflection on the polar wander path is seen. Unfortunately Tananka and Idnurm (1994) did not offer any possible explanation for this large shift in the apparent polar wander path. The copper event, D_4, cratonisation and a shift in polar wander path all seem to have coincided at 1530 Ma.

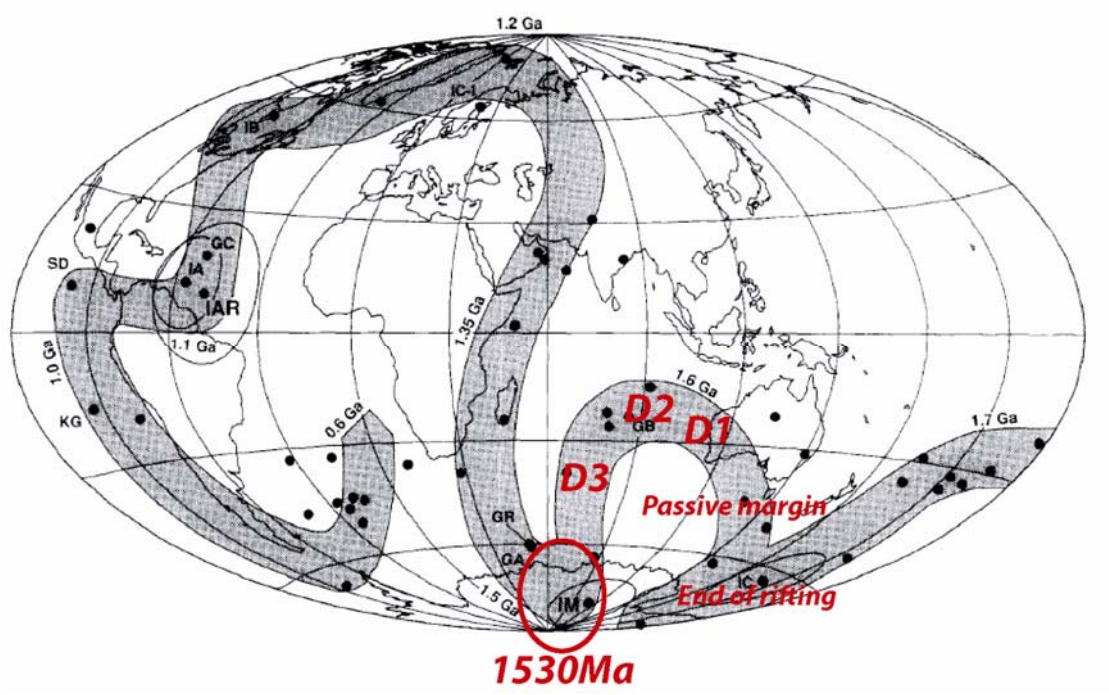

Figure 8.14. (from Tanaka and Irdnum, 1994) The 1530 Ma age data also correlates with an inferred change in the polar wander path for the Australian continent.

Several continental reconstructions involving Australian Proterozoic terranes have been proposed (Wade et al., 2006; Giles et al., 2002, 2004; Fitzsimons, 2003; Betts et al., 2002; Karlstrom et al., 2001; Myers et al., 1996). The relationship between different elements of Proterozoic Australia is particularly uncertain, largely due to the fact that the different tectonic blocks are now separated by large regions of much younger sedimentary cover. Indeed, the boundaries of Proterozoic blocks in Australia are commonly defined by geophysical interpretations made necessary by a lack of outcrop, and by the imposition of younger cover sequences (Fraser and Lyons, 2006).

Most paleomagnetic studies based on the Proterozoic North Australian Craton utilise the AUSWUS or SWEAT reconstructions. Both reconstructions have the North Australian Craton in collision with differing parts of Laurentia at ~1500 Ma (Figure 8.15).

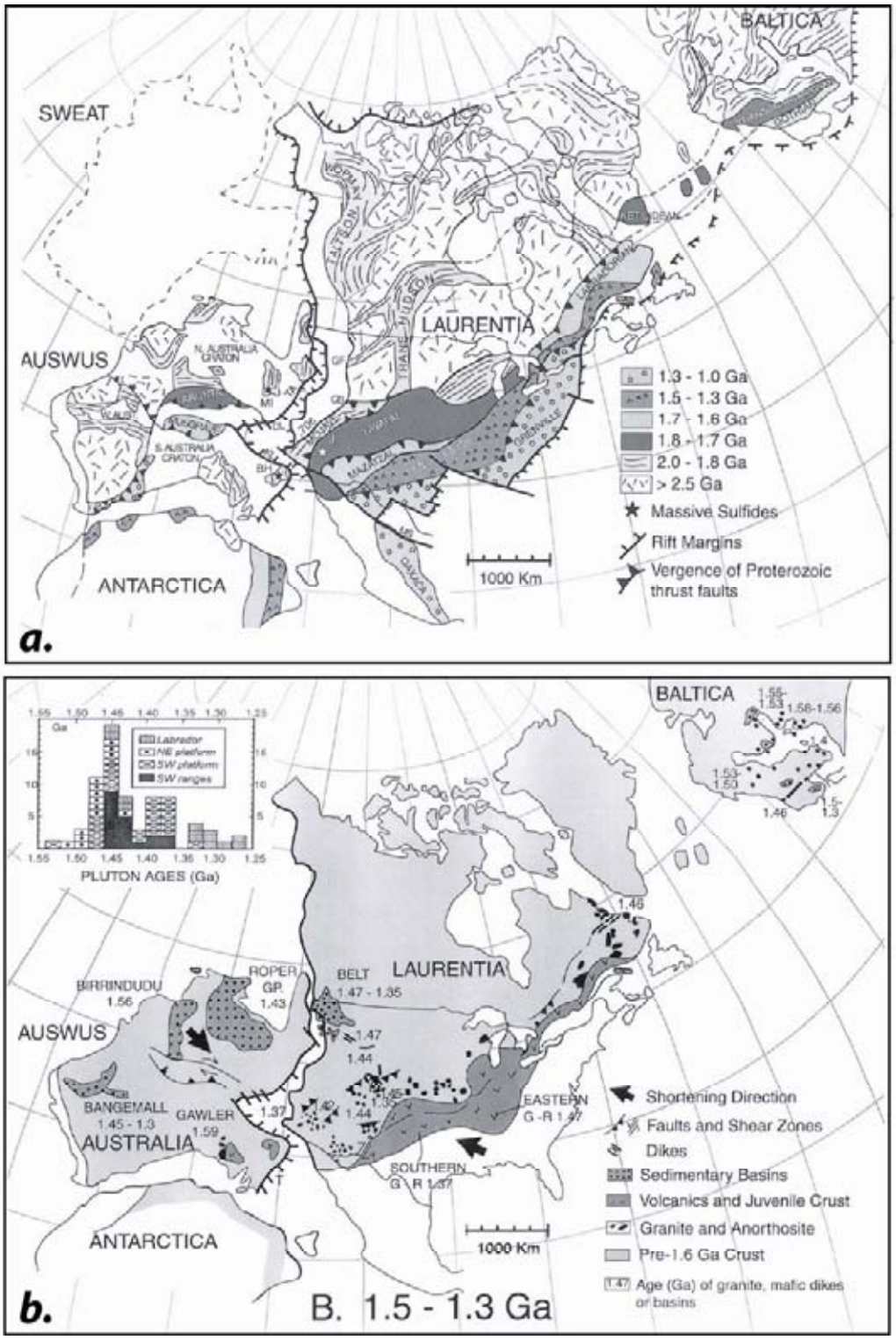

*Figure 8.15. (from Karlstrom et al., 2001) AUSWUS reconstruction for two Proterozoic time slices. Easternmost Australia was removed along the Tasman line (TA; Myers et al., 1996), which marks a major line of truncation of magnetic anomalies in Australia and the western edge of the Paleozoic accreted terranes of the Tasman orogen (Coney, 1990). **(a)** Crustal provinces inferred from U to Pb data; 0.706=Sr 0.706 line; CB=Cheyenne Belt; DL=Diamantina lineament; GF=Great Falls tectonic zone; KL=Koonenberry fault zone; MS=Mojave–Sonora megashear; TA=Tasman Line. **(b)** 1.5–1.3 Ga orogenic belts and A-type granites and anorthosites; G-R=granite rhyolite provinces; histogram shows wide variation in ages of A-type magmatism along the orogen in Laurentia (Hoffman, 1989).*

So did the collision of the North Australian Craton and Laurentia result in, or relate to, a change in the polar wander path at 1530 Ma? Or are there some other potential controls on polar wander and plate tectonics?

Giles et al. (2004) proposed a detachment of the South Australian Craton from the North Australian Craton at ~1500 Ma. Before 1500 Ma the South Australian Craton was part of the larger proto-Australian Craton. Due to conflicting evidence in the paleomagnetic data from the North and South Australian Cratons at ~1500 Ma (Irdnum, 2000), Giles et al. (2004) hypothesise that the South Australian Craton broke away from the North Australian Craton. Coincidently, Fraser and Lyons (2006) have recognised a widespread metamorphic and deformational event at ~1530–1550 Ma across the north-western Gawler Craton. The South Australian and North Australian cratons would recombine sometime after 1100 Ma.

There are also conflicting theories on the collisional tectonics on the opposite side of the Laurentian continent between 1550 and 1450 Ma. Authors such as Åhäll et al. (2000), Pesonen et al. (2007) and Zhao et al. (2004) contend that Baltica was in collision with Eastern Laurentia at approximately the same time as the North Australian Craton was in collision with Western Laurentia (Giles et al., 2004).

The range of tectonic theories at ~1500 Ma was highlighted by Salminem and Pesonen (2007) (Figure 8.16).

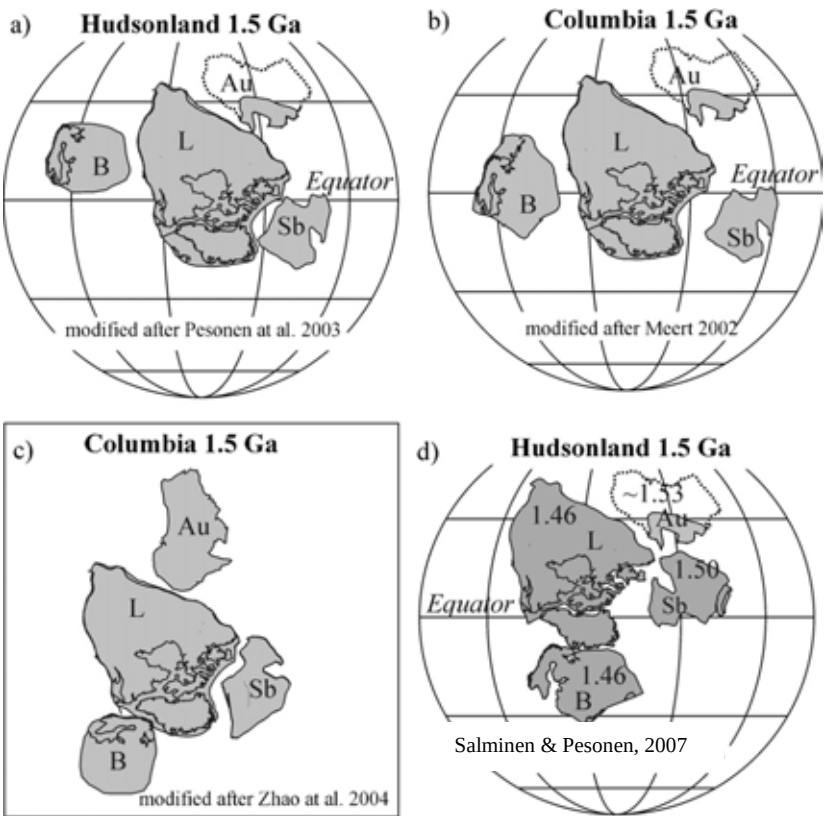

Figure 8.16 (from Salminem and Pesonen, 2007) The proposed Hudsonland (Columbia) supercontinent configurations showing Laurentia, Baltica, North Australia and Siberia. ***(a)*** *The ca. 1.5 Ga paleomagnetic reconstruction of Hudsonland after Pesonen et al., 2003.* ***(b)*** *Paleomagnetic reconstruction of Columbia at ca. 1.5 Ga by Meert (2002) is similar than previous one, but used polarity is opposite.* ***(c)*** *Reconstruction of Columbia by Zhao et al. (2004) based on lithostratigraphic, tectonothermal, geochronological and paleomagnetic data (only continents, which have 1.5 Ga paleomagnetic data are shown). The reconstruction is rotated as a whole so that Laurentia's position is coeval with Pesonen et al. (2003) and Meert (2002).* ***(d)*** *Paleomagnetic reconstruction of Hudsonland based on the work of Salminem and Pesonen (2007).*

8.5.3 Mineralisation at 1530 Ma in Baltica

During the Baltica collision with Laurentia, emplacement of rapakivi granites was coincident with mineralisation. Emplacement of rapakivi granites and ferrolite ores (Fe-Ti-V) in the Mazury Complex in Poland has been dated between 1559 and 1513 Ma. The belt-shaped Mazury complex (Figure 8.17) comprises the Suwałki anorthosite-norite intrusion with ferrolite ores (Fe-Ti-V-bearing) and variously composed felsic and intermediate rocks, such as leucogranite, quartz-monzonite, monzonite, granodiorite, and monzodiorite (Bagiński et al. 2001).

The Mazury Complex is geochronologically consistent with the Ragunda rapakivi-like complex (NE Sweden) and with several smaller complexes in central Sweden which yielded dates between

1530 and 1470 Ma (Persson 1997) as well as the 1547–1530 Ma Salmi rapakivi granite-anorthosite complex in Russia (Amelin et al. 1997).

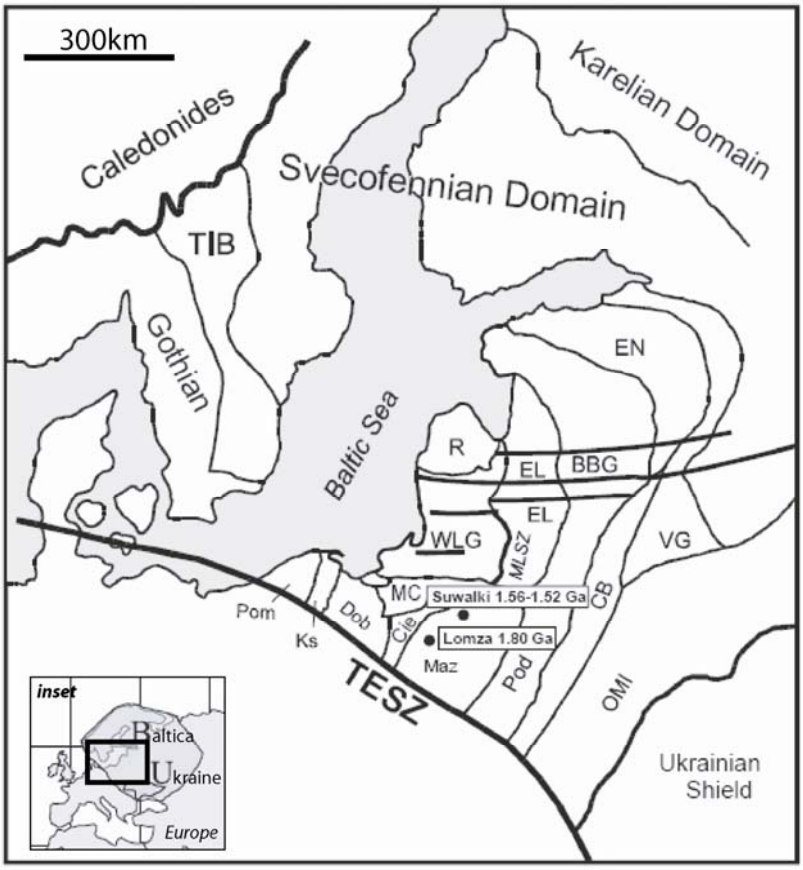

Explanations: R – rapakivi-like granites and related rocks, TIB – Transscandinavian igneous belt, BBG – Baltic – Belarus granulite belt, EL – East Lithuanian belt, WLG – West Lithuanian granulite belt, NE – North Estonian belt, CB – Central Belarus belt, VG – Vitebsk granulite domain, OMI – Osnitsk – Mikashevichi igneous belt; granitoid massifs: Maz – Mazow-sze, Dob – Dobrzyń; Pom – Pomorze; metamophic complexes: Lub – Lublin; Pod – Podlasie; Cie –Ciechanów; Ks – Kaszuby, Mesoproterozoic structures: MC – Mazury Complex with rapakivi-like granitoids and anorthosite massifs.

Figure 8.17 (from Wiszniewska, 2005) Tectonic outline of the western part of East European Craton after Bogdanowa (1999) with the structural units after Kubicki, Ryka (1982). The Transeuropean Suture Zone (TESZ; cf. Gaal, Gorbatschev 1987)

The Suwałki anorthosite massif (SAM) and associated rocks belong to the widespread, magmatic AMCG suite (anorthosite-mangerite-charnockite-granite of rapakivi type) and they are connected with Proterozoic deep crustal structures (Wiszniewska, 2005). The Suwałki anorthosite contains Fe-Cu-Co-Ni-Ti-V ores and Re-Os dating of sulphide ores has yielded ages of the Krzemianka and Jezioro Okrągłe ores of 1559±37 Ma and the age of Udryń ores of 1556±94 Ma (Wiszniewska et al. 1999). The U-Pb (zircon-titanite) age determinations yielded age values of 1525±4 Ma (Krasnopol), 1522±2 Ma (Bartoszyce), 1512±1.1 Ma (Boksze) as well as 1499±4 Ma and 1502±2 Ma for two other quartz monzonites (Dörr et al. 2001). These well constrained dates imply a ~25 Ma long emplacement period for the felsic and intermediate rocks of the Mazury AMCG complex (Wiszniewska, 2005).

The ca. 1425 Ma Ar-Ar dates from the Boksze and Krasnopol rocks refers to the age of cooling of the intrusion. The time interval between zircon crystallisation at 900 °C and the calculated biotite Ar-Ar age values is ca. 100 Ma. The obtained initial isotope Os/Os ratios (which yielded 1.16±0.06 Ma for Krzemianka and 0.87±0.20 Ma for Udryń) and εNd (-1.56 to -6.3) indicate a lower crustal source of the parental Suwałki anorthosite magma (Morgan et al. 2000). Rocks of the gabbro-norite composition, remelted at a depth interval corresponding to a pressure of 10-13 kbars and temperature of ca. 1300 ºC, are believed to be the most probable protolith of anorthosites. Fe-Ti-V ore mineralisation was concentrated in the marginal parts of the massif (Krzemianka, Jezioro Okrągłe and Jeleniewo ore fields), as a result of granulation and polygenisation processes of anorthosites, as well as filter-pressing and squeezing out the ore-mineral mush into tectonic cracks and faults (Wiszniewska et al. 2001). The δ34S and δ13C values confirm the magmatic origin of pyrrhotite, pentlandite, chalcopyrite in ores and the same sulfides and graphite dispersed in anorthosite.

Major activity in Baltica at ~1525 Ma may provide a reasonable explanation for the change in polar wander path, and by implication cratonisation and mineralisation, in the Mount Isa Block. It is possible that collision of Baltica on the other side of Laurentia resulted in a change of the convergence direction of Laurentia and the NAC. This may have been sufficient to trigger strike-slip faulting on earlier faults, allowing rapid vertical permeability connection and thus the right conditions to allow mixing (for example) between copper-bearing fluids and reactive host rocks or other fluids. Simultaneously, the emplacement of the Williams Batholith may have provided a source for some of these fluids, but also resulted in strengthening of the lower crust by melt removal, consequent exhumation, cratonisation and the perfect conditions for fault-related copper mineralisation. It is the combination of final cratonisation, a change in far field stresses to allow vertical fracture permeability, and appropriate copper fluid reservoirs that has resulted in development of one of the premier copper provinces of the world.

CONCLUSIONS

Copper mineralisation in the Mt Isa Inlier is typically hosted in faults and breccias in a variety of rock types. With only one known exception to date (the Osborne Mine) copper mineralisation in the Mt Isa Inlier is between 1530 Ma and 1505 Ma old. These dates broadly correlate with the D_4 deformation event at 1527±4 Ma, determined by dating a foliation associated with the intrusion of the Saxby Granite in the Snake Creek area. The foliation was determined to have formed in an ESE-WNW oriented shortening event (Rubenach *et al.,* 2007).

The D_4 deformation event occurs late in the Isan Orogeny, prior to cratonisaton and is expressed as predominantly brittle structures, for example forming large breccias within and adjacent to faults formed in the deformation events preceding. D_4 deformation also occurs as ductile fabrics i.e. where the D_4 deformation is seen to have a ductile character, forming ductile foliations and porphyroblast growth, the 1530 Ma granites of the Williams and Naraku batholiths are typically in close proximity.

Individual deposit studies conducted in this thesis determined that the D_4 event was actually an Inlier-wide event, responsible for the formation of copper-hosting breccias seen at a range of mines. Conventional structural mapping and palaeostress inversions were conducted at the Mt Gordon Mines and determined a shortening orientation consistent with the ESE-WNW D_4 event recorded at Snake Creek (approximately 200 km away). Distinct element modelling of the Mt Gordon Mines fault array tested a range of structural hypotheses and supported the findings of the structural mapping.

The distinct element modelling was applied to other mineral deposits in the Mt Isa Inlier with great success. The D_4 ESE-WNW shortening event is inferred to be responsible for the formation of copper-hosting breccias at Mt Isa, Mt Kelly, Ernest Henry and Greenmount. The Investigator Fault system, south of Mt Gordon was numerically modelled and in sites predicted to be dilatant, large hematite-chlorite filled breccias were seen at surface. The Investigator area remains a highly prospective region for Mammoth Mine and Esperanza Mine analogues.

The ESE-WNW shortening event was compared to copper prospectivity studies conducted on both the Eastern and Western Successions of the Mt Isa Inlier. The previous prospectivity studies determined that specific fault intersections and fault bends had a high spatial correlation with known

copper deposits. The highest ranking fault intersections and fault bends determined from the prospectivity study would be expected to be obvious sites for dilation during ESE-WNW shortening.

Brittle deformation can only occur under certain pressure and temperature conditions. Temperatures of greater than 350 ºC are not optimal for brittle failure. Techniques such as Ar-Ar dating of minerals such as hornblende and biotite, record the dates of temperature closure of certain minerals, for example the nominal closure temperature of argon in biotite is ~300 °C and of argon in hornblende ~550 °C. It is apparent that most of the copper deposits in the Mt Isa Inlier are found in areas where biotite Ar-Ar ages were indicate the rocks had cooled sufficiently to behave brittley at around 1530 Ma. Conversely, rocks adjacent to granites or otherwise show protracted cooling histories (e.g. Ar-Ar in hornblende younger than 1520 Ma) and did not cool quickly enough to allow the coincidence of brittle deformation and the possibility for significant copper mineralisation to occur. A potentially useful exploration technique may involve collating all the spatially constrained published Ar-Ar dates collected through the Mt Isa Inlier and constructing a map of rocks that would have the potential to fail via brittle modes between 1530 and 1500 Ma.

REFERENCES

Aha¨ll, K. I. & Connelly, J. 1998, 'Intermittent 1.53–1.13 Ga magmatism in western Baltica; age constraints and correlations within a postulated supercontinent', *Precambrian Research*, vol. 92, pp. 1–20.

Alston, T. 2004, *Flitch plan interpretation of the Greenmount ore zone*, [unpublished company report].

Anderson, E.M. 1951, *The Dynamics of Faulting*, Oliver & Boy, Edinburgh, p. 206.

Angelier, J. 1979, 'Determination of the mean principal direction of stresses for a given fault population', *Tectonophysics*, vol. 56, T17-T26.

Angelier, J. 1984, 'Tectonic analysis of fault slip data sets', *Journal of Geophysical Research*, vol. 89, pp. 5835-5848.

Angelier, J. 1989, 'From orientation to magnitudes in paleostress determinations using fault slip data', *Journal of Structural Geology*, vol. 11, no. 1-2, pp. 37-50.

Angelier, J., Lymberis, N., Le Pichon, X., Barrier, E. & Huchon, P. 1982, 'The tectonic development of the Hellenic arc and sea of Crete: a synthesis', *Tectonophysics*, vol. 86, pp.159-196.

Anonymous, 1981, *1:5000 Geological Map of the Investigator Fault Zone for Anaconda Resources*.

Anonymous, 1994, *A regional structural overview of the Mammoth copper deposit Gunpowder, Queensland*, [confidential company report], ERA-MAPTEC Australia.

Arthaud, F. 1996, 'Méthode de détermination graphique des directions de raccourcissement, d'allongement et intermédiaire d'une population de failles', *Bull. Soc. Géol. Fr*, vol. 1, no. 7, pp. 729–737.

Austin, J. R. & Blenkinsop, T. G. 2008, 'The Cloncurry Fault Zone: strain partitioning vs. multiple deformations in a long-lived, crustal-scale structure in the Mount Isa Inlier', *Precambrian Research*, in press.

Aviles, C.A., Scholz, CH. & Boatwright, J. 1987, 'Fractal analysis applied to characteristic segments of the San Andreas Fault', *Journal of Geophysical Research*, v. 92, pp. 331-344.

Baker, T., and Laing, W. P. 1998, 'Eloise Cu-Au deposit, east Mount Isa block: Structural environment and structural controls on ore', *Australian Journal of Earth Sciences*, v. 45, p. 429–444.

Baker, T., Perkins, C., Blake, K.L., Williams, P.J. 2001, 'Radiogenic and stable isotope constraints on the genesis of the Eloise Cu–Au deposit, Cloncurry District, northwest Queensland', *Economic Geology*, vol. 96, pp. 723–742.

Barrier, E. & Angelier, J. 1986, 'Active collision in eastern Taiwan; the Coastal range', *Tectonphysics*, vol. 125, pp. 39-72.

Bell, T. H. 1983, 'Thrusting and duplex formation at Mt Isa, Queensland, Australia', *Nature*, vol. 304, pp. 493-497.

Bell, T.H., Perkins, W.G., & Swager, C.P. 1988, 'Structural controls on development and localization of syntectonic copper mineralization at Mount Isa, Queensland', *Economic Geology*, vol. 83, pp. 69–85.

Betts, P. G., Giles, D., Lister, G. S., Frick, L. R., 2002, 'Evolution of the Australian lithosphere', *Australian Journal of Earth Science*, vol. 49, pp. 661–695.

Bierlein, F. (Eds.) 2005, *Mineral Deposit Research: Meeting the Global Challenge*. Proceedings of the 8th Biennial SGA Meeting, Beijing, China, Springer Verlag, vol. 1, pp. 29-32.

Blainey, G. 1965, *Mines in the Spinifex*, Angus and Robertson, Singapore, p. 256.

Blake, D.H. 1987, 'Geology of the Mount Isa Inlier and environs, Queensland and Northern Territory', *BMR Bulletin*, vol. 225, p. 83.

Blake, K., Pollard, P.J., Xu, G. 1997, 'Alteration and mineralisation in the Mount Fort Constantine volcanics, Cloncurry district, northwest Queensland', *Cloncurry base metals and gold: AMIRA P438 Final Report* 11:53.

Blenkinsop, T., Lisle, R. & Ferrill, F. 2006, 'Introduction to the special issue on new dynamics in palaeostress analysis', *Journal of Structural Geology*, vol. 28, pp. 941-942.

Blenkinsop, T., Mustard, R., Bierlein, F.P. 2005, 'Fault Roughness, Length and Mineral Endowment', In: Blenkinsop, T.G. (Ed.), Total Systems Analysis of the Mount Isa Eastern Succession, *I 2+3 Final Report*, Predictive Minerals Discovery Cooperative Research Centre, Townsville, pp. 403-413.

Bowell, R. J., Foster, R. P. & Stanley, C. J., 1990, 'Telluride mineralization at the Ashanti gold mine, Ghana', *Mineralogical Magazine*, vol. 54, pp. 617–627.

Bradshaw, G. A., & Zoback, M. D. 1988, 'Listric normal faulting, stress refraction, and the state of stress in the Gulf Coastal Basin', *Geology*, v. 16, no. 3, pp. 271-274.

Bridges, R. 1970, *Faults and Fractures in 1100 Orebody*, [internal company report], Mt Isa: Mt Isa Mines.

Bridges, R. 1971, *2000-3000N block structural investigations 1100 Orebody*, [internal company report], Mt Isa: Mt Isa Mines.

Brooks, J. H. 1957, *Copper mining in the Cloncurry Mineral Field*, Geological Survey Queensland, p. 7.

Brooks, J. H. 1962, 'Mammoth Copper Mine, Calton Hills-Mount Isa Mineral Field', *Queensland Government Mining Journal*, p. 376-379.

Butera, K., Oliver, N., Rubenach, M., Collins, W., & Cleverley,J. 2005, 'Multiple generations of metal and sulphur contribution from mafic rocks to the IOCG budget of the Mount Isa Eastern Succession', *I2+3 Final Report*, Predictive Mineral Discovery Collaborative Research Committee, Townsville.

Byerlee, J. 1978, 'Friction of rocks', *Pure and applied geophysics*, vol. 116, no.4-5, pp. 615-626.

Chapman, L. H. 2001, 'New constraints on the thermal evolution of the Mount Isa mineralization system', *Geological Society of America Program with Abstracts*, vol. 33, p. 271.

Chapman, L. H., Williams, P. J. 1998, 'Evolution of pyroxene–pyroxenoid–garnet alteration in the southern zone of the Cannington Ag–Pb–Zn deposit, Cloncurry District, Queensland, Australia', *Economic Geology*, vol. 93, pp. 1390–1405.

Clark, A. 1992, *1100 Orebody Fault Study 4200mN to 3200mN*, [internal company report], Mt Isa: Mt Isa Mines.

Clarke, D.J. 2003, *Geology and Genesis of the Mammoth Cu Deposit, Mount Isa Inlier, Australia*, [unpublished PhD thesis], University of Tasmania, pp. 1-259.

Connors, K. 1994, *Regional fault history of the Waggaboonya area*, [unpublished company report], Etheridge Henly Williams for Aberfoyle Resources Ltd.

Connors, K. 1997, *Regional Fault History of the Waggaboonya Are*, [confidential company report], Etheridge Henley Williams, p. 34.

Connors, K. A. & Page, R. W. 1995. 'Relationships between magmatism, metamorphism and deformation in the western Mount Isa Inlier, Australia', *Precambrian Research*, vol. 71, pp. 131-153.

Connors, S. K. A. 1992. *Tectonothermal Evolution of the Mount Novit Ranges, Mount Isa Inlier, Australia*, [unpublished PhD thesis], Monash University, Melbourne.

Couples, G. 1977, 'Stress and shear fracture (fault) patterns resulting from a suite of complicated boundary conditions with applications to the Wind River Mountains', Pure & Applied Geophysics, vol. 115, pp. 113-133.

Cowan, J. A., Beatson, R. K., Fright, W. R., McLennan, T. J. & Mitchell, T. J. 2002. 'Rapid Geological Modelling', *Australian Institute of Geologists International Structural Conference*, Kalgoorlie, WA, Australia.

Coward, M. J, 2000, *Structural Controls on Ore Formation and Distribution at the Ernest Henry Cu-Au Deposit, NW Qld*, [unpublished. Honours thesis], James Cook University, Townsville.

Craske, T. E. 1995, 'Geological aspects of the discovery of the Ernest Henry Cu-Au deposit, northwest Queensland', *Australian Institute of Geoscientists Bulletin*, vol. 16, pp. 95-109.

Crossing, J. 2004, Geological mapping of the Mt Gordon mine leases area, Mt Isa region, [unpublished company report], Birla, Mt Gordon.

Crossing, J. 2007, *Geological mapping of the Mt Kelly and Lady Annie projects*, Mt Isa region, [unpublished company report], for Copperco.

Cundall, P. A. 1980, *UDEC, a generalised distinct element program for modelling jointed rock*, [contract report], U.S. Army European Research Office and Defence Nuclear Agency, DAJA 37-39-C-0548.

Da Costa, R. 2005, *Structural controls in Mt Kelly copper deposits, North West Queensland*, [unpublished honours thesis] University of New South Wales, Sydney.

Davidson, G. J., Large, R. R., Kary, G. & Osborne, R. 1989, 'The deformed iron-formation-hosted Starra and Trough Tank Au-Cu mineralization: A new association from the Proterozoic eastern succession of Mount Isa, Australia', *Economic Geology*, monograph 6, pp.135–150.

Davis, et al. 2001, 'Deformation history of the Naraku Batholith, Mt Isa Inlier, Australia: implications for pluton ages and geometries from structural study of the Dipvale Granodiorite and Levian Granite', *Australian Journal of Earth Sciences*, vol. 48, pp. 113–129.

Davis, T. P. 2004, 'Mine-Scale Structural Controls on the Mount Isa Zn-Pb-Ag and Cu Orebodies', *Economic Geology*, vol. 99, pp. 543-559.

de Jong, G., Williams, P. J. 1995, 'Giant metasomatic system formed during exhumation of mid-crustal Proterozoic rocks in the vicinity of the Cloncurry Fault, northwest Queensland', *Australian Journal of Earth Science*, vol. 42, pp. 281–290.

Derrick, G. M., Wilson, I. H. & Sweet, I. P. 1980, 'The Quilalar and Surprise Creek Formations-New Proterozoic units from the Mount Isa Inlier: their regional sedimentology and application to regional correlation', *BMR Journal of Australian Geology & Geophysics*, vol. 5, pp. 215–223.

Derrick, G.M. 1982, 'A Proterozoic rift zone at Mount Isa, Queensland, and implications for mineralisation', *BMR Journal of Australian Geology & Geophysics*, vol. 7, pp. 81-92.

Eriksson, K.A., Simpson, E.L. & Jackson, M.J. 1993, 'Stratigraphical evolution of a Proterozoic syn-rift to post-rift basin: constraints on the nature of lithospheric extension in the Mount Isa Inlier, Australia', *International Association of Sedimentologists Special Publication*, vol. 20, pp. 203-221.

Etheridge, M. A., Rutland, R. W. R., & Wyborn, L. A. I. 1987, 'Orogenesis and tectonic process in the Early to Middle Proterozoic of northern Australia', *Proterozoic lithosphere evolution: American Geophysical Union Geodynamics Series*, vol. 17, pp. 131–147.

Evans, J. P., Forster, C. B., & Goddard, J. V. 1997, 'Permeability of fault-related rocks, and implications for hydraulic structure of fault zones', *Journal of Structural Geology*, vol. 19, no. 11, pp. 1393-1404.

Fitzsimons, I. C .W. 2003, 'Proterozoic basement provinces of southern and south-western Australia, and their correlation with Antarctica',*Proterozoic East Gondwana: Supercontinent Assembly and Breakup*, vol. 206.

Ford, A., Blenkinsop, T. G. 2007, 'Combining fractal analysis of mineral deposit clustering with weights of evidence to evaluate patterns of mineralization: Application to copper deposits of the Mount Isa Inlier, NW Queensland, Australia', *Ore Geology Reviews*, accepted.

Foster, D. R. W. 2003, *Protereozoic low-pressure metamorphism in the Mount Isa Inlier, northwest Queensland, Australia, with particular emphasis on the use of calcic amphibole chemistry as temperature-pressure indicators*, [unpublished PhD thesis], James Cook University.

Foster, D. R. W. & Rubenach, M. J. 2006, 'Isograd pattern andregional low-pressure, high-temperature metamorphism of pelitic, mafic and calc-silicate rocks along an east–west section through the Mt Isa Inlier', *Australian Journal of Earth Sciences*, vol. 53, no. 1, pp. 167-186.

Foy, M. 1964, *Transverse Faulting in the mine area*, [Internal Company Report], Mt Isa: Mt Isa Mines.

Fraser, G. L. & Lyons, P. 2006, 'Timing of Mesoproterozoic tectonic activity in the northwestern Gawler Craton constrained by $^{40}Ar/^{39}Ar$ geochronology', *Precambrian Research*, vol. 151, pp. 160–184.

Fry, N. 1992, 'Stress ratio determinations from striated faults: A spherical plot for cases of near-vertical principal stresses', *Journal of Structural Geology*, vol. 14, no. 10, pp. 1121-1131.

Gapais, D., Cobbold, P.R., Bourgeois, O., Rouby, D., de Urreiztieta, M. 2000, 'Tectonic significance of fault-slip data', *Journal of Structural Geology*, vol. 22, pp.881–888.

Gauthier, L., Hall, G., Stein, H., Schaltegger, U. 2001 'The Osborne deposit, Cloncurry district: a 1595 Ma Cu–Au skarn deposit', In: Williams PJ (ed) *A hydrothermal odyssey, new developments in metalliferous hydrothermal systems research*, extended conference abstracts, EGRU, vol. 59, pp. 58–59.

Gessner, K. 2004, 'Numerical process models of the Mount Isa Copper mineralisation synthesis and implications for targeting', In: 'Predictive Discovery of Mount Isa Style Iron-Sulphide Copper Mineralisation', *I4 Final Report*, Predictive Minerals Discovery Cooperative Research Centre, pp.1-146.

Gessner, K., Jones, P. A., Wildeand, A. R. & Kühn, M. 2006, 'Significance of strain localization and fracturing in relation to hydrothermal mineralization at Mount Isa, Australia', *Journal of Geochemical Exploration*, vol. 89, no.1-3, pp. 129-132.

Gibson, G. M., 2006, 'Chronostratigraphy and geodynamic evolution of the Western Succession', *I1 Final Report*, Predictive Mineral Discovery Collaborative Research Committee, Canberra, Australia.

Giles, D., Betts, P. G. & Lister, G. S. 2002, 'A continental back-arc setting for early to middle proterozoic basins of northeastern Australia,' *Geology*, vol. 30,pp. 823–826.

Giles, D., Betts, P.G. & Lister, G.S. 2004, '1.8–1.5 Ga links between the North and South Australian Cratons and the Early-Middle Proterozoic configuration of Australia', *Tectonophysics*, vol. 380, pp. 27-41.

Giles, D., Nutman, A. P. 2002, 'SHRIMP U–Pb monazite dating of 1600–1580 Ma amphibolite facies metamorphism in the southeastern Mt Isa Block, Australia', *Australian Journal of Earth Science*, vol. 49, pp. 455–465.

Glikson, A. Y., Derrick G. M., Wilson, I. H. & Hill, R. M. 1976, 'Tectonic evolution and crustal setting of the Middle Proterozoic Leichhardt River fault trough, Mount Isa region, northwestern Queensland', *BMR Journal of Australian Geology & Geophysics*, vol. 1, pp. 115-472.

Gow, P. 2004, *Mineral maps for the Ernest Henry deposit*, [unpublished company report], Xstrata Copper.

Gunton, C. G. 1999, *A study of molybdenum at the Ernest Henry Cu–Au deposit, Northwest Queensland*, [unpublished BSc (Hons) thesis],Australian National University.

Hafner, W. 1951, 'Stress distributions and faulting', *Bulletin of Geological Society of America*, vol. 62, pp. 373-398.

Heinrich, C. A., Andrew, A. S, Wilkins, R. W. T. & Patterson, D. J. 1989, 'A fluid inclusion and stable isotope study of synmetamorphic copper ore formation at Mount Isa, Australia', *Economic Geology*, vol. 84, pp. 529-550.

Heinrich, C. A., Bain, J. H. C., Mernagh, T. P., Wyborn, L. A. I., Andrew, A. S., and Waring, C. L., 1995, 'Fluid and mass transfer during metabasalt alteration and copper mineralization at Mount Isa, Australia', *Economic Geology*, v. 90, p. 705-730.

Hitzman, M. W. , Oreskes, N., Einaudi, M.T. 1992, 'Geological characteristics and tectonic setting of Proterozoic iron oxide (Cu–U–Au–REE) deposits', *Precambrian Research*, vol. 58, pp. 241-287.

Hoadley, E., Rubenach, M. J., Coleburn, D., Sisois, I. & Fanning, M. 2001, ‘Significance of an amphibolite facies shear zone event synchronous with the emplacement of the Sybella Batholith, Mount Isa’, *Geological Society of Australia Abstracts*, vol. 64, p. 83.

Hobbs, B. E., Means, W. D., & Williams, P. F. 1976, *An Outline of Structural Geology*, Wiley, New York, USA.

Holyland, P. W. & Ojala, V. J. 1997, 'Computer-aided structural targeting in mineral exploration: Two- and three-dimensional stress mapping', *Australian Journal of Earth Sciences*, vol.44, no. 4, pp. 421-432.

Holyland, P. W., 1990, *The nature of the lithosphere: cracks and blocks?*, Terra Sancta, Perth.

Homberg, C., Hu, J.C., Angelier, J., Bergerat, F. & Lacombe, O. 1997, ‘Characterization of stress perturbations near major fault zones: insights from 2D distinct- element numerical modelling and field studies (Jura mountains)’, *Journal of Structural Geology*, vol. 19, no. 5, pp. 703-718.

Honman, C. S. 1938, *The Mount Oxide Area: Canberra, Aerial, Geological and Geophysical Survey of Northern Australia*, p. 7.

Hoyland, P. W. 1990, ‘Stress mapping in the Mt. Isa region’, *Mt Isa Inlier Geology Conference*, Monash University, Melbourne, pp. 76-77.

Hsu, T. L. 1976,‘Neotectonics of the Longitudinal Valley, Eastern Taiwan’, *Bulletin of the Geological Survey of Taiwan*, vol. 25, pp. 53-62.

Hu, J. C., Angelier, J., Yu, S. B. 1996,‘An interpretation of the active deformation of southern Taiwan based on numerical simulation and GPS studies’, *Tectonphysics*, vol. 274, pp. 145-169.

Hubbert, M. K. 1951, 'Mechanical basis for certain familiar geologic structures', *Bulletin of Geological Society of America*, vol. 62, pp. 355-372.

Hutton, L. J., & Wilson, I. H., 1985, *Mammoth Mines Region, Queensland. 1:100 000 Geological Map Commentary,* Geological Survey of Queensland, Canberra, p. 26.

Isaacs, E.H and Srivastava, R.M. 1989, *Applied Geostatics*. Oxford University Press, New York.

ITASCA. 2000, *UDEC, Universal Disctinct Element Code Command Reference*, Itasca Consulting Group Inc., Minnesota, USA.

Jackson, M.J., Scott, D.L. & Rawlings, D.J. 2000, 'Stratigraphic framework for the Leichhardt and Calvert Superbasins: review and correlations of the pre-1700 Ma successions between Mt Isa and McArthur River', *Australian Journal of Earth Sciences*, vol. 47, pp. 381-403.

Jennings, C. W. 1975, 'Fault map of California, 1:750,000', *Geologic Data Map No. 1*, Californian Division of Mines and Geology, California, USA.

Jiang*, Z., Oliver, N. H. S., Barr, T. D., Power, W. L., & Ord, A.*, 1997, 'Numerical modelling of fault-controlled fluid flow in the genesis of tin deposits of the Malage ore field in Gejiu mining district, China', *Economic Geology*, vol. 92, no. 2, pp. 228-247.

Karlstrom, K. E., Ahall, K., Harlan, S. S., Williams, M. L., McLelland, J. & Geissman, J. W. 2001, 'Long-lived (1.8–1.0 Ga) convergent orogen in southern Laurentia, its extensions to Australia and Baltica, and implications for refining Rodinia', *Precambrian Research*, vol. 111, pp. 5-30.

Kendrick, M.A., Duncan, R. & Phillips, D. 2006, 'Noble gas and halogen constraints on mineralizing fluids of metamorphic versus surficial origin: Mt Isa, Australia', *Chemical Geology*, vol. 235, pp. 325-351.

Keys, D. L. 2002, *Copper System Fault Study :2CBS0181dlk*, [internal company report] Mt Isa: Mt Isa Mines.

King, S. & Hy, B. 1994, Structural analysis of the Greenmount Au-Cu-Co orebody, Marimo Basin, Queensland. [unpublished report], ERA-Maptec

King, S. & Hy, B. 1997, *Structural interpretation of the Marimo Basin, Cloncurry Mapping Project, North Queensland*. [unpublished report], ERA-Maptec.

Knuepfer, P. L. K., Bamberger, M. J., Turko, J. M. & Coppersmith, K. J 1987, 'Characteristics of the boundaries of historical surface fault ruptures', *Seismological Research Letters*, vol. 58, p. 31.

Krcmarov, R. L. 1995, *Greenmount Cu-Au-Co Deposit, Cloncurry District*, [unpublished M. Sc. Thesis], University of Tasmania, Hobart.

Krcmarov, R. L. and Stewart, J. I. 1998, 'Geology and mineralisation of the Greenmount Cu-Au-Co deposit, southeastern Marimo Basin, Queensland', *Australian Journal of Earth Sciences*, vol. 45, no. 3, pp. 463-482.

Krois, L. A. 2002, *Enterprise mine Fault Study*, [Internal Company Report], Mt Isa:Mt Isa Mines.

Laing, W. P. 2003, The Ernest Henry structural-metasomatic project, [unpublished company report], for Xstrata Copper.

Laing, W. P. 2004, *The White Range Structural Metasomatic Greenmount Project: Preliminary mapping and lode architecture*, [internal company report], Matrix Metals.

Law, S. 2001, *Copper Mine Visitors Guide*, [internal company report], Mt Isa:Mt Isa Mines.

Lisle, R.J. & Orife, T., 2002, 'STRESSTAT: a *Basic* program for numerical evaluation of multiple stress inversion results', *Computers & Geosciences*, vol. 28, no. 9, pp.1037-1040.

MacCready, T. 2006, 'Structural evolution of the southern Mt Isa Valley', *Australian Journal of Earth Sciences*, vol.53, no, 1, pp. 27- 40.

Maiden, K. 1999*, Assessment of Reefway's tenement application areas in the Mt Gordon Fault Zone, Western Mount Isa Block*, [unpublished company report].

Maiden, K., Hewitt, D. & Stephens, M. 2000, *Mount Kelly: A Mount Isa type copper-gold deposit in the Western Mt Isa Block, Queensland*, [internal company report].

Mair, J. L., Ojala, V. J., Salier, B. P., Groves, D. I. & Brown, S. M. 2000, 'Application of stress mapping in cross-section to understanding ore geometry, predicting ore zones and development of drilling strategies', *Australian Journal of Earth Sciences*, vol. 47, pp. 895-912.

Mark, G. 1998, 'Albitite formation by selective pervasive sodic alteration of tonalite plutons in the Cloncurry district, NW Queensland', *Australian Journal of Earth Science*, vol.45, pp. 765–774.

Mark, G. & Crookes, R. A. 1999, 'Epigenetic alteration at the Ernest Henry Fe-oxide-(Cu–Au) deposit, Australia', In: *Mineral Deposits: Processes to Processing*, Society for Geology Applied to Mineral Deposits, London, pp. 185–8.

Mark, G, & Foster, D. R. W. 2000, 'Magmatic albite-actinolite-apatite rich rocks from the Cloncurry district, Northwest Queensland, Australia', *Lithos*, vol. 51, pp.223–245.

Mark, G., Oliver, N. H. S., Williams, P. J. 2006, 'Mineralogical and chemical evolution of the Ernest Henry Fe oxide-Cu-Au ore system, Cloncurry district, Northwest Queensland, Australia', *Mineralium Deposita*, vol. 40, no. 8, pp. 769-801.

Marrett, D.C.P., & Peacock, R. 1999, 'Strain and stress', reply, *Journal of Structural Geology*, vol. 22, no. 9, pp. 1369-1378.

Marrett, R., Allmendinger, R.W. 1990, 'Kinematic analysis of fault-slip data', *Journal of Structural Geology*, vol.12, pp. 973–986.

Marshak, S. & Mitra, G. 1988, *Basic methods of structural geology*, Prentice Hall, Englewood Cliffs, N.J.

Marshall, L. J. & Oliver, N. H. S. 2005, 'Monitoring fluid chemistry in iron oxide–copper–gold-related metasomatic processes, eastern Mt Isa Block, Australia', *Geofluids*, vol.5, pp.1–22.

Mason, D. R. 1994, *Petrographic and mineralogical studies on a suite of eight samples, Northwestern Queensland*, [unpublished report]. Report to Homestake Gold of Australia Limited.

Matthäi, S.K., Heinrich, C.A., & Driesner, T. 2004, 'Is the Mount Isa copper deposit the product of forced brine convection in the footwall of a major reverse fault?', *Geology*, vol. 32, pp. 357-360.

McLaren, S., Sandiford, M., & Hand, M. 1999, 'High radiogenic heat-producing granites and metamorphism- An example from the western Mount Isa inlier, Australia', *Geology*, v. 27, p. 679–682.

McLaren, S., Sandiford, M. & Powell, R. 2005, 'Contrasting styles of Proterozoic crustal evolution: a hot-plate tectonic model for Australian terranes', *Geology*, vol. 33, pp. 673– 676.

McLellan, J.G., Oliver, N.H.S. 2007. 'Discrete element modelling applied to mineral prospectivity analysis in the eastern Mount Isa Inlier', *Precambrian Research*, in press.

McLellan, J. G. 2007, 'Discrete element modelling applied to mineral prospectivity analysis in the Western Succession of the Mount Isa Inlier', [unpublished report], pmd*CRC I7.

Meert, J. G. 2002, 'Paleomagnetic evidence for a Paleo-Mesoproterozoic supercontinent Columbia', *Gondwana Research*, vol. 5, pp. 207–215.

Miller, J., McLellan, J. G. 2006, 'Structural controls on the Cu distribution Mt Isa', July 2004. [Interim project report], QLD, p***md****CRC*, p. 17.

Mills, P. 1978, *Mining geology of 4200mN to 4500mN block of 1100*, [internal company report], Mt Isa: Mt Isa Mines.

Mitchell, J. W. & Moore, G. P. 1975, 'The Mammoth copper deposit', *in* Knights, C. L., ed., *Economic Geology of Australia and Papua New Guinea, 1*, Australasian Institute of Mining and Metallurgy, Melbourne, pp. 383-389.

Moore, J. M. 1975, 'A major lineament in the Arabian Shield and its relationship to mineralization', *Mineralium Deposita*, vol. 11, no. 3, pp. 323-328.

Morgan, J. W., Stein, H. J., Hannah, J. L., Markey, R. J. & Wiszniewska, J. 2000, 'Re-Os study of Fe-Ti-V oxides and Fe-Cu-Ni sulfide deposites, Suwałki Anorthosite Massif, NE Poland', *Mineralium Deposita*, vol. 35,pp. 391-401.

Moore, G. P., & Stoakes, C. A . 1975, *The geology and mineralisation of the Mammoth copper deposit, in Queensland Division Field Conference, Mt. Isa Region,* Geological Society of Australia, Queensland Division, Brisbane, pp 34–40.

Muller, O. H. & Pollard, D. D. 1977, 'The stress state near Spanish Peaks, Colorado determined from a dike pattern, Pure & Applied Geophysics, vol. 115, pp 69-86.

Mustard, R., Blenkinsop, T.G., Foster, D.R.G., Mark, G., McKeagney, C., Huddlestone-Holmes, C., Partington, G. & Higham, M. 2005, 'Critical ingredients in Cu–Au–iron oxide deposits, NW

Queensland: an evaluation of our current understanding using GIS spatial data modeling', *I 2+3 Final Report*, Predictive Minerals Discovery Cooperative Research Centre, pp.291–324.

Myers, J. S., Shaw, R. D., & Tyler, I. M. 1996, 'Tectonic evolution of Proterozoic Australia', *Tectonics*, vol. 15, no.6, pp. 1431–1446.

Neudert, M. 1983, *A depositional model for the Upper Mt Isa Group and its implications ore formation,* [unpublished. PhD thesis], Australian National University, Canberra.

Neumann, N. L., Southgate, P. N., Gibson, G. M. & MCintyre, A. 2006, 'New SHRIMP geochronology for the Western Fold Belt of the Mt Isa Inlier: developing a 1800 - 1650 Ma event framework ', *Australian Journal of Earth Sciences*, vol. 53, no. 6, pp. 1023-1039.

O'Dea, M.G., Lister, G.S., McCready, T., Betts, P. G., Oliver, N.H.S., Pound, K.S., Huang, W. & Valenta, R.K. 1997, 'Geodynamic evolution of the Proterozoic Mount Isa terrain', *In*: Burg J.P. & Ford M. eds, *Orogeny Through Time*, *Geological Society of London Special Publication*, vol. 121, pp. 99-122.

Ode, H. 1957, 'Mechanical analysis of the dike pattern of the Spanish Peaks area, Colorado', *Bulletin of Geological Society of America*, vol. 68, pp. 567-576.

Ojala V. J., Ridley J. R., Groves D. I. & Hall G. C. 1993, 'The Granny Smith gold deposit: the role of heterogeneous stress distribution at an irregular granitoid contact in a greenstone facies terrane', *Mineralium Deposita*, vol. 28, pp. 409-419.

Oliver, N. H. S., 2001, 'Linking of regional and local hydrothermal systems in the mid crust by shearing and faulting', *Tectonophysics*, vol. 335, pp. 147–161.

Oliver, N. H. S., Cleverley, J. S., Mark, G., Pollard, P. J., Fu, B., Marshall, L. J., Rubenach, M. J., Williams, P.J., Baker, T. 2004, 'Modelling the role of sodic alteration in the genesis of iron oxide–copper–gold deposits; eastern Mt. Isa Block, Australia', *Economic Geology*, vol. 99, pp. 1145–1176.

Oliver, N. H. S., Rawling, T. J., Cartwright I & Pearson, P. J. 2006, 'High-temperature fluid-rock interaction and scapolitization in an extension-related hydrothermal system, Mary Kathleen, Australia', *Journal of Petrology*, vol. 35,no. 6, pp. 1455-1491.

Oliver, N. H. S.,Butera, K. M., Rubenach, M. J., Marshall, L. J., Cleverley, J. S, Mark, G., Tullemans, F. & Esser, D. 2007, 'The protracted hydrothermal evolution of the Mount Isa Eastern Succession: A review and tectonic implications', *Precambrian Research*, in press

Oliver, N.H.S., Holcombe, R.J., Hill, E.J., and Pearson, P.J. 1991, 'Tectonometamorphic evolution of the Mary Kathleen fold belt, northwest Queensland: A reflection of mantle plume processes?', *Australian Journal of Earth Sciences*, v. 38, pp. 425–455.

Oliver, N.H.S., Pearson, P.J., Holcombe, R.J., Ord, A., 1999, 'Mary Kathleen metamorphic–hydrothermal uranium-rare-earth deposit: ore genesis and a numerical model of coupled deformation and fluid flow', *Australian Journal of Earth Science*, vol. 46, pp. 467–484.

Oliver, S., Valenta, R. K., Wall, V. J. 1990, 'The effect of heterogeneous stress and strain on metamorphic fluid flow, Mary Kathleen, Australia, and a model for large-scale fluid circulation', *Journal of Metamorphic Geology*, vol. 8, pp. 311-331.

Ord, A. & Oliver, N. H. S. 1997 'Mechanical controls on fluid flow during regional metamorphism: some numerical models', *Journal of Metamorphic Geology*, vol. 15, no. 3, pp. 345-359.

Orife, T., & Lisle, R.J. 2006, 'Assessing the statistical significance of palaeostress estimates: simulations using random fault-slips', Journal of Structural Geology, vol. 28, no. 4, pp. 952–956.

Page, R. W. & Sun, S.-S. 1998, 'Aspects of geochronology and crustal evolution in the Eastern Fold Belt, Mt Isa Inlier', *Australian Journal and Earth Sciences*, vol. 45, pp. 343-361.

Page, R. W. 1983, 'Chronology of magmatism, skarn formation and uranium mineralisation, Mary Kathleen, Queensland, Australia', *Economic Geology*, vol. 78, pp. 838 – 853.

Page, R.W. & Bell, T. H. 1986, 'Isotopic and structural responses of granite to successive deformation and metamorphism', *Journal of Geology*, vol. 94,no. 3, pp. 365-379.

Page, R.W. 1998, 'Links between Eastern and Western fold belts in the Mount Isa Inlier, based on SHRIMP U-Pb studies', *Geological Society of Australia abstracts*, vol. 49, p. 349.

Page, R. W., Sweet, I. P. 1998, 'Geochronology of basin phases in the western Mount Isa Inlier, and correlation with the McArthur Basin', *Australian Journal of Earth Science*, vol. 45, pp. 219–232.

Painter, M. G. M., Golding, S. D., Hannan, K. W. & Neudert, M. K. 1999, 'Sedimentologic, petrographic, and sulfur isotope constraints on fine-grained pyrite formation at Mount Isa Mine and environs, Northwest Queensland, Australia', *Economic Geology*, vol. 94, pp. 883-912.

Parsons, T., & Thompson, G. A., 1993, 'Does magmatism influence low-angle normal faulting?', *Geology*, v. 21, no. 3, pp. 247-250.

Pearson, P. J., Holcombe, R. J. & Page, R.W. 1992, 'Synkinematic emplacement of the Middle Proterozoic Wonga Batholith into a midcrustal extensional shear zone, Mount Isa Inlier, Queensland, Australia', *Australian Geological Survey Organisation Bulletin*, pp. 289-328, 243.

Perkins, C., Heinrich, C A. & Wyborn, L. A. I. 1999, '40 Ar/ 39 Ar geochronology of copper mineralization and regional alteration, Mount Isa, Australia', Economic Geology, vol. 94, no. 1; pp. 23-36.

Perkins, C. and Wyborn, L. A. I. 1998, 'Age of Cu-Au mineralisation, Cloncurry district, eastern Mt Isa Inlier, Queensland, as determined by 40Ar/39Ar dating ', *Australian Journal of Earth Sciences*, 45:2, 233 – 246.

Perkins, W. 1984, 'Mount Isa silica dolomite and copper orebodies; the result of a syntectonic hydrothermal alteration system', *Economic Geology*, vol. 79, pp. 601-637.

Perring, C. S., Pollard, P. J., Dong, G., Nunn, A. J. and Blake, K. L. 2000, 'The Lightning Creek sill complex, Cloncurry District, northwest Queensland: a source of fluids for Fe oxide Cu-Au mineralization and sodic-calcic alteration', *Economic Geology*, vol. 95, pp. 1067-1089.

Petit, J-P., & Mattauer, M. 1995, 'Palaeostress superimposition deduced from mesoscale structures in limestone: the Matelles exposure, Languedoc, France', *Journal of Structural Geology*, vol. 17, no. 2, pp. 245-256.

Pollard, D. D., & Aydin, A. 1988, 'Progress in understanding jointing over the past century', *Geological Society of Australia Bulletin*, v. 100; no. 8; pp. 1181-1204.

Pollard, D.D., Saltzer, S.D., Rubin, A.M. 1993, 'Stress inversion methods; are they based on faulty assumptions?', *Journal of Structural Geology*, vol. 15, pp. 1045–1054.

Pollard, P.J., McNaughton, N.J. 1997, 'U/Pb geochronology and Sm/Nd isotope characterization of Proterozoic intrusive rocks in the Cloncurry district, Mount Isa inlier, Australia', *AMIRA P438 Cloncurry Base Metals and Gold Final Report*, section 4, p.19.

Ranalli, G. 2000, 'Rheology of the crust and its role in tectonic reactivation', *Journal of Geodynamics*, vol 30, pp.3-15.

Ramsay, J.G. & Lisle, R.J. 2000, *The Techniques of Modern Structural Geology. Vol. 3: Applications of Continuum Mechanics in Structural Geology*. Academic Press, London.

Raymond, S. 1990, *Geology of the southern 1100 orebody (34200mN - 33440mN)*, [internal company report], Mt Isa: Mt Isa Mines.

Richardson, S. 2000, *E Lens Oriented Core Measurements*, Western Metals Corporation, p. 13.

Richardson, S. M. & Moy, A. D. 1998, 'Gunpowder Copper Deposits', *in* Berkman, D. A., and Mackenzie, D. H., eds., *Geology of Australian and Papua New Guinean Mineral deposits*, The Australian Institute of Mining and Metallurgy, Melbourne, p. 743-752.

Robertson, C. W. 1975, 'The stratigraphy and geochemistry of the southern portion of the 110 copper orebody at Mount Isa, north west Queensland, and its implication on the genesis of the copper mineralisation', [unpublished MSc thesis], Queensland, James Cook University.

Robertson, C.W. 1982, 'The role of pre-existing sulfides in copper-ore formation at Mount Isa, Queensland: Bureau of Mineral Resources', *Journal of Australian Geology and Geophysics*, vol. 7, pp. 119–124.

Rosenstreich, M., Stewart, J. I.. & Medina, C. C. 1988-1990. [internal reports], Homestake Gold of Australia.

Rubenach, M. J., Foster, D. R. W., Evins, P.M., Blake, K.L. & Fanning, C.M. 2007, 'Age constraints on the tectonothermal evolution of the Selwyn Zone, Eastern Fold Belt, Mount Isa Inlier', *Precambrian Research*, in press.

Rubenach, M. J and Foster, D. R. W. 2007,'Age constraints on the tectonothermal evolution of the Selwyn Zone, Eastern Fold Belt, Mount Isa Inlier', *Precambrian Research*, In press

Rubenach, M. J. 1992. 'Proterozoic low-pressure/high temperature metamorphism and an anticlockwise P–T–t path for the Hazeldene area, Mount Isa Inlier', *Journal of Metamorphic Geology*, vol. 10, pp. 333 – 346.

Rubenach, M. J. 2005, 'Tectonothermal evolution of the Eastern Fold Belt, Mt Isa Inlier', In: Blenkinsop, T.G. (Ed.), 'Total systems analysis of the Mount Isa Eastern Succession', *I 2+3 Final Report*, Predictive Minerals Discovery Cooperative Research Centre, pp.99–169.

Rubenach, M.J., Adshead, N.D., Oliver, N.H.S., Tullemans, F., Esser, D., and Stein, H. 2001, 'The Osborne Cu-Au deposit: Geochronology and genesis of mineralization in relation to host albitites and ironstones', *Economic Geology Research Unit Contribution*, Townsville, Australia, James Cook University, School of Earth Sciences, vol. 59, pp. 172–173.

Ryan, A. 1998, 'Ernest Henry copper-gold deposit', In: Berkman DA, Mackenzie DH (eds) *Geology of Australian and Papua New Guinean Mineral Deposits*,. Australasian Institute of Mining and Metallurgy, vol. 22, pp. 759–768.

Salminen, J. & Pesonen, L. J. 2007, ' Paleomagnetic and rock magnetic study of the Mesoproterozoic sill, Valaam island, Russian Karelia', Precambrian Research, vol. 159, pp.212–230.

Sayab, M. 2005, *N– S shortening during orogenesis in the Mt Isa Inlier: the preservation of W–E structures and their tectonic and metamorphic significance.* [unpublished PhD thesis], James Cook University, Townsville.

Sayab, M. 2007, Correlating multiple deformation events across the Mesoproterozoic NE Australia using foliation intersection axes (FIA) preserved within porphyroblasts, *Gondwana Research*, accepted.

Scholz, C. H. 1977, 'Transform fault systems of California and New Zealand: similarities in their tectonic and seismic styles', *Journal of the Geological Society of London*, vol. 133, pp. 215-230.

Scholz, C. H. 1988, 'The brittle-plastic transition and the depth of seismic faulting', *International Journal of Earth Sciences*, vol. 77, no. 1, pp. 319-328.

Scot, R. J. & Berry, R. F. 2004, 'A new method for obtaining and quantifying the reliability of structural data from axially-oriented drill core using a fabric of known orientation', *Journal of Structural Geology*, vol. 26, no.4, pp. 643-658.

Secis, J. 1992, *Faults in the northern 1100 orebody*, [internal company report], Mt Isa: Mt Isa Mines.

Secor, D. T. 1965, 'Role of fluid pressure in jointing', *American Journal of Science*, vol 263, pp 633-646.

Shepherd, S. R. L. 1946, 'Some mines on the Cloncurry Field', *Queensland Government Mining Journal*, vol. 47, p. 48-49.

Sibson, R. H. 1984, 'Roughness at the base of the seismogenic zone: contributing factors', *Journal of Geophysical Research*, vol. 89, pp. 5791-5799.

Sibson, R. H. 1986, 'Earthquakes and lineament infrastructure', *Philosophical Transactions of the Royal Society of London*, vol. A317, pp. 63-79.

Sibson, R. H. 1989, 'Earthquake faulting as a structural process', *Journal of Structural Geology*, vol. 11. pp. 1-14.

Sibson, R.H. 2001, 'Seismogenic framework for hydrothermal transport and ore deposition', In: J.P. Richards and R.M. Tosdal, Editors, 'Structural Controls on Ore Genesis', *Reviews in Economic Geology*, vol 14, pp. 25–47.

Sims, 1992, *Review of the Buck Quartz Fault's geometrical relationship to the 1100 orebody and surrounding rocks*, [internal company report], Mt Isa: Mt Isa Mines.

Spear, F. S. 1993, *Metamorphic phase equilibria and pressure-temperature-time paths*, Mineralogical Society of America, Monograph, Boulder, pp. 371–405 p. 799.

Spikings, R. A., Foster, D. A., Kohn, B. P. & Lister, G. S. 2001, 'Postorogenic (<1500 Ma) thermal history of the Proterozoic Eastern Fold Belt, Mount Isa Inlier, Australia', *Precambrian Research*, vol. 109, pp. 103 – 144.

Stark, M. 2003, *Strike slip faulting in the Mount Isa Inlier, Australia*, [unpublished honours thesis], James Cook University, Townsville.

Stegman, C. L. 1994, *CRAE combined report for the period 1/7/92 to 30/6/93*, vol. 1, CRA Exploration, Report Number 19546.

Stein, S. & Wysession, M. 2002, *An Introduction to Seismology, Earthquakes and Earth Structure*, Blackwell Science, Malden, MA.

Stephens, M. 2001, A review of the potential of the Mount Kelly area north of Mount Isa, Queensland. Reefway Pty Ltd.

Stewart A. J. & Blake D. H. eds. Detailed Studies of the Mount Isa Inlier, *Australian Geological Survey Organization Bulletin*, vol. 243, pp. 147-160.

Stewart, J. I. 1991, *Proterozoic Geology and Gold Geochemistry of the Marimo Basin area. Cloncurry, NW Queensland*, [unpublished MSc thesis], James Cook University, Townsville.

Stoker, I. 1976, *2000-3000N block structural investigations 1100 Orebody*, [internal company report], Mt Isa: Mt Isa Mines.

Swager, C. P. 1985, 'Syndeformational carbonate-replacement model for the copper mineralization at Mount Isa, Northwest Queensland; a microstructural study', *Economic Geology*, vol. 80; no. 1; pp. 107-125.

Tanaka, H., Idnurm, M. 1994, 'Paleomagnetism of Proterozoic mafic intrusions and host rocks of the mount Isa Inlier, Australia', *Precambrian Research*, vol. 69, pp. 241–258.

Tear, S. 2005, *Copper orebody distribution in the Mammoth Mine, Aditya Birla*, [unpublished internal company report], pp. 1-5.

Thurston, P. C. 2002, 'Tectonic controls on mafic magmatism in the Superior Province, Canada', *International Platinum Symposium*, 9th, pp. 445-448.

Tsai, Y. B., Teng, T. L., Chiu, J. M. & Liu, H. L. 1977,'Tectonic implications of the seismicity in the Taiwan region', *Mem. Geol. Soc. China*, vol. 2, pp. 13-41.

Turcotte, D. L., & Schubert, G. 2002, *Geodynamics*, Cambridge University Press, Cambridge, UK.

Twyerould, S.C. 1997*, The geology and genesis of the Ernest Henry Fe–Cu–Au deposit, northwest Queensland, Australia*, [unpublished PhD thesis], University of Oregon.

Valenta, R. K. 1989, 'Vein geometry in the Hilton area, Mount Isa, Queensland: implications for fluid behaviour during deformation', *Tectonophysics*, vol.158, no.1-4,pp. 191-207.

Valenta, R. 1994, 'Syntectonic discordant copper mineralization in the Hilton Mine, Mount Isa', *Economic Geology*, vol. 89, pp. 1031-1052.

Valenta, R. K, 2000, *Structural interpretation of the Ernest Henry Cu-Au Mine*, [unpublished company report], Mt Isa Mines.

van Dijk, P. M. 1986, *Copper Mineralization and regional structural geology of the western Mount Isa Block, Australia*, [unpublished PhD thesis], James Cook University, pp. 1-129.

Vermeer P.A. & de Borst, R. 1984, *Non-associated plasticity for Soils, Concrete and Rock*, Herron, London.

Waring, C. L. 1990, 'The distinction between metamorphosed stratiform Pb – Zn – Ag mineralization and metamorphic syntectonic Cu mineralization at Mt. Isa', *Mount Isa Inlier Geology Conference Abstracts*, Monash University and Victorian Institute of Earth and Planetary Sciences, Melbourne, pp. 69-72.

Waring, C. L., Heinrich, C. A., & Wall, V. J. 1998, 'Proterozoic metamorphic copper deposits', *Australian Geological Survey Organisation Journal of Australian Geology and Geophysics*, vol. 17, pp. 239–246.

Webb, M. & Rowston, P. 1995 'The geophysics of the Ernest Henry Cu–Au deposit (N.W.) Queensland', *Exploration Geophysics*, vol. 26, pp.51–59.

Wilde, A. R. & Gessner, K. 2005, 'Is the Mount Isa copper deposit the product of forced brine convection in the footwall of a major reverse fault?', *Geology*, [online publication], Published on the Geological Society of America Database, Available at www.gsajournals.org.

Williams, P.J.& Pollard, P.J. 2003 'Australian Proterozoic iron oxide–Cu–Au deposits: an overview with new metallogenic and exploration data from the Cloncurry district, northwest Queensland', *Exploration Mining Geology*, vol. 10, pp.191–213.

Williams, P. J. & Skirrow, R. G. 2000 'Overview of iron oxide-copper-gold deposits in the Curnamona province and Cloncurry district (Eastern Mount Isa Block), Australia', In: Porter TM (ed) *Hydrothermal*

Iron Oxide Copper-Gold and Related Deposits: A Global Perspective, Australian Minerals Foundation, pp 105–122.

Williams, P. J., Barton, M. D., Fontbote, L., de Haller, A., Johnson, D. A., Mark, G., Marschik, R., & Oliver, N. H. S. 2005, 'Iron oxide-copper-gold deposits: Geology, space-time distribution, and possible modes of origin', *Economic Geology*, 100th Anniversary volume, pp. 371–406.

Wilson, C. J. L. 1973, 'The prograde microfabric in a deformed quartzite sequence, Mount Isa, Australia', *Tectonophysics*, vol. 19, pp. 39-81.

Windsor, C. N. 1986, 'Intermittant folding and faulting in the Lake Moondarra area, Mt Isa, Queensland', *Australian Journal of Earth Sciences*, vol. 33, pp. 27-42.

Wiszniewska, J., Duchesne, J. C., Stein H. J. & Jedrysek, M. O. 2001, 'Petrologic and isotope evidence for crustal source of ore-bearing Suwałki anorthosites, Poland', [in:] Piestrzyński A. (Ed.), *Mineral deposits at the beginning of the 21st century, Proceedings of the Joint Sixth Biennial SGA-SEG Meeting*, Kraków, Poland, pp. 635-638.

Wiszniewska, J. & Krzeminska, E. 2005, 'Precambrian crystalline basement of northeastern Poland – new approach', *Mineralogical Society of Poland*, vol. 26.

Yamaji, A. 2000, 'The multiple inverse method: a new technique to separate stresses from heterogeneous fault–slip data', *Journal of Structural Geology*, vol. 22, no. 4, pp. 441–452.

Zhang, X. & Sanderson, D. J. 2002 *Numerical Modelling and Analysis of Fluid Flow and Deformation of Fractured Rock Masses*, Pergamon, London, UK.

Zhao, G., Sun, M., Wilde, S. A., Li, S. 2004, 'A Paleo-mesoproterozoic supercontinent: assembly, growth and breakup', *Earth Science. Reviews*, vol. 67, pp. 91-123.

APPENDIX A
NUMERICAL MODELLING FILES

The attached discs contain all of the input data and UDEC output files for the numerical modelling conducted. Due to the size of the files, the data is stored on 2 DVD discs.

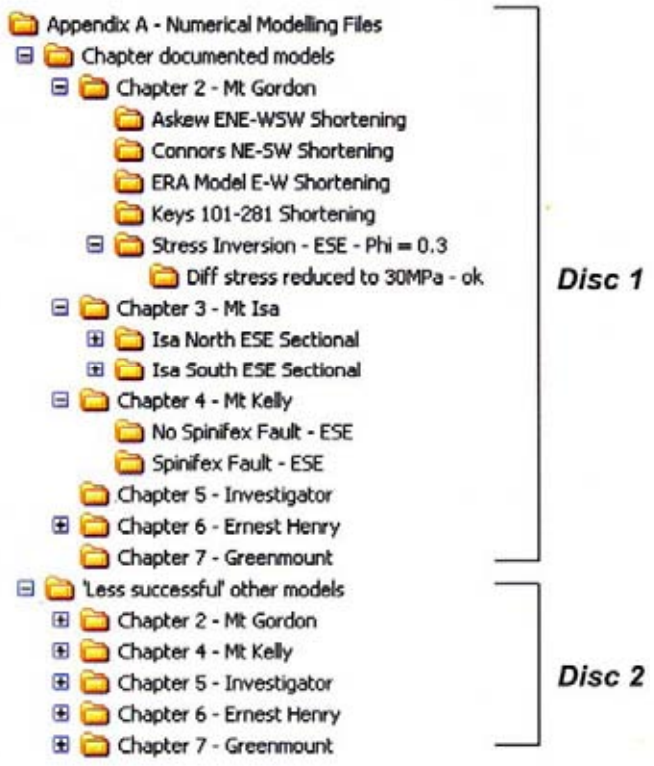

Directory list for the attached DVD's.

Each of the folders contains a range of files. Files with the extension ***.dat*** are the raw data input files for each specific numerical model.

Files with the extension ***.sav*** are the UDEC model output save files. These files record time steps through the modelling run (500 steps/sav file).

DISC 1

File directory for Disc 1. This disc contains the numerical modelling input data and output data save files for all modelling documented throughout the thesis. Specific model folders have been divided on the basis of the chapters to which they are relevant.

DISC 2

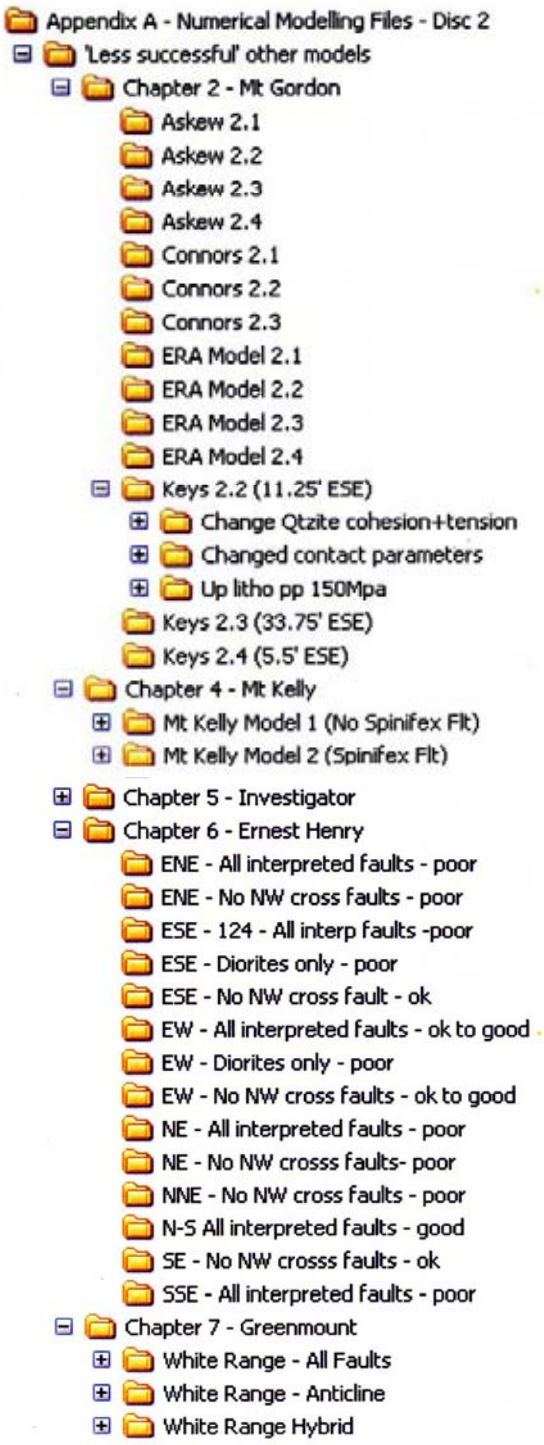

File directory for Disc 2. This disc contains the numerical modelling input data and output data save files for all modelling documented throughout the thesis. Specific model folders have been divided on the basis of the chapters to which they are relevant.